Neutrinos And Quantum Fields In The Universe

by

Mainak Mukhopadhyay

A Dissertation Presented in Partial Fulfillment
of the Requirements for the Degree
Doctor of Philosophy

Approved May 2022 by the
Graduate Supervisory Committee:

Cecilia Lunardini, Chair
Tanmay Vachaspati
Matthew Baumgart
F.X. Timmes

ARIZONA STATE UNIVERSITY

August 2022

ABSTRACT

The first part of this work focuses on the information that neutrinos from core-collapse supernovae (CCSNe) can provide with in the context of multi-messenger astronomy. A CCSN serves as nature's very own laboratory. Neutrinos from the various phases of a CCSN can be used to gain insights and understanding in a much broader context. The localization of a star using presupernova neutrinos is studied and it is shown that their topology can give the direction to the star with an error of $\sim 60^{\circ}$. A new phenomenological description of the neutrino gravitational wave memory effect is built, highlighting its detectability, and physics potential in the present context. It is shown that this effect will be detectable in the near future, for a galactic supernova, at deci-Hertz GW interferometers. A novel idea of how observations of the neutrino GW memory from CCSNe will enable time-triggered searches of supernova neutrinos at megaton (Mt) scale neutrino detectors is also presented. This combination of a deci-Hz GW and a Mt-neutrino detector will allow the latter to detect $\sim 3-30$ supernova neutrino events/Mt/per decade of operation.

The second part of this work focuses on studying quantum fields in time and space-dependent backgrounds. Generically, such quantum fields get excited (a phenomenon known as particle production) and the quantum excitations then backreact on the background. This scenario is important in all areas of physics, specifically in the context of gravitation and cosmology. This work discusses some simplified models pertaining to this. In particular, the dynamics of a classical field rolling down a linear potential while it is bi-quadratically coupled to a quantum field is studied. The formation of global topological defects in d-dimensions as a result of spontaneous symmetry breaking during a quantum phase transition is also studied. Furthermore, a sine-Gordon kink-antikink collision in the presence of interactions with a scalar field is considered and the regimes of breather and long lived oscillon formation are found.

DEDICATION

....to Ma and Baba. I owe everything to you. This is for the both of you....

ACKNOWLEDGMENTS

As I stand here nearing towards concluding this journey of getting a PhD in theoretical Physics, if there is one word that can describe how I feel, it is *gratitude*. I am filled with immense gratitude towards each and everyone, that even in the smallest ways was a part of this journey, right from my childhood to now. It is because of you that I could make it till here, so Thank you.

But there are some people whom I specifically want to mention, without whom this thesis or my journey till here would not have been possible. To begin with, my advisor, Prof. Cecilia Lunardini. I am extremely fortunate to have you as my advisor. You have been a constant support and guided me in the best possible way at every step of my PhD, making sure that I can avail and make the most of every opportunity that comes my way. When I joined ASU, after my 3-year undergraduate program, I was terrified. I did not know if I can make it through the program. The first person who believed in me and offered me an opportunity to work with him was Prof. Tanmay Vachaspati. That was the start, since then I have had countless occasions for which I am thankful to you. I want to thank the other members of my graduate committee besides Cecilia and Tanmay - Prof. Matthew Baumgart and Prof. F.X. Timmes. Your comments, feedback, advice and support has been crucial in my progress in the program and as an individual researcher. Thank you for being a part of my committee.

There are two people who have always had my back, during the last four years. The first is Dr. George Zahariade. I owe to you a lot of what I have learned in the last four years. The second is Dr. Andrew Svesko. Thank you for making time to hear me out no matter how busy you are, and for your constant support and advice in good and especially in bad times. Conversations with you on physics and non-physics topics are something I cherish.

I want to take this opportunity to thank all my collaborators - Dr. Carlos Cardona, Dr. Evangelos Sfakianakis, and Dr. Zidu Lin. It was a pleasure working with you and I had a wonderful time. An integral part of my PhD life has been the Cosmology Student office. Through my good and bad times, my office mates have been there for me. I want to thank all my past and current office mates: Ayush, Billy, Charlie, Jacob, Jesse, Logan, Nik, Nikhil, Omer, Panos, Teerthal, Tucker. With each one of you, I have spent times that I cherish and I will remember forever. I also wanted to thank Pallavi and Akram for their constant support. All of you hold a special place in my heart. Thank you for existing. You made/make work feel like home. I want to thank Araceli Vizcarra, who helped me resolve any bureaucratic issues that came up during my grad school and who was always available to help.

I am fortunate enough to have been introduced to neutrino physics by Prof. D.P. Roy. I want to thank Dr. Abhinav Gupta, Dr. Sanil Unnikrishnan and Dr. Monoranjan Guchait for believing in me. I also want to thank Mitrajyoti, who was instrumental in convincing me to apply to US grad schools after my undergrad. I am forever grateful to my high school Physics and Math teacher, Mr. Anshuman Bhattacharya, who was the first person to kindle my interest in Physics and constantly encourage me. Mrinal, Akanksha, Deepak, Saurabh, and Vaibhav - thanks for sticking right from the school days.

Lastly, I have the deepest appreciation and gratitude for my family: Thaam, Kogo, Kaka, Dudun, Dadu, Popa, Jethu, Moni, Moshai, Chhotopapun, Kamma, Mammam, Maima, Babu, Boroburo Mama, Tukai Mama, Dadabhai, Babai Dada, Bhai, Christy. Thank you for all your love and support. Each one of you have contributed a lot to make this journey possible. Thanks is too less a word for Ma (Mithu Mukhopahdyay) and Baba (Manas Mukhopadhyay). I owe everything to you. This thesis is for the both of you....

TABLE OF CONTENTS

Page

CHAPTER Page

CHAPTER Page

CHAPTER Page

CHAPTER Page

LIST OF TABLES

Table Page

LIST OF FIGURES

Figure Page

Figure Page

Figure Page

Figure Page

Figure Page

PREFACE

Neutrinos and quantum fields in the Universe, is no doubt, one of the broadest titles that one can ever imagine! As a reader, you might wonder, why is that? Well, the title is so because during my PhD, my research interests were broadly divided in two distinct categories - astroparticle physics and theoretical high energy physics. I had once tried and miserably failed to give my entire work in the two distinct fields one unifying title. So, I decided not to repeat that attempt and get rid of the grand unification scheme I had once thought of. The next best possible option was to give it a broad enough title so as to encompass the two parts of my work, hence the the present title. As a result of this grand non-(unification) scheme that I chose, the thesis is divided into two distinct parts. The first part (from chapters 1 to 6), is based on my work in astroparticle physics. The second part (from chapters 7 to 11), focuses on my work in theoretical high energy physics. If I were to provide individual titles to the two parts, they would be called *Multi-messengers from core-collapse supernovae: neutrinos and gravitational waves*, and *Quantum fields in time- and space-dependent backgrounds*, respectively!

In astroparticle physics my main focus is neutrino physics. I am interested in the phenomenology of astrophysical neutrinos, multi-messenger astronomy, and gravitational waves. In theoretical high energy physics, the majority of my focus has been to study dynamical quantum fields on time- and space-dependent classical backgrounds. I am interested in early universe cosmology, field theory, phase transitions, and topological defects.

The first part of this thesis is based on my work with neutrinos from core-collapse supernovae (CCSNe). In particular, what information do these neutrinos provide us with and how they help in the context of multi-messenger astronomy, which is a

promising avenue to probe extreme astrophysical phenomena and our understanding of the Universe. The topics discussed in the first part also contributes to the areas of combined neutrino and GW observations.

We begin the first part of this work with a very general introduction to neutrino physics in chapter 1. The contents of this chapter is heavily derived from published reviews and books on neutrino physics. Some additional information relevant to the chapter is provided in Appendices. A and B. A short introduction to multi-messenger astronomy follows in chapter 2, with particular emphasis on the physics of a CCSN and neutrino emission from its different phases. This chapter is also based on several reviews and books available in the literature. The main motivation behind the first two chapters is to provide a mini-review on things that would be important for the main work and an overview of the field in general. The subsequent chapters form the core of this thesis and is based on original work performed and published during my PhD.

In chapter 3, we explore the potential of presupernova neutrinos in providing directional sensitivity and hence an early alert of a CCSN, facilitating multi-messenger observations. This is based on the work done in Mukhopadhyay *et al.* (2020a). Some additional details relevant to this chapter is provided in Appendices. C and D. In chapter 4, the phenomenology of the neutrino gravitational wave memory (GWM) effect – a multi-messenger channel combining neutrino physics with GW physics, is explored in details. This is based on Mukhopadhyay *et al.* (2021a). Appendix. E provides additional details regarding certain calculations in this chapter. Moreover, we demonstrated that observations of the GWM effect from a CCSN at future Deci-Hz interferometers will enable us to perform time-triggered searches of supernova neutrinos at megaton-scale detectors in Mukhopadhyay *et al.* (2021b). This form the contents of chapter 5. In Appendix. F we provide additional details that were not

included in the chapter. We conclude this part of the thesis in chapter 6, where we summarize our main results, their implications and future possibilities.

The second part of this work deals with quantum fields in time- and space-dependent classical backgrounds and how the dynamics of these fields affect the classical background itself. Numerous systems ranging from condensed matter to cosmology are described by dynamical quantum fields on classical backgrounds. My research investigated such systems in the context of phase transitions, the formation of topological defects and inflationary scenarios.

We begin this part with a general introduction to systems involving particle production and back-reaction in chapter 7. This chapter is based on various existing published works and books. The subsequent chapters contain original work that I contributed to and published during my PhD.

Chapter 8 is based on the work done in Mukhopadhyay and Vachaspati (2019), where we studied the dynamics of a classical field rolling down a linear potential while bi-quadratically coupled to a quantum field. In chapter 9, we investigated the formation and dynamics of global topological defects formed due to a quantum phase transition. This chapter is based on Mukhopadhyay *et al.* (2020b,c). Finally, in chapter 10, we studied kink-antikink scattering in the sine-Gordon model in the presence of interactions with an additional scalar field in its quantum vacuum. This is based on the work that was done in Mukhopadhyay *et al.* (2022). Appendix. G shows some additional details (mostly plots) related to the chapter. This is followed by a conclusion to this part of the work in chapter 11, once again summarizing the main results and insights that they provide along with future directions.

I had some of the most wonderful and memorable times of my life during my PhD research over the last four years. Putting it all together in this thesis, made it seem like, it was yesterday that I started working on the various projects. It gave me a lot

of perspective, insights and I had an amazing time writing it. I hope the reader has a good time reading it as well!

Chapter 1

NEUTRINOS

Approximately a century has passed since the birth of *neutrino physics*. The poltergeist of the past turned out to be a key element in understanding how nature works and has become one of the prime focuses of a big community of physicists. Today it is well-known that *neutrinos* are all around us. They are elusive nevertheless have been detected and form a cornerstone of our understanding of the universe. Neutrinos in the celebrated Standard Model need to be massless. However, it has now been established that neutrinos oscillate and have mass! This is a major breakthrough for the entire physics community since it serves as one of the most important evidences of physics beyond the Standard Model. Time and again neutrinos have provided physicists with complex puzzles, a big portion of which have been solved, but a major chunk still remains to be addressed. In particular, we are yet to decipher the nature of neutrinos - are they Dirac or Majorana particles? What are their absolute masses? Is there a leptonic CP violation? Is there a fourth (sterile) neutrino?... Although these questions originate in neutrino physics, their answers have profound implications in understanding key aspects of nature. This chapter is mostly an introduction to neutrino physics with particular emphasis on some of the things that will be important for later parts of this work.

We begin with a short historical introduction to neutrino physics and how it evolved since the beginning in Sec. 1.1. This is followed by a discussion of neutrinos in the Standard Model in Sec. 1.2. We focus on broadly discussing the standard model in Sec. 1.2.1 and the electroweak Lagrangian in Sec. 1.2.2. The neutrino interactions are discussed in Sec. 1.3. In particular, we focus on discussing the inverse $\beta-$decay in

Sec. 1.3.1, neutrino-electron elastic scattering in Sec. 1.3.2, and the coherent elastic neutrino-nucleus scattering in Sec. 1.3.3. Neutrino oscillations is the focus of Sec. 1.4. The vacuum oscillation case is discussed in Sec. 1.4.1 (the details for the two neutrino case is given in App. A) and the effects due to matter oscillations is briefly mentioned in Sec. 1.4.2. Neutrino masses in particular the normal and inverted ordering of neutrino masses is discussed in Sec. 1.5. The information that supernova neutrinos can provide about neutrino masses is mentioned in Sec. 1.5.1. We conclude this chapter with a discussion of various neutrino detectors in Sec. 1.7. The detectors that are particularly important for this work - scintillator detectors and water Cherenkov detectors are the focus of Sec. 1.7.1 and Sec. 1.7.2 respectively. Other kinds of detectors relevant to supernova neutrinos are mentioned in Sec. 1.7.3.

1.1 A Historical Introduction

The story of neutrino physics begins approximately 100 years ago. This section provides a very brief history of neutrino physics from its origins to the key moments of its development.

In 1920s, physicists were puzzled by the continuous energy spectrum observed in $\beta-$decay (See Fig. 1.1, blue curve) in contrast to $\alpha-$ or $\gamma-$ decays. In the $\beta-$decay process, a nucleus transforms itself into another one with the emission of an electron,

$$ {}^{A}_{Z}X \rightarrow {}^{A}_{Z+1}X' + e^{-}(+\dots)\,. $$

The parent nuclei, daughter nuclei and the electron could be seen. Thus, the expectation based on energy-momentum conservation was the electron would carry away an energy corresponding to the difference in mass between the parent and daughter nuclei (see Fig. 1.1, red curve) implying a monochromatic line in the $\beta-$decay spectrum. Possible solutions to this puzzle was the existence of a new particle or, as Niels

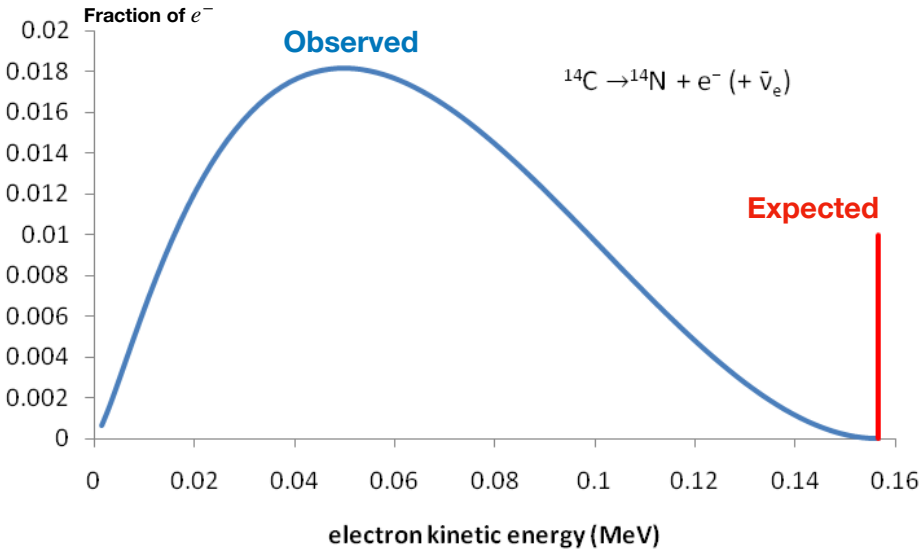

Figure 1.1: Energy spectrum of a $\beta-$ decay. The red spike shows the expected energy spectrum of the electron. The blue curve shows the observed energy spectrum.

Bohr had suggested, energy conservation was valid in a statistical sense only. In 1930, Wolfgang Pauli with utmost trust in the energy conservation principle, proposed the existence of a new particle, thus choosing the former possibility. This new particle according to Pauli would be a neutral, weakly interacting fermion, with mass of the order of an electron. He chose to call this particle a 'neutron' (Pauli, 2000). However, in 1932 James Chadwick, discovered a new and heavy neutral particle which he named *neutron* (Chadwick, 1932). The re-naming of Pauli's particle was done by Enrico Fermi (suggested by Edoardo Amaldi) in 1932, who chose it to be as we know it today, *neutrino*, a little neutron. In 1933, it was shown by Fermi (Fermi, 1933) and Perrin (Perrin, 1933) that neutrinos could be massless. In 1934, Fermi put everything together to construct a theory for $\beta-$decay (Fermi, 1934a,b) that would explain the observations. This was done in terms of a 4-fermion interaction with a coupling strength G_F. Another prediction of this model was the neutrinos scattering off matter - inverse β decay (IBD) ($\bar{\nu} + p \rightarrow n + e^+$), which was a way to detect these still hypothetical particles. The next obvious thing was done by Hans Bethe and

Rudolf Peierls who calculated the strength of the coupling and the cross-section of the process, which unfortunately was extremely miniscule $\sim 10^{-44}\ cm^2$ for a neutrino energy of ~ 2 MeV. This was a major setback for physicists and in favor of Pauli's original fear, *"I have committed the cardinal sin of a theorist. I made a prediction which can never be tested, ever, because this particle is so weakly interacting that it may never be seen."*

Bruno Pontecorvo came to the rescue when he suggested that the large neutrino fluxes from nuclear energy sources can be used to detect neutrinos. In 1950s, Frederick Raines and Clyde Cowan considered various nuclear sources (including an atomic bomb!), and settled on placing a detector to detect neutrinos coming from a nuclear reactor. In 1956, at the Savannah River Plant in South Carolina they managed to finally detect neutrinos! They sent a telegram to Pauli (Reines *et al.*, 1960; Reines, 1996).

Parity was considered to be a respected symmetry in nature. But in the 1950s, ideas of parity violation started emerging, starting with the novel work of T.D. Lee and C.N. Yang (Lee and Yang, 1956). Experimentally, in 1956, Chien-Shiung Wu and collaborators showed that parity violation occurs in case of $\beta-$decay (Wu *et al.*, 1957). In 1958, Goldhaber, Grodzins and Sunyar (Goldhaber *et al.*, 1958) showed that neutrinos are always left-handed, that is, they are polarized in a direction which is opposite to their direction of motion. The fact that neutrinos can be described by a left-handed Weyl spinor was proposed by Lev Landau (Landau, 1957), Lee and Yang (Lee and Yang, 1957), and Abdus Salam (Salam, 1957). This fact was embedded in the V-A theory of weak interactions (Feynman and Gell-Mann, 1958; Sudarshan and Marshak, 1958; Sakurai, 1958). Finally this was also incorporated in the standard model (SM) of particle physics by Sheldon Lee Glashow, Steven Weinberg and Salam (Glashow, 1961; Weinberg, 1967; Salam, 1968).

In 1937, Ettore Majorana suggested that neutrinos and antineutrinos (anti-particle to neutrinos) could be indistinguishable (Majorana, 1937). This basically boils down to understanding whether lepton number is a conserved quantity or not. The concept of lepton number, L was introduced in 1953 by E.J. Konopinski and H.M. Mahmoud (Konopinski and Mahmoud, 1953) to explain some missing decay modes. The idea being leptons like $e^-, \mu^-, \tau^-, \nu_e, \nu_\mu, \nu_\tau$ are assigned $L = 1$, whereas their antiparticles are assigned, $L = -1$. The experiment for finding neutrinos by Reines-Cowan (discussed earlier) was seen to conserve lepton number. But, Ray Davis' experiment to observe $\bar{\nu}_e + {}^{37}Cl \rightarrow {}^{37}Ar + e^-$ violated lepton number[1]. We still haven't solved this puzzle of whether neutrinos are their own anti-particles in which case they will be called Majorana fermions or they have a different anti-particle in which case they are Dirac fermions. Ongoing efforts of observing neutrinoless double beta decay would solve this puzzle on the nature of neutrinos.

In 1937, the muon was discovered by J.C. Street and E.C. Stevenson (Street and Stevenson, 1937) and by S.H. Neddermeyer and C.D. Anderson (Neddermeyer and Anderson, 1937). The muon was heavier than the electron and had Fermi interactions accompanied by a neutrino. So, the main question then was: *is it the same neutrino that is present in $\beta-$decays?*. Once again, Pontecorvo had an idea: he suggested that if the process, $\pi^+ \rightarrow \mu^+ + \nu_\mu$ cannot induce e^-, it would mean ν_e and ν_μ are indeed different particles Pontecorvo (1959). In 1962, Leon M. Lederman, M. Schwartz, J. Steinberger et. al. (Danby *et al.*, 1962) took up the idea and created the first accelerator neutrino beam, from pion decays from a boosted proton beam hitting a target. These neutrinos *did not* induce an electron, thus showing ν_e and ν_μ are indeed two different particles. This was proof that there are at least two different neutrino fami-

[1]Fun fact: This is what led Ray Davis to the making of Homestake solar neutrino experiment with $\bar{\nu}_e$ being replaced by ν_e from the Sun!

lies or flavors. The third family, ν_τ related to the τ lepton was discovered in 2000 by the DONUT experiment (Kodama *et al.*, 2001).

Now that it was established that there are at least more than one family of neutrinos, the question that needed answering was - *can there be mixing and transitions between the different families?* The concept of *neutrino oscillations* was first proposed by Pontecorvo in 1957 (Pontecorvo, 1957b,a). This was motivated by the $K^0 \leftrightarrow \bar{K}^0$ oscillation phenomenon. In 1962, Z. Maki, M. Nagakawa and S. Sakata considered ν_e and ν_μ are mixed states of two mass eigenstates, thus introducing the concept of mixing between mass and flavor states (Maki *et al.*, 1962). Finally, Pontecorvo gave the first intuitive link between neutrino mixing and oscillations (Pontecorvo, 1967) and further solidified it with V.N. Gribov (Gribov and Pontecorvo, 1969). Neutrino oscillations are extremely important since they imply that *neutrinos have mass*. Neutrinos are massless in the SM, hence neutrinos with mass is the first hint of new physics beyond the SM. This makes the SM an effective field theory of an even bigger theory beyond the SM.

The elaborate phenomena of neutrino oscillations have been and continue to be explored experimentally. The very first indications of flavor transitions in neutrinos was observed in the Homestake experiment (Cleveland *et al.*, 1998) by R. Davies, which we mentioned in passing before. This was due to the fact that Davis' experiment observed a lower flux of solar neutrinos (neutrino produced in the sun) than expected from models by John Bahcall and collaborators (Bahcall *et al.*, 1963) and others (Davis *et al.*, 1968; Turck-Chieze *et al.*, 1988; Bahcall and Pinsonneault, 1992; Turck-Chieze and Lopes, 1993; Turck-Chieze *et al.*, 1993; Bahcall and Pinsonneault, 1995; Bahcall *et al.*, 1998, 2001; Turck-Chieze *et al.*, 2001; Couvidat *et al.*, 2003; Pena-Garay and Serenelli, 2008; Serenelli *et al.*, 2009; Asplund *et al.*, 2009; Serenelli *et al.*, 2011; Vinyoles *et al.*, 2017) (see Haxton *et al.* (2013) for a review). Other experiments

like GALLLEX/GNO (Hampel *et al.*, 1999) and Sage (Abdurashitov *et al.*, 2002) confirmed the same. Kamiokande (Fukuda *et al.*, 1996) and Super-Kamiokande (Fukuda *et al.*, 1999) measured the solar neutrino flux with high precision and confirmed the same. Finally, SNO (Ahmad *et al.*, 2002) resolved the solar neutrino deficit problem in 2002. The resolution was the confirmation of neutrino oscillations in the sun due to the Mikheev-Smirnov-Wolfenstein (MSW) resonance conversion effects (Wolfenstein, 1978; Mikheyev and Smirnov, 1985; Mikheev and Smirnov, 1986), that is, ν_e is roughly 1/3rd of the total solar neutrino flux since ν_e produced in the sun oscillate to ν_μ or ν_τ while propagating, which accounts for the reduced ν_e flux that was being observed. In 2002, KamLAND (Gando *et al.*, 2013) also confirmed the oscillation parameters for solar neutrinos. Neutrino oscillations were also seen for atmospheric neutrinos (neutrinos produced in the atmosphere as a result of cosmic rays). In 1998, Super-Kamiokande discovered neutrino oscillations for atmospheric neutrinos (Fukuda *et al.*, 1998).

1.2 Neutrinos In The Standard Model

1.2.1 The Standard Model (SM)

The Standard model (SM) of particle physics Glashow (1961); Weinberg (1967); Salam (1968) is based on the gauge group $SU(3)_C \times SU(2)_L \times U(1)_Y$, where, C denotes color, L denotes left-handed chirality, and Y denotes hypercharge. It contains all elementary particles constituting ordinary matter and describes the strong, the weak and the electromagnetic interactions of elementary particles. The particle content of the SM is shown in Fig. 1.2. There are eight massless gluons, corresponding to the eight generators of $SU(3)_C$, that mediate strong interactions, four gauge bosons amongst which 3 are massive ($W^\pm$ and Z) and 1 is massless: the photon (γ), cor-

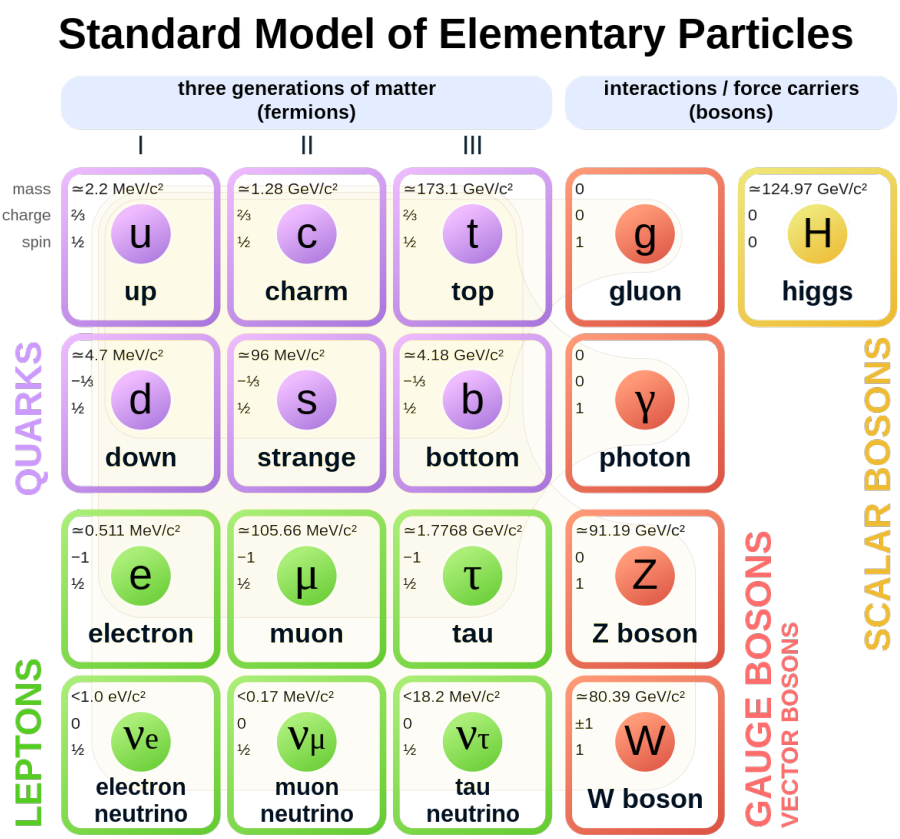

Figure 1.2: The Standard Model Of Particle Physics.

responding to the 3 generators of the $SU(2)_L$ and $U(1)_Y$ gauge groups, which are responsible for electroweak interactions. The fermions come in 3 generations with identical properties but different masses. They are divided into quarks - which participate in all the interactions (strong, electromagnetic, weak and gravitational) and leptons - which participate in all except the strong interactions. Their masses, electric charges and spins are shown in Fig. 1.2. The fermions are all spin 1/2 particles. The antiparticles corresponding to them have the same mass but opposite electric charge and opposite lepton or baryon number depending on whether they are leptons or quarks. The fermion sector of the SM depends on 13 parameters - six quark masses,

three charged lepton masses, three quark mixing angles and one phase[2]. Since we are interested in neutrinos, we will be focusing on the SM interactions of the neutrino in this section.

Neutrinos are singlets of $SU(3)$ but belong to $SU(2)_L$ doublets (weak isospin doublets) along with the charged leptons. They have hypercharge $-1/2$ and are *electrically neutral*. In the SM, neutrinos are left-handed Weyl fermions. Since the neutrinos are massless in the SM their chirality and helicity are the same. The antineutrinos are right-handed to respect the CPT (charge, parity, time reversal) symmetry of the SM.

1.2.2 Electroweak Lagrangian

We consider only $SU(3)_L \times U(1)_Y$ SM symmetry group, to describe the electroweak part of the SM Lagrangian which is relevant for neutrino interactions. The three generation version of the electroweak SM lagrangian is given as:

$$
\begin{aligned}
\mathcal{L} = & \, i \sum_{\alpha=e,\mu,\tau} \overline{L'_{\alpha L}} \not{D} L'_{\alpha L} + i \sum_{\alpha=e,\mu,\tau} \overline{Q'_{\alpha L}} \not{D} Q'_{\alpha L} \\
& + i \sum_{\alpha=e,\mu,\tau} \overline{l'_{\alpha R}} \not{D} l'_{\alpha R} + i \sum_{\alpha=e,\mu,\tau} \overline{q'^{D}_{\alpha R}} \not{D} q'^{D}_{\alpha R} + i \sum_{\alpha=e,\mu,\tau} \overline{q'^{U}_{\alpha R}} \not{D} q'^{U}_{\alpha R} \\
& - \frac{1}{4} \underline{A}_{\mu\nu} \underline{A}^{\mu\nu} - \frac{1}{4} B_{\mu\nu} B^{\mu\nu} \\
& + (D_\rho \Phi)^\dagger (D_\rho \Phi) - \mu^2 \Phi^\dagger \Phi - \lambda (\Phi^\dagger \Phi)^2 \\
& - \sum_{\alpha,\beta=e,\mu,\tau} \left(Y'^{l}_{\alpha\beta} \overline{L'_{\alpha L}} \Phi l'_{\beta R} + Y'^{l*}_{\alpha\beta} \overline{l'_{\beta R}} \Phi^\dagger L'_{\alpha L} \right) \\
& - \sum_{\alpha=1,2,3 \;\; \beta=d,s,b} \left(Y'^{D}_{\alpha\beta} \overline{Q'_{\alpha L}} \Phi q'^{D}_{\beta R} + Y'^{D*}_{\alpha\beta} \overline{q'^{D}_{\beta R}} \Phi^\dagger Q'_{\alpha L} \right) \\
& - \sum_{\alpha=1,2,3 \;\; \beta=u,c,t} \left(Y'^{U}_{\alpha\beta} \overline{Q'_{\alpha L}} \tilde{\Phi} q'^{U}_{\beta R} + Y'^{U*}_{\alpha\beta} \overline{q'^{U}_{\beta R}} \tilde{\Phi}^\dagger Q'_{\alpha L} \right).
\end{aligned}
\tag{1.1}
$$

[2]Neutrinos need to be massless in the SM.

We will once again focus on the leptonic part. The Lagrangian for neutrino interactions governed by the leptonic charged-current weak interaction after some simplifications can be obtained from the first line of Eq. 1.1,

$$\mathcal{L}_{I,L}^{(CC)} = -\frac{g}{2\sqrt{2}}\left(j_{W,L}^{\rho} W_{\rho} + j_{W,L}^{\rho}{}^{\dagger} W_{\rho}^{\dagger}\right), \tag{1.2}$$

where, the leptonic charge current $j_{W,L}^{\rho}$ is defined as,

$$j_{W,L}^{\rho} = 2 \sum_{\alpha=e,\mu,\tau} \overline{\nu_{\alpha L}} \gamma^{\rho} l_{\alpha L} = \sum_{\alpha=e,\mu,\tau} \overline{\nu_{\alpha}} \gamma^{\rho} (1-\gamma^5) l_{\alpha}\,. \tag{1.3}$$

The part of the lagrangian associated with neutrinos for the leptonic neutral-current interactions is given as,

$$\mathcal{L}_{I,\nu}^{(NC)} = -\frac{g}{2\cos\vartheta_W} j_{Z,\nu}^{\rho} Z_{\rho}\,, \tag{1.4}$$

where, g is the coupling, the leptonic neutral current $j_{W,L}^{\rho}$, is defined as,

$$j_{W,L}^{\rho} = \sum_{\alpha=e,\mu,\tau} \overline{\nu_{\alpha L}} \gamma^{\rho} \nu_{\alpha L} = \frac{1}{2} \sum_{\alpha=e,\mu,\tau} \overline{\nu_{\alpha}} \gamma^{\rho} (1-\gamma^5) \nu_{\alpha}\,, \tag{1.5}$$

where, ϑ_W is the weak mixing angle or Weinberg angle (Weinberg, 1967). We will skip more details, which can be found in various textbooks in particular Giunti and Kim (2007). Equipped with this, we will focus on the neutral and charged current interactions of neutrinos in the next section.

1.3 Neutrino Interactions

In this section we discuss the neutrino interactions with electrons and nuclei. Since our primary focus is studying neutrinos from a core-collapse supernova, the relevant neutrino interactions are with neutrino energy $\mathcal{O}(10)$ MeV. The discussion in this section is a mini-review. More detailed information can be found in Burrows *et al.* (2006), textbooks (Giunti and Kim, 2007) and reviews (Freedman *et al.*, 1977; Scholberg, 2012; Sajjad Athar *et al.*, 2022) (and references therein).

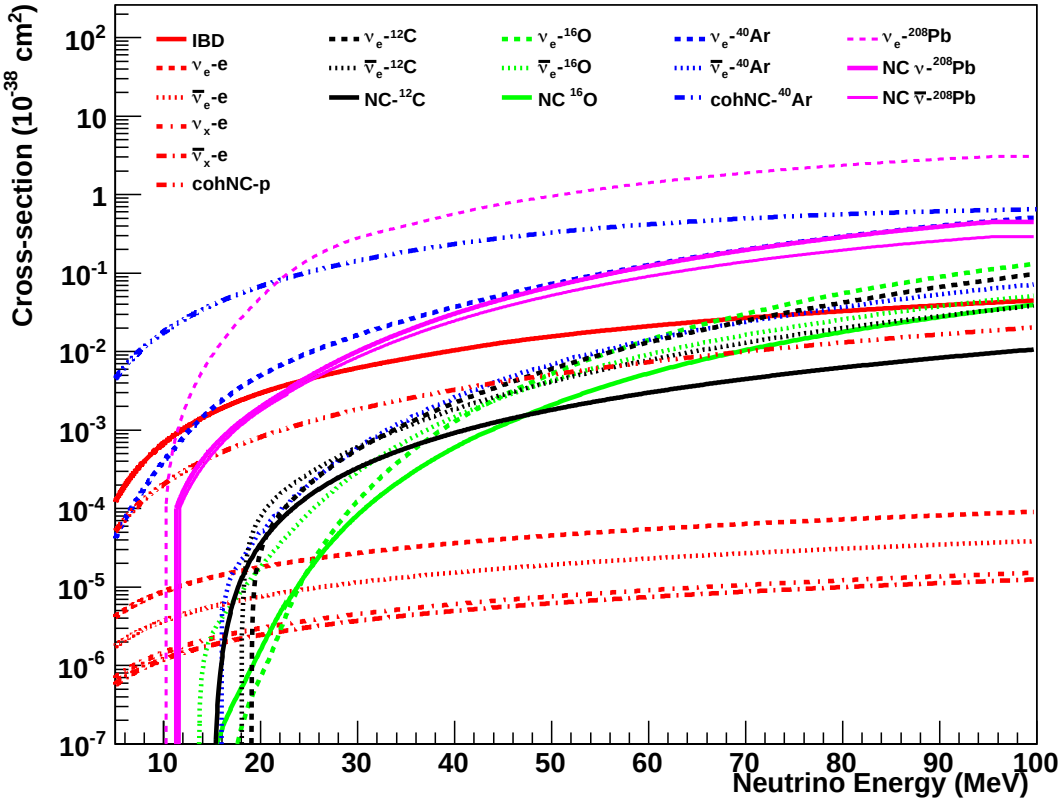

Figure 1.3: Cross-sections per target for relevant neutrino interactions. Abbreviations are: IBD: inverse $\beta-$decay, NC: Neutral current. Figure taken from Scholberg (2012).

Fig. 1.3 shows the cross-sections per target for the relevant interactions. Broadly neutrino interactions are classified as follows:

- **Neutrino-electron interactions**

  – Neutrino-electron elastic scattering:

$$\overset{(-)}{\nu}_\alpha + e^- \rightarrow \overset{(-)}{\nu}_\alpha + e^-, \text{ where, } \alpha = e, \mu, \tau\,. \tag{1.6}$$

– Neutrino-electron quasielastic scattering:

$$\nu_\mu + e^- \rightarrow \nu_e + \mu^- \,. \tag{1.7}$$

– Neutrino-antineutrino pair production:

$$e^+ + e^- \rightarrow \nu + \bar{\nu} \,. \tag{1.8}$$

- **Hadron decays**

– Charged pion decay: This is the most common way to produce muon neutrinos or antineutrinos.

$$\pi^\pm \;\rightarrow\; l^\pm + \overset{(-)}{\nu}, \text{ where, } l = e, \mu \,. \tag{1.9}$$

Similarly, Kaon and D-meson decays produce neutrinos.

– Neutron decay or, famously $\beta-$decay:

$$n \rightarrow p + e^- + \bar{\nu}_e \,. \tag{1.10}$$

- **Neutrino-nucleon and neutrino-nucleus scattering**

– Quasielastic charged-current reactions:

$$\nu_l + n \rightarrow p + l^- \,, \tag{1.11}$$

$$\bar{\nu}_l + p \rightarrow n + l^+ \,, \tag{1.12}$$

this reaction when $l = e$, becomes *inverse-beta decay (IBD)*, $\bar{\nu}_e + p \rightarrow n + e^+$.

– Elastic neutral-current reactions or Coherent elastic neutrino-nucleus scattering (CEνNS):

$$\overset{(-)}{\nu}_l + N \;\rightarrow \overset{(-)}{\nu}_l \; + N, \text{ where, } N = p, n \,. \tag{1.13}$$

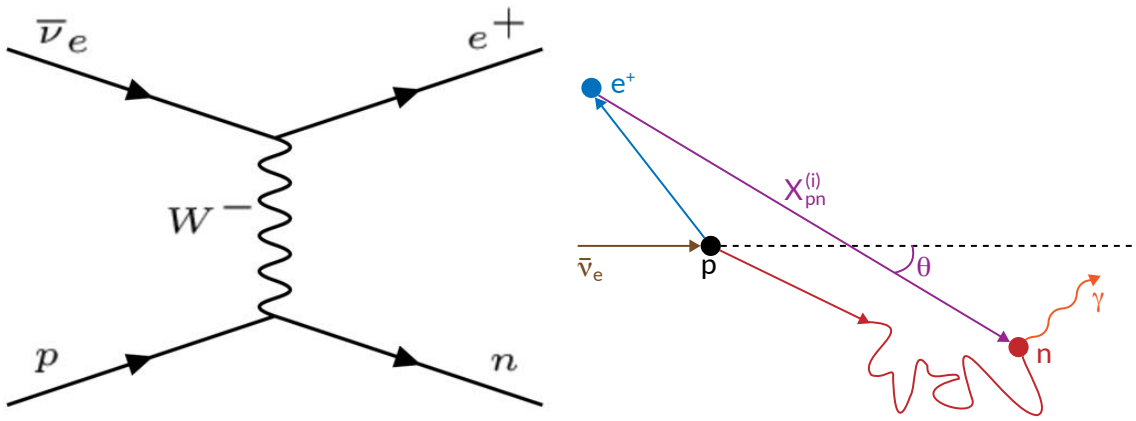

Figure 1.4: *Left:* The Feynman diagram for inverse $\beta-$decay. *Right:* A schematic diagram showing a IBD process.

– Charged-current deep inelastic scattering:

$$\begin{aligned} \nu_l + N &\rightarrow l^- + X\,, \\ \bar{\nu}_l + N &\rightarrow l^+ + X\,, \end{aligned} \tag{1.14}$$

where, $N = p, n$ and X denotes any set of final hadrons.

– Neutral-current deep inelastic scattering:

$$\overset{(-)}{\nu}_l + N \rightarrow \overset{(-)}{\nu}_l + X\,, \tag{1.15}$$

where, $N = p, n$ and X denotes any set of final hadrons.

Details about each of the above processes can be found in Giunti and Kim (2007). We will discuss a few interactions that will be important for the subsequent chapters.

1.3.1 Inverse Beta Decay (IBD)

The inverse beta decay as described in Eq. 1.12, is given by,

$$\bar{\nu}_e + p \rightarrow n + e^+ \tag{1.16}$$

An antineutrino interacts with a proton mediated by a W boson, to produce a positron and neutron. This process is of utmost importance in detecting neutrinos, especially

sub-GeV neutrinos (Vogel and Beacom, 1999; Strumia and Vissani, 2003), like the supernova neutrinos which will be our main interest in the following chapters. There are multiple reasons why IBD is commonly used for neutrino detection:

- It has a relatively large cross-section, approximately $\sim G_F^2 E_\nu^2$, where, G_F is the Ferrmi coupling and E_ν is the neutrino energy.

- The cross-section unlike most of other neutrino interactions can be accurately computed.

- The threshold of IBD is low $E_{\nu_{Th}} = 1.8$ MeV, making it suitable for supernova and very low energy presupernova neutrinos (this will be discussed in chapter 3).

- In the energy regimes for supernova neutrinos, the measurable positron energy is strongly correlated with the incoming antineutrino energy, $E_{e^+} = E_\nu - 1.3$ MeV.

- Neutrino detectors need to be huge to detect neutrino interactions. Thus, to make them cost effective a strategy is to use large amounts of cheap material like water or hydrocarbon based liquid scintillators. These have lots of free protons making IBD the most significant reaction, for supernova neutrinos.

- In scintillator detectors, both the positron and neutron can be tagged, thus reducing backgrounds. The positron annihilation with electrons ($e^+ + e^- \rightarrow \gamma\gamma$), produces 0.511 MeV gamma rays that can be observed, thus tagging the positron. The neutron may be captured on the free protons with an approximately 200 μs thermalization and capture time, producing a deuteron and 2.2 MeV γ ray which can be detected. The neutron can also be captured on another nucleus which gets excited. The nucleus then de-excites by emitting a cascade

of γ rays which is visible in the detector due to Compton scattering. Thus, the neutron is also tagged in the detector.

- The above point also opens up avenues to *dope* the detector with some material that has a high neutron capture cross-section, like Gadolinium (Gd)or Lithium (Tanaka and Watanabe, 2014). For example, Gd has a neutron capture cross-section 1.6×10^5 times that of free protons and reduces the thermalization and capture time scales by an order of magnitude. In chapter 3 we will consider one such doped detector for our analysis.

Cross-section

The details about the IBD cross-section can be found in Vogel and Beacom (1999); Strumia and Vissani (2003). Assigning momentum to the particles involved in IBD, we have from Eq. 1.12,

$$\bar{\nu}_e(p_\nu) + p(p_p) \to n(p_n) + e^+(p_e)\,.$$

The differential cross-section at tree level, summed over all final state polarizations is given by,

$$\frac{d\sigma}{dt} = \frac{G_F^2 \cos^2\theta_C}{2\pi(s - m_p^2)^2}|\mathcal{M}^2|\,, \tag{1.17}$$

where, the Fermi coupling is given by $G_F = 1.16637 \times 10^{-5}/\text{GeV}^2$ and the cosine of the Cabibo angle is, $\cos\theta_C = 0.9746 \pm 0.0008$. $\mathcal{M}$ has a well-known current-current structure details of which can be found in Strumia and Vissani (2003). The cross-section in terms of the neutrino and electron energy in the rest frame of the proton is given by,

$$\frac{d\sigma}{dE_e}(E_\nu, E_e) = 2m_p\frac{d\sigma}{dt}\,,\ \text{if, } E_\nu \geq E_{Th} \equiv \frac{(m_n + m_e)^2 - m_p^2}{2m_p}\,. \tag{1.18}$$

The IBD process has a very slight energy-dependent anisotropy, so it has a low directional sensitivity. In chapter 3 we will discuss in great detail the extent to which this can be used for pointing to supernovae. The zeroth-order cross-section, differential in the angle θ which is the angle between the incoming antineutrino direction and the positron is given as (Vogel and Beacom, 1999),

$$\frac{d\sigma}{d\cos\theta} = \frac{\sigma_0}{2}\left[(f^2+3g^2)+(f^2-g^2)\nu_e\cos\theta\right]E_e p_e\,, \tag{1.19}$$

where, $f=1$ and $g=1.26$ are the vector and axial-vector couplings respectively. σ_0 is the normalizing constant defined as,

$$\sigma_0 = \frac{G_F^2\cos^2\theta_C}{\pi}\left(1+\Delta^R_{inner}\right), \tag{1.20}$$

where, the energy dependent inner radiative correction, $\Delta^R_{inner}\approx 0.024$ (Wilkinson, 1994). The final standard cross-section at zeroth-order is given by,

$$\sigma_{tot} = \sigma_0(f^2+3g^2)E_e p_e = 9.52\times10^{-44}\left(\frac{E_e p_e}{1\text{MeV}^2}\right)\text{cm}^2\,. \tag{1.21}$$

This cross-section is valid at low energies, but is not very suitable for supernova neutrino analyses. The cross-section that we mostly use for supernova neutrinos is taken from Strumia and Vissani (2003) (See Eq. 25 there) and is given by,

$$\begin{aligned}
\sigma(E_\nu) &= 10^{-43}\text{cm}^2\left(p_e(E_\nu)E_e(E_\nu)E_\nu^{\left(-0.07056+0.02018(\log\ E_\nu)-0.001953(\log\ E_\nu)^3\right)}\right),\\
p_e(E_\nu) &= \sqrt{E_e^2-m_e^2}\\
E_e(E_\nu) &= E_\nu-\Delta\,,\\
\Delta &= m_n-m_p = 1.293\ \text{MeV}\,,
\end{aligned} \tag{1.22}$$

where, $p_e(E_\nu)$ is the positron energy in MeV, $E_e(E_\nu)$ is the electron energy in the rest frame of the proton, $m_n=939.565$ MeV, is the rest mass of the neutron, $m_p=938.272$ MeV is the rest mass of the proton and $m_e=0.511$ MeV is the rest mass of the electron.

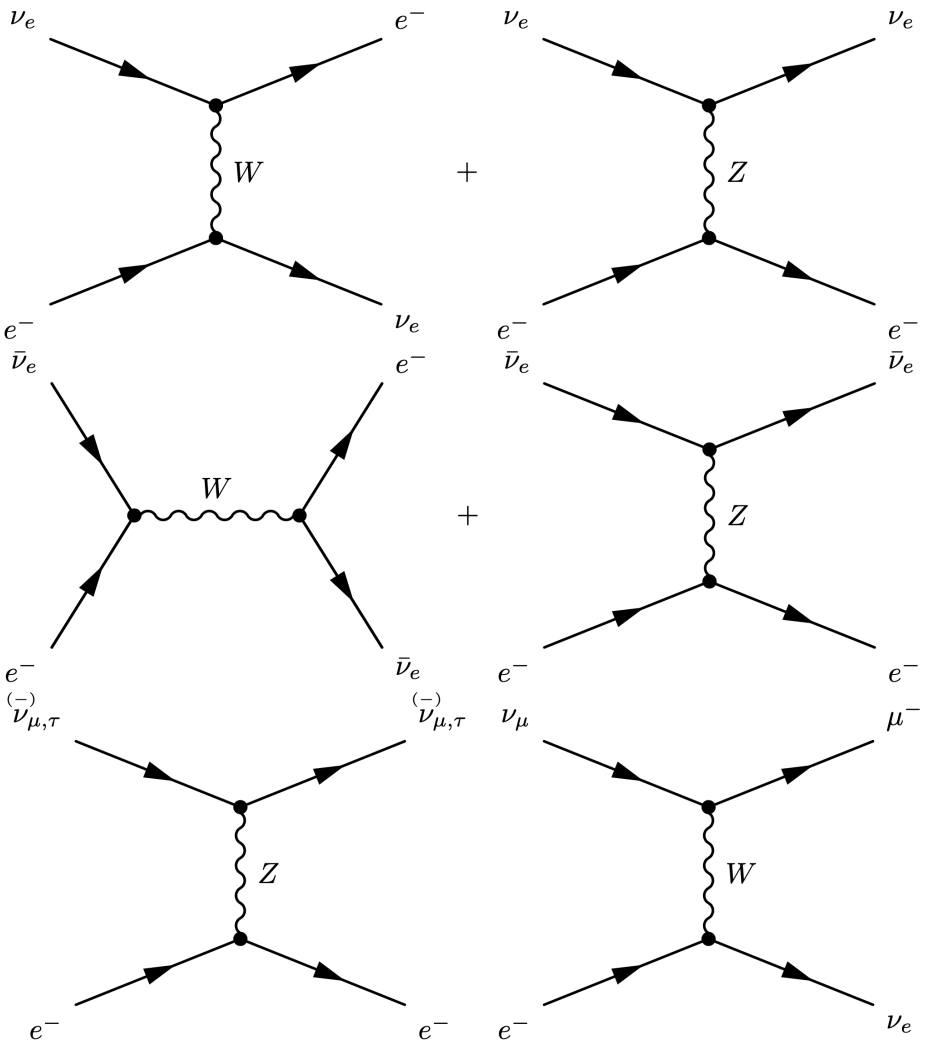

Figure 1.5: *Top row:* Tree level Feynman diagram for elastic scattering of ν_e: charged current (left) and neutral current (right). *Middle row:* Same for $\bar{\nu}_e$: charged current (left) and neutral current (right). *Bottom row:* Same for ν_x for neutral current (left) and only for ν_μ (right) for charged current, where, $x = \mu, \tau$.

1.3.2 Neutrino-electron Elastic Scattering (ES)

This is one of the most common interactions of the neutrino. The theory of elastic neutrino-electron scattering has been studied in detail (Tomalak and Hill (2020) and references therein). Low energy neutrinos interact with electrons through an elastic scattering process. Since in this case the final and the initial states are the same, the

only outcome is a redistribution of the total energy and momentum between the two particles involved. This process can proceed via both charged-current and neutral-current reactions. The possible Feynman diagrams are shown in Fig. 1.5. The tree level Feynman diagrams for,

$$\nu_e + e^- \rightarrow \nu_e + e^- \,, \tag{1.23}$$

is shown in the top row of Fig. 1.5. For the case where we have,

$$\bar{\nu}_e + e^- \rightarrow \bar{\nu}_e + e^- \,, \tag{1.24}$$

the t-channel diagram replaced by the s-channel diagram (see Fig. 1.5 middle row). We can also have the process,

$$\overset{(-)}{\nu}_{\mu,\tau} + e^- \rightarrow \overset{(-)}{\nu}_{\mu,\tau} + e^- \,. \tag{1.25}$$

This has neutral current contributions only (see Fig. 1.5 bottom row).

Although the cross-section for this process is small as compared to IBD or CEνNS (see Fig. 1.3), it has excellent directionality. We don't discuss the directionality of this process in detail in this work. In short, the electron is scattered in a forward direction with respect to the direction of the incoming neutrino. Thus the detector can reconstruct the electron tracks and hence the direction of the incoming neutrino.

Cross-section

In the laboratory frame, the differential cross-section as a function of the kinetic energy of the recoil electron is given by,

$$\frac{d\sigma}{dT_e}(E_\nu, T_e) = \frac{\sigma_0}{m_e}\left[g_1^2 + g_2^2\left(1 - \frac{T_e}{E_\nu}\right)^2 - g_1 g_2 \frac{m_e T_e}{E_\nu^2}\right], \tag{1.26}$$

where,

$$\sigma_0 = \frac{2G_F^2 m_e^2}{\pi} \approx 88.06 \times 10^{-46}\mathrm{cm}^2 \,. \tag{1.27}$$

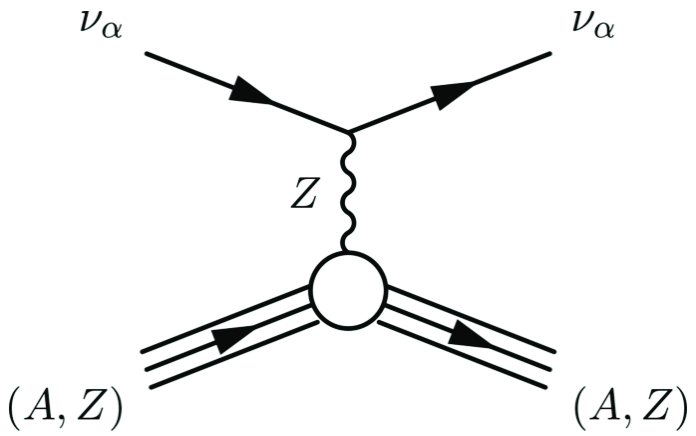

Figure 1.6: Feynman diagram for the CEνNS process.

The value of g_1 and g_2 are neutrino flavor dependent.

$$\begin{aligned} g_1^{(\nu_e)} &= g_2^{\bar{\nu}_e} \approx 0.73\,, \\ g_2^{(\nu_e)} &= g_1^{\bar{\nu}_e} \approx 0.23\,, \\ g_1^{(\nu_{\mu,\tau})} &= g_2^{\bar{\nu}_{\mu,\tau}} \approx -0.27\,, \\ g_2^{(\nu_{\mu,\tau})} &= g_1^{\bar{\nu}_{\mu,\tau}} \approx 0.23\,. \end{aligned} \tag{1.28}$$

In the laboratory frame, the electron is initially at rest. We can neglect the tiny neutrino mass such that, one of the relativistic Mandelstam invariant is, $s = 2m_e E_\nu$. For, $\sqrt{s} \gg m_e$, the ν_e^- cross-section is ~ 2.4 times larger than the $\bar{\nu}_e - e^-$ cross-section; ~ 6.2 times larger than the $\nu_{\mu,\tau} - e^-$ cross-section; and ~ 7.1 times the $\bar{\nu}_{\mu,\tau} - e^-$ cross-section.

1.3.3 Coherent Elastic Neutrino-nucleus Scattering (CEvNS)

Another very important class of neutrino interactions is the elastic neutral-current reactions mediated by the Z boson Fig. 1.6. The CEνNS pocess was first discussed in Freedman (1974). Neutrinos with energy in MeV range, coherently scatter off protons or entire nuclei via neutral current weak interactions. The interaction rate is very high due to the comparatively large cross-section $\sim 10^{-39}$ cm^2 (see Fig. 1.3).

However, the slight drawback is the fact that the recoil energies are very low, so the detectors need to have a very low energy threshold. An important characteristic of this process is that it is flavor blind.

Cross-section

The SM cross-section for this process is given by (Freedman *et al.*, 1977),

$$\frac{d\sigma^I}{dE_r}(E_\nu, E_r) = \frac{G_F^2 m_I}{4\pi} Q_W^2 \left(1 - \frac{m_I E_r}{2E_\nu^2}\right) F_I^2(E_r)\,, \tag{1.29}$$

where, m_I is the target nuclide mass, once again the Fermi coupling constant $G_F = 1.1664 \times 10^{-5}$ GeV^{-2}, $F_I(E_r)$ is the form factor, taken to be the Helm form factor (Helm, 1956), the weak nuclear charge $Q_W = [(1 - 4\sin^2\theta_W)Z_I - N_I]$, N_I is the number of neutrons and Z_I is the number of protons and θ_W is the Weinberg angle. At low energies, $\sin^2\theta_W = 0.23867$ (Erler and Ramsey-Musolf, 2005). The minimum neutrino energy required to produce a recoil of energy E_r is given by,

$$E_\nu^{min} = \sqrt{\frac{m_I E_r}{2}}\,. \tag{1.30}$$

The maximum recoil energy produced due to collision with a neutrino of energy E_ν is,

$$E_r^{max} = \frac{2E_\nu^2}{m_I + 2E_\nu}\,. \tag{1.31}$$

When the target consists of entire nuclei, the recoil energies are extremely low (a few keV to to a few 10 keV) (Freedman *et al.*, 1977; Drukier and Stodolsky, 1984) which is out of reach for conventional detectors. But detectors designed for dark matter may be able to see these recoils. The use of dark matter detectors as neutrino detectors using the CEνNS process is being thoroughly explored (Reichard *et al.*, 2017; Khaitan, 2018; Aalbers *et al.*, 2022).

1.4 Neutrino Oscillations

Neutrino oscillation is a consequence of leptonic mixing and non-degenerate neutrino mass. It is a quantum mechanical phenomenon related to the flavor and mass eigenstates. It is important to note that in the SM neutrinos must be massless and if that were true there would be no neutrino oscillations unless other exotic physics is invoked. But we have seen neutrino oscillations in various neutrino experiments (see Sec. 1.1), implying neutrinos do have a non-zero mass and hinting at the first evidence of physics beyond the SM. In this section we briefly discuss neutrino oscillations. Detailed reviews can be found in Bilenky and Pontecorvo (1978); Bilenky *et al.* (1999); Strumia and Vissani (2006); Nunokawa *et al.* (2008); Giunti and Kim (2007); Roy (2009); Gonzalez-Garcia *et al.* (2016); Farzan and Tortola (2018).

The basic idea is that the description of neutrino production and detection is in terms of the flavor states. Now each flavor eigenstate is a *coherent* superposition of mass eigenstates with slightly different masses. These massive states propagate over long distances with different phases. This results in a slight change in its phase. Finally, when the neutrino is detected, the flavor state is once again projected out and there is a probability that a different flavor is found as compared to the initial flavor. One key aspect of neutrino oscillation is coherence. Coherence is needed during production and propagation.

1.4.1 Neutrino Oscillations In Vacuum

Let us discuss the simple case of neutrino oscillations in vacuum. We will use the most commonly used plane-wave approximation technique for discussing the oscillation probability. The main assumption is once again is, the initial state is a coherent superposition of massive states with momentum, $p \equiv |\mathbf{p}|$. Say, we have a neutrino ν_α

produced at time $t = 0$. The initial state is described as,

$$|\nu, t = 0\rangle = |\nu_\alpha\rangle = \sum_i U^*_{\alpha i} |\nu_i\rangle, , \tag{1.32}$$

where, U is the PMNS (Pontecorvo-Maki-Nakagawa-Sakata) matrix (defined later) and is unitary, $\alpha = e, \mu, \tau$ and $i = 1, 2, 3$. The mass states are eigenstates of the free Hamiltonian $\hat{H}$ with energy eigenvalues given by, $E_i = \sqrt{\mathbf{p}^2 + m_i^2}$. Time evolution of the initial state is given as,

$$|\nu, t\rangle = \exp(-i\hat{H}t)|\nu_a\rangle = \sum_i U^*_{\alpha i} \exp(-iE_i t)|\nu_i\rangle \, . \tag{1.33}$$

The transition probability from ν_α at time $t = 0$, to ν_β at time $t = t$ is given by,

$$P(\nu_\alpha \to \nu_\beta, t) = |\langle \nu_\beta | \nu, t\rangle|^2 = \left| \sum_i U_{\beta i} U^*_{\alpha i} \exp(-iE_i t) \right|^2 . \tag{1.34}$$

In writing the above expression, we use $\langle \nu_j | \nu_i \rangle = \delta_{ij}$. In most cases, the neutrinos are highly relativistic and a series of approximations follow, $E_i - E_j \approx (m_i^2 - m_j^2)/2p$, where, E_i is the energy of $|\nu_i\rangle$, $L = t$, where, L is the distance between the source and detector, and $E \simeq p$. We define, $\Delta m^2_{ij} \equiv m_i^2 - m_j^2$. This finally gives us the neutrino oscillation probability in vacuum as,

$$P(\nu_\alpha \to \nu_\beta, t) = |\langle \nu_\beta | \nu, t\rangle|^2 = \left| \sum_i U_{\beta i} U^*_{\alpha i} \exp\left(-i \frac{\Delta m^2_{ij}}{2E} t \right) \right|^2 . \tag{1.35}$$

There are a few interesting things that can be noted from the above expression (Eq. 1.35) right away:

- Neutrino oscillations require leptonic mixing, $U \neq 1$ and the neutrinos need to have a finite non-zero mass as discussed earlier.

- Neutrino oscillation conserves lepton number, that is, the neutrino does not oscillate to an antineutrino. But lepton flavor is not conserved.

- Only the mass-squared difference between the different mass states play a role in neutrino oscillations, thus making individual absolute value of neutrino masses irrelevant.

- Since neutrino oscillation is a lepton number conserving process, the Majorana phases do not come in.

- When, $\alpha = \beta$ Eq. 1.35 is called the *survival probability* or disappearance channel. For $\alpha \neq \beta$ Eq. 1.35 is called the *transition probability* or appearance channel.

The neutrino oscillation probability obtained in Eq. 1.35 is simple but misses a lot of the subtle aspects. A more precise treatment is done using wave packets (Nussinov, 1976; Kayser, 1981; Kiers *et al.*, 1996). However, we will not go into the details of that. The case of two neutrino oscillation is discussed in Appendix A. The transition probability for the 2 neutrino case is given by,

$$P(\nu_\alpha \to \nu_{\beta\neq\alpha}) = \sin^2\theta \sin^2\left(\frac{\Delta m^2 L}{4E}\right), \tag{1.36}$$

where, θ and $\Delta m^2 = m_2^2 - m_1^2$ are the mixing angle and mass-squared difference in this case.

Moving a step further, the general neutrino oscillation probability for the three flavors is given by,

$$P(\nu_\alpha \to \nu_\beta) = \sum_{i,j} U_{\alpha i} U^*_{\beta i} U_{*\alpha j} U_{\beta j} \exp\left(-i\frac{\Delta m^2_{ij}}{2}\frac{L}{E}\right) \tag{1.37}$$

Motivated from the atmospheric and solar neutrino oscillation experiments, the unitary PMNS matrix U can be parameterized in terms of 3 mixing angles, θ_{ij} and 1

phase parameter δ_{CP},

$$\mathbf{U} = \begin{pmatrix} 1 & 0 & 0 \\ 0 & c_{23} & s_{23} \\ 0 & -s_{23} & c_{23} \end{pmatrix} \begin{pmatrix} c_{13} & 0 & s_{13}e^{-i\delta_{CP}} \\ 0 & 1 & 0 \\ -s_{13}e^{i\delta_{CP}} & 0 & c_{13} \end{pmatrix} \begin{pmatrix} c_{12} & s_{12} & 0 \\ -s_{12} & c_{12} & 0 \\ 0 & 0 & 1 \end{pmatrix}. \tag{1.38}$$

Here, $c_{ij} = \cos\theta_{ij}$ and $s_{ij} = \sin\theta_{ij}$. Some remarks based on the PMNS matrix are:

- θ_{23} is called the *atmospheric mixing angle*, since it determines the oscillations of atmospheric muon neutrinos to the leading order.
- θ_{12} is referred to as the *solar mixing angle*. This is because it describes the solar neutrino oscillations to the leading order.
- θ_{13} is small, as a result of which atmospheric and solar neutrino oscillations can be treated independently within a good approximation.
- If neutrinos are Majorana, there are 2 additional phases. These can be added to the diagonal of the matrix, U. These phases cannot be measured in neutrino oscillations.
- $\sin\delta_{CP} \neq 0$, will imply CP violation.

Owing to the mass hierarchy[3], in most cases the simpler two flavor neutrino oscillation (discussed in App. A) is a reasonable approximation.

1.4.2 Matter Effects In Neutrino Oscillation

We discussed neutrino oscillations in vacuum in the previous section (Sec.1.4.1). However, in most realistic cases neutrinos propagate though matter. This is particularly true in the sun or a core-collapse supernova. Therefore, an interesting question

[3]This will be discussed in the next section.

arises: *what happens to the phenomenon of neutrino oscillations in the presence of matter?*

Before we discuss the answer to the above question, let us take a small detour. When neutrinos propagate through matter they scatter off its constituents, for example, electrons, protons and neutrons. A very crude calculation of the cross-section for such scattering processes shows, $\sigma_\nu \sim 10^{-38}$ cm$^2 EM/\text{GeV}^2$, where E is the neutrino energy and M is the mass of the target in the medium, like nucleons. The mean free path is defined as, $\lambda = 1/(\sigma_\nu n)$, where, n is the density of the medium. This mean free path for earth densities is $\sim 10^{14}$ cm at 1 GeV neutrino energy! What this means is, the earth is practically transparent to neutrinos, since the mean free path is much larger than the diameter of the earth. Thus, to trap the neutrinos, it would require a very high density environment, which can be the case in a core-collapse supernova.

This brings us back to the main question, what happens to neutrino propagation in the low density environments like in the sun or in the earth. The matter contributes to changing the effective neutrino mass. This is accounted for by writing an effective matter potential. The matter effects on neutrino oscillations is discussed in detail in Barger *et al.* (1980); Lunardini and Smirnov (2001); Freund (2001); Friedland *et al.* (2004a,b); Giunti and Kim (2007); Roy (2009); Hannestad *et al.* (2006); Mirizzi *et al.* (2016). Here we will discuss it very briefly and give the main results.

The oscillation probabilities get modified because of the effective matter potential. For simplicity consider the two flavor case in Eq. 1.37. The parameters θ and Δm^2 are modified to θ_m and Δm^2_m to account for the matter effects. The size of the matter will of course depend on the density and composition of the medium. For the relatively simple case of constant matter density, we obtain,

$$\sin^2 2\theta_m = \frac{\sin^2 2\theta}{(A/\Delta m^2 - \cos 2\theta)^2 + \sin^2 2\theta}\,, \tag{1.39}$$

where, $A = 2\sqrt{2}G_F N_e E$ and the electron number density is given by N_e. The case of a varying matter density is also possible, but we will not discuss it here. It is discussed in detail in Wolfenstein (1978); Mikheyev and Smirnov (1985); Mikheev and Smirnov (1986) and is known as the MSW effect. The generic case of 3 flavor mixing implies that neutrino oscillations are described by 6 parameters: 3 mixing angles (θ_{12}, θ_{13} and θ_{23}), 2 independent mass splittings (Δm^2_{21} and Δm^2_{32}, or Δm^2_{31}) and one CP phase (δ_{CP}). Terrestrial and astrophysical neutrino sources (see Sec. 1.6) have enabled us to measure all the mixing angles, Δm^2_{21} and the magnitude of Δm^2_{32}. However, δ_{CP} and the sign of Δm^2_{32} is still unknown. Atmospheric neutrinos constrains θ_{23} and gives us, $|\Delta m^2_{31}|$. The solar and reactor neutrinos helped constrain θ_{12} and Δm^2_{21} and showed the sign of Δm^2_{21} is positive. Reactor neutrinos provide with the most precise measurement of θ_{13}, the smallest mixing angle. The current status of the oscillation parameters based on global fits can be found in Sajjad Athar *et al.* (2022).

1.5 Neutrino Masses

We discussed in the previous section, how neutrinos oscillations which have been experimentally confirmed, reveals that neutrinos have non-zero masses. Neutrino oscillation depends on several parameters, one of which is the neutrino mass-squared difference Δm^2_{ij}. The next important question to answer is, *what can be said about the neutrino mass-squared differences in terms of observations?*

Solar and atmospheric neutrino oscillations have provided us with two mass squared differences. Let us label them as Δm^2_{SOL} and Δm^2_{ATM}. Past generation neutrino experiments like KamLAND and K2K have confirmed these measurements independently. Recall, from Sec. 1.4, the mass-squared differences in the case of three neutrino

oscillation is given as,

$$\begin{aligned}\Delta m^2_{21} &\equiv m^2_2 - m^2_1\,,\\ \Delta m^2_{31} &\equiv m^2_3 - m^2_1\,,\\ \Delta m^2_{32} &\equiv m^2_3 - m^2_2\,.\end{aligned} \tag{1.40}$$

This allows us to show right away, that combining th above gives,

$$\Delta m^2_{32} + \Delta m^2_{21} - \Delta m^2_{31} = 0\,. \tag{1.41}$$

From the experiments we observed, $\Delta m^2_{SOL} \ll \Delta m^2_{ATM}$. The neutrino mass states are generally labeled as, m_1, m_2, m_3. We choose (arbitrarily) the sates such that, $\Delta m^2_{SOL} = \Delta m^2_{21}$ and $\Delta m^2_{ATM} = |\Delta m^2_{31}|$. This implies,

$$\begin{aligned}\Delta m^2_{21} &\ll \Delta m^2_{31} \simeq \Delta m^2_{32}\,,\\ \Delta m^2_{32} &= \Delta m^2_{31} - \Delta m^2_{SOL}\,.\end{aligned} \tag{1.42}$$

From the above discussion, it is clear that the mass-squared differences can be accommodated in two different ways as shown in Fig. 1.7[4]:

- **Normal Ordering**:

$$m_1 < m_2 < m_3 \implies \Delta m^2_{31} > 0\,. \tag{1.43}$$

The individual neutrino masses can then be expressed in terms of just one unknown parameter, the lightest neutrino mass, say m_{MIN},

$$\begin{aligned}m_1 &= m_{MIN}\,,\\ m_2 &= \sqrt{m^2_{MIN} + \Delta m^2_{21}} = \sqrt{m^2_{MIN} + \Delta m^2_{SOL}}\,,\\ m_3 &= \sqrt{m^2_{MIN} + \Delta m^2_{31}} = \sqrt{m^2_{MIN} + \Delta m^2_{ATM}}\,.\end{aligned} \tag{1.44}$$

[4]The content of each massive neutrino state can be determined from the PMNS matrix **U** corresponding to $|U_{\alpha i}|^2$.

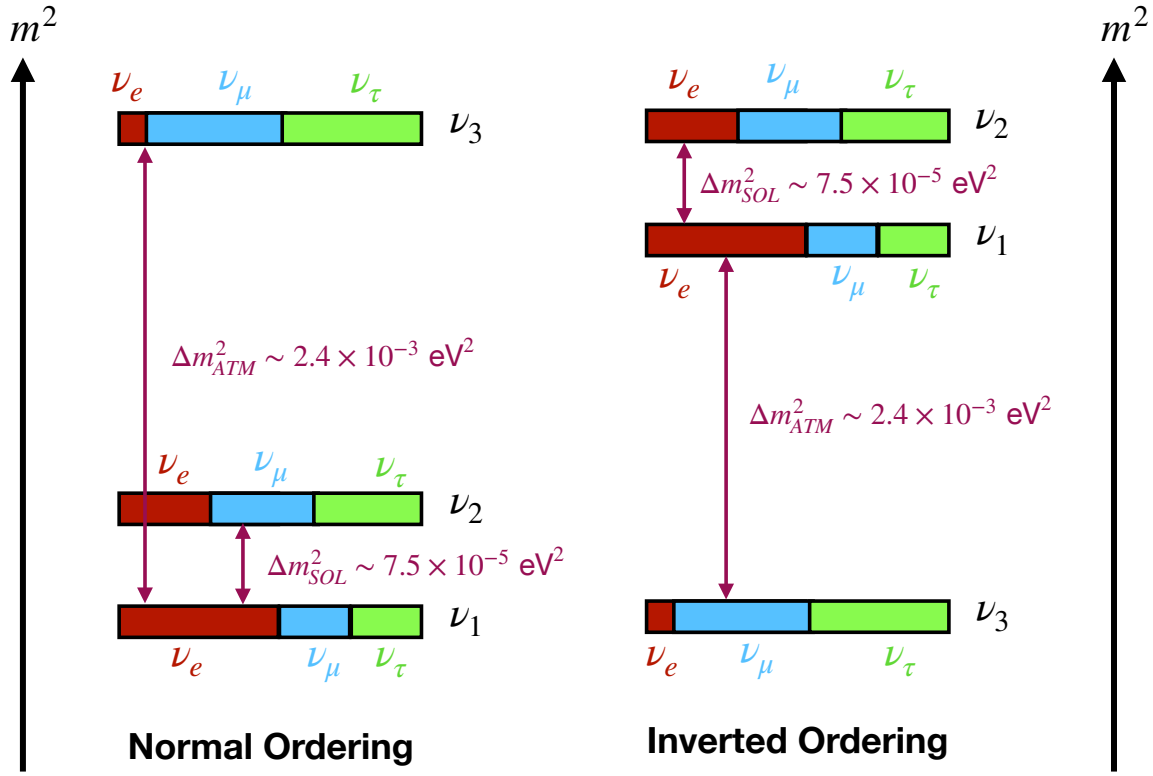

Figure 1.7: A schematic diagram to show the normal and inverted ordering of neutrino masses. The fractional flavor content of each mass eigenstate ν_i is also shown based on the best fit values of mixing angles.

- **Inverted Ordering**:

$$m_3 < m_1 < m_2 \implies \Delta m^2_{31} < 0\,. \tag{1.45}$$

The individual neutrino masses in this case are given by,

$$\begin{aligned} m_3 &= m_{MIN}\,, \\ m_1 &= \sqrt{m^2_{MIN} - \Delta m^2_{31}} = \sqrt{m^2_{MIN} + \Delta m^2_{ATM}}\,, \\ m_2 &= \sqrt{m^2_1 + \Delta m^2_{21}} = \sqrt{m^2_{MIN} + \Delta m^2_{ATM} + \Delta m^2_{SOL}}\,. \end{aligned} \tag{1.46}$$

There is another possibility if $m_{MIN} \gg \sqrt{|\Delta m^2_{31}|}$, it would imply the three mass eigenstates are almost degenerate, that is, $m_1 \simeq m_2 \simeq m_3 \simeq m_{MIN}$. Based on current data from neutrino experiments, neutrino oscillations imply a *lower bound* of

0.06 eV for the normal ordering and 0.10 eV for the inverted ordering, for the sum of neutrino masses. The *upper bound* for the same is ≤ 1 eV. The absolute neutrino masses are being probed experimentally in various way like: neutrinoless double beta decay experiments ($0\nu 2\beta$) (Elliott and Vogel, 2002; Elliott and Engel, 2004), beta decay experiments (Eitel, 2005) and precision cosmology experiments (Hu *et al.*, 1998; Bennett *et al.*, 2003; Tegmark *et al.*, 2004; Seljak *et al.*, 2005).

There are different ways of extending the SM to account for the neutrino masses leading to various scenarios of beyond SM physics. These include adding a right-handed heavy neutrino to the SM, introducing a Majorana mass term leading to the see-saw mechanisms (Type-I, II and III) (Minkowski, 1977; Mohapatra and Senjanovic, 1980; Schechter and Valle, 1980; Foot *et al.*, 1989) and many others. We will not go discuss or go into the details of those in this work.

1.5.1 Neutrino Masses From Supernova Neutrinos

Since the main focus of our work is supernova neutrinos (see Sec. 2.3), it may be useful to discuss what information do supernova neutrinos give us about neutrino masses. This idea was discussed in Zatespin (1968); Cabibbo (1980); Piran (1981).

The group velocity of an extremely relativistic neutrino with mass $m \ll E$ propagates with group velocity,

$$v = \frac{p}{E} = \sqrt{1 - \frac{m^2}{2E^2}} \simeq 1 - \frac{m^2}{2E^2}\,. \tag{1.47}$$

If the source in this case say a core-collapse supernova is at a distance D. The time delay for the massive neutrino to travel the distance D with respect to say a photon emitted at the same time is,

$$\Delta t = D\left(\frac{1}{v} - 1\right) \simeq \frac{m^2}{2E^2} D = (5 \times 10^{-3}) \left(\frac{m}{1\text{ eV}}\right)^2 \left(\frac{E}{10\text{ MeV}}\right)^{-2} \left(\frac{D}{10\text{ kpc}}\right) \text{s}\,. \tag{1.48}$$

In the above equation, we have used the speed of light, $c = 3 \times 10^8$ m/s. Neutrinos produced at the same time with different energies will reach the detector with a delay ΔT, where,

$$\Delta T \simeq \frac{m^2}{2}\frac{2\Delta E}{E^3}D = \frac{m^2}{E^2}D\frac{\Delta E}{E}\,, \tag{1.49}$$

where, we assume the supernova neutrino spectrum has mean energy E and the width ΔE. This expression can be obtained from differentiating Eq. 1.48 with respect to energy. We can define the intrinsic time scale of neutrino production in the core-collapse supernova as ΔT_0, the observed time interval of the neutrino burst at the detector as ΔT_{obs}. To obtain an estimate of the upper bound of the neutrino mass that does not depend on the specific physical conditions or details of neutrino production, we need to have, $\Delta T < \Delta T_0 \leq \Delta T_{obs}$. Particularly, $\Delta T \leq \Delta T_{obs}$ allows us to set the upper bound on the neutrino mass m_ν,

$$m_\nu \leq E\sqrt{\frac{E}{\Delta E}\frac{\Delta T_{obs}}{D}} \simeq 31.2 \text{ eV} \left(\frac{E}{10 \text{ MeV}}\right) \sqrt{\frac{E}{\Delta E}} \sqrt{\frac{\Delta T_{obs}}{10 \text{ s}}} \sqrt{\frac{10 \text{ kpc}}{D}}\,. \tag{1.50}$$

The ideal conditions for obtaining information about the neutrino mass would be to make the upper bound as low as possible. This can be is achieved by a large distance, a low neutrino energy, a wide ΔE. However, the neutrino flux falls of as $1/D^2$ with distance, the supernova neutrino mean energy is $\sim$ 10 MeV. Thus, we are limited to nearby (galactic scale) supernova for obtaining this information. But the rate of galactic supernovae is extremely low (see Sec. 2.6). This makes it a challenging and less optimistic process to constrain neutrino masses with supernova neutrino observations.

From SN1987A (see Sec. 2.7 for details), which was at a distance $D = 50$ kpc ($E \simeq 15$ MeV, $\Delta E \sim 15$ MeV, and $\Delta T_{obs} = 12$ s), we could put a bound on the electron flavor neutrino as Schramm (1987),

$$m_{\nu_e} \leq 23 \text{ eV}\,,$$

The above is a very rough estimate (see Schramm (1987) for details): we neglect neutrino mixing and consider only electron antineutrino events. The bounds provided by other methods are much more competitive and recent.

1.6 Neutrino Sources

In this section, we discuss various neutrino sources. A complete and detailed review can be found in Vitagliano *et al.* (2020); Sajjad Athar *et al.* (2022). Neutrinos are emitted from a variety of sources ranging from cosmological to geological. Neutrinos from some sources have been detected and well studied, and there are some sources from which neutrinos are yet to be detected experimentally. The neutrinos from various sources have different energies. They contribute to understanding the properties of the source itself. Fig. 1.8 is a plot of neutrino flux ϕ as a function of energy and shows the grand unified neutrino spectrum at earth, integrate and summed over all flavors (see Fig. caption for more details). Below, we list the various sources with a very brief description for each one.

- **Cosmic neutrino background (CνB):**

  The cosmic neutrino background is a background of relic neutrinos from the early universe when it was $\sim$ 1 second old, similar to the CMB (cosmic microwave background). It is constituted by $\sim$ 112 cm^{-3} neutrinos and antineutrinos per flavor. In fact it is the largest neutrino density at earth. The neutrinos from CνB have never been detected. If detected they would shed light on the nature of neutrinos, that is, they would provide information about neutrino masses and their Dirac or Majorana nature (Long *et al.*, 2014).

- **Neutrinos from the Big Bang nucleosynthesis:**

  In the Big Bang nucleosynthesis, the universe produces the observed light ele-

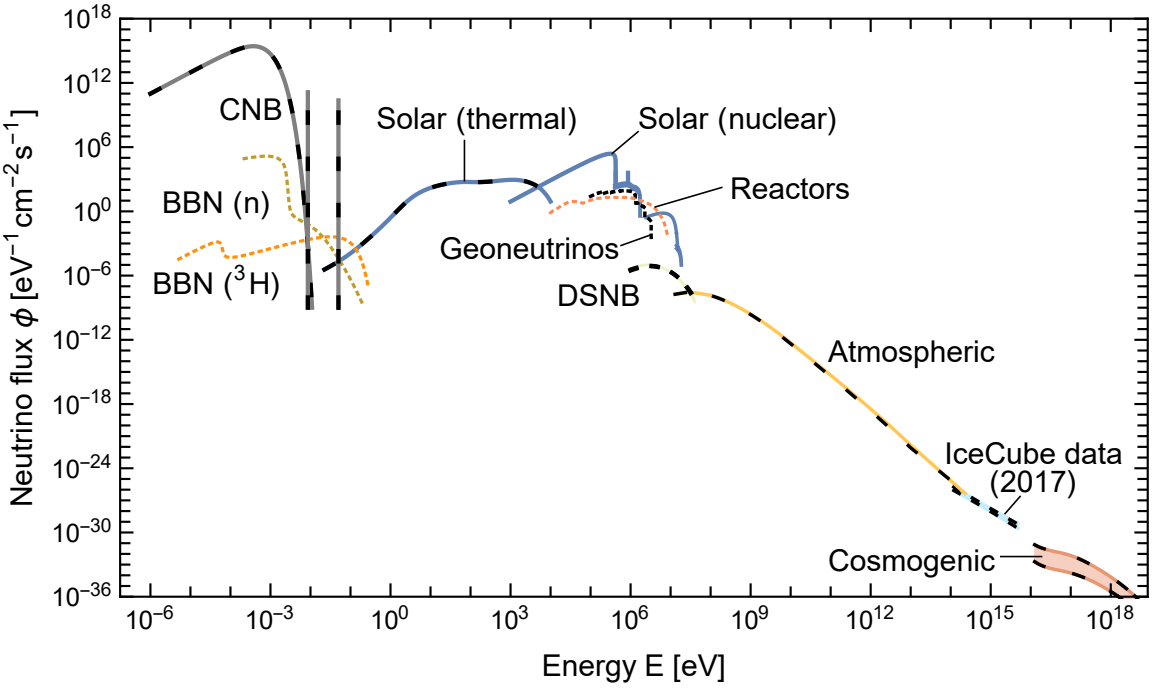

Figure 1.8: Grand Unified Neutrino Spectrum at Earth, integrated over directions and summed over flavors. The plots shows neutrino flux ϕ as a function of energy. Solid lines are for neutrinos, dashed or dotted lines for antineutrinos, superimposed dashed and solid lines for sources of both ν and $\bar{\nu}$. The fluxes from BBN, the Earth, and reactors encompass only antineutrinos, the Sun emits only neutrinos, whereas all other components include both. The CNB is shown for a minimal mass spectrum of $m_1 = 0, m_2 = 8.6$, and $m_3 = 50$ meV, producing a blackbody spectrum plus two monochromatic lines of nonrelativistic neutrinos with energies corresponding to m_2 and m_3. The supernova neutrino spectrum is not shown because it is a transient source. In general, supernova neutrinos have energy ~ 10 MeV. Figure taken from Vitagliano *et al.* (2020).

ments during the first few minutes. This is followed by the decay of neutrons ($n \rightarrow p + e + \bar{\nu}_e$) and tritons ($^3H \rightarrow {}^3He + e + \bar{\nu}_e$). These decays produce a small electron antineutrino flux with energy ranging from $10 - 100$ MeV. These neutrinos have never been detected and the chances of detecting them with the current neutrino experiments are low. However, if detected, they will enable us to probe the primordial nucleosynthesis.

- **Solar neutrinos:**

Solar neutrinos are the neutrinos that are produced in the sun. They can be further classified into:

- **Neutrinos from nuclear reactions in the sun:**

  The effective fusion reaction in the sun, $4p + 2e^- \rightarrow {}^4He + 2\ \nu_e + 26.73$ MeV, while proceeding through several reaction chains (pp chains) and cycles (CNO cycle) produce neutrinos. In fact, the sun emits $\sim 2.3\%$ of its nuclear energy in the form of neutrinos which are called the solar neutrinos. These neutrinos have energy in the MeV range. The solar neutrino events have been one of the most detected and well studied neutrino events. They were first observed in the Homestake experiment (Davis *et al.*, 1968) and since then many experiments have studied solar neutrinos, in particular, the Super-Kamiokande (Abe, 2016), SNO (Aharmim *et al.*, 2010), Gallex (Hampel *et al.*, 1999), SAGE (Abdurashitov *et al.*, 2009), Borexino (Agostini *et al.*, 2020). Their detection led to the discovery of flavor conversion and matter effects in neutrino oscillation. They also help in modeling the sun, provide valuable information about its chemical composition and solar interiors. Future neutrino experiments like SNO+ (Andringa *et al.*, 2016) and JUNO (An, 2016) will also study solar neutrinos.

- **Thermal neutrinos from the sun:**

  Thermal processes in the sun produce neutrino pairs of all flavors. These neutrino have energies in the keV range. The main production channels include plasmon decay, Compton process and electron bremsstrahlung. These neutrinos are the dominant flux on earth below 4 keV of neutrino energy. These neutrinos have never been detected and the prospects of detection in the upcoming detectors are also absent. However, if these

neutrinos are detected, they will provide us with information about the sun's chemical composition.

- **Geoneutrinos:**

  When the long-lived radioactive isotopes in the earth, like ^{238}U, ^{232}Th and ^{40}K decay, they produce an antineutrino flux in the MeV-range, which are known as geoneutrinos. The geoneutrino flux exceeds 10^{25} s^{-1}. They are produced from various activities like plate tectonics and vulcanism leading to radiogenic heat production. The geoneutrinos can be used to study the earth's interior using a technique called neutrino tomography (Donini *et al.*, 2019). These neutrinos have been detected by the KamLAND and Borexino experiments.

- **Reactor neutrinos:**

  Nuclear fission reaction in nuclear power plants produce electron antineutrinos in the MeV energy range. The very first neutrino detection by Cowan and Reines (see Sec. 1.1), were reactor neutrinos. They provide crucial information about neutrino mixing parameters and the existence of sterile neutrinos.

- **Supernova neutrinos:**

  Massive stars ($\geq 8\ M_\odot$) mostly die by core-collapse followed by an explosion called supernova. This phenomenon of core-collapse is accompanied by copious amounts of neutrino emission. The entire gravitational binding energy of the star 3×10^{53} ergs is released on the form of neutrinos. These neutrinos are known supernova neutrinos. They have energies of the order of 10 MeV. We will discuss the phenomena of core-collapse supernova and supernova neutrino properties in great detail in the following chapters. Neutrinos from a core-collapse supernova is the main focus of this work. Experimentally, supernova neutrinos were detected in 1987 from SN1987A (see Sec. 2.7 for details). Note

that in Fig. 1.8 this neutrino flux is not shown because it is a transient flux.

- **Diffuse supernova neutrino background (DSNB):**

  The diffuse supernova neutrino background comprises of the neutrinos from all collapsing stars in the visible universe. The DSNB neutrino energies dominate in the range of $10 - 25$ MeV. There are a lot of on-going efforts to detect the DSNB,, since it will provide us with crucial information about the supernova redshift distribution, supernova neutrino mean energies, successful and failed supernovae. The upcoming detectors like JUNO and the Gd-enriched Super Kamiokande (Beacom and Vagins, 2004) have good chances of detecting the DSNB neutrinos (de Gouvêa *et al.*, 2022).

- **Atmospheric neutrinos:**

  When cosmic rays interact with the earth's or sun's atmosphere they produce neutrinos which are called atmospheric neutrinos (Barr *et al.*, 1989; Honda *et al.*, 1996). These neutrinos were detected by Super-Kamiokande which helped in understanding flavor oscillations (Fukuda *et al.*, 1998; Abe *et al.*, 2013). Atmospheric neutrinos are used to probe neutrino masses and mixing parameters (see Kajita (2014) for a review).

- **Cosmic high-energy neutrinos:**

  These are very high energy neutrinos (energies in the range of a few TeV to a few PeV). The main sources of these extremely high energy are thought to be dim or choked astrophysical jets, star-forming galaxies (SFGs), gamma-ray bursts (GRBs) and active galactic nuclei (AGNs). In fact our own galaxy may account for $\sim 1\%$ of the observed flux. These neutrinos are detected in the IceCube neutrino observatory. These are produced by cosmic-ray interactions in the source,, surroundings or while propagation to earth. The reactions involved are

proton-proton (pp) or proton-gas (pγ) interactions. The sources of these high energy neutrinos are still a mystery.

1.7 Neutrino Detectors

Having discussed neutrino interactions in Sec. 1.3 and various neutrino sources in Sec. 1.6, we now focus on the various past, present and future neutrino detectors. In general, the neutrino detectors are built with specific science goals, that is, to observe neutrinos in a particular energy regime. Since, our focus in this work is on supernova neutrinos we will mainly discuss the neutrino detectors relevant to detecting supernova neutrinos. Furthermore, we will discuss in detail the neutrino detectors that will be relevant in the later chapters. A complete review can be found in Nakamura *et al.* (2010); Scholberg (2012) and references therein. The main principle on which neutrino detectors operate is: the neutrinos from the various sources as discussed in Sec. 1.6 interact in the detector (in the detector medium) based on the processes mentioned in Sec. 1.3 and produce other particles which are then detected by a wide variety of detection techniques which include but are not limited to, collecting photons or charge proportional to ionization energy loss, collecting Cherenkov photons or detecting neutrons.

The expected event rates of observed particles for a given neutrino interaction process in a detector can be computed by combining the supernova neutrino flux with the cross-section and detector response. This is given by (Scholberg, 2012),

$$\frac{dN}{dE'} = \int_0^\infty \int_0^\infty dE\, d\hat{E}\, \Phi(E)\, \sigma(E)\, k(E-\hat{E})\, T(\hat{E})\, V(\hat{E}-E')\,, \tag{1.51}$$

where, E is the neutrino energy, $\hat{E}$ is the energy of the particle produced, E' is the measured energy of the product particle, the total cross-section of the process is $\sigma(E)$, $k(E-\hat{E})$ provides the energy distribution of the produced particle, the detector threshold is given by $T(\hat{E})$, and $V(\hat{E}-E')$ gives the energy response of the detector.

Let us begin the discussion by listing, in general *what are the characteristics of an ideal supernova neutrino detector?* An ideal supernova neutrino detector needs to:

- **Have good timing resolution:** this would enable the detector to separate one event from another.
- **Have good energy resolution:** this would enable the detector to measure the incoming neutrino energy with precision.
- **Have good directionality:** which would enable the detector to have a good directional sensitivity, that is, the ability to point back to the source, supernova.
- **Be sensitive to all neutrino flavors:** this will enable to have the maximum flux since the supernova neutrinos are approximately distributed one-third in each flavor.
- **Tag interactions:** this will provide valuable information to separate events associated with different flavors, like, ν_e, $\bar{\nu}_e$ and ν_x events.
- **Have low backgrounds:** Any event which is not a part of the signal event is background. The backgrounds for supernova neutrino detection depend on the detector and its location. In general, the common background events include, ambient radioactivity, reactor $\bar{\nu}_e$, solar ν_e, low energy atmospheric neutrinos and antineutrinos, and cosmic ray related backgrounds. In general, for a nearby supernova the backgrounds is not a big issue, however as we will see in chapter 5 for supernova at $\mathcal{O}(1)$ Mpc, the backgrounds totally dominate the signal events.

In reality, however, we are far from ideal detectors. We have made immense progress in making better and perhaps bigger neutrino detectors and it is a field of on-going research. Let us discuss the most common supernova neutrino detectors that are relevant for this work.

1.7.1 *Scintillation Detectors*

These detectors are mainly constituted of mineral oils (C_nH_{2n}). The main process employed in these detectors for SN neutrinos is IBD, which we discussed in detail in Sec. 1.3.1. The $\gamma-$rays that are produced as a result, are then viewed by photo-multiplier tubes (PMTs). The detectors hence have the structure of large homogeneous volume of liquid hydrocarbon surrounded by PMTs. The scintillation detectors generally have very good energy resolution and low threshold. But the main drawback is there is very little directional information associated with the observed events. However, doping the liquid scintillator with a suitable element like Gd or Li may lead to a good vertex resolution which will then provide some directional information (see chapter 3 for details). There detectors also detect some elastic scattering processes.

Past detectors of this kind include the famous KamLAND detector (Eguchi *et al.*, 2003), Borexino (Cadonati *et al.*, 2002; Monzani, 2006). Prominent upcoming detectors include JUNO (An *et al.*, 2016; Beacom *et al.*, 2017), which is a spherical detector with $\sim$ 20 kt of linear alkylbenzene, and SNO+ (Kraus and Peeters, 2010). A few surface detectors of this kind that may be sensitive to nearby supernova neutrinos include MiniBOONE (Sharp *et al.*, 2002; Aguilar-Arevalo *et al.*, 2010), NOνA (Ayres *et al.*, 2004). Some reactor neutrino detectors (mostly Gd dissolved) of this kind may also see supernova neutrinos. These include: Double CHOOZ (Ardellier *et al.*, 2006), Daya Bay (Ochoa-Ricoux, 2011), and RENO (Ahn *et al.*, 2010).

1.7.2 *Water Cherenkov Detectors*

Water Cherenkov detectors consist of large volumes of ultra-pure water along with photomultiplier tubes (PMTs). Water is most easily available and has a lot of free

protons making it a suitable medium for neutrino detectors. The charged particles are detected via the Cherenkov light emission, which forms a 42° cone for relativistic particles. The number of photons detected is proportional to the energy loss. The Cherenkov ring produced also allows one to reconstruct the interaction vertices and direction. The main drawback of these detectors are there relatively high threshold energy, leading to a poor detection efficiency for supernova neutrinos. However, the directional information that can be obtained from these detectors is very precise. There are also scintillations produced by the dominant IBD reactions in water. However, once again due to the Cherenkov threshold they are difficult to detect. These detectors may also detect other sub-dominant interactions like interactions with Oxygen.

Well-known past detectors in this category include IMB (Becker-Szendy *et al.*, 1993) and Kamiokande (Hirata *et al.*, 1991) which observed the supernova neutrinos from SN1987A (we will discuss this in Sec. 2.7). SNO (Boger *et al.*, 2000) was a heavy-water detector. At present, Super-Kamiokande (Ikeda *et al.*, 2007) is also an example of a large water Cherenkov detector. The most promising future water Cherenkov detector is Hyper-Kamiokande (Abe *et al.*, 2011), which will have a fiducial volume of ~ 260 kt.

1.7.3 Miscellaneous

In this section, we briefly mention the detectors that are important and can detect supernova neutrinos but are not directly relevant for this work. A detailed discussion on these detectors can be found in Scholberg (2012) and references therein. The various other detectors are mentioned below:

- **Long-string water Cherenkov detectors**

  These detectors are basically long strings of PMTs suspended in water or ice.

These are generally designed to study high energy ($\mathcal{O}(1)$ TeV or more) astrophysical neutrinos, But they may also be able to detect supernova neutrinos (for a galactic scale, ≤ 10 kpc supernova). The main detection channel is once again IBD, which would produce large number of photons to be picked up by the PMTs. A prime example of these kinds of detectors is IceCube (Abbasi *et al.*, 2011), which has 86 strings with 60 PMTs each, suspended 1 - 2 km below the ice surface in Antarctica. Another example is the ANTARES (Ageron *et al.*, 2012). A future detector of this kind is KM3NET (Leisos *et al.*, 2013).

- **Liquid Argon time-projection chambers (LArTPC)**

  LArTPC consists of a large liquid argon time projection chamber. In these detectors, the ionization charge is drifted by an electric field following which signals are collected on wire planes. Once the charges arrive the readout planes, the three-dimensional tracks can be reconstructed and the identification of particles can be implemented by the rate of energy loss along these tracks. Scintillations are also produced in Argon, which can be collected in the PMTs thus providing timing information. These detectors have a low threshold, good energy resolution along with good directional information. A prime example of these kinds of detector is DUNE (Abi *et al.*, 2021), which has a total volume of 70-kt of liquid argon and is located deep underground, 1.5 km below the surface. ICARUS (Bueno *et al.*, 2003) is another detector in this class.

- **Detectors employing heavy nuclei**

  The charged-current and neutral-current weak interactions of neutrinos with heavy nuclei like iron or lead is the main detection channel for these detectors. Leptons and nucleons that are ejected in the process may be observed. These detectors will provide us with information on the supernova neutrino spectra.

A particularly optimistic detector material is lead, since it is stable, and ease of handling. The current example of this class of detector is HALO (Duba *et al.*, 2008).

- **Low threshold detectors (Dark Matter detectors)**

  These detectors mainly consist of detectors that can detect neutrinos via the CEνNS process (see Sec. 1.3.3). This is particularly interesting since the CEνNS process is flavor blind. But owing to the very low energy threshold of the nuclear recoils in the CEνNS process only very clean and radioactively quiet detectors are useful. In general, the detectors developed for dark matter detection are able to do this. These detectors can use solid-state, noble liquids like Xenon, Argon or Neon. The detectors in these category include COHERENT (Akimov *et al.*, 2017), CLEAN (Horowitz *et al.*, 2003), CONUS (Bonet *et al.*, 2021).

Chapter 2

MULTI-MESSENGER ASTRONOMY

The current era of physics and astrophysics has the gift of a new avenue to explore the universe - multi-messenger astronomy. In this era of multi-messenger astronomy, gravitational wave (GW), neutrino, photon, and cosmic ray observations are combined to extract information about astrophysical sources and phenomena in the universe. Because of the energy scales involved, these sources can help to test particle and exotic physics. Multi-messenger science has been a very recent phenomenon. However, since its birth, multi-messenger astronomy has made rapid progress. Initially most multi-messenger channels would be limited to cosmic ray and photon observations, but now all the four messengers provide us with promising information about the Universe. The most notable multi-messenger observations include: IceCube's discovery of the diffuse astrophysical neutrino flux (Aartsen *et al.*, 2013), the first observation of gravitational waves by LIGO (Abbott *et al.*, 2016b), and the first joint detections in gravitational waves and photons (Abbott *et al.*, 2017c) and in neutrinos and photons (Aartsen *et al.*, 2018a). The reason why multi-messenger astronomy is so effective and provides a lot of information is because each of the messengers has its own speciality and strength. For example, gravitational waves (GWs) provide us with information about astrophysical environments where gravity is at its peak helping us understand and test general relativity and beyond. Photons associated with gamma ray emission, provide crucial information about particle acceleration and high energy collisions, jets. Cosmic rays are associated with particles at the highest energy scales ever probed, which for a comparison can be up to ten million times the energies probed at the LHC. Neutrinos propagate mostly unobstructed and complement areas

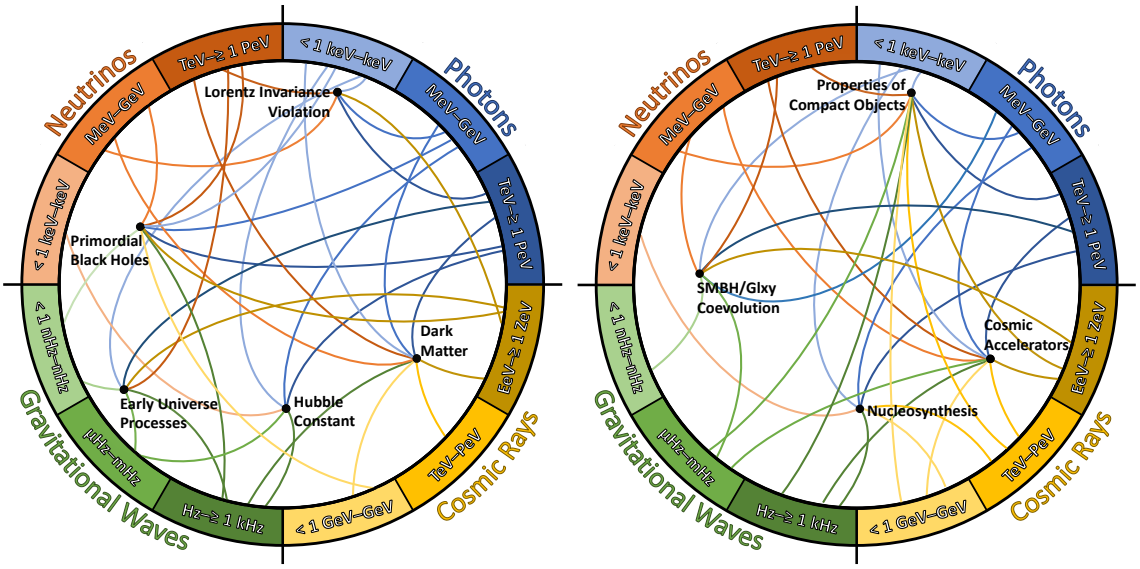

Figure 2.1: *Left:* Connections between messengers and fundamental physics topics. *Right:* Connections between messengers and particle astrophysics topics. Figure taken from Engel *et al.* (2022).

where photons are difficult to observe from, helping us probe hadronic processes and nuclear physics.

The potential of these messengers increase even more when they are combined with one another. In Fig. 2.1 we show the connections between the various messengers and fundamental physics (left) and particle astrophysics (right). GWs and photons can together test general relativity, constrain various modified gravity models and perform measurements of the expansion of the Universe. The energy scales involved in most astrophysical process is extremely high as compared to any man-made collider. The neutrinos, cosmic rays and gamma rays from these sources help understand the workings of nature at such enormous energy scales. Besides multi-messenger physics is a good probe of dark matter, early universe cosmology, and physics beyond the SM.

On October 16, 2017 the first multi-messenger co-detection was announced. On August 17, 2017 a binary neutron star merger was detected by the LIGO/Virgo col-

laboration (Abbott *et al.*, 2017a). Around 1.7 seconds later, Fermi-GBM saw a short gamma-ray burst (GRB) from the same patch in sky (Evans *et al.*, 2017; Kasliwal *et al.*, 2017). This was the first ever direct evidence that linked short GRBs with binary neutron star merger. This was theoretically predicted (Paczynski, 1986; Eichler *et al.*, 1989; Narayan *et al.*, 1992), had subtle indirect evidences from Swift (Fox *et al.*, 2005; Barthelmy *et al.*, 2005) but no direct evidence was observed prior to this event. This led to an even more thorough search in the other channels - EM signals (Abbott *et al.*, 2017c) and neutrinos (Albert *et al.*, 2017). This resulted in successfully localizing the host galaxy where the merger occurred (NGC4993). Besides, it also provided the very first unambiguous detection of a kilonova, the broadband signature of r-process nucleosynthesis in the merger ejecta (Li and Paczynski, 1998; Kulkarni, 2005; Metzger *et al.*, 2010).

On July 13, 2018, the first extragalactic gamma-ray, neutrino co-detection was announced (Aartsen *et al.*, 2018a,b). The IceCube, Fermi-LAT, MAGIC, AGILE, HAWC, H.E.S.S., INTEGRAL, and KANATA collaborations an September 22, 2017 announced the simultaneous production of neutrinos and gamma-rays from blazar TXS 0506+056. The detection of neutrinos from a blazar has profound implications on our understanding of particle energetics near supermassive black holes, as well as the origin of cosmic rays and astrophysical neutrinos (Aartsen *et al.*, 2013). Recently, a real time coincidence analysis for multimessenger astrophysics called AMON (Astrophysical Multi-messenger Observatory Network) (Smith *et al.*, 2013; Ayala Solares *et al.*, 2020b) has been developed. This consists of the HAWC and IceCube experiments data (Ayala Solares *et al.*, 2020a) and Fermi-LAT and ANTARES data (Ayala Solares *et al.*, 2019). A similar multi-messenger themed network of detectors for supernova neutrinos, SNEWS (SuperNova Early Warning System) (Antonioli *et al.*, 2004; Scholberg, 2008; Al Kharusi *et al.*, 2020) has also been developed. Thus, the

field of multi-messenger astronomy is currently growing at an unprecedented rate.

A detailed review on multi-messenger science can be found in Engel *et al.* (2022). For this work however, we will focus on core-collapse supernovae. A core-collapse supernova (CCSN) is amongst the most fascinating astrophysical sources with a huge potential for multimessenger studies. In this chapter, we will discuss the dynamics of core-collapse supernova and most importantly focus on the various multi-messenger signals from a core-collapse supernova. The main focus will of course be neutrinos, but we will also briefly discuss GW emissions.

In Sec. 2.1 of this chapter we provide an introduction to core-collapse supernovae. The various multi-messengers from a CCSN is discussed in Sec. 2.2. Amongst the various messengers we discuss neutrinos in detail in Sec. 2.3. The dynamics and processes involved prior to core-collapse is discussed in Sec. 2.3.1. The dynamics of a core-collapse supernova from the onset of collapse is discussed in Sec. 2.3.2. We discuss the case of a failed supernova or a black hole forming collapse in Sec. 2.3.3. The different phases and properties of neutrino emission from a core-collapse supernova is discussed in sec. 2.4. We focus on the presupernova neutrino emission phase prior to collapse in Sec. 2.4.1, the neutronization burst phase in Sec. 2.4.2, the accretion phase is discussed in Sec. 2.4.3, and the cooling phase in Sec. 2.4.4. The neutrino emission properties from a failed supernova is the focus of Sec. 2.4.5. A discussion of the supernova neutrino emission spectra is provided in Sec. 2.4.6. A very brief discussion about another messenger - gravitational waves from CCSNe is provided in Sec. 2.5. The rate of CCSNe is discussed in Sec. 2.6, and an analytical calculation of the cummulative CCSN rate is shown in Sec. 2.6.1. We conclude this chapter with a discussion of SN1987A and its relevance in facilitating multi-messenger astronomy in Sec. 2.7.

2.1 Core-collapse Supernova (CCSN)

Stars have a life-cycle of their own. They are born, they live, going through various stages of nuclear burning, and finally they die. The extremely powerful explosion that leads to the death of some stars is known as a supernova. During their lifetime, stars synthesize various light and heavier elements which are ejected upon their death. These form an integral part in the formation of galaxies, stars, planets and for the existence of life itself. In some cases compact objects like a neutron star or a black hole are formed as a result of supernovae. Supernovae (SNe) have been studied in great detail since the 1930s . Some galactic supernovae have even been observed with the naked eye. The energy scales involved ($\sim 10^{51} - 10^{53}$ ergs) make them nature's own laboratories to study and gain insights in various fields of physics including but not limited to physics beyond the standard model, plasma physics, nuclear physics, cosmology.

Supernovae are classified into different types based on their spectroscopic characteristics, light curves, and mechanism leading to the supernova. Fig. 2.2 shows a schematic representation of the same. The wide categorization is based on the presence or absence of hydrogen lines. Further (and more relevant) classification is based on the mechanism generating the supernova: *thermonuclear* versus *core-collapse* which distinguishes type Ia from types Ib, Ic and II. Some good introductions and reviews can be found in Trimble (1982, 1983).

Types Ib, Ic and II SNe are generated by core-collapse. In particular, Type II SNe are generated by the core collapse of red or blue supergiants with masses ranging between $8 - 9\ M_\odot$ and $40 - 60\ M_\odot$. These will be important to us for following chapters. As an illustration, we have shown the red and the blue supergiants near to us (within 1 kpc) in Fig. 2.3. A Mollweide projection for the same is shown in

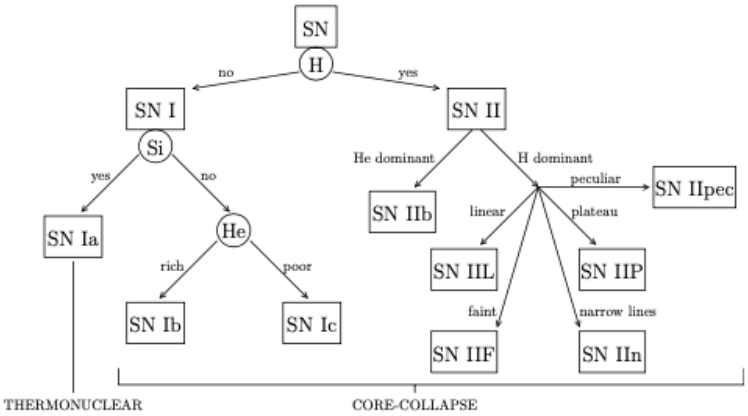

Figure 2.2: Classification of supernovae. Figure taken from Giunti and Kim (2007).

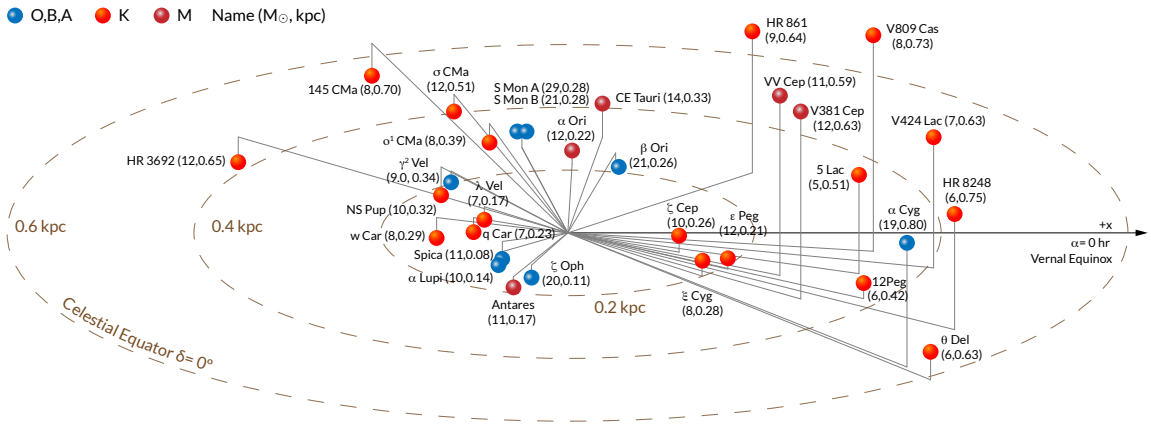

Figure 2.3: Illustration of nearby ($D \leq 1$ kpc) core collapse supernova candidates. Each star's spectral type, name, mass and distance is shown in labels. See Table D.1 for details and references.

Fig. 2.4. A detailed table corresponding to the figure is given in App. D. Finally, the distribution of these stars with distance form earth and mass is shown in Fig. 2.5.

Types Ib, Ic and II SNe are particularly interesting to us since they produce a huge flux of neutrinos of all flavors. Core-collapse supernova is the death of a massive star ($M \geqslant 8\ M_{\odot}$). The massive stars die violently by the collapse of their core leaving behind a compact remnant in the form of a neutron star or a black-hole (BH).

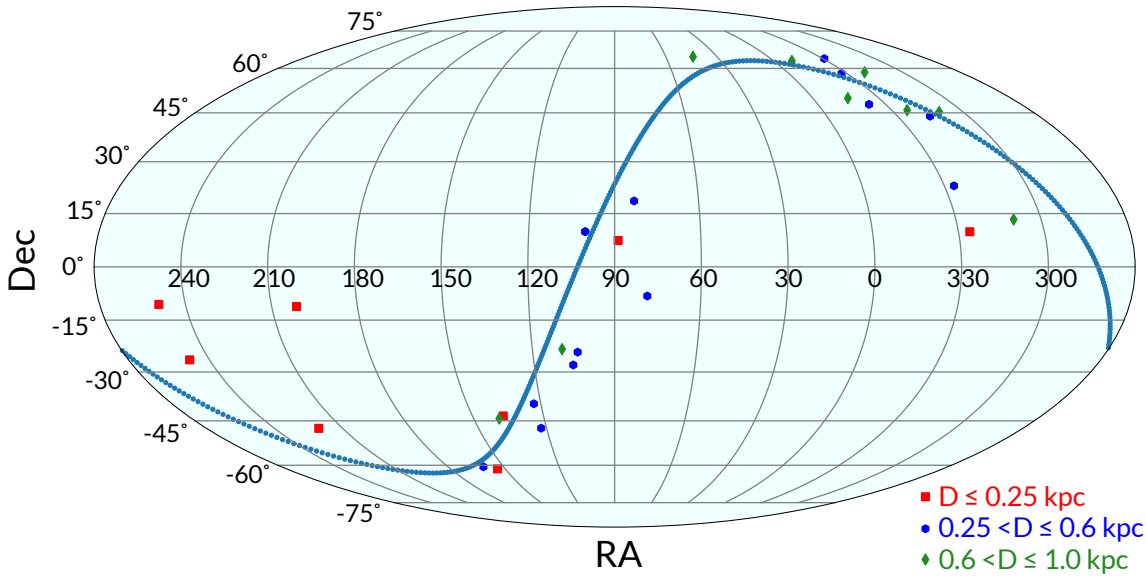

Figure 2.4: Mollweide projection of nearby ($D \leq 1$ kpc) core collapse supernova candidates. Symbols and colors correspond to distance intervals. The dotted line indicates the Galactic Plane. The red square near the center of the map is α Ori, best known as Betelgeuse.

2.2 Multi-messengers From A Core-collapse Supernova

Core-collapse supernovae (CCSNe) have been a prime focus of research since long. Most importantly, it is an astrophysical phenomena which can be analyzed in great detail using the multi-messengers. CCSNe emit neutrinos, GWs and electromagnetic (EM) signals. We will focus on the details including the mechanism of core-collapse supernova in the next sections. In this section, we will mainly discuss CCSNe in the context of multi-messenger astronomy.

Hundreds of CCSNe have been observed through the optical (EM) channel in recent years (Sako *et al.*, 2008; Leaman *et al.*, 2011). But these are mostly in distant galaxies. Owing to the distance from us these extra-galactic CCSNe have provided us with only one channel of detection. While this is good, it is not enough to understand the extremely complicated mechanisms that happen in a collapsing star (see Sec. 2.3.2 for details). In a sense, the EM signals are seen once the star explodes, thus failing

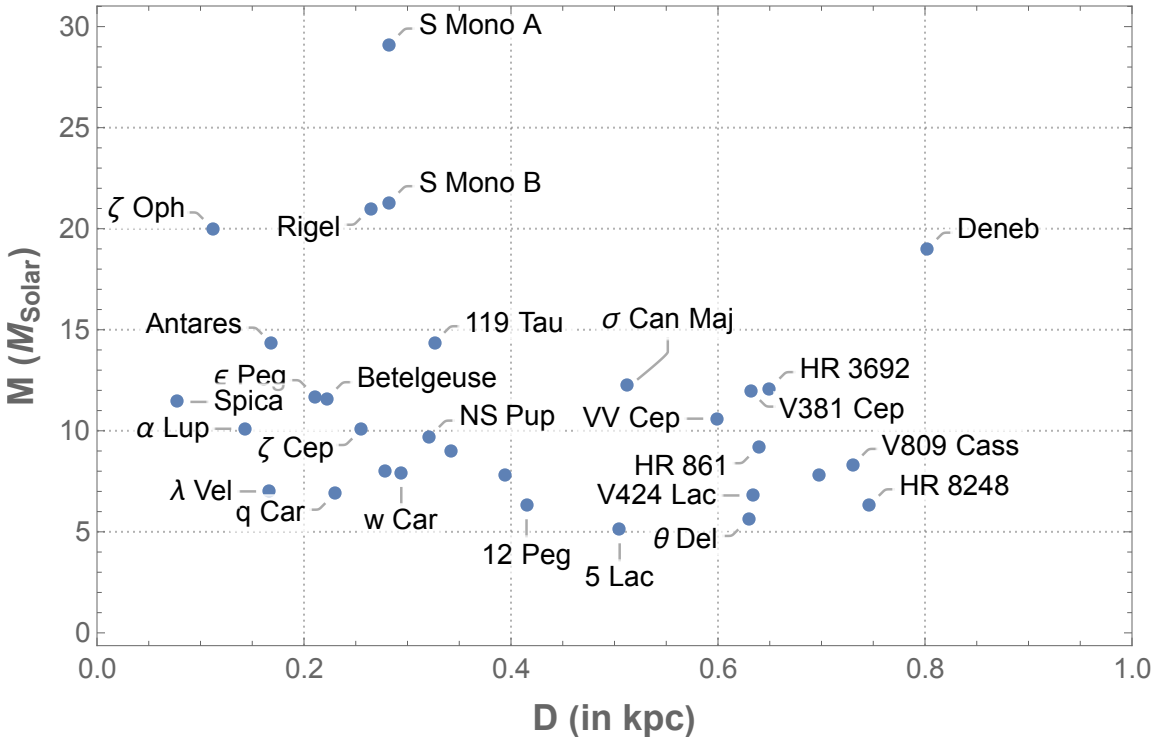

Figure 2.5: Graphical rendering of nearby ($\sim$ 1 kpc) red and blue supergiants as listed in Table D.1. The distance from earth is shown in kpc on the x-axis and y-axis shows the mass of the progenitor.

to provide us with any information about the inner dynamics, composition and properties. Moreover, in certain cases EM signals from CCSNe can even be absent (like in a failed CCSN, see Sec. 2.3.3).

A CCSN in our own Milky Way or neighbouring galaxies however will completely change the paradigm. It will enable us to study the phenomena with various messengers like neutrinos (Scholberg, 2012), GWs (Ott, 2009; Kotake, 2013), and nuclear gamma rays (Gehrels *et al.*, 1987; Horiuchi and Beacom, 2010). Altogether, it will provide us with an unique opportunity to study the inner dynamics of a CCSN. In particular, neutrinos and GWs will probe the explosion mechanism. Existing and planned neutrino detectors like Super-Kamiokande (SK), IceCube, Jiangmen Underground Neutrino Observatory (JUNO), Hyper-Kamiokande (HK), and Deep Under-

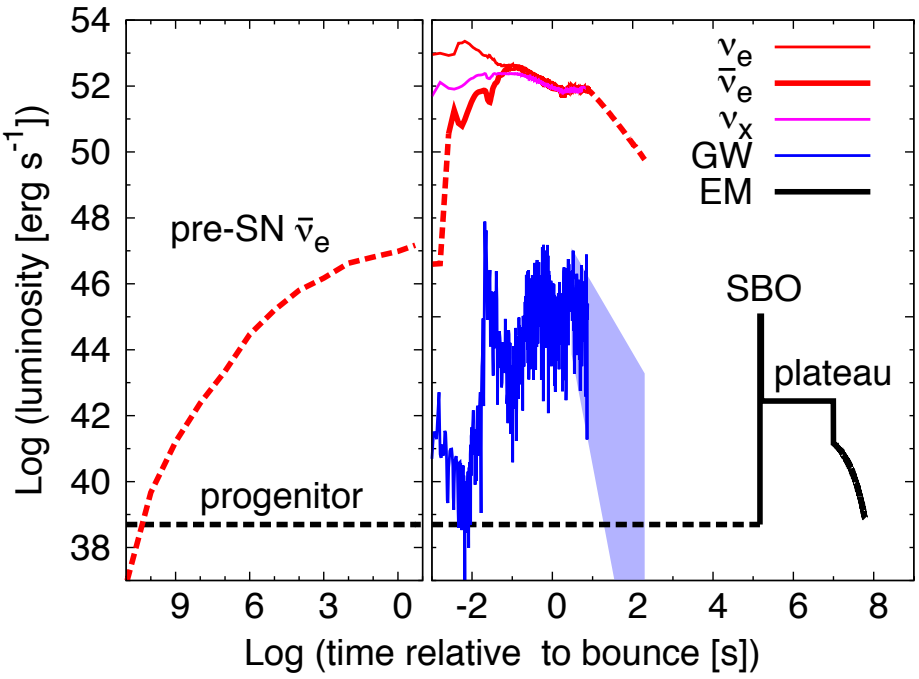

Figure 2.6: Various messengers from a CCSN with time at which they are emitted. Figure taken from Nakamura *et al.* (2016).

ground Neutrino Experiment (DUNE), will see the neutrino signals with high statistics from a galactic scale ($D \leq 10$ kpc) CCSN. Current and next generation GW detectors like Advanced LIGO (ALIGO), Advanced VIRGO, KAGRA and the einstein Telescope (ET) have the potential to see the GWs from a nearby CCSN.

Recent numerical simulations have shown that neutrinos are emitted even prior to the collapse of a massive star during the advanced stages of nuclear burning. These neutrinos called presupernova neutrinos (see Sec. 2.3.1) have been shown to be detectable at the upcoming neutrino detectors (Odrzywolek *et al.*, 2004b; Patton *et al.*, 2017a). This right away helps in using the presupernova neutrino signatures as an early warning system for a CCSN. An early warning system would give enough time to make the necessary preparations for observing the other messengers from a CCSN including the supernova neutrinos. Moreover, the presupernova neutrinos (see

chapter 3) and supernova neutrinos (Vogel and Beacom, 1999; Tomas *et al.*, 2003) can be used for pointing to the collapsing star. This is valuable information since it enables the telescopes to see the shock breakout (SBO) emission photons as a bright flash of ultraviolet and X-rays. Due to the short duration of SBO, it is quite challenging to detect it and knowing the approximate location definitely definitely increases the detection prospects of the emitted photons.

Extensive research has been conducted in studying CCSNe using the various multi-messenger channels. A detailed investigation of utilizing a joint analysis of GW and neutrino data, in the context of failed CCSNe can be found in Leonor *et al.* (2010). The connection of SBO to multimessenger observations has been discussed in Kistler *et al.* (2013). The importance of neutrino warning and pointing for observing the early CCSN light curve is the focus of Adams *et al.* (2013). In chapter 4, we discuss in detail the observation of GWs sourced by supernova neutrino emission, which is another example of a multi-messenger observation giving us key information about stellar dynamics during the collapse. In fact, these GWs can then be used as triggers to detect clean supernova neutrino samples from $\mathcal{O}(100)$ Mpc, which can provide valuable insights into CCSN theory. This is discussed extensively in chapter 5. More details on multi-messengers from CCSN simulations can be found in Nakamura *et al.* (2016).

The various multi-messengers from a CCSN are shown in Fig. 2.6 along with the time at which they are emitted. The presupernova neutrino emission (Odrzywolek *et al.*, 2004b), the neutrino burst and gravitational energy release predicted directly from the numerical simulation, and the analytic bolometric light curve of SBO, plateau, and tail signals are shown and labeled in the figure. The neutrino burst luminosity is extrapolated up to 200 seconds based on the gravitational energy release rate from the shrinking protoneutron star. The GW energy emission rate is estimated using

a quadrupole formula (Müller *et al.*, 2013). The height of the curves do not reflect the energy output in each messenger; total energy emitted after bounce in the form of anti-electron neutrino, photons, and GW is $\sim 6 \times 10^{52}$ erg, $\sim 4 \times 10^{49}$ erg, and $\sim 7 \times 10^{46}$ erg, respectively. In this work, we have primarily focused on discussing in detail one of the multi-messengers from a CCSN - neutrinos (Sec. 2.3). We do discuss GW emissions from a CCSN very briefly in Sec. 2.5.

2.3 Neutrinos From A Core-collapse Supernova

Neutrino physics has been largely enriched by the study and detection of supernova neutrinos - neutrinos emitted as a result of a core-collapse supernova. Copious amounts of these neutrinos are produced and emitted during the process of a CCSN. Around 99% of the gravitational binding energy of the star $\sim 3 \times 10^{53}$ ergs is emitted in neutrinos of average energy 10 MeV. The number of neutrinos emitted $\sim 10^{58}$, is an order of magnitude higher than the lepton number of the collapsed core. This makes neutrinos one of the best messengers from a CCSN, providing crucial information about the inner dynamics and the various stages of evolution of a CCSN. Let us now discuss, the various stages of a CCSN including its dynamics.

2.3.1 Precollapse Phase

Massive stars evolve through nuclear burning of elements in the periodic table starting from hydrogen. In the advanced stages, they have a onion-shell like structure as shown in Fig. 2.7. When carbon burning begins, the star's energy loss is dominated by neutrino emission. The neutrinos have a very fast diffusion timescale which in turn speeds up the advanced nuclear burning stages, generally occurring within months or hours before the star collapses and explodes to a supernova or implodes to form a black hole. The neutrinos from the advanced stages have never been

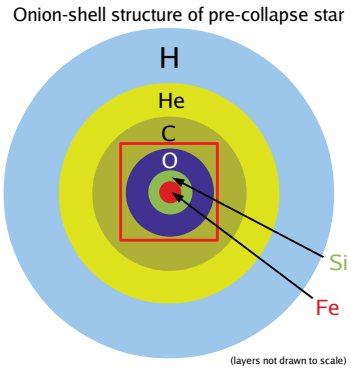

Figure 2.7: Schematic onion-shell structure of a supernova progenitor star before core collapse. Only the main elemental constituents of the different composition shells, which contain the products and ashes of the sequence of nuclear burning stages, are indicated. Note that the radial thickness of the layers is not drawn to scale.

observed, however the next generation neutrino detectors provide new opportunities to observe them. If observed these neutrinos would provide us with valuable information facilitating understanding of the interiors of the star leading to collapse. This also has a multi-messenger aspect to it since the progenitor about to collapse has been observed in the electromagnetic band.

We will mainly focus on the neutrino emission mechanism in the precollapse phase. The neutrinos emitted in the precollpase phase are known as presupernova neutrinos. Studies on presupernova neutrino emission began in the early 2000. The fact that next generation neutrino experiments can detect a presupernova neutrino flux from nearby ($\sim$ 1 kpc) massive stars was was shown in Odrzywolek *et al.* (2004a,b); Kutschera *et al.* (2009); Odrzywolek and Heger (2010). The various production mechanisms involved in the stellar core, for example, thermal processes were studied in detail in Ratkovic *et al.* (2003); Dutta *et al.* (2004); Misiaszek *et al.* (2006); Odrzywolek (2007). The state of the art numerical simulations for obtaining the time-independent presupernova neutrino flux on earth was done by Kato *et al.* (2015, 2017); Yoshida *et al.* (2016); Patton *et al.* (2017b,a); Patton *et al.* (2019). Another main production

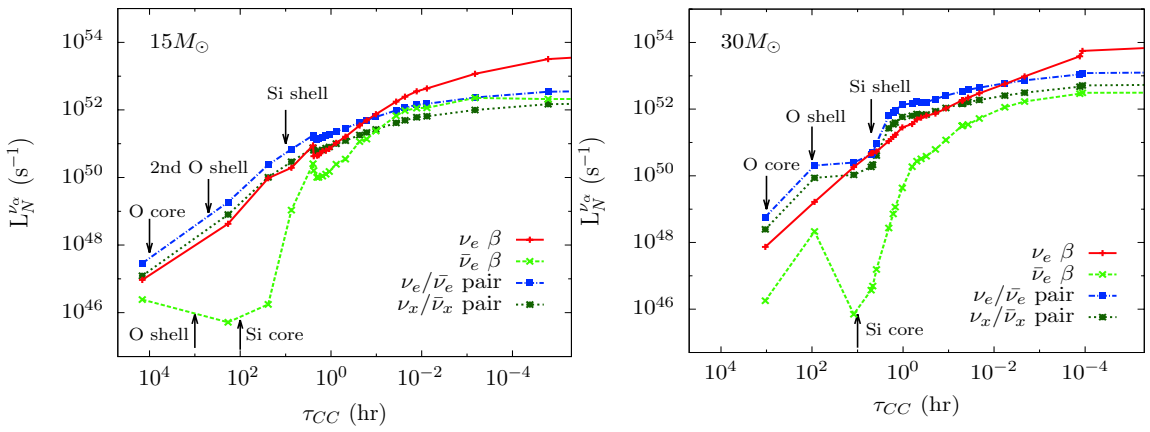

Figure 2.8: The time evolution of the presupernova neutrino luminosities for different production channels for the cases of 15 $M_\odot$ an 30 $M_\odot$ respectively. τ_{CC} is the time to core-collapse in hours. The arrows indicate approximate times of ignition for the different fuels. Figure taken from Patton *et al.* (2017a).

process for presupernova neutrinos is $\beta-$processes. For these processes, the development has been comparatively slow. Dedicated studies were initially performed in Odrzywolek (2009); Odrzywolek and Heger (2010). More recent detailed studies has been done in Patton *et al.* (2017b), which also included state of the art simulations of the neutrino emissivity in these processes. Below, we discuss the major processes in the stellar interiors that lead to the production of presupernova neutrinos. The following section are based on Patton *et al.* (2017b,a).

Presupernova neutrino production

Around a 1000 years prior to collapse, the fusion of heavy elements begin in the stellar core. Carbon is fused leading to a increase in temperature and density, followed by the subsequent fusion of Ne, O and Si. The hot and dense environment during these last stages produce abundant amounts of neutrinos through various processes. The main processes involved are discussed below and the total presupernova neutrino luminosity

due to these processes[1] is shown in Fig. 2.8 for the case of 15 $M_\odot$ and 30 $M_\odot$ stars.

- **Thermal processes**

  - Plasmon decay: $\gamma^* \rightarrow \nu_\alpha + \bar{\nu}_\alpha$

    This is defined as a process in which an excitation in the plasma called a plasmon, decays into a neutrino-antineutrino pair. These dominate the emissivity at high densities. Further details of this process can be found in Itoh and Kohyama (1983); Ratkovic *et al.* (2003); Odrzywolek (2007); Asakura and KamLAND Collaboration (2016).

  - Photoneutrino production: $e^\pm + \gamma \rightarrow e^\pm + \nu_\alpha + \bar{\nu}_\alpha$

    This is basically the photoproduction of neutrino pairs. The charged current W - exchange channel produces only ν_e and $\bar{\nu}_e$, whereas the neutral Z - exchange results in pairs of all three neutrino (e, μ, and τ) flavors. The photoneutrinos dominate the total emissivity at a few loations in the outer shells of the star. This process is discussed in detail in Dutta *et al.* (2004).

  - Pair annihilation: $e^+ + e^- \rightarrow \nu_\alpha + \bar{\nu}_\alpha$

    The neutrinos from this process are emitted from the centre of the star where the temperature and density are the highest. This is one of the dominant channels in the late time presupernova neutrino emission. Fig. 2.8 shows the total neutrino luminosity from $\nu/\bar{\nu}_e$ pair annihilation (blue, dot dashed line) and $\nu_x/\bar{\nu}_x$ where, $x = \mu, \tau$ pair annihilation (dark green, dotted line). More details about this process can be found in Misiaszek *et al.* (2006).

- **Beta processes**

[1]Since the thermal processes except pair annihilation is subdominant at late times, they are not shown in the plot.

- $\beta^{\pm}$ decay: $A(N,Z) \rightarrow A(N-1,Z+1) + e^{-} + \bar{\nu}_e$

  $A(N,Z) \rightarrow A(N+1,Z-1) + e^{+} + \nu_e$

- Positron (e^{+}) capture: $A(N,Z) + e^{+} \rightarrow A(N-1,Z+1) + e^{-} + \bar{\nu}_e$

- Electron (e^{-}) capture: $A(N,Z) + e^{-} \rightarrow A(N+1,Z-1) + e^{-} + \nu_e$

The late time neutrino emission is completely dominated by the beta processes and pair annihilation. The contribution of thermal processes discussed above is subdominant. The rates for the beta processes can be found in Fuller *et al.* (1980, 1982b,a, 1985); Oda *et al.* (1994); Martinez-Pinedo *et al.* (2000). A much more recent attempt at modeling the $\beta-$processes was done by Patton *et al.* (2017b).

We now discuss Fig. 2.8 in detail, especially focusing on the features of the pair annihilation and beta processes and comparing the two for the 15 $M_{\odot}$ and 30 $M_{\odot}$ models. The important features are listed below:

- A general remark is, the ν_e luminosity from the $\beta-$processes grows faster than that of the thermal processes. Quantitatively speaking, for the 15 $M_{\odot}$ case (Fig. 2.8, left), it is $\sim 30\%$ of the contribution from pair annihilation when oxygen burning occurs, it becomes comparable to pair annihilation at ~ 6 minutes prior to collapse, finally at the onset of collapse it is an order of magnitude more than the pair annihilation contribution. For the 30 $M_{\odot}$ case (Fig. 2.8, right panel), the contribution the numbers are $\sim 10\%$, 7 s prior to collapse and 30% greater at the onset of collapse.

- The $\bar{\nu}_e$ luminosity from the $\beta-$ processes traces the phases of the stellar evolution closely. It suffers a drop after oxygen burning ends in the core. It starts increasing once again as silicon burning starts.

- At the start of core-collapse $\beta-$ processes contribute $\sim 40\%$ of the pair processes

for the 15 $M_\odot$ case and $\sim 20\%$ for the 30 $M_\odot$ case.

- Towards the end (the last few hours prior to collapse), the neutrino luminosity from pair annihilation increases at a comparatively slow rate. This can be understood by the fact that neutrino production in pair annihilation is independent of density for a fixed temperature. Thus the slow rate increase is because of the corresponding slow increase in the temperature.

- For the 15 $M_\odot$ model (Fig. 2.8, left panel), one can notice a short sharp drop in the neutrino luminosities for all species. This occurs shortly after shell silicon-burning begins and is followed by a smooth increase. The profiles for the 30 $M_\odot$ star are smoother. This can be understood by the core carbon burning phases, which proceeds convectively for the 15 $M_\odot$ model and radiatively for the 30 $M_\odot$ model.

An important thing to note is, the features of the neutrino luminosity and processes discussed above is in general agreement with that observed from other works like . But there are slight differences leading to higher presupernova neutrino luminosity in some models than others. This leads to certain models being more optimistic than others.

2.3.2 CCSN Dynamics

Decades of scientific research and hard work has gone into understanding the dynamics of a CCSN. The process is extremely non-trivial, requires very high computational power to perform simulations and requires theoretical concepts from general relativity, fluid hydrodynamics, nuclear physics to name a few. Numerous dedicated studies and reviews exist on the topic. A selected few include: Woosley and Weaver (1986); Janka *et al.* (2002); Woosley *et al.* (2002); Woosley and Janka (2005); Janka

et al. (2012); Scholberg (2012); Pejcha and Thompson (2012); Janka *et al.* (2016); Janka (2017); Müller (2019); Burrows and Vartanyan (2021) and references therein. This section provides a mini-review, especially focusing on the elements we would require for the subsequent chapters. The review is based on Janka (2017) and Giunti and Kim (2007).

The various stages in the evolution of a CCSN is discussed below. Since we are concerned with the neutrino emission, our main focus would be on the different neutrino emission phases.

The beginning of core-collapse:

Massive stars go through nuclear burning from hydrogen all the way to iron. Finally, the core is constituted of iron and is surrounded by concentric shells of lighter elements as shown in Fig. 2.7. The subsequent burning of shells leads to a further increase in the mass of the core until gravitational instability finally sets in. The core reaches the Chandrashekhar mass with a diameter off $\sim$ 3000 km, a central temperature of $\sim$ 1 MeV and a central density of $\sim 10^9$ g/cm^3. At this point, the thermal γ photons partially disintegrate the iron-group nuclei to produce α-particles and free nucleons. This leads to the conversion of thermal energy to overcome the binding energy of the nucleons in heavy nuclei. This process is endothermic and lowers the effective adiabatic index below a critical value. In other words, now, the increase in density leads to a reduction of pressure. As density keeps increasing, electron captures on nuclei becomes dominant, which leads to loss in lepton number by the production and escape of electron neutrinos. This causes even more loss of pressure and the collapse accelerates. See, Fig. 2.9 top left panel.

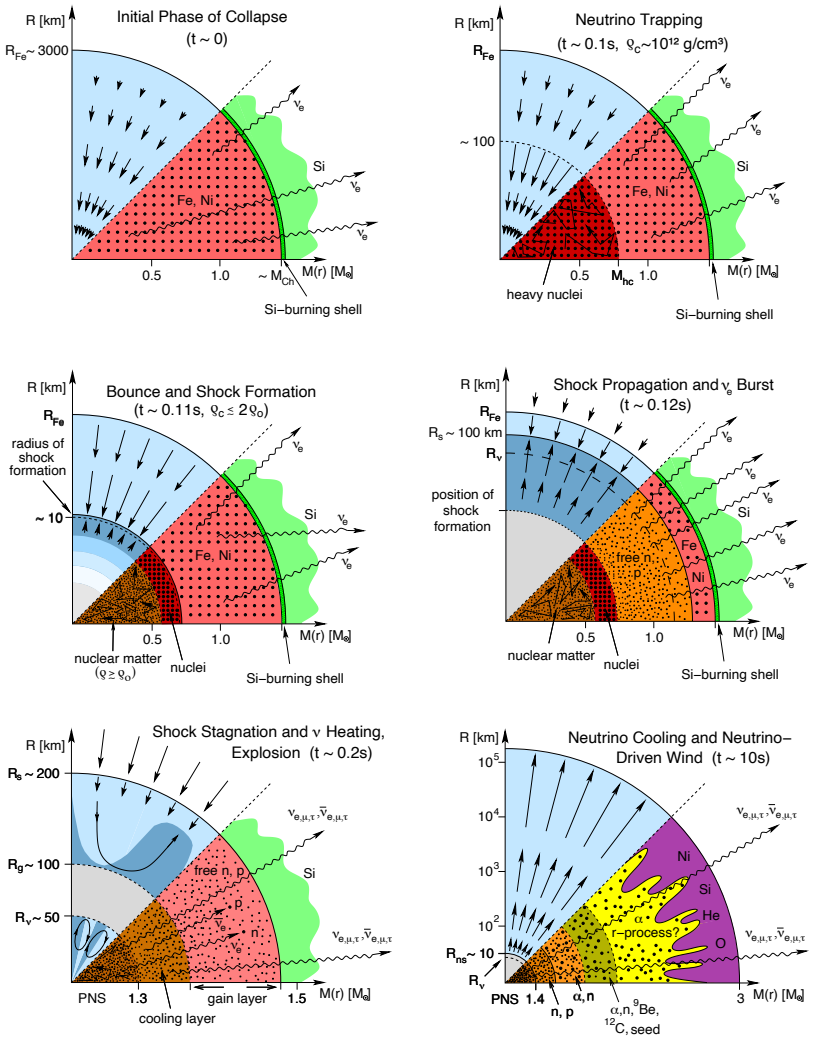

Figure 2.9: Schematic representation of the evolutionary stages from stellar core collapse through the onset of the supernova explosion to the neutrino-driven wind during the neutrino-cooling phase of the proto-neutron star (PNS). The panels display the dynamical conditions in their upper half, with arrows representing velocity vectors. The nuclear composition as well as the nuclear and weak processes are indicated in the lower half of each panel. The horizontal axis gives mass information. MCh means the Chandrasekhar mass and Mhc the mass of the subsonically collapsing, homologous inner core. The vertical axis shows corresponding radii, with R_{Fe}, R_s, R_v, R_g, and R_{ns} being the iron core radius, shock radius, gain radius, neutron star radius, and neutrinosphere, respectively. The PNS has maximum densities ρ above the saturation density of nuclear matter (ρ_0). Figure taken from Janka *et al.* (2007).

The trapping of neutrinos:

When the density of the collapsing core exceeds $\sim 10^{11}\text{g/cm}^3$, neutrinos begin to get trapped in it. The neutrino production by electron captures still happening, are swept inward with the in-falling matter (see Fig. 2.9 top right panel). The outer core collapse which is supersonic accelerated to nearly free fall. The inner core which is subsonic implodes with a velocity proportional to its radius.

The bounce of the core and formation of the shock:

If we focus on the inner core, within milliseconds after neutrino trapping, the center reaches nuclear densities of order 10^{12}g/cm^3. Matter at such high densities have been shown to be incompressible due to the repulsive nuclear forces. This results in the inner core-collapse coming to an abrupt stop followed by it bouncing back. This bounce shock begins to move outwards against the outer core - the overlying iron-core material. See Fig. 2.9 middle left panel.

The propagation of the shock and the neutronization burst at the shock breakout:

A huge production of ν_e as a result of electron capture on free protons continues behind the outer moving shock front. The dense post shock matter however forces them to stay trapped. When the shock reaches low densities, the ν_e diffuse faster than the shock propagates. At this point, the breakout burst - a luminous flash of ν_e, is emitted. See Fig. 2.9 middle right panel.

The stagnation of the shock and the revival by neutrino heating:

The initial high mass accretion rate leads to the accumulation of a thick layer of dense matter behind the shock. The decay of this mass accretion rate, combined

with the energy loss through neutrinos leads to the radial shock coming to a stop. This happens around a radius of 100 km - 200 km and has an enclosed mass of 1 $M_{\odot}$. Note that this is still well within the collapsing iron core. Thus, the bounce-shock mechanism essentially fails to generate supernova explosion.

A lot of research has been dedicated to understand the shock revival mechanism. Here, we will discuss the one that is most widely accepted - the intense neutrino flux from the nascent neutron star re-energizes the shock against the pressure of the collapsing surrounding stellar core. This is done by ν_e and $\bar{\nu}_e$ captures on free nucleons. Numerical simulations show non-radial hydrodynamic instabilities like convection, standing accretion-shock instability (SASI), and non-spherical flows are crucial for the explosion. This is of utmost importance to us, since these anisotropies in the progenitor are important reasons for CCSNe to be an excellent source to study the *gravitational wave memory effect*. This is discussed in detail in Sec. 2.4.3 and also in chapter 4. As a last remark, before the re-acceleration of the shock, the shock feeds a massive accretion flow onto the neutron star. The hot mantle around the neutron star emits large amounts of ν_e and $\bar{\nu}_e$. The luminosity in this accretion phase adds to the emission of all species of neutrinos and antineutrinos. See, Fig. 2.9, bottom left panel.

The cooling of the proto-neutron star (PNS) and the neutrino driven wind:

Accretion time scales vary depending on various properties of the progenitor star. It can be sustained for $\sim 100 - 1000$ ms by the newly formed neutron star. The end of this phase is marked by the gradual decrease of the speed of shock expansion and finally the PNS entering the cooling phase. The remaining gravitational binding energy is lost by the PNS by emission of neutrinos and anti-neutrinos of all flavors. The PNS cools by neutrino losses. These neutrinos deposit their energies on the outer

cooler layers which lead to a continuous dilute outflow of mass from the neutron star surface. This phenomenon is known as neutrino-driven wind (See Fig. 2.9, bottom right panel).

2.3.3 Failed Supernova

We discussed the probable shock revival mechanism and how it aids in re-energizing the shock which is crucial for a *successful* CCSN explosion. Such explosions form a compact object as a neutron star and are called *neutron star forming collapses (NSFCs)*.

In some cases, it is possible that the shock wave produced during the collapse followed by bounce of the core is not sufficiently energetic to eject its mantle (Burrows, 1986; O'Connor and Ott, 2011). Failure to revive the stalled shock leads to the supernova being "absorbed" and forming a black hole. These *unsuccessful* CCSNe, that implode into a black hole are known as *black hole forming collapses (BHFCs)* or *failed supernovae*. A failed supernova may be the outcome of -

1. a weak CCSN fallback accretion pushes the nascent neutron star over its Chandrashekhar mass limit,

2. nuclear phase transitions during the PNS cooling phase or the cooling phase leading to a reduced pressure support in a hyper-massive PNS,

3. the CCSN mechanism lacking efficacy and failing to revive the shock, where continued accretion pushes the PNS over its maximum possible Chandrashekhar mass.

An important thing to note is the formation of the BH in no circumstance is prompt. Prior to the BH formation, there is the extended PNS phase which produces large

amounts of neutrinos before it is engulfed by the BH horizon. There has been extensive theoretical work (O'Connor and Ott, 2011; Ugliano *et al.*, 2012; Sukhbold *et al.*, 2016) and observational evidence (Gerke *et al.*, 2015; Smartt, 2015; Adams *et al.*, 2017a,b) for BHFCs.

Observationally, BHFCs emit a faint electromagnetic (EM) signal which originates from the stripping of the hydrogen core. This weak (dim) signal may be difficult to detect using the EM channel, thus neutrinos and GWs may be our best bet for their detections. It is currently unclear what percentage of progenitors lead to NSFCs and BHFCs. This is a topic of extensive research. It is expected anywhere between $10\% - 40\%$ of all CCSNe end up forming a BH.

The neutrino emission properties from a failed CCSN is discussed in Sec. 2.4.5. The BHFCs will be relevant for this work in the context of gravitational wave memory in chapters 4 and 5.

2.4 Phases And Properties Of CCSN Neutrino Emission

We discuss the various phases and properties of neutrino emission corresponding to the various stages of the CCSN dynamics discussed in Sec. 2.3.2. The main phases of CCSN neutrino emission are: a) presupernova neutrino emission phase, b) the neutronization burst, c) the accretion phase, and d) the cooling phase. A schematic diagram illustrating the different phases is shown in Fig. 2.10, which also depicts the time scales involved.

2.4.1 Presupernova Neutrino Emission

We discuss the presupernova neutrino energy spectra in this section. In Fig. 2.10 this is neutrino emission curve shown before $\text{Time}_{\text{post-bounce}} = 0$. Fig. 2.11 shows the number luminosities differential in energy for each neutrino species st seven different

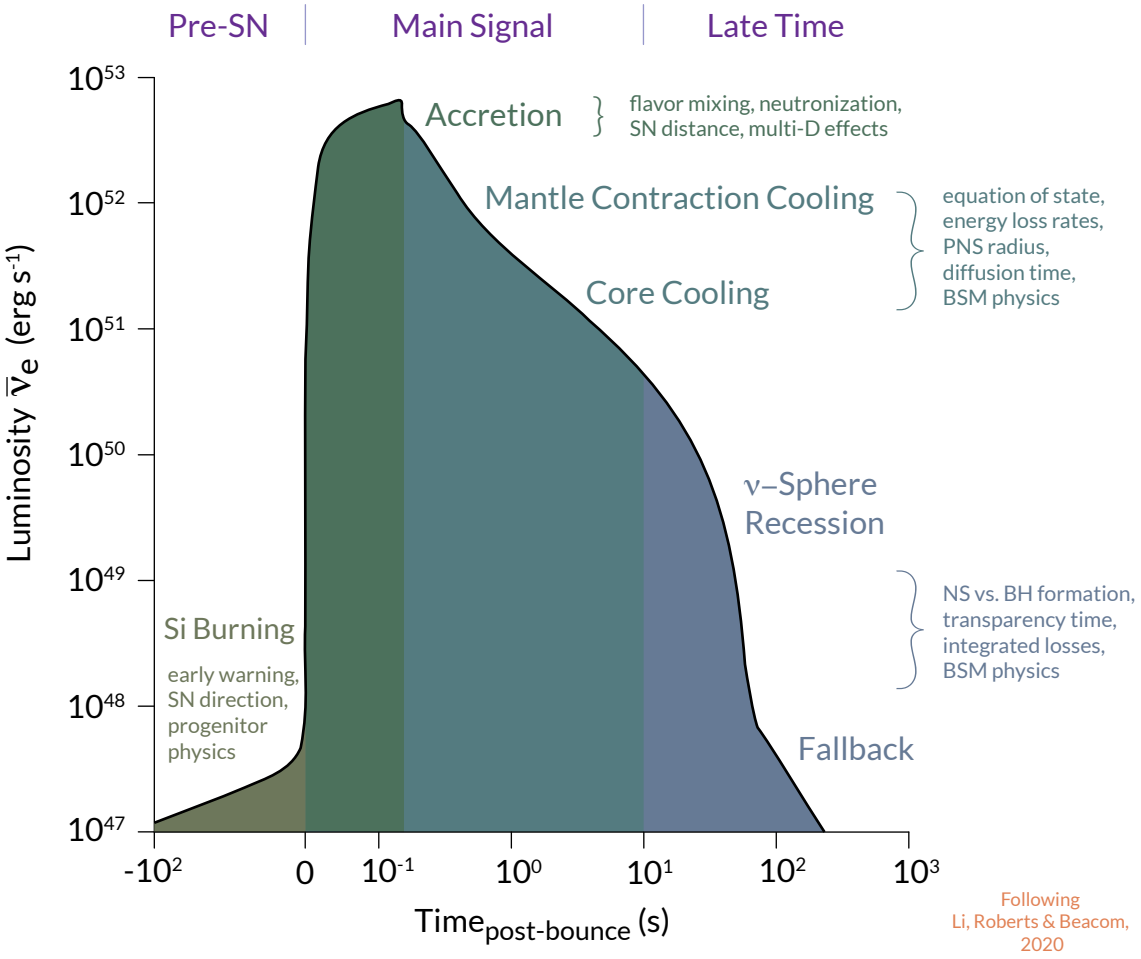

Figure 2.10: Schematic figure showing the neutrino luminosity as a function of time for the various neutrino emission phases namely: the presupernova neutrinos, the main burst signal, the late time cooling phase neutrinos. The figure is based on Li *et al.* (2020). Credits: Prof. Frank Timmes (SESE, ASU).

instances in the evolution. The top panel shows the number luminosity for ν_e, middle panel for $n\bar{u}_e$ and the bottom panel for ν_x. The percentage of ν_e and $\bar{\nu}_e$ luminosities from $\beta-$ processes is shown in the smaller panels. The main thing to note from the figure is the pre-supernova neutrinos are *low energy* neutrinos with energy peaked at around $1-3$ MeV. In particular the ν_e spectrum is always dominated by $\beta-$processes beyond 4 MeV. The $\bar{\nu}_e$ production from $\beta-$processes is lower. One of the reasons for this is the lower number density of positrons (relative to electrons) available for

capture.

Presupernova neutrino flux and detection

One of the most interesting things about presupernova neutrinos is they will be detectable on earth for a nearby ($\leq$ 1 kpc) star. In fact, this is one of the integral aspects that chapter 3 is based on. Therefore, it is important to discuss the expected flux of presupernova neutrinos on earth. Just as before, we will restrict our discussion to the Patton *et al.* (2017a) model. The flavor of presupernova neutrinos change while they propagate from the star to earth due to neutrino oscillations (see Sec. 1.4 for details). Thus, for doing an analysis of presupernova neutrino detection prospects, it is important to take those into account. Fig. 2.12 shows the presupernova neutrino flux on earth for a star at $D = 1$ kpc at different instances in time. The two cases in consideration are the 15 $M_\odot$ and 30 $M_\odot$ models. Both the normal and inverted hierarchy is shown (see Sec. 1.5 for details). These fluxes do take into neutrino oscillation while they propagate but ignore oscillation effects like collective oscillations in the stellar system and earth matter effects. It can be shown that these oscillation effects are safe to be ignored (Patton *et al.*, 2017a). Fig. 2.12 also shows the relevant backgrounds for each case. It is evident that for ν_e presupernova neutrino flux the most significant background is the solar neutrino flux (see Sec. 1.6 for details on different neutrino sources) and that for the $\bar{\nu}_e$ is the reactor and geoneutrino fluxes. Other irrelevant backgrounds include the DSNB and atmospheric neutrinos.

A striking feature that can be observed from the figure is, around 2 hours prior to collapse the ν_e presupernova neutrino flux dominates over the background flux. This is what ensures that the prospect of detection of presupernova neutrinos is possible. The flux increases as the time of collapse nears, implying the chances of detection go up with time. The inverted hierarchy has a slightly higher ν_e flux as compared to

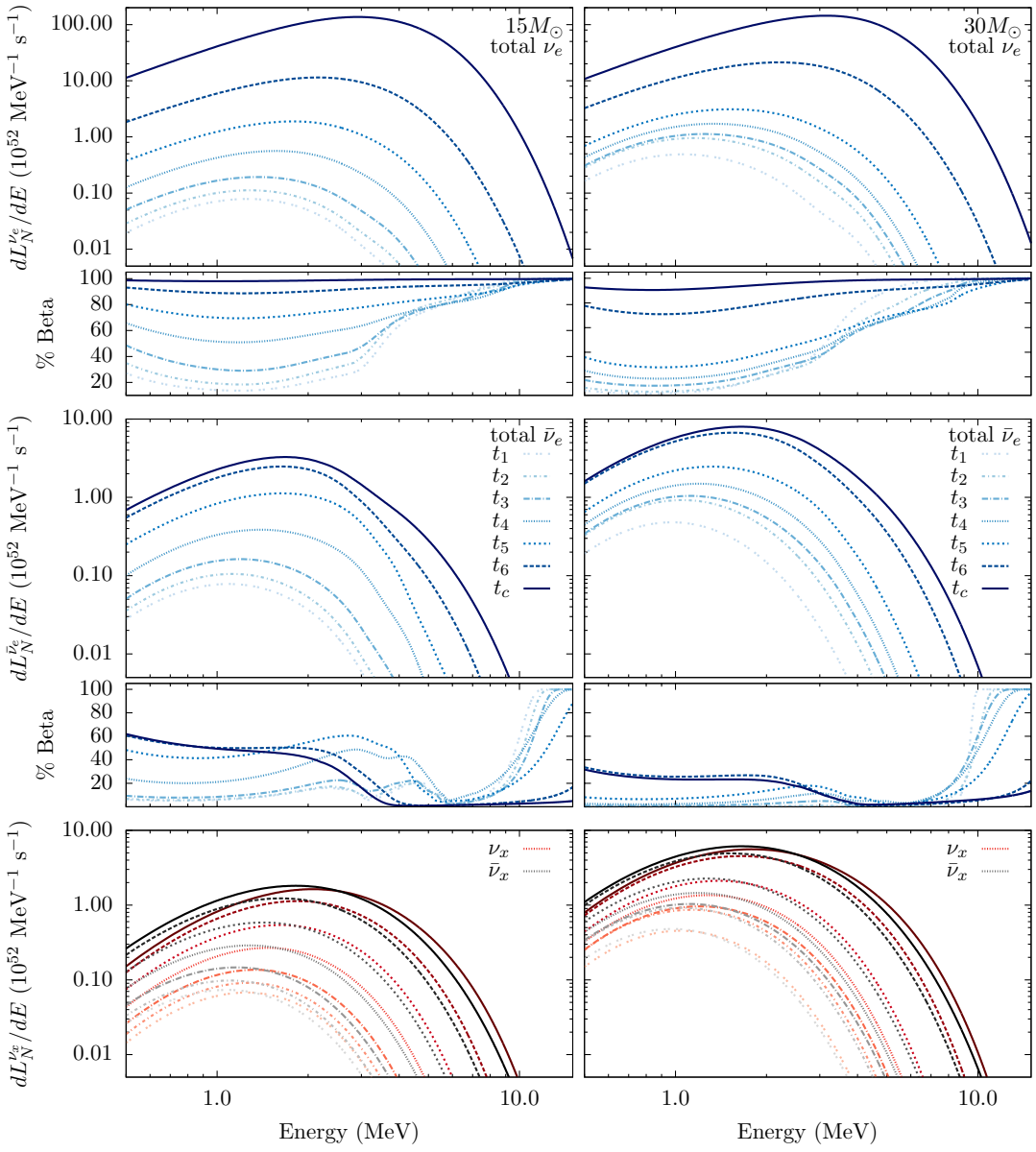

Figure 2.11: The presupernova neutrino spectra at selected times prior to collapse for 15 $M_\odot$ and 30 $M_\odot$ models. Each set of curves shows times t_1 through t_c (lower to upper curves), where t_c is the time of collapse. Figure taken from Patton *et al.* (2017a).

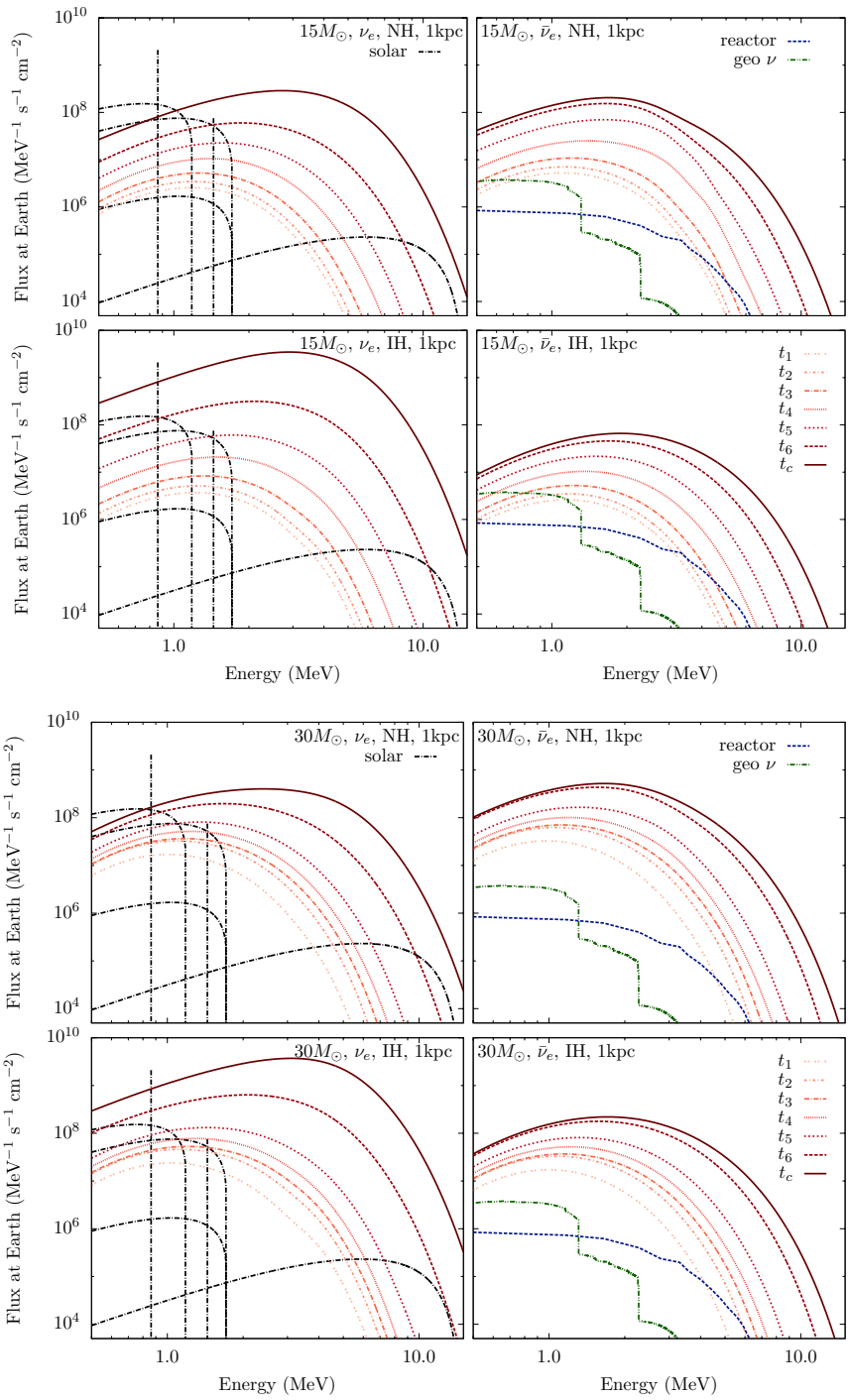

Figure 2.12: The flux of ν_e and $\bar{\nu}_e$ expected at earth for the 15 $M_\odot$ and 30 $M_\odot$ cases located at $D = 1$ kpc from earth. Each set of curves shows times t_1 through t_c (lower to upper curves), where t_c is the time of collapse. Both the normal and the inverted hierarchy cases are shown. Neutrino oscillations are taken into account. Figure taken from Patton *et al.* (2017a).

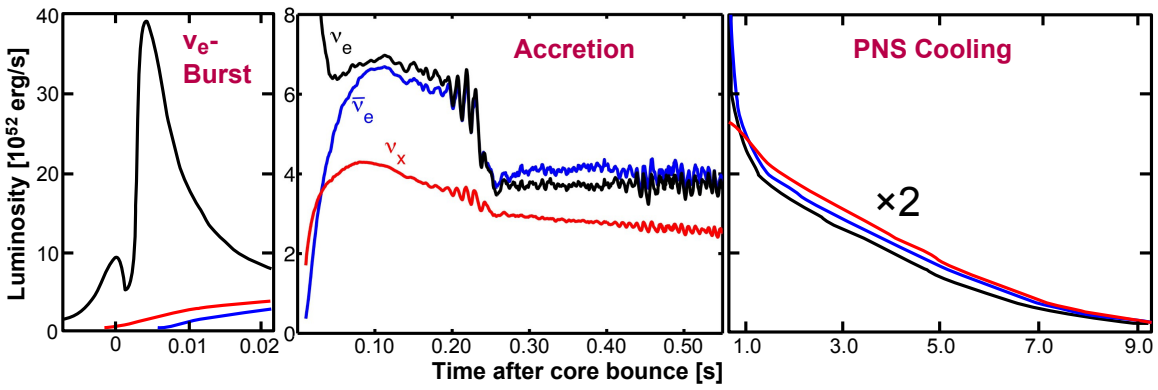

Figure 2.13: Neutrino luminosities (ν_e: black; $\bar{\nu}_e$: blue; ν_x as one species of ν_μ, $\bar{\nu}_\mu$, ν_τ, $\bar{\nu}_\tau$: red) during the main neutrino-emission phases. The *left panel* shows the prompt burst of electron neutrinos associated with the moment of shock breakout into the neutrino-transparent outer core layers only milliseconds after bounce ($t = 0$). The *middle panel* corresponds to the post-bounce accretion phase before shock revival as computed in a three-dimensional simulation (see Tamborra *et al.*, 2014). The quasi-periodic luminosity variations are a consequence of modulations of the mass-accretion rate by the neutron star caused by violent non-radial motions due to hydrodynamic instabilities (in particular due to the standing accretion-shock instability or SASI) in the post-shock layer. The *right panel* displays the decay of the neutrino luminosities over several seconds in the neutrino-cooling phase of the newly formed neutron star (the plotted values are scaled up by a factor of 2). Figure taken from Janka (2017).

the normal hierarchy. The prospects of detection considerably go up for the 30 $M_\odot$ progenitor owing to its higher presupernova neutrino luminosity. Similarly the $\bar{\nu}_e$ flux, also dominates over the background as time to collapse reduces.

Finally, let us discuss the main types of neutrino detectors that would see the presupernova neutrino flux. These include: liquid scintillator, water Cherenkov and liquid argon detectors (See Sec. 1.7 for details on types of neutrino detectors). The dominant channels for water Cherenkov and liquid scintillator detectors is IBD and for liquid argon detectors it is ν_e charged current scattering on Argon nuclei (see Sec. 1.3 for details about neutrino interactions). Overall, IBD is the most optimistic detection channel for presupernova neutrino because of its extremely low energy threshold ($\sim$ 1.8 MeV). Thus, a next generation liquid scintillator detector like JUNO (An, 2016) is the best candidate for presupernova neutrino detection.

2.4.2 The Neutronization Burst

Let us now discuss, the neutrino emission happening after the core-collapse, $\text{Time}_{\text{post-bounce}} > 0$. The sharp peak in neutrino luminosity, signifying a highly luminous flash of neutrinos is known as the neutronization burst (see Fig. 2.13, left panel). These neutrinos are radiated when the shock transitions from opaque to a neutrino-transparent layer in the iron core. This occurs at ~ 2 ms post-bounce. The peak neutrino luminosity reached is $\sim 4 \times 10^{53}$ ergs/s resulting in an energy release of $\sim 2 \times 10^{51}$ ergs within ~ 20 ms. The ν_es that are produced in large quantities due to efficient electron capture on free protons escape. The mean energy of the radiated ν_es is $\sim 12 - 13$ MeV. From, Fig. 2.13 (left panel) we notice two other important features: the initial rise in the ν_e luminosity before the core bounce, and the small dip just before the burst. The former is caused due to increasingly efficient electron capture due to increased core density because of compression, and the latter due to strong compression and Doppler redshifting of the main ν_e region.

2.4.3 The Accretion Phase

This phase follows the neutronization burst. The ν_e luminosity decreases with time post-bounce and forms a plateau (See Fig. 2.13, middle panel). The charged current processes in the hot mantle of the PNS produce large amounts of ν_e and $\bar{\nu}_e$. As seen in the figure, the ν_e and $\bar{\nu}_e$ luminosities are identical during this phase.[2] The luminosities of ν_x is low owing to the fact that they are produced in the denser core region. The neutrino emission luminosities in this phase are highly sensitive to two important quantities - a) the mass accretion rate and b) the mass of the PNS. It has been shown that more compact stars (which also implies higher mass) have higher

[2]There is a slight excess in the ν_e luminosity due to deleptonization.

neutrino luminosities and harder neutrino spectra (Qian and Woosley, 1996; Otsuki *et al.*, 2000; Thompson *et al.*, 2001; Arcones *et al.*, 2007). The mean energy increases in this phase, for all species and is steeper for ν_e and $\bar{\nu}_e$ than for ν_x. The mean energy is given by the proportionality, $\langle E_\nu \rangle \propto M_{ns}(t)$, where, M_{ns} is the mass of the PNS. The luminosities of the muon and tau neutrinos in the accretion phase can be estimated as a Stefan-Boltzmann like formula,

$$L_{\nu_x} = 4\pi\phi s_\nu R_{ns}^2 T_\nu^4 \,, \tag{2.1}$$

where, ϕ is a greyness factor obtained from numerical simulations (Müller and Janka, 2014) and ranges from $\sim 0.4 - 0.85$, $s_\nu = 4.50 \times 10^{35}$ erg MeV^{-4}cm$^{-2}s^{-1}$ for a single ν_x species, the effective spectral temperature T_ν is related to the average energy as $\langle E \rangle = 3.15 T_\nu$, and R_{ns} is the radius of the PNS. The sum of ν and $\bar{nu}_e$ luminosities is given by,

$$L_{\nu_e} + L_{\bar{\nu}_e} = 2\beta_1 L_{\nu_x} + \beta_2 \frac{G M_{ns} \dot{M}}{R_{ns}} \,, \tag{2.2}$$

where, $\beta_1$andβ_2 are obtained using statistical methods and are around unity, L_{ν_x} is given in Eq. 2.1, M_{ns} is the mass of the PNS, and $\dot{M}$ is the mass accretion rate of the PNS.

The appearance of anisotropies in neutrino luminosity

We discussed the appearance of non-radial instabilities in Sec. 2.3.2. These instabilities develop during the accretion phase since they require finite time to develop post-bounce. This results in large-scale modulations of the accretion flow onto the PNS, which leads time and *direction dependent*, large amplitude, quasi-periodic fluctuations of the neutrino luminosities and mean energies (Lund *et al.*, 2012; Tamborra *et al.*, 2013, 2014). The final result of this is an anisotropic (direction-dependent) neutrino emission. These may be caused by:

- rotationally deformed PNSs (Müller *et al.*, 2004; Kotake *et al.*, 2006; Dessart *et al.*, 2006)
- convective overturn and SASI (Mueller and Janka, 1997a; Müller *et al.*, 2004; Ott *et al.*, 2006; Kotake *et al.*, 2007a)
- global asymmetries in the (precollapse) matter distribution (Burrows and Hayes, 1996; Fryer *et al.*, 2004).

2.4.4 The Cooling Phase

The accretion phase is followed by the cooling phase, which is also called the Kelvin-Helmholtz cooling phase. The transition from accretion phase to cooling phase is gradual. The PNS continues to emit neutrinos of all flavors for $\mathcal{O}(10)$s. All neutrino and antineutrino flavors in this phase have similar luminosities, which keeps declining with time (see Fig. 2.13, right panel). Although, $\bar{\nu}_e$ has a higher mean energy than ν_e to maintain a net lepton number flux out of the PNS. Besides, the mean energies of ν_x is slightly lower than that of $\bar{\nu}_e$ due to recoil energy transfer in the scattering layers. The cooling of the outer layers of the PNS results in the mean energy of the radiated neutrinos also going down with time and the differences shrink. The decline in the neutrino luminosity with time (in seconds) is nearly *exponential*.

The average luminosities during this phase is roughly given by,

$$L^{\nu}_{tot} \equiv \sum_{i=e,\mu,\tau} L_{\nu_i} L_{\bar{\nu}_i} \sim \frac{E_b}{t_E} \sim \text{a few } 10^{52}\ ergs/s\,, \tag{2.3}$$

where, E_b is the binding energy,

$$E_b \sim E_g \approx \frac{3}{5}\frac{GM^2_{ns}}{R_{ns}} \approx 3.6 \times 10^{53} \left(\frac{M_{ns}}{1.5\ M_\odot}\right)^2 \left(\frac{R_{ns}}{10\ \text{km}}\right)^{-1} \text{erg}\,, \tag{2.4}$$

where, E_g is the gravitational energy, M_{ns} and R_{ns} is the mass and radius of the neutron star formed, and $t_E \sim 10$ s is the energy loss time scale. We assume that the

neutron star formed is approximately spherical.

The cooling phase serves as an even better laboratory for nuclear physics than the accretion phase. Various physical conditions deep in the PNS leave their imprints on the neutrino emission in this phase. Furthermore, the neutrino emission in this phase can be used constrain physics beyond the Standard Model. For example, the neutrino signal can be used to place bounds on axion emission (Turner, 1988; Mayle *et al.*, 1988; Raffelt and Seckel, 1988; Janka *et al.*, 1996; Keil *et al.*, 1997), sterile neutrino emission (Raffelt *et al.*, 1996; Esmaili *et al.*, 2014), non-standard neutrino interactions (Esteban-Pretel *et al.*, 2007), and so on. Besides, helping probe the conditions deep within the PNS, the neutrinos in the cooling phase also provide insights into the explosion dynamics. This includes but are not limited to probes of MSW flavor conversions, collective oscillations, etc.

2.4.5 Neutrino Emission From A Failed SN

We discussed the case of a failed supernova or BHFC in Sec. 2.3.3. Here we discuss the neutrino emission properties in case of failed supernovae. Not much is known about the dynamics of failed supernovae, making it a major research area. However, neutrino luminosities can provide some insights into this phenomena. Perhaps the most significant indication of a BHFC is the sharp cut-off in the neutrino luminosities as a result of the PNS forming a BH. This is generally preceded by a gradual rise in the neutrino luminosities and mean energies.[3] The neutrino luminosity and mean energy from a BH forming collapse for a 40 $M_\odot$ and 75 $M_\odot$ model is shown in Fig. 2.14. The neutrino signal terminates at 572 and 250 ms for the 40 $M_\odot$ and 75 $M_\odot$ models respectively, indicating the formation of a BH.

[3]Some works also claim a considerable rise in the neutrino luminosities and mean energies (Fischer *et al.*, 2009).

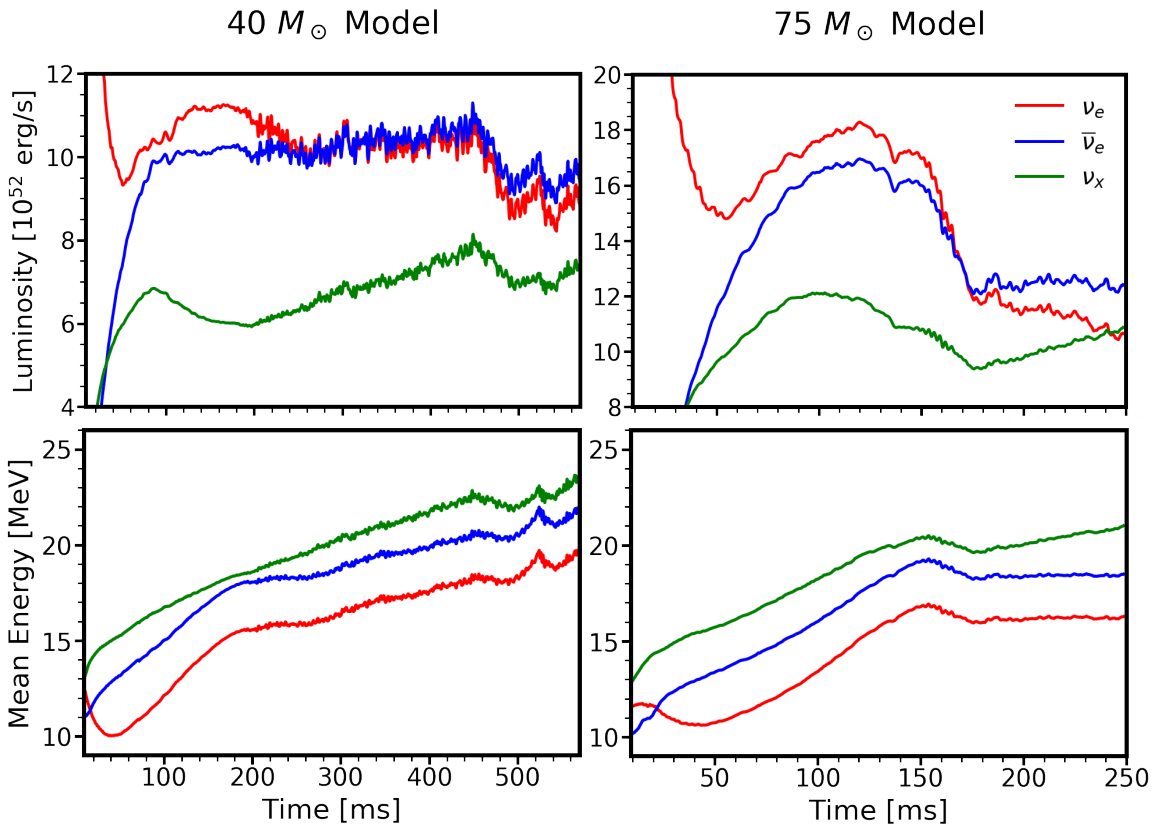

Figure 2.14: *Top panels:* Luminosity of each neutrino flavor ($\nu_e, \overline{\nu}_e$ and ν_x in red, blue, and green, respectively) for the 40 $M_\odot$ (left) and 75 $M_\odot$ (right) models after integrating over all observer directions. *Bottom panels:* Mean energies (i.e., energy flux divided by number flux) of each neutrino flavor as a function of time. The neutrino signal terminates at 572 and 250 ms for the 40 $M_\odot$ and 75 $M_\odot$ models respectively, indicating the formation of a BH. Figure taken from Walk *et al.* (2020a).

An important thing to note regarding BHFCs is they may have high anisotropies in the neutrino emission. This is evident from the right panel in Fig. 2.14 where one can see large amplitude modulations due to strong spiral SASI. This once again develops in the accretion phase. The SASI motions of the postshock layers modulate the accretion flow onto the PNS leading to the large amplitude variations seen in Fig. 2.14 (right panel).

Neutrinos from a BHFC will help resolve major questions in nuclear physics and astrophysics. For example, the neutrino emission and the time of formation of a

BH depend on the equation of state used, properties of the progenitor. Thus more information can be obtained about them. The neutrino signal may also signal the occurrence of a phase transition in the PNS. This is of importance since the phase transition can create a secondary shock which may then be responsible for the explosion (Sagert *et al.*, 2009; Fischer *et al.*, 2018). The signature of this secondary shock would be a *secondary neutrino burst.* Multi-messenger observations can also help in understanding the phenomenon of BHFCs.

2.4.6 Supernova Neutrino Emission Spectra

The supernova neutrino emission spectra can be well approximated by the Fermi-Dirac distribution,

$$f(E) \propto \frac{E^2}{1+\exp\left(E/T-\eta\right)}\,, \tag{2.5}$$

where, T is the temperature of the emission in energy units, and η is an effective degeneracy parameter (Janka and Hillebrandt, 1989)[4]. The proportionality constant is $L/(F((\eta)T^4)$, where, L is the total neutrino luminosity. Thus, the emission spectra can be written as,

$$\begin{aligned} \frac{dN}{dE} &= \frac{L}{F(\eta)T^4}\frac{E^2}{1+\exp\left(E/T-\eta\right)}\,, \\ F(\eta) &= \int_0^\infty dx\ \frac{x^3}{\exp\left(x-\eta\right)+1}\,. \end{aligned} \tag{2.6}$$

A slightly more convenient representation is to parameterize the neutrino spectrum as follows (Keil *et al.*, 2003; Giunti and Kim, 2007; Nakamura *et al.*, 2016),

$$\frac{dN_{\nu_x}}{dE} = \frac{(1+\beta_{\nu_x})^{(1+\beta_{\nu_x})}}{\Gamma(1+\beta_{\nu_x})}\frac{E^{tot}_{\nu_x}}{\langle E_{\nu_x}\rangle^2}\left(\frac{E}{\langle E_{\nu_x}\rangle}\right)^{\beta_{\nu_x}}\exp\left(-\frac{(1+\beta_{\nu_x})E}{\langle E_{\nu_x}\rangle}\right), \tag{2.7}$$

[4]This can also be thought as a chemical potential.

where,

$$
\begin{aligned}
E^{tot}_{\nu_x} &= \int_0^t dt\ L_{\nu_x}(t)\,, \\
\beta_{\nu_x} &= \frac{(2\langle E_{\nu_x}\rangle^2 - \langle E^2_{\nu_x}\rangle)}{(\langle E_{\nu_x}\rangle^2 - \langle E^2_{\nu_x}\rangle)}\,, \\
\langle E\rangle &= \frac{\int dE E(dN/dE)}{\int dE(dN/dE)} \\
\langle E^2\rangle &= \frac{\int dE E^2(dN/dE)}{\int dE(dN/dE)}\,,
\end{aligned}
\tag{2.8}
$$

where, $E^{tot}_{\nu_x}$ is the total energy emitted in a single neutrino species, L_{ν_x} is the luminosity of a single neutrino species, $\langle E\rangle$ is the mean neutrino luminosity, β_{ν_x} is the amount of spectral pinching (spectral shape parameter) for a given neutrino species, computed using the two lowest moments of the spectrum.

A Maxwell-Boltzmann spectrum has $\beta = 2$, a Fermi-Dirac spectrum has $\beta \approx 2.3$ ($\eta = 0$), and a *pinched* Fermi-Dirac spectrum has $\beta \gtrsim 2.3$. Appendix B contains a table with details of the various luminosity parameters of neutrino emission spectra. Fig. 2.15 shows the time-integrated spectra of the supernova neutrino luminosity shown in Fig. 2.13. For this case the integrated spectra follows approximately a Maxwell-Boltzmann distribution. The mean energy as discussed earlier is ~ 10 MeV. The total number of particles emitted is the highest for ν_e (3.2×10^{57}) owing to its highest overall luminosity. This is followed by $\bar{\nu}_e$ (2.4×10^{57}) and then ν_μ, $\bar{\nu}_m u$, ν_τ, and $\bar{\nu}_\tau$ (2.3×10^{57} each).

2.5 Gravitational Waves From A Core-collapse Supernova

The GW emission from a CCSN is imprinted with the various processes that happen inside the progenitor including but not limited to, explosion mechanism, the complex hydrodynamics involved, the properties of the shock. The GW emission is highly dependent on stellar properties, mass, etc. It is dominated by the dynamics of

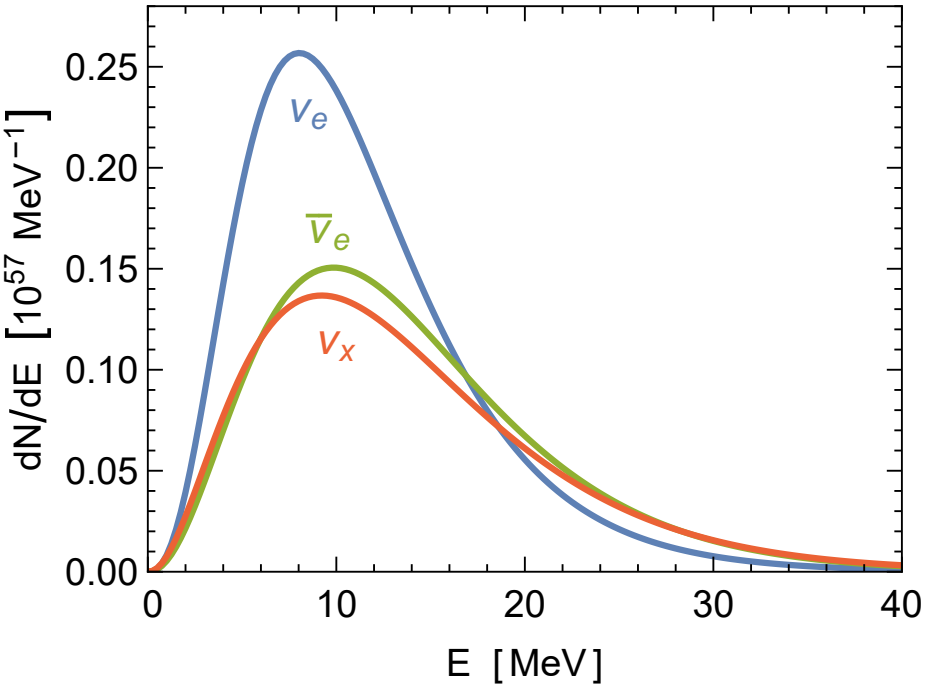

Figure 2.15: Time-integrated supernova neutrino emission spectra corresponding to neutrino luminosity in Fig. 2.13.

the proto-neutron star (PNS) (see Sec. 2.3.2 for details). In this section, we provide a very brief description of the main properties of GW emission from CCSNe. We encourage the interested reader to look at Kotake *et al.* (2007a); Ott (2009) for more details. In Fig. 2.16 we illustrate the GW emission from a CCSN in time domain (top panel) and the associated GW energy spectrum (bottom panel) (see Murphy *et al.* (2009) for details). The main properties associated with GW emission from a CCSN are as follows (this is based on Gossan (2019)):

- For progenitors with rotational pre-collapse cores, whose rotational periods exceeds a few 10 seconds:
  - The PNS oscillations produce the strongest GW emissions. The PNS oscillations are excited by convective plumes and hydrodynamic waves (Murphy *et al.*, 2009; Yakunin *et al.*, 2010; Mueller *et al.*, 2013; Yakunin *et al.*, 2015).

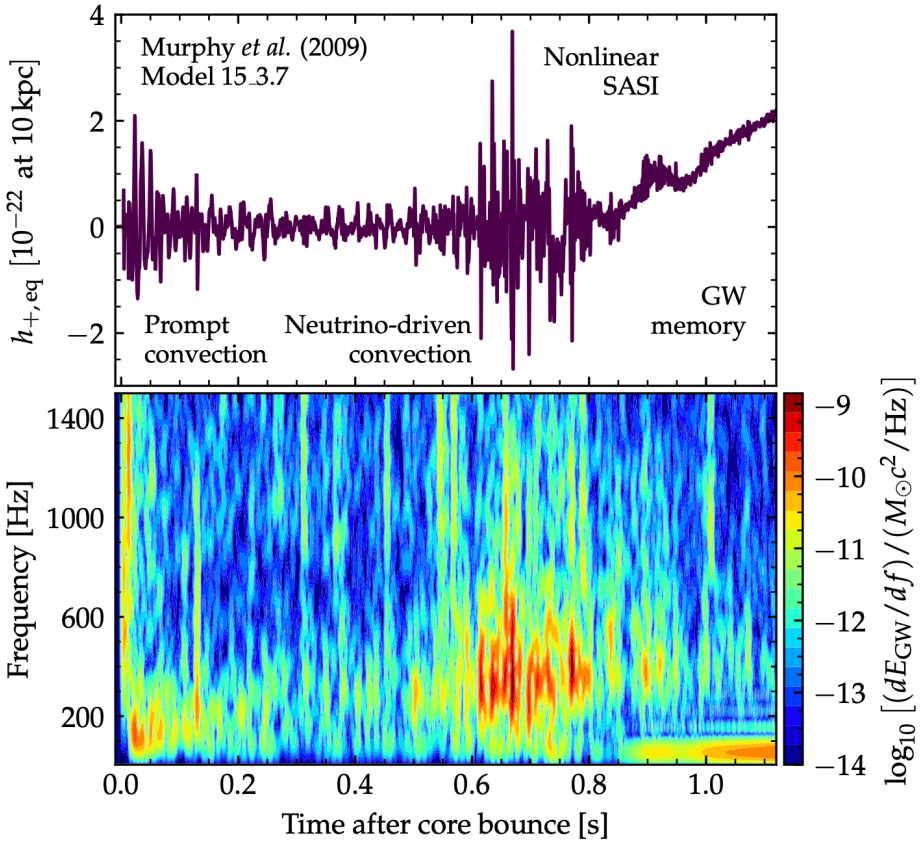

Figure 2.16: In the context of an equatorial observer at 10 kpc , the time domain strain (top panel) and time-frequency evolution of the spectral GW energy (bottom panel) for model $15_3.7$ from Murphy *et al.* (2009). The regions where emission originates from prompt convection, neutrino-driven convection, non-linear SASI, and GW memory are highlighted. Figure taken from Gossan (2019).

– The dominant PNS surface g-mode frequency dictates the peak frequency of the GW emission. The peak frequency increases quasi-linearly with time from $\sim 100 - 200$ Hz to above 1 kHz. This is as a result of the PNS accreting fallback material, contracting and finally deleptonizing. However, the oscillation spectrum consists of broad and complex excitations (Cerdá-Durán *et al.*, 2013; Sotani and Takiwaki, 2016; Morozova *et al.*, 2018).

– At frequencies between $100 - 300$ Hz, prompt convection leads to GW emission. The prompt convection develops after the neutronization burst

in the accretion phase ($\sim$ 10 ms after bounce) and fades by $\sim$ 100 ms. The puffy nature of the PNS leads to their development.

- The GW emission between $\sim 300 - 1000$ Hz is sourced by the neutrino-driven convection.
- SASI (see Sec. 2.3.2 for details) further induces quadrupolar oscillations around $100 - 200$ Hz at later times during accretion. This begins at $\sim$ 100 ms post-bounce. The GW emission frequency is related to the characteristic frequency of the advective-acoustic cavity in which it develops (Murphy *et al.*, 2009; Mueller *et al.*, 2013; Kuroda *et al.*, 2016). The phase of emission is stochastic, owing to the highly chaotic nature of SASI (Kotake *et al.*, 2009a).

  This is of particular interest for this work since the anisotropies produced as a result of SASI and other turbulent activity in the accretion phase, leads to an anisotropic neutrino emission. This anisotropic neutrino emission sources GWs which is different from the ones due to the motion of the PNS itself. These GWs from the anisotropic neutrino emission have a *memory* associated with them, which can be detected and can provide us with crucial information about the interior post-collapse. This will be the focus of chapter 4.

- For progenitors with pre-collapse cores with considerable angular momentum, the PNS deforms into an oblate spheroid. This is because of the high centrifugal support around the equatorial regions. A strong quadrupole is sourced when the PNS decelerates and rebounds, which results in a big spike in the GW signal at core bounce. This is followed by the ringdown of the PNS as it settles to a new equilibrium state (Dimmelmeier *et al.*, 2008; Ott, 2009; Fuller *et al.*, 2015). For

this case, the GW signal depends on the inner core's mass, angular momentum distribution and the equation of state of the nuclear matter (Fryer *et al.*, 2002; Ott *et al.*, 2005, 2007; Scheidegger *et al.*, 2010; Kuroda *et al.*, 2014).

- A significant enhancement in GW emissions after ~ 50 ms post-bounce may develop in progenitors with pre-collapse cores with extreme rapid rotation and/or strong differential rotation, non-axisymmetric rotational instabilities driven by rotational shear (O'Connor and Ott, 2011; Clausen *et al.*, 2015; Ugliano *et al.*, 2012).

- The GW emissions from a BHFC (failed supernova) are characterized a short burst and ringdown. The peak ringdown frequency is inversely proportional to the mass of the nascent BH, with typical ringdown spectra for stellar mass BH formation peaking $\sim \mathcal{O}(1)$ kHz (Kuroda *et al.*, 2018; Cerdá-Durán *et al.*, 2013; Pan *et al.*, 2019; Ott *et al.*, 2011).

2.6 CCSN Rates

A key ingredient required for studying CCSN is information about how frequently they occur, in short, their rates and the variation of rates with distance and other physical quantities. The CCSN rate in our galaxy and the local volume is of particular importance. In general the rate of CCSN in the galaxy is believed to be $3.2^{+7.3}_{-2.6}$ per century (Adams *et al.*, 2013). Fig. 2.17 shows the comoving supernova rate (SNR) (all types of luminous core collapses including Type II and Type Ibc) as a function of redshift. The SNR predicted from the cosmic star formation rate (SFR) fit and its supporting data (Hopkins and Beacom, 2006), as well as that predicted from the mean of the local SFR measurements, are plotted and labeled. The fit to the measured cosmic SNR, with a fixed slope of $(1+z)^{3.4}$ taken from the cosmic SFR, is

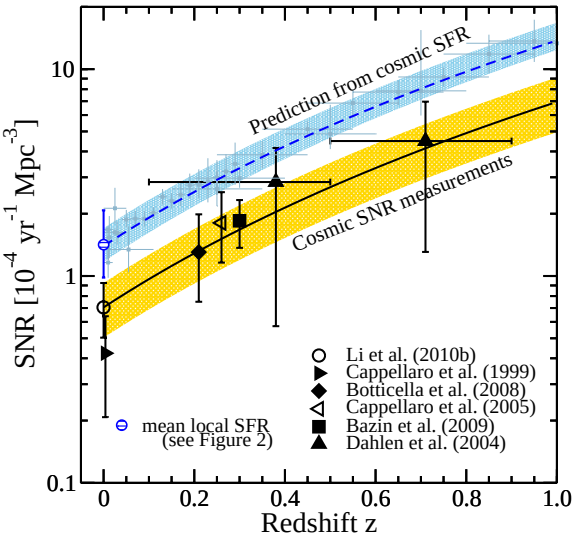

Figure 2.17: Comoving SNR (all types of luminous core collapses including Type II and Type Ibc) as a function of redshift. The SNR predicted from the cosmic SFR fit and its supporting data (Hopkins and Beacom, 2006), as well as that predicted from the mean of the local SFR measurements, are plotted and labeled. The fit to the measured cosmic SNR, with a fixed slope of $(1 + z)^{3.4}$ taken from the cosmic SFR, is shown with the uncertainty band from the LOSS measurement. Figure taken from Horiuchi *et al.* (2011).

shown with the uncertainty band from the LOSS measurement. The predicted and measured cosmic SNR are consistently discrepant by a factor of 2, which is called the supernova rate problem. However, rates from SN catalogs in the very local volume do not show such a large discrepancy. Here, we will not discuss the supernova rate problem.

For this work, we will require the CCSN rate in the local volume (within 11 Mpc) and beyond. This will be relevant in chapter 5. In the local volume, the cummulative CCSN rate has been estimated in Nakamura *et al.* (2016). But beyond 11 Mpc, the rate needs to be calculated analytically. In Sec. 2.6.1 below, we show an analytical calculation of the cummulative CCSN rate beyond 11 Mpc.

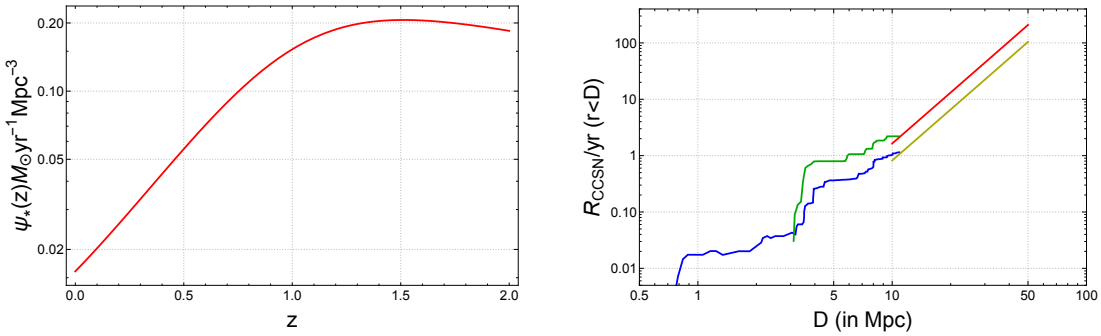

Figure 2.18: Left: a) The cosmic star formation rate for $f_* = 2.3$ with redshift (z). Right: b) The cumulative CCSN rates with distance D.

2.6.1 Cummulative CCSN Rate Beyond 11 Mpc

The CCSN rate calculated analytically needs to be used beyond the local volume of 11 Mpc. The rate is based on the SFR. The model we use is based on Ando and Sato (2004) (See Sec. - 2.2 there). We begin by writing the functional form for the SFR per unit comoving volume ($\psi_*(z)$),

$$\psi_*(z) = 0.32\ f_*\ h_{70}\ \frac{\exp{(3.4z)}}{\exp{(3.8z)} + 45}\ \frac{\sqrt{\Omega_m(1+z)^3 + \Omega_\Lambda}}{(1+z)^{3/2}}\ M_\odot\ yr^{-1} Mpc^{-3}\,, \qquad (2.9)$$

where, f_* is a factor of order unity. The local SFR varies within a range based on various models, the common range is $\psi_*(0) = (0.5 - 2.9) \times 10^{-2} h_{70}\ M_\odot\ yr^{-1} Mpc^{-3}$. Hence, f_* is in a way a correction factor. For example, choosing $f_* = 1$ gives $\psi_*(0) = 0.7 \times 10^{-2} h_{70}\ M_\odot\ yr^{-1} Mpc^{-3}$, whereas $f_* = 2.3$ implies $\psi_*(0) = 1.6 \times 10^{-2}\ M_\odot\ yr^{-1} Mpc^{-3}$ which is what was obtained in Strigari *et al.* (2004). We choose $f_* = 2.3$ in our work. Based on standard ΛCDM cosmology, the matter density parameter, $\Omega_m = 0.3$ and the dark energy density parameter, $\Omega_\Lambda = 0.7$. z is the redshift. The reduced Hubble constant, $h_{70} = H_0/70\ km\ s^{-1}\ Mpc^{-1}$. The present day Hubble constant $H_0 = 70\ km\ s^{-1}\ Mpc^{-1}$. The SN rate ($R_{SN}(z)$) can be obtained using (2.9) by assuming the Salpeter IMF ($\phi(m) \propto m^{-2.35}$) with a lower cut-off around 0.5 $M_\odot$

and that all stars $M > 8\ M_\odot$ explode as CCSN,

$$R_{SN}(z) = \lambda \frac{\int_{8M_\odot}^{125M_\odot} dm\ \phi(m)}{\int_0^{125M_\odot} dm\ m\phi(m)} = 0.0122\ {M_\odot}^{-1}\ \psi_*(z)\,, \tag{2.10}$$

where, λ is the parameter to fix conservative and optimistic (observed) rates. We choose, $\lambda = 1$ for conservative rates and $\lambda = 2$ for optimistic (observed) rates. The IMF is assumed to be constant in time which is a good approximation (See Ando and Sato (2004) for a detailed discussion). The results are also insensitive to the upper limit of integration. The cumulative rate of CCSN is obtained by performing the volume integral,

$$R_{CCSN}(r_0) = \int_0^{r_0} r^2 dr \int_{-1}^{1} d(\cos\theta) \int_0^{2\pi} d\phi\ \lambda R_{SN}(r) = 4\pi \int_0^{r_0} r^2 dr\ R_{SN}(r)\ yr^{-1}\,, \tag{2.11}$$

where, r_0 is the distance in Mpc at which the cumulative CCSN rate is required. The relation between redshift z and distance (D) in Mpc for small distances is, $z = DH_0/c$, where the speed of light, $c = 3 \times 10^8\ ms^{-1}$.

2.7 SN1987A: Multi-messenger Astronomy Using CCSN

Before concluding this chapter, it is imperative to discuss SN1987A - the only CCSN from which we detected neutrino signals. SN1987A was discovered in the Large Magellanic Cloud, located at $\sim$ 50 kpc from our solar system. It was a very bright type-II SN observed on 24 February, 1987. The progenitor in this case was blue supergiant Sanduleak (Sonneborn *et al.*, 1987).

The neutrino detectors active during that period were: Kamiokande-II , Baksan , IMB and LSD . The events in Kamiokandde-II, Baksan and IMB happened nearly simultaneously, however the events in LSD were five hours prior to the other ones. Thus, LSD events are generally not included when talking of observed neutrino events from SN1987A. The observed events was $\sim$ 10 MeV and spread over a 10s time inter-

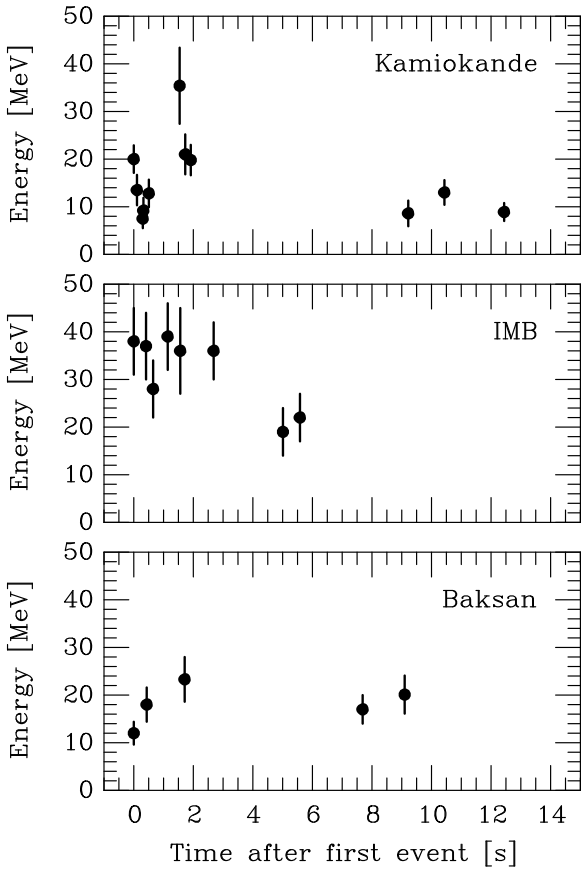

Figure 2.19: SN1987A neutrino events observed by Kamiokande, IMB and Baksan showed that the neutrino burst lasted about 13 s. Figure taken from Janka (2017)

val. Fig. 2.19 shows the pbserveed neutrino events in the three detectors. This was hours before SN1987A was optically discovered.

SN1987A opened up the avenues to perform multi-messenger studies of CCSN, since not only was it studied using the detected neutrino events, but also on all electromagnetic bands: radio (Manchester *et al.*, 2005), infrared (Bouchet *et al.*, 2004, 2006), optical (Graves *et al.*, 2005; Sugerman *et al.*, 2005), ultraviolet (Kirshner *et al.*, 1987; Sonneborn *et al.*, 1987), and x-rays (Hasinger *et al.*, 1996; Burrows *et al.*, 2000; Shtykovskiy *et al.*, 2005; Park *et al.*, 2005a,b; Zhekov *et al.*, 2005; Park *et al.*, 2006). Besides, it was also the first SN visible to the naked eye following Kepler SN in 1604.

It is exciting to think that the physics of core-collapse supernovae and neutrinos

have come such a long way with just one instance of CCSN neutrino observation. Thanks to the immense research initiatives including but not limited to complicated numerical simulation codes, nuclear physics and fluid hydrodynamics inputs, etc. The future prospects of supernova neutrino detections look very promising with the advent of next generation neutrino detectors: HyperKamiokande (Abe, 2016), DUNE (Acciarri *et al.*, 2016) and JUNO (An, 2016; Li, 2014; Brugière, 2017), to name a few. Combined with the massive improvements in neutrino detectors, the new and improved astronomical telescopes are available to confirm the occurrence of a CCSN. Finally, the gravitational wave (GW) detectors like LIGO-VIRGO (Abbott *et al.*, 2016c, 2017b, 2020a,b) and Adv.LIGO (Aasi *et al.*, 2015b) will also detect the GWs from a CCSN, making it a multi-messenger observation. The next step is to probably wait for a galactic scale ($\sim$ 10 kpc) CCSN, to open up immense opportunities to gain insights into the dynamics of a CCSN, neutrino properties, and also test physics beyond the standard model.

Chapter 3

POINTING USING PRESUPERNOVA NEUTRINOS

In section 2.3, we discussed in detail the neutrinos from a core-collapse supernova (CCSN). The focus of this chapter is - pointing using presupernova neutrinos. As discussed before, presupernova neutrinos are the neutrinos of $\sim$ 0.1 - 5 MeV energy that accompany, with increasing luminosity, the last stages of nuclear burning of a massive star in the days leading to its core collapse and final explosion as a supernova, or implosion into a black hole (a "failed" supernova). These neutrinos are produced by thermal processes – mainly pair-production – that depend on the ambient thermodynamic conditions (Fowler and Hoyle, 1964; Beaudet *et al.*, 1967; Schinder *et al.*, 1987; Itoh *et al.*, 1996) – and by weak reactions – mainly electron/positron captures and nuclear decays – that have a stronger dependence on the isotopic composition (Fuller *et al.*, 1980, 1982b,a, 1985; Langanke and Martínez-Pinedo, 2000, 2014; Misch *et al.*, 2018), and thus on the network of nuclear reactions that take place in the stellar interior.

Building on early calculations (Odrzywolek *et al.*, 2004a,b; Kutschera *et al.*, 2009; Odrzywolek, 2009), recent numerical simulations with state-of-the-art treatment of the nuclear processes (Kato *et al.*, 2015; Yoshida *et al.*, 2016; Patton *et al.*, 2017b,a; Kato *et al.*, 2017; Guo *et al.*, 2019) have shown that the presupernova neutrino flux increases dramatically, both in luminosity and in average energy, in the hours prior to the collapse, and it becomes potentially detectable when silicon burning is ignited in the core of the star. In particular, for stars within $\sim$1 kpc of Earth like Betelgeuse, presupernova neutrinos will be detected at multi-kiloton neutrino detectors like the current KamLAND (see Araki *et al.* (2005) for a dedicated study), Borexino (Borexino

Collaboration, 2018), SNO+ (Andringa *et al.*, 2016), Daya Bay (Guo *et al.*, 2007) and SuperKamiokande (Simpson, 2019), and the upcoming HyperKamiokande (Abe, 2016), DUNE (Acciarri *et al.*, 2016) and JUNO (An, 2016; Li, 2014; Brugière, 2017). Next generation dark matter detectors like XENON (Newstead *et al.*, 2019), DARWIN (Aalbers, 2016), and ARGO (Aalseth, 2018) will also observe a significant signal (Raj *et al.*, 2020). Therefore, presupernova neutrinos are a prime target for the SuperNova Early Warning System network (SNEWS, Antonioli *et al.*, 2004) – which does or will include the neutrino experiments mentioned above – and its multi-messenger era successor SNEWS 2.0, whose mission is to provide early alerts to the astronomy and gravitational wave communities, and to the scientific community at large as well. The observation of presupernova neutrinos from an impending core-collapse supernova will: (i) allow numerous tests of stellar and neutrino physics, including tests of exotic physics that may require pointing to the collapsing star (e.g. axion searches, see Raffelt *et al.* (2011)); and (ii) enable a very early alert of the collapse and supernova, thus extending – perhaps crucially, especially for envelope-free stellar progenitors that tend to explode shortly after collapse – the time frame available to coordinate multi-messenger observations.

In this chapter, we explore presupernova neutrinos as early alerts. In particular, we focus on the question of localization: *can a signal of presupernova neutrinos provide useful positional information? Can it identify the progenitor star?* From a recent exploratory study (Li *et al.*, 2020), we know that the best potential for localization is offered by inverse beta decay events at large ($\mathcal{O}(10)$ kt mass) liquid scintillator detectors, where, for optimistic presupernova flux predictions and a star like Betelgeuse (distance of 0.2 kpc), a signal can be discovered days before the collapse, and the direction to the progenitor can be determined with a $\sim 80^\circ$ error.

This article is the first dedicated study on the localization question for presuper-

nova neutrinos. Using a state-of-the-art numerical model for the neutrino emission, we examine a number of questions that were not previously discussed, having to do with the diverse stellar population of nearby stars (including red and blue supergiants, of masses between ~ 10 and ~ 30 times the mass of the Sun, and clustered in certain regions of the sky) and with the rich possibilities of improving the directionality of the liquid scintillator technology in the future.

In Section 3.1 we discuss presupernova neutrino event rates and nearby candidates. In Section 3.2 we present our main results for the angular sensitivity. In Section 3.3 we discuss progenitor identification. Sec. 3.4 we discuss the effects on the angular pointing abilities of a detector in the presence of backgrounds. In Appendix. C we discuss some additional technical details and in Appendix D we detail the distance and mass estimates of nearby presupernova candidates.

3.1 Presupernova Neutrino Event Rates And Candidates

A liquid scintillator is ideal for the detection of presupernova neutrinos, through the inverse beta decay process (henceforth IBD, $\bar{\nu}_e + p \rightarrow n + e^+$) due to its low energy threshold (1.8 MeV), and its timing, energy resolution, and background discrimination performance. The expected signal from a presupernova in neutrino detectors has been presented in recent articles (e.g., Asakura and KamLAND Collaboration, 2016; Kato *et al.*, 2015; Yoshida *et al.*, 2016; Patton *et al.*, 2017b; Kato *et al.*, 2017; Li *et al.*, 2020).

We consider an active detector mass of 17 kt, which is expected for JUNO, with detection efficiency of unity, and we use the IBD event rates in Patton *et al.* (2017b); Patton *et al.* (2019). Figure 3.1 shows the numbers of events and cumulative numbers of events for progenitor stars of zero age main-sequence (ZAMS) masses of 15 $M_\odot$ and 30 $M_\odot$ (here $M_\odot = 1.99\,10^{33}$ g is the mass of the Sun) at a distance of D=0.2 kpc (rep-

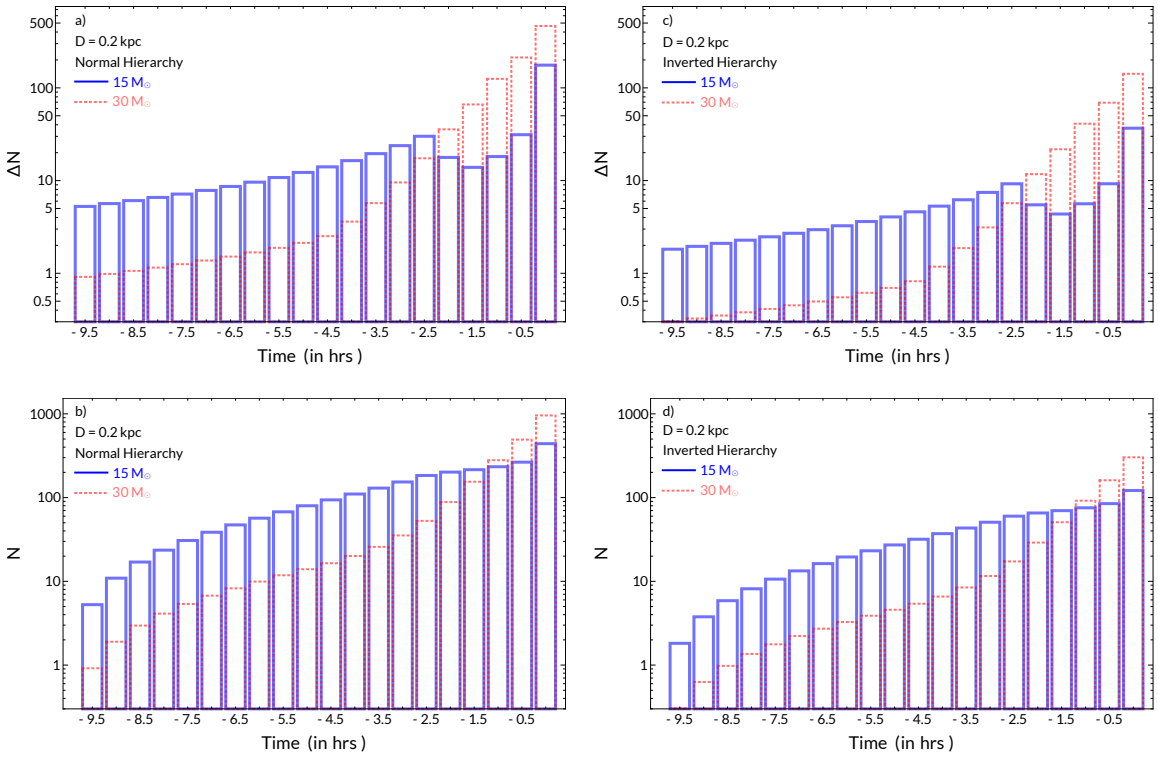

Figure 3.1: Top row a) and c): Number of presupernova neutrino events at a 17 kt liquid scintillator detector, in time bins of width $\Delta t = 0.5$ hrs as a function of time before core-collapse. Bottom row or b) and d): Cumulative numbers of events in half-hour increments. Shown are the cases of a ZAMS 15 $M_\odot$ (blue histogram) and a ZAMS 30 $M_\odot$ (red histogram) progenitor, at a distance D=0.2 kpc, for the normal (left column) and inverted (right column) neutrino mass hierarchy.

resentative of Betelgeuse). Results are shown for the normal and inverted hierarchy of the neutrino mass spectrum. Times are negative, being relative to the time of core-collapse.

Figure 3.1 shows that a few hundred events are expected in the hours before core-collapse. For the 15 $M_\odot$ model, the neutrino signal exceeds $\simeq$100 events at t=−4 hr and has a characteristic peak at $t \simeq -2.5$ hours, which marks the beginning of core silicon burning. For the 30 $M_\odot$ model, the neutrino signal exceeds $\simeq$100 events at t=−2 hr. The number of events then increases steadily and rapidly, leading to a cumulative number of events that is larger than in the 15 $M_\odot$ model.

For the detector background, we follow the event rates estimated in An (2016) (see also Yoshida *et al.* (2016)) for JUNO: $r_{Bkg}^{on} \simeq 2.66$/hr and $r_{Bkg}^{off} \simeq 0.16$/hr in the reactor-on and reactor-off cases respectively. In addition to reactor neutrinos, other backgrounds are due, in comparable amounts (about 1 event per day each), to geoneutrinos, cosmogenic ^{8}He/^{9}Li, and accidental coincidences due to various radioactivity sources, like the natural decay chains, etc. For the latter, it is assumed that an effective muon veto will be in place, see An (2016) for details[1]. Roughly, a signal is detectable if the number of events expected is at least comparable with the number of background events in the same time interval ($N \gtrsim N_{\rm bkg}$). Using the reactor-on background rate, the most conservative presupernova event rate in Figure 3.1, and the fact that the number of signal events scales like D^{-2}, we estimate that a presupernova can be detected to a distance $D_{\rm max} \simeq 1$ kpc.

What nearby stars could possibly undergo core collapse in the next few decades? To answer this question, we compiled a new list of 31 core collapse supernova candidates; see Appendix D and Table D.1. Figure 2.3 gives an illustration of their names, positions, distances, masses, and colors. Figure 2.4 shows the equatorial coordinate system positions of the same stars, colored by distance bins, in a Mollweide projection. These candidates lie near the Galatic Plane, with clustering in directions associated with the Orion A molecular cloud (Großschedl *et al.*, 2019) and the OB associations Cygnus OB2 and Carina OB1 (Lim *et al.*, 2019). We find that for the stars in Table D.1 the minimum separation (i.e., the separation of a star from its nearest neighbor in the same list) is, on average, $\langle \Delta\theta \rangle \simeq 10.4^\circ$, and that 70% of the candidate stars have $\Delta\theta \lesssim 12.8^\circ$ (see Table D.2). Therefore, a sensitivity of $\simeq 10^\circ$ is

[1] Although we use detector-specific background rates, we emphasize that our results are given as a function of the forward-backward asymmetry of the data set at hand, and therefore are broadly applicable to different detector setups. See Sec. 3.2.

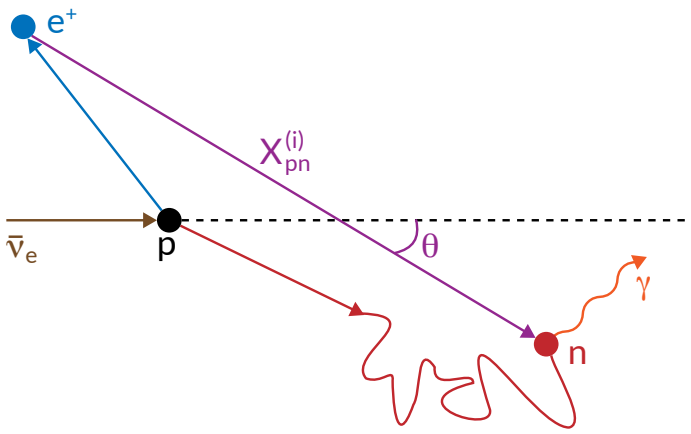

Figure 3.2: The geometry of Inverse Beta Decay in liquid scintillator. Shown are the incoming anti-neutrino (brown), proton (black), outgoing positron and its annihilation point (blue), outgoing neutron, its subsequent scattering events and its capture point (red), and the outgoing photon (orange). The vector $X_{pn}^{(i)}$ originates at the positron annihilation location and points in the direction of the neutron capture point. θ is the angle between $X_{pn}^{(i)}$ and the incoming neutrino momentum.

desirable for complete disambiguation of the progenitor with a neutrino detector.

3.2 Angular Resolution And Sensitivity

Here we discuss the angular sensitivity of a liquid scintillator detector for realistic numbers of presupernova neutrino events. We consider two cases: a well tested liquid scintillator technology (henceforth LS) based on Linear AlkylBenzene (LAB), as is used in SNO+ (Andringa *et al.*, 2016) and envisioned for JUNO; and a hypothetical setup where a Lithium compound is dissolved in the scintillator for enhanced angular sensitivity (henceforth LS-Li), as discussed for geoneutrino detection (Tanaka and Watanabe, 2014). As a notation definition, let us assume that the total number of events in the detector is $N = N_S + N_{\rm Bkg}$, where N_S is the number of signal events and $N_{\rm Bkg}$ is the number of background events.

The IBD process in LS is illustrated in Figure 3.2. Overall, the sensitivity of this process to the direction of the incoming neutrino is moderate, with the emitted positron (neutron) momentum being slightly backward (forward)-distributed, see

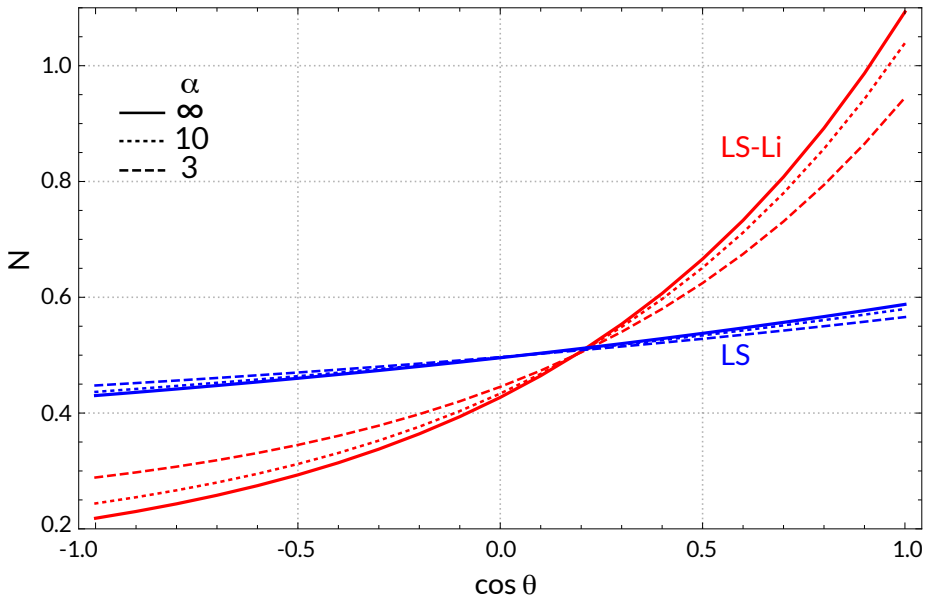

Figure 3.3: Normalized distributions of $\cos\theta$ for LS and LS-Li, for different values of the signal-to-background ratio, $\alpha = N_S/N_{\rm Bkg}$ (numbers in legend). Here, $\alpha = \infty$ means absence of background, $N_{\rm Bkg} = 0$.

Beacom and Vogel (1999) and Vogel and Beacom (1999) for a detailed overview. Here, we follow the pointing method proposed and tested by the CHOOZ collaboration (Apollonio, 2000), which we describe briefly below.

Let us first consider a background-free signal, $N_{\rm Bkg} = 0$. For each detected neutrino ν_i $(i = 1, 2, \ldots, N)$, we consider the unit vector $\hat{X}_{pn}^{(i)}$ that originates at the positron annihilation location and is directed towards the neutron capture point. Let θ be the angle that $\hat{X}_{pn}^{(i)}$ forms with the neutrino direction (see Figure 3.2). The unit vectors $\hat{X}_{pn}^{(i)}$ carry directional information – albeit with some degradation due to the neutron having to thermalize by scattering events before it can be captured – and possess a slightly forward distribution. The angular distributions expected for LS and LS-Li are given by Tanaka and Watanabe (2014) (in the context of geoneutrinos) in graphical form; we find that they are well reproduced by the following functions:

$$\begin{aligned} f_{LS}(\cos\theta) &\simeq 0.2718 + 0.2238 \ \exp\left(0.345\cos\theta\right) \\ f_{LS-Li}(\cos\theta) &\simeq 0.1230 + 0.3041 \ \exp\left(1.16\cos\theta\right). \end{aligned} \tag{3.1}$$

Using these, one can find the forward-backward asymmetry, which is a measurable parameter:

$$\frac{a_0}{2} = \frac{N_F - N_B}{N_F + N_B} \ . \tag{3.2}$$

Here N_F and N_B are the numbers of events in the forward ($\theta \leq \pi/2$) and backward ($\theta > \pi/2$) direction respectively. We obtain $a_0 \simeq 0.16$ for LS, which is consistent with the distributions shown in Apollonio (2000), and $a_0 \simeq 0.78$ for LS-Li.

Let us now generalize to the case with a non-zero background, and define the signal-to-background ratio, $\alpha = N_S/N_{\rm Bkg}$. For simplicity, the background is modeled as isotropic and constant in time. Suppose that N_S, α, and a_0 are known. In this case, the total angular distribution of the N events will be a linear combination of two components, one for the directional signal

$$N_{B,S} = \frac{N_S}{2}\left(1 - \frac{a_0}{2}\right) \qquad N_{F,S} = \frac{N_S}{2}\left(1 + \frac{a_0}{2}\right), \tag{3.3}$$

and the other for the isotropic background

$$N_{B,\rm Bkg} = \frac{N_{\rm Bkg}}{2} \qquad N_{F,\rm Bkg} = \frac{N_{\rm Bkg}}{2}. \tag{3.4}$$

The two distributions have a relative weight of α, which yields the forward-backward asymmetry as

$$\frac{a}{2} = \frac{(N_{F,S} + N_{F,\rm Bkg}) - (N_{B,S} + N_{B,\rm Bkg})}{(N_{F,S} + N_{F,\rm Bkg}) + (N_{B,S} + N_{B,\rm Bkg})}. \tag{3.5}$$

In the small background limit, $N_{\rm Bkg} \to 0$, then $\alpha \to \infty$ and $a \to a_0$. In the large background limit $N_{\rm Bkg} \to \infty$, then $\alpha \to 0$ and $a \to 0$.

Figure 3.3 shows the angular distribution for different signal-to-noise ratios α (see Table 3.1 for the corresponding values of a). For LS the $\alpha = \infty$ curve (blue solid) is taken from Equation (3.1), and for LS-Li the $\alpha = \infty$ curve (red solid) is taken from Equation (3.1). For LS-Li, an enhancement in the directionality is achieved as a result of an improved reconstruction of the positron annihilation point and a shortening of

α	Standard LS	Enhanced LS
∞	0.1580	0.7820
10.0	0.1418	0.7165
3.0	0.1170	0.5911

Table 3.1: Values Of a For The Curves In Figure 3.3.

the neutron capture range. Enhancement in the directionality decreases for LS and LS-Li as the background becomes larger.

From here on, for all cases we adopt an approximate linear distribution[2] for the N events in the detector:

$$f(\cos\theta) = \frac{1}{2}\Big(1 + a\cos\theta\Big) \ . \tag{3.6}$$

This form is accurate – yielding results that are commensurate with those obtained from the distributions in Figure 3.3 – and it allows to describe our results as functions of the varying parameter a in a general and transparent manner.

Rigorously, a depends on the neutrino energy. We investigated the uncertainty associated with treating a as a (energy-independent) constant, and found it to be negligible in the present context where larger errors are present from, for example, uncertainties associated with modeling of the presupernova neutrino event rates. In addition, the values of a used in the literature for supernova neutrinos, reactor neutrinos and geoneutrinos (e.g., Apollonio, 2000; Tanaka and Watanabe, 2014; Fischer *et al.*, 2015) vary only by $\simeq$10-20% over a wide range of energy. The values of a in Table 3.1 for the background-free $\alpha = \infty$ cases are used in Tanaka and Watanabe (2014) and Fischer *et al.* (2015) for geoneutrinos, which have an energy range

[2]A more general case of an exponential distribution is discussed in App. C. It can be inferred from the figure there, that the approximate linear distribution is a very good approximation for the original exponential case, and does not alter our results significantly.

($E \simeq$2-5 MeV) and spectrum that is similar to those of presupernova neutrinos.

3.2.1 *Pointing To The Progenitor Location*

For a signal of N IBD events in the detector from a point source on the sky, and therefore a set of unit vectors $\hat{X}_{pn}^{(i)}$ $(i = 1, 2, \ldots, N)$, an estimate of the direction to the source is given by the average vector $\vec{p}$ (Apollonio, 2000; Fischer *et al.*, 2015):

$$\vec{p} = \frac{1}{N} \sum_{i=1}^{N} \hat{X}_{pn}^{(i)} \ . \tag{3.7}$$

This vector offers an immediate way to estimate the direction to the progenitor star in the sky. The calculation of the uncertainty in the direction is more involved (Apollonio, 2000), and requires examining the statistical distribution of $\vec{p}$, as follows.

Consider a Cartesian frame of reference where the neutrino source is on the negative side of the z-axis. In the limit of very high statistics ($N \to \infty$), the averages of the x- and y- components of the vectors $\hat{X}_{pn}^{(i)}$ vanish. The average of the z- component can be found from Equation (3.6), and is $\langle z \rangle = a/3$. Thus, the mean of $\vec{p}$ is:

$$\vec{p}_m = (0, 0, |\vec{p}|) = (0, 0, a/3) \ . \tag{3.8}$$

For the linear distribution in Equation (3.6), the standard deviation is,

$$\sigma = (\sqrt{3 - a^2})/3 \simeq 1/\sqrt{3} \, ,$$

where, the approximation introduces a relative error of the form $a^2/6$, which is negligible in the present context. For $N \gg 1$, the Central Limit Theorem applies, and the distribution of the three components of $\vec{p}$ are Gaussians[3] centered at the components of $\vec{p}_m$, and with standard deviations $\sigma_x = \sigma_y = \sigma_z = \sigma = 1/\sqrt{3N}$. Hence, the

[3]This statement (and therefore Equation (3.9)) is only valid in the assumed frame of reference, which is centered at the detector, with the neutrino source being on the z-axis. In a generic frame of reference, the three components of $\vec{p}$ are not statistically independent, and their probability distribution takes a more complicated form.

probability distribution of the vector $\vec{p}$ is

$$P(p_x, p_y, p_z) = \frac{1}{\left(2\pi\sigma^2\right)^{\frac{3}{2}}} \exp\left(\frac{-p_x^2 - p_y^2 - (p_z - |\vec{p}|)^2}{2\sigma^2}\right) . \tag{3.9}$$

The angular uncertainty on the direction to the supernova progenitor is given by the angular aperture, β, of the cone around the vector $\vec{p}_m$, containing a chosen fraction of the total probability (e.g., $I = 0.68$ or $I = 0.90$):

$$\int P(p_x, p_y, p_z)\ dp_x dp_y dp_z = I\ , \tag{3.10}$$

or, in spherical coordinates:

$$\int_0^\infty p^2 dp \int_{\cos\beta}^1 d\cos\theta \int_0^{2\pi} d\phi\ P(p_x, p_y, p_z) = I\ . \tag{3.11}$$

The latter form reduces to[4]:

$$\frac{1}{2}\left[1 + \mathrm{Erf}(k) - \cos\beta\ \exp\left(-k^2 \sin^2\beta\right)\Big(1 + \mathrm{Erf}(k\cos\beta)\Big)\right] = I\ , \tag{3.12}$$

where $k = \sqrt{3N/2}\ |\vec{p}| = a\sqrt{N/6}$, and the error function is,

$$\mathrm{Erf}(z) = 2/\sqrt{\pi} \int_0^z \exp(-t^2)\ dt\,.$$

For a fixed value of I, Equation (3.12) can be solved numerically to find $\beta = \beta(k, I)$, and therefore to reveal the dependence of β on N and a. Figure 3.4 shows the dependence of β on N, for two confidence levels (C.L.). The figure illustrates the (expected) poor performance of LS: we have $\beta \simeq 70^\circ$ at 68% C.L. and $N = 100$, improving to $\beta \simeq 40^\circ$ at $N = 500$. For the same C.L. and values of N, LS-Li would allow an improvement in the error by nearly a factor of 4, giving $\beta \simeq 18^\circ$ and $\beta \simeq 10^\circ$ in the two cases respectively. The degree of improvement in performance with increasing a is shown in Figure 3.5, where $N = 200$ is kept fixed.

[4]The steps involved in obtaining Eq. 3.12 from Eq. 3.9 is shown in App. C.

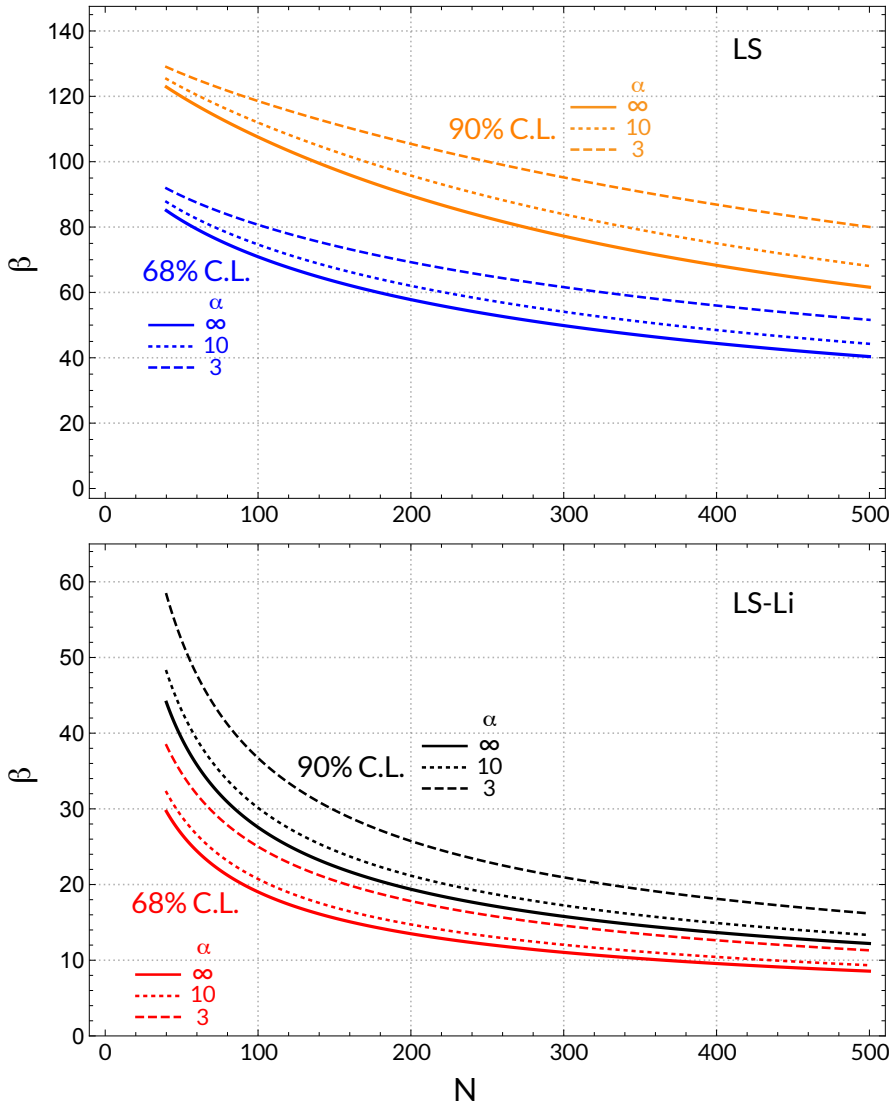

Figure 3.4: The angular uncertainty, β, as a function of the number of events, for LS and LS-Li, two different confidence levels, and three values of the signal-to-background ratio, α (see figure legend).

					LS			LS-Li		
Time to CC	N_{Total}	N_{Sig}	N_{Bkg}	α	a	68%	90%	a	68%	90%
4.0 hr	93	78	15	5.20	0.1308	78.43°	116.17°	0.6610	23.24°	33.98°
1.0 hr	193	170	23	7.39	0.1374	63.92°	98.42°	0.6942	15.47°	22.26°
2 min	314	289	25	11.56	0.1435	52.72°	81.79°	0.7254	11.63°	16.67°

Table 3.2: Parameters and results for Betelgeuse, Figure 3.6, left panels. The angular errors at a given confidence level (C.L.) are in degrees.

					LS			LS-Li		
Time to CC	N_{Total}	N_{Sig}	N_{Bkg}	α	a	68%	90%	a	68%	90%
4.0 hr	161	146	15	9.73	0.1414	66.27°	101.59°	0.7147	16.44°	23.70°
1.0 hr	333	310	23	13.48	0.1452	51.11°	79.24°	0.7337	11.16°	15.98°
2 min	543	518	25	20.72	0.1488	41.02°	62.70°	0.7519	8.54°	12.19°

Table 3.3: Parameters and results for Antares, Figure 3.6, right panels.

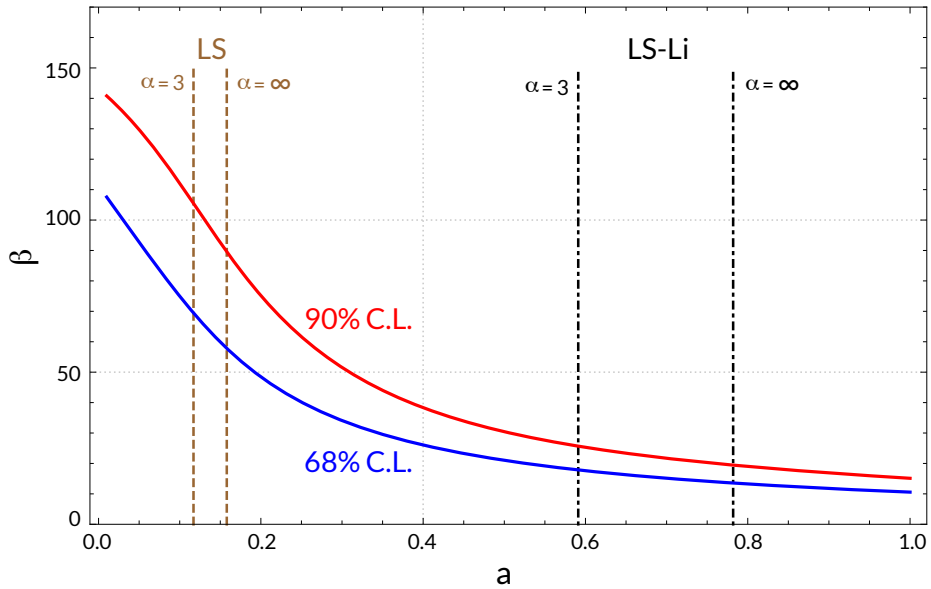

Figure 3.5: The angular uncertainty, β, as a function of the forward-backward asymmetry, a, for two different confidence levels (see figure legend) and fixed number of events, $N = 200$. The vertical lines indicate the values of a corresponding to $\alpha = \infty,\ 3$ for LS (dashed lines) and LS-Li (dot-dashed), see Table 3.1.

					LS		**LS-Li**	
Time to CC	N_{Total}	N_{Sig}	N_{Bkg}	α	a	68%	a	68%
2.0 hr	31	20	11	0.55	0.0553	103.28°	0.2797	71.43°
1.0 hr	36	23	13	0.56	0.0560	102.54°	0.2829	68.32°
2 min	58	25	33	1.32	0.0887	93.56°	0.4484	41.57°

Table 3.4: Parameters and results for σ Canis Majoris, Figure 3.7, left panels.

					LS		**LS-Li**	
Time to CC	N_{Total}	N_{Sig}	N_{Bkg}	α	a	68%	a	68%
2.0 hr	44	20	24	1.20	0.0850	96.53°	0.4300	48.26°
1.0 hr	141	23	118	5.13	0.1305	71.60°	0.6596	19.00°
2 min	420	25	395	15.80	0.1466	46.28°	0.7413	9.84°

Table 3.5: Parameters and results for S Monocerotis A, Figure 3.7, right panels

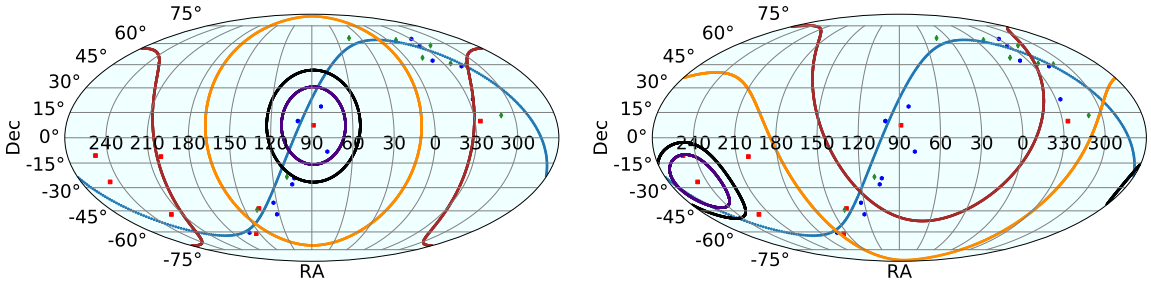

t = -4.0 hours

t = -4.0 hours

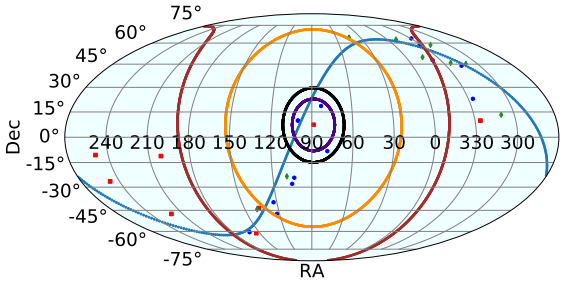

t = -1.0 hour

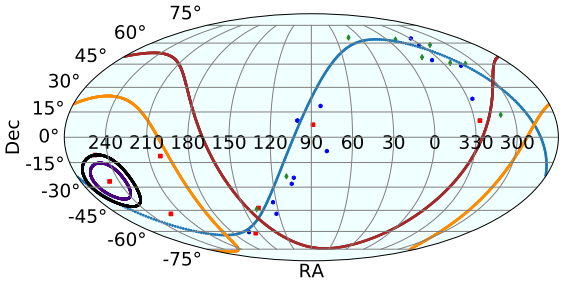

t = -1.0 hour

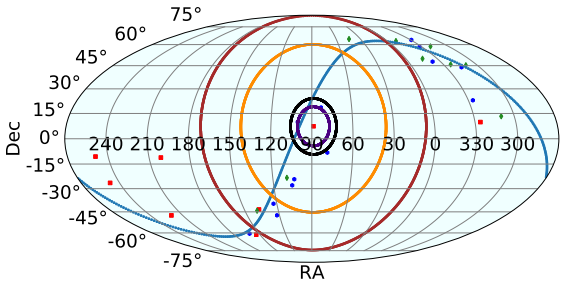

t = -2 minutes

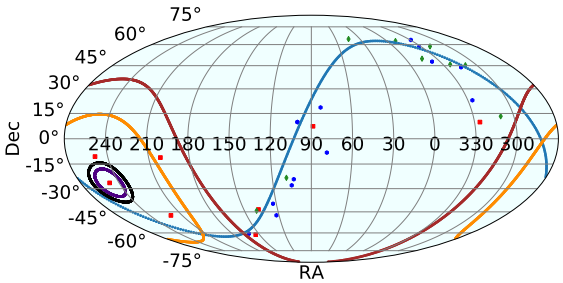

t = -2 minutes

Figure 3.6: Angular error cones at 68% C.L. and 90% C.L. for LS (orange and maroon contours), and LS-Li (indigo and black contours) at 4 hours, 1 hour and 2 minutes prior to the core collapse. The left panels correspond to Betelgeuse (D= 0.222 kpc, $M \simeq 15\ M_{\odot}$); the right panels to Antares (D= 0.169 kpc, $M \simeq 15\ M_{\odot}$). The presence of background is considered in all cases according to An (2016). The number of events is based on the model by Patton *et al.* (2017a).

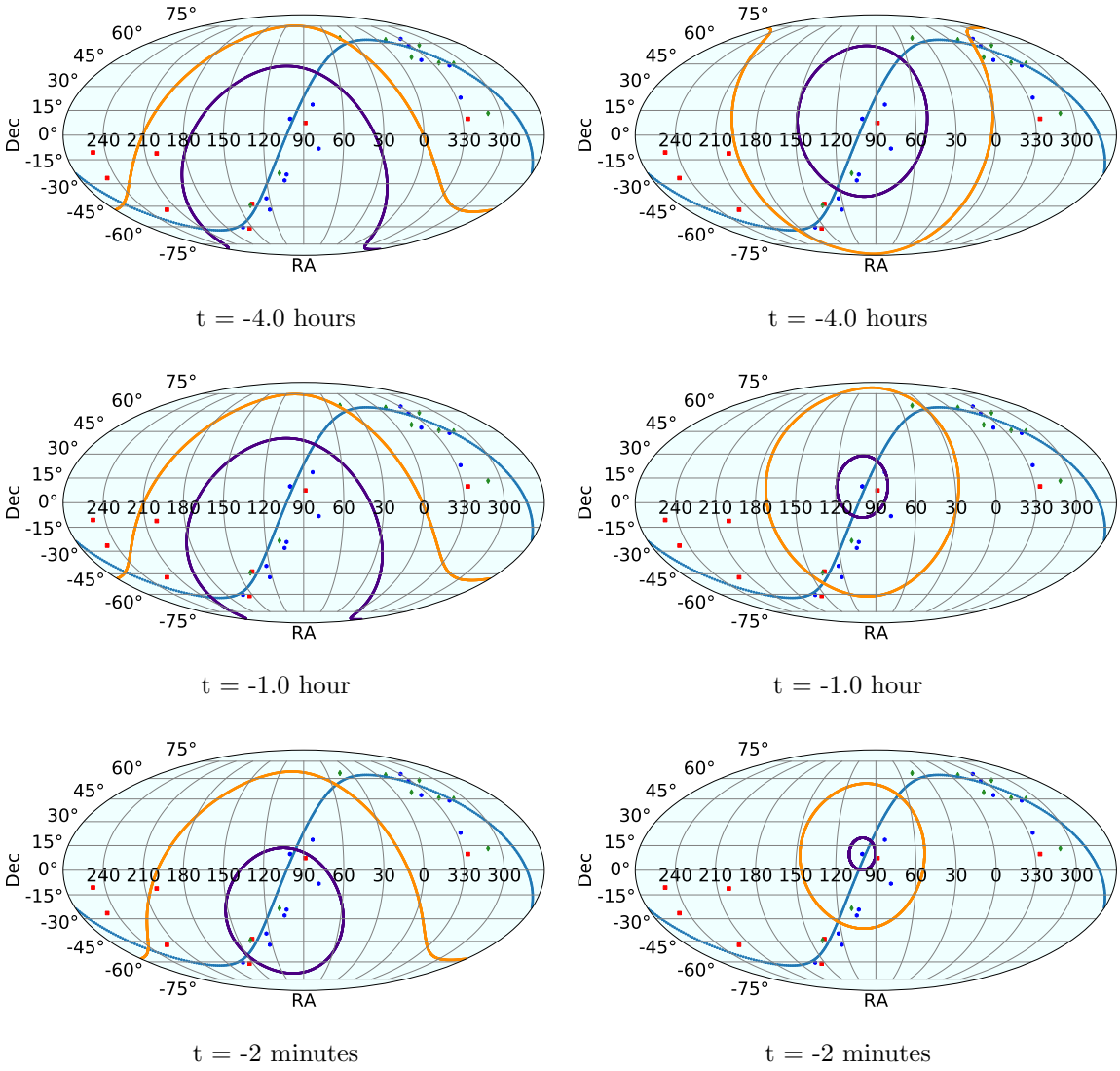

Figure 3.7: Same as Figure 3.6, but for σ Canis Majoris (left panels, D= 0.513 kpc, $M \simeq 15\ M_{\odot}$) and S Monocerotis A (right panels, D= 0.282 kpc, $M \simeq 30\ M_{\odot}$). Only 68% C.L. contours are shown here, for LS (orange) and LS-Li (indigo).

In the case of isotropic background the mean vector, $\vec{p}_m$, still points in the direction of the progenitor star. That is no longer true in the general case of anisotropic background, which would introduce a systematic shift in the direction of $\vec{p}_m$. A naive estimate for a point-like source of background gives an (average) shift in direction by an angle $\delta \lesssim N_{Bkg}/N_S$ (valid if $N_{Bkg} \ll N_S$ and independent of a), corresponding to $\delta \lesssim 4^\circ - 10^\circ$ for parameters typical of Betelgeuse (see Table 3.2). A comparison with the typical values of β indicates that the shift is probably negligible for LS ($\beta \gg \delta$, typically) but might have to be considered for LS-Li. A more accurate estimate of δ depends on site-specific information and is beyond the scope of the present paper.

Another source of potential uncertainty is in the site-specific number of accidental coincidences in the detector (e.g., a coincidence between a positron from a cosmic muon decay and a neutron capture from a different process). Although here we assume a strong muon veto (An, 2016), the actual performance of the veto in a realistic setting may be different and contribute to larger background levels that would negatively affect the presupernova localization. See Cao and Wang (2017) and references therein for technical information on realistic veto designs and their expected performance.

3.3 Progenitor Identification

Attempts at progenitor identification will involve a complex interplay of different information from different channels. Here, we discuss a plausible, although simplified, scenario where two essential elements are combined: (i) pointing information from a single liquid scintillator detector, using the method in Section 3.2; and (ii) a rough estimate of the distance to the star, from the comparison of the signal with models[5].

[5]Circumstances that could further narrow the list of candidate stars include unusual electromagnetic activity from a candidate in the weeks or days preceding the signal, improving the distance

Both these indicators will evolve with time over the duration of the presupernova signal, with the list of plausible candidates becoming shorter as higher statistics are collected in the detector. We emphasize that the goal here is not necessarily to reduce to a single star; even reducing the list to a few stars (3 or 4, for example) can be useful to the gravitational wave and electromagnetic astronomy communities.

Consider the two case studies shown in Figure 3.6 and detailed in Tables 3.2 and 3.3. The left column refers to Betelgeuse and the right column to Antares, both with a time distribution of IBD events as in Figure 3.1 for 15 $M_\odot$. The three panels show how the 68% and 90% C.L. angular errors decrease with time, leading to a progressively more accurate estimate of the position[6]. An algorithm to plot angular error cones om Mollweide projections is discussed in App. C.

For the case of LS, at $t = -1$ hr pre-collapse, as many as $\sim$10 progenitor stars are within the angular error cone, with only a minimal improvement at later times. Therefore, the identification of the progenitor can not be achieved using the angular information alone. It might be possible, however, in the presence of a rough distance estimation from the event rate in the detector. In both examples, a possible upper limit of $D < 0.25$ kpc (red squares in Figure 3.6, also see Figure 2.4) results in a single pre-supernova being favored. For LS-Li, the angular information alone is sufficient to favor 3-4 stars as likely progenitors already $\sim$4 hours pre-collapse. At $t = -1$ hr, a single progenitor can be identified in the case of Antares.

A less fortunate scenario is shown in the left panels in Figure 3.7 (details in Table 3.4) for σ Canis Majoris (distance $D = 0.513$ kpc). The number of events was calculated according to the 15 $M_\odot$ model in Figure 3.1. The lower signal statistics (the

estimate using data from multiple detectors, etc.

[6]In a realistic situation, the center of the angular error cone would be shifted away from the true position of the progenitor star by a statistical fluctuation. This effect is not included here.

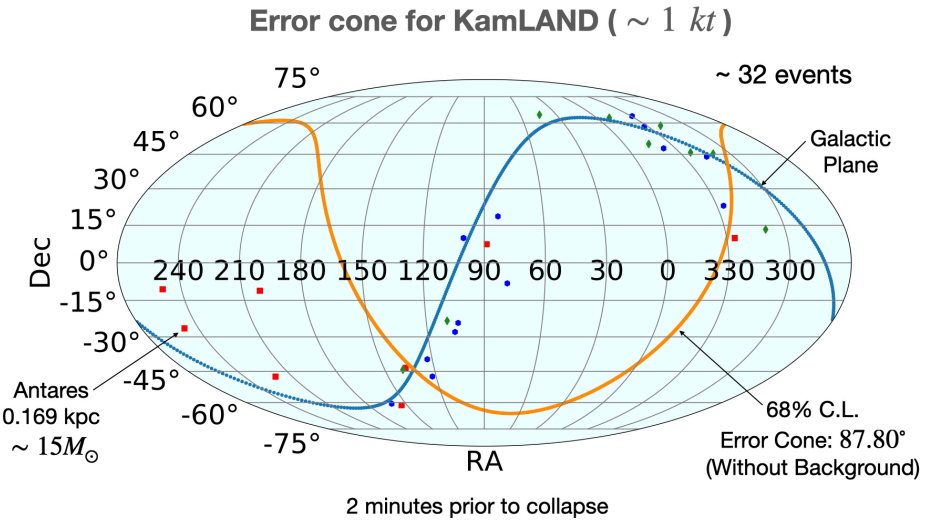

Figure 3.8: The angular uncertainty cone for KamLAND at 2 minutes prior to collapse. Only the 68% C.L. is shown. The progenitor assumed in this case is Antares.

number of events barely reaches 60), and the larger relative importance of the background result in a decreased angular sensitivity. We find that LS will only eliminate roughly half of the sky if we use the 68% C.L. error cone. When combined with an approximate distance estimate, this coarse angular information might lead to identifying ~ 10 stars as potential candidates. With LS-Li, the list of candidates might be slightly shorter but a unique identification would be very unlikely, even immediately before collapse.

A $30\,M_\odot$ case is represented by the right panels in Figure 3.7 (and detailed in Table 3.5) for S Monocerotis A (distance $D = 0.282$ kpc). An hour prior to the collapse $\simeq$ 120 events are expected, allowing LS to shorten the progenitor list to $\simeq$ 12 stars within the error cone at 68% C.L. Whereas, LS-Li narrows the progenitor list down to $\simeq 3$ stars with the same C.L. one hour prior to the collapse. When combined with a rough distance estimate, the progenitor might be successfully identified.

Having established the directional pointing abilities of JUNO, it is worth asking how would the previous and current generation neutrino detectors perform in the context of directional pointing. Since we focused on the IBD channel, liquid scin-

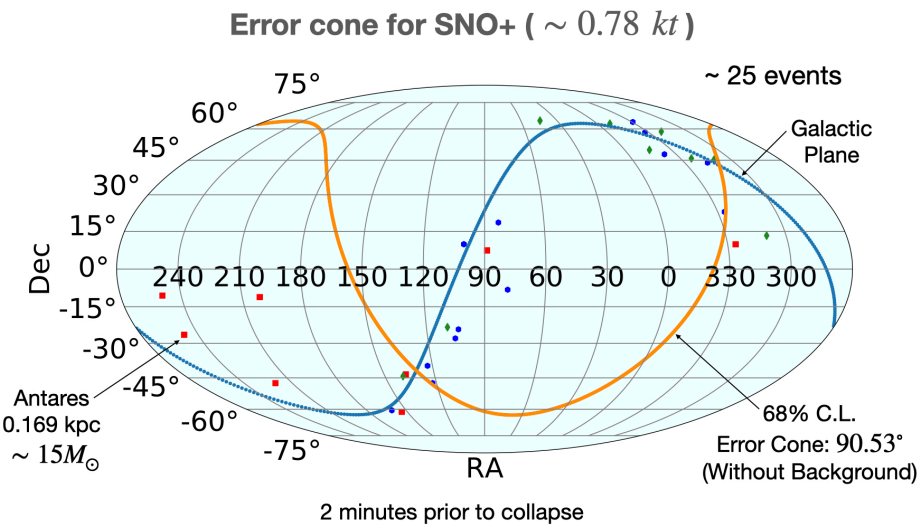

Figure 3.9: Same as Fig. 3.8 but for SNO+.

tillator detectors would ideal and suited to the analysis. Fig. 3.8 shows a plausible outcome for the KamLAND detector and Fig. 3.9 for the SNO+ detector. In both cases because of the small fiducial masses of the two detectors we are limited to very nearby presupernova candidates like Antares. The figures show the 68% confidence level 2 minutes prior to collapse for both the detectors. In both cases, the angular uncertainty cones are $\mathcal{O}(90^\circ)$ which is not very optimistic. KamLAND primarily due to its slightly bigger fiducial mass has the ability to perform slightly better than SNO+.

In closing of this section, let us elaborate on the potential of estimating the distance to the star by comparing the observed neutrino event rate with models. The accuracy of such estimate depends on the uncertainty on model predictions, which in principle can be estimated from the spread in the presupernova neutrino number luminosity from different models in the current literature that begin with the same zero-age main sequence mass. Unfortunately, the presupernova models in the present literature do not allow a reasonable direct comparison due to key, yet often undisclosed, modelling choices made during the evolution of a stellar model (although see

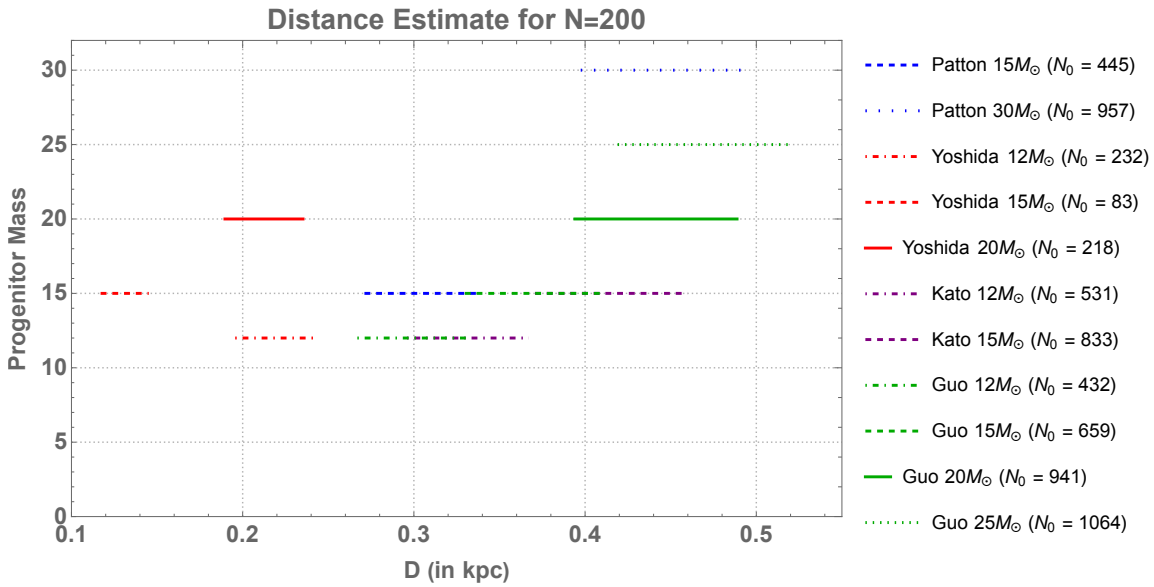

Figure 3.10: Distance cuts based on different models of presupernova neutrino emission. The total number of events predicted by the different models at 0.2 kpc is denoted by N_0. The horizontal lines show the distance corresponding to a 3σ value around the number of events. (Note: The models are referenced in the text).

Patton *et al.* (2017a) for an exception). For example, the neutrino number luminosity can change by more than an order of magnitude due to the prescription used for mass loss by stellar winds over the evolution of the model, the treatment of convective boundaries, the spatial (mass) and temporal resolution of the model over its evolution, the global conservation of energy by the model over its evolution, the number of isotopes evolved by the nuclear reaction network, and how nuclear burning is coupled to the hydrodynamics (operator split versus fully coupled vs post-processing) especially during the advanced stages of massive star evolution. We must conclude, therefore, that the idea to use models to place distance constraints will become realistic only in the future, after more progress is achieved on presupernova emission models. However, to have a current understanding of the situation, we show the distance estimates assuming a fixed number of events ($N = 200$) versus the mass of the

progenitor in Fig. 3.10. We know,

$$N = N_{Total}\left(\frac{D_{Model}}{D}\right)^2 \tag{3.13}$$

Thus,

$$D = (D_{Model})\sqrt{\frac{N_{Total}}{N}} \tag{3.14}$$

The results are shown in Fig. 3.10, assuming a 3σ value around the number of events to predict the distance cuts.

3.4 Backgrounds

The presence of background needs to be addressed since it will affect the pointing abilities negatively. In this section we discuss how the presence of noise affects the error cone and hence the pointing precision using our method. We start with an isotropic case of background.[7] Since pre-supernova neutrinos are low energy neutrinos, the main source of backgrounds will be the low energy geoneutrinos and reactor neutrinos. For a detector like JUNO which we used for our analysis, the main source of background would be the reactor neutrinos. Figure 3.11 shows the half-hourly and the cumulative distribution of background events for JUNO in the reactor on and off phases. The background events are modeled from Apollonio (2000).

The background events should be compared with the number of signal events (see Fig. 3.1 which depend on the distance of the progenitor from Earth. For nearby (~ 0.2 kpc) stars the background can be considered to be fairly low.

The way we put in the background is by introducing a parameter α which is

[7]We think it can be generalized to a more complicated case of a directional background. The directional background will affect the error cone in a way that it would not be centered around the star as it is in the present case which is discussed.

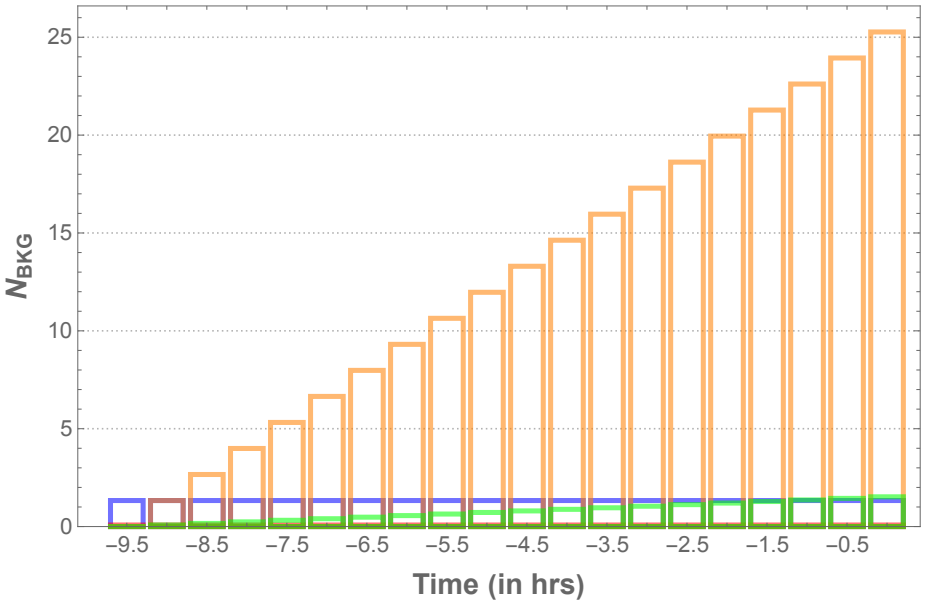

Figure 3.11: Number of background events per half an hour prior to the SN explosion - a) In reactor off phase (Red); b) In reactor on phase (Blue). Cumulative number of events per half an hour prior to the SN explosion - a) In reactor off phase (Green); b) In reactor on phase (Orange).

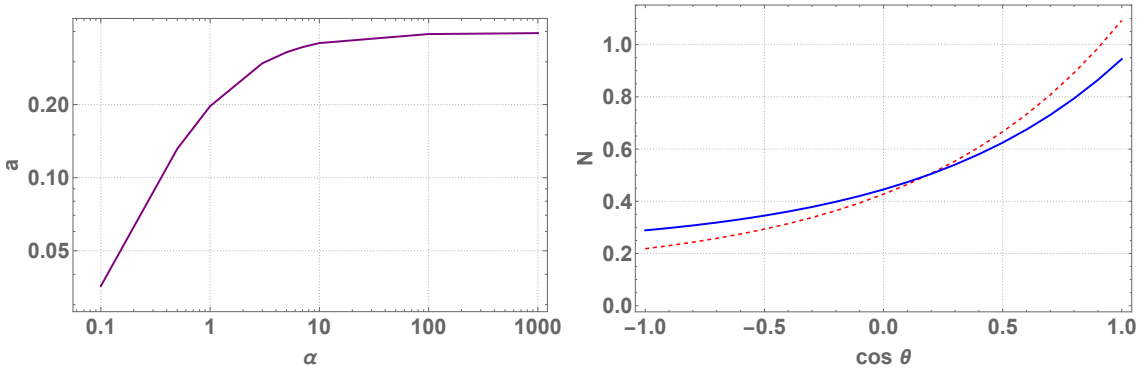

Figure 3.12: Effects on angular uncertainty due to background: *Left Panel:* the variation of asymmetry factor a with α; *Right Panel:* angular distribution of events in the presence of background (blue, solid curve) ($\alpha = 3$) and in the absence of background (red, dashed curve).

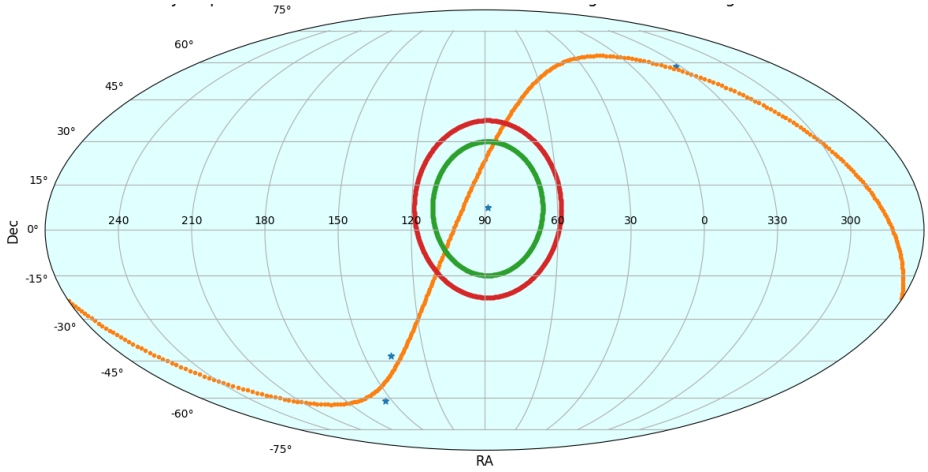

Figure 3.13: Angular uncertainty in the presence (red) and absence (green) of background.

defined as:

$$\alpha = \frac{Signal}{Noise} \tag{3.15}$$

We consider the angular distribution of events, normalize this distribution, and introduce the isotropic time-independent background. This helps in calculating the parameter α. We then re-normalize all of this combined together. Recall, that the main aspect of such a distribution is the number of forward (N_f) and backward (N_b) events which lets us decide the asymmetry parameter a. Fig. 3.12 (left panel) shows the variation of asymmetry factor a with α. As expected, for smaller values of a implying a high background, the asymmetry is very low, i.e., the number of forward and backward events are nearly equal. This results in the angular uncertainty being large and reduces the pointing capabilities. As, α increases to large values implying tiny backgrounds.

3.4.1 Effects On Angular Uncertainty

The angular distribution of events comparing the cases of with and without background is shown in Fig. 3.12 (right panel). The presence of background makes the

Subject	D Small	D Large
D (in kpc)	0.20	0.63
N_{Sig}	200	20
N_{Bkg}	20	20
With Bkg	220	40
Without Bkg	200	20
α	10	1
a	0.3583	0.1970
β (With Bkg)	29.15°	78.52°
β (Without Bkg)	26.72°	66.07°

Table 3.6: Table Showing The Parameters Used In Figure 3.14

distribution flatter implying less asymmetry, thus resulting in an increased angular uncertainty (error cone). Having obtained the value of a corresponding to the background (or α) will change the error cone as shown in Fig. 3.13. As expected, the error cone in the presence of background (red) is larger than in the case without background (green).

As discussed before, the impact of the background on the pointing sensitivities is closely related to the distance to the progenitor. Assuming a fixed background, the main idea is, the closer the progenitor more is the signal events as compared background and larger is α. As distance to progenitor increases the signal and background events become comparable, leading to a small value of α and increased angular uncertainty. The effect of distance on the uncertainty is shown in Fig. 3.14 and corresponding table Tab. 3.6.

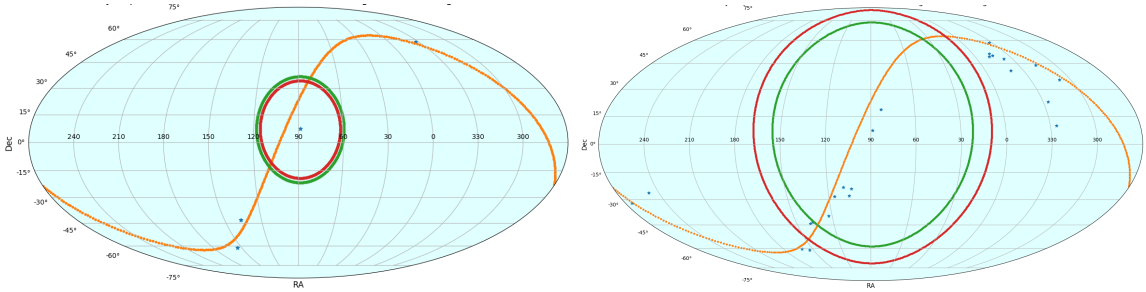

Figure 3.14: Angular uncertainty in the presence of background for: *left panel:* small D (~ 0.2 kpc), and *right panel:* large D.

Chapter 4

THE NEUTRINO GRAVITATIONAL-WAVE MEMORY EFFECT

Neutrino- and gravitational wave-astronomy are emerging players in the new field of multi-messenger astronomy. They both have the potential to investigate "dark" phenomena like the core collapse of a massive star and its possible implosion into a black hole, and the process of inspiral and merger of a binary systems involving at least one neutron star. After the LIGO-Virgo observation of binary mergers (Abbott *et al.*, 2016c, 2017b, 2020a,b), such exploration is already a reality for gravitational waves (GW), and a similar level of steady progress might be achieved in the next decades with the next generation of low background neutrino observatories reaching up to a Megaton mass. While neutrino and GW physics are still mostly developing separately, their potential as complementary probes of the same astrophysical phenomena has recently been recognized, and dedicated, interdisciplinary research has begun.

Surprisingly, so far only limited attention has been paid to the most *direct* connection between neutrinos and GW: the *gravitational memory* caused by (anisotropic) neutrino emission. The essence of this effect has been known since the 1970's (Zel'dovich and Polnarev, 1974; Braginskii and Thorne, 1987): anisotropic neutrino emission, for example by a core collapse supernova, would cause a non-oscillatory, *permanent* strain in the spacetime metric that would in principle be visible at a powerful GW detector (Epstein, 1978; Turner, 1978). The theory of the memory effect is well established, having been developed at the formal level for a generic emitter of radiation and matter (Sago *et al.*, 2004; Suwa and Murase, 2009; Favata, 2010). Early applications to a core collapse supernova were developed as well, analytically and numerically (Epstein, 1978; Turner, 1978; Burrows and Hayes, 1996; Mueller and Janka, 1997a).

Results showed that, in a GW detector, the neutrino-induced memory from a galactic supernova would appear as a signal with typical frequency of $0.1 - 10$ Hz and (dimensionless) strain of $\sim 10^{-22} - 10^{-20}$, which is well below the sensitivity of LIGO and its immediate successors. Long considered unobservable, the memory has thus largely remained a textbook-case curiosity.

This situation is about to change with the third generation of GW detectors, especially those designed to explore the Deci-Hz frontier (Seto *et al.*, 2001; Yagi and Seto, 2011a; Luo *et al.*, 2016; Graham *et al.*, 2016; Shuichi Sato and Masaki Ando, 2017; Pau Amaro-Seoane and Stanislav Babak, 2017; Ruan *et al.*, 2020), namely the region centered at frequency $f \sim 0.1$ Hz. Ambitious projects like the DECi-hertz Gravitational-wave Observatory (DECIGO) (Seto *et al.*, 2001; Yagi and Seto, 2011a) and the Big Bang Observer (BBO) (Yagi and Seto, 2011a) will reach a sensitivity of $\sim 10^{-24}$ in strain, and therefore will be able to observe the supernova neutrino memory. An experimental test of the memory, with its distinctive hereditary nature, would be an important confirmation of general relativity. The new observational prospects have stimulated several modern studies of the supernova neutrino memory, based on state-of-the art hydrodynamic simulations in two and three dimensions (Burrows and Hayes, 1996; Kotake *et al.*, 2007b, 2009a; Muller *et al.*, 2012; Yakunin *et al.*, 2015; Vartanyan and Burrows, 2020), where the detailed time structure of the neutrino luminosity and of the anistropy parameter are modeled. Due to computational cost, simulations have been conducted for isolated examples of progenitor star, and reproduce only part of the memory evolution, up to about 1 s after the core bounce.

In the light of the recent advancements on modeling the memory effect numerically, the time is now mature for the development of phenomenological studies, for the benefit of the broader community, with the goal of assessing the detectability and physics potential of the supernova neutrino memory effect. These studies will

necessarily require a parametric description that captures the essential features of the memory over the entire ~ 10 s of duration of the neutrino burst, and can be applied to wide variety of phenomenological scenarios, corresponding to different stellar progenitors, different outcomes of the collapse (successful explosion or implosion into a black hole), etc. Such description can be useful as a foundation for more advanced phenomenological studies, and as a template to simulate the response of a GW detector to a memory signal.

This work is a first effort in this direction. We develop a phenomenological model of the neutrino-induced memory strain both in time and frequency domain. Our model is sufficiently realistic – because it is based on realistic (although simplified) assumptions, motivated by numerical results for the memory and at the same time is sufficiently simple to be used widely. We apply it to a number of plausible core collapse scenarios, and discuss the physics potential of a joint detection of a neutrino burst and a memory signal from a galactic supernova. Our study extends and complements previous analytical description of the memory, which were developed for long gamma-ray bursts (GRBs) (Sago *et al.*, 2004) where the memory from a single jet and a unified model of the GRB were considered along with the angular dependence of the wave-form, supermassive stars (Li *et al.*, 2018) which estimated the memory strain magnitude from supermassive stars ($\sim 5 \times 10^4 M_\odot$) and discussed the prospects of their detection and hypernovae (Suwa and Murase, 2009) using spherically symmetric and oblate-spheroidal accretion discs and constant neutrino anisotropy parameter.

This chapter is structured as follows. In Sec. 4.1 the formalism describing the memory signal is summarized, and general upper bounds are derived. Our model is introduced in Sec. 4.2; then in Sec. 4.3 we present applications and discuss the detectability of the supernova neutrino memory at future Deci-Hz interferometers.

Some technical details are included in App. E.

4.1 Formalism

In this section we summarize the formalism that describes the memory strain due the anisotropic emission of radiation (massless particles) by a generic source, and specialize it to neutrinos from a core collapse supernova.

4.1.1 Memory Wave Form

For completeness, here we review the theoretical framework of the memory, following closely some classic papers on the subject (Weinberg, 1972; Misner *et al.*, 1973; Epstein, 1978). For brevity, certain derivations are omitted; we refer the reader to appendix E for those.

The starting point is Einstein's field equation,

$$R_{\mu\nu} - \frac{1}{2} R g_{\mu\nu} = -8\pi G T_{\mu\nu} \,, \tag{4.1}$$

where, $R_{\mu\nu}$ is the Ricci tensor, the Ricci scalar $R = 8\pi G T^{\mu}_{\mu}$, $g_{\mu\nu}$ is the metric, G is the Newton's universal gravitational constant and $T_{\mu\nu}$ is the stress-energy tensor[1].

Here it suffices to work in the weak-field approximation, where the metric is nearly flat, with small perturbations $h_{\mu\nu}$:

$$g_{\mu\nu} = \eta_{\mu\nu} + h_{\mu\nu}. \tag{4.2}$$

In this approximation, the field equations (4.1) are still invariant under coordinate transformations that preserve the weak-field condition. We can use this gauge freedom to choose a convenient gauge: $g^{\mu\nu}\Gamma^{\lambda}_{\mu\nu} = 0$ ($\Gamma^{\lambda}_{\mu\nu}$ is the Christoffel symbol defined in Appendix E). By keeping only terms up to first order in $h_{\mu\nu}$, from (4.1) we get the

[1]The detailed expressions for each are given in Appendix E

following wave equation in flat space for the field perturbation,

$$\Box^2 h_{\mu\nu} = -16\pi G S_{\mu\nu}\,, \tag{4.3}$$

where the effective stress-energy tensor (in presence of matter) is $S_{\mu\nu} = T_{\mu\nu} - \frac{1}{2}\eta_{\mu\nu}T^{\lambda}_{\lambda}$. One can solve the wave equation by using the retarded Green's function corresponding to the D'Alembert operator in four-space time dimensions, so to obtain the expression:

$$h_{\mu\nu} = 4G \int d^3\vec{x}' \Big(\frac{S_{\mu\nu}(\vec{x}', t - |\vec{x} - \vec{x}'|)}{|\vec{x} - \vec{x}'|} \Big)\,. \tag{4.4}$$

The gauge choice leading us to this solution does not fix completely all the gauge freedom and an additional constraint should be imposed to leave only the physical degrees of freedom. This is done by projecting the source tensor $S_{\mu\nu}$ into its transverse-traceless (TT) components (see for example Misner *et al.* (1973)). Doing this and without loss of generality, we will use the following very well known ansatz for the source term proposed in Epstein (1978),

$$S^{ij}(t, x) = \frac{(n^i n^j)_{TT}}{r^2} \int_{-\infty}^{\infty} \sigma(t') f(\Omega', t') \delta(t - t' - r) dt', \tag{4.5}$$

where, $\vec{n} = \vec{x}/r$, $r = |\vec{x}|$ and the sub index (TT) denotes the transverse-traceless component. This source term represents the effect of emitted radiation from the source origin at $x = 0$ [2]. Here $\sigma(t)$ denotes the rate of energy loss, and $f(\Omega', t')$ is the angular distribution of emission, where the argument Ω' is a shorthand notation indicating the dependence on the angles ϑ' and φ'. $d\Omega'$ is the differential solid angle, $d\Omega' = \sin(\vartheta')d\vartheta' d\varphi'$ (see Fig. 4.1), so that $f(\Omega', t') \geq 0$ and $\int f(\Omega', t') d\Omega' = 1$. After substituting the ansatz (4.5) into the wave form (4.4), and integrating, we obtain the following expression for the wave form:

$$h^{ij}_{TT}(t, x) = 4G \int_{-\infty}^{t-r} \int_{4\pi} \frac{(n^i n^j)_{TT} f(\Omega', t') \sigma(t')}{t - t' - r\cos\theta} d\Omega' dt'\,, \tag{4.6}$$

[2] Due to the conservation of the stress-energy tensor, we only need to consider the spatial index of the tensor

where θ is the angle between the observer position and the radiation source point. Following Mueller and Janka (1997a), we assume that the observer is situated at a distance $r = |x| \to \infty$ from the source. The radiation that reaches the observer at a time t was actually emitted at time, $t' = t - r/c$, physically representing a case where the neutrino pulse itself causes a gravitational wave signal. We can now rewrite (4.6) in this approximation as,

$$h^{ij}_{TT}(t,x) = \frac{4G}{rc^4}\int_{-\infty}^{t-r/c} dt' \int_{4\pi} \frac{(n^i n^j)_{TT}}{1-\cos\theta}\frac{dL_\nu(\Omega',t')}{d\Omega'}d\Omega', \tag{4.7}$$

where, $f(\Omega',t')\sigma(t') = \frac{dL_\nu(\Omega',t')}{d\Omega'}$, which is the direction dependent neutrino luminosity.

Fig. 4.1 shows the orientation of the coordinate axes for the observer and the source. The different angles involved are also shown. The wave $h^{ij}_{TT}(t,x)$ can be either '+' or '×' polarized. We denote the '+' polarization as, $h^{xx}_{TT} = -h^{yy}_{TT} = -h^{+}_{TT}$. With this in mind, we now need to compute the different pieces of (4.7). One obtains (see Appendix E) $(n^x n^x)_{TT} = \frac{1}{2}(1-\cos^2\theta)(2\cos^2\phi - 1) = \frac{1}{2}(1-\cos^2\theta)\cos 2\phi$. Substituting this in Eq. (4.7) gives,

$$h^{xx}_{TT} = \frac{2G}{rc^4}\int_{-\infty}^{t-r/c} dt' \int_{4\pi} (1+\cos\theta)\cos 2\phi \frac{dL_\nu(\Omega',t')}{d\Omega'}d\Omega'. \tag{4.8}$$

The '×' polarization, $h^{xy}_{TT} = h^{\times}_{TT}$ can be found by simply replacing $\cos 2\phi$ by $\sin 2\phi$. One can isolate the angular dependence by defining the *anisotropy parameter* $\alpha(t)$ as,

$$\alpha(t) = \frac{1}{L_\nu(t)}\int_{4\pi} d\Omega'\ \Psi(\vartheta',\varphi')\ \frac{dL_\nu(\Omega',t)}{d\Omega'}\,, \tag{4.9}$$

where $\Psi(\vartheta',\varphi')$ is an angle-dependent function that depends solely on the location of the observer with respect to the source, i.e., θ and ϕ appearing in Eq. (4.8) are expressed in terms of ϑ' and φ' based on the observer's location with respect to the source (see Mueller and Janka (1997a); Kotake *et al.* (2009a) for example and details.)

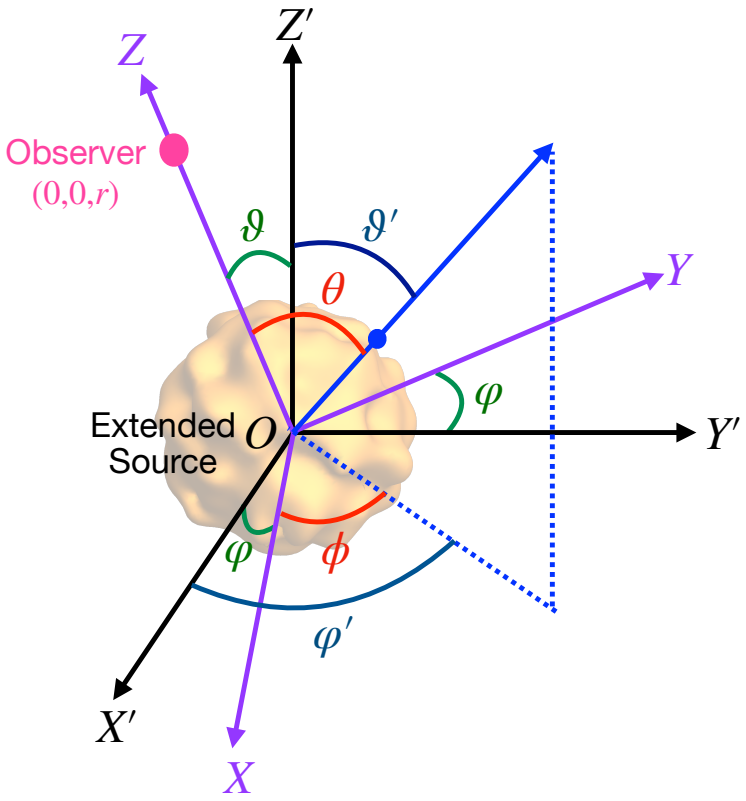

Figure 4.1: Setup of the coordinate systems - (XYZ) (Purple): Coordinate system for observer , $(X'Y'Z')$ (Black): Coordinate system for source (source is treated as an extended source, centered at the origin; denoted by yellow blob). The blue dot is a point on the surface of the extended source and the corresponding position vector is shown as a blue arrow. (ϑ', φ') (Dark Blue): Radiation direction in the source frame $(X'Y'Z')$; (θ, ϕ) (Red): Radiation direction in the observer's frame (XYZ), (ϑ, φ) (Dark Green): Orientation of observer's frame (XYZ) with respect to the source frame $(X'Y'Z')$. Observer (Pink) is located along the Z-axis at a distance, r $(0, 0, r)$.

This enables us to write (4.8) in the following convenient form,

$$h^{xx}_{TT} = h(t) = \frac{2G}{rc^4} \int_{-\infty}^{t-r/c} dt' L_\nu(t') \alpha(t') \,. \tag{4.10}$$

The anisotropy parameter plays a very significant role in determining the amplitude of the gravitational wave strain $h(t)$. It is mainly governed by the complex dynamics of the source. We will discuss its role in more detail in later sections. It is important to note here that if an ideal gravitational wave detector has two freely falling masses which have a vectorial separation of l_k, the gravitational wave strain

changes their separation by δl_j where,

$$\delta l_j = \frac{1}{2} h^{TT}_{jk} l^k \,. \tag{4.11}$$

Of course in Eq. (4.10), we have just considered the strain in the x-directon. It may also be useful to express the gravitational wave strain $h(t)$ in frequency space,

$$\tilde{h}(f) = \int_{-\infty}^{\infty} h(t)\, e^{2\pi i\, ft}\, dt \,, \tag{4.12}$$

where, $\tilde{h}(f)$ is the Fourier transform of $h(t)$. Finally, we define the characteristic strain $h_c(f)$ (Sago *et al.*, 2004; Li *et al.*, 2018) as,

$$h_c(f) = 2f|\tilde{h}(f)| \,. \tag{4.13}$$

This is a dimensionless quantity (the f appearing above makes it dimensionless), which helps in computing the signal to noise ratio (SNR) for a given gravitational wave detector and compare the signal to the sensitivity curve of the detector to predict the prospects of detection of the signal using the given detector.

4.1.2 General Properties Of The Neutrino Memory Signal

In this section we discuss properties of the memory signal, in the time and frequency domain, that stem directly from its expression as an integral over time, Eq. (4.10), and therefore have general validity.

Time domain: evolution and upper bound

Considering the finite duration ($\Delta t \sim 10$ s) of the neutrino burst, from (4.10) we expect the metric perturbation $h(t)$, to transition from an asymptotic value $h = 0$ at earlier times ($t \to -\infty$) to a different asymptotic value $h = \Delta h$ at later times ($t \to +\infty$), as sketched in Fig. 4.2. The characteristic rise time must be $\delta t \lesssim$

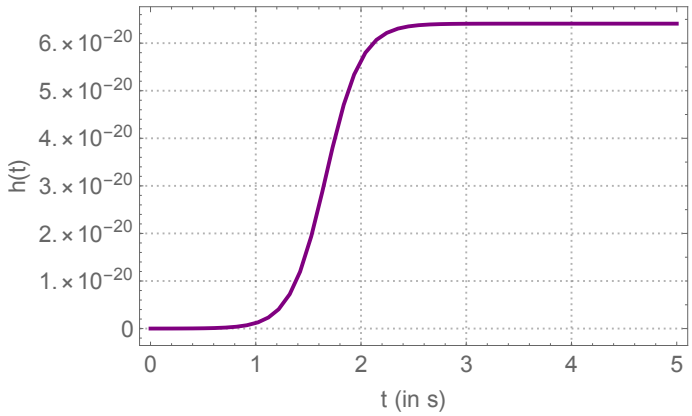

Figure 4.2: Sketch of a typical gravitational wave memory strain profile, $h(t)$.

Δt, depending on the time dependence of $\alpha(t)$. In physical terms, the gravitational memory accumulates from the arrival of the first neutrinos to Earth until the neutrino burst has passed completely.

We can place a conservative upper limit on $h(t)$ from the following inequality:

$$|h(t)| \leq \frac{2G}{rc^4} \int_{-\infty}^{\infty} L_\nu(t) |\alpha(t)| dt \leq \frac{2G}{rc^4} |\alpha|_{max} E_{tot} \ . \tag{4.14}$$

Here we accounted for the possibility that $\alpha(t)$ may be negative and change sign (see Sec. 4.2.2), and $|\alpha|_{max}$ is the maximum of its value (in modulus). $E_{tot} = \int_{-\infty}^{\infty} L_\nu(t) dt \simeq 3 \times 10^{53}$ ergs is the total energy emitted by neutrinos. Numerically, Eq. (4.14) gives:

$$|h(t)| \leq 6.41 \ 10^{-20} \left(\frac{|\alpha|_{max}}{0.04} \right) \left(\frac{E_{tot}}{3 \ 10^{53} \text{ ergs}} \right) \left(\frac{r}{10 \text{ kpc}} \right)^{-1} \ . \tag{4.15}$$

The same bound holds for $|\Delta h|$, as one can easily verify.

Frequency domain: limiting cases

Let us now discuss the main features of $h_c(f)$ (Eq. 4.13). We expect it to be dominated by frequencies of the order of $f_c \sim 1/2\pi\delta t \gtrsim 1/2\pi\Delta t \sim 0.02$ Hz.

In agreement with previous literature (Turner, 1978; Favata, 2011), in the *zero frequency limit* (ZFL), $f \ll f_c$, $h_c(f)$ tends to a constant value. This can be proven by observing that:

$$\lim_{f\to 0} h_c(f) = \lim_{f\to 0} |2f\tilde{h}| = \lim_{f\to 0} \left|\frac{i}{\pi}\dot{\tilde{h}}\right| \,, \tag{4.16}$$

where we used the well known property relating the Fourier Transform of a function to the Fourier Transform of its derivative ($\tilde{\dot{g}}(f) = -2\pi i\, f\tilde{g}(f)$) (see appendix E for the validity of this property in the case at hand). Now, we note that

$$\lim_{f\to 0} \dot{\tilde{h}} \;=\; \lim_{f\to 0} \int_{-\infty}^{\infty} \dot{h}(t) e^{2\pi i\, f\, t} dt = \int_{-\infty}^{\infty} \dot{h}(t) dt = \Delta h \,, \tag{4.17}$$

leading immediately to the result

$$\lim_{f\to 0} h_c = \frac{|\Delta h|}{\pi} \,, \tag{4.18}$$

which does not depend on f. Therefore, we expect a flat behaviour of h_c at low frequencies, characterized by the strength of the metric change Δh [3].

When combined with Eq. (4.14), Eq. (4.18) gives an upper limit:

$$\lim_{f\to 0} h_c \leq \frac{2G}{\pi r c^4} |\alpha|_{max} E_{tot} \simeq 2.0\ 10^{-20} \left(\frac{|\alpha|_{max}}{0.04}\right) \left(\frac{E_{tot}}{3\ 10^{53}\ \text{ergs}}\right) \left(\frac{r}{10\ \text{kpc}}\right)^{-1} \,. \tag{4.19}$$

The latter bound can be shown to be valid at all frequencies. Indeed, consider that, from Eq. (4.8), we can write

$$\dot{h}(t) = \frac{2G}{rc^4} L_\nu(t)\alpha(t) \,. \tag{4.20}$$

Therefore

$$|\dot{\tilde{h}}| = \frac{2G}{rc^4} \left| \int_{-\infty}^{\infty} L_\nu(t)\alpha(t) e^{2\pi i\, f\, t} dt \right| \leq \frac{2G}{rc^4} \int_{-\infty}^{\infty} L_\nu(t)\, |\alpha(t)| dt \,. \tag{4.21}$$

[3] The ZFL provides a good estimate of the wave strain when the time scale of the burst is much longer than the neutrino emission process (Turner, 1978). Additionally, at the ZFL the neutrino quantum production can be computed classically.

This result can then be combined with Eqs. (4.14), and (4.18), to confirm the bound in Eq. (4.19).

Let us now study the behavior of the $h_c(f)$ in the high frequency regime, $f \gg f_c$. A good starting point is the derivative $\dot{h}$, Eq. (4.20). On physical grounds we know that the luminosity $L_\nu(t)$ is positive and bounded from above. Furthermore, it is natural to assume that product $L_\nu(t)\alpha(t)$ is zero outside a finite interval of time. This because the neutrino burst has a characteristic duration of tens of seconds (with a sharp decline of $L_\nu(t)$ at $t \sim 30 - 40$ s post-bounce, when the neutrino emission transitions from surface to volume emission). Furthermore, numerical simulations (see for example Kotake *et al.* (2007b, 2009a); Vartanyan and Burrows (2020)) suggest that the anisotropy parameter $\alpha(t)$ be mainly due to the spiral SASI, which has a characteristic duration of $\mathcal{O}(10^{-1})$ s.

These arguments justify us to treat $\dot{h}(t)$ as a function that has compact support in a given time interval:

$$\begin{cases} \dot{h}(t) \neq 0 & t_1 \leq t \leq t_2 \\ \dot{h}(t) = 0 & \text{otherwise} \end{cases} . \tag{4.22}$$

We can then use one of the incarnations of the Paley–Wiener theorem, which asserts (see for example Stein and Weiss (1971)):

The Paley–Wiener theorem: *Let $g(t)$ be a C^∞ function vanishing outside an interval $[A, B]$, then $\tilde{g}(f)$ is an analytic function of exponential type $\sigma = \max\{|A|, |B|\}$*[4] *and is rapidly decreasing, i.e, $|\tilde{g}(f)| \leq c_N \left(1 + \frac{f}{f_c}\right)^{-N}$ for all N, where f is the frequency in the present context.* Which immediately implies that [5],

[4] An analytic function is said to be of exponential type σ if for every $\epsilon > 0$ there exists a real constant A such that $|\tilde{g}(z)| \leq A\, e^{(\sigma+\epsilon)|z|}$ for $|z| \to \infty$

$$|\tilde{\dot{h}}(f)| \leq c_N \left(1 + \frac{f}{f_c}\right)^{-N} \tag{4.23}$$

Using (4.16), we have

$$h_c(f) = \frac{|\tilde{\dot{h}}(f)|}{\pi} \leq \frac{c_N}{\pi} \left(1 + \frac{f}{f_c}\right)^{-N} , \tag{4.24}$$

for all integers N. By staying as conservative as possible, we can take the less constraining integer $N = 1$. In principle, as the theorem states, c_N can be any constant that allows the bound to exist, but we can estimate it in our case, by comparing it with the zero-frequency limit, in other words, taking $f = 0$ in the expression above, we have,

$$h_c(f) \leq \frac{c_1}{\pi} , \tag{4.25}$$

which combined with (4.18) allow us to state that the high-frequency behaviour of the characteristic strain should satisfy the decaying property,

$$h_c(f) \leq \frac{|\Delta h|}{\pi} \left(1 + \frac{f}{f_c}\right)^{-1} . \tag{4.26}$$

This result provides us with a nice interpolation between the zero frequency limit – which leads us to the flat bound (frequency-independent) in Eq. (4.19) – and a increasingly stringent bound at higher frequencies. Such trend will be confirmed in all our phenomenological models, as will be seen in Sec. 4.3.

4.2 A Phenomenological Model Of Neutrino Memory

In this section we construct a phenomenological model for the memory effect, first by taking inspiration from the results of numerical simulations, and then generalizing to a broader range of situations. To keep the model sufficiently simple, in its analytical

[5]Notice that the constant c_N has to be positive and f_0 is the typical frequency scale of the particular model.

form, we will concentrate on reproducing the features of the neutrino luminosity and of the anisotropy parameter that develop over time scales of 0.1 s or larger. These correspond to frequency scales ($f \lesssim 10$ Hz) at or close to the Deci-Hz range, which is most promising experimentally.

4.2.1 Neutrino Luminosity And Anisotropy Parameter

This subsection contains a brief overview of neutrino emission from a supernova – with emphasis on the aspects most relevant to the memory – for the benefit of the broader readership.

The aging process of a massive star ($M \geq 8\ M_{\odot}$) involves several phases of nuclear burning, finally culminating in a pressure loss, which leads to the gravitational collapse of the star's core. Due to a sharp rise in the incompressibility of nuclear matter, the collapse eventually comes to an abrupt stop, and the core bounces back, producing a forward moving shockwave. The shockwave is initially stalled for a fraction of a second, and then it either dies out (leading to black hole formation) or is launched due to energy deposition by neutrinos, thus causing the explosion of the star.

As a result of the core collapse and bounce, $E_{tot} \sim 3\ 10^{53}$ ergs of gravitational energy is released, and most of it is emitted in thermal neutrinos and anti-neutrinos of all flavors, over a time scale of $\sim 1 - 10$ s. The emission is largely isotropic, however, transient anisotropies of the order of $\sim 10^{-3} - 10^{-2}$ are expected to develop. We can distinguish three main phases for the neutrino emission:

- The *neutronization burst*. The initial emission of neutrinos after core collapse is dominated by electron neutrinos (ν_e) due to the absorption of electrons on neutrons and nuclei. The signature of this processes is a sharp peak in $L_\nu(t)$, of about ~ 2 ms width. Numerical simulations (Kotake *et al.*, 2007b, 2009a; Var-

tanyan and Burrows, 2020) show that, at this stage, the anisotropy parameter is negligible ($\alpha(t) \leq 0.001$); an indication that the shock maintains spherical symmetry. Here we will assume $\alpha = 0$ during neutronization.

- The *accretion phase*. Until $t \sim 0.2 - 1.0$ s post-bounce, when the shockwave is stalled, the neutrino emission is approximately thermal and it is powered by the influx of matter accreting on the collapsed core. The neutrino luminosity time profile, after the sharp neutronization peak, becomes nearly flat, reaching a plateau value of $L_\nu \simeq few\ 10^{52}$ erg s^{-1}. Numerical simulations confirm that in the accretion phase the physics near the core is complex, being characterized by turbulence and hydrodynamical instabilities, like the Standing Accretion Shock Instability (SASI), which causes fluctuations of the neutrino luminosity around the plateau value with a characteristic time scale $\delta t \simeq 10^{-2}$ s (Blondin and Shaw, 2007; Kotake *et al.*, 2007b, 2009a; Walk *et al.*, 2020b). The same phenomena lead to anisotropies in the neutrino emission; in particular, the *spiral* SASI mode has been found to be associated to an anisotropy parameter $|\alpha| \sim 10^{-3} - 10^{-2}$ (Mueller and Janka, 1997a; Kotake *et al.*, 2009a). α could change sign over time, transitioning between positive and negative, as the orientation of plane of the spiral SASI changes relative to the observer (Kotake *et al.*, 2009a); see Fig. 4.3b for an example.

- The post-accretion time: *cooling phase*. If the shock is launched, the neutrino emission continues beyond the accretion phase (otherwise, in the case of black hole formation, it drops sharply at $t \sim 0.5 - 1$ s post-bounce, see e.g., Kuroda *et al.* (2017, 2018); Vartanyan *et al.* (2019); Walk *et al.* (2020b); Shibagaki *et al.* (2021)). The collapsed core – which is now a newly-born proto-neutron star – and its surrounding regions slowly cool by thermally radiating neutrinos of all

flavors. The neutrino luminosity and average energy decline smoothly with time, over a scale of $\mathcal{O}(10)$ s. Since the state-of-the-art numerical simulations stop at or before the end of the accretion phase, there are no quantitative estimates of the anisotropy parameter in the cooling phase. Intuitively, one may expect a relaxation of the system into a more symmetric configuration (smaller anisotropy), however the question remains open.

4.2.2 Phenomenological Description Of The Neutrino Memory

Let us now construct a phenomenological description of the memory strain that well approximates the results of numerical simulations, and can serve as a template for generalizations to a wider range of cases (Sec. 4.3).

To fix the ideas, we first consider a scenario where the neutrino emission has anisotropy only in the accretion phase, and therefore only this phase contributes to the memory effect. As discussed in Sec. 4.2.1, during the accretion phase $L_\nu(t)$ has an irregular behavior over time scales $\delta t \sim 0.01$ s or so, due to turbulence and SASI, however its global shape over a time interval $\Delta t \gtrsim 1$ s – which is most relevant to capture the spectrum at low frequency, as will be shown later – can be approximately described by the functional form

$$L_\nu(t) = \lambda + \beta \ \exp\big(-\chi\, t\big) \ , \tag{4.27}$$

(see Fig. 4.3). Here l, β and χ are phenomenological parameters, and it is assumed that Eq. (4.27) is only valid locally (i.e., for a finite interval of time post-bounce), since $L_\nu(t)$ should vanish at $t \to \pm\infty$.

Inspired by published numerical results (Kotake *et al.*, 2007b, 2009a; Vartanyan and Burrows, 2020; Suwa and Murase, 2009), we model the asymmetry function as a

multi-Gaussian, added to a constant component:

$$\alpha(t) = \kappa + \sum_{j=1}^{N} \xi_j \ \exp\left(- \frac{(t-\gamma_j)^2}{2\sigma_j^2} \right) , \tag{4.28}$$

for $t > 0$ [6]. While largely oversimplified, this form captures the essential physical features of $\alpha(t)$ (Sec. 4.2.1), as is shown in Fig. 4.3, where Eq. (4.28) is compared to a numerical result. Furthermore, Eqs. (4.27) and (4.28) lead to reasonably accurate results for the memory strain, as is discussed below.

By substituting the expressions (4.27) and (4.28) in Eq. (4.10), one obtains a closed form for the memory strain as a function of time:

$$\begin{aligned} h(t) = \sum_{j=1}^{N} \Bigg\{ & \left[h_{1j} \left(\operatorname{erf}\left(\rho_j \ \tau_{1j}\right) + \operatorname{erf}\left(\rho_j (t - \tau_{1j})\right) \right) \right] \\ & + \left[h_{2j} \left(\operatorname{erf}\left(\rho_j \ \tau_{2j}\right) + \operatorname{erf}\left(\rho_j (t - \tau_{2j})\right) \right) \right] \Bigg\} \\ & + \left[h_3 \left(\frac{\beta}{\chi} \left(1 - \exp\left(-t\chi\right) \right) + \lambda t \right) \right] , \end{aligned} \tag{4.29}$$

where,

$$\begin{aligned} h_{1j} &= \frac{2G}{rc^4} \sqrt{\frac{\pi}{2}} \beta \xi_j \sigma_j \exp\left(\frac{\chi}{2} (-2\gamma_j + \sigma_j^2 \chi) \right) , \\ \rho_j &= \frac{1}{\sqrt{2}\sigma_j} , \\ \tau_{1j} &= \gamma_j - \sigma_j^2 \chi , \\ h_{2j} &= \frac{2G}{rc^4} \sqrt{\frac{\pi}{2}} \lambda \xi_j \sigma_j , \\ \tau_{2j} &= \gamma_j , \\ h_3 &= \frac{2G}{rc^4} \kappa . \end{aligned} \tag{4.30}$$

[6] For the sake of obtaining closed analytical formulae for the memory in time and frequency space, we imposed $\alpha(t) = 0$ for $t \leq 0$; this is immaterial for the conclusions of this work.

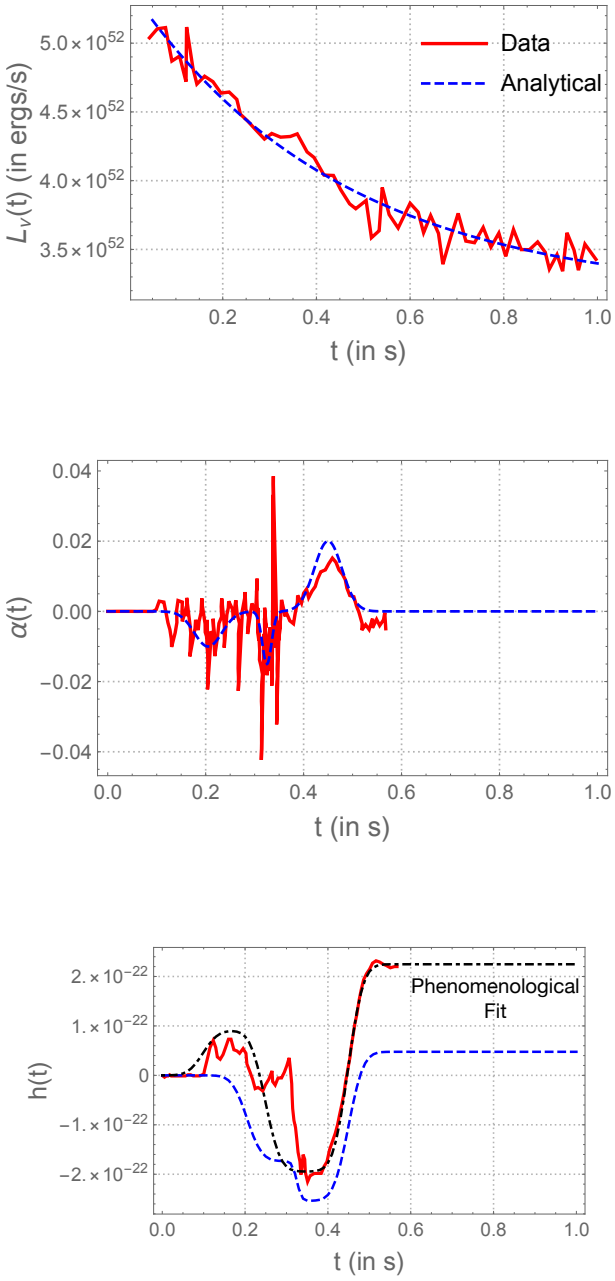

Figure 4.3: Phenomenological curves from our model (dashed lines), in comparison with numerical results (solid lines) for: (a) the neutrino (ν_e) luminosity, $L_\nu(t)$; (b) anisotropy parameter $\alpha(t)$; and (c) the GW strain, $h(t)$. The numerical results in (a) are from Vartanyan and Burrows (2020), whereas those in (b) and (c) are from Kotake *et al.* (2009a) In (c), the dashed (blue) curve is obtained using the same parameters as the curves in (a) and (b). An additional line (dot-dashed, black) is plotted, showing a phenomenological fit to the numerical data using Eq. (4.29).

Here erf (x) is the error function, erf $(x) = \frac{2}{\sqrt{\pi}} \int_0^x \exp(-t^2) dt$, and a factor of $2G/rc^4 = 5.34 \times 10^{-65}$ (10 kpc$/r$) m has been isolated where possible, to facilitate the comparison with Eq. (4.10).

In the expression (4.29), we can identify the main features of the memory signal. For a single Gaussian anisotropy bump ($N = 1$), there are three distinct terms. The first and second terms are due to the exponential and constant part of L_ν, respectively, in combination with the Gaussian part of $\alpha(t)$. They show the typical rise and plateau behavior expected from the theory (Sec. 4.1.2, Fig. 4.2), where the timescale of the rise is, naturally, given by the width of the anisotropy Gaussian, σ_j. The third term is proportional to the constant part of the anisotropy parameter, and therefore the time-scale of its rising and plateauing is the time-scale of the neutrino luminosity, $1/\chi$. Finally, in Eq. (4.29) one may notice a term of the form $\kappa\lambda t$, which is due to the constant terms in L_ν and in $\alpha(t)$; this term vanishes in realistic realizations (see next section), and therefore it is not a cause of concern.

Let us now describe the memory strain in the frequency domain. From Eq. (4.29), a closed form is obtained for the Fourier transform of h:

$$\begin{aligned}\tilde{h}(f) = \sum_{j=1}^{N} \Bigg[\Bigg(& h_{1j} \frac{i}{\pi f} \exp\left(\frac{-\pi^2 f^2}{\rho_j^2}\right) \exp\left(i 2\pi f \tau_{1j}\right) \Bigg) \\ & + \left(h_{2j} \frac{i}{\pi f} \exp\left(\frac{-\pi^2 f^2}{\rho_j^2}\right) \exp\left(i 2\pi f \tau_{2j}\right) \right) \Bigg] \\ & + \left(\sqrt{2\pi}\, h_3 \frac{\beta}{\chi} \left(\frac{1}{i 2\pi f} - \frac{1}{-\chi + i 2\pi f} \right) \right),\end{aligned} \tag{4.31}$$

where i is the imaginary unit.

Here we analyze the structure of Eq. (4.31) to infer the properties of $h_c(f) = f|\tilde{h}(f)|$. In Eq. (4.31), the terms proportional to f^{-1} produce the expected low-frequency limit, where $h_c(f)$ tends to a constant value (see Sec. 4.1.2). We also observe that $f\tilde{h}$ vanishes in the high frequency limit, thus reproducing the expected

drop, $h_c(t) \to 0$. The the transition between the two regimes (low and high f limits) is determined by the inverse width of the Gaussian asymmetry factors, $f_i \approx 1/2\pi\sigma_j$ (first two terms of Eq. (4.31)) or, in the case of constant asymmetry, by the inverse time scale of the neutrino luminosity, $f_\nu \approx \chi/2\pi$.

Let us now give an illustration of how our model reproduces the expected features of a memory signal. In Fig. 4.3 we compare the phenomenological forms for L_ν, $\alpha(t)$ and $h(t)$ (Eqs. (4.27), (4.28) and (4.29), respectively) with the results of numerical simulations for the accretion phase. Due to the sparseness of published numerical results, we consider information from different sources, and in particular, $L_\nu(t)$ from Vartanyan and Burrows (2020) (see Fig. 1 (left) there, 15 $M_\odot$ model) and $\alpha(t)$ from Kotake *et al.* (2009a). These are well reproduced, in their global structure, by the phenomenological curves (with a tri-Gaussian structure for $\alpha(t)$, $N = 3$), for appropriately chosen parameters (given in Table 4.10). For the *same* parameters, the memory strain, $h(t)$ from Eq. (4.29) is plotted in Fig. 4.3c. For comparison, the figure also shows the numerically calculated $h(t)$ from Kotake *et al.* (2009a). The two curves are in good qualitative agreement in the general time structure of the strain, although differences by a factor of up to $\sim 4-5$ exist. We stress that a quantitative agreement is not expected because of our extracting information on L_ν and α from different sources, therefore the qualitative agreement noted above is a satisfactory validation of our model.

Our master formula, Eq. (4.29), can serve an effective phenomenological description of data (or numerically-generated results) for $h(t)$, if its parameters are treated as fit parameters. The dot-dashed curve in Fig. 4.3c shows an example of this: the dot-dashed curve has been obtained from Eq. (4.29) (with $N = 3$) by setting the parameters so to best reproduce the numerically calculated $h(t)$ from Kotake *et al.* (2009a). The agreement is acceptable, and can be further improved by increasing N.

As a note in closing, let us mention that our phenomenological forms for $h(t)$ and $\tilde{h}(f)$ are in general agreement with earlier, simpler toy models, like those presented by M. Favata (Favata, 2011). In those, $h(t)$ has the form of a hyperbolic tangent. A comparison with our Eq. (4.29) becomes intuitive if one considers the well known approximation (see, e.g. Vedder (1987)):

$$\mathrm{erf}\,(x) \simeq \tanh\,(mx), \text{ with } m = \sqrt{\pi}\log(2)\,, \tag{4.32}$$

which we checked to be very precise (less than 1% difference) at the time/frequency regimes of interest here.

Using Eq. (4.32), our master equation for $h(t)$, Eq. (4.29), can be rewritten as:

$$h(t) = \sum_{j=1}^{N}\left[\left\{h_{1j}\left(\tanh\left(m\rho_j\ \tau_{1j}\right) + \tanh\left(m\rho_j(t-\tau_{1j})\right)\right)\right\} + \left\{h_{2j}\left(\tanh\left(m\rho_j\ \tau_{2j}\right)\right.\right.\right.$$
$$\left.\left.\left. + \tanh\left(m\rho_j(t-\tau_{2j})\right)\right)\right\}\right] + \left\{h_3\left(\frac{\beta}{\chi}\left(1-\exp\left(-t\chi\right)\right)+\lambda t\right)\right\}, \tag{4.33}$$

and its Fourier transform takes the form:

$$\begin{aligned}\tilde{h}(f) = \sum_{j=1}^{N}\Bigg[&\left(h_{1j}\frac{i\pi}{m\rho_j}\,\mathrm{csch}\left(\frac{\pi^2 f}{m\rho_j}\right)\exp\left(i2\pi f\tau_{1j}\right)\right)\\ &+\left(h_{2j}\frac{i\pi}{m\rho_j}\,\mathrm{csch}\left(\frac{\pi^2 f}{m\rho_j}\right)\exp\left(i2\pi f\tau_{2j}\right)\right)\Bigg]\\ &+\left(\sqrt{2\pi}\ h_3\frac{\beta}{\chi}\left(\frac{1}{i2\pi f}-\frac{1}{-\chi+i2\pi f}\right)\right).\end{aligned} \tag{4.34}$$

4.3 Generalization: Plausible Phenomenological Scenarios

We now present five models that are a generalization of the framework discussed in Sec. 4.2.2. These models represent possibilities that have not yet been investigated numerically, but are nevertheless plausible. In the remainder of this section, for each model we provide some physics motivation, and justify the choice of the parameters (given in Table 4.11).

4.3.1 *Case Studies*

To fix the ideas, let us examine the following specific situations:

- *Accretion-only models.* Taking direct inspiration from numerical results (Sec. 4.2), we present three realizations where only the accretion phase contributes to the neutrino memory. They are illustrated in Fig. 4.4. The first model, the *accretion phase-three gaussians model* (Ac3G), has already been introduced in Sec. 4.2 and Fig. 4.3 as a description of numerical simulations, and therefore can be considered especially well motivated.

  A variation of the previous model is the *accretion phase-one Gaussian model* (Ac1G), where the anisotropy parameter $\alpha(t)$ has a simpler time-dependence, and is described by a single Gaussian profile. This scenario may be realistic for cases where the spiral SASI activity is weaker and shorter, for example in supernovae from smaller mass progenitors, see e.g., Tamborra *et al.* (2013, 2014); Walk *et al.* (2018, 2019).

  As a third realization, we consider the *long accretion phase-three Gaussian model* (LAc3G), where optimistic choices of the parameters are made. Here, the neutrino luminosity is kept constant at a relatively high value, and the anisotropy parameter is the sum of three overlapping Gaussian curves, extending to $t \sim 0.7$ s (refer to Table 4.11 for details). The net shape of the $\alpha(t)$ function is a curve that has a fast rising and declining time scales, similarly to the Ac1G model, but is wider than a single Gaussian. This model could be descriptive of a black-hole forming collapse (failed supernova), where the high rate of mass accretion and the long-stalling shockwave favor a highly luminous and sustained neutrino emission and prolonged spiral SASI, see for example the simulation for a 40 $M_\odot$ progenitor in Walk *et al.* (2020b), where a complex SASI dynamics (suggesting

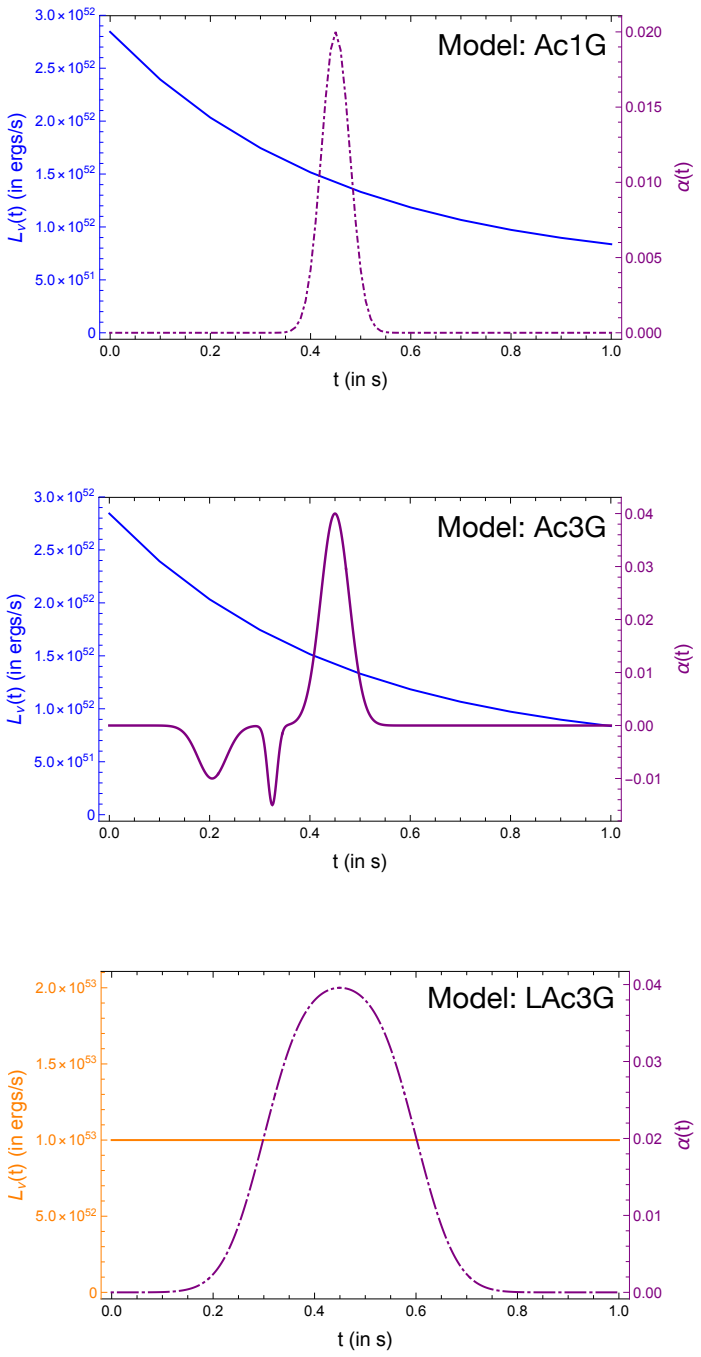

Figure 4.4: Neutrino luminosity (exponential curve, vertical scale on the right) and anisotropy parameter (single- or multi-Gaussian curve, vertical scale on the left) as functions of time post-bounce, for the three accretion-only models, where only the accretion phase of the neutrino emission contributes to the memory. See Table 4.11 for details.

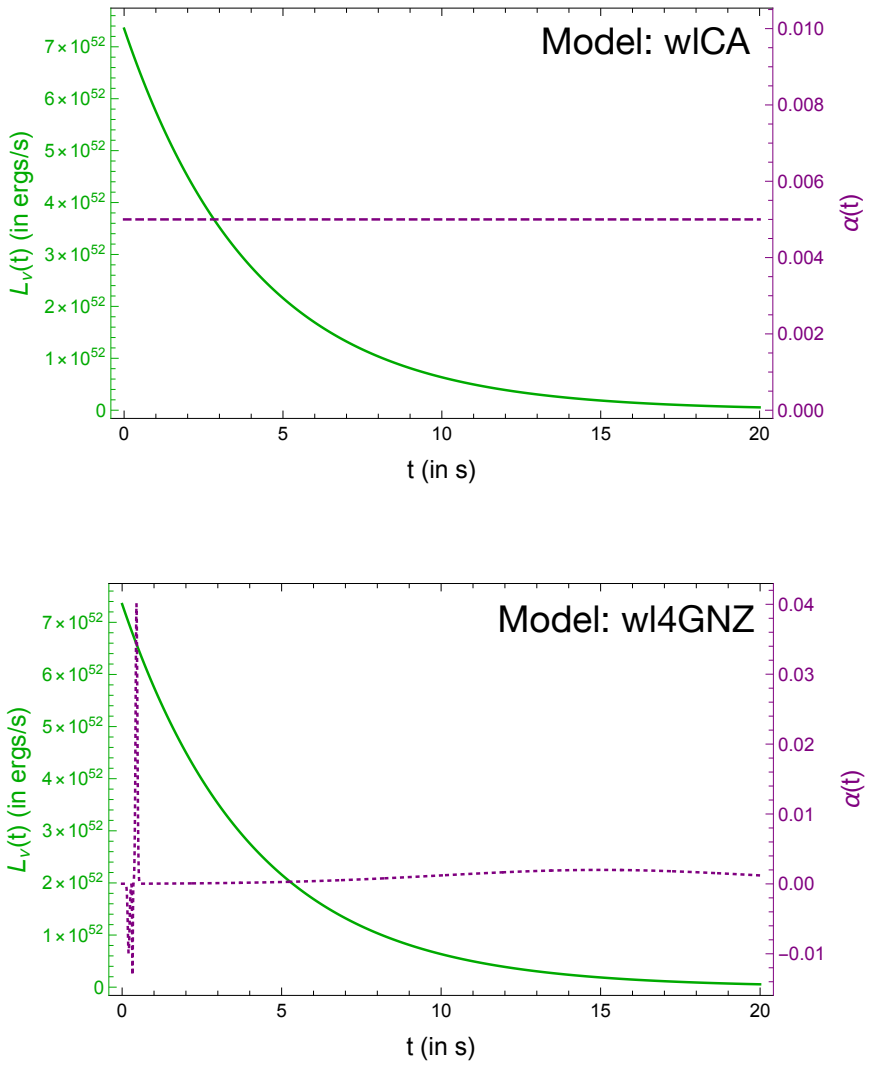

Figure 4.5: The same as Fig. 4.4 for the whole-luminosity models, where both the accretion and cooling phases contribute to the memory. See Table 4.11 for details.

a multi-Gaussian structure of $\alpha(t)$) is found, and the collapse to a black hole is obtained a at $t = 0.570$ s post-bounce.

- *Long-term evolution models.* We now discuss scenarios where the entire ~ 10 s neutrino burst contributes to the memory due to a residual, non-zero long-term anisotropy, see Fig. 4.5. While the idea of a multi-second long anisotropic emis-

sion is perhaps speculative, it is motivated by the fact that some numerical simulations reach $t \sim 1$ s post-bounce (where they end due to computational cost) with a non-zero $\alpha(t)$ (Vartanyan *et al.*, 2019), thus suggesting that anisotropy could be present beyond $t \sim 1$ s post-bounce in certain cases.

The first scenario, the *whole luminosity-constant alpha model* (wlCA, show in Fig. 4.5, top pane) is the simplest realization, having a constant anisotropy parameter. Consistently with the idea of a residual effect, here α is fixed at a relatively small value ($\alpha = 5\ 10^{-3}$) compared to the accretion-only models. A constant, feature-less anisotropy parameter could be realized if the SASI is very weak or absent and the anisotropy has a different physical origin, i.e., in the structure of the progenitor star. This model might also be useful for comparison with prior theory works where a constant anisotropy was assumed, for example Suwa and Murase (2009), where the case of a system composed of an accretion disk and a jet (producing a Gamma Ray Burst) was examined.

In the second scenario, called the *whole luminosity-four Gaussians non-zero alpha model* (wl4GNZ), we attempt a more realistic description by combining the time structure of α for the accretion phase ($\alpha(t)$ is the same as in model Ac3G at for $t < 1$ s), with an additional extended anisotropy, represented by a wide Gaussian centered at several seconds post-bounce, reaching a maximum value of $\alpha \simeq 0.002$. Physically, this late time feature of α could correspond to a weak revival of the anisotropy due to late time effects. We note that here the product $L_\nu(t)\alpha(t)$ is a smoothly decreasing function of t (for $t \gtrsim 1$ s). Therefore – in the absence of a direct physical interpretation of the parameters – this model could simply be considered as a purely phenomenological description of a multi-second long memory effect.

4.3.2 *Results: Memory In The Time- And Frequency-domain*

We now present results for the memory strain in the time and frequency domain, $h(t)$ and h_c, for the phenomenological models of Sec. 4.3.1 (Table 4.11). They are shown in Fig. 4.6[7].

For the accretion-only model, $h(t)$ reaches a plateau in less than one second, corresponding to the characteristic duration of the episodes when the anisotropy parameter is non-zero (see Sec. 4.2.2). Before the plateau, $h(t)$ can change sign due to the change of sign in $\alpha(t)$, as can be seen for the Ac3G model. Consistently with the upper bound, Eq. (4.19), the late time, asymptotic value of $h(t)$ is $h \sim 10^{-22}$ m for the two more conservative scenarios (the value being the same for the Ac1G and Ac3G models is accidental, due to the choice of parameters, see Table 4.11); it is largest – approaching $\sim 10^{-20}$ – for the most optimistic choice parameters, in the LAc3G model.

For the long-term emission models, $h(t)$ evolves over the cooling time scale of several seconds. In the simplest case of constant anisotropy (wlCA model), it rises up smoothly to a value close to $\sim 10^{-20}$. The rise time reflects the decay time of the neutrino luminosity, and therefore it is directly comparable to the time profile of the detected neutrino signal. For the more realistic case of a time-evolving anisotropy parameter with a multi-second-wide Gaussian (wl4GNZ model), the evolution of $h(t)$ is the same as for the Ac3G model, with a weak late time rise that brings it to reach $\sim 10^{-21}$ at $t \sim 20$ s.

In the figures for $h_c(f)$, one can check that the zero-frequency limit (ZFL) is indeed

[7]Note: The results for the models are color coded: The line color represents the luminosity for a particular phase from Figs. 4.4 and 4.5 and the line styles denote the corresponding anisotropy parameter from the same figures. In all the results shown above the distance to the source is taken to be 10 kpc.

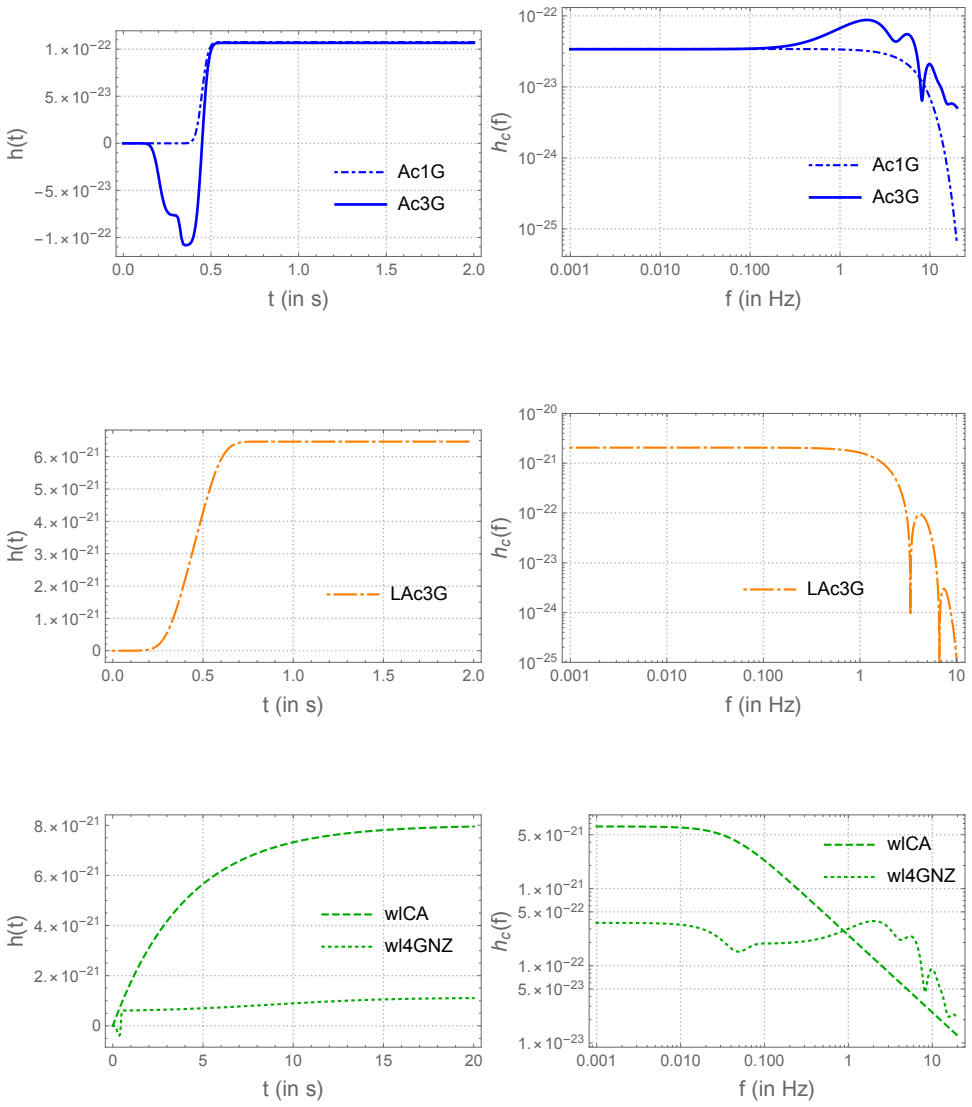

Figure 4.6: *Left panel :* Plots showing the dimensionless gravitational wave strain $h(t)$ for various models: (a) Solid blue line - accretion phase-three bumps model (Ac3G), Dot-dashed blue line - accretion phase-one bump model (Ac1G); (c) Dot-long dashed orange line - long accretion-three bumps model (LAc3G); (e) Dashed green line - whole luminosity-constant α model (wlCA), Dotted green line - whole luminosity-four bumps non-zero α model (wl4GNZ). *Right panel :* Plots showing the characteristic gravitational wave strain $h_c(f)$ (in Hz) for various models: (b) Solid blue line - accretion phase-three bumps model (Ac3G), Dot-dashed blue line - accretion phase-one bump model (Ac1G); (d) Dot-long dashed orange line - long accretion-three bumps model (LAc3G); (f) Dashed green line - whole luminosity-constant α model (wlCA), Dotted green line - whole luminosity-four bumps non-zero α model (wl4GNZ).

proportional (by factor $1/\pi$) to the difference between the initial and final values of $h(t)$, Eq. (4.18) (Sec. 4.1.2). For the accretion only models, the ZFL is realized at $f \lesssim 0.1$ Hz. Above this value, one can start to see structures related to the time scale of the episode(s) of non-zero anisotropy. We note how, for models where the anisotropy parameter does not change sign, h_c is maximum at the ZFL. In the case of the Ac3G model, instead, where $\alpha(t)$ changes sign, the fast variability in $h(t)$ at $t \lesssim 0.5$ s causes h_c to have a maximum at higher frequency, $f \sim 2$ Hz. The same feature is seen, as expected, in the wl4GNZ model. For the two long-term evolution models, the ZFL is reached only at $f \lesssim 10^{-2}$ Hz, consistently with the longer evolution time scale. Note that these two models (wlCA and wl4GNZ) give comparable values of h_c at $f \sim 1$ Hz, but are drastically different above and below this point, with the wlCA (wl4GNZ) model having significantly more power at lower (higher) frequency, as expected from the different time scales of $h(t)$ in the two models.

4.3.3 Detectability

To estimate the potential for a memory signal to be detected at realistic GW detectors, we compare the characteristic strains $h_c(f)$ with a typical characteristic detector noise amplitude, $h_n(f)$, averaged over the source position and polarization angle. Broadly, if $h_c(f) \gtrsim h_n(f)$ for a sufficiently wide frequency interval, the memory can be considered likely to be detectable, although a detailed estimate of detectability is waveform specific, and would require a dedicated study.

Following Li *et al.* (2018), $h_n(f)$ can be expressed as

$$h_n(f) = \frac{\sqrt{f S_n(f)}}{\langle F_+^2(\theta, \phi, \psi)\rangle^{1/2}}\,, \tag{4.35}$$

where $S_n(f)$ is the detector's one-sided noise spectral density, in units of s (Hz^{-1}) and $F_+(\theta, \phi, \psi)$ is defined as the detector's beam pattern function (see Sathyaprakash

and Schutz (2009a); Moore *et al.* (2014); Schmitz (2021) for details). We choose the DECIGO as representative of the potential of future detectors at the Deci-Hz scale. DECIGO is planned to start, in prototype form, in the next decade (Kawamura *et al.*, 2020).

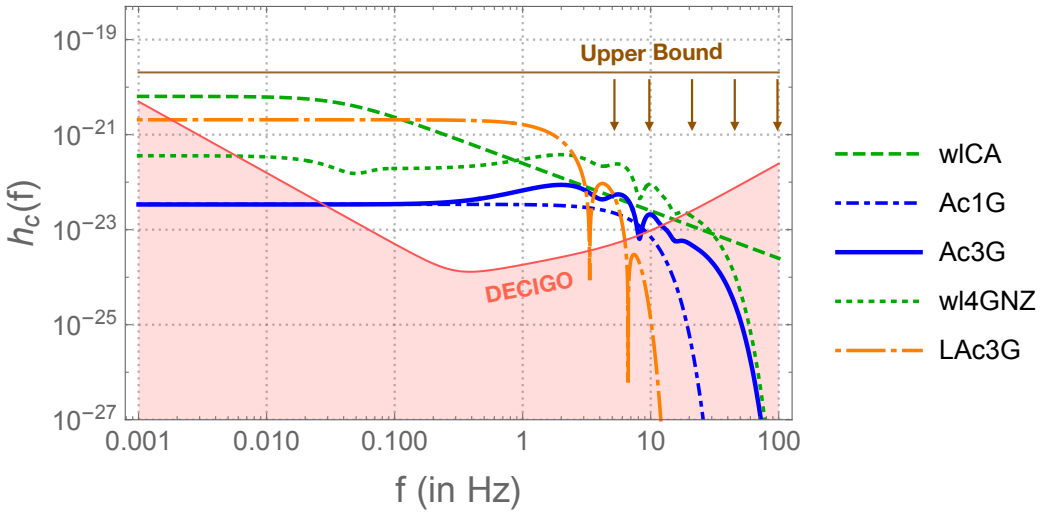

Figure 4.7: Characteristic strain from the models along with a typical sky-averaged noise curve from DECIGO Seto *et al.* (2001); Yagi and Seto (2011a); Shuichi Sato and Masaki Ando (2017). In all the results shown above (including the bound) the distance to the source is taken to be 10 kpc. The upper bound, $h_c = 2.04 \times 10^{-20}$, Eq. (4.19), is shown as a horizontal line (with arrows).

Fig. 4.7 shows the sensitivity curve of DECIGO, compared with the results from the phenomenological models of Fig. 4.6, for a supernova at distance $r = 10$ kpc. It appears that, for all our models, the memory signal is detectable up to frequencies $f \sim 10$ Hz, and the zero frequency limit is observable (although only barely for the wlCA model). We note that for $f > 3$ Hz or so, the accretion only-models give the strongest signal, whereas for $f < 0.1$ Hz h_c is largest for the model with the strongest long-term memory contribution (the wlCA model). Interestingly, in the intermediate range, $f \sim 0.1 - 3$ Hz, the LAc3G model would give the strongest signal, indicating that long accretion collapses (e.g., failed supernovae) might be an especially promising target for Deci-Hz detectors. Considering the $1/r$ dependence

of the memory strain, from Fig. 4.7 we estimate that a signal similar to the LAc3G model might be detectable at DECIGO for distances up to $r \sim 10$ Mpc or so.

In Fig. 4.9 we illustrate the potential of different detector concepts to observe the neutrino memory from a supernova. A signal from an optimistic model, the LAc3G model, is shown for different distances to the supernova. For comparison, we also plot the sensitivity curves for different next-generation detectors. We distinguish between the ground-based, space-based and atom-interferometer detectors. Ground-based interferometers (Fig. 4.9a) have limited performance at sub-Hz frequencies (due to seismic noise), and furthermore are not perfectly inelastic, a fact that would lead to the dissipation of memory effect signatures over time (Favata, 2010). Among these, the Einstein Telescope (ET) (Sathyaprakash and Schutz, 2009a; M Punturo and F Acernese, 2010; Michele Maggiore and Nicola Bartolo, 2020) has the best potential, being able to observe the memory at $f \sim 1 - 5$ Hz up to several kpc of distance to see the memory for a nearby ($\lesssim 1$ kpc) supernova. In the same frequency range, the Advanced Laser Interferometer Gravitational-wave Observatory (ALIGO) (Sathyaprakash and Schutz, 2009a; Aasi *et al.*, 2015a) and Cosmic Explorer (CE) (Reitze *et al.*, 2019) could see a signature only for a near-Earth star like Betelgeuse ($r \sim 0.1$ kpc).

The drawbacks suffered by ground based detectors are overcome by space-based interferometers (Fig. 4.9b), which have peak-performance at $f \sim 0.01 - 1$ Hz. These are (in principle) completely inelastic, and therefore capable of preserving memory signatures indefinitely. The most powerful proposed detectors of this type are the BBO (Yagi and Seto, 2011a), and DECIGO; for both of them the sensitivity to the signal extends up to ~ 10 Mpc. The most optimistic detector scenario, representative of the distant future potential, is Ultimate DECIGO (Seto *et al.*, 2001; Yagi and Seto, 2011a; Shuichi Sato and Masaki Ando, 2017), for which the distance of

sensitivity exceeds 100 Mpc. Although less powerful, the Advanced Laser Interferometer Antenna (ALIA) (Bender *et al.*, 2013) and Laser Interferometer Space Antenna (LISA) (Sathyaprakash and Schutz, 2009a; Pau Amaro-Seoane and Stanislav Babak, 2017) should both be capable to detect a supernova at a typical galactic distance ($r \sim 10$ kpc). Note that LISA will probe the zero-frequency limit, since it has peak sensitivity at the milli-Hz scale.

Interestingly, atom interferometry (Fig. 4.9c) has recently emerged as an alternative to large scale traditional interferometers. After an initial stage on ground, most atom interferometer projects are envisioned to be in space, where their ultimate potential will be realized[8]. A space-based version of the Mid-band Atomic Gravitational Wave Interferometric Sensor (MAGIS) experiment (Graham *et al.*, 2016), at the Km-length scale, might be sensitive to a galactic supernova. A prototype of MAGIS (with baseline of 100 m) is now approved for construction at the Fermi National Laboratory (Graham *et al.*, 2016, 2017; Coleman, 2019). A similar performance as MAGIS is expected for the Atomic Experiment for Dark matter and Gravity Exploration in space (AEDGE) (El-Neaj *et al.*, 2020), which is being reviewed by the European Space Agency within its Voyage 2050 programme, the Atom Interferometer Observatory and Network (AION) (Badurina *et al.*, 2020) in its 1 km configuration, and the European Laboratory for Gravitation and Atom-interferometric Research (ELGAR) (Canuel *et al.*, 2020a,b).

Other sensitivity curves shown in Fig. 4.9 are for TianQuin (Luo *et al.*, 2016), the Gravitational-wave Lunar Observatory for Cosmology (GLOC) (Jani and Loeb, 2020), the Astrodynamical Middle-frequency Interferometric Gravitational wave Observatory (AMIGO) (Ni, 2018; Ni *et al.*, 2020) and the Zhaoshan long-baseline Atom

[8]An exception is the Zhaoshan long-baseline Atom Interferometer Gravitation Antenna (ZAIGA) Zhan *et al.* (2019), which will be based underground.

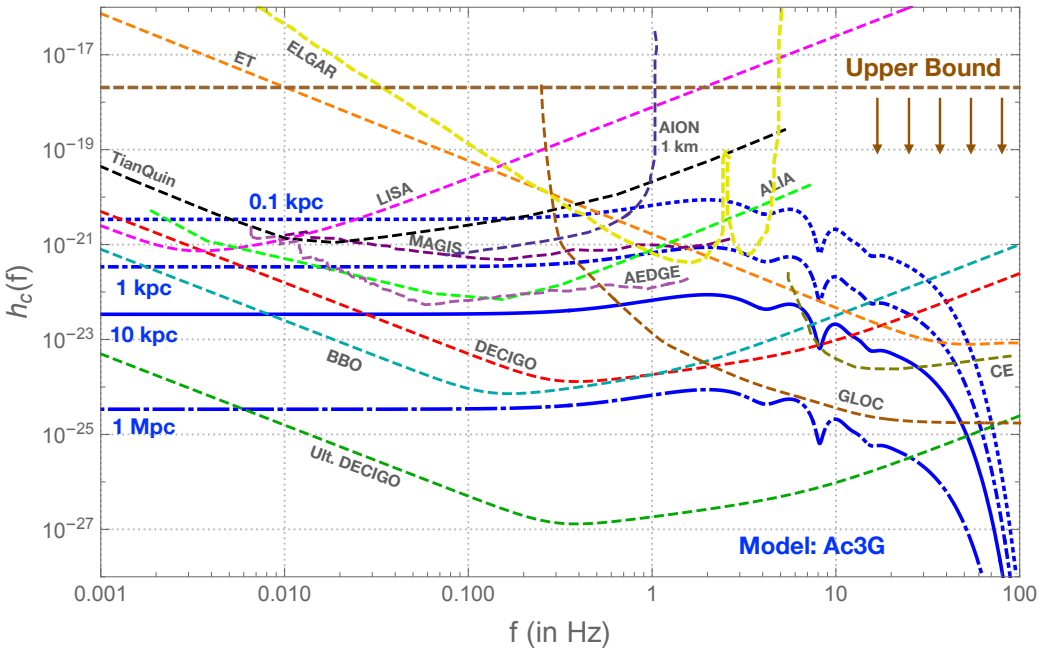

Figure 4.8: The same as Fig. 4.9, for the Ac3G model. For simplicity, only sensitivity curves that intersect our theoretical predictions are plotted in a single panel.

Interferometer Gravitation Antenna (ZAIGA) (Zhan *et al.*, 2019).

A more conservative case for the observation of the memory effect is given by the Ac3G model, as shown in Fig. 4.8. For this model, the distance of sensitivity of each detector is reduced by about one order of magnitude, with MAGIS and DECIGO being limited to under 1 kpc and 1 Mpc respectively.

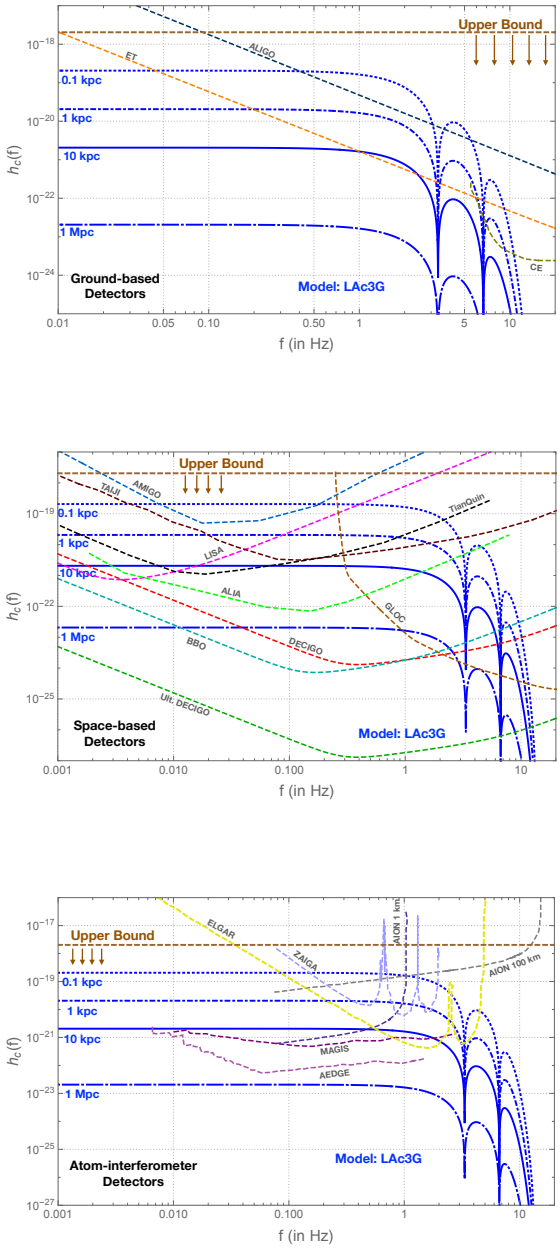

Figure 4.9: Characteristic strain of the supernova neutrino memory from the LAc3G model for a supernova at distance $r = 0.1, 1, 10, 10^3$ kpc, along with the upper bound from Eq. (4.19) (shown for $r = 0.1$ kpc). Detector sensitivity curves are shown, grouped in different panels as follows: a) Ground-based detectors: ALIGO, ET, CE; b) Space-based detectors: LISA, DECIGO, Ultimate DECIGO, BBO, TAIJI, TianQuin, ALIA, GLOC, AMIGO ; c) Atom-interferometers: MAGIS, AEDGE, AION (1 km and 100 km), ZAIGA and ELGAR. See text for the full names of these projects and references.

Curve	$L_\nu(t)$ Parameters	$\alpha(t)$ Parameters	Effective Parameters
Analytical (Blue Dashed)	$\lambda = 3.16 \times 10^{52}$ ergs/s, $\beta = 2.25 \times 10^{52}$ ergs/s, $\chi = 2.24\ s^{-1}$	$N = 3$, $\kappa = 0.0$, $\xi_1 = -0.01$, $\xi_2 = -0.015$, $\xi_3 = 0.02$, $\gamma_1 = 0.205$ s, $\gamma_2 = 0.325$ s $\gamma_3 = 0.45$ s, $\sigma_1 = 0.04/\sqrt{2}$ s, $\sigma_2 = 0.04/3\sqrt{2}$ s, $\sigma_3 = 0.04/\sqrt{2}$ s	$h_{11} = 3.12 \times 10^{-23}$, $h_{12} = -1.03 \times 10^{-23}$, $h_{13} = -2.69 \times 10^{-23}$, $\rho_1 = 25$ Hz, $\rho_2 = 75$ Hz, $\rho_3 = 25$ Hz, $\tau_{11} = 0.4482$ s, $\tau_{12} = 0.3248$ s, $\tau_{13} = 0.2032$ s, $h_{21} = 1.20 \times 10^{-22}$, $h_{22} = -2.99 \times 10^{-23}$, $h_{23} = -5.98 \times 10^{-23}$, $\tau_{21} = 0.45$ s, $\tau_{22} = 0.325$ s, $\tau_{23} = 0.205$ s, $h_3 = 0.0$
Phenomenological (Black Dot-dashed)	$\lambda = 5.97 \times 10^{51}$ ergs/s, $\beta = 2.25 \times 10^{52}$ ergs/s, $\chi = 2.24\ s^{-1}$	$N = 3$, $\kappa = 0.0$, $\xi_1 = 0.01$, $\xi_2 = -0.04$, $\xi_3 = 0.078$, $\gamma_1 = 0.100$ s, $\gamma_2 = 0.250$ s $\gamma_3 = 0.450$ s, $\sigma_1 = 0.04/\sqrt{2}$ s, $\sigma_2 = 0.04/\sqrt{2}$ s, $\sigma_3 = 0.04/\sqrt{2}$ s	$h_{11} = 1.22 \times 10^{-22}$, $h_{12} = -9.74 \times 10^{-23}$, $h_{13} = 3.41 \times 10^{-23}$, $\rho_1 = 25$ Hz, $\rho_2 = 25$ Hz, $\rho_3 = 25$ Hz, $\tau_{11} = 0.4482$ s, $\tau_{12} = 0.2482$ s, $\tau_{13} = 0.0982$ s, $h_{21} = 8.81 \times 10^{-23}$, $h_{22} = -4.52 \times 10^{-23}$, $h_{23} = 1.13 \times 10^{-23}$, $\tau_{21} = 0.45$ s, $\tau_{22} = 0.25$ s, $\tau_{23} = 0.10$ s, $h_3 = 0.0$

Figure 4.10: Figure of a table showing the parameters relevant for luminosity $L_\nu(t)$ and anisotropy parameter $\alpha(t)$ along with the respective effective parameters as defined in (4.30), corresponding to the different curves in Fig. 4.3. Note: The normalization for the luminosity is different for the two curves, since the analytical curve is just a curve superimposed on the raw data.

Model Name	Acronym	$L_\nu(t)$ Parameters	$\alpha(t)$ Parameters	Effective Parameters
Accretion phase - three bumps	Ac3G (N=3)	$\lambda = 5.97\times10^{51}$ ergs/s, $\beta = 2.25\times10^{52}$ ergs/s, $\chi = 2.24\ s^{-1}$	$\kappa = 0.0$, $\xi_1 = -0.01$, $\xi_2 = -0.015$, $\xi_3 = 0.04$, $\gamma_1 = 0.205$ s, $\gamma_2 = 0.325$ s $\gamma_3 = 0.45$ s, $\sigma_1 = 0.04/\sqrt{2}$ s, $\sigma_2 = 0.04/3\sqrt{2}$ s, $\sigma_3 = 0.04/\sqrt{2}$ s	$h_{11} = 6.23\times10^{-23}$, $h_{12} = -1.03\times10^{-23}$, $h_{13} = -2.69\times10^{-23}$, $\rho_1 = 25$ Hz, $\rho_2 = 75$ Hz, $\rho_3 = 25$ Hz, $\tau_{11} = 0.4482$ s, $\tau_{12} = 0.3248$ s, $\tau_{13} = 0.2032$ s, $h_{21} = 4.52\times10^{-23}$, $h_{22} = -5.65\times10^{-24}$, $h_{23} = -1.13\times10^{-23}$, $\tau_{21} = 0.45$ s, $\tau_{22} = 0.325$ s, $\tau_{23} = 0.205$ s, $h_3 = 0.0$
Accretion phase - one bump	Ac1G (N=1)	$\lambda = 5.97\times10^{51}$ ergs/s, $\beta = 2.25\times10^{52}$ ergs/s, $\chi = 2.24\ s^{-1}$	$\kappa = 0.0$, $\xi_1 = 0.02$, $\gamma_1 = 0.45$ s, $\sigma_1 = 0.04/\sqrt{2}$ s	$h_{11} = 3.12\times10^{-23}$, $\rho_1 = 25.0$ Hz, $\tau_{11} = 0.4482$ s, $h_{21} = 2.26\times10^{-23}$, $\rho_2 = 25.0$ Hz, $\tau_{21} = 0.45$ s, $h_3 = 0.0$
Long Accretion phase - three bumps	LAc3G (N=3)	$\lambda = 1.0\times10^{53}$ ergs/s, $\beta = 0.0$, $\chi = 0.0$	$\kappa = 0.0$, $\xi_1 = \xi_2 = \xi_3 = 0.023$, $\gamma_1 = \gamma_2 = \gamma_3 = 0.35$ s, $\sigma_1 = \sigma_2 = \sigma_3 = 0.07$ s	$h_{1i} = 0.0$, $\rho_1 = \rho_2 = \rho_3 = 10.10$ Hz, $\tau_{21} = 0.35$ s, $\tau_{22} = 0.45$ s, $\tau_{23} = 0.55$ s, $h_{21} = h_{22} = h_{23} = 1.08\times10^{-21}$, $h_3 = 0.0$
Whole Luminosity - constant alpha	wlCA (N=0)	$\lambda = 0.0$, $\beta = 7.35\times10^{52}$ ergs/s, $\chi = 0.245\ s^{-1}$	$\kappa = 0.005$	$h_{1i} = 0.0$, $h_{2i} = 0.0$, $h_3 = 2.67\times10^{-67}$
Whole Luminosity - four bumps non-zero alpha	wl4GNZ (N=4)	$\lambda = 0.0$, $\beta = 7.35\times10^{52}$ ergs/s, $\chi = 0.245\ s^{-1}$	$\kappa = 0.0$, $\xi_1 = -0.01$, $\xi_2 = -0.015$, $\xi_3 = 0.04$, $\xi_4 = 0.002$, $\gamma_1 = 0.205$ s, $\gamma_2 = 0.325$ s $\gamma_3 = 0.45$ s, $\gamma_4 = 15.0$ s, $\sigma_1 = 0.04/\sqrt{2}$ s, $\sigma_2 = 0.04/3\sqrt{2}$ s, $\sigma_3 = 0.04/\sqrt{2}$ s, $\sigma_4 = 5.0$ s	$h_{11} = 4.98\times10^{-22}$, $h_{12} = -6.42\times10^{-23}$, $h_{13} = -1.32\times10^{-22}$, $h_{14} = 2.64\times10^{-22}$, $\rho_1 = 25$ Hz, $\rho_2 = 75$ Hz, $\rho_3 = 25$ Hz, $\rho_4 = 0.1414$ Hz, $\tau_{11} = 0.4498$ s, $\tau_{12} = 0.3250$ s, $\tau_{13} = 0.2048$ s, $\tau_{14} = 8.875$ s, $h_{2i} = 0.0$, $h_3 = 0.0$

Figure 4.11: Figure of a table showing the parameters relevant for the luminosity $L_\nu(t)$ and anisotropy parameter $\alpha(t)$ for different analytical models constructed along with the respective effective parameters as defined in (4.30). Here, N is the number of Gaussians in $\alpha(t)$.

Chapter 5

MEMORY-TRIGGERED SUPERNOVA NEUTRINO DETECTION

In chapter 2, we discussed how neutrinos are major players in the emerging field of multi-messenger astronomy. With gravitational waves (GWs) and photons, they have the potential to probe the most extreme astrophysical phenomena in unprecedented detail. Since SN1987A (see Sec. 2.7 for details), core collapse supernovae (CCSNe) have been prime targets of multi-messenger observations, where neutrinos dominate the energy output and carry direct information on the extremely dense environment surrounding the collapsed core (see Sec. 2.3 for details). The $\sim$ 10 s burst of neutrinos from a supernova will also allow tests of particle physics beyond the Standard Model.

The detection of an individual supernova neutrino burst is exciting as well as

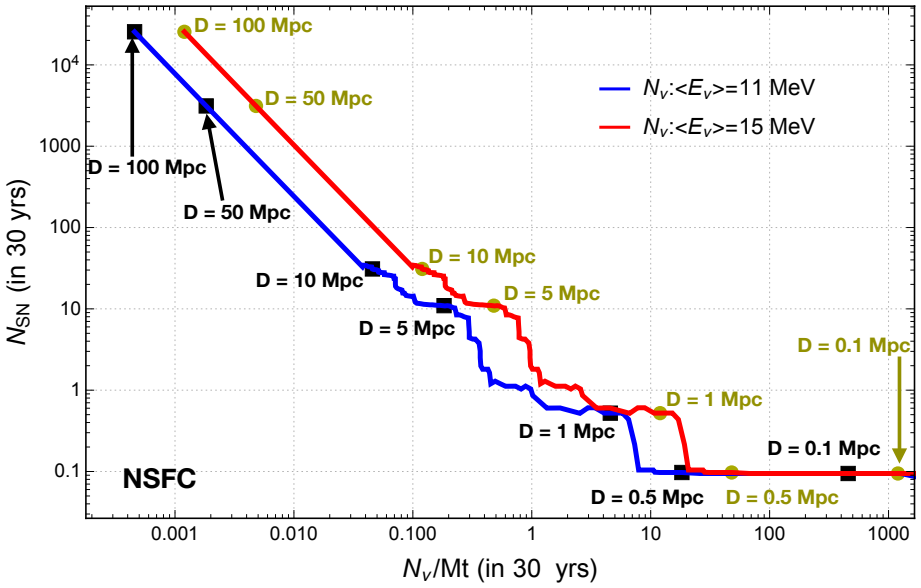

Figure 5.1: Plot showing the total number of core-collapse supernovae in 30 years versus the total number of neutrinos obtained per megaton from the supernovae in 30 years. The mean neutrino energy is varied 11 MeV (blue) and 15 MeV (red). The distance from earth is marked by markers in both cases. We have assumed neutron-star forming collapses (NSFC) only (see Sec. 2.3.2 for details).

challenging. A statistically significant observation is possible only for supernovae within 1-3 Mpc from Earth (Ando *et al.*, 2005; Kistler *et al.*, 2011), where collapses are rare, resulting in decades of waiting time. Fig. 5.1 illustrates this fact. We have plotted the total number of core-collapse supernovae in 30 years versus the total number of neutrinos obtained per megaton from the supernovae in 30 years. This is done for mean supernova neutrino energy of 11 and 15 MeV. The distance from earth is marked by markers in both cases. We assume only neutron-star forming collapses (NSFC) only (see Sec. 2.3.2 for details). The details of the parameters and the formulae required to obtain the plot will be discussed later in the chapter. But the evident fact is for nearby distances which would lead to very high statistics, the rate of core-collapse supernova is extremely low. For large distances, the number of core-collapse supernova is very large but because the neutrino flux falls off as $1/D^2$ the statistics is extremely low.

An alternative is to search for the Diffuse Supernova Neutrino Background (DSNB), from all the supernovae in the universe (Bisnovatyi-Kogan and Seidov, 1982; Krauss *et al.*, 1984; Beacom, 2010; Lunardini, 2017), which has a substantial cosmological component. $\mathcal{O}(10-100)$ DSNB neutrinos could be detected in a decade (see, e.g., De Gouvêa *et al.* (2020)), and preliminary data could be available in just a few years (Beacom and Vagins, 2004; Zhang *et al.*, 2015; An *et al.*, 2016; Abe *et al.*, 2018a; Askins *et al.*, 2020; Abi *et al.*, 2020).

Burst and DSNB searches lack sensitivity to the local universe, $r \sim 3-100$ Mpc, where many supernova-rich galaxies are situated. Ideas to overcome this gap typically rely on time-triggers that would allow to identify a single neutrino as signal instead of background. One could use either a neutrino self-trigger — where $2-3$ neutrinos observed less than 10 s apart can be attributed to a supernova with high confidence (Ando *et al.*, 2005; Adams *et al.*, 2013) — , or the time coincidence with the $O(10^2)$

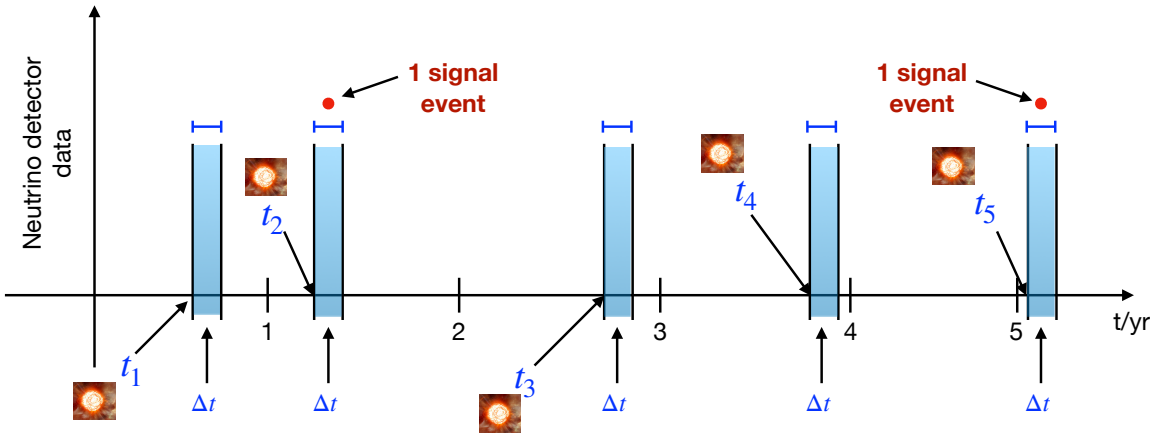

Figure 5.2: Schematic diagram to illustrate the idea of memory-triggered supernova neutrino detection.

Hz supernova GW signal from interferometers like LIGO-Virgo and its successors (Pagliaroli *et al.*, 2009; Abbott *et al.*, 2016a; Abe *et al.*, 2021). Both methods are still limited to a few Mpc distance, except for the most optimistic GW models (see, e.g., Szczepanczyk *et al.* (2021) and references therein) and futuristic multi-Megaton neutrino detectors (Kistler *et al.*, 2011)[1].

In this chapter, we propose a new time-triggered method to detect supernova neutrinos, which is potentially sensitive to supernovae up to $\sim$ 100 Mpc. The time trigger is the observation of the gravitational memory signal caused by the neutrino emission itself. Fig. 5.2 shows a schematic representation of the main idea. The core-collapse supernova leads to an observable GW memory signal in the GW detectors say at different times, $t_1, t_2, t_3, t_4, \ldots$. We know the time duration of a supernova neutrino burst, $\Delta t \sim 10$ s (see Sec. 2.3 for details). Now, one can go back to the neutrino detector data and analyze the events within time-windows, $t_1 + \Delta t, t_2 +$

[1]Astronomical observations of supernovae can not serve as time triggers, due to the $\mathcal{O}(1)$ hour uncertainty in the time delay between the neutrino and the electromagnetic signal from the same star.

$\Delta t, t_3 + \Delta t, t_4 + \Delta t, \ldots$. Since, the background in each of the time-windows is very low, owing to the time duration of just ~ 10 s; the probability of finding a signal event (in this case a supernova neutrino) is high. This method of reducing the background events by using a triggered time-window of a short duration allows collecting a clean sample of signal events over time.

The memory is a non-oscillatory, permanent distortion of the local space time due to the anisotropic emission of matter or energy by a distant source. The memory due to neutrino emission by a supernova at distance r has characteristic strain $h_c \sim 10^{-23} - 10^{-21}(10 \text{ kpc}/r)$ and frequencies in the Deci-Hz band, $f \sim 0.1 - 3$ Hz (Burrows and Hayes, 1996; Mueller and Janka, 1997b; Kotake *et al.*, 2009b; Muller *et al.*, 2012; Li *et al.*, 2018; Vartanyan and Burrows, 2020). The memory develops ~ 0.1 s from the start of the neutrino emission, thus being an ideal time-trigger. Next generation powerful Deci-Hz GW detectors, like the Deci-hertz Interferometer Gravitational wave Observatory (DECIGO) (Seto *et al.*, 2001; Yagi and Seto, 2011b; Sato *et al.*, 2017; Kawamura *et al.*, 2021) and the Big Bang Observer (BBO) (Yagi and Seto, 2011b) will provide robust triggers for supernovae at 10 Mpc and beyond (Mukhopadhyay *et al.*, 2021a). These would result in a nearly pure sample of $\sim 10 - 100$ supernova neutrino events from the local universe within a few decades; see our summary figure, Fig. 5.6. Here we illustrate our proposed methodology and its physics potential.

5.1 Formalism

5.1.1 Gravitational Memory Signals

The supernova neutrino memory strain can be expressed as (Epstein, 1978; Turner, 1978; Mueller and Janka, 1997b)

$$h^{xx}_{TT} = h(r,t) = \frac{2G}{rc^4} \int_{-\infty}^{t-r/c} dt' L_\nu(t') \alpha(t') \,. \tag{5.1}$$

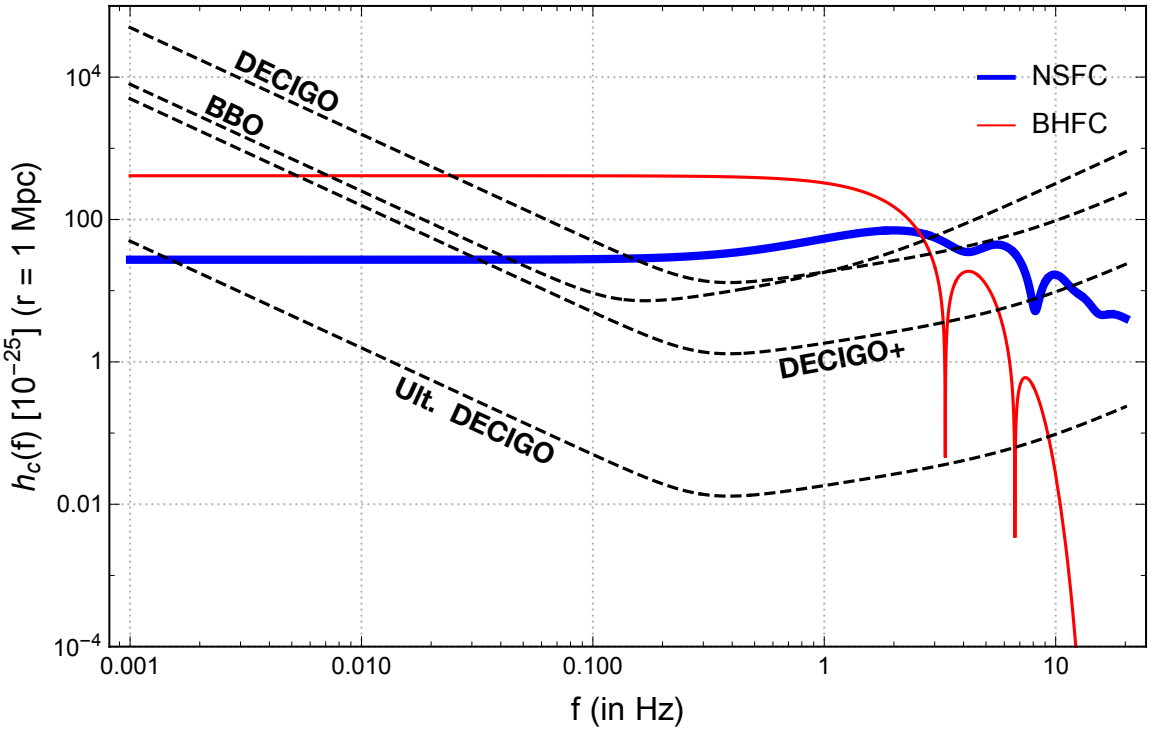

Figure 5.3: Solid: the characteristic gravitational memory strain $h_c(f)$ for the NSFC and BHFC models (thin and thick lines respectively). The distance to the supernova is $r = 1$ Mpc. Dashed: sky-averaged noise curves for representative detectors (see fig. 5.6).

where c is the speed of light, t is the time post bounce and G is the universal gravitational constant. L_ν is the all-flavors neutrino luminosity and $\alpha \sim \mathcal{O}(10^{-3} - 10^{-2})$ is the time-varying anisotropy parameter[2]. Simulations show that $\alpha(t)$ becomes non-zero within a few ms post-collapse, during the accretion phase, and can change sign multiple times within the first second, as a result of the dynamics of the matter near the collapsed core. The behavior of $\alpha(t)$ at $t > 1$ s, during the cooling phase, is unknown. Following Mukhopadhyay *et al.* (2021a), we consider two phenomenological models for the memory: the first, characterized by a weaker and shorter anisotropic

[2]We consider the case where the observer is in a coordinate system where the '×' component of the strain vanishes, see Mueller and Janka (1997b); Kotake *et al.* (2009b).

phase, is representative of a neutron-star-forming collapse (NSFC) (see Sec. 2.3.2 for details); the second has larger and prolonged anisotropy, and could represent a black-hole-forming collapse (BHFC) (see Sec. 2.3.3 for details). In both models, $\alpha = 0$ for $t > 1$ s[3]. Maximum values of $rh(r,t) \sim 26.5$ cm and $rh(r,t) \sim 400$ cm are obtained for the two models respectively. In Fig. 5.3, we show the memory characteristic strain, $h_c(r,f) = 2f|\tilde{h}(r,f)|$, where $\tilde{h}(r,f)$ is the Fourier Transform of $h(r,t)$. Also shown are the noise curves of Deci-Hz detectors, which are given by the quantity $h_n(f) = \Upsilon\sqrt{5\ f\ S_n(f)}$, where $S_n(f)$ is the power spectral noise density (Sathyaprakash and Schutz, 2009b). We choose $\Upsilon = 1, 10^{-1}, 10^{-3}$; the first and last correspond to DECIGO and its optimal (futuristic) realization, Ultimate DECIGO (Seto *et al.*, 2001; Yagi and Seto, 2011b; Sato *et al.*, 2017); the middle value represents an hypothetical intermediate case (DECIGO+ from here on).

The detectability of a memory signal is determined by the signal-to-noise (SNR) ratio of the detector, which is defined as (Moore *et al.*, 2015)

$$\rho^2(r) = \int_{-\infty}^{\infty} d(\log f) \left(\frac{h_c(r,f)}{h_n(f)}\right)^2 . \tag{5.2}$$

We compute the probability of detecting a CCSN memory, P_{det}^{GW}, for a fixed false alarm probability $P_{FA}^{GW} = 0.1$ (see App. F for details). This requires producing Receiver Operating Curves (ROCs) (see App. F for details) in the plane $P_{det}^{GW} - P_{FA}^{GW}$, which we do following the formalism in Jaranowski and Krolak (2000) for $N = 3$ degrees of freedom (here N is set equal to the number of Gaussian functions used to represent $\alpha(t)$, see Mukhopadhyay *et al.* (2021a)). The result is that P_{det}^{GW}, at a fixed P_{FA}^{GW}, is an increasing function of $\rho(r)$, through which it depends on the distance, r. We define the GW detector distance of sensitivity, r_{max}^{GW} such that $P_{det}^{GW}(r_{max}^{GW}) = 0.5$. $P_{det}^{GW}(r)$ is shown in fig. 5.4 for our cases of reference. For DECIGO, and for NSFC and

[3](See App. F for details on neutrino luminosity and anisotropy parameter in the two models).

BHFC respectively, we have $r_{max}^{GW} \simeq 4$ Mpc and $r_{max}^{GW} \simeq 33$ Mpc. We find $r_{max}^{GW} \simeq 40$ Mpc and $r_{max}^{GW} \simeq 335$ Mpc for DECIGO+; for Ultimate DECIGO, $r_{max}^{GW} > 350$ Mpc for both population models.

5.1.2 Neutrino Signals

For neutrino detection, we consider a water Cherenkov experiment, where the main channel of sensitivity is inverse beta decay (IBD), $\bar{\nu}_e + p \rightarrow n + e^+$. For the time-integrated (over $\Delta t = 10$ s) $\bar{\nu}_e$ flux at Earth, $\Phi(r, E_\nu)$ we use analytical quasi-thermal spectra of the form given in Keil *et al.* (2003). The average $\bar{\nu}_e$ energy is varied in an interval motivated by numerical simulations (Sukhbold *et al.*, 2016; Ertl *et al.*, 2016; Kresse *et al.*, 2021), in a way to effectively account for neutrino oscillations. The spectrum shape parameter, β, and the total energy in $\bar{\nu}_e$ are fixed. See Table 5.1 for details.

Model	**Energy** ($\times 10^{53}$**ergs**)		β	$\langle E_\nu \rangle$ **(in MeV)**	
	Ac. ph.	$\bar{\nu}_e$		Lower	Upper
NSFC	1.2	0.5	3	11	15
BHFC	2	0.45	2	15	20

Table 5.1: The neutrino flux parameters, from numerical simulations Sukhbold *et al.* (2016); Ertl *et al.* (2016); Kresse *et al.* (2021). The Ac. ph. and $\bar{\nu}_e$ columns refer to the all flavor energy in the accretion phase only (which contributes to the memory signal, see text) and to the energy in $\bar{\nu}_e$ emitted over the time-triggered interval of 10 s. β is related to the second momentum of the spectrum: $\beta = (2\langle E_\nu \rangle^2 - \langle E_\nu^2 \rangle)/(\langle E_\nu^2 \rangle - \langle E_\nu \rangle^2)$.

The predicted number of events in the detector from a CCSN at distance r is:

$$N(r) = \int_{E_\nu^{th}}^{E_\nu^{max}} N_p \eta \sigma(E_\nu) \Phi(r, E_\nu)\, dE_\nu\,, \tag{5.3}$$

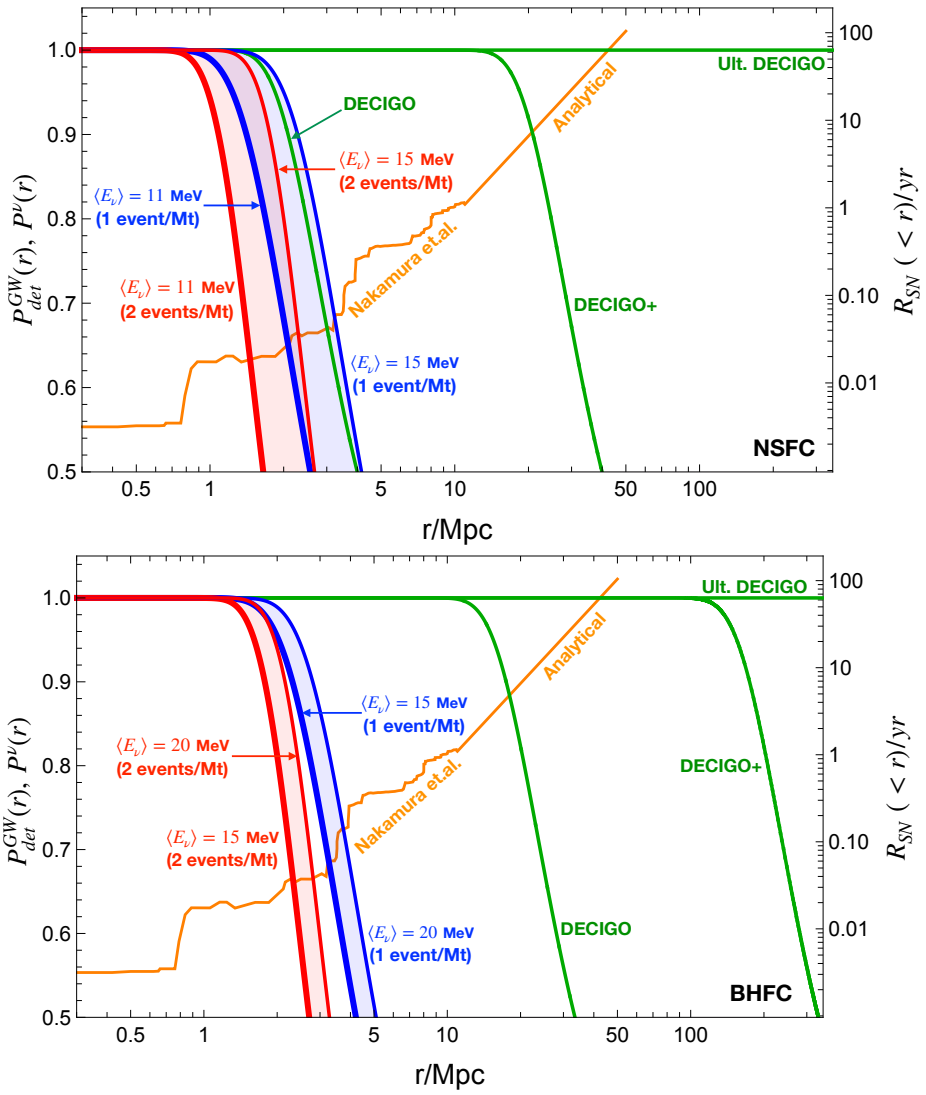

Figure 5.4: Detection probabilities for a memory signal, $P^{GW}_{det}(r)$, at three GW detectors of reference, and neutrino detection probabilities, $P^{\nu}(1,r)$ and $P^{\nu}(2,r)$ (see eq. (5.4)). Shadings describe the variations with the varying neutrino spectrum, see Table 5.1. The left (right) panel is for NSFC (BHFC). Also shown is the cumulative rate of core collapses (vertical axis on the right). See labels on the curves for details.

.

where N_p is the number of target protons, $\eta = 0.9$ is the detection efficiency (Hirata *et al.*, 1988; Abe *et al.*, 2011; Kyutoku and Kashiyama, 2018) and $\sigma(E_\nu)$ is the IBD cross-section (Strumia and Vissani, 2003). We take an energy interval $\left[E_\nu^{th}, E_\nu^{max}\right] = [19.3, 50]$ MeV to avoid the spallation background at low energy and the atmospheric neutrino background at high energy (Abe *et al.*, 2011, 2018a; Kunxian, 2015). We find $N(1\text{ Mpc}) \simeq 5 - 12$ and $N(1\text{ Mpc}) \simeq 12 - 18$ for NSFC and BHFC respectively, by varying the mean $\bar{\nu}_e$ energy in the intervals given in Table 5.1.

The Poisson probability of observing $N \geq N_{min}$ neutrino events in a detector is

$$P^\nu(N_{min}, r) = \sum_{n=N_{min}}^{\infty} \frac{N^n(r)}{n!} e^{-N(r)}\,. \tag{5.4}$$

It is plotted for $N_{min} = 1,\ 2$ in fig. 5.4 for the two models of reference. As expected, $P^\nu(N_{min}, r)$ declines rapidly at $r \gtrsim 3$ Mpc.

5.2 Memory-triggered Neutrino Observations

5.2.1 Event Rates

To estimate the rate of memory-triggered neutrino events, we model the rate of core collapses as a function of r. For $r \lesssim 11$ Mpc, we use the rates for individual galaxies from Nakamura *et al.* (2016). For $r > 11$ Mpc we assume a constant volumetric rate of $R_{SN} = 1.5\ 10^{-4}$ Mpc^{-3}yr^{-1} (the evolution with redshift is negligible for the distances of interest here). The cumulative rate (total rate of core collapses with $r < D$) is shown in fig. 5.4.

The number of memory-triggered neutrino events from all supernovae within a distance D, over a detector running time ΔT can be calculated as a sum over all the galaxies (index $j = 1, 2, ...$), at distance $r_j < D$:

$$N_\nu^{trig}(D) = \Delta T \sum_{j, r_j < D} R_j N(r_j) P_{det}^{GW}(r_j)\,, \tag{5.5}$$

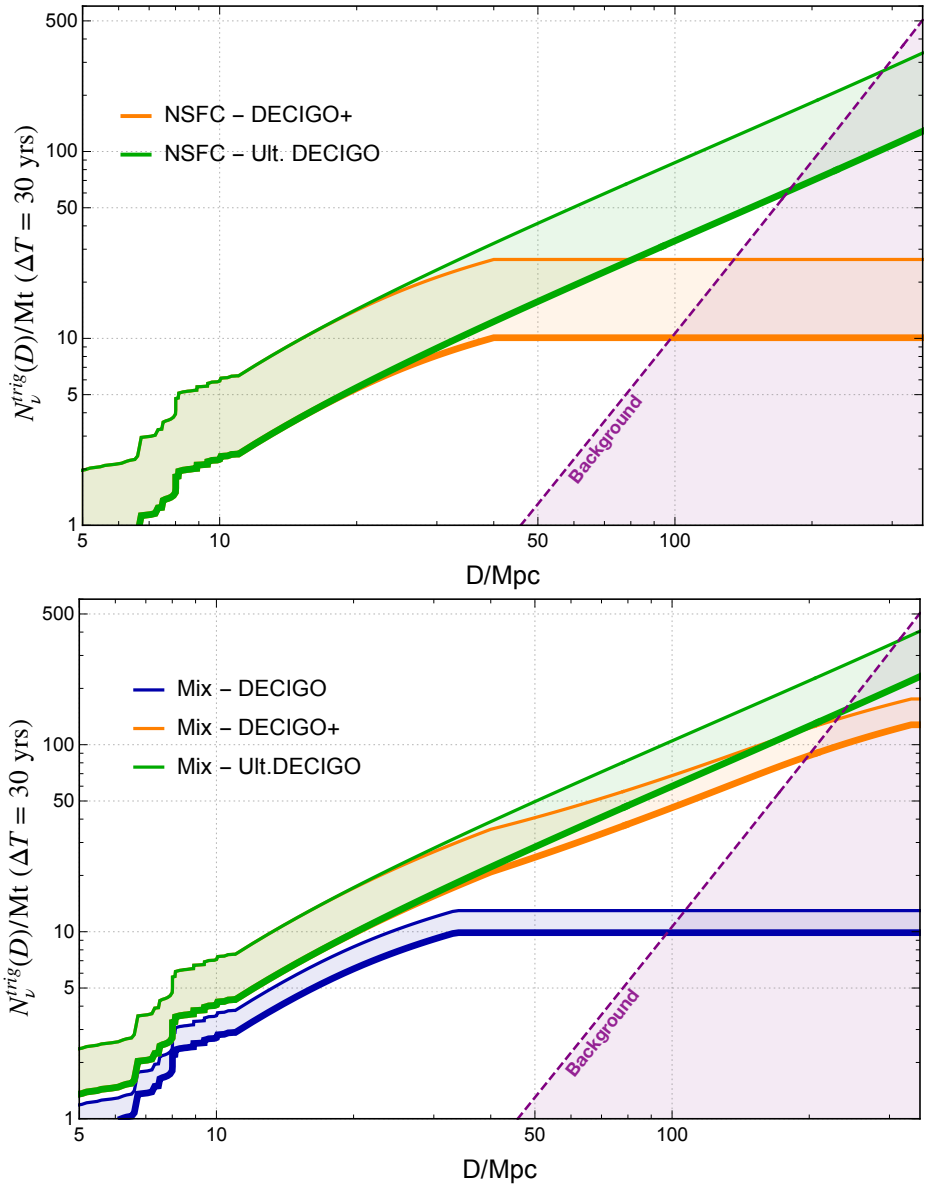

Figure 5.5: Number of background events and of memory-triggered neutrino events from collapses at distance $r < D$, as a function of D, for a Mt water Cherenkov detector and 30 years running time. The upper to lower shaded regions are for triggers from Ultimate DECIGO, DECIGO+ and DECIGO (the latter is invisible in the left panel). Shadings describe the effect of varying the neutrino spectrum, see Table 5.1. Left panel: homogeneous NSFC population. Right: mix of 60% NSFC and 40% BHFC.

where R_j indicates the supernova rate in the galaxy j. This discrete expression is replaced by a continuum one, involving an integral, for $D > 11$ Mpc, where the cosmological supernova rate is used.

We now discuss the background of the time-triggered neutrino search. The number of supernova memory signals observed in the time ΔT is, $N_{SN}^{trig}(D) = \Delta T \sum_{j,r_j<D} R_j P_{det}^{GW}(r_j)$, and the number of expected background events is,

$$N_{bckg}^{trig}(D) = N_{SN}^{trig}(D)\lambda\Delta t\,,$$

where, $\lambda \simeq 1313$ events/year is the background rate[4] in the detector (Abe *et al.*, 2011, 2018a; Kunxian, 2015). Note that the background level is reduced by a factor $\epsilon_{bckg=} N_{SN}^{trig}(D)\Delta t/\Delta T$ compared to an un-triggered search.

We limit our study to neutrino events (eq. (5.5)) from CCSNe in the cosmic volume with $4 < D < 350$ Mpc, thus accounting for the fact that a nearby supernova ($D < 4$ Mpc) is unlikely to occur in three decades time. The upper bound on D is justified because beyond it the total event rate becomes dominated by background. Experimentally, a distance cut can be accomplished in different ways. For NSFC, one can make a selection using estimates of D from astronomy follow ups, which will benefit from the alerts from the memory detection and should have excellent sensitivity to supernovae in the local universe (see, e.g., Kochanek *et al.* (2017); Hiramatsu *et al.* (2021a); Valenti *et al.* (2016); Spiro *et al.* (2014); Hosseinzadeh *et al.* (2018) for dedicated projects). In the absence of an optical counterpart (BHFC), a similar (although less efficient) data selection can be performed using minimal input from theoretical models, e.g. to obtain conservative upper limits on the distances of individual observed BHFCs via GW memory signals. In the mature stage of this

[4]Some details about background events and a discussion on triggered and untriggered background rates is provided in App. F.

search, specifically designed data-analysis algorithms – exploiting the correlation of multiple observables – could reduce the level of model-dependency to a minimum.

5.2.2 Results

Our main results are in Fig. 5.5 and Fig. 5.6 for $\Delta T = 30$ yrs and for two scenarios: (i) a supernova population entirely comprised of NSFC; and (ii) a mixed population with 60% NSFC and 40% BHFC. Fig. 5.5 shows $N_\nu^{trig}(D)$ as a function of D. We observe the (expected) trend $N_\nu^{trig}(D) \propto D$ for $D \lesssim r_{max}^{GW}$ [5], with a flattening of the curves at larger D due to the loss of sensitivity of the GW detector. For case (i), time triggers from DECIGO+ will result in $N_\nu^{trig} \sim 10 - 30$. For Ult. DECIGO, $N_\nu^{trig} \sim 100 - 300$ is expected[6]. For the mixed population (case (ii)), results for Ult. DECIGO change only minimally, due to the different neutrino parameters between NSFC and BHFC. Instead, N_ν^{trig} increases dramatically, surpassing 100, for DECIGO+, due to the larger distance of sensitivity to BHFC. Indeed, the number of triggered neutrino events from collapses with $30 < D < 350$ Mpc is dominated by BHFC (see also Fig. 5.4). For this mixed population scenario, even DECIGO could be effective, providing a few triggers of BHFC up to $D \sim 30$ Mpc, resulting in $N_\nu^{trig} \sim 10$. As Fig. 5.5 shows, in all cases the signal exceeds the background for triggers with $r \lesssim 100$ Mpc. For Ultimate DECIGO, even for the largest D the signal is comparable to the background, and would cause a statistically significant excess.

Our summary figure, Fig. 5.6, shows $N_\nu^{trig}(350\ \mathrm{M}pc)$, as a function of h_n, together with representative values of r_{max}^{GW}. Roughly, we find $N_\nu^{trig} \propto 1/h_n$, for $h_n \gtrsim 10^{-26}$, with a flattening at lower values of h_n, due to upper cutoff on D. It appears that,

[5] Recall that, in the continuum limit, the number of supernovae scales like D^3 and the flux dilution factor like D^{-2}.

[6] For comparison, our estimated number of CCSNe within 350 Mpc is $N_{SN}^{trig} \sim 1.21 \times 10^6$.

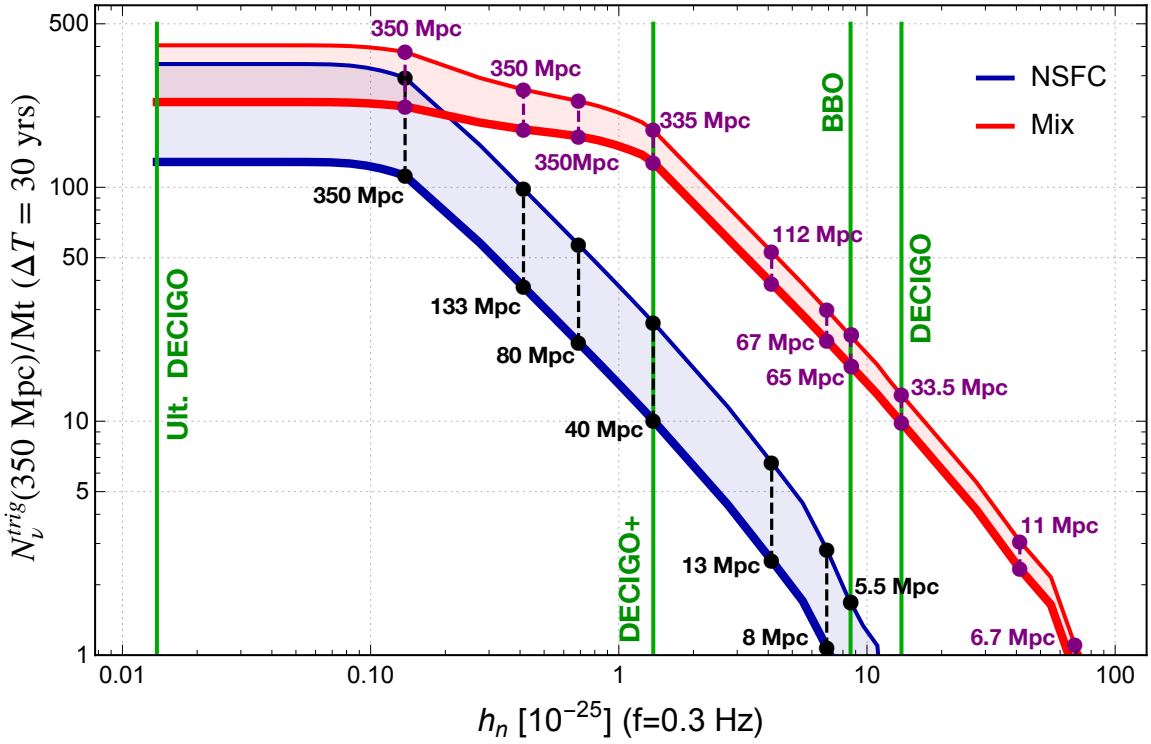

Figure 5.6: The number of memory-triggered supernova neutrinos detected at a 1 Mt water Cherenkov detector in 30 years, as a function of the noise of the GW detector at $f = 0.3$ Hz. The vertical lines mark specific experiments considered here. The lower and upper shaded regions refer respectively to a homogeneous population with moderate memory strain and a mixed population where 40% of collapses have stronger memory strain; the shading describes the effect of varying the neutrino spectrum, see Table 5.1. The dots (upper set: NSFC and lower set: BHFC) and legends on the curves give the GW distance of sensitivity (r_{max}^{GW}, see text below Eq. (5.2)) corresponding to the noise on their abscissa.

even for the most conservative parameters, a $\mathcal{O}(10)$ noise abatement with respect to DECIGO (i.e., DECIGO+) is sufficient to obtain a signal at a Mt scale detector in $\sim 20 - 30$ years.

Chapter 6

DISCUSSIONS AND CONCLUSION - I

The overall theme of this work has been to investigate what information does neutrino emission from a core-collapse supernova provide us with, especially at the dawn of multi-messenger astronomy. In the era of multi-messenger astronomy gravitational, neutrino and gamma ray observations are combined to extract information about astrophysical sources and phenomena in the universe. Some of these are at the largest energy scales known and hence act as nature's own laboratories to test particle and exotic physics. This may help in extending the current Standard Model. Since neutrinos are produced in most of these extreme environments (in the Sun, supernovae. . .), they have become a centerpiece of modern astronomy.

CCSN is the process by which a massive star ($> 10\ M_{\odot}$) dies. Its lifetime involves several stages of nuclear burning which finally lead to pressure loss and ultimately the gravitational col- lapse of the star's core and its explosion. The core collapse is followed by the release of $\sim 3 \times 10^{53}$ ergs of gravitational energy, most of which (99%) is emitted in the form of neutrinos over a time-scale of $\sim 10s$. These supernova neutrinos are detectable in current (Super-Kamiokande) and future (Hyper-Kamiokande, DUNE, JUNO) neutrino detectors, making them ideal to probe the phenomena of CCSN and understand the nature of neutrino in general.

We focused our efforts to study the directional information carried by presupernova neutrinos and how it can be used to localize a CCSN and ultimately an early warning system (see chapter 3). Our work is the first dedicated study of the localization of a star using pre-supernova neutrinos. Since it serves as an early alert it will allow astronomers, for the first time, to observe a star prior to and during collapse.

This would help constrain models of stellar evolution. For fast exploding stars pre-supernova neutrinos would be the only useful alert since they precede the supernova neutrino burst by hours. An early alert will also help in testing the emission of exotic particles (e.g., axions) during a CCSN by providing information about where to point detectors. It will also help in preparing gravitational wave (GW) detectors to observe GWs from the CCSN, thus facilitating multi-messenger observations.

We have also explored the potentials of the next generation deci-Hz GW detectors to observe an unique effect produced by supernova neutrinos - the gravitational wave memory effect (see chapter 4). This in essence is a multimessenger effort which would combine the neutrino observations with the GW observations from a CCSN, to provide crucial information about the internal dynamics of the collapse and help in constraining models. It also complements numerical calculations of the memory which are computationally intensive. After verifying that our phenomenological models are robust and match the existing numerical simulations, we predicted the GW strain for plausible scenarios including the case of a star collapsing into a black hole. We found that the GW strain for a galactic supernova ($D \leq 10$ kpc) is of the order $\sim 10^{-22} - 10^{-21}$, and develops over a time scale related to the anisotropy of the neutrino emission. We also analyzed the potential of various kinds of GW detectors (ground, space, atom interferometers) to detect the memory signatures. The ideal detectors to observe the GWM would be the future space-based ones like DECIGO and BBO. An ideal version of DECIGO called Ultimate DECIGO would be able to see the memory effect from a CCSN at 100 Mpc or more which is far beyond the reach of neutrino detectors.

This led us to the novel idea of using these GW memory observations as triggers for neutrino detectors, to collect a clean sample of supernova neutrinos from CCSN upto ~ 100 Mpc (see chapter 5). This combination of a deci-Hz GW detector and a

Mt neutrino detector will allow the latter to surpass its current sensitivity limits to detect a nearly background-free sample of $\sim 3-30$ supernova neutrino events per Mt per decade of operation, from large distances ($\sim 10-100$Mpc), which will open a new avenue to studying supernova neutrinos.

We hope our work, will prove to be a tiny yet significant contribution in these areas. In this chapter, we discuss the main highlights of our work including some general comments and relevant future directions.

In chapter 3, we demonstrated that it will be possible to use the neutrino IBD signal at a large liquid scintillator detector to obtain an early localization of a nearby pre-supernova ($D \lesssim 1$ kpc). The method we propose is robust, as it has been used successfully for reactor neutrinos, and it is sufficiently simple that it can be implemented during a pre-supernova signal detection. For a detector where the forward-backward asymmetry is about 10% (realistic for JUNO), and 200 events detected (also realistic at JUNO, for a star like Betelgeuse) the angular resolution is $\beta \simeq 60°$, which is moderate, but sufficient to exclude a large number of potential candidate progenitors.

The method has the potential to become even more sensitive if it is used with LS-Li, and therefore it provides further motivation to develop new experimental concepts in this direction. For example, 200 signal events with forward-backward asymmetry of $\sim$40% would result in a resolution of about 15°, and the possibility to uniquely identify the progenitor star.

In a realistic situation, as soon as a presupernova signal is detected with high confidence (a few tens of candidate events), an alert with a coarse localization information can be issued, followed by updates with improved angular resolution in the minutes or hours leading to the neutrino burst detection.

Using the Patton *et al.* (2017a) presupernova model, we find that (see Figure 3.6) when the number of events reaches $N = 100$ ($\simeq 1$ hour pre-collapse for Betelgeuse),

the angular information is already close to optimal, since only a minimal improvement of the positional estimate can be gained at subsequent times. Note, however, that our results are conservative. According to other simulations where the presupernova neutrino luminosity reaches a detectable level over a time scale of days (Kato *et al.*, 2015; Guo *et al.*, 2019), it might be possible to detect a larger number of events, resulting in even better angular resolutions in the last 1-2 hours before the core collapse.

It is possible that, when a nearby star reaches its final day or hours before becoming a supernova, a new array of neutrino detectors will be available. A large liquid scintillator experiment like the proposed THEIA (Askins *et al.*, 2019), which could reach 80 kt (fiducial) mass, could observe more than 10^3 IBD events, with an angular resolution of at least $\sim 30°$. The resolution of THEIA would be improved by using a water-based liquid scintillator, where the capability to separate the scintillation and Cherenkov light would result in enhanced pointing ability (e.g., Askins *et al.*, 2019) for IBD, and in the possibility to use neutrino-electron elastic scattering for pointing. A subdominant, but still useful, contribution to the pointing effort – at the level of tens of events – will come from $\mathcal{O}(1)$ kt liquid scintillator projects like SNO+ (Andringa *et al.*, 2016) and the Jinping Neutrino Experiment (Beacom *et al.*, 2017), for which the deep underground depth will result in very low background levels. Further activities on directionality in scintillators are ongoing (e.g., Biller *et al.*, 2020). Data from elastic scattering events at water Cherenkov detectors like SuperKamiokande (Simpson, 2019) and possibly the planned HyperKamiokande ($\mathcal{O}(100)$ kt) (Abe, 2016), will also contribute, despite the loss of statistics (compared to liquid scintillator) due to the higher energy threshold ($\sim 5-7$ MeV). In these detectors, a possible phase with Gadolinium dissolved in the water, like in the upcoming SuperK-Gd, (Beacom and Vagins, 2004; Simpson, 2019), will allow better discrimination of the IBD events,

resulting in an enhanced pointing potential.

In addition to new experimental scenarios, a different theoretical panorama may be realized as well, and there might be novel avenues to conduct fundamental science tests (e.g., searches for exotic light and weakly interacting particles) using presupernova neutrinos.

In chapter 4, we present a dedicated study of the phenomenology and detectability of the gravitational memory effect due to the neutrino emission from a core collapse supernova. We place a theoretical upper bound on the strain, $h(t)$ (Eq.(4.15)), and present phenomenological (analytical) description of the expected signal in time and frequency domain (Eqs. (4.29) and (4.31)). This description reproduces the results of numerical simulations well, and its analytical form can be considered a generalization of earlier toy models of the memory (e.g., Favata (2011)). We find that, depending on the type of scenario and on the choice of parameters, $h(t)$ and $h_c(f)$ vary between $\sim 10^{-23}$ and $\sim 10^{-20}$. Due to the time-varying anisotropy parameter, $\alpha(t)$, the memory signal is generally not straightforwardly related to the time profile of the neutrino luminosity profile. Rather, it could receive its dominant contribution from the second (or less)-long accretion phase, thus having substantial power at $f \gtrsim 1$ Hz.

Naturally, large uncertainties affect our models, mostly due to our incomplete knowledge of the size and time evolution of the anisotropy parameter. While the accretion-only models are supported by state-of-the art numerical simulations of supernovae, models with long-term anisotropy are necessarily more speculative, and have a character of plausibility. They suffer of uncertainties at the order of magnitude level. Let us also note that the *total*, net memory observed at Earth is uncertain due to the (uncertain) contribution of anisotropic matter ejection, which adds to the term due to neutrinos. The matter memory should be subdominant at low frequency ($f \lesssim 1$ Hz), and become progressively more important in the high frequency regime,

see, e.g., Kotake *et al.* (2009a); Vartanyan and Burrows (2020).

Our results confirm that, with the advent of Deci-Hz detectors, the observation of the gravitational memory from a collapsing star will be realistic. Therefore, the study of memory waveforms will become an important part of the multi-messenger approach to studying stellar core collapse, together with the observations of the neutrino burst at neutrino detectors (and, for near-Earth stars, of the pre-supernova neutrino emission, Patton *et al.* (2017a); Mukhopadhyay *et al.* (2020a)), of gravitational waves at 10-100 Hz, and of the electromagnetic emission (if the collapse results in a supernova explosion). The best prospects for the supernova memory detection are at the most powerful Deci-Hz detectors like BBO and DECIGO, for which the distance of sensitivity can reach $\sim$ 10 Mpc for the most optimistic models, and $\sim$ 1 Mpc for more conservative scenarios. Interestingly, these distances of sensitivity are comparable, or even larger than the typical reach of the largest realistic neutrino detector, a 0.3-1 Mt water Cherenkov detector like the approved HyperKamiokande Abe *et al.* (2018b). This implies that a memory detection might be an important early supernova alert for extragalactic supernovae, that can be used for astronomy and neutrino follow ups.

The most immediate physics potential of the observation of a neutrino memory signal is the possibility to probe the anisotropy parameter, $\alpha(t)$. From the memory alone – especially if probed over a wide range of frequencies, through the interplay of multiple interferometers – it might be possible to distinguish between drastically different scenarios. In particular, a fast-rising, fast-plateauing memory signal, with frequency peak at or beyond 1 Hz would be an indication of an accretion-only scenario, whereas a slower rising (multi-second time scale), lower frequency (peak at $f \lesssim 1$ Hz) memory strain will indicate the presence of a long-term anisotropy.

For a galactic supernova, the interplay with a high statistics observation of the neutrino burst will open the possibility of precision measurement, because $\alpha(t)$ can be

extracted by comparing the memory data with the *measured total neutrino luminosity* (for which high sensitivity to the non-electron neutrino flavor is important, a fact that strengthens the motivations of efforts on this front). The measured anisotropy parameter could carry imprints of the hydrodynamics happening during the core-collapse, such as SASI, turbulence and chaotic dynamics, thus providing an important test of numerical models of core collapse. A detailed comparison of the memory features with SASI signatures observed in neutrinos and/or in gravitational waves at ~ 100 Hz may allow to pinpoint important events in the dynamics of the collapsed star, such as a change in the plane of the spiral SASI. Using the neutrino burst data, it might also be possible to disentangle the matter contribution to the memory from the neutrino one, thus offering a new handle on the phenomena that contribute to it.

Outside the field of multimessenger astronomy, the theme of neutrinos as sources of the gravitational memory is worth further exploration for its significance in general relativity. In particular, beyond the linear memory studied in this work, it would be worth to ask if neutrino emissions would play any significant role into the non-linear memory effect Christodoulou (1991); Blanchet and Damour (1992), which accounts for the contribution to the memory from the gravitational wave itself. It has been shown Thorne (1992) that the non-linear memory can be described by a linear memory in which the sources are the individual radiated gravitons; therefore, one might wonder if an analogous effect occurs from the emitted neutrinos. Even more recently, it has been argued Favata (2010) that the non-linear memory has a large contribution in the gravitational waveform which enter at leading order in a post-Newtonian expansion. The reason of this large contribution being the hereditary nature of the memory, which can be build from long times for some long lived asymmetries of the source. Another exciting aspect of the non-linear memory, is its connection to the group of symmetries for asymptotically flat space-time metrics Strominger (2014) which is directly related

to the study of the vacuum in quantum gravity and the infrared structure of gravity. Along the same lines, it has been shown that the non-linear memory is just equivalent to Weinberg's theorem for soft graviton production Strominger and Zhiboedov (2016). All these new developments motivate a study of the non-linear memory in the novel context of neutrino emission.

The gravitational memory could be the next major prediction of general relativity to receive an impressive experimental confirmation, in a not-too-distant future. It is interesting that such a first observation will be directly linked to another exciting event, the detection of a neutrino burst from a galactic (or near-galactic) supernova. Learning about gravity from neutrinos, and vice-versa, will be a new and fascinating development in multimessenger astronomy.

In chapter 5, we described a new multimessenger approach to core collapse supernovae, where a time-triggered search of supernova neutrinos is enabled by observing the gravitational memory caused by the neutrinos themselves. This scenario could be realized a few decades from now, when powerful Deci-Hz interferometers (noise $h_n \lesssim 10^{-25}$) and Mt-scale neutrino detectors start operating. For optimistic parameters, DECIGO and HyperKamiokande (mass $M = 0.260$ Mt) might already achieve a low statistics observation. This approach will also enable joint analyses of neutrino, GW and light curves of CCSNe in local universe.

Our proposed method will deliver a sample of neutrino events from supernovae in the *local* universe, from which the main neutrino properties – i.e, the (population-averaged) energy spectra and time profiles– will be measured. These can then be compared to the same quantities from (1) SN 1987A, to measure the deviation between SN1987A and an average local supernova (the same exercise can be done for a future nearby supernova burst, if it occurs); (2) the DSNB, to distinguish the contributions to the DSNB by CCSNe in the distant universe and by other transients (e.g.

binary mergers). The comparison between cosmological and local contributions to the DSNB will test hypotheses of how the supernova progenitor population evolves with the distance. Even within the local-neutrino sample, one could test the evolution with distance, if the latter is estimated for each supernova using multi-messenger observations (e.g., the amplitude of the memory signal and astronomical imaging).

Correlating memory and neutrino data might reveal two distinct populations, like those described here (NSFC and BHFC), which could be statistically separated. For example, events having a relatively large neutrino-memory time separation (bigger than 1 s, as black hole formation typically occur within 1 s, cutting off the neutrino luminosity (Woosley *et al.*, 2002; Sumiyoshi *et al.*, 2006; O'Connor and Ott, 2011)) and(or) followed by electromagnetic (EM) signals of a CCSN could be attributed to NSFC. The possibility to study such sub-population individually is unique of this local-collapses neutrino sample. Additionally, our method provides a unique chance to jointly analyze neutrino and follow-up EM signals (LSST Science Collaboration, 2009; Kochanek *et al.*, 2017) from the *same* NSFC. Although only ≈ 1 event would be detected from a specific NSFC, it can help to determine the time when the core of a NSFC collapses and the shock is formed. Such estimation would be relatively precise, considering that the neutrino burst from a NSFC only lasts for ≈ 10 s. A supernova EM signal is delayed relative to the neutrinos, by at least the time it takes the shock to propagate through the envelope, typically hours. Measuring this time delay will provide a crucial confirmation and can test the variation of the CCSNe explosion mechanism.

To conclude, we have demonstrated that the interplay between neutrino detectors and sub-Hz GW observatories will open a new path to studying supernova neutrinos. Although several decades may pass before the first results become available, the work of designing the next generation of experiments is well under way, and we hope that

our work will contribute to its progress.

When the next galactic core-collapse supernova happens, it will be a very important event for the entire physics community, especially the neutrino physics community. Immense progress will be made in the context of understanding the complex dynamics of a CCSN and understanding the nature of neutrinos. Perhaps, if one is optimistic, it will also take us closer to answering a lot of the open questions we mentioned in the introduction (see chapter 1). We hope this work will be an aid to that effort. For now, we wait and continue to extend the ideas, so that when the day comes we are prepared to take the next leap.

Chapter 7

QUANTUM FIELDS IN TIME- AND SPACE-DEPENDENT BACKGROUNDS

An important avenue of research in theoretical physics is the dynamics of quantum fields on classical backgrounds. The interplay of classical and quantum degrees of freedom (Cooper and Mottola, 1989a; Brout *et al.*, 1995; Anderson, 1995; Halliwell, 1998; Hertzberg, 2016) has been of interest and is particularly relevant in the context of cosmology (Birrell and Davies, 1984; Ford, 2021; Armendariz-Picon, 2020), gravitational collapse (Hawking, 1975; Narlikar, 1978; Alberghi *et al.*, 2001; Vachaspati, 2009), condensed matter systems (Kasper *et al.*, 2016), etc. What generically happens in such systems is, the quantum fields get excited. This phenomenon is known as particle production. Particle production generally happens whenever the background, that a quantum field is coupled to, has some associated time-dependence. When the background is time-dependent, the time-translation symmetry is broken. Then the energy of the quantum particles need not be conserved, and the quantum field may absorb energy from the background. Particle production has been well-studied (Zeldovich and Starobinsky, 1971; Hu, 1974; Berger, 1975; Hu and Parker, 1977, 1978). But, one might choose to go a step forward and ask, *what happens to the background itself as a result of particle production?* The simple answer is to this is, the quantum excitations backreact on the classical field and modify its dynamics. A key question that arises out of this is: how does one account for this in various physical systems? The answer to this question is what we address in the following chapters.

Interesting phenomenon involving particle production and backreaction include backreaction of Hawking radiation during gravitational collapse (Hawking, 1975), particle production during inflation (Kofman *et al.*, 1994) and the backreaction of

Schwinger pair production on the background electric field (Schwinger, 1951; Cooper and Mottola, 1989b; Kluger *et al.*, 1991; King *et al.*, 2012), systems of simple harmonic oscillators with quadratic couplings (Vachaspati, 2017). For example, in inflationary cosmology the inflaton rolls down some potential while exciting other quantum fields to reheat the universe. Phase transitions in which an order parameter evolves to develop a vacuum expectation value while also interacting with other quantum degrees of freedom, are also examples of phenomenon involving interplay between classical and quantum degrees of freedom. Such problems have a rich history but the attention has mostly focused on the quantum effects in fixed classical backgrounds.

Mathematically speaking, assume a quantum field ψ in a time-dependent background. The field ψ will obey the classical equation of motion as follows,

$$\Box\psi + \omega^2(t)\ \psi = 0\,, \tag{7.1}$$

where, the D'Alembertian operator may also include a time-dependent metric and ω^2 may arise due to interactions with the space-time dependent background field. The trivial case, $\psi(t, x) = 0$, is of course obtained if we have trivial initial conditions, $\psi(t = 0, x) = 0$ and $\dot{\psi}(t = 0, x) = 0$. This represents a situation when there is no radiation. But the story is different in case you treat the system quantum mechanically. In that case, quantum modes of ψ will get excited leading to radiation. This is what leads to particle production in the systems mentioned above.

The way we tackle these class of problems involving quantum fields coupled to a classical time-dependent background is by using a technique called the *Classical Quantum Correspondence (CQC)*. This was developed in Vachaspati and Zahariade (2018a,b). The CQC enables us to study particle production and the effects on the dynamics of the classical background due to backreaction. The CQC is similar to the semiclassical approach in which the classical background dynamics couples to the

expectation value of the quantum operators in the equation of motion. The catch is that the expectation value is to be taken in a quantum state of the fields that itself depends on the dynamics of the classical background. In the CQC it is realized that the expectation value can be evaluated in a quantum state in an arbitrary background in terms of certain classical variables that satisfy classical equations of motion with specific initial conditions. The solution of the full classical problem obtained using CQC contains all information about the quantum variables and also the backreacted dynamics of the classical background. This is what makes the CQC a powerful and a well-suited method for tackling such problems. However, it should be noted that the CQC method is identical to the "mode function method" used previously in the literature (Aarts and Smit, 2000; Borsanyi and Hindmarsh, 2008, 2009; Saffin *et al.*, 2014).

We will review the CQC for a quantum simple harmonic oscillator in Sec. 7.1. It is generalized for the case of fields in Sec. 7.1.1. We conclude the chapter with a brief discussion of the various systems where the CQC has been used to investigate in Sec. 7.2. The other applications of the CQC, relevant to this work has been discussed in detail in the following chapters 8, 9, and 10.

7.1 The Classical Quantum Correspondence (CQC)

In this section we reproduce the derivation of CQC as done in Vachaspati and Zahariade (2018a). The most simple case that we can consider to understand the CQC, is a quantum simple harmonic oscillator (SHO with a time-dependent frequency. In the CQC, we will show that the quantum dynamics of this one-dimensional SHO can be mapped to a two-dimensional classical dynamics equation with some particular initial conditions. We will work in the Heisenberg picture. The Hamiltonian for the

quantum simple harmonic oscillator with a time-dependent frequency is given by,

$$\hat{H} = \frac{\hat{p}^2}{2m} + \frac{m\omega(t)^2}{2}\hat{x}^2\,, \tag{7.2}$$

where, $\omega(t)$ is some time-dependent frequency. The creation and the annihilation operators defined in the usual way are,

$$\hat{a} = \frac{\hat{p} - im\omega\hat{x}}{\sqrt{2m\omega}}, \quad \hat{a}^\dagger = \frac{\hat{p} + im\omega\hat{x}}{\sqrt{2m\omega}}\,. \tag{7.3}$$

We can show that from above, $[\hat{a}, \hat{a}^\dagger] = 1$. The Hamiltonian can then be expressed in terms of the creation and annihilation operators as,

$$\hat{H} = \omega(t)\left(\hat{a}^\dagger\hat{a} + \frac{1}{2}\right)\,. \tag{7.4}$$

Differentiating the creation and annihilation operators with respect to time gives,

$$\frac{\partial\hat{a}}{\partial t} = -\frac{\dot{\omega}}{2\omega}\hat{a}^\dagger, \quad \frac{\partial\hat{a}^\dagger}{\partial t} = -\frac{\dot{\omega}}{2\omega}\hat{a}\,. \tag{7.5}$$

Recall, in the Heisenberg picture, an operator $\hat{O}$ evolves in time as,

$$\frac{d\hat{O}}{dt} = -i[\hat{O}, \hat{H}] + \frac{\partial\hat{O}}{\partial t} \tag{7.6}$$

Thus for $\hat{a}$ and $\hat{a}^\dagger$, in the Heisenberg picture we have,

$$\frac{d\hat{a}}{dt} = -i[\hat{a}, \hat{H}] + \frac{\partial\hat{a}}{\partial t} = -i\omega\hat{a} - \frac{\dot{\omega}}{2\omega}\hat{a}^\dagger \tag{7.7}$$

$$\frac{d\hat{a}^\dagger}{dt} = -i[\hat{a}, \hat{H}] + \frac{\partial\hat{a}}{\partial t} = +i\omega\hat{a}^\dagger - \frac{\dot{\omega}}{2\omega}\hat{a} \tag{7.8}$$

Particle production is generally treated using the Bogoliubov transformations. This involves writing the creation and annihilation operators at time t as a linear combination of the creation and annihilation operators at the initial time $t_0 = t = 0$ with some arbitrary time-dependent coefficients. In this case, to obtain the excitation of the SHO because of $\omega(t)$, we can write the Bogoliubov transformations as,

$$\hat{a}(t) = \alpha(t)\hat{a}_0 + \beta(t)\hat{a}_0^\dagger, \quad \hat{a}^\dagger(t) = \alpha^*(t)\hat{a}_0^\dagger + \beta^*(t)\hat{a}_0 \tag{7.9}$$

where $\hat{a}_0$ and $\hat{a}_0^\dagger$ are the annihilation and creation operators in Eq. (7.3) at the initial time, $t = 0 = t_0$, α and β are some arbitrary complex coefficcients. From Eqs. (7.7), (7.8), we can write,

$$\dot{\alpha} = -i\omega\alpha - \frac{\dot{\omega}}{2\omega}\beta^* \tag{7.10}$$

$$\dot{\beta} = -i\omega\beta - \frac{\dot{\omega}}{2\omega}\alpha^* \tag{7.11}$$

The expectation value of the energy of the qunatum SHO in the vacuum state is thus given by,

$$E_q(t) \equiv \langle H \rangle = \omega(t)\left(|\beta|^2 + \frac{1}{2}\right). \tag{7.12}$$

We can now define a new complex-variable z, $z \equiv \xi + i\chi$, where, ξ and χ are its real and imaginary parts. Rewriting, Eqs. (7.10) and (7.11) in terms of z gives us the following,

$$\alpha = \sqrt{\frac{m}{2\omega}}\left(\dot{z}^* - i\omega z^*\right), \tag{7.13}$$

$$\beta = \sqrt{\frac{m}{2\omega}}\left(\dot{z} - i\omega z\right), \tag{7.14}$$

One can notice right away that, the expressions for α and β are identical to the definition of the annihilation operator a in Eq. (7.3) if we think of z and $m\dot{z}$ as representing the complexified position and momentum operators for one dynamical variable and similarly z^* and $m\dot{z}^*$ for a second dynamical variable. Similarly the complex conjugates α^* and β^* then correspond to the expression for the creation operator $a^\dagger$ in Eq. (7.3). The equation of motion for z can be found by inserting Eqs. (7.13) and (7.14) in Eqs. (7.10) and (7.11). It is given by,

$$\ddot{z} + \omega^2(t)z = 0\,, \tag{7.15}$$

which as mentioned earlier, describes the dynamics of a two-dimensional complex SHO. It is easy to see that ξ and χ satisfy the classical equations of motion

$$\ddot{\xi} + \omega^2(t)\xi = 0, \quad \ddot{\chi} + \omega^2(t)\chi = 0. \tag{7.16}$$

Recall, that this method only works for some particular set of initial conditions. We can find them by noticing that, $a(0) = a_0$, corresponds to: $\alpha(0) = 1$, $\beta(0) = 0$, which implies,

$$z(0) = \frac{-i}{\sqrt{2m\omega_0}}, \quad \dot{z}(0) = \sqrt{\frac{\omega_0}{2m}}, \tag{7.17}$$

In terms of ξ and χ, the above initial condditions can be easily reqritten as,

$$\xi(0) = 0, \ \dot{\xi}(0) = \sqrt{\frac{\omega_0}{2m}} \ ; \ \chi(0) = \frac{-1}{\sqrt{2m\omega_0}}, \ \dot{\chi}(0) = 0 \tag{7.18}$$

where $\omega_0 = \omega(t = 0)$. The quantum dynamical problem has thus been completely reduced to a classical evolution problem for arbitrary backgrounds, $\omega(t)$. All the information required is contained in the complex variable z, which solves a classical equation of motion. The backreaction on the classical background due to the quantum particle production is taken into account using the semi-classical approximation and is evaluated using z. This will be discussed for specific models in later chapters (see chapters 8, 9, and 10).

7.1.1 CQC For Fields

In this section we elaborate how the CQC discussed above can be generalized to quantum fields. This is a rederivation of one of the main results from Vachaspati and Zahariade (2018b). In essence, we will follow the same sequence of steps as above but now deal with fields. We can think of the field consisting of N coupled quantum simple harmonic oscillators. The Hamiltonian for such a system is given by,

$$H = \frac{1}{2}\mathbf{p}^T\mu^{-2}\mathbf{p} + \frac{1}{2}\mathbf{x}^T\mu\Omega^2\mu\mathbf{x} \ , \tag{7.19}$$

where $\mathbf{p} = (p_1, \ldots, p_N)^T$ are the momentum operators corresponding to the position operators $\mathbf{x} = (x_1, \ldots, x_N)^T$, and ^{T} denotes matrix transposition, $\mu = [\mu_{ij}]_{1\leq i,j\leq N}$, and $\Omega = [\Omega_{ij}]_{1\leq i,j\leq N}$ are assumed to be real and symmetric positive definite which can

depend on time. The creation operator, $\mathbf{a}^\dagger = (a_1^\dagger, \ldots, a_N^\dagger)$ and annihilation operator, $\mathbf{a} = (a_1, \ldots, a_N)^T$ can be defined in the usual way, as we did earlier.

$$\mathbf{a} = \frac{1}{\sqrt{2}}\left(\sqrt{\Omega}^{-1}\mu^{-1}\mathbf{p} - i\sqrt{\Omega}\mu\mathbf{x}\right) , \tag{7.20}$$

$$\mathbf{a}^\dagger = \frac{1}{\sqrt{2}}\left(\mathbf{p}^T\mu^{-1}\sqrt{\Omega}^{-1} + i\mathbf{x}^T\mu\sqrt{\Omega}\right) . \tag{7.21}$$

The Hamiltonian as before can be rewritten in terms of the creation and annihilation operators as,

$$H = \mathbf{a}^\dagger\Omega\mathbf{a} + \frac{1}{2}\mathrm{Tr}(\Omega) . \tag{7.22}$$

We work in the Heisenberg picture like before. We can check that the creation and annihilation operators verify, $[a_i, a_j^\dagger] = \delta_{ij}$, $[a_i, a_j] = 0 = [a_i^\dagger, a_j^\dagger]$, and $[\mathbf{a}, H] = \Omega\mathbf{a}$, $[\mathbf{a}^\dagger, H] = -\mathbf{a}^\dagger\Omega$. The Heisenberg equations are then given by,

$$\frac{d\mathbf{a}}{dt} = -i\Omega\mathbf{a} + \frac{\partial\mathbf{a}}{\partial t} , \tag{7.23}$$

$$\frac{d\mathbf{a}^\dagger}{dt} = +i\mathbf{a}^\dagger\Omega + \frac{\partial\mathbf{a}^\dagger}{\partial t} , \tag{7.24}$$

This can be further expanded and written out as,

$$\frac{\partial\mathbf{a}}{\partial t} = \frac{1}{2}\left[\frac{d}{dt}\left(\sqrt{\Omega}^{-1}\mu^{-1}\right)\mu\sqrt{\Omega}\left(\mathbf{a} + \mathbf{a}^{\dagger T}\right) - \frac{d}{dt}\left(\sqrt{\Omega}\mu\right)\mu^{-1}\sqrt{\Omega}^{-1}\left(\mathbf{a}^{\dagger T} - \mathbf{a}\right)\right] \tag{7.25}$$

$$\frac{\partial\mathbf{a}^\dagger}{\partial t} = \frac{1}{2}\left[\left(\mathbf{a}^T + \mathbf{a}^\dagger\right)\sqrt{\Omega}\mu\frac{d}{dt}\left(\mu^{-1}\sqrt{\Omega}^{-1}\right) - \left(\mathbf{a}^T - \mathbf{a}^\dagger\right)\sqrt{\Omega}^{-1}\mu^{-1}\frac{d}{dt}\left(\mu\sqrt{\Omega}\right)\right] \tag{7.26}$$

We once again want to focus on particle production, for which we define the Bogoliubov coefficient as before,

$$\mathbf{a} = \alpha\ \mathbf{a}_0 + \beta\ \mathbf{a}_0^{\dagger T}, \tag{7.27}$$

$$\mathbf{a}^\dagger = \mathbf{a}_0^\dagger\ \alpha^\dagger + \mathbf{a}_0^T\ \beta^\dagger, \tag{7.28}$$

where, $\alpha(t)$ and $\beta(t)$ are complex matrices this time and is defined as, $\alpha = [\alpha_{ij}(t)]_{1\leq i,j\leq N}$ and $\beta = [\beta_{ij}(t)]_{1\leq i,j\leq N}$. From the Heisenberg equations and 7.28 we can write

$$\frac{d\alpha}{dt} = -i\Omega\alpha + \frac{1}{2}\left[\frac{d}{dt}\left(\sqrt{\Omega}^{-1}\mu^{-1}\right)\mu\sqrt{\Omega}\,(\alpha+\beta^*) - \frac{d}{dt}\left(\sqrt{\Omega}\mu\right)\mu^{-1}\sqrt{\Omega}^{-1}\,(\beta^*-\alpha)\right] \tag{7.29}$$

$$\frac{d\beta}{dt} = -i\Omega\beta + \frac{1}{2}\left[\frac{d}{dt}\left(\sqrt{\Omega}^{-1}\mu^{-1}\right)\mu\sqrt{\Omega}\,(\alpha^*+\beta) - \frac{d}{dt}\left(\sqrt{\Omega}\mu\right)\mu^{-1}\sqrt{\Omega}^{-1}\,(\alpha^*-\beta)\right] \tag{7.30}$$

The initial conditions are $\alpha = 1$ and $\beta = 0$. We can define new variables to simplify the above equations. We can then write 7.29 and 7.30 as,

$$\alpha = \frac{1}{\sqrt{2}}\left(\sqrt{\Omega}^{-1}\mu^{-1}P^* - i\sqrt{\Omega}\mu Z^*\right)\,, \tag{7.31}$$

$$\beta = \frac{1}{\sqrt{2}}\left(\sqrt{\Omega}^{-1}\mu^{-1}P - i\sqrt{\Omega}\mu Z\right)\,, \tag{7.32}$$

where, the variable redefinitions are,

$$P = \frac{1}{\sqrt{2}}\mu\sqrt{\Omega}(\alpha^*+\beta)\,, \tag{7.33}$$

$$iZ = \frac{1}{\sqrt{2}}\mu^{-1}\sqrt{\Omega}^{-1}(\alpha^*-\beta)\,, \tag{7.34}$$

In these variables the simplified equations are,

$$\dot{P} = -\mu\Omega^2\mu Z \quad \text{and} \quad \dot{Z} = \mu^{-2}P\,, \tag{7.35}$$

The initial conditions can be expressed as,

$$P_0 = \frac{1}{\sqrt{2}}\mu_0\sqrt{\Omega_0} \quad \text{and} \quad Z_0 = -\frac{i}{\sqrt{2}}\mu_0^{-1}\sqrt{\Omega_0}^{-1}\,. \tag{7.36}$$

The classical Hamiltonian in terms of Z, P is given by,

$$H_c = \frac{1}{2}\mathrm{Tr}\left[P^\dagger\mu^{-2}P + Z^\dagger\mu\Omega^2\mu Z\right], \tag{7.37}$$

The above expression which is like rewriting the original Hamiltonian for $\mathbf{x}$, $\mathbf{p}$ in (7.19) in terms of the new variables Z, P. Once again Z contains all the information about the field. The backreaction is once again taken into account using the semi-classical

approximation and evaluating the vacuum expectation values of the quantum field in terms of Z. This will be discussed in specific contexts in the following chapters (see chapters 8, 9, and 10).

7.2 Applications Of The CQC

The CQC, since it was outlined in Vachaspati and Zahariade (2018a) and generalized for fields in Vachaspati and Zahariade (2018b), has been applied to investigate various systems and scenarios. In this section, we briefly discuss the applications of the CQC to gain insights into coupled quantum and classical systems, in particular particle production and backreaction. The applications of CQC in the context of a rolling quantum field relevant for early universe cosmology (Ch. 8), formation of topological defects due to a quantum phase transition (Ch. 9), and the collision of a sine-Gordon kink-antikink in the presence of a quantum field (Ch. 10), form the core of this work and will be discussed in great detail in the subsequent chapters.

Ref. Vachaspati and Zahariade (2019), considers a quantum scalar field in the gravitational background of a collapsing spherical shell. It was shown that for a toy model representative of the actual situation, the CQC can yield Hawking radiation as well as the slow down of the collapse due to radiation backreaction. The quantum evaporation of a classical sine-Gordon like breather was studied in Olle *et al.* (2019). The complete treatment of the backreaction of quantum radiation on the classical dynamics of oscillons was considered. The breather decay rate was also calculated as function of coupling strength.

The Schwinger process in a uniform non-Abelian electric field was studied in Cardona and Vachaspati (2021). The approach used was dynamical where, initially a color electric field background and the quantum excitations in their non-interacting ground state was considered. Then, this system was evolved using the CQC. The

spectral energy density and number density in the excitations were evaluated as functions of time. It was found that there is an ultraviolet divergence associated with the total energy density which can be tamed using asymptotic freedom. Furthermore, the number density of the excitations had an infrared divergence which may be resolved by confinement.

Until now, the main discussion was always revolving around particle production and back reaction in the context of quantum fields in time-dependent backgrounds. But one can also ask the exact opposite question - *are there quantum fields in time-dependent classical backgrounds, that have no net particle production?* This question was addressed in Vachaspati (2022a), where the author chose to call the background *unexciting*. A quantum simple harmonic oscillator with a time-dependent frequency was considered. For this simple setup, it was found that there exists an infinite set of unexciting backgrounds, that is, any variations of the frequency, including rapid variations, would lead to no net particle production. Generalizing the problem to quantum fields, the spatially homogeneous case was considered first. This problem can be reduced to infinite simple harmonic oscillators each with a time-dependent frequency. In this case, the conclusion was that a *homogeneous background cannot be unexciting*. The reason being, one can choose a suitable background time-dependence to suppress the excitations of some modes, but there are always some modes that get excited by the time-dependent background. The problem was then generalized to the case of inhomogeneous time-dependent backgrounds. In this case, it was possible to derive idealized (non-physical) backgrounds, that lead no net particle production. The no net particle production can be physically understood in the sense that particles are produced and then later absorbed so that the net particle production vanishes.

But then one can wonder, *are there quantum fields in time-dependent classical backgrounds, for which there is no particle production at all times?* The answer is yes

and an easy example is a boosted soliton coupled to a quantum degree of freedom. A boosted soliton is time-dependent but does not produce radiation. In these special class of backgrounds there is no quantum dissipation and hence there is no need of an external driver to prevent the background from decaying. In Vachaspati (2022b), electric field backgrounds in a non-Abelian theory were investigated. A pure non-Abelian $SU(2)$ gauge theory with a background ("color") electric field was considered with masless and charged "gluons" as the quantum excitations. Remarkably, it was found that in this model, one can construct an electric field background that has no particle production at all times. Thus, the electric field found was stable against quantum dissipation due to Schwinger pair production.

With this we conclude this section, the other applications of CQC relevant to this work, is discussed in detail in the following chapters.

Chapter 8

ROLLING WITH A QUANTUM FIELD

In this chapter, we will consider rolling in field theory; some earlier works on this problem using different approaches and approximations can be found in Refs. Bardeen and Bublik (1987); Boyanovsky and de Vega (1993); Mrowczynski and Muller (1994); Ramsey and Hu (1997); Bedingham and Jones (2003); Aarts and Tranberg (2008); Asnin *et al.* (2009). To be more specific, we will consider a model with two scalar fields, ϕ and ψ, where ϕ is the classical background and ψ is the quantum field interacting with this background. The Lagrangian (in 1+1 dimensions) is,

$$L = \frac{1}{2}(\partial_\mu \phi)^2 + \frac{1}{2}(\partial_\mu \psi)^2 - V(\phi) - \frac{m^2}{2}\psi^2 - \frac{1}{2}\lambda\phi^2\psi^2 \tag{8.1}$$

where we will mostly focus on the case of a linear potential $V(\phi) = -\kappa\phi$ on which ϕ can roll. One approach to solving for the dynamics is to realize that the Lagrangian is quadratic in the quantum field ψ. Thus it can be integrated out in the path integral. This will yield a term in the effective action that has the form $\ln(\mathrm{Det}\hat{O}[\phi])$ where $\hat{O}[\phi]$ is an operator that depends on the background ϕ (see Peskin and Schroeder (1995) for example). Usually, at this stage, one adopts a perturbative approach and assumes ϕ is a known background to lowest order in some coupling. Then it may be possible to diagonalize $\hat{O}$ and to evaluate $\ln(\mathrm{Det}\hat{O}[\phi])$ perturbatively or in some other approximation scheme (Bardeen and Bublik, 1987; Boyanovsky and de Vega, 1993; Mrowczynski and Muller, 1994; Ramsey and Hu, 1997; Bedingham and Jones, 2003; Aarts and Tranberg, 2008; Asnin *et al.*, 2009).

In contrast, in the CQC, one does not try to eliminate ψ from the action. Instead the CQC equations *simultaneously* evolve the background ϕ as coupled to the expec-

tation value of ψ^2 and the quantum operator ψ in the ϕ background. This becomes possible by rewriting the quantum operator ψ in terms of new c-number variables denoted by a complex matrix Z and the initial quantum operators. The evolution of ψ is given entirely by the evolution of Z (Vachaspati and Zahariade, 2018b) and the expectation of ψ^2 that enters the ϕ equation takes the form Z^*Z. In this way, we obtain a set of differential equations for ϕ and Z that are solved with specific initial conditions to obtain the full dynamics. The background is completely general and need not be homogeneous, and perturbation theory is not employed. The only assumption is that the background is classical and it couples to the expectation value of ψ^2 evaluated in its dynamical quantum state.

To understand the CQC equations more quantitatively, we write the semiclassical equation of motion for ϕ,

$$\Box\phi + V'(\phi) + \lambda\langle\psi^2\rangle\phi = 0, \tag{8.2}$$

where the expectation value $\langle\psi^2\rangle$ is in the (unknown) instantaneous quantum state for the ψ fields. The evolution of the quantum operator ψ is given by the Heisenberg equation,

$$\dot{\psi} = \pi, \tag{8.3}$$

$$\dot{\pi} = \nabla^2\psi + (m^2 + \lambda\phi^2)\psi \tag{8.4}$$

where π denotes the conjugate momentum to ψ. This equation for quantum ψ can be solved in terms of a c-number variable in two spatial dimensions, $Z(t, x, y)$, by writing,

$$\psi(t, x) = \int dy \, \Big[Z^*(t, x, y)a_0(y) + Z(t, x, y)a_0^\dagger(y)\Big] \tag{8.5}$$

where a_0 and $a_0^\dagger$ are annihilation and creation operators at the initial time. a_0 is

defined by

$$a_0(y) = \frac{1}{\sqrt{2}}\left(\sqrt{\Omega_0}^{-1}\,\pi_0(y) - i\sqrt{\Omega_0}\,\psi_0(y)\right) \tag{8.6}$$

and $a_0^\dagger(y)$ is the Hermitian conjugate of a_0. Also $\Omega_0^2 = \nabla_y^2 + m^2 + \lambda\phi_0^2$ and $\phi_0 = \phi(t = 0, y)$ may depend non-trivially on y. Inserting (8.5) in (8.4) we obtain the equation of motion for Z,

$$\ddot{Z} - \nabla_x^2 Z + (m^2 + \lambda\phi^2)Z = 0 \tag{8.7}$$

Thus Z satisfies the classical equation of motion (independently of y). The initial conditions for Z can be obtained from the initial conditions for ψ and π, and we will write these explicitly in Sec. 8.1.

Next we assume that the initial state is the vacuum and is annihilated by a_0. Then we find

$$\langle\psi^2\rangle = \int dy\, Z^* Z \tag{8.8}$$

where recall that we are working in the Heisenberg picture so the quantum state at all times is given by the initial vacuum state. Inserting the expectation value in (8.2) gives,

$$\Box\phi + V'(\phi) + \lambda\left(\int dy\, Z^* Z\right)\phi = 0 \tag{8.9}$$

So the CQC equations consist of (8.9) and (8.7). In practice these need to be solved numerically for which they must be discretized. A convenient discretization is discussed in Sec. 8.1.

A simplification occurs if attention is restricted to static solutions. Then the background is fixed and the CQC approach is equivalent to the effective potential. It is only when we are interested in dynamical questions that the CQC becomes a powerful tool. For example, if we consider the model in Eq. (8.1), we can find static solutions for ϕ by locating the extrema of the effective potential, or equivalently by finding static solutions to the CQC equations. If on the other hand, we want to

know the dynamical solution, the effective potential is not useful whereas the CQC approach leads to the solution. The underlying reason is that the effective potential assumes the quantum state of the fields, for example the vacuum state or a thermal state, and expectation values of operators are taken in this state. In a dynamical process, the quantum state itself will be determined by the dynamics and will in general be different from the vacuum (or other) state assumed in the calculation of the effective potential. One situation where the effective potential may suffice is if there is dissipation in the system (for example, an expanding universe) and then the quantum fields are consistently driven to their vacuum state. Even in this case, the CQC can be used to describe the approach to the asymptotic state whereas the effective potential can only describe the final asymptotic state after the quantum fields have dissipated into their vacuum state.

In this chapter, we start by describing the discretized CQC formulation in Sec. 8.1. Then we discuss static solutions in Sec. 8.2. This exercise is completely equivalent to the effective potential formulation. In Sec. 8.3 we first discuss homogeneous dynamics. This leads to a very different picture from that obtained by simply considering static solutions of the effective potential. In Sec. 8.3 we also study dynamics with inhomogeneous initial conditions to see if homogeneous solutions might be unstable to developing inhomgeneities. We do not find an instability and this means that translational invariance is not spontaneously broken.

8.1 Lattice CQC

The CQC reformulation of the system in (8.1) follows that in Vachaspati and Zahariade (2018b); Olle *et al.* (2019). One difference is that we will employ periodic boundary conditions whereas Dirichlet boundary conditions were used in Refs. Vachaspati and Zahariade (2018b); Olle *et al.* (2019).

The first step is to latticize the field theory. The lattice points are given by $x = na$ where $n = 1, \ldots, N$. The discrete Lagrangian is

$$\begin{aligned} L' = \quad & a\sum_{n=1}^{N}\Big[\frac{1}{2}\dot{\phi}_n^2 + \frac{1}{2a^2}\phi_n\left(\phi_{n+1} - 2\phi_n + \phi_{n-1}\right) \\ & + \frac{1}{2}\dot{\psi}_n^2 + \frac{1}{2a^2}\psi_n\left(\psi_{n+1} - 2\psi_n + \psi_{n-1}\right) \\ & - V(\phi_n) - \frac{m^2}{2}\psi_n^2 - \frac{\lambda}{2}\phi_n^2\psi_n^2\Big] \end{aligned} \tag{8.10}$$

where $V(\phi)$ is a potential for ϕ that we will choose later. We assume periodic boundary conditions and n should be considered to be an integer mod N.

The ψ dependent part can be written as

$$L'_\psi = a\left[\frac{1}{2}\dot{\Psi}^T\dot{\Psi} - \frac{1}{2}\Psi^T\Omega^2\Psi\right] \tag{8.11}$$

where Ψ denotes a column vector with components ψ_i and

$$\Omega_{ij}^2 = \begin{cases} +2/a^2 + m^2 + \lambda\phi_i^2, & i = j \\ -1/a^2, & i = j \pm 1, \\ -1/a^2 & i = 1, j = N;\ i = N, j = 1 \\ 0, & \text{otherwise} \end{cases} \tag{8.12}$$

Using the CQC, the quantum field variables $\{\psi_i\}$ map into $N \times N$ complex classical field variables $\{Z_{ij}\}$ that satisfy the equation of motion (Vachaspati and Zahariade, 2018b),

$$\ddot{Z}_{nj} + \sum_{k=1}^{N}\Omega_{nk}^2 Z_{kj} = 0. \tag{8.13}$$

The CQC equation of motion for ϕ is

$$\ddot{\phi}_n - \frac{1}{a^2}(\phi_{n+1} - 2\phi_n + \phi_{n-1}) + V'(\phi_n) + \lambda\left(\frac{1}{a^2}\sum_{j=1}^{N} Z_{nj}^* Z_{nj}\right)\phi_n = 0. \tag{8.14}$$

These equations of motion have to be solved with initial conditions for Z that correspond to ψ being in its vacuum state,

$$Z_0 = -i\sqrt{\frac{a}{2}}\sqrt{\Omega_0}^{-1}, \quad \dot{Z}_0 = \sqrt{\frac{a}{2}}\sqrt{\Omega_0} \tag{8.15}$$

The initial conditions for ϕ are fixed by the problem of interest,

$$\phi_n = \phi_n(0), \quad \dot{\phi}_n = \dot{\phi}_n(0). \tag{8.16}$$

The sum over Z's in the last term of (8.14) will lead to renormalization of the mass of ϕ as we will discuss in Sec. 8.2.2.

8.2 Statics

We look for static solutions of ϕ but Z_{ij} may be time dependent. Then we set $\ddot{\phi}_n$ in (8.14) to zero. The equation is consistent only if we can show that the $Z-$dependent factor in the last term is time independent. This factor is proportional to $ZZ^\dagger$ and hence we define,

$$F = ZZ^\dagger \tag{8.17}$$

Then

$$\dot{F} = \dot{Z}Z^\dagger + Z\dot{Z}^\dagger, \tag{8.18}$$

$$\ddot{F} = 2\dot{Z}\dot{Z}^\dagger - (\Omega^2 F + F\Omega^2), \tag{8.19}$$

From the initial conditions in (8.15) we get

$$Z_0 Z_0^\dagger = \frac{a}{2}\Omega_0^{-1}, \quad \dot{Z}_0 Z_0^\dagger = i\frac{a}{2} = -Z_0\dot{Z}_0^\dagger \tag{8.20}$$

$$\dot{Z}_0\dot{Z}_0^\dagger = \frac{a}{2}\Omega_0 = \Omega_0^2 Z_0 Z_0^\dagger = \Omega_0^2 F(0) \tag{8.21}$$

From here it is straightforward to check that $\dot{F}(0) = 0 = \ddot{F}(0)$. Also note that Ω_0^2 and $F_0 = a\Omega_0^{-1}/2$ commute. Then all higher derivatives of F when evaluated at the

initial time will also vanish. For example,

$$\dddot{F}_0 = -2(\Omega_0^2 Z_0 \dot{Z}_0^\dagger + \dot{Z}_0 Z_0^\dagger \Omega_0^2) - (\Omega_0^2 \dot{F}_0 + \dot{F}_0 \Omega_0^2) = 0 \tag{8.22}$$

Hence it is consistent to set $\ddot{\phi} = 0$ in (8.14) and to obtain the static equation,

$$-\frac{1}{a^2}(\phi_{n+1} - 2\phi_n + \phi_{n-1}) + V'(\phi_n) + \frac{\lambda}{2a}\Omega_{0,nn}^{-1}\phi_n = 0 \tag{8.23}$$

where there is no sum over the repeated index n.

Note that $\Omega_{0,nn}$ depends on $\{\phi_i\}$. So (8.23) is a highly non-linear (and implicit) equation for ϕ_n. We now discuss the solution under the assumption that ϕ is homogeneous [1].

8.2.1 Static Homogeneous Solution

Under the assumption that ϕ_n is independent of n, we will write $\phi_n = \phi_0$. This will be a self-consistent assumption only if $\Omega_{0,nn}^{-1}$ in (8.23) is independent of n. We now check this.

With the assumption of homogeneity, Ω^2 can be diagonalized explicitly. For $N \geq 3$ we can write

$$\Omega^2 = O^\dagger D O \tag{8.24}$$

where

$$O_{lk} = \frac{1}{\sqrt{N}} e^{ilk2\pi/N} \tag{8.25}$$

and

$$D_{lk} = \left[\frac{4}{a^2}\sin^2\left(\frac{\pi l}{N}\right) + m^2 + \lambda\phi_0^2\right]\delta_{lk} \tag{8.26}$$

Then

$$\Omega_0^{-1} = O^\dagger \sqrt{D}^{-1} O \tag{8.27}$$

[1] Inhomogeneous solutions would also be of interest as they would represent solitons that are supported by the quantum vacuum (Huang and Tipton, 1981).

but since $|O_{lk}|^2 = 1/N$ for every l, k we find

$$\frac{1}{2a}\Omega^{-1}_{0,nn} = \frac{1}{2aN}\sum_{k=1}^{N}(\sqrt{D}^{-1})_{kk} = \frac{1}{2aN}\sum_{k=1}^{N}\frac{1}{\sqrt{\frac{4}{a^2}\sin^2\left(\frac{\pi k}{N}\right)+M^2}} \tag{8.28}$$

where

$$M = \sqrt{m^2 + \lambda\phi_0^2} \tag{8.29}$$

Note that $\Omega^{-1}_{0,nn}/2a$ (no sum over n) is independent of n when ϕ_0 is homogeneous and the homogeneity assumption is self-consistent. This completes our check.

To connect with the continuum calculation we take the $a \to 0$ and $L = aN \to \infty$ limit. In the limit $a \to 0$, only terms with $\sin^2(\pi k/N) \to 0$ will contribute to the sum in (8.28). So we can approximate $\sin^2(\pi k/N) \sim (\pi k/N)^2$. Define $q = 2\pi k/(aN)$ and also consider the $L = aN \to \infty$ limit. Then

$$\frac{1}{2a}\Omega^{-1}_{0,nn} \to \frac{1}{2\pi}\int_0^\infty \frac{dq}{\sqrt{q^2+M^2}} \tag{8.30}$$

The quantity $\Omega^{-1}_{0,nn}/2a$ in (8.23) is completely equivalent to the vacuum expectation value of ψ^2. In the usual quantum field theory treatment, with constant $\phi = \phi_0$, ψ is a free field with mass M. The standard treatment then gives

$$\langle\psi^2\rangle = \frac{1}{2\pi}\int_0^\infty \frac{dp}{\sqrt{p^2+M^2}} \tag{8.31}$$

exactly as in (8.30).

8.2.2 Renormalization

Eq. (8.23) depends on $\Omega^{-1}_{0,nn}/2a$ which is given by (8.28). Let us evaluate this term in the $N \to \infty$ limit while keeping the lattice spacing, a, fixed. Then,

$$\frac{1}{2a}\Omega^{-1}_{0,nn} = \frac{1}{L}\sum_{k=1}^{N/2}\frac{1}{\sqrt{\frac{4}{a^2}\sin^2\left(\frac{\pi k}{N}\right)+M^2}} \tag{8.32}$$

For $\pi k/N < \pi/4$, we approximate $\sin^2(\pi k/N) \sim (\pi k/N)^2$, while for $\pi k/N > \pi/4$ we approximate $\sin^2(\pi k/N) \sim 1$ and take $Ma \ll 1$. Then

$$\frac{1}{2a}\Omega^{-1}_{0,nn} \approx \frac{1}{L}\sum_{k=1}^{N/4} \frac{1}{\sqrt{\frac{4\pi^2k^2}{L^2}+M^2}} + \frac{1}{L}\sum_{k=N/4}^{N/2}\frac{L}{2N} = \frac{1}{2\pi}\int_{q_0}^{q_\infty}\frac{dq}{\sqrt{q^2+M^2}} + \frac{1}{8} \qquad (8.33)$$

where $q \equiv 2\pi k/L$, $q_0 = 2\pi/L$ and $q_\infty = \pi N/(2L)$. The integral can be evaluated to give

$$\begin{aligned}
\frac{1}{2a}\Omega^{-1}_{0,nn} &\approx \frac{1}{4\pi}\ln\left[\frac{\sqrt{p^2+M^2}+p}{\sqrt{p^2+M^2}-p}\right]^{q_\infty}_{q_0} + \frac{1}{8} \\
&\approx \frac{1}{4\pi}\ln\left[\frac{2}{M^2/(2q_\infty^2)}\right] - 0 + \frac{1}{8} \\
&\approx \frac{1}{2\pi}\ln(q_\infty a) - \frac{1}{2\pi}\ln(Ma) + \frac{1}{4\pi}\ln(4) + \frac{1}{8} \\
&\approx -\frac{1}{2\pi}\ln(Ma) + C \qquad (8.34)
\end{aligned}$$

where we have used $ML \gg 2\pi$, in which case the q_0 contribution approximates to 0. We have also denoted the remaining terms by C as these are sensitive to the approximations we have made.

Next we consider the consequences of changing the lattice spacing. If we rescale a to ξa for some constant ξ, then $\Omega^{-1}_{0,nn}/2a$ shifts by $-\ln(\xi)/2\pi$. This shift contributes to the mass of ϕ and can be compensated for by introducing a suitable bare mass contribution in the classical potential $V(\phi)$. Then the physical mass of ϕ will not depend on rescalings of the lattice spacing. However, we still need a measurement to tell us the physical mass of ϕ at a given renormalization scale. This is normally determined by experiment. For our purposes, we will take the renormalization scale μ to be $1/a$. If we wish to use a different lattice spacing, say $a \to \xi a$, then to compare results we must also change the potential: $V \to V + \lambda\ln(\xi)\phi^2/4\pi$.

The existence of the energy scale μ is also necessitated by our treatment of ϕ as a classical background field. Strictly, ϕ should also be quantized. In those cases

that ϕ can effectively be described as a classical background, we expect the classical treatment to break down if we probe the background on very short length scales, that is, at very high energies. For example, if the classical background is the spacetime metric, we expect that a quantum treatment will become essential at energies above the Planck scale. Similarly for a solitonic background, we might expect that a quantum treatment will become necessary for energy much larger than the mass scale of the soliton.

Now from (8.23), we see that the CQC formulation for static, homogeneous ϕ_0 is completely equivalent to the effective potential,

$$\begin{aligned} V_{\text{eff}}(\phi_0) &= V(\phi_0) + \frac{\lambda}{2a}\int^{\phi_0} d\phi\, \Omega^{-1}_{0,nn}[\phi]\,\phi \\ &\approx V(\phi_0) - \frac{M^2}{4\pi}\ln(Ma) + \lambda\left(C + \frac{1}{4\pi}\right)\frac{\phi_0^2}{2} + \frac{m^2}{8\pi} \end{aligned} \tag{8.35}$$

where M is given by (8.29). Note that $-\ln(Ma) = +\ln(\mu/M) > 0$ since μ is an ultra-violet cutoff.

To summarize, we will write (8.23) for the static, homogeneous background case as

$$\frac{\lambda}{2a}\Omega^{-1}_{0,nn}\phi_0 = -V'(\phi_0). \tag{8.36}$$

We now consider static solution for two simple choices for $V(\phi)$, namely a linear potential and an inverted quadratic potential.

8.2.3 Conditions For Static Solutions In Simple Cases

Linear potential

First we consider a linear potential

$$V_1(\phi) = -K\phi \tag{8.37}$$

Then (8.36) becomes

$$\frac{\lambda}{2a}\Omega^{-1}_{0,nn}\phi_0 = +K \tag{8.38}$$

In Fig. 8.1a we have plotted the left-hand side of this equation. The right-hand side will be a horizontal line at K and there is clearly a solution. However, if K is larger than the cutoff value of the left-hand side, *i.e.* when it is evaluated at $M = \mu$, then we cannot be sure that there is a solution since (8.36) is only valid below the cutoff. Hence the condition for a solution is

$$0 < K < K_{\max} \tag{8.39}$$

where

$$K_{\max} = \sqrt{\lambda}\,\mu \left[\frac{1}{2a}\Omega^{-1}_{0,nn}\right]_{M=\mu} \approx C\sqrt{\lambda}\,\mu \tag{8.40}$$

where we have used (8.34). Since for large ϕ_0 the potential is quadratic and increasing, the solution is a minimum. Hence there is a non-trivial minimum of the potential that is entirely due to quantum vacuum fluctuations of ψ provided the coupling is strong, as given by

$$\lambda \gtrsim \frac{K^2}{C^2\mu^2} = 2.4a^2K^2 \tag{8.41}$$

where the value of C is determined using (8.32) with $M = \mu = 1/a$ and gives $C = 0.643$. For weaker couplings, there is no solution for non-trivial ϕ_0 within the range of values in which our treatment holds.

Inverted quadratic potential

Next we consider an inverted quadratic potential

$$V_2(\phi) = -\frac{\kappa^2}{2}\phi^2 \tag{8.42}$$

Then (8.36) becomes

$$\frac{\lambda}{2a}\Omega^{-1}_{0,nn}\phi_0 = +\kappa^2\phi_0 \tag{8.43}$$

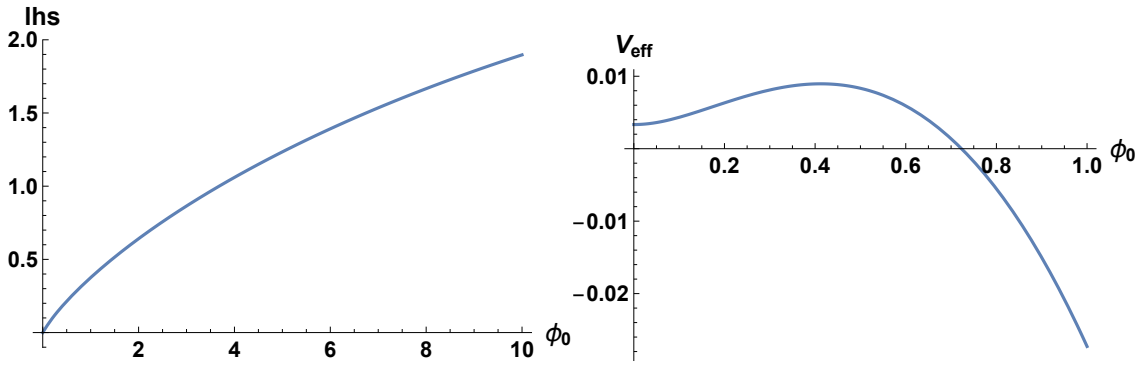

(a) (b)

Figure 8.1: (a) Plot of the left-hand side of (8.36) versus ϕ_0 for $\lambda = 0.5$, $a = 0.001$, $L = 100$, $m = 0$. (b) Plot of the effective potential for the inverted quadratic case for $\kappa = 1$, $m_\psi = 0.1$, $a = 0.25 = 1/\mu$, and $\lambda = 1.0$. As given below (8.41), $C = 0.643$.

The left-hand side is plotted in Fig. 8.1a while the right-hand side is a straight line passing through the origin and with slope κ^2. There is a non-trivial intersection point if the slope κ^2 is less than the slope of the left-hand side at $\phi_0 = 0$ and greater than the slope of the line joining the origin to the point where the left-hand side is evaluated at the cutoff value $\mu/\sqrt{\lambda}$.

Near the origin, we can expand the left-hand side (lhs) of (8.43) for small ϕ_0

$$\text{lhs}(\phi_0 \to 0) = \lambda \left[\frac{1}{2\pi}\ln(\mu/m) + C\right]\phi_0. \tag{8.44}$$

and the coefficient of ϕ_0 is the slope at the origin. At the cutoff, the left-hand side evaluates to

$$\text{lhs}(\phi_0 = \mu/\sqrt{\lambda}) = \lambda\left[-\frac{m^2}{4\pi\mu^2} + C\right]\phi_0 \tag{8.45}$$

and the slope of the line joining the origin with the cutoff point is given by the pre-factor of ϕ_0. Therefore we only have a non-trivial ($\phi_0 \neq 0$) solution if

$$\lambda\left[\frac{1}{2\pi}\ln(\mu/m) + C\right] > \kappa^2 > \lambda\left[-\frac{m^2}{4\pi\mu^2} + C\right] \tag{8.46}$$

which we can also write as

$$\frac{\kappa^2}{C - m^2/4\pi\mu^2} > \lambda > \frac{\kappa^2}{C + \ln(\mu/m)/2\pi} \tag{8.47}$$

To understand the range of couplings for which there is a solution, note that λ cannot be too small because then the quantum effects are negligible. On the other hand a very large value of λ means that the quantum effects are very strong and make the classical inverted potential upright at all ϕ_0. Then the only solution is the trivial $\phi_0 = 0$. However, evaluating the second derivative of the effective potential at $\phi_0 = 0$ shows that it is positive if the conditions in (8.47) are satisfied. This implies that the effective potential has a minimum at the origin and the non-trivial solution is a maximum. Thus the quantum corrections for the inverted quadratic potential can provide a metastable vacuum at $\phi_0 = 0$ in the range of parameters in (8.47) as shown in the example in Fig. 8.1b.

8.3 Dynamics

The effective potential is not suitable for describing the evolution of the background because the derivation assumes that the quantum field ψ is in its vacuum. In the dynamical problem, as the field ϕ rolls, quanta of ψ are excited and the field ψ is no longer in its vacuum. The production of ψ quanta backreacts on the dynamics of ϕ. We shall now solve this dynamical problem, separately considering homogeneous and inhomogeneous backgrounds.

8.3.1 Dynamics With Homogeneity

The first question we ask is if the initial conditions for ϕ are homogeneous, can the dynamics make ϕ inhomogeneous? As this is a dynamical question, we use the CQC equations in (8.13) and (8.14) and check that homogeneous evolution is self-consistent.

For homogeneous ϕ, Eq. (8.12) can be written in a more convenient way as

$$\Omega_{ij}^2 = -\nabla_{ij}^2 + M^2\delta_{ij} \tag{8.48}$$

where $M^2 = m^2 + \lambda\phi^2$ and the Laplacian matrix is given by,

$$a^2\nabla^2_{ij} = \delta_{i+1,j} - 2\delta_{ij} + \delta_{i-1,j} \tag{8.49}$$

where the indices are integers mod N. The ∇^2 has translational symmetry, *i.e.*

$$\nabla^2_{ij} = \nabla^2_{i+s,j+s} \tag{8.50}$$

where s is any integer. Alternately, ∇^2_{ij} only depends on the difference $i-j$ (mod N). Then Ω^2_{ij} is also translationally invariant and only depends on the difference $i-j$

$$\Omega^2_{i+s,j+s} = \Omega^2_{i,j} \tag{8.51}$$

In particular, this implies Ω^2_{nn} is independent of n, as already discussed below (8.30).

Using Eqs. (8.24), (8.25) and (8.26) we can check that the initial conditions for Z_{ij} are also translationally invariant,

$$Z_{0;i+s,j+s} = Z_{0;i,j}, \quad \dot{Z}_{0;i+s,j+s} = \dot{Z}_{0;i,j} \tag{8.52}$$

when ϕ is homogeneous.

Next we consider the equation for $Z_{n+s,j+s}$ in (8.13).

$$\begin{aligned} 0 &= \ddot{Z}_{n+s,j+s} + \sum_{k=1}^{N} \Omega^2_{n+s,k}\, Z_{k,j+s} \\ &= \ddot{Z}_{n+s,j+s} + \sum_{l=1}^{N} \Omega^2_{n+s,l+s}\, Z_{l+s,j+s} \\ &= \ddot{Z}_{n+s,j+s} + \sum_{l=1}^{N} \Omega^2_{n,l}\, Z_{l+s,j+s} \end{aligned} \tag{8.53}$$

In the above derivation we have changed the summation index from k to $l+s$ in the second line and used (8.51) in the third line. Now subtracting (8.13) gives

$$(\ddot{Z}_{n+s,j+s} - \ddot{Z}_{n,j}) + \sum_{l=1}^{N} \Omega^2_{n,l}(Z_{l+s,j+s} - Z_{l,j}) = 0 \tag{8.54}$$

With the initial conditions in (8.52), the solution is

$$Z_{n+s,j+s}(t) = Z_{n,j}(t) \tag{8.55}$$

i.e. $Z_{n,j}$ is invariant under translations while ϕ is homogeneous.

Making use of the translational symmetry, we can write $Z_{nj} = a\chi_{n-j}$. Then going back to the equation for ϕ in (8.14), we see

$$\frac{1}{a^2}\sum_{j=1}^{N} Z^*_{nj}Z_{nj} = \sum_{j=1}^{N} \chi^*_{n-j}\chi_{n-j} = \sum_{k=1}^{N} \chi^*_k\chi_k$$

which is independent of n. Thus the ϕ_n equation is independent of n and the evolution of ϕ is homogeneous. Thus homogeneous initial conditions will lead to homogeneous evolution.

8.3.2 CQC For Fields With Homogeneous Background

The result above, that translational symmetry of the background is preserved on evolution, suggests that the system of CQC equations simplify when the background is homogeneous. Indeed we will show here that translational symmetry of the background implies that our quantum system corresponds to a classical field theory. Whereas the quantum system has the real scalar fields ϕ and ψ, the classical system has the background ϕ and a *complex* scalar field χ that is to be evolved with specific initial conditions.

For homogeneous backgrounds we have already introduced $\chi_{n-j} = Z_{nj}/a$ above (8.56). Then the ϕ equation becomes

$$\ddot{\phi} + V'(\phi) + \lambda\left(\sum_{j=1}^{N} \chi^*_j\chi_j\right)\phi = 0 \tag{8.56}$$

where we have written ϕ_n as ϕ since it is homogeneous. Similarly, after some manipulation, (8.13) with (8.48) leads to

$$\ddot{\chi}_n - \frac{1}{a^2}(\chi_{n+1} - 2\chi_n + \chi_{n-1}) + M^2\chi_n = 0 \tag{8.57}$$

which is the discretized version of

$$\Box\chi + M^2\chi = 0 \tag{8.58}$$

where $\Box$ is the D'Alembertian operator and note that χ is complex. Hence the original system where we had a classical field ϕ and a quantum field ψ has been transformed into a system with ϕ and a classical complex field χ.

We would now like to solve the system of equations in (8.56) and (8.57) with initial conditions following from those specified in Sec. 8.1,

$$\chi_q(t=0) = \frac{-i}{\sqrt{2a}N}\sum_{k=1}^{N}\frac{e^{-ikq2\pi/N}}{\left[\frac{4}{a^2}\sin^2\left(\frac{\pi k}{N}\right)+M_0^2\right]^{1/4}} \tag{8.59}$$

$$\begin{aligned}\dot{\chi}_q(t=0) &= \frac{1}{\sqrt{2a}N}\sum_{k=1}^{N}\left[\frac{4}{a^2}\sin^2\left(\frac{\pi k}{N}\right)+M_0^2\right]^{1/4} \\ &\quad\times e^{-ikq2\pi/N}\end{aligned} \tag{8.60}$$

where $M_0^2 = m^2 + \lambda\phi(t=0)^2$.

We can simplify the equations further by performing a discrete Fourier transform,

$$\chi_n = \frac{1}{\sqrt{N}}\sum_k c_k(t)e^{-ink2\pi/N} \tag{8.61}$$

Then the equation for the mode coefficients c_k are ordinary differential equations

$$\ddot{c}_k + \left[\frac{4}{a^2}\sin^2\left(\frac{\pi k}{N}\right)+M^2\right]c_k = 0 \tag{8.62}$$

with the initial conditions

$$c_k(t=0) = \frac{-i}{\sqrt{2aN}}\left[\frac{4}{a^2}\sin^2\left(\frac{\pi k}{N}\right)+M_0^2\right]^{-1/4} \tag{8.63}$$

$$\dot{c}_k(t=0) = \frac{1}{\sqrt{2aN}}\left[\frac{4}{a^2}\sin^2\left(\frac{\pi k}{N}\right)+M_0^2\right]^{1/4} \tag{8.64}$$

Further reduction in the number of variables can be obtained at the cost of introducing some non-linearity by letting

$$c_k = \rho_k e^{i\theta_k} \tag{8.65}$$

Then angular momentum ($\rho_k^2 \dot{\theta}_k$) conservation together with the initial conditions gives

$$\dot{\theta}_k = \frac{1}{2L\rho_k^2} \tag{8.66}$$

and the equation for ρ_k is

$$\ddot{\rho}_k + \left[\frac{4}{a^2}\sin^2\left(\frac{\pi k}{N}\right) + M^2\right]\rho_k = \frac{1}{4L^2\rho_k^3} \tag{8.67}$$

with initial conditions

$$\rho_k(0) = \frac{1}{\sqrt{2L}}\left[\frac{4}{a^2}\sin^2\left(\frac{\pi k}{N}\right) + M_0^2\right]^{-1/4}, \tag{8.68}$$

$$\dot{\rho}_k(0) = 0. \tag{8.69}$$

Advantage can also be taken of the symmetry $k \to N - k$ and then we only need to solve for $N/2 + 1$ of the ρ_k's.

In terms of the ρ_k's, the equation for ϕ is,

$$\ddot{\phi} + V'(\phi) + \lambda \sum_{k=1}^{N} \rho_k^2 \, \phi = 0 \tag{8.70}$$

To summarize our results in this section, a quantum real scalar field in a homogeneous time-dependent ("rolling") background field is equivalent to a classical complex scalar field in the same background with specific interactions with the background and specific initial conditions. In the discretized version, the quantum rolling problem is thus equivalent to $2N + 1$ (recall that c_k's are complex) second order ordinary differential equations (8.62), (8.70) with the initial conditions (8.63), (8.64) and chosen initial conditions for homogeneous ϕ. The problem can be reduced to $(N/2 + 1) + 1$ second order ordinary differential equations by going to the real ρ_k variables and using the $k \to N - k$ symmetry.

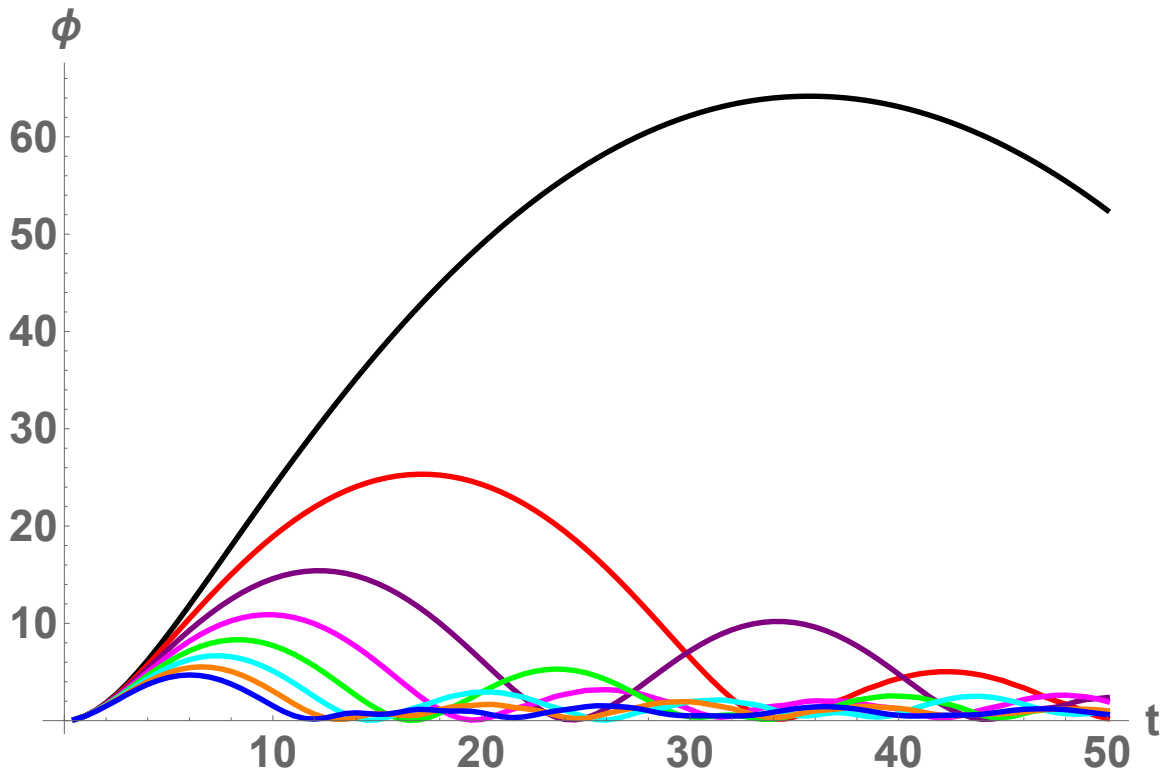

Figure 8.2: Plot of ϕ versus time for $\lambda = 0.3$ (black), 0.4 (red), 0.5 (dark purple), 0.6 (light purple), 0.7 (dark green), 0.8 (light green), 0.9 (orange) and 1.0 (blue), and other parameters as given in the text.

8.3.3 Dynamics In A Linear Potential

For the particular case of a linear potential, we have solved for the evolution of ϕ using the CQC equations in Sec. 8.1 with the potential in (8.37) ($K = -1$) and the ϕ initial conditions $\phi_n(0) = 0 = \dot{\phi}_n(0)$. The solutions for $\phi(t)$ for several different values of λ and with parameters $a = 0.25$, $N = 400$, $L = 100$, $m = 0.1$, are shown in Fig. 8.2.

The plots show that ϕ does not increase monotonically as we might expect based on rolling on a classical linear potential; instead ϕ oscillates, as one might expect based on the effective potential analysis. To compare the CQC dynamics with that of

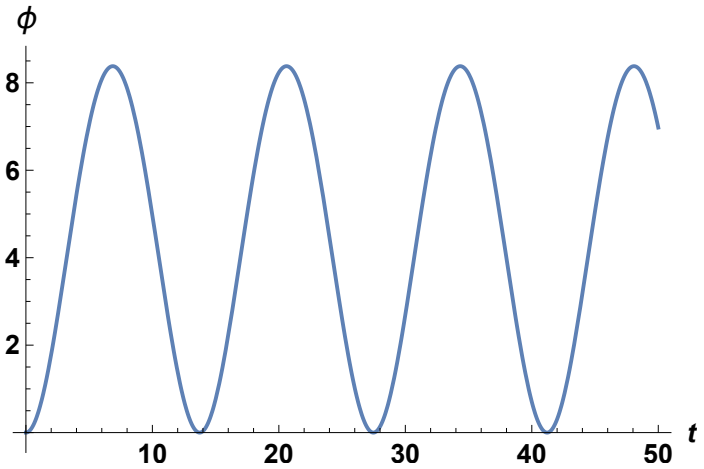

Figure 8.3: Plot of ϕ versus time for $\lambda = 0.3$ using the effective potential. This is to be contrasted with the CQC solution for $\lambda = 0.3$, shown as the black curve in Fig. 8.2.

rolling on the effective potential, we have solved the "effective equation of motion",

$$\ddot{\phi} + V'_{\text{eff}}(\phi) = 0 \tag{8.71}$$

where $V_{\text{eff}}(\phi)$ is given in (8.35) and $V(\phi) = -\phi$. Fig. 8.3 shows the rolling solution on the effective potential for $\lambda = 0.3$. It is to be compared to the corresponding curve in Fig. 8.2.

A few features of the dynamics stand out: the field ϕ oscillates in the full dynamics (Fig. 8.2) but at a much smaller frequency than in the effective potential treatment (Fig. 8.3); the amplitude of oscillations in the effective potential stays constant and is much smaller than in the CQC. This is surprising since the physical argument is that ψ particles are produced during rolling and this is what causes differences between the full dynamics and the dynamics on the effective potential. However, increased particle production might be expected to increase $\langle\psi^2\rangle$ and this should cause the ϕ oscillations in the full dynamics to have *smaller* amplitude than in the effective potential. The resolution is that even though there is particle production, $\langle\psi^2\rangle$ actually *decreases* as is evident in Fig. 8.4. This can happen if most of the energy in particle production

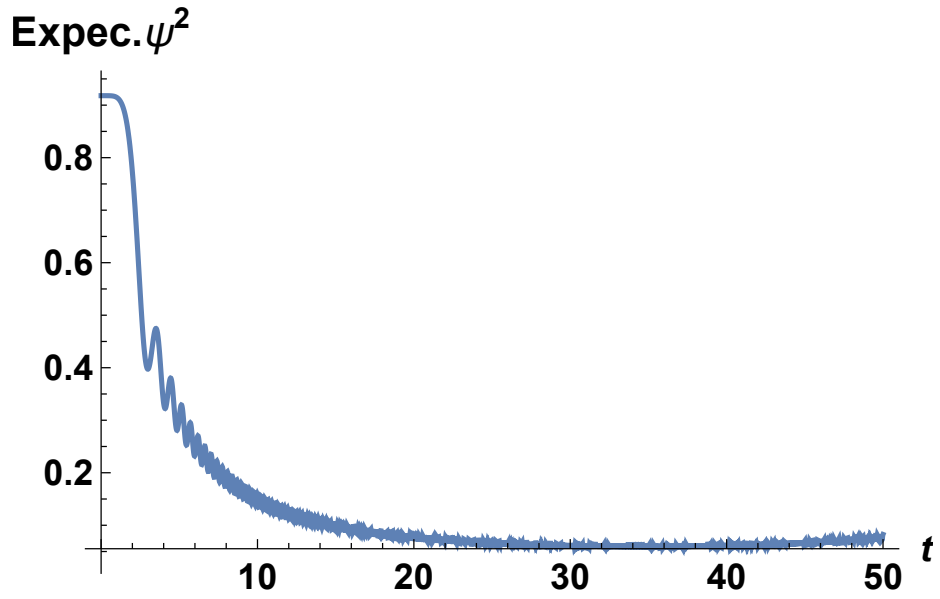

Figure 8.4: Plot of $\langle\psi^2\rangle$ versus time for $\lambda = 0.3$.

goes into the kinetic energy and not in $\langle\psi^2\rangle$. Then with a smaller $\langle\psi^2\rangle$ we do expect the ϕ oscillations to have larger amplitude in the full dynamics.

In the CQC solution, let us denote the first maximum value of ϕ by $\phi_{\rm max}$ and the time at which this value is reached by $t_{\rm max}$. In Fig. 8.5a we show $\phi_{\rm max}$ as a function of λ on a log-log plot. It is clear that the data is not fit by a power law as the fit varies from $\phi_{\rm max} \sim \lambda^{-3.2}$ for smaller λ to $\phi_{\rm max} \sim \lambda^{-1.7}$ at larger λ. Fig. 8.5b shows $t_{\rm max}$ versus λ on a log-log plot. Here too the fit varies from $t_{\rm max} \sim \lambda^{-1.9}$ to $\sim \lambda^{-0.9}$ at larger λ.

Even though we have shown that homogeneous initial conditions lead to homogeneous evolution, there remains the possibility that the evolution is unstable to developing inhomogeneities. We now address this question numerically by including small perturbations to homogeneous initial conditions.

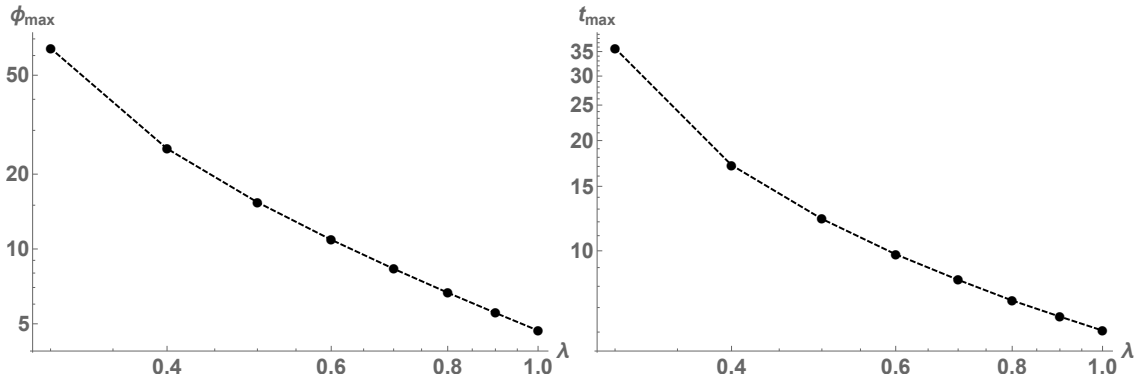

(a) (b)

Figure 8.5: (a) Log-log plot of the value of ϕ at the first turning point versus λ. The fit is not a straight line, ranging from $\phi_{\max} \sim \lambda^{-3.2}$. (b) Log-log plot of the value of t at the first turning point versus λ. The fit is not a straight line, ranging from $t_{\max} \sim \lambda^{-1.9}$ for smaller values of λ and $\sim \lambda^{-0.9}$ for the larger values.

8.3.4 Dynamics With Small Initial Inhomogeneities

To introduce inhomogeneous perturbations, we solve the CQC equations in (8.14), (8.13) but with the initial conditions

$$\phi_n(t=0) = 0, \quad \dot{\phi}_n(t=0) = \epsilon \sin\left(\frac{2\pi n\nu}{N}\right) \tag{8.72}$$

where ϵ is a small amplitude and the integer ν sets the wavenumber of the perturbation. The Z initial conditions are still given by (8.15). The advantage of introducing the inhomogeneities in the time derivative $\dot{\phi}_n$ while keeping ϕ_n homogeneous is that then we can continue to use (8.24) with the formula for O and D given in Sec. 8.2.1.

We now write the field ϕ as

$$\phi = \bar{\phi} + \delta\phi \tag{8.73}$$

where the homogeneous part is

$$\bar{\phi}(t) \equiv \frac{1}{N}\sum_{n=1}^{N} \phi_n \tag{8.74}$$

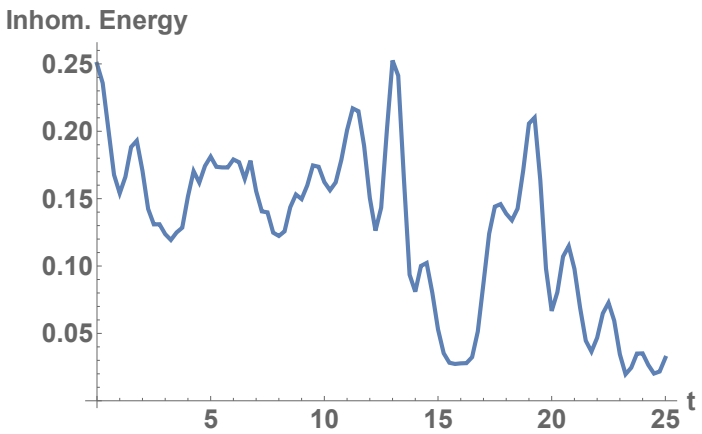

Figure 8.6: Energy in inhomogeneity versus time for $\lambda = 1.0$ $\epsilon = 0.1$ and $\nu = N/10$.

The energy in the inhomogeneous part is

$$E_{\rm inhom} = a \sum_{n=1}^{N} \left[\frac{1}{2} (\delta\dot{\phi}_n)^2 + \frac{1}{2} \left(\frac{\delta\phi_{n+1} - \delta\phi_{n-1}}{2a} \right)^2 \right] \tag{8.75}$$

In Fig. 8.6 we show $E_{\rm inhom}$ versus t for $\lambda = 1.0$, $\epsilon = 0.1$ and $\nu = N/10$. It is clear that the energy in the inhomogeneities decreases with time, though with some fluctuations, and there is no instability in the system. We find similar evolution for other values of ν.

Chapter 9

QUANTUM FORMATION OF TOPOLOGICAL DEFECTS

9.1 Topological Defects

Topological defects are expected to arise during phase transitions in the early universe. These can include domain walls (Saikawa, 2020; Hiramatsu *et al.*, 2013; Vilenkin and Everett, 1982; Sikivie, 1982), cosmic strings (Vilenkin, 1985; Blanco-Pillado *et al.*, 2018; Dufaux *et al.*, 2010; Damour and Vilenkin, 2000; Vachaspati and Vilenkin, 1984, 1985; Hindmarsh and Kibble, 1995; Kibble, 1976), monopoles ('t Hooft, 1974; Nambu, 1974; Gibbons and Manton, 1986; Mavromatos and Mitsou, 2020) and textures (Gueron and Letelier, 1997; Notzold, 1991; Spergel and Turok, 1992; Durrer *et al.*, 1991; Turok, 1989; Brandenberger and Jiao, 2020), depending on the symmetry breaking pattern. While topological defects have not yet been observed in a cosmological context (Ade *et al.*, 2014), they are abundant in condensed matter systems (Zurek, 1985; Pal *et al.*, 2017; del Campo *et al.*, 2010; Chuang *et al.*, 1991; Bowick *et al.*, 1994; Hendry *et al.*, 1994; Ruutu *et al.*, 1996; Bäuerle *et al.*, 1996; Monaco *et al.*, 2002; Carmi *et al.*, 2000; Maniv *et al.*, 2003; Beugnon and Navon, 2017), with intriguing analogies between the two areas of research (Kibble, 2002; Vachaspati, 1998; Zurek, 1996).

Topological defects are also an ideal setting for studying quantum effects in space-time dependent classical backgrounds. Significant effort has already gone into the quantization of topological defects (Rajaraman, 1982; Coleman, 1985; Christ and Lee, 1975; Goldstone and Jackiw, 1975; Cahill, 1974; Dashen *et al.*, 1974a,b,c), in which case the topological defects form space-dependent backgrounds for quantum fields.

Less effort has been invested in time-dependent problems that involve quantum fields in the background of dynamical topological defects (Dashen *et al.*, 1975). Going one step further, the quantum fields will backreact on the dynamics of the topological defects and lead to non-trivial interplay between the quantum and classical degrees of freedom.

The formation of topological defects during a quantum phase transition is a novel process in which the quantum vacuum spontaneously breaks up into classical objects. In a thermal phase transition, the formation of defects is also a transition from a collection of particles above the critical temperature to a collection of a complex of particles (defects) and new excitations at low temperatures. It is no surprise that there has been so much theoretical and experimental (Kibble, 1976, 1980; Zurek, 1985, 1993, 1996; Zurek *et al.*, 2005; Vachaspati, 2010; Kibble, 2007; Chuang *et al.*, 1991; del Campo *et al.*, 2010; Dodd *et al.*, 1998; Bowick *et al.*, 1994; Hendry *et al.*, 1994; Ruutu *et al.*, 1996; Bäuerle *et al.*, 1996; Monaco *et al.*, 2002; Carmi *et al.*, 2000; Maniv *et al.*, 2003; Ducci *et al.*, 1999; Eltsov *et al.*, 1998; Beugnon and Navon, 2017; Monaco *et al.*, 2006b,a) interest in understanding details of defect formation.

The number density of defects formed during a phase transition is sensitive to the rates at which external parameters are changed to pass through the phase transition. The leading theoretical framework for estimating the number density of defects is the "Kibble-Zurek" analysis (Kibble, 1976, 1980; Zurek, 1985, 1993, 1996; Zurek *et al.*, 2005). Numerical simulations have further strengthened the model (Antunes *et al.*, 1999; Hindmarsh and Rajantie, 2000; Yates and Zurek, 1998; Stephens *et al.*, 1999; Laguna and Zurek, 1997; Donaire *et al.*, 2007; Koyama *et al.*, 2006). However predictions of the Kibble-Zurek model have not yet gained universal confirmation, with most experiments in systems involving ^{4}He, liquid crystals, superconductors, superfluids in agreement (Chuang *et al.*, 1991; del Campo *et al.*, 2010; Dodd *et al.*,

1998; Bowick *et al.*, 1994; Hendry *et al.*, 1994; Ruutu *et al.*, 1996; Bäuerle *et al.*, 1996; Monaco *et al.*, 2002; Carmi *et al.*, 2000; Maniv *et al.*, 2003; Ducci *et al.*, 1999; Eltsov *et al.*, 1998; Beugnon and Navon, 2017; Monaco *et al.*, 2006b,a) and others in disagreement (Dodd *et al.*, 1998; Carmi and Polturak, 1999; Maniv *et al.*, 2003) with the predictions. In particular, the appearance of vortices in ^{4}He was claimed in Hendry *et al.* (1994) but was retracted in Dodd *et al.* (1998) since it was found that the vortices in the former case were an externally induced artifact. Overall, the analysis of the phenomenon of defect formation in various systems is an ongoing field of research and has broad implications.

In this chapter we solve for the number density of defects (kinks, vortices and monopoles) formed during a quantum phase transition. The analysis is rigorous and without recourse to approximation but the quantum field theory models we consider are "free", the only interaction being with external parameters that drive the phase transition. These models provide us with zeroth order solvable problems in different dimensions that we fully analyze. Even with these minimal interactions, the analysis is highly non-trivial and in part has to be done numerically. We discuss how other interactions may be included in the analysis using perturbation theory and under what conditions we expect the zeroth order approximation to be accurate.

We are generally interested in Poincaré invariant field-theoretic models in $d+1$ spacetime dimensions, featuring an internal (global) $O(d)$ symmetry which is spontaneously broken during a quantum phase transition. In particular we will be considering d real scalar fields $\Phi_1, \ldots, \Phi_d$ assembled in an $O(d)$-multiplet $\mathbf{\Phi} \equiv (\Phi_1, \ldots, \Phi_d)^T$

whose dynamics are given by the Lagrangian density[1]

$$\mathcal{L}^{(d)} = \frac{1}{2}\partial^{\mu}\mathbf{\Phi}^{T}\partial_{\mu}\mathbf{\Phi} - V_{\beta}\left(\mathbf{\Phi}^{T}\mathbf{\Phi}\right) . \tag{9.1}$$

Here the potential V_β is $O(d)$-invariant and depends on a (possibly time-dependent) external parameter β. We assume that V_β is such that the vacuum manifold is $O(d)$-symmetric for $\beta < 0$ and $O(d-1)$-symmetric for $\beta > 0$. In other words, as the parameter β increases from negative to positive values, the system transitions from a higher symmetry phase to a lower symmetry one, and the average vacuum field configuration starts exhibiting topological defects. These defects then annihilate with one another and eventually disappear. It is precisely this dynamics of formation and annihilation of topological defects that we are concerned with in this paper. In fact, our main purpose will be to determine the number density of topological defects as a function of time and its dependence on the external parameter β, using a combination of analytical and numerical methods.

For concreteness we will take β to be the (time-dependent) mass squared of the field, so that

$$V_{\beta}\left(\mathbf{\Phi}^{T}\mathbf{\Phi}\right) = \frac{1}{2}m_2(t)\mathbf{\Phi}^{T}\mathbf{\Phi} + \frac{\lambda}{4}\left(\mathbf{\Phi}^{T}\mathbf{\Phi}\right)^{2} , \tag{9.2}$$

where

$$m_2(t) = -m^2 \tanh\left(\frac{t}{\tau}\right) , \tag{9.3}$$

and λ, m, τ are positive parameters. In particular, the quench parameter τ is a time scale quantifying the rate of change of the potential during the phase transition. It is clear that for $t \ll -\tau$, the vacuum manifold reduces to the null field configuration $\Phi = 0$ and is therefore $O(d)$-symmetric, while for $t \gg \tau$ it includes all field configurations

[1] In this paper we use a mostly plus signature for the Minkowski metric and natural units, $\hbar = c = 1$.

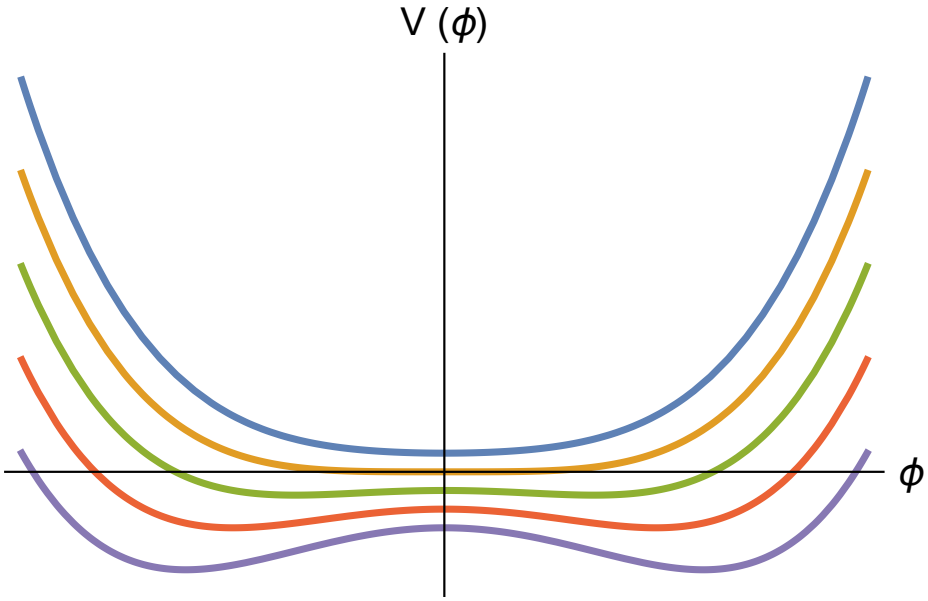

Figure 9.1: Snapshots of the $d = 1$ potential at a few different times. The plots have been shifted vertically for clarity.

on the $O(d-1)$-symmetric hypersphere given by

$$\lambda \mathbf{\Phi}^T \mathbf{\Phi} = m^2 \,. \tag{9.4}$$

In Fig. 9.1 we sketch the potential (9.2) at a few different times.

It is well known that these models have topological defects – kinks ($d = 1$) in one spatial dimension, vortices ($d = 2$) in two spatial dimensions, and monopoles ($d = 3$) in three spatial dimensions (Vilenkin and Shellard, 2000). In each of these cases the vacuum manifold described by (9.4) has non-trivial topology: for $d = 1$ it is 2 points, for $d = 2$ it is a circle, and for $d = 3$ it is a two-sphere. The defect locations are described by zeros of $\mathbf{\Phi}$ even in the symmetry broken phase. The zeros are trapped due to the non-trivial topology of the vacuum manifold. We realize that the topology persists even if we set $\lambda = 0$ and the problem of defect formation simplifies. Then the $\lambda = 0$ problem can be thought of as the zeroth order problem. We discuss the $\lambda \neq 0$ problem for $d = 1$ in greater detail in Sec. 9.5 where we find that λ dependent corrections are small if $\lambda\tau/m \ll 1$.

The overall strategy will be to regulate both the IR and UV behaviors of the field theory by working in a finite box of size L^d (with periodic boundary conditions) and discretize space on a N^d point lattice (with lattice spacing $a = L/N$). Then we can determine an exact expression for the field probability density functional as a function of a finite number of quantities that can be computed numerically. We then find the average expectation value of a judiciously constructed quantum operator that counts the number density of zeros of the field multiplet $\mathbf{\Phi}$ in the limit of the finite resolution imposed by the lattice. We finally take both the continuum limit $N \to \infty$, $a \to 0$, and the infinite volume limit, $L \to \infty$ (in this exact order), to recover the full field theory result. Up to spurious zeros due to vacuum fluctuations that can consistently be discarded, this accurately gives the number density of topological defects. The case of a sudden phase transition ($\tau = 0$) can be treated analytically but the general case will be treated numerically.

It should be mentioned that the so-called *spinodal decomposition* – where one phase evolves into domains of other phases in the absence of phase barriers – during quantum phase transitions has been the subject of extensive work in the literature (Calzetta, 1989; Liu and Mazenko, 1991, 1992b,a; Halperin, 1980; Boyanovsky, 1993; Boyanovsky *et al.*, 2000; Rivers, 1995). These studies were in the context of the Ginzburg-Landau model and in a more general field theoretic context but were limited to instantaneous quenches (Ibaceta and Calzetta, 1999; Liu and Mazenko, 1991, 1992b,a; Rivers, 1995). Our purely quantum approach applies to non-instantaneous quenches and is readily generalizable to the case of d-dimensional global topological defects. The present work aims to describe it in an elementary and self-contained manner. We find, for different quench time-scales τ, the behavior of the average defect number density. We observe that defects start being produced immediately after the phase transition and their number density reaches a maximum within a short time, after which they start

annihilating with each other and their number density goes down. The efficiency of topological defect production is found to depend on the details of the phase transition. Indeed the defect number density increases faster and to higher maximum values as τ decreases and the phase transition becomes more sudden. On the contrary, the late-time mutual annihilation of topological defects exhibits universal characteristics. After a transient regime, the number density of defects decays as a power law $t^{-d/2}$ with a coefficient that only depends on the spatial dimension d and not on τ. Hence the $\tau = 0$ result is an attractor for the dynamics of defect formation and subsequent decay for a large class of quantum phase transitions. Our comprehensive analysis thus provides a unifying picture of defect formation and decay during *non-instantaneous quenches* and fills a gap in the literature. We are however limited to the regime where the $\lambda = 0$ approximation holds and we discuss this limitation in some detail in Sec. 9.5.

The chapter is structured as follows. In Sections 9.2 and 9.3 we fully describe the average dynamics of kink ($d = 1$) and vortex ($d = 2$) condensation respectively. In Section 9.4 we extend these results to 3 and higher dimensions. In Sec. 9.5 we discuss how the previous results constitute only the zeroth order approximation in a perturbative expansion in λ and estimate the next-order corrections.

9.2 One Dimension: Kinks

One of the challenges in finding the number density of kinks is to first define a kink in the quantum field theory given by (9.1) with $d = 1$, where we denote the single-component scalar field $\mathbf{\Phi}$ by ϕ. This can be done using the Mandelstam "kink operator" (Mandelstam, 1975), which is a two-component *fermionic* operator, $\hat{\chi}$. A

key property of $\hat{\chi}$ is that it satisfies the equal time commutation relations,

$$\left[\hat{\phi}(t,y),\hat{\chi}(t,x)\right] = \begin{cases} \eta\,\hat{\chi}(t,x), & y<x\,, \\ 0, & y>x\,, \end{cases} \tag{9.5}$$

where η is a real number. If $|s\rangle$ is an eigenstate of $\hat{\phi}(t,y)$ such that $\hat{\phi}|s\rangle = 0$ (for all y), then we find that the state $|s'\rangle \equiv \hat{\chi}(t,x)|s\rangle$ satisfies

$$\hat{\phi}(t,y)|s'\rangle = \begin{cases} \eta\,|s'\rangle, & y<x \\ 0, & y>x \end{cases} \tag{9.6}$$

Hence the operator $\hat{\chi}$ has created a step in the value of ϕ at x by an amount η. If $\phi = 0$ and $\phi = \eta$ are two possible vacuum expectation values of ϕ, $\hat{\chi}$ would have created a kink that interpolates between two vacua. The number density of χ quanta would then correspond to the number density of kinks.

Unfortunately the relation between χ and ϕ is quite complicated – χ involves exponentials of ϕ and $\dot{\phi}$ and other quantum field theory subtleties – and we do not have a clear way to utilize the Mandelstam operator. Instead we find it useful to work entirely with the ϕ field, simply defining the kink to be a jump in the value of ϕ as further discussed in Sec. 9.2.2. Our definition of the kink operator is also helpful in the case of vortices and monopoles for $d = 2, 3$ as these objects correspond to intersections of domain walls *i.e.* kinks extended to higher dimensions.

9.2.1 Setup And Quantization

We start by treating the $d = 1$ case in detail. The relevant Lagrangian density for the real scalar field ϕ is thus

$$\mathcal{L}^{(1)} = \frac{1}{2}(\partial_\mu\phi)^2 - \frac{1}{2}m_2(t)\phi^2 - \frac{\lambda}{4}\phi^4\,. \tag{9.7}$$

Clearly, for $t < 0$ the model has a unique vacuum $\phi = 0$ while for $t > 0$ it has two degenerate vacua at $\phi = \pm m/\sqrt{\lambda}$ corresponding to the two minima of the double-well potential. It is well-known that in the $t \gg \tau$ limit (where $m_2(t) \approx -m^2$), there exist static classical kink and anti-kink solutions given by

$$\phi_{\pm}(x) = \pm \frac{m}{\sqrt{\lambda}} \tanh\left(\frac{mx}{\sqrt{2}}\right) . \tag{9.8}$$

These solutions are non-perturbative and topologically non-trivial: they interpolate between the two vacua over a spatial scale $\sim 1/m$. Of course, Poincaré invariance allows the construction of displaced or even "dynamical" kinks from the above solutions but, whatever the frame, they will always be characterized by their topological charge

$$q = \int_{-\infty}^{\infty} dx\, \partial_x \phi = \phi(\infty) - \phi(-\infty) . \tag{9.9}$$

In fact, a kink always has positive topological charge since the field undergoes a negative to positive sign change, while an anti-kink has the exact opposite property.

Multi-kink and anti-kink solutions can be constructed as well, but these will not be static anymore since the kinks and anti-kinks will attract each other and they will eventually annihilate. If separations are large and the different kinks and anti-kinks are initially at rest, such configurations will however be approximately static. Even though the topological charge of such field configurations does not inform us about the number of kinks or anti-kinks involved (since the topological charge is a binary valued quantity), one can however in principle recognize the presence of individual kinks and anti-kinks in a given field configuration by focusing on the points where the field changes sign: a negative-to-positive sign change will be identified as a kink while a positive-to-negative one will be identified as an anti-kink. Of course this is only part of the picture because not every sign change should be counted as a kink or anti-kink especially if it occurs on time and distance scales shorter than the characteristic width

of $1/m$. We will discuss this subtlety in Sec. 9.2.2.

We are interested in the production of kinks during a quantum phase transition and in particular in how their average number density scales with time. As we have discussed in Sec. 9.1, we will first be analyzing the $\lambda = 0$ case and the Lagrangian density we will work with will thus be

$$\mathcal{L}^{(1)} = \frac{1}{2}(\partial_\mu \phi)^2 - \frac{1}{2} m_2(t) \phi^2 \,. \tag{9.10}$$

We now need to quantize this model. We start by assuming that the volume (or length since $d = 1$) of space is finite of size L and that the field obeys periodic boundary conditions. (We can alternatively think of space as a circle of length L.) We then discretize space on a lattice consisting of N points separated by a distance $a = L/N$. At each lattice point $x_j \equiv ja$, we define the discretized field $\phi_j \equiv \phi(x_j)$ and the full Lagrangian of the discretized theory reads

$$L^{(1)}_{\text{disc.}} = \frac{a}{2} \dot{\boldsymbol{\phi}}^T \dot{\boldsymbol{\phi}} - \frac{a}{2} \boldsymbol{\phi}^T \Omega_2(t) \boldsymbol{\phi} \,, \tag{9.11}$$

where we have assembled the discretized fields in a column vector $\boldsymbol{\phi} \equiv (\phi_1, \ldots, \phi_N)^T$ and the matrix Ω_2 is defined by

$$[\Omega_2]_{jl} = \begin{cases} +2/a^2 + m_2(t) \,, & j = l \\ -1/a^2 \,, & j = l \pm 1 \pmod N \\ 0 \,, & \text{otherwise} \,. \end{cases} \tag{9.12}$$

Introducing the canonically conjugate momentum fields, $\pi_j \equiv a\dot{\phi}_j$, and assembling them in a column vector $\boldsymbol{\pi} \equiv (\pi_1, \ldots, \pi_N)^T$, we can promote both the ϕ_js and π_js to operators satisfying canonical commutation relations $[\hat{\phi}_j, \hat{\pi}_l] = i\delta_{jl}$. The quantum Hamiltonian of the discretized theory (Vachaspati and Zahariade, 2018b) then reads

$$\hat{H}^{(1)}_{\text{disc.}} = \frac{1}{2a} \hat{\boldsymbol{\pi}}^T \hat{\boldsymbol{\pi}} + \frac{a}{2} \hat{\boldsymbol{\phi}}^T \Omega_2(t) \hat{\boldsymbol{\phi}} \,, \tag{9.13}$$

where hats denote operator valued quantities. It is apparent from (9.13) that the discretized theory describes the quantum dynamics of a set of N quadratically coupled, simple harmonic oscillators.

We are interested in how the (unique) quantum vacuum before the phase transition (at a time $t_0 \ll -\tau$ when the potential is upright and $m_2(t_0) \approx m^2$) is destabilized by the quench and evolves into a more complicated state featuring dynamical kinks and anti-kinks. To understand the dynamics of this process we need to solve the functional Schrödinger equation associated with (9.13),

$$i\frac{\partial \Psi}{\partial t} = -\frac{1}{2a}\Delta\Psi + \frac{a}{2}\boldsymbol{\phi}^T\Omega_2(t)\boldsymbol{\phi}\ \Psi\,, \tag{9.14}$$

where the wave functional $\Psi[\phi_1, \ldots, \phi_N; t]$ is such that $|\Psi|^2$ gives the probability density of a given field configuration at time t, and the Laplacian operator is defined by

$$\Delta \equiv \frac{\partial^2}{\partial\phi_1^2} + \cdots + \frac{\partial^2}{\partial\phi_N^2}\,. \tag{9.15}$$

One can easily check that the wave functional for the vacuum state at $t = t_0$ is

$$\Psi(t_0) = \mathcal{N}\exp\left[-\frac{a}{2}\boldsymbol{\phi}^T\Omega_2(t_0)^{1/2}\,\boldsymbol{\phi}\right], \tag{9.16}$$

where

$$\mathcal{N} = \left(\frac{a}{\pi}\right)^{N/4}\det\left(\Omega_2(t_0)\right)^{1/8}\,, \tag{9.17}$$

and fractional powers of the positive-definite matrix $\Omega_2(t_0)$ are unambiguously defined in the standard way. For instance $\Omega_2^{1/2} = O\,\mathrm{Diag}\left(\lambda_1^{1/2}, \ldots, \lambda_N^{1/2}\right)O^T$, where O is the orthogonal matrix diagonalizing Ω_2, and λ_j are the (positive) eigenvalues of Ω_2. Given this initial condition, the solution for the wave functional at time t will be given by

$$\Psi(t) = \mathcal{N}\exp\left[-\frac{1}{2}\int_{t_0}^{t} dt'\mathrm{Tr}\,M(t') + \frac{ia}{2}\boldsymbol{\phi}^T M(t)\,\boldsymbol{\phi}\right], \tag{9.18}$$

where the $N \times N$ complex symmetric matrix $M(t)$ verifies

$$\dot{M} + M^2 + \Omega_2(t) = 0\,, \tag{9.19}$$

and $M(t_0) = i\Omega_2(t_0)^{1/2}$. Introducing the complex $N \times N$ matrix $Z(t)$ defined by

$$\ddot{Z} + \Omega_2(t) Z = 0\,, \tag{9.20}$$

and

$$Z(t_0) = -\frac{i}{\sqrt{2a}}\Omega_2(t_0)^{-1/4}\,, \tag{9.21}$$

$$\dot{Z}(t_0) = \frac{1}{\sqrt{2a}}\Omega_2(t_0)^{1/4}\,, \tag{9.22}$$

we can write

$$M = \dot{Z} Z^{-1}\,. \tag{9.23}$$

Indeed, using (9.20), (9.21) and (9.22), it is easy to check that this expression yields a symmetric matrix since $\dot{Z}Z^{-1} - (\dot{Z}Z^{-1})^T$ is a conserved quantity which vanishes at time t_0. We can now write the probability density functional as

$$|\Psi(t)|^2 = |\mathcal{N}|^2 \exp\left[-\frac{1}{2}\int_{t_0}^{t} dt' \mathrm{Tr}\left(M(t') + M(t')^\dagger\right) + \frac{ia}{2}\boldsymbol{\phi}^T\left(M(t) - M(t)^\dagger\right)\boldsymbol{\phi}\right]. \tag{9.24}$$

To simplify this expression we first use the fact that

$$\int_{t_0}^{t} dt' \mathrm{Tr}\left(M(t') + M(t')^\dagger\right) = \mathrm{Tr}\left(\log K\right)\Big|_{t_0}^{t}\,, \tag{9.25}$$

where $K \equiv ZZ^\dagger$ is a real positive definite symmetric matrix; indeed, using (9.20), (9.21) and (9.22), it is easy to check that $ZZ^\dagger - Z^* Z^T$ is a conserved quantity which vanishes at time t_0. Next, we make use of another conserved quantity

$$Z^\dagger \dot{Z} - \dot{Z}^\dagger Z = i/a\,, \tag{9.26}$$

which can also be verified via (9.20), (9.21) and (9.22), to show that

$$M(t) - M(t)^\dagger = iK^{-1}/a\,. \tag{9.27}$$

Finally, plugging (9.25) and (9.27) into (9.24) yields a simplified (and manifestly normalized) expression for the probability density functional

$$|\Psi(t)|^2 = \frac{1}{\sqrt{\det(2\pi K)}} e^{-\boldsymbol{\phi}^T K^{-1} \boldsymbol{\phi}/2} \,. \tag{9.28}$$

This expression (along with (9.20), (9.21) and (9.22)) contains all the information that we will need in order to determine the average number density of kinks in the lattice. Note that K is a time-dependent matrix, whose time-dependence is given by that of the matrix Z.

Before going any further, we mention a separate interpretation of the matrix Z. Working in Heisenberg picture with respect to time t_0, we can define creation and annihilation operators at time t_0 by

$$\hat{\boldsymbol{a}}(t_0) \equiv \frac{1}{\sqrt{2a}} \left(\Omega_2^{-1/4} \hat{\boldsymbol{\pi}}(t_0) - ia\Omega_2^{1/4} \hat{\boldsymbol{\phi}}(t_0) \right) , \tag{9.29}$$

$$\hat{\boldsymbol{a}}^\dagger(t_0) \equiv \frac{1}{\sqrt{2a}} \left(\Omega_2^{-1/4} \hat{\boldsymbol{\pi}}(t_0) + ia\Omega_2^{1/4} \hat{\boldsymbol{\phi}}(t_0) \right) . \tag{9.30}$$

Notice that we have used column vector notation here but that the dagger refers to the adjoint operation on the Hilbert space only: it does not turn column vectors into row vectors. Then we can expand the Heisenberg picture discretized field operators at time t as follows

$$\hat{\boldsymbol{\phi}}(t) = Z(t)^* \hat{\boldsymbol{a}}(t_0) + Z(t) \hat{\boldsymbol{a}}^\dagger(t_0) \,. \tag{9.31}$$

Eqs. (9.20), (9.21) and (9.22) ensure that the Heisenberg equations as well as the proper initial conditions at t_0 are verified. Now it is easy to see that the matrix K is simply the covariance matrix of the discretized field since, using (9.31),

$$\langle 0 | \hat{\phi}_j \hat{\phi}_l | 0 \rangle = \sum_{k=1}^{N} Z_{jk}^* Z_{lk} = K_{lj} \,. \tag{9.32}$$

Here the Heisenberg picture vacuum $|0\rangle$ is time-independent and defined by the wave functional (9.16).

In principle we now have all the ingredients needed to discuss the quantum production of kinks during the phase transition. Indeed equation (9.28) along with the N^2 complex linear ordinary differential equations (9.20) fully determine the quantum dynamics of the field configuration. However, it turns out that not all components of the matrix Z are relevant and we can reduce the number of differential equations that need to be solved. It can be shown that the matrix Z is *circulant* (Mukhopadhyay and Vachaspati, 2019) i.e., its matrix elements Z_{jl} only depend on $j - l \pmod N$. We can therefore diagonalize it via the discrete Fourier transform:

$$Z_{jl} = \frac{1}{\sqrt{N}} \sum_{n=1}^{N} c_n(t) e^{-i(j-l)2\pi n/N} \,. \tag{9.33}$$

This allows us to recast (9.20), (9.21) and (9.22) in terms of the complex mode functions $c_n(t)$ thus obtaining

$$\ddot{c}_n + \left[\frac{4}{a^2}\sin^2\left(\frac{\pi n}{N}\right) + m_2(t)\right] c_n = 0 \,, \tag{9.34}$$

and

$$c_n(t_0) = \frac{-i}{\sqrt{2L}} \left[\frac{4}{a^2}\sin^2\left(\frac{\pi n}{N}\right) + m_2(t_0)\right]^{-1/4} , \tag{9.35}$$

$$\dot{c}_n(t_0) = \frac{1}{\sqrt{2L}} \left[\frac{4}{a^2}\sin^2\left(\frac{\pi n}{N}\right) + m_2(t_0)\right]^{1/4} . \tag{9.36}$$

Rewriting the dynamical equations in terms of mode coefficients provides an enormous computational gain: we now only have to solve N equations instead of N^2. Additionally, as we will shortly see, mode coefficients are particularly well suited to discussing problems related to the $N \to \infty$ limit and divergences related to vacuum fluctuations of the quantum field. We can achieve further simplification by writing the mode functions in trigonometric form

$$c_n \equiv \rho_n e^{i\theta_n} \,, \tag{9.37}$$

where ρ_n and θ_n are respectively the modulus and argument of the complex number c_n, and making use of the conserved quantity (9.26), which in this representation takes the form of a conserved angular momentum,

$$\rho_n^2 \dot{\theta}_n = 1/2L\,. \tag{9.38}$$

Then (9.34) reduces to a set of N real (but non-linear) ordinary differential equations,

$$\ddot{\rho}_n + \left[\frac{4}{a^2}\sin^2\left(\frac{\pi n}{N}\right) + m_2(t)\right]\rho_n = \frac{1}{4L^2\rho_n^3}\,, \tag{9.39}$$

with initial conditions

$$\rho_n(t_0) = \frac{1}{\sqrt{2L}}\left[\frac{4}{a^2}\sin^2\left(\frac{\pi n}{N}\right) + m_2(t_0)\right]^{-1/4}\,, \tag{9.40}$$

$$\dot{\rho}_n(t_0) = 0\,. \tag{9.41}$$

Even though working in terms of modes is computationally advantageous, kinks are configurations (field zeros) in physical space. Thus we have to straddle the two descriptions as in the following Sec. 9.2.2.

9.2.2 Average Kink Number Density

We are now in a position to tackle the problem of kink production during the phase transition. As mentioned earlier, since kinks and anti-kinks occur at zeros of the field configuration we first introduce a quantum operator $\hat{n}_Z$ that gives the number density of zeros in a given field configuration:

$$\hat{n}_Z = n_Z\left(\hat{\boldsymbol{\phi}}\right) \equiv \frac{1}{L}\sum_{j=1}^{N}\frac{1}{4}\left[\mathrm{sgn}\left(\hat{\phi}_j\right) - \mathrm{sgn}\left(\hat{\phi}_{j+1}\right)\right]^2 = \frac{N}{2L} - \frac{1}{2L}\sum_{j=1}^{N}\mathrm{sgn}\left(\hat{\phi}_j\hat{\phi}_{j+1}\right)\,. \tag{9.42}$$

More precisely, such an operator is sensitive to the number of sign changes that occur between adjacent points on the lattice. We should stress that this is only accurate up to the finite resolution given by the lattice spacing a. It may in fact

undercount the number of zeros of the actual continuous field configuration (if there are multiple sign changes within a lattice spacing). We expect however that, as N becomes large enough, this operator will become more and more accurate. This assumption is reasonable as long as we can find a way to disregard high frequency noise-like fluctuations due to the quantum vacuum thus only counting "true" kinks and anti-kinks.

We now calculate the vacuum expectation value of this operator or, in Heisenberg picture

$$\langle \hat{n}_Z \rangle \equiv \langle 0 | \hat{n}_Z(t) | 0 \rangle \,. \tag{9.43}$$

Given that we know the probability density functional explicitly for the Schrödinger picture time-dependent state we can write

$$\langle \hat{n}_Z \rangle = \frac{1}{\sqrt{\det(2\pi K)}} \int d^N \boldsymbol{\phi} \; n_Z(\boldsymbol{\phi}) e^{-\boldsymbol{\phi}^T K^{-1} \boldsymbol{\phi}/2} = \frac{N}{2L} - \frac{1}{2L} \sum_{j=1}^{N} \left\langle \mathrm{sgn}\left(\hat{\phi}_j \hat{\phi}_{j+1}\right) \right\rangle \,, \tag{9.44}$$

where

$$\left\langle \mathrm{sgn}\left(\hat{\phi}_j \hat{\phi}_{j+1}\right) \right\rangle \equiv \frac{1}{\sqrt{\det(2\pi K)}} \times \int d^N \boldsymbol{\phi} \; \mathrm{sgn}\left(\phi_j \phi_{j+1}\right) e^{-\boldsymbol{\phi}^T K^{-1} \boldsymbol{\phi}/2} \,. \tag{9.45}$$

Introducing the permutation (shift) matrix

$$P = \begin{pmatrix} 0 & 1 & 0 & \cdots & \cdots & 0 \\ \vdots & \ddots & \ddots & \ddots & & \vdots \\ \vdots & & \ddots & \ddots & \ddots & 0 \\ \vdots & & & \ddots & \ddots & 1 \\ 0 & 0 & & & \ddots & 0 \\ 1 & 0 & \cdots & \cdots & 0 & 0 \end{pmatrix} \,, \tag{9.46}$$

and performing the change of variables $\boldsymbol{\phi} \to P^{1-j} \boldsymbol{\phi}$, we can rewrite (9.45) as

$$\left\langle \mathrm{sgn}\left(\hat{\phi}_j \hat{\phi}_{j+1}\right) \right\rangle = \frac{1}{\sqrt{\det(2\pi K)}} \times \int d^N \boldsymbol{\phi} \; \mathrm{sgn}\left(\phi_1 \phi_2\right) e^{-\boldsymbol{\phi}^T P^{j-1} K^{-1} P^{1-j} \boldsymbol{\phi}/2} \,. \tag{9.47}$$

As mentioned earlier, Z is a circulant matrix and, consequently, it has to be polynomial in P. Therefore, the matrix $K = ZZ^\dagger$ is also circulant and K^{-1} is seen to commute with P. This implies that,

$$\left\langle \mathrm{sgn}\left(\hat{\phi}_j\hat{\phi}_{j+1}\right)\right\rangle = \left\langle \mathrm{sgn}\left(\hat{\phi}_1\hat{\phi}_2\right)\right\rangle = \frac{1}{\sqrt{\det(2\pi K)}}\int d^N\boldsymbol{\phi}\ \mathrm{sgn}\left(\phi_1\phi_2\right) e^{-\boldsymbol{\phi}^T K^{-1}\boldsymbol{\phi}/2}\,, \tag{9.48}$$

and the average number density of zeros simply reduces to

$$\langle \hat{n}_Z\rangle = \frac{N}{2L}\left[1 - \left\langle \mathrm{sgn}\left(\hat{\phi}_1\hat{\phi}_2\right)\right\rangle\right]\,. \tag{9.49}$$

Let it be mentioned here that the circulant property of the covariance matrix K is the mathematical counterpart of the fact that the system has translational invariance (which is maintained at a discretized level by our choice of periodic boundary conditions). In other words, it is a consequence of the fact that two-point correlation functions $\langle\phi(x)\phi(y)\rangle$ only depend on the relative position $|x-y|$.

We now need to evaluate (9.48) more explicitly. We start by writing

$$\left\langle \mathrm{sgn}\left(\hat{\phi}_1\hat{\phi}_2\right)\right\rangle = \frac{1}{\sqrt{\det(2\pi K)}}\times\sum_{Q=I}^{IV}\int_Q d\phi_1 d\phi_2\ \mathrm{sgn}(\phi_1\phi_2)\int d\phi_3\ldots d\phi_N\, e^{-\boldsymbol{\phi}^T K^{-1}\boldsymbol{\phi}/2}\,, \tag{9.50}$$

where the sum runs over the four quadrants in the (ϕ_1,ϕ_2) plane (denoted by Roman numerals). We then decompose K^{-1} into suitably sized blocks,

$$K^{-1} = (ZZ^\dagger)^{-1} = \begin{pmatrix} A & B \\ B^T & C\end{pmatrix}, \tag{9.51}$$

where A and C are real symmetric matrices of respective sizes 2×2 and $(N-2)\times(N-2)$, while B is a $2\times(N-2)$ real matrix, and introduce the notations $\boldsymbol{\chi} = (\phi_1,\phi_2)^T$, $\boldsymbol{\xi} = (\phi_3,\ldots,\phi_N)^T$. We also assume that C is invertible, which will be true generically. This allows us to rewrite the bilinear in the exponent in (9.50) as

$$\boldsymbol{\phi}^T K^{-1}\boldsymbol{\phi} = (\boldsymbol{\xi} + C^{-1}B^T\boldsymbol{\chi})^T C(\boldsymbol{\xi} + C^{-1}B^T\boldsymbol{\chi}) + \boldsymbol{\chi}^T(A - BC^{-1}B^T)\boldsymbol{\chi}\,. \tag{9.52}$$

Using

$$\int d^{N-2}\boldsymbol{\xi}\; e^{-(\boldsymbol{\xi}+C^{-1}B^T\boldsymbol{\chi})^T C(\boldsymbol{\xi}+C^{-1}B^T\boldsymbol{\chi})/2} = \frac{(2\pi)^{(N-2)/2}}{\sqrt{\det(C)}}\,, \tag{9.53}$$

we can perform the Gaussian integral over $\phi_3, \ldots, \phi_N$ and obtain

$$\begin{aligned}\left\langle \mathrm{sgn}\left(\hat{\phi}_1\hat{\phi}_2\right)\right\rangle &= \frac{1}{2\pi\sqrt{\det(K)\det(C)}} \times \\ &\sum_{Q=I}^{IV}\int_Q d\phi_1 d\phi_2\; \mathrm{sgn}(\phi_1\phi_2)\; \exp\left[-\frac{1}{2}(\phi_1,\phi_2)A'\begin{pmatrix}\phi_1\\ \phi_2\end{pmatrix}\right],\end{aligned} \tag{9.54}$$

where

$$A' \equiv A - BC^{-1}B^T \tag{9.55}$$

is the so-called *Schur complement* of C. The left-over two-dimensional quadrant integrals

$$I_Q \equiv \int_Q d\phi_1 d\phi_2\; \mathrm{sgn}(\phi_1\phi_2)\; \exp\left[-\frac{1}{2}(\phi_1,\phi_2)A'\begin{pmatrix}\phi_1\\ \phi_2\end{pmatrix}\right], \tag{9.56}$$

can also be carried out. For the first quadrant, for example, $\mathrm{sgn}(\phi_1\phi_2) = +1$ and we can write

$$\begin{aligned} I_I &= \int_0^\infty\int_0^\infty d\phi_1 d\phi_2 \times \quad \exp\left[-\frac{1}{2}\left(A'_{11}\phi_1^2 + 2A'_{12}\phi_1\phi_2 + A'_{22}\phi_2^2\right)\right] \\ &= \int_0^\infty ds \int_0^\infty \phi_2\, d\phi_2 \times \quad \exp\left[-\frac{1}{2}\left(A'_{11}s^2 + 2A'_{12}s + A'_{22}\right)\phi_2^2\right] \\ &= \int_0^\infty ds \frac{1}{A'_{11}s^2 + 2A'_{12}s + A'_{22}} = \frac{1}{\sqrt{A'_{11}A'_{22} - A'_{12}}}\left[\frac{\pi}{2} - \tan^{-1}\left(\frac{A'_{12}}{\sqrt{A'_{11}A'_{22} - A'_{12}}}\right)\right] \\ &= \frac{1}{\sqrt{\det(A')}}\left[\frac{\pi}{2} - \tan^{-1}\left(\frac{A'_{12}}{\sqrt{\det(A')}}\right)\right], \end{aligned} \tag{9.57}$$

where in going from the first to the second line we used the change of variables $\phi_1 \to s\phi_2$.

The integrals over the remaining three quadrants are readily obtained from I_I as follows. To begin with, the change of variables $\phi_1 \to -\phi_1$ and $\phi_2 \to -\phi_2$ makes it

clear that $I_{III} = I_I$, and $I_{II} = I_{IV}$. Furthermore, notice that the change of variables $\phi_1 \to -\phi_1$ (leaving ϕ_2 unchanged) on I_{II} has the same effect (up to an overall sign) as changing A'_{12} into $-A'_{12}$ in (9.57). We thus obtain

$$I_{II} = -\frac{1}{\sqrt{\det(A')}}\left[\frac{\pi}{2} + \tan^{-1}\left(\frac{A'_{12}}{\sqrt{\det(A')}}\right)\right], \tag{9.58}$$

and all the four integrals I_Q appearing in (9.54) are accounted for. We can achieve further simplification by taking advantage of the properties of the matrix A'. In particular since

$$K^{-1} = \begin{pmatrix} I & BC^{-1} \\ 0 & I \end{pmatrix}\begin{pmatrix} A' & 0 \\ 0 & C \end{pmatrix}\begin{pmatrix} I & 0 \\ C^{-1}B^T & I \end{pmatrix}, \tag{9.59}$$

we have

$$\det\left(K^{-1}\right) = \frac{1}{\det\left(K\right)} = \det\left(A'\right)\det\left(C\right) \tag{9.60}$$

and (9.54) collapses to

$$\left\langle \mathrm{sgn}\left(\hat{\phi}_1\hat{\phi}_2\right)\right\rangle = -\frac{2}{\pi}\tan^{-1}\left(\frac{A'_{12}}{\sqrt{\det(A')}}\right). \tag{9.61}$$

But we can go even further. Indeed inverting (9.59),

$$K = \begin{pmatrix} I & 0 \\ -C^{-1}B^T & I \end{pmatrix}\begin{pmatrix} A'^{-1} & 0 \\ 0 & C^{-1} \end{pmatrix}\begin{pmatrix} I & -BC^{-1} \\ 0 & I \end{pmatrix}, \tag{9.62}$$

shows that A'^{-1} coincides with the upper-left 2×2 block of the matrix K. More explicitly we can write,

$$A'^{-1} = \begin{pmatrix} \alpha & \beta \\ \beta & \alpha \end{pmatrix} \tag{9.63}$$

where, using (9.33) and the reality of K,

$$\alpha \equiv K_{11} = \sum_{n=1}^{N} |c_n|^2, \tag{9.64}$$

$$\beta \equiv K_{12} = \sum_{n=1}^{N} |c_n|^2 \cos(2\pi n/N). \tag{9.65}$$

Thus

$$A' = \frac{1}{\alpha^2 - \beta^2} \begin{pmatrix} \alpha & -\beta \\ -\beta & \alpha \end{pmatrix} \tag{9.66}$$

and (9.61) becomes

$$\left\langle \mathrm{sgn}\left(\hat{\phi}_1 \hat{\phi}_2\right) \right\rangle = \frac{2}{\pi} \tan^{-1}\left(\frac{\beta}{\sqrt{\alpha^2 - \beta^2}}\right) = \frac{2}{\pi} \sin^{-1}\left(\frac{\beta}{\alpha}\right) . \tag{9.67}$$

Finally we obtain the average number density of zeros

$$\langle \hat{n}_Z \rangle = \frac{N}{2L}\left[1 - \frac{2}{\pi} \sin^{-1}\left(\frac{\beta}{\alpha}\right)\right] . \tag{9.68}$$

Recall however that we are interested in the average number density of kinks which may differ from the number density of zeros as given in (9.68) because the latter includes zeros due to vacuum fluctuations of the quantum field. The difference between the two quantities is most clear long before the phase transition, where the field is in its unique vacuum and its expectation value vanishes everywhere on the lattice. However the field fluctuates about zero and there is a non-zero average number density of zeros. This is to be contrasted with the average number density of kinks which should be exactly zero before the phase transition. Moreover the average number density of zeros is expected to be highly sensitive to the number of lattice points N since the finer the resolution, the more zeros can be identified. This is again different for the average number density of kinks which are supposed to be extended objects whose separation is set by the correlation length of the field fluctuations. We therefore need a systematic procedure to eliminate the spurious zeros from the result in (9.68). One way is to restrict the sums in (9.64), (9.65) to those modes $c_n(t)$ that are *not* oscillating (Karra and Rivers, 1997), in other words to indices n verifying

$$\omega_2^{(n)}(t) \equiv \frac{4}{a^2} \sin^2\left(\frac{\pi n}{N}\right) + m_2(t) \leq 0 . \tag{9.69}$$

It is indeed the presence of such unstable modes that allows for the production of the non-perturbative kink and anti-kink solutions. Then the formula for the average

number density of kinks, n_K, is obtained by restricting the modes that enter (9.68), giving us

$$n_K = \frac{N}{2L}\left[1 - \frac{2}{\pi}\sin^{-1}\left(\frac{\bar{\beta}}{\bar{\alpha}}\right)\right], \tag{9.70}$$

where now

$$\bar{\alpha} \equiv \sum_{\omega_2^{(n)}\leq 0} |c_n|^2, \tag{9.71}$$

$$\bar{\beta} \equiv \sum_{\omega_2^{(n)}\leq 0} |c_n|^2 \cos(2\pi n/N)\,. \tag{9.72}$$

These equations only apply for $t \geq 0$ when the modes start to become unstable. For $t < 0$, there are only fluctuating modes and we set $n_K = 0$. We will discuss the difference between $\langle \hat{n}_Z \rangle$ and n_K in Sec. 9.2.4.

After the phase transition and as long as the lattice spacing a is small enough, $a < 2/\sqrt{|m_2(t)|}$ for all times $t > 0$, we can introduce $n_c(t)$, the time-dependent critical value of n that separates unstable modes from modes that oscillate,

$$n_c(t) \equiv \left\lfloor \frac{N}{\pi}\sin^{-1}\left(\frac{a\sqrt{|m_2(t)|}}{2}\right)\right\rfloor . \tag{9.73}$$

where $\lfloor\,\rfloor$ denotes the integer part function. Then $n_c(t) < N/2$ and (9.71), (9.72) can be rewritten in a more explicit way

$$\bar{\alpha} \equiv \sum_{|n|\leq n_c(t)} |c_n|^2 = |c_0|^2 + 2\sum_{n=1}^{n_c(t)} |c_n|^2, \tag{9.74}$$

$$\begin{aligned}\bar{\beta} &\equiv \sum_{|n|\leq n_c(t)} |c_n|^2 \cos(2\pi n/N) \\ &= |c_0|^2 + 2\sum_{n=1}^{n_c(t)} |c_n|^2 \cos(2\pi n/N)\,.\end{aligned} \tag{9.75}$$

Here we have identified c_{-n} with c_{N-n} for concision, and exploited the symmetry $c_{N-n} = c_n$ (valid for $1 \leq n \leq N-1$) which can be checked directly via (9.34), (9.35), (9.36). Since the ratio $\bar{\beta}/\bar{\alpha}$ belongs to the interval $[0,1]$ one can also rewrite (9.70) as

$$n_K = \frac{N}{\pi L}\cos^{-1}\left(\frac{\bar{\beta}}{\bar{\alpha}}\right). \tag{9.76}$$

Before diving into analytical and numerical estimates of n_K we need to discuss the continuum and infinite volume limits of our discretized theory. We start with the continuum limit. Keeping L fixed, and noticing that, for all N, $n_c(t) \leq mL/4$, we can safely take the $N \to \infty$ limit in expressions involving n/N. In particular

$$\omega_2^{(n)}(t) \approx \left(\frac{2\pi n}{L}\right)^2 + m_2(t)\,, \tag{9.77}$$

and

$$n_c(t) \approx \left\lfloor \frac{L\sqrt{|m_2(t)|}}{2\pi} \right\rfloor . \tag{9.78}$$

Then the expression for the ratio $\bar{\beta}/\bar{\alpha}$ reads

$$\frac{\bar{\beta}}{\bar{\alpha}} \approx 1 - \frac{2\pi^2}{N^2} \frac{\sum_{\omega_2^{(n)}(t)\leq 0} n^2 |c_n|^2}{\sum_{\omega_2^{(n)}(t)\leq 0} |c_n|^2}\,. \tag{9.79}$$

Now, it is clear that this expression is of the form $1-2x^2$ with $x \in [0,1]$ and therefore we may use the identity

$$\cos^{-1}\left(1-2x^2\right) = 2\sin^{-1} x\,, \tag{9.80}$$

to simplify (9.76) and obtain

$$n_K = \frac{2N}{\pi L} \sin^{-1}\left(\frac{\pi}{N}\sqrt{\frac{\sum_{\omega_2^{(n)}(t)\leq 0} n^2|c_n|^2}{\sum_{\omega_2^{(n)}(t)\leq 0} |c_n|^2}}\right) = \frac{2}{L}\sqrt{\frac{\sum_{\omega_2^{(n)}(t)\leq 0} n^2|c_n|^2}{\sum_{\omega_2^{(n)}(t)\leq 0} |c_n|^2}}\,. \tag{9.81}$$

This is the expression of the continuum limit ($N \to \infty$) average number density of kinks. The main property of this expression is that is does not depend on N anymore. Indeed, although the system's dynamics is governed by an infinite number of mode functions, only a finite number appears in the formula; it is only those modes with $n \leq mL/2\pi$ that trigger the instabilities required for the production of kinks. This means that the result is stable in the UV limit and does not depend on the resolution of our discretization. Physically, the contribution of the vacuum fluctuations of the quantum field has been discarded.

Let us now end this section by discussing the infinite volume (or length since we are working in one spatial dimension) limit $L \to \infty$. This is readily done by noticing that the finite size of the spatial dimension is responsible for the discreteness of the wave vectors

$$k_n \equiv \frac{2\pi n}{L}\,, \tag{9.82}$$

corresponding to different modes. As L increases, however, these wave vectors become more and more numerous and densely packed until they form a continuum spanning the entire interval $[-m, m]$. At this point, it is convenient to switch notations and index any relevant quantities by k_n instead of just n. Then

$$\omega_2^{(k_n)}(t) = k_n^2 + m_2(t)\,, \tag{9.83}$$

and

$$k_c(t) \equiv \frac{2\pi n_c(t)}{L} = \sqrt{|m_2(t)|}\,. \tag{9.84}$$

The average kink number density can therefore be rewritten

$$n_K = \frac{1}{\pi}\sqrt{\frac{\sum_{|k_n|\leq k_c(t)} k_n^2 |c_{k_n}|^2}{\sum_{|k_n|\leq k_c(t)} |c_{k_n}|^2}}\,. \tag{9.85}$$

In the $L \to \infty$ limit the sums over k_n become integrals over k, so that

$$n_K \approx \frac{1}{\pi}\sqrt{\frac{\int_0^{k_c(t)} dk\, k^2 |c_k|^2}{\int_0^{k_c(t)} dk\, |c_k|^2}}\,. \tag{9.86}$$

Here we have tacitly introduced the infinite volume mode functions c_k verifying

$$\ddot{c}_k + \left(k^2 + m_2(t)\right) c_k = 0\,, \tag{9.87}$$

and used their $k \to -k$ symmetry properties. We now have all the tools required to perform simple analytical estimates of the average kink number density.

9.2.3 *Analytical Estimate*

In the limit of a sudden phase transition ($\tau = 0$), we can solve (9.34) exactly since $m_2(t) = -m^2\Theta(t)$ (where Θ is the Heaviside function). In fact one may then choose the initial time to be $t_0 = 0_-$ and solve the differential equations

$$\ddot{c}_n + \left[\frac{4}{a^2}\sin^2\left(\frac{\pi n}{N}\right) - m^2\right] c_n = 0\,, \tag{9.88}$$

with initial conditions

$$c_n(0) = \frac{-i}{\sqrt{2L}}\left[\frac{4}{a^2}\sin^2\left(\frac{\pi n}{N}\right) + m^2\right]^{-1/4}, \tag{9.89}$$

$$\dot{c}_n(0) = \frac{1}{\sqrt{2L}}\left[\frac{4}{a^2}\sin^2\left(\frac{\pi n}{N}\right) + m^2\right]^{1/4}. \tag{9.90}$$

Since the time dependence of the frequency has disappeared, the above differential equations can be solved analytically. This yields the unstable mode functions $c_n(t)$ involved in the formula for the average number density of kinks (9.70) i.e. those verifying $|n| \leq N\sin^{-1}(ma/2)/\pi$. More precisely we have

$$\begin{aligned} c_n(t) &= \frac{-i}{\sqrt{2L}}\left[\frac{4}{a^2}\sin^2\left(\frac{\pi n}{N}\right) + m^2\right]^{-1/4}\cosh\left(\kappa_n t\right) \\ &\quad + \frac{1}{\sqrt{2L}}\left[\frac{4}{a^2}\sin^2\left(\frac{\pi n}{N}\right) + m^2\right]^{1/4}\frac{\sinh(\kappa_n t)}{\kappa_n}, \end{aligned} \tag{9.91}$$

where $\kappa_n = \sqrt{m^2 - \frac{4}{a^2}\sin^2\left(\frac{\pi n}{N}\right)}$. Taking first the continuum limit $N \to \infty$ while keeping L fixed we obtain, for $|n| \leq mL/2\pi$,

$$\begin{aligned} c_{k_n}(t) &\approx \frac{-i}{\sqrt{2L}}\left(k_n^2 + m^2\right)^{-1/4}\cosh\left(t\sqrt{m^2 - k_n^2}\right) \\ &\quad + \frac{1}{\sqrt{2L}}\left(k_n^2 + m^2\right)^{1/4}\frac{\sinh\left(t\sqrt{m^2 - k_n^2}\right)}{\sqrt{m^2 - k_n^2}}, \end{aligned} \tag{9.92}$$

where we labelled the mode functions by $k_n = 2\pi n/L$ as in the previous section. In the $L \to \infty$ limit, the discrete variable k_n becomes continuous and we can write an

analytical formula for the average kink number density as in (9.86):

$$n_K = \frac{1}{\pi}\left\{\int_0^m dk\,\left[\frac{k^2\left(m^2\cosh\left(2t\sqrt{m^2-k^2}\right)-k^2\right)}{(m^2-k^2)\sqrt{k^2+m^2}}\right]\right\}^{1/2} \left\{\int_0^m dk\,\left[\frac{m^2\cosh\left(2t\sqrt{m^2-k^2}\right)-k^2}{(m^2-k^2)\sqrt{k^2+m^2}}\right]\right\}^{-1/2} . \tag{9.93}$$

With this expression in hand we can immediately estimate a few important quantities. First of all, we can predict the late time behavior of the average kink number density. Indeed for large t the integrals simplify considerably and it is easy to see that they are dominated by values of $k \ll m$. We can then estimate (9.93) to be

$$n_K \approx \frac{1}{\pi}\left[\frac{\int_0^m dk\,k^2\exp\left(-tk^2/m\right)}{\int_0^m dk\,\exp\left(-tk^2/m\right)}\right]^{1/2} \approx \frac{1}{\pi}\sqrt{\frac{m}{2t}} \tag{9.94}$$

Using Eq. (9.93), one can also estimate the maximum number density of kinks that are produced after the phase transition. In fact, taking a time derivative of (9.93), it is easy to convince oneself that this maximum occurs at $t = 0_+$, in other words, immediately after the phase transition. Moreover its value can be computed exactly to be

$$\begin{aligned} n_K(0) &= \frac{1}{\pi}\left(\frac{\int_0^m dk\,k^2/\sqrt{k^2+m^2}}{\int_0^m dk/\sqrt{k^2+m^2}}\right)^{1/2} \\ &= \frac{m}{\pi}\left(\frac{\sqrt{2}-\sinh^{-1}(1)}{2\coth^{-1}\left(\sqrt{2}\right)}\right)^{1/2} \approx 0.175m\,. \end{aligned} \tag{9.95}$$

Both the power law for the asymptotic behavior of the average kink number density and the maximum number of kinks value will be numerically confirmed in the following subsection. Our analytic results agree with previous work on sudden phase transitions in thermal quenches studied in Boyanovsky (1993); Boyanovsky *et al.* (2000); Ibaceta and Calzetta (1999); Calzetta (1989) using different techniques.

9.2.4 Numerical Results

We now discuss our numerical results for the time evolution of n_K for different values of the quench parameter τ. In principle this involves solving the complex differential equations (9.34) with initial conditions (9.35) and (9.36), for the unstable mode functions $c_n(t)$ – those with $|n| \leq n_c(t)$. We can then directly evaluate the average number density of kinks using (9.70). However, since this formula only involves $|c_n(t)| = \rho_n(t)$, considerable computational gain can be achieved by instead solving the real differential equations (9.39) with initial conditions (9.40), (9.41).

It turns out that this system of ordinary differential equations presents a major computational difficulty caused by the fact that $\rho_n(t)$ grows exponentially for $|n| \leq n_c(t)$. Therefore the numerical evolution is limited to short time periods after the phase transition beyond which the numbers involved become extremely large and results cannot be trusted. One way to get around this problem is to factor out the exponential growth, *i.e.* the zero mode $\rho_0(t) = \rho_N(t)$, from the other modes and evolve it separately. So we write,

$$\rho_n(t) = \rho_0(t) r_n(t)\,, \tag{9.96}$$

for $n = 1, \ldots, N-1$. With this redefinition it can be shown that the differential equation (9.39) now becomes,

$$\ddot{r}_n + 2\frac{\dot{\rho}_0}{\rho_0}\dot{r}_n + \left(\omega_2^{(n)} - \omega_2^{(0)} + \frac{1}{4L^2\rho_0^4}\left(1 - \frac{1}{r_n^4}\right)\right) r_n = 0\,, \tag{9.97}$$

and its corresponding initial conditions are given by,

$$r_n(t_0) = \frac{1}{\sqrt{2L}} \frac{\omega_2^{(n)}(t_0)^{-1/4}}{\rho_0(t_0)}\,, \tag{9.98}$$

$$\dot{r}_n(t_0) = 0\,. \tag{9.99}$$

Recall here that

$$\omega_2^{(n)} = \frac{4}{a^2}\sin^2\left(\frac{\pi n}{N}\right) + m_2(t)\,, \tag{9.100}$$

and $\omega_2^{(0)} = \omega_2^{(N)}$. Furthermore, one can also efficiently solve for $\rho_0(t)$ by introducing the auxiliary function $q(t) = \ln \rho_0(t)$, verifying

$$\ddot{q} + \dot{q}^2 + \omega_2^{(0)} = \frac{e^{-4q}}{4L^2}\,, \tag{9.101}$$

with initial conditions,

$$\begin{aligned} q(t_0) &= \ln\left[\frac{1}{\sqrt{2L}}\Big(m_2(t_0)\Big)^{-1/4}\right], \\ \dot{q}(t_0) &= 0\,. \end{aligned} \tag{9.102}$$

By going to the $q(t)$ variable we avoid the exponential growth of $\rho_0(t)$. Thus, both the differential equation for $r_n(t)$ (9.97) and its corresponding initial conditions can be rewritten in terms of this auxiliary function:

$$\ddot{r}_n + 2\dot{q}\dot{r}_n + \left(\omega_2^{(n)} - \omega_2^{(0)} + \frac{e^{-4q}}{4L^2}\left(1 - \frac{1}{r_n^4}\right)\right) r_n = 0\,, \tag{9.103}$$

with initial conditions,

$$\begin{aligned} r_n(t_0) &= \left(\frac{\omega_2^{(0)}(t_0)}{\omega_2^{(n)}(t_0)}\right)^{1/4}, \\ \dot{r}_n(t_0) &= 0\,. \end{aligned} \tag{9.104}$$

In summary, the numerically efficient way to study the dynamics of kink formation in our model, is to solve (9.101) and (9.103) with respective initial conditions (9.102) and (9.104). The computational problem we had is indeed resolved since we managed to eliminate the exponential growth of $\rho_n(t)$ by suitable function redefinitions. The numerics can now be trusted for much longer periods of time.

In our numerical work we work in units where $m = 1$ and pick $t_0 = -200$. To get accurate results we choose large L and N. Most of our results are for $L = 6400$ and $N = 12800$. The evolution of the average number density of kinks n_K for different quench time scales τ is shown in Fig. 9.2a. The different curves exhibit the same

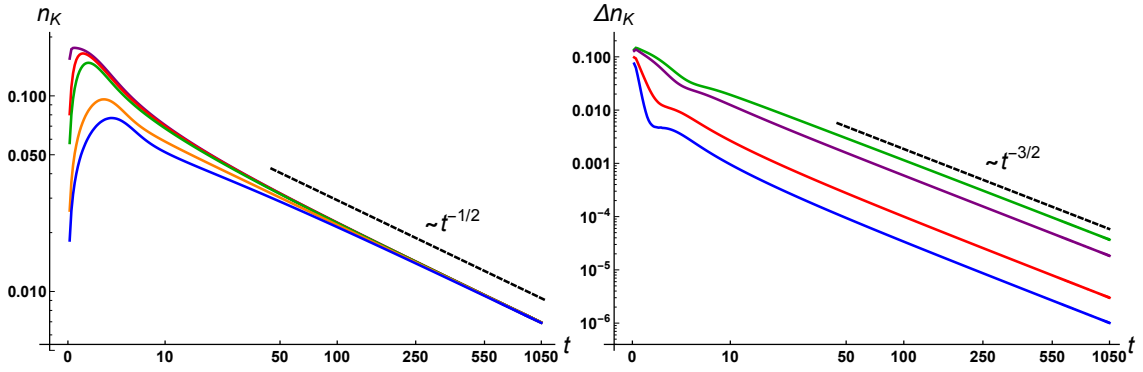

(a) (b)

Figure 9.2: (a) Log-log plot of n_K versus time for τ =0.1 (Purple, topmost curve), 0.5 (Red), 1.0 (Green), 5.0 (Orange), 10.0 (Blue). The black dashed line shows the exhibited power law at late times, *i.e.* $t^{-1/2}$. (b) Log-log plot of the differences between the average kink number density for different values of τ, $n_K(t, \tau_1 = 0.1) - n_K(t, \tau_2)$ vs. time for $\tau_2 = 0.5$ (Blue), 1.0 (Red), 5.0 (Purple), 10.0 (Green). The black dashed line shows the exhibited power law, *i.e.* $t^{-3/2}$.

qualitative behavior: immediately after the phase transition ($t = 0$) the average number density of kinks increases from 0 to a maximum value $(n_K)_{\max}$ within a time $t_{\max}$, and this is followed by a gradual decrease that asymptotically converges to a power law. Physically this corresponds to the production of a random distribution of kinks and anti-kinks during the phase transition, followed by their mutual annihilation over time. Noticeably, the asymptotic behavior of the average kink number density is independent of the quench time scale: at late times the plots for different values of τ converge to the *same* function that falls off as $t^{-1/2}$. (We have also cross-checked this result by computing the correlation length $\xi(t)$ of field fluctuations and showing that it scales as $1/n_K \sim t^{1/2}$, as expected from existing results in the literature (Liu and Mazenko, 1991, 1992a; Boyanovsky, 1993; Boyanovsky *et al.*, 2000; Liu and Mazenko, 1992b). This scaling law also agrees with the analytical estimate of Eq. (9.94) and shows that the $\tau = 0$ solution is a universal attractor. To analyze the rate at which the kink densities for different values of τ converge, we plot $\Delta n_K(t, \tau_1, \tau_2) \equiv n_K(t, \tau_1) -$

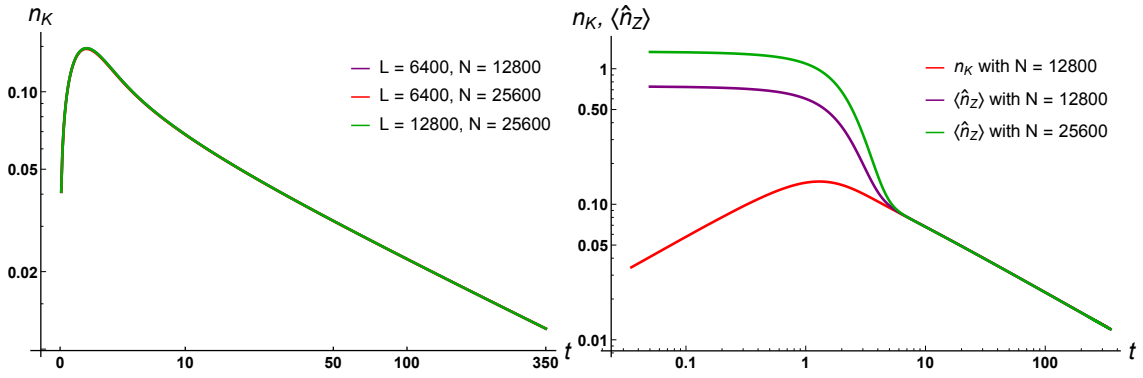

(a) (b)

Figure 9.3: (a) Log-log plot of $n_K(t)$ versus time for $\tau = 1.0$ for various values of L and N as given in (9.70). (b) Log-log plot of n_K and $\langle \hat{n}_Z \rangle$ versus time for $\tau = 1.0$, $L = 6400$ and various values of N.

$n_K(t, \tau_2)$ versus t in Fig. 9.2b. We observe that at late times these differences fall off as $t^{-3/2}$. We can therefore conclude that

$$n_K(t) = C_K \sqrt{\frac{m}{t}} + \mathcal{O}\left(t^{-3/2}\right), \tag{9.105}$$

where $C_K \approx 0.22$ is a constant of proportionality which is independent of the quench time scale τ. This agrees well with the analytical estimate found in Eq. (9.94): $1/(\pi\sqrt{2}) \approx 0.225$.

We can explicitly check, as shown in Fig. 9.3a, that our results are independent of both L and N as long as they are sufficiently large and $a = L/N$ is sufficiently small. In Fig. 9.3b we have also plotted $\langle \hat{n}_Z \rangle$ and n_K for different values of N. Although the curves depend on N (or are UV sensitive) near the phase transition, the late time behaviors are universal. This is to be expected since unstable modes grow exponentially and dominate the sums in (9.74) and (9.75). Thus our technique of restricting the mode sums to differentiate between field zeros and kinks is reasonable and gets rid of the artifacts arising due to finite N.

The plots of $(n_K)_{\max}$ versus τ, and $t_{\max}$ versus τ, are shown in Fig. 9.4a and

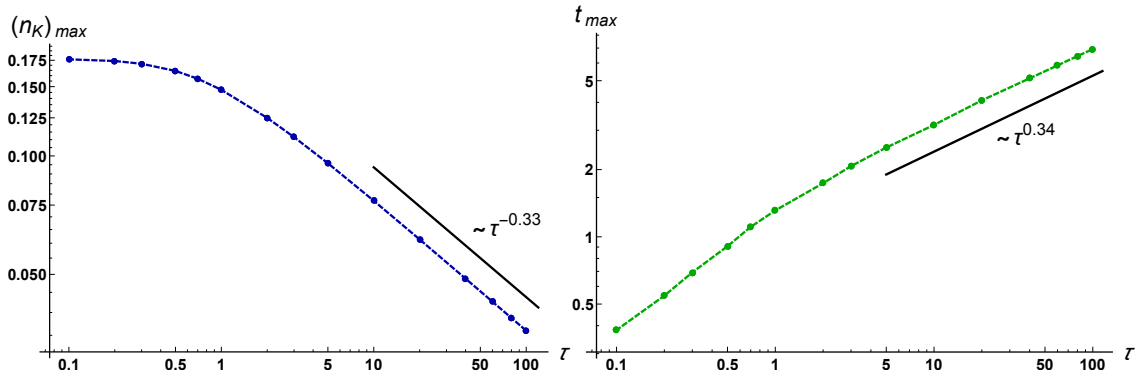

(a) (b)

Figure 9.4: (a) Log-Log plot of the maximum average kink number density $(n_K)_{\max}$ vs. τ. For larger values of τ the maximum average kink number density falls off as $\tau^{-0.33}$. (b) Log-Log plot of the time at which maximum average kink number density $(n_K)_{\max}$ occurs $(t_{\max})$ vs. τ. For larger values of τ, $t_{\max}$ grows as $\tau^{0.34}$.

Fig. 9.4b respectively. From these we note that the faster the phase transition (smaller quench time τ), the more kinks and anti-kinks are produced and the faster their maximum number density is attained. In Fig. 9.4a we see that the maximum density of kinks $(n_K)_{\max}$ flattens, *i.e.* it becomes a constant as quench time scales approach zero. The value of $(n_K)_{\max}$ for which this happens is seen to be approximately 0.175. This agrees remarkably well with the analytical estimate in Eq. (9.95).

9.3 Two Dimensions: Vortices

The analysis done in Section 9.2 can be generalized to the $d = 2$ case. We will be considering a two-dimensional complex scalar field Φ whose dynamics are described by the Lagrangian density

$$\mathcal{L}^{(2)} = \frac{1}{2}\partial_\mu \Phi^* \partial^\mu \Phi - \frac{1}{2} m_2(t) \Phi^* \Phi - \frac{1}{4}\lambda \left(\Phi^* \Phi\right)^2 . \tag{9.106}$$

This theory is known to possess solitonic solutions called *vortices*, characterized by a topological charge known as the *winding number*. Assuming a vortex field configuration $\Phi(x, y) = r(x, y)e^{i\theta(x,y)} = \phi(x, y) + i\psi(x, y)$ centered at a point (x_0, y_0), the

winding number is given by

$$\Gamma = \frac{1}{2\pi} \oint_{\mathcal{C}} d\theta = \frac{1}{2\pi} \int_{\mathcal{C}} \frac{1}{r^2} (\phi d\psi - \psi d\phi) \,, \tag{9.107}$$

where $\mathcal{C}$ is any closed loop around (x_0, y_0). Generically a non-zero winding number along a closed loop implies the existence of a vortex configuration and the vanishing of the field somewhere within the bounded region. Therefore, as in the case of kinks, vortices are to be found among zeros of Φ.

To study the production of vortices during the quantum phase transition we will thus do a similar analysis to the one we did for kinks. We start by setting λ to zero and express the Lagrangian density in terms of the two real scalar fields ϕ and ψ, respectively defined as the real and imaginary part of the complex field Φ:

$$\mathcal{L}^{(2)} = \frac{1}{2}(\partial_\mu \phi)^2 + \frac{1}{2}(\partial_\mu \psi)^2 - \frac{1}{2} m_2(t)(\phi^2 + \psi^2) \,. \tag{9.108}$$

This is a model for two non-interacting real scalar fields in two spatial dimensions. In order to apply the methods outlined in Section 9.2, we need to discretize this model. We first compactify both spatial dimensions by assuming periodic boundary conditions, $\phi(x+L, y) = \phi(x, y+L) = \phi(x, y)$ (and similarly for ψ). Space is thus seen to be a 2-torus of area L^2. We then discretize it on a regular square lattice consisting of N^2 points separated by a distance $a = L/N$ along both the x and y directions. Now for each lattice point $(x_j, y_l) \equiv (ja, la)$ we can define the discretized fields $\phi_{jl} \equiv \phi(x_j, y_l)$ and $\psi_{jl} \equiv \psi(x_j, y_l)$. Writing the discretized Lagrangian and quantizing it can be done analogously to the one-dimensional case, with the understanding that any vectors and matrices are now N^2 and $N^2 \times N^2$ dimensional respectively. For example, the vector of discretized field values of ϕ is given by

$$\boldsymbol{\phi} \equiv (\phi_{11}, \phi_{12}, ..., \phi_{1N}, \phi_{21}, ..., \phi_{2N}, ..., \phi_{NN-1}, \phi_{NN})^T. \tag{9.109}$$

More generally, any $N^2 \times N^2$ matrix A will be represented by a two-dimensional array of matrix elements $A_{ij,kl}$ arranged in the following way:

$$A = \begin{pmatrix} A_{11,11} & A_{11,12} \cdots\cdots A_{11,1N} & A_{11,21} & A_{11,22} \cdots\cdots \\ A_{12,11} & A_{12,12} \cdots\cdots A_{12,1N} & A_{12,21} & A_{12,22} \cdots\cdots \\ \vdots & \vdots \qquad\qquad \vdots & \vdots & \vdots \\ A_{1N,11} & A_{1N,12} \cdots\cdots A_{1N,1N} & A_{1N,21} & A_{1N,22} \cdots\cdots \\ A_{21,11} & & & \\ A_{22,11} & & & \\ \vdots & & & \end{pmatrix}$$

With these conventions in mind (where matrices are four index objects and vectors are two index objects), we can directly generalize the computations in Sec. 9.2.1 to solve the functional Schrödinger equation for the wave-functional is $\Psi[\phi_{ij}, \psi_{ij}; t]$. In fact, we can define a new $N^2 \times N^2$ matrix Z obeying Eqs. (9.20), (9.21) and (9.22) as long as the matrix elements of Ω_2 are given by

$$[\Omega_2]_{ij,kl} = \begin{cases} +2/a^2 + m_2(t)\,, & i = k, j = l \\ -1/a^2\,, & i = k \pm 1, j = l \pm 1 \pmod N \\ 0\,, & \text{otherwise}\,. \end{cases} \tag{9.110}$$

It is then easy to write the probability density functional as in Eq. (9.28),

$$|\Psi(t)|^2 = \frac{1}{\det(2\pi K)} e^{-\boldsymbol{\phi}^T K^{-1} \boldsymbol{\phi}/2} e^{-\boldsymbol{\psi}^T K^{-1} \boldsymbol{\psi}/2}\,. \tag{9.111}$$

where the matrix K is still related to Z via $K = ZZ^\dagger$.

We can be even more explicit by realizing that the matrix $Z(t)$ is once again real and *circulant*, *i.e.*, the matrix elements of Z, $Z_{pq,rs}$ depend only on $p - r \pmod N$ and $q - s \pmod N$. We can therefore again diagonalize Z using the discrete Fourier

transform:

$$Z_{pq,rs} = \frac{1}{N}\sum_{n,n'=1}^{N} c_{n,n'}(t) e^{-i(p-r)2\pi n/N} e^{-i(q-s)2\pi n'/N} \,. \tag{9.112}$$

Using equations (9.20),(9.21) and (9.22), the complex mode functions $c_{n,n'}(t)$ verify

$$\ddot{c}_{n,n'} + \left[\frac{4}{a^2}\left\{\sin^2\left(\frac{\pi n}{N}\right) + \sin^2\left(\frac{\pi n'}{N}\right)\right\} + m_2(t)\right] c_{n,n'} = 0\,, \tag{9.113}$$

and

$$c_{n,n'}(t_0) = \frac{-i}{\sqrt{2a}}\frac{1}{N}\left[\frac{4}{a^2}\left\{\sin^2\left(\frac{\pi n}{N}\right) + \sin^2\left(\frac{\pi n'}{N}\right)\right\} + m_2(t_0)\right]^{-1/4}, \tag{9.114}$$

$$\dot{c}_{n,n'}(t_0) = \frac{1}{\sqrt{2a}}\frac{1}{N}\left[\frac{4}{a^2}\left\{\sin^2\left(\frac{\pi n}{N}\right) + \sin^2\left(\frac{\pi n'}{N}\right)\right\} + m_2(t_0)\right]^{1/4}. \tag{9.115}$$

Note that $c_{n,n'} = c_{n',n}$ which immediately implies that $Z_{pq,rs} = Z_{qp,sr}$ and again we assume the initial time t_0 to be such that $t_0 \ll -\tau$. This follows from the rotational symmetry of the system.

9.3.1 Average Vortex Number Density

To find the vortex number density, we first need a quantum operator that counts the number of zeros n_Z of the complex field Φ (as in Sec. 9.2.2), or in other words, coincident zeroes of both the fields ϕ and ψ. Since space is discretized, such an operator necessarily yields a coarse-grained estimate of the actual number of zeros of a given field configuration. As the number of lattice points N^2 increases so does the operator's resolution: while certain "zeros" cease to be counted, new ones are revealed. In the limit where $N \to \infty$ we expect divergences, just as in the kink case, and we will return to this point later on.

We think of the vortex as the intersection of a domain wall of ϕ – for our purposes, a domain wall is a curve on which $\phi = 0$ – with a domain wall of ψ. Then, as shown in Fig. 9.5, there could be a situation where a ϕ domain wall enters a plaquette through

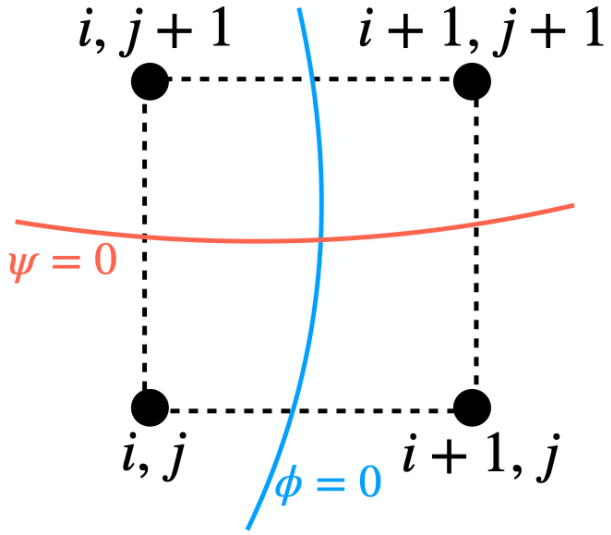

Figure 9.5: A plaquette showing how zeros are counted.

one edge and leaves through the opposite edge, while a ψ domain wall passes through the plaquette in the orthogonal direction. Then the two domain walls must intersect, leading to coincident zeros that correspond to a vortex within that plaquette. Other possibilities include the case where the ϕ wall enters the plaquette from the lower edge but leaves from the right edge in Fig. 9.5 while the ψ domain wall goes through as shown or bends to exit from the top edge. It is ambiguous whether a coincident zero exists in these other cases but the ambiguity is minimized as the lattice resolution is increased ($N \to \infty$). Hence we can count zeros of Φ in the large N limit by counting the plaquettes in which ϕ and ψ domain walls enter across orthogonal edges.

Then, motivated by the discussion in Sec. 9.2.2, we can define the number density of zeros of Φ by, $\hat{n}_Z = n_Z\left(\hat{\boldsymbol{\phi}}, \hat{\boldsymbol{\psi}}\right)$,

$$\begin{aligned}\hat{n}_Z &\equiv \frac{1}{L^2}\sum_{i,j=1}^{N}\frac{1}{16}\Big[\left\{\mathrm{sgn}\left(\hat{\phi}_{ij}\right)-\mathrm{sgn}\left(\hat{\phi}_{i+1,j}\right)\right\}^2\left\{\mathrm{sgn}\left(\hat{\psi}_{ij}\right)-\mathrm{sgn}\left(\hat{\psi}_{i,j+1}\right)\right\}^2+(\phi\leftrightarrow\psi)\Big] \\ &= \frac{1}{4L^2}\sum_{i,j=1}^{N}\Big[\left\{1-\mathrm{sgn}\left(\hat{\phi}_{i,j}\hat{\phi}_{i+1,j}\right)\right\}\left\{1-\mathrm{sgn}\left(\hat{\psi}_{ij}\hat{\psi}_{i,j+1}\right)\right\}+\left\{1-\mathrm{sgn}\left(\hat{\psi}_{ij}\hat{\psi}_{i+1,j}\right)\right\} \\ &\quad \left\{1-\mathrm{sgn}\left(\hat{\phi}_{ij}\hat{\phi}_{i,j+1}\right)\right\}\Big].\end{aligned}$$

We can now write down the vacuum expectation value of the operator $\hat{n}_Z$: $\langle \hat{n}_Z \rangle \equiv \langle 0|\hat{n}_Z(t)|0\rangle$. Using the fact that the fields ϕ and ψ are independent and that, consequently, the probability density functional factorizes as in Eq. (9.111), we first notice that

$$\left\langle \mathrm{sgn}\left(\hat{\phi}_{ij}\hat{\phi}_{i,j+1}\right)\right\rangle = \frac{1}{\sqrt{\det(2\pi K)}} \times \int d^N\boldsymbol{\phi}\ \mathrm{sgn}\left(\phi_{ij}\phi_{i,j+1}\right) e^{-\boldsymbol{\phi}^T K^{-1}\boldsymbol{\phi}/2}\,. \tag{9.116}$$

Then, using the fact that the matrix K^{-1} is circulant and, moreover, symmetric under interchange of its first (or last) two indices – properties that are inherited from Z, we can establish that

$$\left\langle \mathrm{sgn}\left(\hat{\phi}_{ij}\hat{\phi}_{i,j+1}\right)\right\rangle = \left\langle \mathrm{sgn}\left(\hat{\phi}_{11}\hat{\phi}_{12}\right)\right\rangle = \left\langle \mathrm{sgn}\left(\hat{\phi}_{11}\hat{\phi}_{21}\right)\right\rangle = \left\langle \mathrm{sgn}\left(\hat{\phi}_{ij}\hat{\phi}_{i+1,j}\right)\right\rangle\,. \tag{9.117}$$

Physically, this set of equalities is a manifestation of the translational and rotational invariance of the system. It is also clear that, ϕ being a dummy variable in the integral of Eq. (9.116),

$$\left\langle \mathrm{sgn}\left(\hat{\psi}_{ij}\hat{\psi}_{kl}\right)\right\rangle = \left\langle \mathrm{sgn}\left(\hat{\phi}_{ij}\hat{\phi}_{kl}\right)\right\rangle\,. \tag{9.118}$$

These properties thus allow us to write the average number of zeros of the field in a very simple form:

$$\langle \hat{n}_Z \rangle = \frac{N^2}{2L^2}\left[1 - \left\langle \mathrm{sgn}\left(\hat{\phi}_{11}\hat{\phi}_{12}\right)\right\rangle\right]^2. \tag{9.119}$$

From this point on, the computation of the average number of zeros follows along the same lines as in Sec. 9.2, and we obtain

$$\langle \hat{n}_Z \rangle = \frac{N^2}{2L^2}\left[1 - \frac{2}{\pi}\sin^{-1}\left(\frac{\beta}{\alpha}\right)\right]^2, \tag{9.120}$$

where α and β are now defined as

$$\alpha \equiv K_{11,11} = \sum_{n,n'=1}^{N} |c_{n,n'}|^2, \tag{9.121}$$

$$\beta \equiv K_{11,12} = \sum_{n,n'=1}^{N} |c_{n,n'}|^2 \cos(2\pi n'/N)\,. \tag{9.122}$$

Here, once again, we have used the reality of the matrix Z.

Eq. (9.120) gives us the number density of field zeros but we are interested in counting the number density of *vortices*. We have already discussed how quantum fluctuations can induce a non-zero number density of zeros of the field even in the absence of spontaneous symmetry breaking. We thus need to eliminate such spurious zeros by restricting the sums in (9.121) and (9.122) to the mode functions $c_{n,n'}(t)$ that are *non-oscillating*. In this case we include the modes corresponding to n and n' verifying,

$$\omega_2^{(n,n')}(t) \equiv \frac{4}{a^2}\left\{\sin^2\left(\frac{\pi n}{N}\right) + \sin^2\left(\frac{\pi n'}{N}\right)\right\} + m_2(t) \leq 0\,. \tag{9.123}$$

The average number density of vortices formed after the phase transition is finally given by,

$$n_V = \frac{N^2}{2L^2}\left[1 - \frac{2}{\pi}\sin^{-1}\left(\frac{\bar{\beta}}{\bar{\alpha}}\right)\right]^2\,, \tag{9.124}$$

where,

$$\bar{\alpha} \equiv \sum_{\omega_2^{(n,n')}\leq 0} |c_{n,n'}|^2, \tag{9.125}$$

$$\bar{\beta} \equiv \sum_{\omega_2^{(n,n')}\leq 0} |c_{n,n'}|^2 \cos(2\pi n'/N)\,. \tag{9.126}$$

Similar to the case of kinks (see discussion in Sec. 9.2.2), this result only makes sense after the phase transition; it is ill-defined before. As might be intuitively expected, the average number density of vortices is obtained, up to a combinatorics factor due to the $\phi \leftrightarrow \psi$ symmetry, by squaring the average number density of kinks. In the next subsections we will see that this intuition is supported by both analytical and numerical estimates of the asymptotic dynamics of the problem.

Analogously to Sec. 9.2.2, Eq. (9.124) can be further simplified by first taking the

continuum limit $N \to \infty$ (at fixed volume L) to obtain

$$n_V \approx \frac{8}{L^2} \frac{\sum_{\omega_2^{(n,n')} \leq 0} n'^2 |c_{n,n'}|^2}{\sum_{\omega_2^{(n,n')} \leq 0} |c_{n,n'}|^2} \,, \tag{9.127}$$

where the sums run over pairs of integers $(n, n') \in \mathbb{Z}^2$ verifying

$$\omega_2^{(n,n')}(t) \approx \left(\frac{2\pi n}{L}\right)^2 + \left(\frac{2\pi n'}{L}\right)^2 + m_2(t_0) \leq 0 \,, \tag{9.128}$$

and it is understood that $c_{-n,n'} \equiv c_{N-n,n'}$, $c_{n,-n'} \equiv c_{n,N-n'}$ for $0 \leq n, n' \leq N-1$. Relabelling the mode functions by the discrete two-dimensional wave vector

$$\vec{k}_{n,n'} = \left(k_x^{(n)}, k_y^{(n')}\right) \equiv \left(\frac{2\pi n}{L}, \frac{2\pi n'}{L}\right) \,, \tag{9.129}$$

and taking the large L limit, Eq. (9.127) can be recast as

$$n_V \approx \frac{2}{\pi^2} \frac{\int_{k \leq k_c(t)} d^2k \, k_y^2 |c_{\vec{k}}|^2}{\int_{k \leq k_c(t)} d^2k \, |c_{\vec{k}}|^2} \,. \tag{9.130}$$

Here we have once again introduced the infinite volume mode functions $c_{\vec{k}}$ – labelled by a continuum of two-dimensional wave vectors $\vec{k} \equiv (k_x, k_y)$ – verifying

$$\ddot{c}_{\vec{k}} + \left(k^2 + m_2(t)\right) c_{\vec{k}} = 0 \,, \tag{9.131}$$

and defined $k \equiv |\vec{k}|$ and $k_c(t) = \sqrt{|m_2(t)|}$ as in Sec. 9.2.2. Noticing that $c_{\vec{k}}$ only depends[2] on k and going to polar coordinates, we can turn the double integrals in (9.130) into single integrals to finally obtain the continuum, infinite volume limit of the average vortex number density:

$$n_V \approx \frac{1}{\pi^2} \frac{\int_0^{k_c(t)} dk \, k^3 |c_{\vec{k}}|^2}{\int_0^{k_c(t)} dk \, k |c_{\vec{k}}|^2} \,. \tag{9.132}$$

With the possible exception of our particular choice of UV cutoff, this formula is in agreement with known results in the literature (see *e.g.* Eq. (5) in Ibaceta and Calzetta (1999)).

[2]This can be checked explicitly using Eqs. (9.113), (9.114), (9.115) and is a consequence of the rotational invariance of the problem.

9.3.2 *Analytical Estimate*

Just as we did in the case of kinks in Sec. 9.2.3, we can also compute the average number density of vortices at late times in the limit of a sudden phase transition ($\tau = 0$). This can be achieved once again by exactly solving the differential equations for the mode coefficients $c_{n,n'}(t)$. As we saw in Sec. 9.3 these differential equations are as follows,

$$\ddot{c}_{n,n'} + \left[\frac{4}{a^2}\left\{\sin^2\left(\frac{\pi n}{N}\right) + \sin^2\left(\frac{\pi n'}{N}\right)\right\} - m^2\right] c_{n,n'} = 0\,, \tag{9.133}$$

with initial conditions

$$c_{n,n'}(0) = \frac{-i}{\sqrt{2a}}\frac{1}{N}\left[\frac{4}{a^2}\left\{\sin^2\left(\frac{\pi n}{N}\right) + \sin^2\left(\frac{\pi n'}{N}\right)\right\} + m^2\right]^{-1/4}\,, \tag{9.134}$$

$$\dot{c}_{n,n'}(0) = \frac{1}{\sqrt{2a}}\frac{1}{N}\left[\frac{4}{a^2}\left\{\sin^2\left(\frac{\pi n}{N}\right) + \sin^2\left(\frac{\pi n'}{N}\right)\right\} + m^2\right]^{1/4}\,. \tag{9.135}$$

The solution to these equations can be obtained analytically. In fact they look very similar to the ones we obtained in the kinks case but now involve two indices instead of just one. This gives the unstable mode functions $c_{n,n'}(t)$ involved in the formula for the average number density of vortices:

$$\begin{aligned} c_{n,n'}(t) = {} & \frac{-i}{\sqrt{2L}}\left[\frac{4}{a^2}\left\{\sin^2\left(\frac{\pi n}{N}\right) + \sin^2\left(\frac{\pi n'}{N}\right)\right\} + m^2\right]^{-1/4}\cosh\left(\kappa_{n,n'}t\right) \\ & + \frac{1}{\sqrt{2L}}\left[\frac{4}{a^2}\left\{\sin^2\left(\frac{\pi n}{N}\right) + \sin^2\left(\frac{\pi n'}{N}\right)\right\} + m^2\right]^{1/4}\frac{\sinh(\kappa_{n,n'}t)}{\kappa_{n,n'}} \end{aligned} \tag{9.136}$$

where

$$\kappa_{n,n'} = \sqrt{m^2 - \frac{4}{a^2}\left\{\sin^2\left(\frac{\pi n}{N}\right) + \sin^2\left(\frac{\pi n'}{N}\right)\right\}}\,. \tag{9.137}$$

Now, taking first the continuum limit $N \to \infty$ while keeping L fixed we obtain, for $n^2 + n'^2 \leq (mL/2\pi)^2$,

$$\begin{aligned} c_{\vec{k}_{n,n'}}(t) \approx {} & \frac{-i}{\sqrt{2L}}\left(k_x^{(n)2} + k_y^{(n')2} + m^2\right)^{-1/4}\cosh\left(t\sqrt{m^2 - k_x^{(n)2} - k_y^{(n')2}}\right) \\ & + \frac{1}{\sqrt{2L}}\left(k_x^{(n)2} + k_y^{(n')2} + m^2\right)^{1/4}\frac{\sinh\left(t\sqrt{m^2 - k_x^{(n)2} - k_y^{(n')2}}\right)}{\sqrt{m^2 - k_x^{(n)2} - k_y^{(n')2}}} \end{aligned} \tag{9.138}$$

where we have relabelled the mode functions by $\vec{k}_{n,n'} = (k_x^{(n)}, k_y^{(n')})$ and recall that $k_x^{(n)} = 2\pi n/L$, $k_y^{(n')} = 2\pi n'/L$. In the limit $L \to \infty$, the discrete variables $\vec{k}_{n,n'}$ become continuous and, as in Eq. (9.132), we can write an analytical formula for the average number density of vortices:

$$n_V \approx \frac{1}{\pi^2} \left\{ \int_0^m dk \left[\frac{k^3 \left(m^2 \cosh\left(2t\sqrt{m^2-k^2}\right) - k^2 \right)}{(m^2-k^2)\sqrt{k^2+m^2}} \right] \right\} \left\{ \int_0^m dk \left[\frac{k \left(m^2 \cosh\left(2t\sqrt{m^2-k^2}\right) - k^2 \right)}{(m^2-k^2)\sqrt{k^2+m^2}} \right] \right\}^{-1} . \tag{9.139}$$

Using this equation, we can once again estimate the late time behavior of the average number of vortices. In the limit, $k, k' \ll m$, we have

$$n_V \approx \frac{1}{\pi^2} \frac{\int_0^m dk\, k^3 \exp\left(-tk^2/m\right)}{\int_0^m dk\, k \exp\left(-tk^2/m\right)} \approx \frac{m}{\pi^2 t} = 2!\, n_K^2 . \tag{9.140}$$

As mentioned below Eq. (9.126), the vortex number density is obtained by squaring the kink number density and multiplying by the combinatorial factor 2! due to the exchange symmetry $\phi \leftrightarrow \psi$.

Furthermore, like in the case of kinks, the maximum number density of vortices can be estimated using Eq. (9.139). This maximum is reached immediately after the phase transition, at time $t = 0_+$ and is found to be

$$\begin{aligned} (n_V)_{\max} &= \frac{1}{\pi^2} \frac{\int_0^m dk\, k^3/\sqrt{k^2+m^2}}{\int_0^m dk\, k/\sqrt{k^2+m^2}} \\ &= \frac{m^2\sqrt{2}}{3\pi^2} \approx 0.0478\, m^2 . \end{aligned} \tag{9.141}$$

9.3.3 Numerical Results

We use numerical techniques to solve (9.113) and then calculate the average vortex number density using (9.124). For reasons discussed earlier, the parameters L and N that we choose for our numerical simulations need to be sufficiently large to accurately

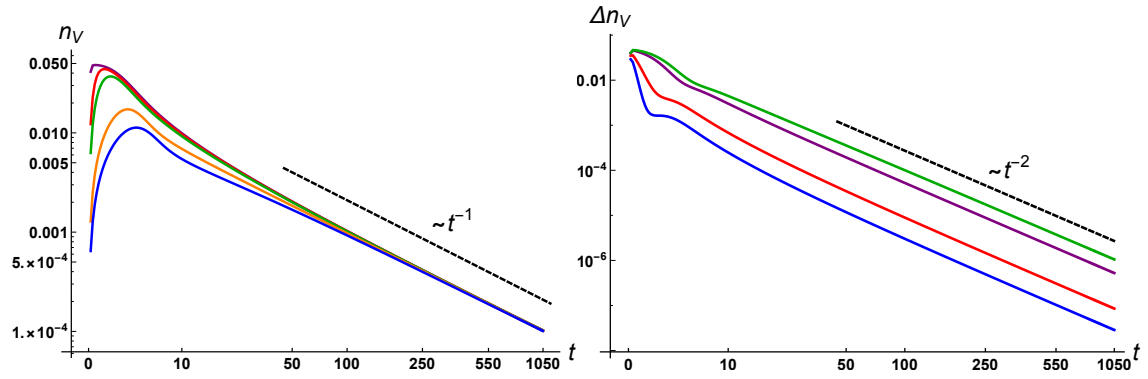

(a) (b)

Figure 9.6: (a) Log-log plot of $n_V(t)$ versus time for τ =0.1 (Purple, topmost curve), 0.5 (Red), 1.0 (Green), 5.0 (Orange), 10.0 (Blue). The black dashed line shows the exhibited power law at late times, *i.e.* t^{-1}. (b) Log-log plot of the differences between the average vortex number density for different values of τ, $n_V(t, \tau_1 = 0.1) - n_V(t, \tau_2)$ vs. time for $\tau_2 = 0.5$ (Blue), 1.0 (Red), 5.0 (Purple), 10.0 (Green). The black dashed line shows the exhibited power law, *i.e.* t^{-2}.

describe the continuum infinite volume limit. We choose, $L = 2000$ and $N = 4000$. As in the case of kinks, the results are insensitive to the UV and IR cutoffs. In practice, because of the order N^2 computational complexity of the problem and the exponential growth of the magnitudes of mode functions, we directly solve for $\rho_{n,n'} = |c_{n,n'}|$ and factor out the zero mode to improve the numerical accuracy (see Sec. 9.2.4 for details).

In Fig. 9.6a we show the average vortex number density for different quench parameters τ as a function of time. As in the kink case, the plots of n_V vs. t for different τ converge to the same function and decay as t^{-1} as we expect from the analytical estimate in (9.140). The result also agrees with the intuition that a vortex corresponds to the intersection of two independent domain walls.

Fig. 9.6a also shows that immediately after the phase transition, n_V increases from zero to some maximum value $(n_V)_{\max}$ in a time $t_{\max}$. As time goes on n_V starts to decay. At very early times, after the phase transition, randomly distributed vortices of positive and negative winding number are produced, but then the system starts

relaxing, the vortices-antivortices start annihilating, and the dynamics reaches its scaling regime.

We can also plot the differences of vortex number densities for different values of τ as we did in the case of kinks: $\Delta n_V(t, \tau_1, \tau_2) \equiv n_V(t, \tau_1) - n_V(t, \tau_2)$. This is shown in Fig. 9.6b which shows that $\Delta n_V(t, \tau_1, \tau_2)$ decays as t^{-2} at late times. We thus deduce the asymptotic form,

$$n_V(t) = C_V\left(\frac{m}{t}\right) + \mathcal{O}\left(t^{-2}\right), \tag{9.142}$$

where, C_V is some constant of proportionality which is independent of the quench time scale τ. Numerically, we find $C_V \approx 0.092$. This is again in reasonable agreement with the value we calculated analytically for a sudden phase transition ($\tau = 0$) in Eq. (9.140), more precisely $1/\pi^2 \approx 0.101$.

The plots of $(n_V)_{\max}$ versus τ, and $t_{\max}$ versus τ are shown in Fig. 9.7a and Fig. 9.7b respectively. The intuitive understanding that a faster phase transition (smaller quench time scale τ) leads to greater and more rapid vortex production is confirmed by these plots. Moreover, from Fig. 9.7a we see that the maximum number density of vortices $(n_V)_{\max}$ flattens as the quench time scale τ approaches zero. This happens for a value $(n_V)_{\max} \approx 0.0483$ which is once again in good agreement with our analytical result in Eq. (9.141).

As a final remark, comparing Fig. 9.4a to Fig. 9.7a shows us right away that for the same quench time-scales τ, the maximum vortex number density $(n_V)_{\max}$ is much lower than the maximum kink number density $(n_K)_{\max}$. For example, in the limiting case of $\tau \to 0$, $(n_V)_{\max} \approx 0.050$ while $(n_K)_{\max} \approx 0.175$. This is again to be expected since the formation of a vortex requires the simultaneous vanishing of two fields, which is less probable than the vanishing of a single field necessary for the formation of a kink in one dimension.

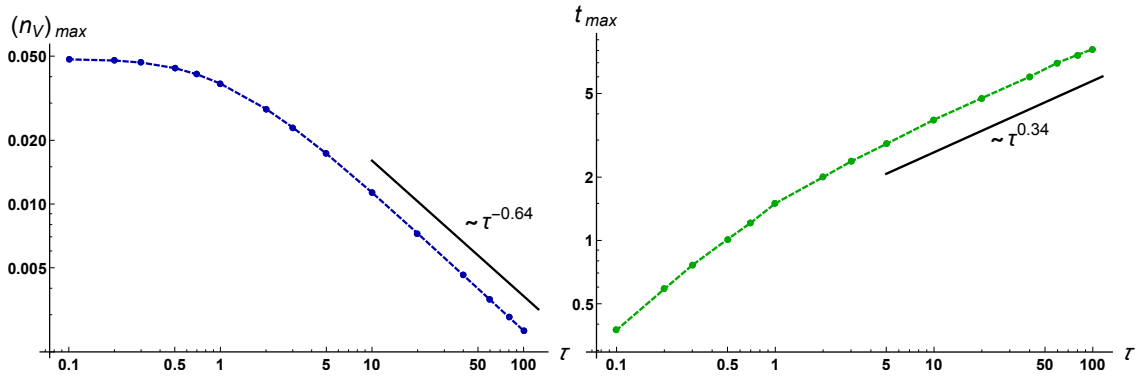

(a) (b)

Figure 9.7: (a) Log-Log plot of the maximum average vortex number density $(n_V)_{\max}$ vs. τ. For larger values of τ the power law manifested is $\sim \tau^{-0.64}$. (b) Log-Log plot of the time at which maximum average vortex number density $(n_V)_{\max}$ occurs $(t_{\max})$ vs. τ. For larger values of τ the power law exhibited is $\sim \tau^{0.34}$.

9.4 Higher Dimensions: Monopoles

Having worked out the details of the $d = 1$ and $d = 2$ cases, it is easy to see that the methods described in the previous sections directly generalize to higher dimensions. Without going into the details of a rigorous proof, the average number density of zero-dimensional topological defects n_D formed in the d dimensional field theory discussed in Sec. 9.1 is given by

$$n_D = d! n_K^d = \frac{d!}{2^{d/2}\pi^d} \left(\frac{m}{t}\right)^{d/2} + \mathcal{O}\left(t^{-(d+2)/2}\right) \tag{9.143}$$

for late times. The factor of $d!$ arises because of permutation symmetry. To get a monopole in d dimensions we need coincident zeros of d fields in a cell of the lattice. As in Sec. 9.3, the point $\Phi = 0$ corresponds to the intersection of d orthogonal domain walls. The $d!$ permutations of the wall positions preserves the $\Phi = 0$ point which leads to the $d!$ prefactor in (9.143).

In Fig. 9.8a we show numerical results for $d = 3$ for the monopole number density as a function of time, obtaining the first term on the right-hand side of (9.143). In

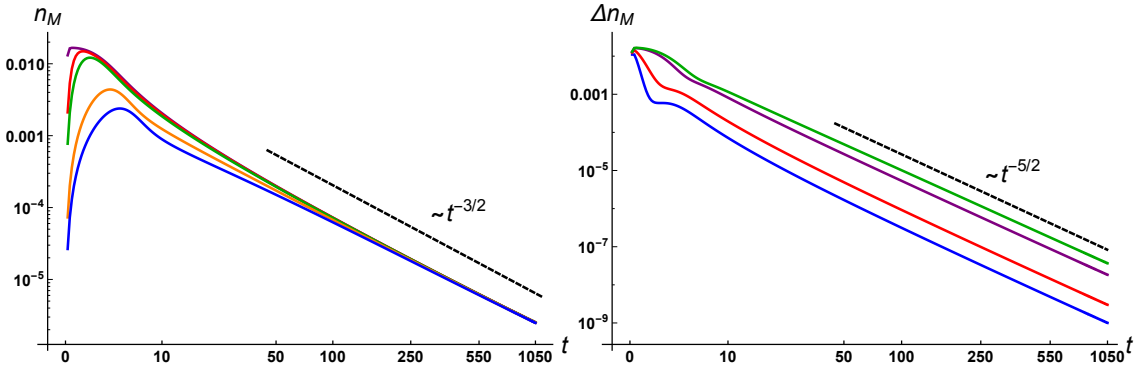

(a) (b)

Figure 9.8: (a) Log-log plot of $n_M(t)$ versus time for τ =0.1 (Purple, topmost curve), 0.5 (Red), 1.0 (Green), 5.0 (Orange), 10.0 (Blue). The black dashed line shows the exhibited power law at late times, *i.e.* $t^{-3/2}$. Here we use $L = 800$, $N = 1600$. (b) Log-log plot of the differences between the average monopole number density for different values of τ, $n_M(t, \tau_1 = 0.1) - n_M(t, \tau_2)$ vs. time for $\tau_2 = 0.5$ (Blue), 1.0 (Red), 5.0 (Purple), 10.0 (Green). The black dashed line shows the exhibited power law, *i.e.* $t^{-5/2}$.

Fig. 9.8b we provide evidence for the second term on the right-hand side of (9.143).

9.5 Effect Of Self-interactions

A key question is to understand the range of parameters for which our results are a good approximation even when $\lambda \neq 0$. We will address this in the context of the model in one spatial dimension given in (9.7). We check for self-consistency of our solution and examine the conditions under which it breaks down.

Our solution for the wavefunction is a Gaussian at all times and so $\langle\phi^4\rangle = 3\langle\phi^2\rangle^2$. With $\lambda \neq 0$, the evolution of the wavefunctional, $\Psi[\phi, t]$, will depend on λ. As long as Ψ can be approximated by a Gaussian centered at $\phi = 0$ we can use the Hartree approximation (*e.g.* Baym (2018)) to write $\lambda\phi^4$ as $3\lambda\langle\phi^2\rangle\phi^2$. Taking into account mass renormalization at lowest order in λ we obtain an effective mass squared $m_2^{\rm eff}(t)$,

$$m_2^{\rm eff}(t) = m_2(t) + \frac{3}{2}\lambda\langle\phi^2\rangle_{\rm in} - \frac{3}{2}\lambda\langle\phi^2\rangle\,. \tag{9.144}$$

where the "in" subscript refers to evaluation at the initial time ($t \to -\infty$). The mass counterterm $3\lambda\langle\phi^2\rangle_{\rm in}/2$ is chosen such that the effective mass equals m at the initial time. Therefore, in the Hartree approximation, the effects of interactions are negligible if the λ dependent corrections to m_2 are small and $m_2^{\rm eff}(t) \approx m_2(t)$, or,

$$3\lambda\left[\langle\phi^2\rangle - \langle\phi^2\rangle_{\rm in}\right] \ll 2|m_2|\,. \tag{9.145}$$

The condition in (9.145) will fail in two circumstances. First, around the time of the phase transition, $t \sim 0$, when $m_2 \sim -m^2 t/\tau$ (see (9.3)) is very small; second, at late times, when $\langle\phi^2\rangle$ grows large. We can make these statements more precise by noticing that (9.145) is strongly violated whenever the function

$$f_{\lambda,\tau}(t) \equiv 2|m_2| - 3\lambda\left[\langle\phi^2\rangle - \langle\phi^2\rangle_{\rm in}\right] \tag{9.146}$$

becomes negative. It turns out that, generically, $f_{\lambda,\tau}$ has three zeros that we denote as t_1, t_2, t_3 and it is negative on the intervals $[t_1, t_2]$ and $[t_3, \infty)$ (see Fig. 9.9 for a qualitative sketch of $f_{\lambda,\tau}$). The late time violation is not important for us as long as by that time all the kinks have already been formed. Moreover their mutual interactions are exponentially suppressed on distances longer than $1/m$ in $d = 1$, and they can be completely neglected given that the average separation of the kinks is larger than $\sim (n_K)^{-1}_{\rm max} \sim 6/m$. On the other hand, the early time violation in the interval $[t_1, t_2]$ can be important as it might interfere with kink production and change the maximum kink number density.

We can thus deduce three necessary conditions for the kink number density in the $\lambda = 0$ model to be a good approximation to that in the $\lambda \neq 0$ case:

(i) The duration of early time violation of (9.145) needs to be finite *i.e.* $t_2 < \infty$.

(ii) All the kinks need to have been produced by the time the late time violation of (9.145) sets in *i.e.* $t_{\rm max} < t_3$

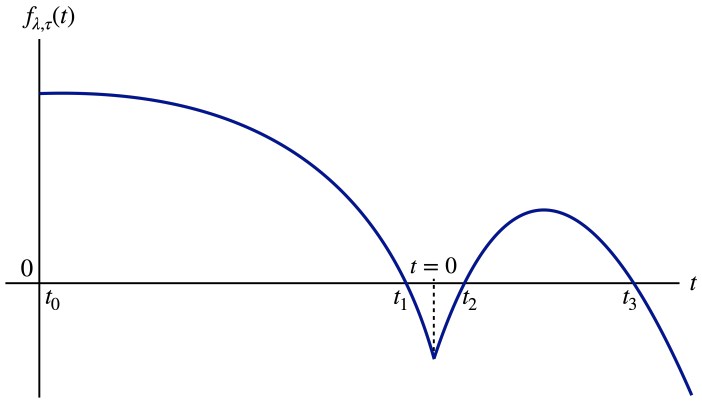

Figure 9.9: Sketch of $f_{\lambda,\tau}(t)$ to show its generic features.

(iii) The duration of the early time violation of (9.145) needs to be much smaller than the fastest timescales of variation of the wave-functional *i.e.* $\Delta t \equiv t_2 - t_1 \ll 1/m$.

We have swept the (λ, τ) parameter space to determine the regions where the above conditions are verified. This has been done numerically by approximating $f_{\lambda,\tau}$ via

$$f_{\lambda,\tau}(t) \approx 2|m_2| - 3\lambda \sum_{n=1}^{N} \left(|c_n(t)|^2 - |c_n(t_0)|^2 \right) , \tag{9.147}$$

and determining the corresponding values of t_1, t_2, t_3 for a wide range of values of λ and τ. The results are shown in Fig. 9.10 where we used the same numerical parameters as in Sec. 9.2.4. The regions shaded in red, orange and pink are excluded by the necessary conditions (i), (ii) and (iii) respectively. Alternatively we expect the $\lambda = 0$ model to be accurate inside the green region. Remarkably, the $\lambda\tau/m = 1$ curve lies deep inside this region which indicates that $\lambda\tau/m \ll 1$ is a sufficient condition for the approximation to be valid.

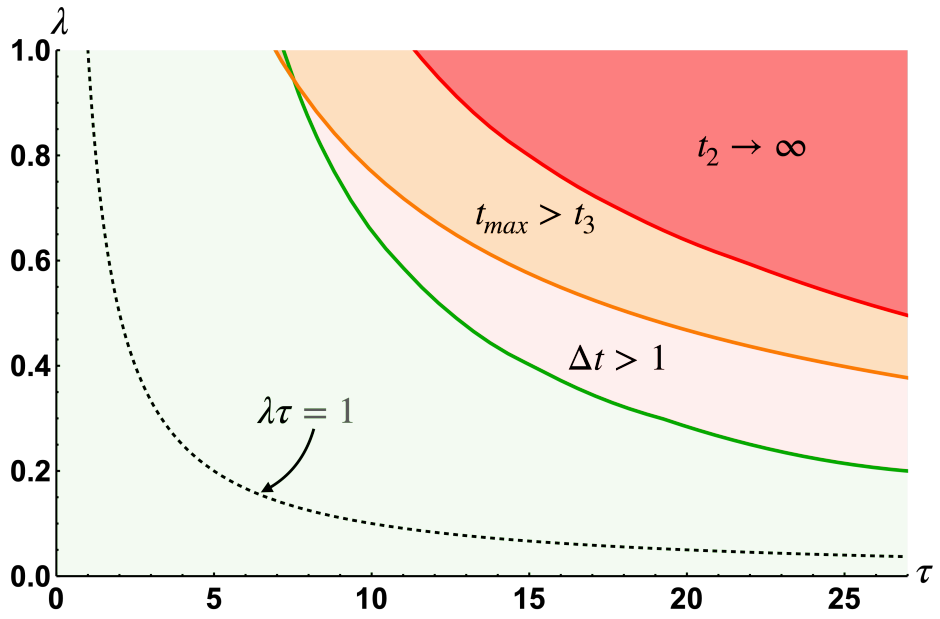

Figure 9.10: Plot showing the allowed and disallowed regions of the (λ, τ) parameter space in units where $m = 1$.

Chapter 10

KINK-ANTIKINK SCATTERING IN A QUANTUM VACUUM

The sine-Gordon equation in one spatial dimension holds a special place in the soliton literature, since it is integrable and allows for the construction of multi-soliton solutions by the use of the Bäcklund transformation. The solitons (or kinks) of the sine-Gordon equation are solutions which interpolate between two successive minima of the potential. The sine-Gordon model has been analyzed in great detail (Rajaraman, 1982; Coleman, 1985; Vachaspati, 2010) and kink-antikink scattering is known to be trivial – the kink and antikink pass through each other albeit with a time delay – a result that holds even when ϕ is treated in quantum field theory. In this chapter, we study kink-antikink scattering in a model where the sine-Gordon scalar field, ϕ, is coupled to a second scalar field, ψ. The kink and antikink propagate in the quantum vacuum of ψ, deforming the vacuum around them. (Alternately, the kink and antikink get dressed by the ψ field.) Upon kink-antikink scattering, ψ particles (wavepackets) are radiated. Depending on the parameters, the quantum radiation of ψ particles can lead to the production of a kink-antikink bound state that is known as a "breather" in the sine-Gordon literature (Rajaraman, 1982; Coleman, 1985; Vachaspati, 2010). In this case, the breather oscillates and continues to radiate ψ particles. (This was more specifically studied in Ref. Olle *et al.* (2019), albeit in a slightly different model.) Surprisingly we find that the breather eventually settles into another oscillating configuration that radiates very slowly, resembling an "oscillon". Oscillons are long-lived localized configurations arising in a variety of scalar field theories and have been shown to emerge naturally in scenarios ranging from preheating to bubble collisions (see e.g. Amin *et al.* (2012); Copeland *et al.* (1995); Gleiser and Sicilia

(2009); Farhi *et al.* (2005); Graham (2007); Zhou *et al.* (2013); Fodor *et al.* (2008); Hiramatsu *et al.* (2021b); Van Dissel and Sfakianakis (2020); Zhang *et al.* (2020); Zhang (2021)).

Our analysis is once again enabled by the "classical-quantum correspondence" (CQC). Quantum backreaction on the classical background is included in the analysis in the semiclassical approximation in which quantum operators occurring in the classical equations of motion are replaced by their dynamical expectation values. Special attention is given to the renormalization issues that arise, since a divergent part of the expectation values contributes to the mass parameter of the background field.

In Sec. 10.1 we introduce the field theoretic model, as well as the equations that will be solved numerically to determine the full dynamics of the kink-antikink collision. We take care to distinguish the no backreaction case, where the kink-antikink background is fixed, from the general case with backreaction. In Secs. 10.2 and 10.3 we outline the results of our numerical analysis: we determine the region of parameter space where a breather-like bound state is formed after the collision and discuss the different phases of its decay. We use natural units where $\hbar = c = 1$ throughout.

10.1 Setup

We work in 1+1 dimensions and consider a sine-Gordon field $\varphi(t, x)$ coupled to a massive scalar field $\psi(t, x)$ according to the Lagrangian density

$$\begin{aligned}\mathcal{L} = &\frac{1}{2}\dot{\varphi}^2 - \frac{1}{2}\varphi'^2 - \frac{m^2}{\kappa^2}(1 - \cos(\kappa\varphi)) + \frac{1}{2}\dot{\psi}^2 - \frac{1}{2}\psi'^2 - \frac{1}{2}\mu^2\psi^2 \\ &- \frac{\lambda}{2}(1 - \cos(\kappa\varphi))\psi^2 \,.\end{aligned} \tag{10.1}$$

Here m, μ are the masses of the two fields, κ is a parameter introduced for future convenience and λ is a coupling constant. We will assume that conditions are such that the φ field can be treated classically, while the ψ field is treated fully quantum mechanically. In general, the (potentially space and time-dependent) classical "back-

ground" field φ excites the quantum "radiation" field ψ, and the excitations of ψ in turn backreact on φ. In the following it will be useful to make the field redefinition $\varphi \to \phi = \kappa\varphi$ and to work with the rescaled field $\phi(t,x)$. With this new field variable, the Lagrangian density becomes

$$\mathcal{L} = \frac{1}{\kappa^2}\left[\frac{1}{2}\dot{\phi}^2 - \frac{1}{2}\phi'^2 - m^2(1-\cos\phi)\right] + \frac{1}{2}\dot{\psi}^2 - \frac{1}{2}\psi'^2 - \frac{1}{2}\mu^2\psi^2 - \frac{\lambda}{2}(1-\cos\phi)\psi^2 \quad (10.2)$$

We see that the coupling between the two fields ϕ and ψ is such that the discrete shift symmetry $\phi \to \phi + 2\pi n$, $n \in \mathbb{Z}$, is maintained.

10.1.1 Neglecting Backreaction

Background dynamics

We start by discussing the limit $\kappa \to 0$ which corresponds to the case where the dynamics of the ϕ field doesn't feel the presence of the radiation field ψ. If ψ is entirely neglected, this is also the limit when ϕ is classical because, in the path integral, $\kappa \to 0$ is equivalent to $\hbar \to 0$. In this "no backreaction" case, the ϕ field equation reduces to the sine-Gordon equation

$$\ddot{\phi} - \phi'' + m^2 \sin\phi = 0\,. \quad (10.3)$$

It is worth mentioning that, in this case, one can define the (conserved) energy of the sine-Gordon field unambiguously by

$$E_\phi = \frac{1}{\kappa^2}\int dx \left[\frac{1}{2}\dot{\phi}^2 + \frac{1}{2}\phi'^2 + m^2(1-\cos\phi)\right]\,, \quad (10.4)$$

and it is easy to see that the $\kappa \to 0$ limit is equivalent to the energy of the sine-Gordon field ϕ being much larger than the (renormalized) vacuum energy of the field ψ. We will come back to this point in Sec. 10.3.

Eq. (10.3) has well-known kink and anti-kink solutions,

$$\phi_\pm(t,x) = \pm 4\arctan\left(e^{\gamma m(x-x_0-v(t-t_0))}\right)\,, \quad (10.5)$$

which describe a soliton (or antisoliton depending on the sign) whose center is at x_0 at time t_0 and which moves to the right with velocity v, with $\gamma = 1/\sqrt{1-v^2}$ being the Lorentz factor. It is worth noting that the energy of this configuration is

$$E_{\pm}(v) = \frac{8\gamma m}{\kappa^2}\,. \tag{10.6}$$

The integrability properties of the sine-Gordon equation allow for the analytical construction of more complicated solutions involving a kink and an antikink. The first one is the so-called *breather* solution which can be understood as a bound state of a kink and an antikink and which reads

$$\phi_{\text{breather}}(t,x) = 4\arctan\left(\frac{\eta\sin(\omega t)}{\cosh(\eta\omega x)}\right)\,. \tag{10.7}$$

Here ω is the angular frequency of the breather and $\eta = \sqrt{m^2-\omega^2}/\omega$. The energy of the breather is

$$E_{\text{breather}} = \frac{16\eta\omega}{\kappa^2} = \frac{16m}{\kappa^2}\sqrt{1-\frac{\omega^2}{m^2}}\,, \tag{10.8}$$

and is seen to be less than the sum of the energy of a static kink and a static antikink.

The other important solution, which will be the main focus of our attention in the remainder of this paper, can be obtained from the breather solution by making the formal substitution $\omega = im\gamma v$. It reads

$$\phi_{K\bar{K}}(t,x) = 4\arctan\left(\frac{\sinh(\gamma m v t)}{v\cosh(\gamma m x)}\right)\,, \tag{10.9}$$

and describes the elastic scattering of a kink and an antikink infinitely separated at $t = -\infty$ and moving towards each other with velocity v. The collision occurs at $t = x = 0$ and the kink and antikink pass through each other with a time delay. As expected, the energy of this field configuration is simply the sum of the energies of a kink and an antikink moving with velocity v,

$$E_{K\bar{K}} = \frac{16\gamma m}{\kappa^2} = 2E_{\pm}(v)\,. \tag{10.10}$$

Having summarized some important features of the sine-Gordon equation, we are ready to study the quantum field ψ living in the background of the latter solution.

Quantum radiation

Integrability of the sine-Gordon model implies that the scattering of a kink-antikink pair is trivial i.e. never forms a bound state, and that a breather never decays. These are classical properties of the sine-Gordon model but they are maintained when taking the quantum fluctuations of the field into account. However, in our case, the classical sine-Gordon field is coupled to an external quantum scalar field and the energy exchange between the classical field configuration and the quantum bath is expected to invalidate these properties.

We thus turn our attention to the quantum radiation that occurs during kink-antikink scattering, equivalently particle production in the time-dependent background $\phi_{K\bar{K}}(t,x)$ given in Eq. (10.9), using the framework of the classical- quantum correspondence (CQC) (Vachaspati and Zahariade, 2018a,b; Olle *et al.*, 2019) that we briefly describe below. Since in the limit $\kappa \to 0$ the dynamics of the background field ϕ is insensitive to the presence of the field ψ, we will work with the truncated Lagrangian density

$$\mathcal{L}_\psi = \frac{1}{2}\dot{\psi}^2 - \frac{1}{2}\psi'^2 - \frac{1}{2}\left\{\mu^2 + \lambda\left[1 - \cos\phi_{K\bar{K}}(t,x)\right]\right\}\psi^2 \,. \tag{10.11}$$

It is easy to understand why this model leads to excitations of the quantum field ψ. Indeed this Lagrangian density describes a free scalar field with a space and time dependent mass-squared $M^2(t,x) = \mu^2 + \lambda\left[1 - \cos\phi_{K\bar{K}}(t,x)\right]$. The non-adiabatic variation of $M^2(t,x)$ will lead to particle production and is expected to occur mostly at the time of kink-antikink collision at $t = 0$.

To study the scattering more quantitatively using numerical methods, we start by

compactifying the spatial dimension on a circle of length L which we then discretize on a regular lattice consisting of N evenly spaced points. The lattice spacing is therefore $a = L/N$. We can further define the discretized field values $\psi_i = \psi(t, -L/2 + ia)$ and $\phi_i = \phi_{K\bar{K}}(t, -L/2 + ia)$ for $i = 1, \ldots, N$, and use the following differencing scheme to estimate the second spatial derivative,

$$\psi''(t, ia) \longrightarrow \frac{\psi_{i+1} - 2\psi_i + \psi_{i-1}}{a^2} \,. \tag{10.12}$$

With these conventions, and after a spatial integration by parts, the Lagrangian of this discretized model can be written as

$$L_{\psi,\text{disc.}} = \frac{a}{2}\dot{\boldsymbol{\psi}}^T.\dot{\boldsymbol{\psi}} - \frac{a}{2}\boldsymbol{\psi}^T.\boldsymbol{\Omega}^2.\boldsymbol{\psi} \,, \tag{10.13}$$

where we have arranged the discretized values of the field ψ in a column vector $\boldsymbol{\psi} = (\psi_1, \psi_2, \ldots, \psi_N)^T$ and introduced the $N \times N$ matrix

$$[\boldsymbol{\Omega}^2]_{ij} = \begin{cases} +2/a^2 + \mu^2 + \lambda\left[1 - \cos\phi_i\right] \,, & i = j \\ -1/a^2 \,, & i = j \pm 1 \pmod N \\ 0 \,, & \text{otherwise} \,. \end{cases} \tag{10.14}$$

In this form, the discretized Lagrangian is immediately seen to describe a collection of N harmonic oscillators (located at each lattice point) coupled to each other via quadratic interactions. The total energy and energy density at each lattice point i for the ψ field in this discretized model are also well-defined and given by[1]

$$H_{\psi,\text{disc.}} = \frac{a}{2}\dot{\boldsymbol{\psi}}^T.\dot{\boldsymbol{\psi}} + \frac{a}{2}\boldsymbol{\psi}^T.\boldsymbol{\Omega}^2.\boldsymbol{\psi} \,, \tag{10.15}$$

$$\mathcal{H}_{\psi,\text{disc.},i} = \frac{1}{2}\dot{\psi}_i^2 + \frac{1}{4a^2}\left[(\psi_{i+1} - \psi_i)^2 + (\psi_i - \psi_{i-1})^2\right] + \frac{1}{2}\left\{\mu^2 + \lambda\left[1 - \cos\phi_i\right]\right\}\psi_i^2 \tag{10.16}$$

[1]Here, in order to get a more accurate discretized estimate of the local gradient energy, the average between its forward differencing and backward differencing approximations is used. This allows us to integrate Eq. (10.16) into Eq. (10.15). Notice however that simply choosing a forward or backward differencing scheme for the estimation of this component of the energy density would also have been consistent.

The next step is to quantize the theory (in the Heisenberg picture) by promoting the discretized field values ψ_i to operators $\hat{\psi}_i$ and introducing the time-dependent matrix $\boldsymbol{Z}$ whose (complex) elements Z_{ij} satisfy the relation

$$\hat{\psi}_i = Z^*_{ij}\hat{a}_j(t_0) + Z_{ij}\hat{a}^\dagger_j(t_0)\,. \tag{10.17}$$

Here the reference time t_0 is chosen so that the background for $t \leq t_0$ can be approximated by a slowly-moving kink-antikink pair separated by a large distance (much larger than their typical size). This is equivalent to specifying a reference vacuum state $|0\rangle$, the state annihilated by all the $\hat{a}_i(t_0)$. (The ladder operators $\hat{a}_i(t_0)$ and $\hat{a}^\dagger_i(t_0)$ refer to the quantum harmonic oscillators located at each lattice point.) Now the dynamics of the field $\hat{\psi}$ is simply given by the Heisenberg equations

$$\ddot{\boldsymbol{Z}} + \boldsymbol{\Omega}^2.\boldsymbol{Z} = 0\,, \tag{10.18}$$

with initial conditions

$$\boldsymbol{Z}(t_0) = -\frac{i}{\sqrt{2a}}\boldsymbol{\Omega}(t_0)^{-1/2} \quad \text{and} \quad \dot{\boldsymbol{Z}}(t_0) = \frac{1}{\sqrt{2a}}\boldsymbol{\Omega}(t_0)^{1/2}\,. \tag{10.19}$$

Since Ω^2 is a symmetric positive definite matrix, $\Omega^{\pm 1/2}$ is computed by first diagonalizing Ω^2 and then applying the desired power function to its positive eigenvalues. Notice that these initial conditions only define the vacuum of the theory unambiguously when the background $\boldsymbol{\Omega}^2(t)$ is approximately constant for $t \leq t_0$. In other words if the time evolution of the background before the time t_0 is adiabatically slow, a different choice of initial time smaller than t_0 will not modify the quantum dynamics. More precisely the initial conditions (10.19) define the 0-th order adiabatic vacuum (which corresponds to the lowest order approximation of the mode functions within the WKB approximation (Birrell and Davies, 1984)). In particular, if the background is such that no t_0 obeying the required properties can be found, then we can expect

spurious excitations of the field ψ to occur and one should strive to minimize them. In the case at hand, the kink and antikink are moving towards each other with velocity v at $t = -\infty$ and we find ourselves exactly in the latter situation. However, we expect that for small v (in practice less than 0.3) the initial conditions (10.19) will still give reasonable results (and we will come back to this later in Sec. 4.3).

Observables

The evolution of ψ is given by the system of equations given in matrix form in Eq. (10.18). Initialized by Eqs. (10.19), they are particularly simple and they can readily be solved numerically. Moreover, the Z_{ij} variables allow for the easy computation of various observable quantities of interest. For example, the expression for the vacuum expectation value of the energy in the radiation field can be written as

$$E_\psi \equiv \langle 0|\hat{H}_{\psi,\text{disc.}}|0\rangle = \frac{a}{2}\text{Tr}\left[\dot{\boldsymbol{Z}}^\dagger.\dot{\boldsymbol{Z}} + \boldsymbol{Z}^\dagger.\boldsymbol{\Omega}^2.\boldsymbol{Z}\right] . \tag{10.20}$$

This is equal to the total (classical) energy in the Z_{ij} variables. Similarly, the vacuum expectation value of the energy density at the i-th lattice point is

$$\begin{aligned}\rho_{\psi,i} &\equiv \langle 0|\hat{\mathcal{H}}_{\psi,\text{disc.},i}|0\rangle \\ &= \sum_{j=1}^{N}\Bigg(\frac{1}{2}|\dot{Z}_{ij}|^2 + \frac{1}{4a^2}\left[|Z_{i+1,j} - Z_{ij}|^2 + |Z_{ij} - Z_{i-1,j}|^2\right] \\ &+ \frac{1}{2}\left\{\mu^2 + \lambda\left[1 - \cos\phi_i\right]\right\}|Z_{ij}|^2\Bigg) .\end{aligned} \tag{10.21}$$

Moreover the spatial two-point function of the radiation field can be written as

$$C_{ij} \equiv \langle 0|\hat{\psi}_i\hat{\psi}_j|0\rangle = \sum_{k=1}^{N} Z^*_{ik}Z_{jk} . \tag{10.22}$$

In order to render these expressions insensitive to the discretization scale a, we first renormalize the spatial two-point function by subtracting its $\lambda = 0$ counterpart,

$$C^{(R)}_{ij} = C_{ij} - C_{ij}|_{\lambda=0} , \tag{10.23}$$

and then use it to renormalize the λ-dependent part of the energy and energy density. This procedure is closely related to point-splitting (Birrell and Davies, 1984). The resulting renormalized quantities are thus

$$\rho^{(R)}_{\psi,i} = \rho_{\psi,i} - \frac{1}{2}\lambda\left[1-\cos\phi_i\right] C_{ii}|_{\lambda=0} - \rho_{\psi,i}|_{\lambda=0} \ , \tag{10.24}$$

$$E^{(R)}_{\psi} = E_{\psi} - \sum_{i=1}^{N} \frac{a}{2}\lambda\left[1-\cos\phi_i\right] C_{ii}|_{\lambda=0} - E_{\psi}|_{\lambda=0} \ . \tag{10.25}$$

In both these equations, the last term corresponds to the subtraction of the (constant) zero-point energy.

We can therefore compute any quantity of interest for the study of ψ particle production in the $\phi_{K\bar{K}}$ background by studying the classical dynamics of the variables Z_{ij} (with well-chosen initial conditions). We thus trade N real quantum variables (corresponding to the discretized field values ψ_i) for $N\times N$ complex classical variables (the Z_{ij}). This is the essence of the CQC and it is closely related to the mode function and Bogoliubov coeffcient methods (Vachaspati and Zahariade, 2018b).

Initial conditions and vacuum structure

The renormalized energy density observable $\rho^{(R)}_{\psi,i}$ allows us to visualize the vacuum structure of the quantum field ψ. Fig. 10.1 shows the renormalized energy density in the ψ field at the initial time superimposed over the background kink-antikink profile. (The parameter a will always be chosen such that the lattice provides a good approximation of the continuum limit and therefore we will liberally identify the discretized quantities $\rho^{(R)}_{\psi,i}(t)$ and $\phi_i(t)$ to their continuous counterparts $\rho^{(R)}_{\psi}(t,x)$ and $\phi(t,x)$ for $x=-L/2+ia$.) We see that the presence of the background induces a dip in the energy density around the kink and antikink, akin to two clouds of ψ particles. The width of these clouds is set by the kink and antikink width i.e. $1/m$. However, as shown in Fig. 10.2, the depth of the underdensities depends on the coupling λ and

the mass of the ψ field μ. In particular, the trough of the ψ energy density around the kink-antikink position increases for larger λ and smaller μ. Moreover, for some parameters, the energy density of ψ shows some non-trivial features that reflect the relevance of the additional length scales μ^{-1} and $\lambda^{-1/2}$.

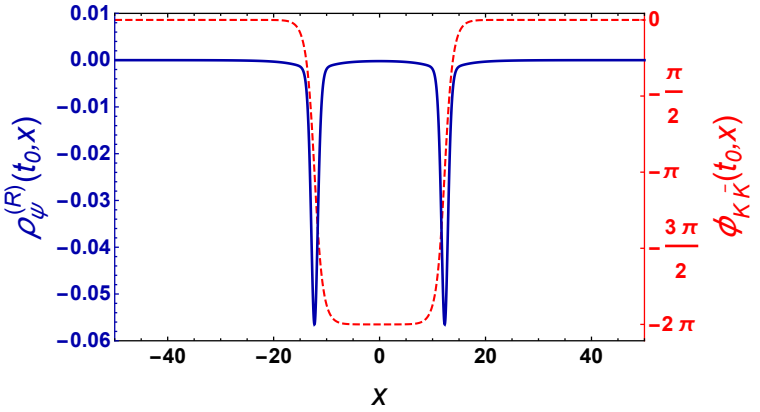

Figure 10.1: Example of the renormalized initial energy density in ψ and the initial kink-antikink profile. The kinks are dressed in ψ particles whose energy within the kink is lower than that outside the kink, *i.e.* they form bound states. The kink-antikink profile is shown as a red dashed line (vertical scale on the right) and the clouds of ψ particles (represented by the renormalized energy density of ψ) are shown in dark blue (vertical scale on the left). The parameters are $L = 100$, $N = 500$, $m = 1$, $v = 0.1$, $\mu = 0.1$, $\lambda = 0.3$, $\kappa \to 0$ and the initial time is chosen as $t_0 = -100$.

10.1.2 Including Backreaction

The results above assumed that backreaction can be neglected. This is certainly a good approximation when κ is small but what happens when backreaction can no longer be neglected? This constitutes the main part of this work, to which we now turn.

We thus consider the case $\kappa \neq 0$ so that the field equation for the ϕ field gets a contribution from the ψ field:

$$\ddot{\phi} - \phi'' + \left(m^2 + \frac{\lambda\kappa^2}{2}\psi^2\right)\sin\phi = 0\,. \tag{10.26}$$

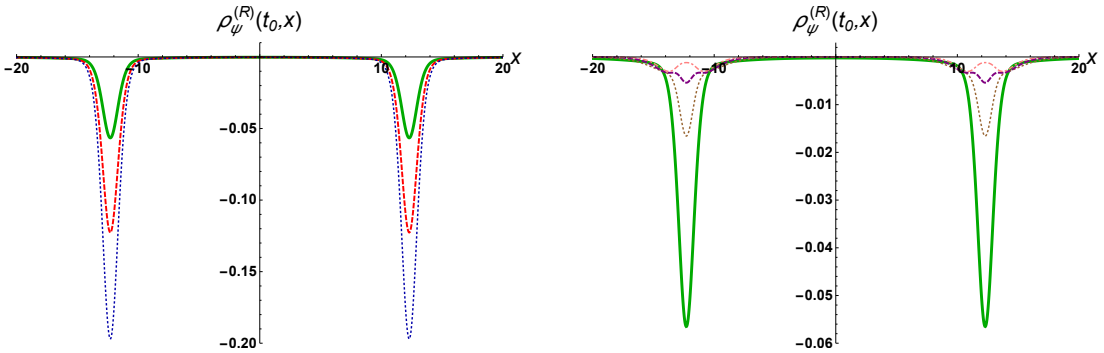

Figure 10.2: (a) Renormalized initial energy density in ψ ($\rho_\psi^{(R)}$) for various values of λ: 0.3 (solid green), 0.5 (dashed red), 0.7 (dotted dark blue) for $\mu = 0.1$. (b) Renormalized initial energy density in ψ for various values of μ: 0.1 (solid green), 0.3 (dotted brown), 0.5 (dashed purple), 0.7 (dot-dashed pink) for $\lambda = 0.3$. The other parameters are $L = 100$, $N = 500$, $m = 1$, $v = 0.1$, $\kappa \to 0$ and the initial time is $t_0 = -100$. Note that the solid green lines correspond to the same set of parameters ($\lambda = 0.3$, $\mu = 0.1$) in both the panels.

Of course this equation is fully classical and one would need to decide how the quantum excitations in the ψ field couple to the classical background ϕ by modifying the coupling term proportional to $\psi^2 \sin\phi$. The most straightforward way is to use the semiclassical approximation[2] which simply entails replacing $\psi(t,x)^2$ by $\langle 0|\hat{\psi}(t,x)^2|0\rangle$. Therefore the ϕ field equation becomes

$$\ddot{\phi} - \phi'' + \left(m^2 + \frac{\lambda\kappa^2}{2}\langle 0|\hat{\psi}^2|0\rangle\right)\sin\phi = 0\,. \tag{10.27}$$

To make contact with the methods described in the previous section, we need the discretized version of this equation,

$$\ddot{\phi}_i - \frac{1}{a^2}(\phi_{i+1} - 2\phi_i + \phi_{i-1}) + \left(m^2 + \frac{\lambda\kappa^2}{2}\langle 0|\hat{\psi}_i^2|0\rangle\right)\sin\phi_i = 0\,, \tag{10.28}$$

[2]Another procedure for incorporating backreaction is based on the stochastic method, where the initial conditions for the field ψ are sampled from a distribution similar to Eq. (10.19). Several simulations, each with different samples for the initial conditions, would be performed and then averaged. We leave the interesting comparison between the two methods for future work.

where $\phi_i = \phi(t, -L/2 + ia)$ is not given by the non-dynamical kink-antikink solution $\phi_{K\bar{K}}$ anymore, rather it will have to be solved for subject to the initial conditions $\phi_i(t_0) = \phi_{K\bar{K}}(t_0, -L/2 + ia)$ and $\dot{\phi}_i(t_0) = \dot{\phi}_{K\bar{K}}(t_0, -L/2 + ia)$. Solving Eq. (10.28) requires being able to compute the dynamics of the quantity $\langle 0|\hat{\psi}_i^2|0\rangle$. This can be done by using the results of the previous section and in particular Eq. (10.22) to make the substitution

$$\langle 0|\hat{\psi}_i^2|0\rangle = \sum_{j=1}^{N} |Z_{ij}|^2 \tag{10.29}$$

with Z_{ij} given by Eqs. (10.18) and (10.19), where background field values ϕ_i in the definition of $\mathbf{\Omega}^2$ are replaced by the corresponding dynamical values. Because $\sum_{j=1}^{N} |Z_{ij}|^2$ is a 1+1 dimensional two-point function in the coincident point limit, in other words C_{ii} given in Eq. (10.22), it is logarithmically sensitive to the discretization scale a, and it would produce infinite backreaction in the continuum limit (Vachaspati and Zahariade, 2018a,b; Olle *et al.*, 2019). This can be remedied by noticing that the parameter m appearing in the field equations is actually the bare mass of the sine-Gordon field, and using it to renormalize the divergence. We therefore define the physical mass $m_{\rm phys}$ of the sine-Gordon field by

$$m^2 = m_{\rm phys}^2 - \frac{\lambda\kappa^2}{2}\sum_{j=1}^{N} |Z_{ij}|^2\Big|_{\lambda=0} = m_{\rm phys}^2 - \frac{\lambda\kappa^2}{4a}\left[\mathbf{\Omega}_0^{-1}\right]_{ii} = m_{\rm phys}^2 - \frac{\lambda\kappa^2}{4L}\,\mathrm{Tr}\,\mathbf{\Omega}_0^{-1}\,. \tag{10.30}$$

Here, in the second equality, we used the fact that, when $\lambda = 0$, $\mathbf{\Omega}^2(t) \equiv \mathbf{\Omega}_0^2$ is a constant matrix, and therefore Eq. (10.18) has the simple solution

$$\boldsymbol{Z}(t) = -\frac{i}{\sqrt{2a}} e^{i\mathbf{\Omega}_0(t-t_0)}\mathbf{\Omega}_0^{-1/2}\,. \tag{10.31}$$

Moreover in the third equality of Eq. (10.30) we use the fact that all the diagonal coefficients of the $\mathbf{\Omega}_0^{-1}$ matrix are equal to each other (see Eq. (10.14)). Overall this procedure is equivalent to replacing the two-point function C_{ii} by its renormalized counterpart $C_{ii}^{(R)}$ in Eq. (10.28), and m by $m_{\rm phys}$ in every equation where it appears.

Notice that, in the non-backreacting case ($\kappa \to 0$), the bare mass m and the physical mass $m_{\rm phys}$ are one and the same. Henceforth, we will simply choose $\kappa = 1$ when taking backreaction into account.

Summing up, the backreacted dynamics (within the semiclassical approximation) are given by the system of coupled differential equations

$$\ddot{\phi}_i - \frac{1}{a^2}(\phi_{i+1} - 2\phi_i + \phi_{i-1}) + \left[m^2_{\rm phys} + \frac{\lambda\kappa^2}{2} \sum_{j=1}^{N} \left(|Z_{ij}|^2 - |Z_{ij}|^2\big|_{\lambda=0} \right) \right] \sin\phi_i = 0 \,, \quad (10.32)$$

and

$$\ddot{\boldsymbol{Z}} + \boldsymbol{\Omega}^2 \boldsymbol{Z} = 0 \,, \quad (10.33)$$

with initial conditions

$$\phi_i(t_0) = \phi_{K\bar{K}}(t_0, -L/2 + ia) \,, \qquad \dot{\phi}_i(t_0) = \dot{\phi}_{K\bar{K}}(t_0, -L/2 + ia) \,, \quad (10.34)$$

$$\boldsymbol{Z}(t_0) = -\frac{i}{\sqrt{2a}} \boldsymbol{\Omega}(t_0)^{-1/2} \,, \qquad \dot{\boldsymbol{Z}}(t_0) = \frac{1}{\sqrt{2a}} \boldsymbol{\Omega}(t_0)^{1/2} \,, \quad (10.35)$$

where we recall that

$$\phi_{K\bar{K}}(t, x) = 4 \arctan\left(\frac{\sinh(\gamma m_{\rm phys} v t)}{v \cosh(\gamma m_{\rm phys} x)} \right) \quad (10.36)$$

and where the matrix $\boldsymbol{\Omega}^2$ defined in Eq. (10.14) depends on the fully dynamical background $\phi_i(t)$. Note that the mass of the ϕ field used in the initial conditions is the physical mass $m_{\rm phys}$, as shown in the above equation.

Before discussing the results of our simulations, let us say a few words about the observables that we are going to use in our study of particle production and the associated backreaction during kink-antikink collisions. These need to accurately account for the energy exchanged between the background and the quantum radiation bath. Of course, in general, in a fully interacting theory it is impossible to separate the energy of a particular subsystem. However, as long as the coupling λ is not too big (smaller than $m^2_{\rm phys}$ in practice) we can assume that Eqs. (10.25) and (10.24) still

provide a useful measure of the (renormalized) energy, respectively energy density, in the quantum field ψ. Under these assumptions, the energy in the kink-antikink background is given by

$$E_\phi \equiv \frac{a}{\kappa^2}\sum_{i=1}^{N}\left[\frac{1}{2}\dot{\phi}_i^2 + \frac{1}{4a^2}\left[(\phi_{i+1}-\phi_i)^2+(\phi_i-\phi_{i-1})^2\right] + m_{\rm phys}^2(1-\cos\phi_i)\right] . \quad (10.37)$$

Notice that the total (conserved) energy of the coupled system is given by

$$E = E_\phi + E_\psi^{(R)} , \quad (10.38)$$

where E_ϕ and $E_\psi^{(R)}$ are given by Eq. (10.37) and Eq. (10.25) respectively.

10.2 Results

In this section we present our numerical results. We will always work in units where $m_{\rm phys} = 1$. which is equivalent to rescaling space, time, μ and λ by $m_{\rm phys}$. Our lattice is a circle of physical size $L = 100$ and is sampled by $N = 500$ equally spaced points ($a = 0.2$). We use an explicit Crank-Nicholson method with two iterations to solve the system of coupled ordinary differential equations given in Eqs. (10.32) and (10.33) with the initial conditions of Eqs. (10.34) and (10.35). The initial time is taken to be $t_0 = -100$. Because most interesting effects are expected to occur at or around the time of collision, $t = 0$, and to make sure that finite lattice size effects don't spoil any physical effects, we only evolve the equations for one light-crossing time after the collision i.e. up to $t = L = 100$. We have also made sure that the results do not strongly depend on the UV and IR cutoffs ($a = L/N$ and L) and that our renormalization scheme is sufficient to eliminate any UV sensitivity (see Fig. G.3). Of course, decreasing a would improve the resolution of the simulations but, given the N^2 complexity of the code, this is not feasible without significantly more computational cost. Similarly a larger lattice would allow us to track the dynamics of the system for

a longer time but maintaining spatial resolution would again require a corresponding increase in N. In the current work, energy non-conservation due to numerical error *over the whole duration of time evolution* is of the order of 0.1%.

The range over which we will vary the different parameters λ, v and μ will depend on numerical accuracy as well as on the intrinsic limitations of our model. To avoid strong coupling effects we will be allowing λ to vary between 0 and 1. Since our initial conditions for the Z_{ij} variables are strictly only valid when the background is adiabatically varying, we limit ourselves to velocities v smaller than 0.3.[3] Moreover, we require the kink-antikink pair to be well-separated at the initial time t_0 which, because of the finite size of our periodic lattice, limits the range of v to the interval $(0.05, 0.4)$. Since the background field ϕ is assumed to behave classically, its mass m_{phys} is expected to be larger than the mass of the radiation field ψ. Thus μ is constrained to be smaller than 1.

We start by presenting the two qualitatively different possible outcomes of the inelastic kink-antikink scattering studied in this paper: pure scattering, or formation of a bound state, *i.e.* a breather-like structure. Then we will discuss what role the different parameters of the model play in the occurrence of these two outcomes.

10.2.1 Scattering Or Formation Of A Bound State

In Fig. 10.3 we show the renormalized energy density in the ψ field as a function of x (horizontal axis) and t (vertical axis) with and without backreaction for two different sets of parameters. The color coding represents the value of the energy density from its minimum value in dark blue to its maximum value in bright red. Since

[3] Because of this violation of adiabaticity at $t = t_0$, a small amount of spurious particle production is observed for the $v = 0.3$ case but the corresponding dissipated energy is of the order of 0.1% of E_ϕ which can safely be neglected.

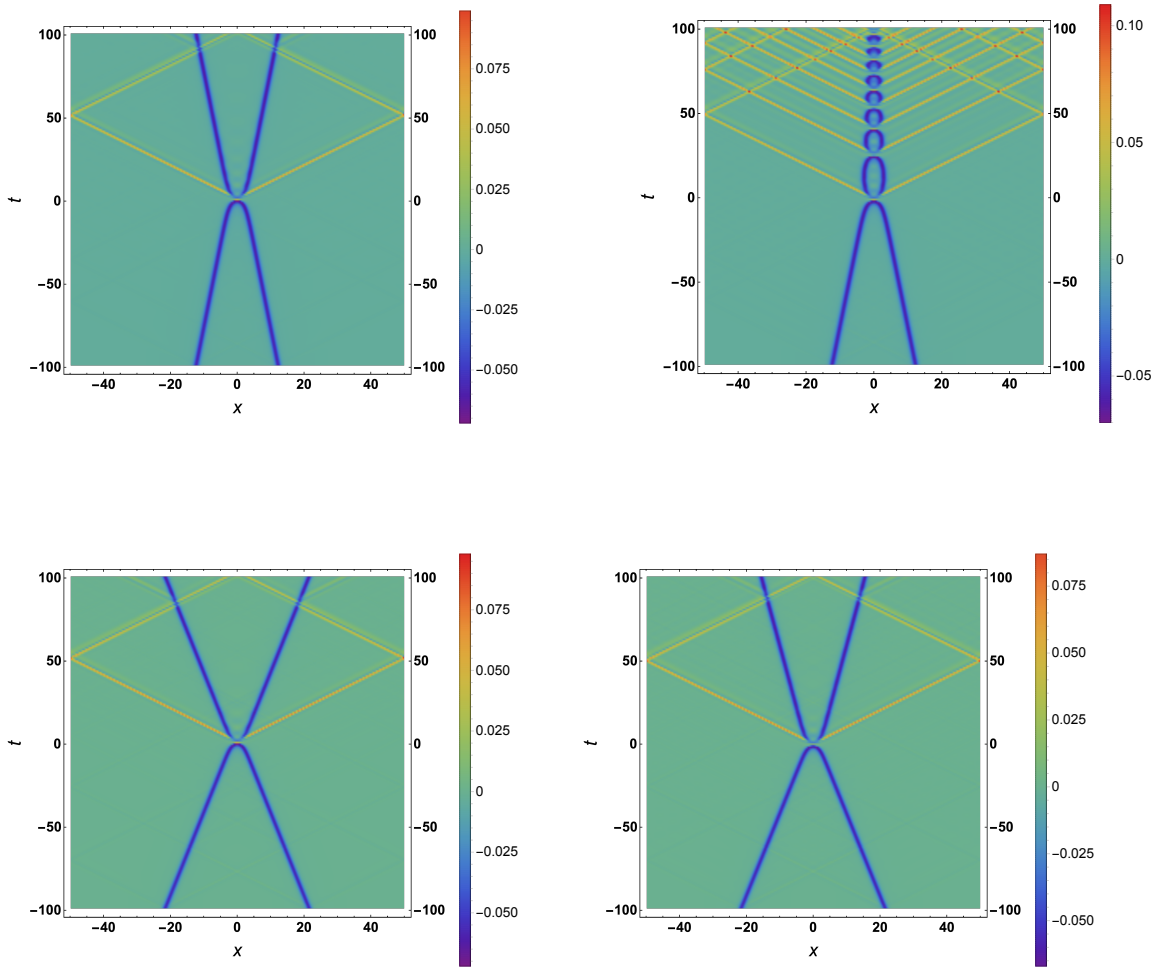

Figure 10.3: Time evolution of the renormalized energy density in ψ ($\rho_\psi^{(R)}$). (a) For, $\kappa \to 0$, i.e., no backreaction; $v = 0.1$, $\lambda = 0.3$; (b) For, $\kappa = 1$, i.e., with backreaction; $v = 0.1$, $\lambda = 0.3$. (c) For, $\kappa \to 0$, i.e., no backreaction; $v = 0.2$, $\lambda = 0.3$; (d) For, $\kappa = 1$, i.e., with backreaction; $v = 0.2$, $\lambda = 0.3$. The universal parameters are $L = 100$, $N = 500$, $\mu = 0.1$, $m_{\rm phys} = 1$, and $t_0 = -100$. The collision happens at $t = 0$. The animations corresponding to the different cases can be found at https://sites.google.com/asu.edu/mainakm.

the clouds of ψ particles (thick dark blue lines) track the kink and antikink perfectly, this representation is particularly well suited for visualizing both the dynamics of the kink-antikink background and any radiation bursts (thin orange lines) occurring during their collision. It serves as an accurate spacetime diagram of the collision. The first thing we notice, in Figs. 10.3a and 10.3c, is that when $\kappa \to 0$ i.e. when backreaction is neglected, the kink and antikink dynamics are unperturbed by the collision (as they should be); there are however two bursts of radiation originating and $x = t = 0$ i.e. at the collision, and propagating away from the kink-antikink pair (one to the left the other to the right) at or near the speed of light. When reaching the end of the lattice they wrap around and come back towards the center by virtue of the periodic boundary conditions. The origin of the bursts of radiation can be explained intuitively by the high degree of non-adiabaticity of the background at the moment of collision.

More interestingly, Figs. 10.3b and 10.3d, including backreaction effects, show two radically distinct behaviors. In Fig. 10.3d, the parameters are such that the collision does not lead to the formation of a bound state. Just like in the non-backreacting case of Fig. 10.3c, the clouds of ψ particles tracking the kink-antikink pair describe an X-like pattern: they are seen to converge, collide and subsequently diverge from one another. The collision is again accompanied by the emission of two bursts of radiation. However, unlike in Fig. 10.3c, the outgoing relative velocity of the kink-antikink pair in Fig. 10.3d is smaller than the initial velocity as background kinetic energy has been converted in quantum radiative energy. In Fig. 10.3b, the parameters are such that the collision leads to the formation of a breather-like kink-antikink bound state. The cactus (or caterpillar) pattern described by the clouds of ψ particles after the initial collision at $t = 0$ represents the multiple subsequent collisions that the kink and antikink undergo, each accompanied by a burst of radiative energy. The first

burst of energy depletes enough kinetic energy that the kink and antikink are not able to break away from their mutual attraction and must form a bound state. We will study the evolution of the energy in ϕ, E_ϕ, in more detail in the next subsection.

10.2.2 Parameter Dependence Of The Outcome Of The Collision

To understand the influence of the parameters of the model on the dynamics of the collision (with backreaction taken into account), we turn our attention to the energy in the kink-antikink pair. In Figs. 10.4, 10.5 and 10.6 we plot E_ϕ as a function of time for different values of the parameters v, λ and μ. We can make a few general comments before going into the details of the plots. First we notice that before the collision E_ϕ is constant, which is to be expected because the kink and antikink are effectively decoupled until their relative distance becomes of the order of the kink width $1/m_{\text{phys}}$. At the collision, the energy decreases abruptly which corresponds to the initial burst of radiation seen in the previous subsection. The energy then quickly stabilizes to a new plateau. If the value of this new energy plateau is larger than the energy of a static kink-antikink pair i.e. $2E_\pm(0) = 16m_{\text{phys}}$, then a breather-like object does not form and the kink-antikink pair remains unbound after the collision (E_ϕ remains constant after the collision). On the contrary, if the first burst of energy is large enough to make the value of the energy plateau fall below this threshold energy, then a bound state is formed. This is followed by a cascade of subsequent bursts of energy that lead to the decay of E_ϕ into lower and lower plateaus of shorter and shorter duration. This cascade is readily understood. After the first collision, the kinks separate out more than their widths which leads to the formation of an energy plateau (because kinks radiate only when they overlap). Eventually though, after a certain number of subsequent collisions, they don't manage to separate out and the plateau shape is lost. The radiation thus transitions through different behaviors

which we will discuss in more detail in the next section.

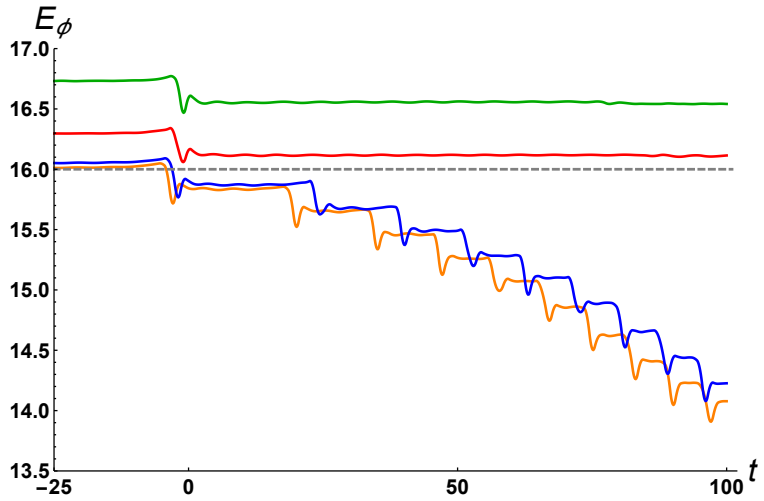

Figure 10.4: The energy in the background ϕ (E_ϕ) as a function of time for various values of v: 0.07 (Orange), 0.1 (Blue), 0.2 (Red) and 0.3 (Green). The other parameters are $L = 100$, $N = 500$, $\mu = 0.1$, $m_{\text{phys}} = 1$, $\lambda = 0.3$, $\kappa = 1$ and $t_0 = -100$. The gray dashed line corresponds to $E_\phi = 16$.

Figure 10.4 shows E_ϕ for $\lambda = 0.3$, $\mu = 0.1$, and varying v. The higher the initial relative velocity v the bigger the gap to the threshold energy of bound state formation, $\Delta_{\text{gap}} \equiv 16(\gamma - 1)m_{\text{phys}}$, as seen from Eq. (10.10). We notice that the energy of the first radiation burst doesn't depend strongly on v (see Appendix G) and therefore, as long as it is larger than Δ_{gap}, a breather-like object is formed. This happens in particular for $v = 0.2$ and $v = 0.3$.

Figure 10.5 shows E_ϕ for $v = 0.2$, $\mu = 0.1$, and varying λ. Here, the energy of the first radiation burst increases with λ (it approximately scales as $\lambda^{1.6}$ for the range of parameters considered here) and exceeds Δ_{gap} for $\lambda = 0.5$ and $\lambda = 0.7$, when a breather-like object forms. In the $\lambda = 0.7$ and $\lambda = 0.9$ cases we notice a peculiar change of behavior in E_ϕ around $t = 70$ when the cascading decay becomes an oscillatory decay with a smaller average slope. The bound state then appears to settle to a long-lived, weakly radiating, oscillon-like object. We will come back to this

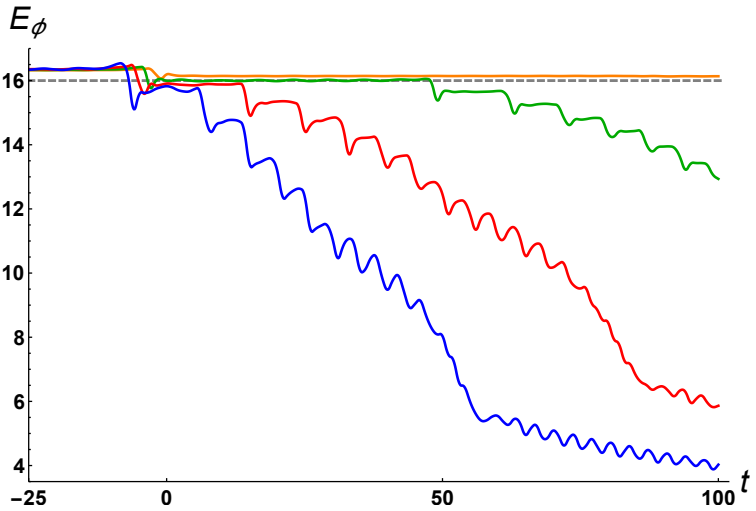

Figure 10.5: The energy in the background ϕ (E_ϕ) as a function of time for various values of λ: 0.3 (Orange), 0.5 (Green), 0.7 (Red) and 0.9 (Blue). The other parameters are $L = 100$, $N = 500$, $\mu = 0.1$, $m_{\text{phys}} = 1$, $v = 0.2$, $\kappa = 1$ and $t_0 = -100$. The gray dashed line corresponds to $E_\phi = 16$.

intriguing configuration in the next section.

Figure 10.6 represents E_ϕ for $v = 0.1$, $\lambda = 0.3$, and varying μ. Here we notice that the lighter the ψ field, the stronger the initial radiation burst after collision (it scales as $\exp(-1.8\mu)$). This is readily understood, as a light field is more easily excited by the time-dependent background. For $\mu \leq 0.5$, a breather-like object forms since the kink-antikink pair releases an energy greater than Δ_{gap} at the collision.

We can even go further and determine the region of (λ, v, μ) parameter space where a breather-like object forms, i.e. the region where the first burst of energy at the collision is larger than Δ_{gap}. We expect that the boundary between the region where a bound state forms and the one where the kink-antikink pair remains unbound after collision, to approximately look like a two-dimensional surface. However, since our determination of Δ_{gap} is imperfect, particularly because the first energy plateau after collision exhibits small oscillations (as can be seen for instance in Figs. 10.4, 10.5 and 10.6), the boundary will necessarily have a thickness. To estimate this thickness

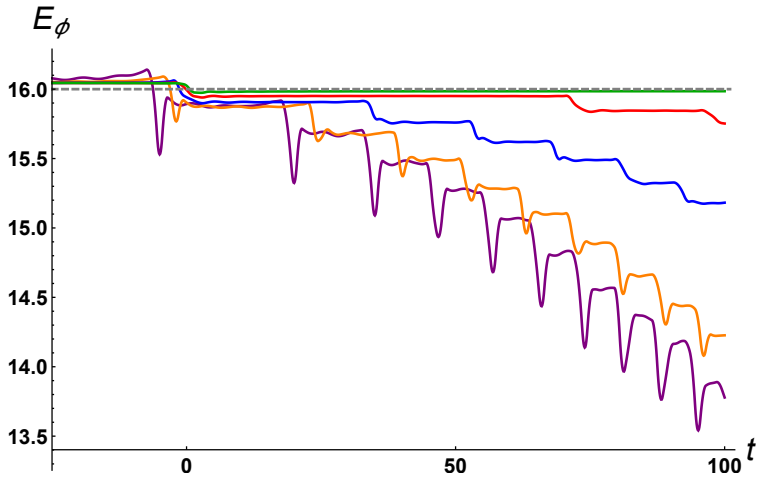

Figure 10.6: The energy in the background ϕ (E_ϕ) as a function time for various values of μ: 0.01(Purple), 0.1 (Orange), 0.3 (Blue), 0.5 (Red) and 0.7 (Green). The other parameters are $L = 100$, $N = 500$, $\lambda = 0.3$, $m_{\text{phys}} = 1$, $v = 0.1$, $\kappa = 1$ and $t_0 = -100$. The gray dashed line corresponds $E_\phi = 16$.

we determine the characteristic amplitude of the small oscillations around the first energy plateau in the worst case scenario (by computing the standard deviation from the mean value σ_{max} in this case) and we conservatively declare that a first energy burst equal to Δ_{gap} with a margin of error of $\pm 2\sigma_{\text{max}}$ doesn't allow us to definitively determine whether a bound state forms or not. Here $\sigma_{\text{max}} = 0.027$. In Fig. 10.7 we show the results of a parameter scan with resolution of 0.25 in λ, 0.01 in v and 0.2 in μ.

10.3 Decay Of The Bound State

We have already seen that, when the parameters of the problem are such that a bound-state forms as a consequence of the kink-antikink collision, the radiation goes through different phases. In this section we highlight two of those phases: the fast decay phase where radiation is emitted via successive energy bursts, and the oscillon phase which is weakly radiating and quasi-stable.

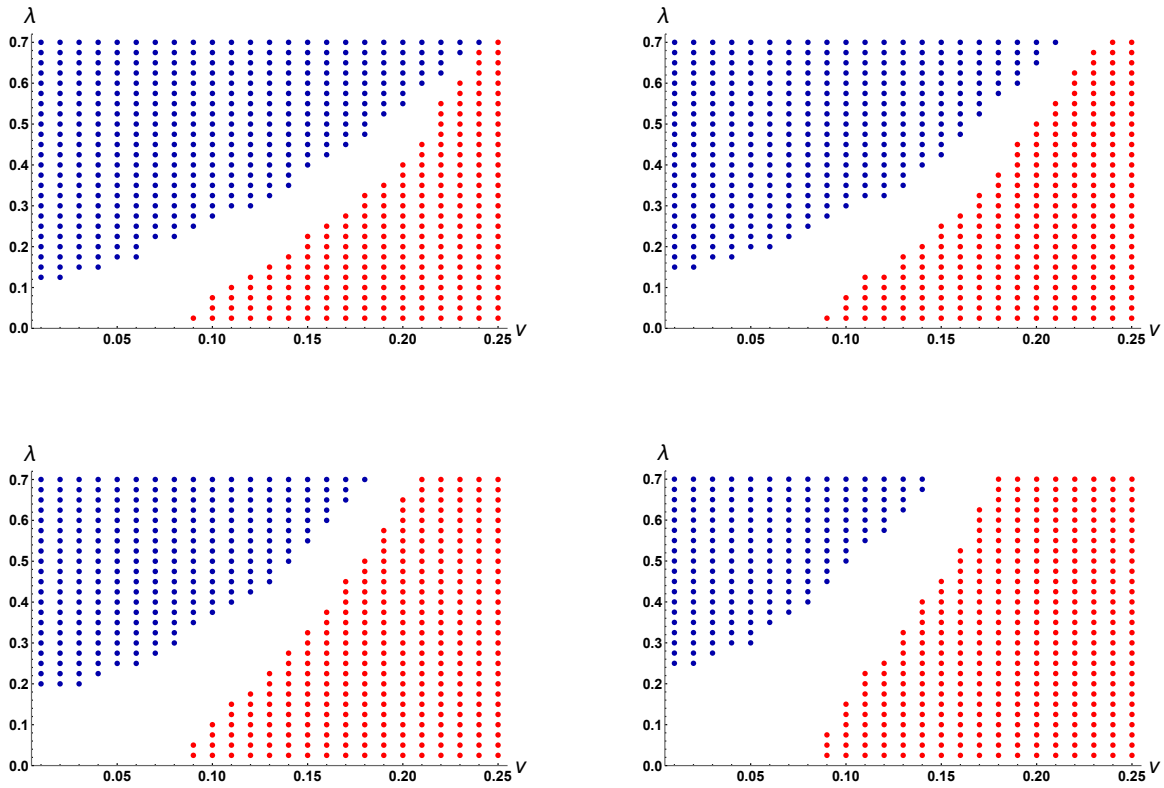

Figure 10.7: Plots showing a parameter scan of the $\lambda - v$ plane for different values of μ: (a) $\mu = 0.1$, (b) $\mu = 0.3$, (c) $\mu = 0.5$, and (d) $\mu = 0.7$. The dark blue points represent a breather-like object being formed. The blank space denotes the region of uncertainty where a breather-like object may or may not form. The red points denote where a breather-like object does not form. The other parameters are $L = 100$, $N = 500$, $\kappa = 1$, and $m_{\text{phys}} = 1$. Because of the long computation time required to generate these plots, we exceptionally choose $t_0 = -50$.

10.3.1 The Energy Plateau Phase: Decay Of The Breather-like Object

In cases where the kink and antikink scatter to form a bound state, we observed that there is a cascade of bursts of radiation at decreasing time intervals. In this subsection we focus on the blue curve in Fig. 10.4 corresponding to the choice of parameters $\lambda = 0.3$, $\mu = 0.1$ and $v = 0.1$. This case features particularly well-defined energy plateaus and lends itself to further analysis. We plot $E_{\phi}^{(n)}$, the energy after

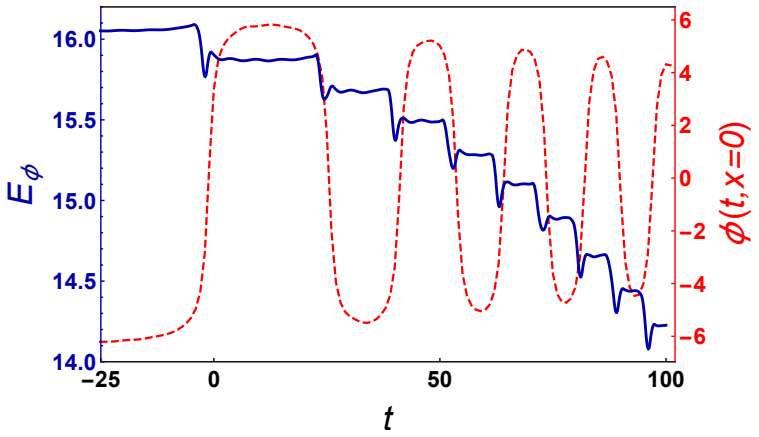

Figure 10.8: Plot of the energy in ϕ (E_ϕ) as a function of time (solid dark blue) superimposed over a plot of $\phi(t,0)$ (dashed-red color). The parameters correspond to the solid blue curve in Fig. 10.4. They are $L = 100$, $N = 500$, $v = 0.1$, $\mu = 0.1$, $\lambda = 0.3$, $m_{\text{phys}} = 1$, $\kappa = 1$ and $t_0 = -100$.

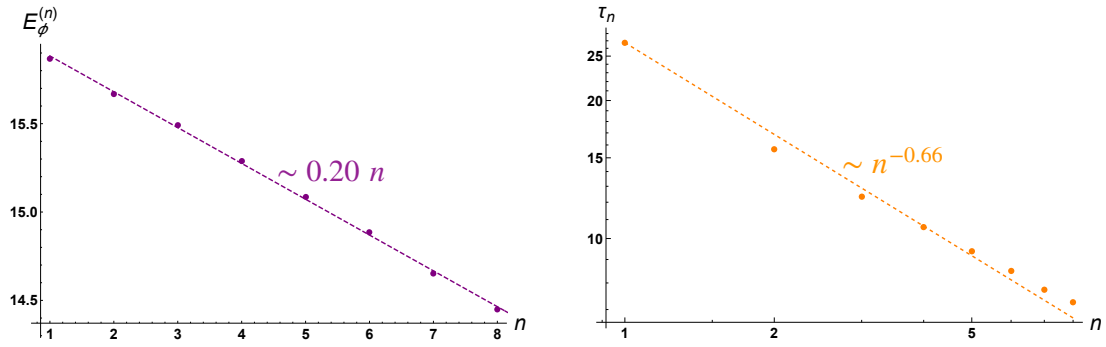

Figure 10.9: (a) Plot of the energy of the n-th plateau of E_ϕ in Fig. 10.8 ($E_\phi^{(n)}$) as a function of n (purple); (b) Plot of the duration of said plateau (τ_n) as a function n (orange). The parameters are $L = 100$, $N = 500$, $v = 0.1$, $\mu = 0.1$, $\lambda = 0.3$, $m_{\text{phys}} = 1$, $\kappa = 1$ and $t_0 = -100$.

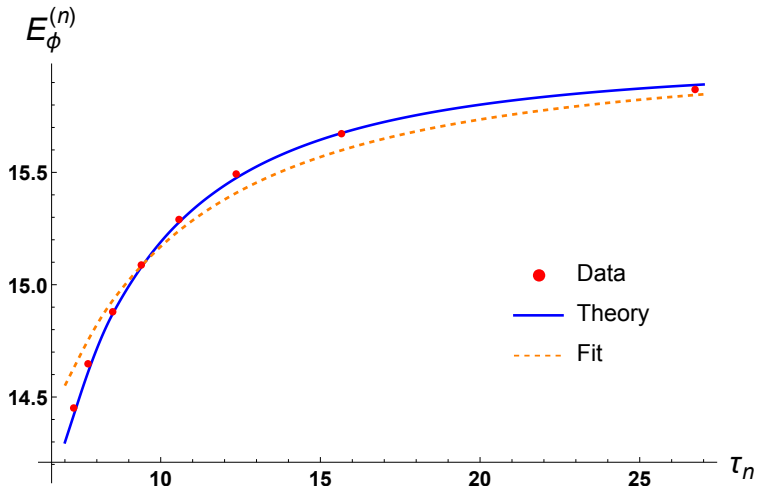

Figure 10.10: Plot of the plateau energy for ϕ ($E_\phi^{(n)}$) as a function of half period τ_n from simulation (red), from theory (10.42) (solid blue) and the analytical fit (10.41) (dashed orange). The parameters for the simulation points correspond to the solid blue curve in Fig. 10.4. They are $L = 100$, $N = 500$, $v = 0.1$, $\mu = 0.1$, $\lambda = 0.3$, $m_{\rm phys} = 1$, $\kappa = 1$ and $t_0 = -100$.

the $n^{\rm th}$ burst as a function of n in Fig. 10.9a and find the fit

$$E_\phi^{(n)} \simeq E_\phi^{(0)} - 0.20\, n\,, \tag{10.39}$$

where $E_\phi^{(0)} \simeq 16.04$ is the initial energy. Using Fig. 10.8 we can also characterize the time intervals τ_n between the $n^{\rm th}$ and $(n+1)^{\rm th}$ bursts (or between two successive zeros of $\phi(t, x = 0)$), as shown in Fig. 10.9b, to get the fit

$$\tau_n \simeq \tau_1 n^{-0.66}\,, \tag{10.40}$$

where $\tau_1 = 26.75$ is the first burst interval. We can then eliminate n to obtain the relation between $E_\phi^{(n)}$ and τ_n,

$$E_\phi^{(n)} \simeq E_\phi^{(0)} - 0.20 \left(\frac{\tau_1}{\tau_n}\right)^{1.52}\,. \tag{10.41}$$

Using the exact solution for the sine-Gordon breathers, the relation between the energy E_ϕ and the half-period τ is

$$E_\phi = 16\sqrt{1 - \frac{\pi^2}{\tau^2}}\,. \tag{10.42}$$

Fig. 10.10 shows an excellent agreement of the numerical data with the analytic sine-Gordon prediction for the relation between the plateau energy and the half-period, showing that the ϕ field decay proceeds discretely through a series of breather states. This decay of the energy continues for a finite number of bursts and then, at a critical time, the system rapidly decays into a new, more stable, oscillon-like phase (which we study in more detail in the next subsection).

10.3.2 Formation Of A Long-lived Oscillon

In this subsection we focus on the particular case $v = 0.2$, $\mu = 0.1$ and $\lambda = 0.9$ (depicted in the blue curve of Fig. 10.5) which prominently features a long-lived oscillon phase and allows us to study its formation and decay. In Figs. 10.11a and 10.11b we show the time evolution of the energy densities in ϕ and ψ respectively. In both cases, we see a qualitative change in the appearance of the breather-like structure occurring around $t = 70$: the spatial extension of the object ceases to decrease and its energy density undergoes small oscillations in amplitude (visible on both plots). Fig. 10.13 shows that the oscillations in the energy of ϕ are accompanied with out-of-phase oscillations in the localized energy of ψ around the origin. As can be seen in Fig. 10.11b the onset of this new regime is preceded by a large burst of radiation that almost completely turns off at $t \sim 70$. Fig. 10.11c shows the amplitude of the value of the ϕ field at the center of the lattice as a function of time. This is in fact a good measure of the ϕ field profile amplitude. The same qualitative change of behavior is observed on this plot: starting with the moment of collision, the ϕ field profile undergoes oscillations of decaying amplitude until a new quasi-stable oscillatory regime is reached around $t = 70$. Although, the amplitude of oscillation continues to decrease, it does so at a very slow rate which justifies the long-lived oscillon nomenclature. Finally, Fig. 10.11d is simply a zoomed in version of the blue curve in Fig. 10.5 allow-

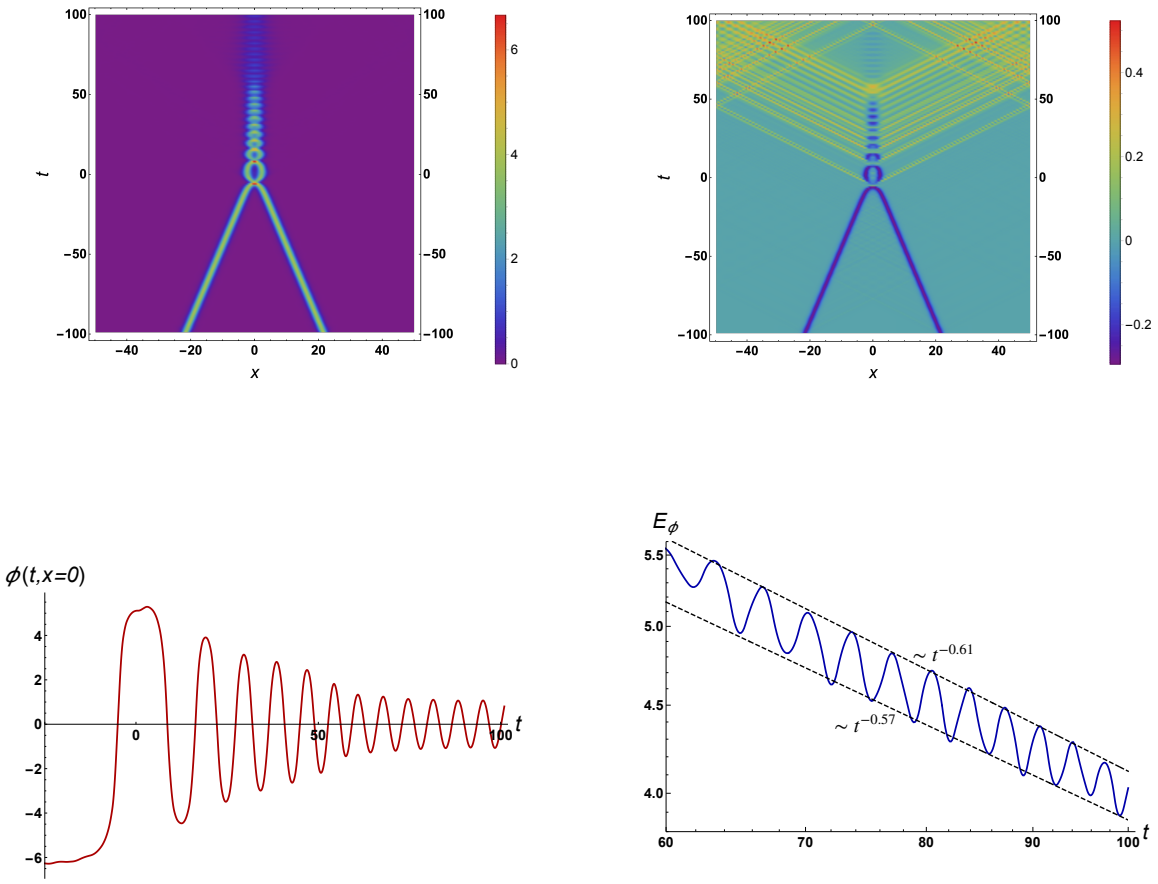

Figure 10.11: Different observables for $\lambda = 0.9$ to highlight the formation of a long-lived oscillon: (a) Time evolution of the energy density in ϕ; (b) Time evolution of the energy density in ψ ($\rho_\psi^{(R)}$); (c) Time evolution of $\phi(t, x = 0)$; (d) Log-log plot of the late-time evolution of the energy in the ϕ (E_ϕ). The parameters are $L = 100$, $N = 500$, $v = 0.2$, $\mu = 0.1$ and $m_{\rm phys} = 1$, $\kappa = 1$ and $t_0 = -100$. The collision happens at $t = 0$. The animation corresponding to this case can be found at https://sites.google.com/asu.edu/mainakm.

ing us to fit a power law to the envelope of E_ϕ within the long-lived oscillon regime. We find a $\sim t^{-0.6}$ power law decay. This is to be contrasted to the approximately linear decay occurring during the immediately preceding phase, where, on average, the energy decreases approximately linearly in time with a slope of -0.16. Given this power-law decay, this object may not be a true "oscillon", since oscillons have been seen to remain highly stable for hundreds or thousands of oscillation times. In order to distinguish it from the more strongly radiating breather state that precedes it, we will adhere to the "oscillon" nomenclature for the remainder of this work.

Fig. 10.12 further showcases the behavior of the field ϕ in the two regimes. We see that for early times, when there is significant energy loss every time ϕ goes through zero, the maxima of the field ϕ match almost exactly to the breather profile of the fully classical Sine-Gordon equation. However, during the second, slowly radiating, part of the evolution, we can see a non-negligible difference between the numerical profile for ϕ and that of a sine-Gordon breather. We can thus conclude that, while the early time evolution can be thought of a series of breathers, with the system "jumping" from one to another every time ϕ crosses zero, the late time evolution exhibits a deformed breather-like structure (which we denote as an oscillon), which is much less radiating. The time between successive ϕ zero-crossings matches rather well with the half-period of Sine-Gordon breathers, as shown in Fig. 10.12d. We also see that both the frequency and the amplitude of the oscillon-like structure remain almost constant.

One potential source of worry is whether the semi-classical approximation remains valid long enough for the oscillon to form. In other words, can the ϕ field still be treated as a classical field, even after a significant amount of its energy has dissipated via quantum radiation? As mentioned in Sec. 10.1, the approximation is valid as long as E_ϕ is larger than $E_\psi^{(R)}$ minus the energy radiated away, or in other words, as long

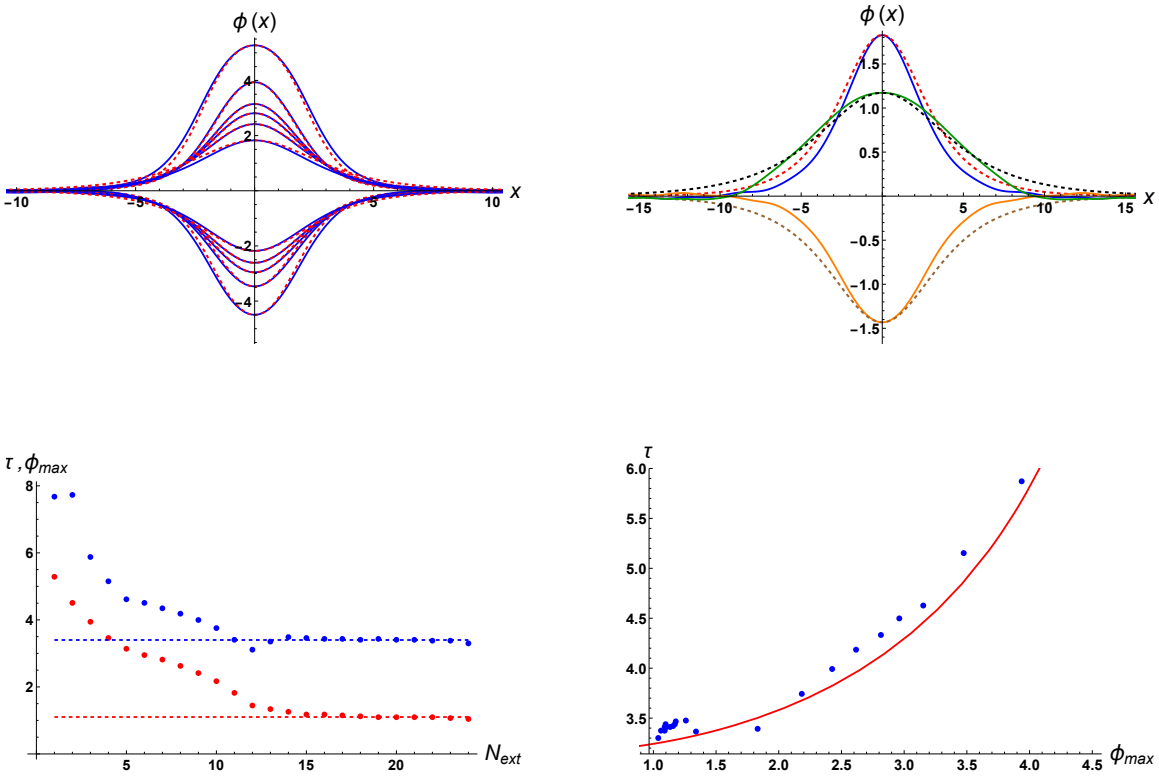

Figure 10.12: (a) The numerically derived profiles of ϕ at the first 11 extrema of Fig. 10.11c (blue). The red-dashed curves correspond to the breather profile of Eq. (10.7) with the frequency parameter ω chosen such that we recover the maximum amplitude $\phi(x = 0)$. We see excellent agreement for almost all curves; (b) The shape of ϕ at the 11^{th}, 12^{th} and 15^{th} extremum (blue,orange and green respectively). The red, brown and black curves correspond to the breather shape of Eq. (10.7); (c) The half-period τ (blue) and maximum central field amplitude $\phi_{\max}$ (red) as a function of the extremum number N_{ext}, as in Fig. 10.11c; (d) The half-period as a function of amplitude extracted from the simulation (blue dots) and computed using the analytical breather solution (red curve).

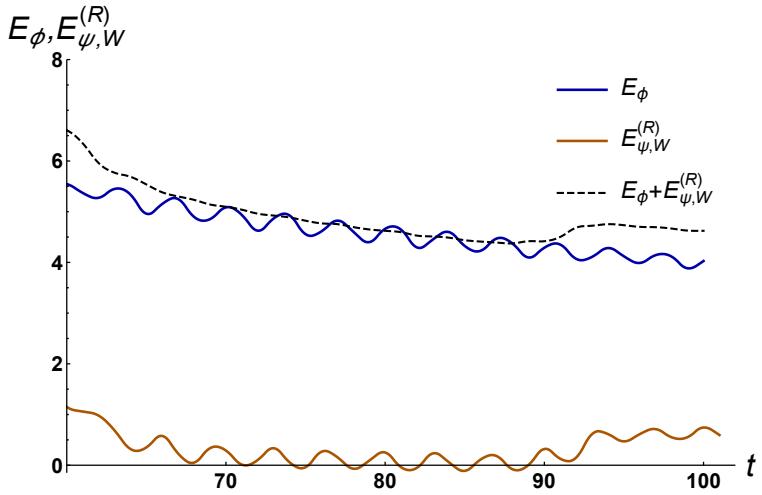

Figure 10.13: The energy in ϕ (E_ϕ) in solid dark blue, and the renormalized energy in ψ within a window ranging from $x = -5$ to $x = 5$ ($E^{(R)}_{\psi,W}$) in solid brown, as a function of time for $\lambda = 0.9$. The sum of the two is denoted by the dashed black line. The parameters are $L = 100$, $N = 500$, $v = 0.2$, $\mu = 0.1$, $m_{\rm phys} = 1$ and $t_0 = -100$. Notice that the slight increase in $E^{(R)}_{\psi,W}$ for $t \gtrsim 90$ is due to the emitted radiation reentering the window because of the periodic boundary conditions.

as the classical energy in the ϕ field is larger than the quantum energy in the clouds of ψ particles "dressing up" the kink-antikink pair. As shown in Fig. 10.13 we have checked that this is indeed the case for the whole duration of the simulation and in particular during the onset of the long-lived oscillon regime.

It would be interesting to understand the profound reasons behind the formation of the long-lived oscillon. However, within the time constraints of our simulation, which we can only evolve until $t \simeq 100$, only a small fraction of the parameter choices allow us to reach this oscillon-like final state. Improved numerics, able to simulate this late-time long-lived state, will allow us to compare it decay rate to analytical estimates (Hertzberg, 2010), thereby further elucidating the truly quantum mechanical nature of the slow decay. Overall, it is important to understand the formation and eventual decay of this slowly radiating object and we will return to this point in the future.

Chapter 11

DISCUSSIONS AND CONCLUSION - II

The main theme for this part of the work has been to investigate the dynamics of quantum fields on classical time- and space-dependent backgrounds. It is relevant for numerous systems from condensed matter physics to cosmology including early universe cosmology. Such systems involving coupled dynamics between classical and quantum degrees of freedom radiate quantum particles and dissipate. The particles however backreact on the classical background which alters its dynamics. Understanding this class of systems shaped this part of the work.

We focused on the dynamics of a classical field rolling down a linear potential, while it is bi-quadratically coupled to a quantum field in chapter 8. Our main findings showed that the dynamics of the classical field slows down because of quantum friction: as the classical field rolls down, some of its energy is transferred to the quantum field leading to particle production.

We studied the formation of global topological defects during a quantum phase transition in chapter. 9. During a quantum phase transition, the vacuum can break up to form these classical defects. We modeled such a phase transition as a time-dependent mass-squared in the potential, which changes sign. We studied the formation and dynamics of the defects by computing their number densities in 1,2 and 3-dimensions (kinks, vortices, and monopoles respectively). We found that they scale as $t^{-d/2}$ (where d is the number of spatial dimensions) and evolve towards attractor solutions that are independent of the externally controlled time dependence.

We looked at kink-antikink scattering in the sine-Gordon model in the presence of interactions with an additional scalar field in its quantum vacuum in chapter 10.

We found that in contrast to the classical scattering, there is quantum radiation in this system and the kink-antikink may form bound states that resemble breathers of the sine-Gordon model. We also quantified the rate of radiation and mapped the parameters for which bound states are formed. Interestingly, these bound states radiate and decay, and eventually there is a transition into an object that resembles a long-lived oscillon.

In this chapter, we discuss the main highlights of our work including some general comments and relevant future directions.

In chapter 8, we solved for the dynamics of a classical rolling field that is coupled to a quantum field using the CQC. Static solutions of the CQC equations are simply the extrema of the effective potential. For the particular model in (8.1) with the linear potential of (8.37), the effective potential has a minimum in the regime of validity of our equations only if the interaction strength is stronger than a critical value as in (8.41). For weaker interactions, there may be a minimum but it would lie beyond our cutoff.

The CQC equations are then used to study the dynamics of rolling on the linear potential. With homogeneous initial conditions, we find that the background field oscillates. This is similar to what we would expect from the effective potential picture but there are sharp differences in the details. These are most easily seen in Figs. 8.2 and 8.3 and are understood by noting that the CQC solves for the full dynamics, including particle production and backreaction, whereas the effective potential picture is limited to static backgrounds. In order to study possible dynamical instabilities, we have also examined the case when the background field is weakly inhomogeneous. Our numerical results show that small inhomogeneities in the initial conditions diminish on evolution and there is no indication of an instability.

Our analysis is directly relevant to phase transitions in which the order parameter

acquires a vacuum expectation value. The CQC equations can be used to study the dynamics of phase transitions, in particular the formation of topological defects. However, it would become necessary to generalize the CQC to the case when the quantum field has self-interactions. One way to deal with self-interactions, *e.g.* a ψ^4 term in the action, is to use perturbation theory on top of the CQC solution. That is, the solution to the CQC equations would serve as the zeroth order solution around which self-interactions could be treated perturbatively. This scheme has not yet been implemented.

Our result that homogeneous initial conditions evolve homogeneously is equivalent to saying that the quantum dynamics does not spontaneously break translational invariance. This is in contrast to the claim that cosmological inflation due to a rolling homogeneous field produces density fluctuations and thus spontaneously breaks translational symmetry (Mukhanov and Chibisov, 1981). However, further investigation of this issue is necessary because there are additional ingredients that go into the inflationary calculation. In particular, quantum fluctuations convert into classical fluctuations once they exit the cosmological horizon (Kiefer *et al.*, 1998), and cosmological expansion provides dissipation. It will be interesting to capture these effects in the CQC formulation.

In chapter. 9, we carried out a thorough analysis of the dynamics of topological defect formation in a quantum field theory where the only interactions are with external parameters that induce a quantum phase transition. We thus worked in the limit where self-interactions can be neglected. Results for the number density of kinks in one spatial dimension are summarized in Fig. 9.2a, for vortices in two spatial dimensions in Fig. 9.6a, and for monopoles in three spatial dimensions in Fig. 9.8a. These results indicate that the number density of topological defects in d spatial dimensions scales as $t^{-d/2}$ and does not depend on the quench time scale, in the late time limit.

Moreover, we showed that the sudden phase transition analytical result is a universal attractor. These novel results stand in contrast to the Kibble-Zurek prediction for a thermal phase transition.

We have also discussed the limit within which our results can be expected to be a good approximation for a more realistic theory where self-interactions are not explicitly set to zero. In the case of kinks ($d = 1$) we found the condition $\lambda\tau/m \ll 1$ where λ is the self-interaction coupling strength, to be a sufficient condition for our results to hold. This condition can be generalized on dimensional grounds to be $\lambda m^{d-2}\tau \ll 1$ in d spatial dimensions.

Finally, in chapter 10, we were able to simulate kink-antikink scattering in a model where a classical sine-Gordon field ϕ (the background) is coupled to a quantum field ψ (the quantum radiation bath) via an interaction term preserving the discrete shift symmetry. As expected the spacetime dependence of the background kink-antikink configuration triggers particle production in the ψ field which can in turn backreact on the field ϕ. As detailed in Sec. 10.1 we used the Classical-Quantum Correspondence (CQC) (Vachaspati and Zahariade, 2018a,b) to study this system numerically. When backreaction is taken into account within the semi-classical approximation, the outcome of the scattering is either an outgoing kink-antikink pair with reduced kinetic energy or a breather-like bound state, which continues to radiate. In Sec. 4.3 we examine the dynamics of this inelastic process and its dependence of the different parameters of the model. Interestingly enough, in the case where a bound state forms, particle production initially occurs in the form of a cascade of strong radiation bursts, but after some time the system appears to settle in a long-lived, weakly-radiating oscillon configuration. Understanding this final state would provide valuable insight into the late-time evolution of realistic systems, like bubble collisions in the early universe. Furthermore, it has been shown that in some cases the presence of specta-

tor fields can enhance the lifetimes of oscillons (Antusch and Orani, 2016). Recent work has also described the properties of multi-component oscillons (Van Dissel and Sfakianakis, 2020), which could be relevant for understanding this configuration. A detailed analytical and numerical investigation of these late-time oscillons falls outside the scope of our current work and will be undertaken in the future.

A limitation of our numerical implementation arises from the fact that working on a periodic lattice prevents us from evolving the dynamical system for a time longer than one light-crossing time after the collision. Beyond that point the emitted radiation comes back to interfere with the kink-antikink pair and our results can no longer be fully trusted. To remedy this would either require parallelizing the code so as to increase the size of the lattice while maintaining spatial resolution, or implementing absorbing boundary conditions. This is necessary for capturing phenomena that develop over long time-scales (like oscillon evaporation) and is currently under development.

One of the other limitations of our numerical setup lies in the choice of the initial conditions given in Eq. (10.35) for the Z_{ij} variables. As mentioned in Section 10.1, these are technically only valid when the background is in a quiescent state at time t_0, *i.e.* when its time variation can be neglected. This is approximately true for non-relativistic collisions such as the ones studied here. However, when γ becomes large, we expect the mismatch of initial conditions to violate adiabaticity strongly around $t = t_0$ thus leading to spurious particle production. Fixing this issue would require going beyond the choice of 0-th order adiabatic vacuum, for example by pasting together the known vacuum modefunctions for a boosted kink and for a boosted antikink (Morse and Feshbach, 1953; Vachaspati, 2010) propagating in the opposite direction to obtain more accurate initial conditions for $\boldsymbol{Z}$. Alternatively one could adiabatically turn on the relative velocity in a well-separated kink-antikink pair but

this again requires better control over numerical error. An amusing fact is that collisions of classical solitons have been analyzed in detail in the opposite regime, that of ultra-relativistic velocities (Amin *et al.*, 2013). There, semi-analytic formulas where derived, albeit neglecting any effect of quantum radiation. Extending the CQC into this regime will allow us to capture the quantum radiation effects on colliding relativistic domain walls in the early universe.

The methods presented here in the context of the simple model of a sine-Gordon potential in one spatial dimensions have a wide applicability to a variety of other scenarios. For example, the analysis carries over directly to kink-antikink collisions in the $\lambda\phi^4$ model (Sugiyama, 1979; Campbell *et al.*, 1983; Anninos *et al.*, 1991; Dorey and Romańczukiewicz, 2018). Moreover its three-dimensional extension would in fact describe domain wall collisions in the early universe in the presence of quantum radiation. This presents an intriguing opportunity to study possible signatures of the interplay between classical and quantum degrees of freedom in a cosmological context (note that the kink-antikink configuration discussed here provides an analogy with the particle production phenomena thought to occur during gravitational collapse, black hole production and evaporation). Furthermore, the formation of oscillons after bubble collisions and their eventual decay will have to be revisited, in order to encompass the backreaction of quantum radiation (Bond *et al.*, 2015).

We hope that our investigations are small but significant steps towards understanding the big picture - the interplay of classical and quantum degrees of freedom in the universe, in broader contexts of gravitation, condensed matter systems and early universe cosmology.

Aalbers, e. a., J., "DARWIN: towards the ultimate dark matter detector", JCAP **2016**, 11, 017 (2016).

Aalbers, J. *et al.*, "A Next-Generation Liquid Xenon Observatory for Dark Matter and Neutrino Physics", (2022).

Aalseth, e., C. E., "DarkSide-20k: A 20 tonne two-phase LAr TPC for direct dark matter detection at LNGS", European Physical Journal Plus **133**, 3, 131 (2018).

Aarts, G. and J. Smit, "Particle production and effective thermalization in inhomogeneous mean field theory", Phys. Rev. D **61**, 025002 (2000).

Aarts, G. and A. Tranberg, "Thermal effects on slow-roll dynamics", Phys. Rev. **D77**, 123521 (2008).

Aartsen, M. G. *et al.*, "Evidence for High-Energy Extraterrestrial Neutrinos at the IceCube Detector", Science **342**, 1242856 (2013).

Aartsen, M. G. *et al.*, "Multimessenger observations of a flaring blazar coincident with high-energy neutrino IceCube-170922A", Science **361**, 6398, eaat1378 (2018a).

Aartsen, M. G. *et al.*, "Neutrino emission from the direction of the blazar TXS 0506+056 prior to the IceCube-170922A alert", Science **361**, 6398, 147–151 (2018b).

Aasi, J., B. P. Abbott, R. Abbott, T. Abbott, M. R. Abernathy, K. Ackley, C. Adams, T. Adams, P. Addesso and et al., "Advanced ligo", Classical and Quantum Gravity **32**, 7, 074001, URL http://dx.doi.org/10.1088/0264-9381/32/7/074001 (2015a).

Aasi, J. *et al.*, "Advanced LIGO", Class. Quant. Grav. **32**, 074001 (2015b).

Abbasi, R. *et al.*, "IceCube Sensitivity for Low-Energy Neutrinos from Nearby Supernovae", Astron. Astrophys. **535**, A109, [Erratum: Astron.Astrophys. 563, C1 (2014)] (2011).

Abbott, B. P. *et al.*, "A First Targeted Search for Gravitational-Wave Bursts from Core-Collapse Supernovae in Data of First-Generation Laser Interferometer Detectors", Phys. Rev. D **94**, 10, 102001 (2016a).

Abbott, B. P. *et al.*, "Observation of Gravitational Waves from a Binary Black Hole Merger", Phys. Rev. Lett. **116**, 6, 061102 (2016b).

Abbott, B. P. *et al.*, "Observation of Gravitational Waves from a Binary Black Hole Merger", Phys. Rev. Lett. **116**, 6, 061102 (2016c).

Abbott, B. P. *et al.*, "GW170817: Observation of Gravitational Waves from a Binary Neutron Star Inspiral", Phys. Rev. Lett. **119**, 16, 161101 (2017a).

Abbott, B. P. *et al.*, "GW170817: Observation of Gravitational Waves from a Binary Neutron Star Inspiral", Phys. Rev. Lett. **119**, 16, 161101 (2017b).

Abbott, B. P. *et al.*, "Multi-messenger Observations of a Binary Neutron Star Merger", Astrophys. J. Lett. **848**, 2, L12 (2017c).

Abbott, B. P. *et al.*, "GW190425: Observation of a Compact Binary Coalescence with Total Mass $\sim 3.4 M_{\odot}$", Astrophys. J. Lett. **892**, 1, L3 (2020a).

Abbott, R. *et al.*, "GW190521: A Binary Black Hole Merger with a Total Mass of $150 M_{\odot}$", Phys. Rev. Lett. **125**, 10, 101102 (2020b).

Abdurashitov, J. N. *et al.*, "Solar neutrino flux measurements by the Soviet-American Gallium Experiment (SAGE) for half the 22 year solar cycle", J. Exp. Theor. Phys. **95**, 181–193 (2002).

Abdurashitov, J. N. *et al.*, "Measurement of the solar neutrino capture rate with gallium metal. III: Results for the 2002–2007 data-taking period", Phys. Rev. C **80**, 015807 (2009).

Abe, e., K., "Real-time supernova neutrino burst monitor at Super-Kamiokande", Astroparticle Physics **81**, 39–48 (2016).

Abe, K. *et al.*, "Letter of Intent: The Hyper-Kamiokande Experiment — Detector Design and Physics Potential —", (2011).

Abe, K. *et al.*, "Evidence for the Appearance of Atmospheric Tau Neutrinos in Super-Kamiokande", Phys. Rev. Lett. **110**, 18, 181802 (2013).

Abe, K. *et al.*, "Hyper-Kamiokande Design Report", (2018a).

Abe, K. *et al.*, "Physics potentials with the second Hyper-Kamiokande detector in Korea", PTEP **2018**, 6, 063C01 (2018b).

Abe, K. *et al.*, "Search for neutrinos in coincidence with gravitational wave events from the LIGO-Virgo O3a Observing Run with the Super-Kamiokande detector", Astrophys. J. **918**, 2, 78 (2021).

Abi, B., R. Acciarri, M. A. Acero, G. Adamov, D. Adams, M. Adinolfi, Z. Ahmad, J. Ahmed, T. Alion, S. A. Monsalve *et al.*, "Deep underground neutrino experiment (dune), far detector technical design report, volume ii: Dune physics", arXiv preprint arXiv:2002.03005 (2020).

Abi, B. *et al.*, "Supernova neutrino burst detection with the Deep Underground Neutrino Experiment", Eur. Phys. J. C **81**, 5, 423 (2021).

Acciarri, R. *et al.*, "Long-Baseline Neutrino Facility (LBNF) and Deep Underground Neutrino Experiment (DUNE)", arXiv e-prints (2016).

Adams, S. M., C. S. Kochanek, J. F. Beacom, M. R. Vagins and K. Z. Stanek, "Observing the Next Galactic Supernova", Astrophys. J. **778**, 164 (2013).

Adams, S. M., C. S. Kochanek, J. R. Gerke and K. Z. Stanek, "The search for failed supernovae with the Large Binocular Telescope: constraints from 7 yr of data", Mon. Not. Roy. Astron. Soc. **469**, 2, 1445–1455 (2017a).

Adams, S. M., C. S. Kochanek, J. R. Gerke, K. Z. Stanek and X. Dai, "The search for failed supernovae with the Large Binocular Telescope: confirmation of a disappearing star", Mon. Not. Roy. Astron. Soc. **468**, 4, 4968–4981 (2017b).

Ade, P. A. R. *et al.*, "Planck 2013 results. XXV. Searches for cosmic strings and other topological defects", Astron. Astrophys. **571**, A25 (2014).

Ageron, M. *et al.*, "The ANTARES Telescope Neutrino Alert System", Astropart. Phys. **35**, 530–536 (2012).

Agostini, M. *et al.*, "Experimental evidence of neutrinos produced in the CNO fusion cycle in the Sun", Nature **587**, 577–582 (2020).

Aguilar-Arevalo, A. A. *et al.*, "A Search for Core-Collapse Supernovae using the MiniBooNE Neutrino Detector", Phys. Rev. D **81**, 032001 (2010).

Aharmim, B. *et al.*, "Low Energy Threshold Analysis of the Phase I and Phase II Data Sets of the Sudbury Neutrino Observatory", Phys. Rev. C **81**, 055504 (2010).

Ahmad, Q. R. *et al.*, "Direct evidence for neutrino flavor transformation from neutral current interactions in the Sudbury Neutrino Observatory", Phys. Rev. Lett. **89**, 011301 (2002).

Ahn, J. K. *et al.*, "RENO: An Experiment for Neutrino Oscillation Parameter θ_{13} Using Reactor Neutrinos at Yonggwang", (2010).

Akimov, D. *et al.*, "Observation of Coherent Elastic Neutrino-Nucleus Scattering", Science **357**, 6356, 1123–1126 (2017).

Al Kharusi, S. *et al.*, "SNEWS 2.0: A Next-Generation SuperNova Early Warning System for Multi-messenger Astronomy", (2020).

Alberghi, G. L., R. Casadio, G. P. Vacca and G. Venturi, "Gravitational collapse of a radiating shell", Phys. Rev. D **64**, 104012, URL https://link.aps.org/doi/10.1103/PhysRevD.64.104012 (2001).

Albert, A. *et al.*, "Search for High-energy Neutrinos from Binary Neutron Star Merger GW170817 with ANTARES, IceCube, and the Pierre Auger Observatory", Astrophys. J. Lett. **850**, 2, L35 (2017).

Amin, M. A., R. Easther, H. Finkel, R. Flauger and M. P. Hertzberg, "Oscillons After Inflation", Phys. Rev. Lett. **108**, 241302 (2012).

Amin, M. A., E. A. Lim and I.-S. Yang, "A scattering theory of ultrarelativistic solitons", Phys. Rev. D **88**, 10, 105024 (2013).

An, e., Fengpeng, "Neutrino physics with JUNO", Journal of Physics G Nuclear Physics **43**, 3, 030401 (2016).

An, F. *et al.*, "Neutrino Physics with JUNO", J. Phys. G **43**, 3, 030401 (2016).

Anderson, A., "Quantum back reaction on 'classical' variables", Phys. Rev. Lett. **74**, 621–625 (1995).

Ando, S., J. F. Beacom and H. Yüksel, "Detection of neutrinos from supernovae in nearby galaxies", Phys. Rev. Lett. **95**, 171101, URL https://link.aps.org/doi/10.1103/PhysRevLett.95.171101 (2005).

Ando, S. and K. Sato, "Relic neutrino background from cosmological supernovae", New J. Phys. **6**, 170 (2004).

Andringa, S. *et al.*, "Current Status and Future Prospects of the SNO+ Experiment", Adv. High Energy Phys. **2016**, 6194250 (2016).

Anninos, P., S. Oliveira and R. A. Matzner, "Fractal structure in the scalar lambda (phi**2-1)**2 theory", Phys. Rev. D **44**, 1147–1160 (1991).

Antonioli, P., R. Tresch Fienberg, R. Fleurot, Y. Fukuda, W. Fulgione, A. Habig, J. Heise, A. B. McDonald, C. Mills, T. Namba, L. J. Robinson, K. Scholberg, M. Schwendener, R. W. Sinnott, B. Stacey, Y. Suzuki, R. Tafirout, C. Vigorito, B. Viren, C. Virtue and A. Zichichi, "SNEWS: the SuperNova Early Warning System", New Journal of Physics **6**, 114 (2004).

Antonioli, P. *et al.*, "SNEWS: The Supernova Early Warning System", New J. Phys. **6**, 114 (2004).

Antunes, N. D., L. M. Bettencourt and W. H. Zurek, "Vortex string formation in a 3-D U(1) temperature quench", Phys. Rev. Lett. **82**, 2824–2827 (1999).

Antusch, S. and S. Orani, "Impact of other scalar fields on oscillons after hilltop inflation", JCAP **03**, 026 (2016).

Apollonio, e., M., "Determination of neutrino incoming direction in the CHOOZ experiment and its application to supernova explosion location by scintillator detectors", "Phys. Rev. D" **61**, 1, 012001 (2000).

Araki, T. *et al.*, "Measurement of neutrino oscillation with KamLAND: Evidence of spectral distortion", Phys. Rev. Lett. **94**, 081801 (2005).

Arcones, A., H.-T. Janka and L. Scheck, "Nucleosynthesis-relevant conditions in neutrino-driven supernova outflows. 1. Spherically symmetric hydrodynamic simulations", Astron. Astrophys. **467**, 1227 (2007).

Ardellier, F. *et al.*, "Double Chooz: A Search for the neutrino mixing angle theta(13)", (2006).

Armendariz-Picon, C., "On the Expected Backreaction During Preheating", (2020).

Asakura, K. and KamLAND Collaboration, "KamLAND Sensitivity to Neutrinos from Pre-supernova Stars", "Astro. Phys. J." **818**, 1, 91 (2016).

Askins, M. *et al.*, "Theia: An advanced optical neutrino detector", arXiv e-prints (2019).

Askins, M. *et al.*, "THEIA: an advanced optical neutrino detector", Eur. Phys. J. C **80**, 5, 416 (2020).

Asnin, V., E. Rabinovici and M. Smolkin, "On rolling, tunneling and decaying in some large N vector models", JHEP **08**, 001 (2009).

Asplund, M., N. Grevesse, A. J. Sauval and P. Scott, "The chemical composition of the Sun", Ann. Rev. Astron. Astrophys. **47**, 481–522 (2009).

Astone, P., K. M. Borkowski, P. Jaranowski and A. Krolak, "Data analysis of gravitational wave signals from spinning neutron stars. 4. An All sky search", Phys. Rev. D **65**, 042003 (2002).

Ayala Solares, H. A. *et al.*, "A Search for Cosmic Neutrino and Gamma-Ray Emitting Transients in 7.3 Years of ANTARES and Fermi LAT Data", Astrophys. J. **886**, 98 (2019).

Ayala Solares, H. A. *et al.*, "Multimessenger Gamma-Ray and Neutrino Coincidence Alerts Using HAWC and IceCube Subthreshold Data", (2020a).

Ayala Solares, H. A. *et al.*, "The Astrophysical Multimessenger Observatory Network (AMON): Performance and science program", Astropart. Phys. **114**, 68–76 (2020b).

Ayres, D. S. *et al.*, "NOvA: Proposal to Build a 30 Kiloton Off-Axis Detector to Study $\nu_\mu \to \nu_e$ Oscillations in the NuMI Beamline", (2004).

Badurina, L. *et al.*, "AION: An Atom Interferometer Observatory and Network", JCAP **05**, 011 (2020).

Bahcall, J. N., S. Basu and M. H. Pinsonneault, "How uncertain are solar neutrino predictions?", Phys. Lett. B **433**, 1–8 (1998).

Bahcall, J. N., W. A. Fowler, J. Iben, I. and R. L. Sears, "Solar Neutrino Flux.", APJ **137**, 344–346 (1963).

Bahcall, J. N. and M. H. Pinsonneault, "Standard solar models, with and without helium diffusion and the solar neutrino problem", Rev. Mod. Phys. **64**, 885–926 (1992).

Bahcall, J. N. and M. H. Pinsonneault, "Solar models with helium and heavy element diffusion", Rev. Mod. Phys. **67**, 781–808 (1995).

Bahcall, J. N., M. H. Pinsonneault and S. Basu, "Solar models: Current epoch and time dependences, neutrinos, and helioseismological properties", Astrophys. J. **555**, 990–1012 (2001).

Bardeen, J. M. and G. J. Bublik, "Quantum Fluctuations and Inflation", Class. Quant. Grav. **4**, 573 (1987).

Barger, V. D., K. Whisnant, S. Pakvasa and R. J. N. Phillips, "Matter Effects on Three-Neutrino Oscillations", Phys. Rev. D **22**, 2718 (1980).

Barr, G., T. K. Gaisser and T. Stanev, "Flux of atmospheric neutrinos", Phys. Rev. D **39**, 3532–3534, URL https://link.aps.org/doi/10.1103/PhysRevD.39.3532 (1989).

Barthelmy, S. D. *et al.*, "An origin for short gamma-ray bursts unassociated with current star formation", Nature **438**, 994 (2005).

Baym, G., *Lectures On Quantum Mechanics* (CRC Press, 2018), URL https://books.google.com/books?id=IGhQDwAAQBAJ.

Beacom, J. and P. Vogel, "Can a supernova be located by its neutrinos?", "Phys. Rev. D" **60**, 3, 033007 (1999).

Beacom, J. F., "The Diffuse Supernova Neutrino Background", Ann. Rev. Nucl. Part. Sci. **60**, 439–462 (2010).

Beacom, J. F. and M. R. Vagins, "Antineutrino spectroscopy with large water Čerenkov detectors", Phys. Rev. Lett. **93**, 171101, URL https://link.aps.org/doi/10.1103/PhysRevLett.93.171101 (2004).

Beacom, J. F. *et al.*, "Physics prospects of the Jinping neutrino experiment", Chin. Phys. **C41**, 2, 023002 (2017).

Beaudet, G., V. Petrosian and E. E. Salpeter, "Energy Losses due to Neutrino Processes", "Astro. Phys. J." **150**, 979 (1967).

Becker-Szendy, R. *et al.*, "IMB-3: A Large water Cherenkov detector for nucleon decay and neutrino interactions", Nucl. Instrum. Meth. A **324**, 363–382 (1993).

Bedingham, D. J. and H. F. Jones, "Quantum field dynamics of the slow rollover in the linear delta expansion", Phys. Rev. **D68**, 025004 (2003).

Bender, P. L., M. C. Begelman and J. R. Gair, "Possible LISA follow-on mission scientific objectives", Classical and Quantum Gravity **30**, 16, 165017, URL https://doi.org/10.1088%2F0264-9381%2F30%2F16%2F165017 (2013).

Bennett, C. L. *et al.*, "First year Wilkinson Microwave Anisotropy Probe (WMAP) observations: Preliminary maps and basic results", Astrophys. J. Suppl. **148**, 1–27 (2003).

Berger, B. K., "Scalar Particle Creation in an Anisotropic Universe", Phys. Rev. D **12**, 368–375 (1975).

Beugnon, J. and N. Navon, "Exploring the kibble–zurek mechanism with homogeneous bose gases", Journal of Physics B: Atomic, Molecular and Optical Physics **50**, 2, 022002, URL https://doi.org/10.1088%2F1361-6455%2F50%2F2%2F022002 (2017).

Bilenky, S. M., C. Giunti and W. Grimus, "Phenomenology of neutrino oscillations", Prog. Part. Nucl. Phys. **43**, 1–86 (1999).

Bilenky, S. M. and B. Pontecorvo, "Lepton Mixing and Neutrino Oscillations", Phys. Rept. **41**, 225–261 (1978).

Biller, S. D., E. J. Leming and J. L. Paton, "Slow Fluors for Highly Effective Separation of Cherenkov Light in Liquid Scintillators", arXiv e-prints (2020).

Birrell, N. D. and P. C. W. Davies, *Quantum Fields in Curved Space*, Cambridge Monographs on Mathematical Physics (Cambridge Univ. Press, Cambridge, UK, 1984).

Bisnovatyi-Kogan, G. S. and Z. F. Seidov, "Medium-Energy Neutrinos in the Universe", SOVAST **26**, 132–138 (1982).

Blanchet, L. and T. Damour, "Hereditary effects in gravitational radiation", Phys. Rev. D **46**, 4304–4319 (1992).

Blanco-Pillado, J. J., K. D. Olum and X. Siemens, "New limits on cosmic strings from gravitational wave observation", Phys. Lett. B **778**, 392–396 (2018).

Blondin, J. M. and S. Shaw, "Linear growth of spiral SASI modes in core-collapse supernovae", Astrophys. J. **656**, 366–371 (2007).

Boger, J. *et al.*, "The Sudbury neutrino observatory", Nucl. Instrum. Meth. A **449**, 172–207 (2000).

Bond, J. R., J. Braden and L. Mersini-Houghton, "Cosmic bubble and domain wall instabilities III: The role of oscillons in three-dimensional bubble collisions", JCAP **09**, 004 (2015).

Bonet, H. *et al.*, "Large-size sub-keV sensitive germanium detectors for the CONUS experiment", Eur. Phys. J. C **81**, 3, 267 (2021).

Borexino Collaboration, "Comprehensive measurement of pp-chain solar neutrinos", Nature **562**, 7728, 505–510 (2018).

Borsanyi, S. and M. Hindmarsh, "Semiclassical decay of topological defects", Phys. Rev. D **77**, 045022 (2008).

Borsanyi, S. and M. Hindmarsh, "Low-cost fermions in classical field simulations", Phys. Rev. D **79**, 065010 (2009).

Bouchet, P., J. M. De Buizer, N. B. Suntzeff, I. J. Danziger, T. L. Hayward, C. M. Telesco and C. Packham, "High resolution imaging of SN 1987A at 10 micron", Astrophys. J. **611**, 394–398 (2004).

Bouchet, P., E. Dwek, I. J. Danziger, R. G. Arendt, I. J. M. De Buizer, S. Park, N. B. Suntzeff, R. P. Kirshner and P. Challis, "SN 1987a after 18 years: Mid-infrared Gemini and Spitzer observations of the remnant", Astrophys. J. **650**, 212–227 (2006).

Bowick, M. J., L. Chandar, E. A. Schiff and A. M. Srivastava, "The Cosmological Kibble mechanism in the laboratory: String formation in liquid crystals", Science **263**, 943–945 (1994).

Boyanovsky, D., "Quantum spinodal decomposition", Phys. Rev. E **48**, 767–771, URL https://link.aps.org/doi/10.1103/PhysRevE.48.767 (1993).

Boyanovsky, D., H. de Vega and R. Holman, "Nonequilibrium phase transitions in condensed matter and cosmology: Spinodal decomposition, condensates and defects", NATO Sci. Ser. C **549**, 139–169 (2000).

Boyanovsky, D. and H. J. de Vega, "Quantum rolling down out-of-equilibrium", Phys. Rev. **D47**, 2343–2355 (1993).

Braginskii, V. B. and K. S. Thorne, "Gravitational-wave bursts with memory and experimental prospects", Nature **327**, 6118, 123–125 (1987).

Brandenberger, R. and H. Jiao, "Cosmic Textures and Global Monopoles as Seeds for Super-Massive Black Holes", JCAP **02**, 002 (2020).

Brout, R., S. Massar, S. Popescu, R. Parentani and P. Spindel, "Quantum back reaction on a classical field", Phys. Rev. D **52**, 1119–1133 (1995).

Brugière, T., "The Jiangmen underground neutrino observatory experiment", Nuclear Instruments and Methods in Physics Research A **845**, 326–329 (2017).

Bueno, A., I. Gil Botella and A. Rubbia, "Supernova neutrino detection in a liquid argon TPC", (2003).

Burrows, A., "Speculations on the Fizzled Collapse of a Massive Star", APJ **300**, 488 (1986).

Burrows, A. and J. Hayes, "Pulsar recoil and gravitational radiation due to asymmetrical stellar collapse and explosion", Phys. Rev. Lett. **76**, 352–355 (1996).

Burrows, A., S. Reddy and T. A. Thompson, "Neutrino opacities in nuclear matter", Nucl. Phys. A **777**, 356–394 (2006).

Burrows, A. and D. Vartanyan, "Core-Collapse Supernova Explosion Theory", Nature **589**, 7840, 29–39 (2021).

Burrows, D. N., E. Michael, U. Hwang, R. McCray, R. A. Chevalier, R. Petre, G. P. Garmire, S. S. Holt and J. A. Nousek, "The x-ray remnant of sn1987a", Astrophys. J. Lett. **543**, L149 (2000).

Bäuerle, C., Y. M. Bunkov, S. N. Fisher, H. Godfrin and G. R. Pickett, "Laboratory simulation of cosmic string formation in the early universe using superfluid 3he", Nature **382**, 6589, 332–334, URL https://doi.org/10.1038/382332a0 (1996).

Cabibbo, N., "Proc. of "Astrophysics and Elementary Particles, Common Problems"", JETP Lett. p. 209 (1980).

Cadonati, L., F. P. Calaprice and M. C. Chen, "Supernova neutrino detection in borexino", Astropart. Phys. **16**, 361–372 (2002).

Cahill, K. E., "Extended Particles and Solitons", Phys. Lett. B **53**, 174–176 (1974).

Calzetta, E., "Spinodal decomposition in quantum field theory", Annals of Physics **190**, 1, 32–58 (1989).

Campbell, D. K., J. F. Schonfeld and C. A. Wingate, "Resonance Structure in Kink - Antikink Interactions in ϕ^4 Theory", Physica D **9**, 1 (1983).

Canuel, B. *et al.*, "ELGAR - a European Laboratory for Gravitation and Atom-interferometric Research", Class. Quant. Grav. **37**, 22, 225017 (2020a).

Canuel, B. *et al.*, "Technologies for the ELGAR large scale atom interferometer array", (2020b).

Cao, L. J. and Y. Wang, "Reactor Neutrino Experiments: Present and Future", Ann. Rev. Nucl. Part. Sci. **67**, 183–211 (2017).

Cardona, C. and T. Vachaspati, "Instability of a uniform electric field in pure non-Abelian Yang-Mills theory", Phys. Rev. D **104**, 4, 045009 (2021).

Carmi, R. and E. Polturak, "Search for spontaneous nucleation of magnetic flux during rapid cooling of $yba_2cu_3o_{7-\delta}$ films through T_c", Phys. Rev. B **60**, 7595–7600, URL https://link.aps.org/doi/10.1103/PhysRevB.60.7595 (1999).

Carmi, R., E. Polturak and G. Koren, "Observation of spontaneous flux generation in a multi-josephson-junction loop", Phys. Rev. Lett. **84**, 4966–4969, URL https://link.aps.org/doi/10.1103/PhysRevLett.84.4966 (2000).

Cerdá-Durán, P., N. DeBrye, M. A. Aloy, J. A. Font and M. Obergaulinger, "Gravitational wave signatures in black-hole-forming core collapse", Astrophys. J. Lett. **779**, L18 (2013).

Chadwick, J., "Possible Existence of a Neutron", Nature **129**, 312 (1932).

Christ, N. H. and T. D. Lee, "Quantum Expansion of Soliton Solutions", Phys. Rev. D **12**, 1606 (1975).

Christodoulou, D., "Nonlinear nature of gravitation and gravitational wave experiments", Phys. Rev. Lett. **67**, 1486–1489 (1991).

Chuang, I., B. Yurke, R. Durrer and N. Turok, "Cosmology in the Laboratory: Defect Dynamics in Liquid Crystals", Science **251**, 1336–1342 (1991).

Clausen, D., A. L. Piro and C. D. Ott, "The Black Hole Formation Probability", Astrophys. J. **799**, 2, 190 (2015).

Cleveland, B. T., T. Daily, R. Davis, Jr., J. R. Distel, K. Lande, C. K. Lee, P. S. Wildenhain and J. Ullman, "Measurement of the solar electron neutrino flux with the Homestake chlorine detector", Astrophys. J. **496**, 505–526 (1998).

Coleman, J., "Matter-wave Atomic Gradiometer InterferometricSensor (MAGIS-100) at Fermilab", PoS **ICHEP2018**, 021 (2019).

Coleman, S., *Aspects of Symmetry: Selected Erice Lectures* (Cambridge University Press, Cambridge, U.K., 1985).

Cooper, F. and E. Mottola, "Quantum back reaction in scalar qed as an initial-value problem", Phys. Rev. D **40**, 456–464, URL https://link.aps.org/doi/10.1103/PhysRevD.40.456 (1989a).

Cooper, F. and E. Mottola, "Quantum Back Reaction in Scalar QED as an Initial Value Problem", Phys. Rev. D **40**, 456 (1989b).

Copeland, E. J., M. Gleiser and H. R. Muller, "Oscillons: Resonant configurations during bubble collapse", Phys. Rev. D **52**, 1920–1933 (1995).

Couvidat, S., S. Turck-Chieze and A. G. Kosovichev, "Solar seismic models and the neutrino predictions", Astrophys. J. **599**, 1434–1448 (2003).

Damour, T. and A. Vilenkin, "Gravitational wave bursts from cosmic strings", Phys. Rev. Lett. **85**, 3761–3764 (2000).

Danby, G., J. M. Gaillard, K. A. Goulianos, L. M. Lederman, N. B. Mistry, M. Schwartz and J. Steinberger, "Observation of High-Energy Neutrino Reactions and the Existence of Two Kinds of Neutrinos", Phys. Rev. Lett. **9**, 36–44 (1962).

Dashen, R. F., B. Hasslacher and A. Neveu, "Nonperturbative Methods and Extended Hadron Models in Field Theory 1. Semiclassical Functional Methods", Phys. Rev. D **10**, 4114 (1974a).

Dashen, R. F., B. Hasslacher and A. Neveu, "Nonperturbative Methods and Extended Hadron Models in Field Theory 2. Two-Dimensional Models and Extended Hadrons", Phys. Rev. D **10**, 4130–4138 (1974b).

Dashen, R. F., B. Hasslacher and A. Neveu, "Nonperturbative Methods and Extended Hadron Models in Field Theory. 3. Four-Dimensional Nonabelian Models", Phys. Rev. D **10**, 4138 (1974c).

Dashen, R. F., B. Hasslacher and A. Neveu, "The Particle Spectrum in Model Field Theories from Semiclassical Functional Integral Techniques", Phys. Rev. D **11**, 3424 (1975).

Davis, R., Jr., D. S. Harmer and K. C. Hoffman, "Search for neutrinos from the sun", Phys. Rev. Lett. **20**, 1205–1209 (1968).

De Gouvêa, A., I. Martinez-Soler, Y. F. Perez-Gonzalez and M. Sen, "Fundamental physics with the diffuse supernova background neutrinos", Phys. Rev. D **102**, 123012 (2020).

de Gouvêa, A., I. Martinez-Soler, Y. F. Perez-Gonzalez and M. Sen, "The diffuse supernova neutrino background as a probe of late-time neutrino mass generation", (2022).

del Campo, A., G. De Chiara, G. Morigi, M. B. Plenio and A. Retzker, "Structural defects in ion chains by quenching the external potential: The inhomogeneous kibble-zurek mechanism", Phys. Rev. Lett. **105**, 075701, URL https://link.aps.org/doi/10.1103/PhysRevLett.105.075701 (2010).

Dessart, L., A. Burrows, C. Ott, E. Livne, S.-Y. Yoon and N. Langer, "Multidimensional simulations of the accretion-induced collapse of white dwarfs to neutron stars", The Astrophysical Journal **644**, 2, 1063 (2006).

Dimmelmeier, H., C. D. Ott, A. Marek and H. T. Janka, "The Gravitational Wave Burst Signal from Core Collapse of Rotating Stars", Phys. Rev. D **78**, 064056 (2008).

Dodd, M. E., P. C. Hendry, N. S. Lawson, P. V. E. McClintock and C. D. H. Williams, "Nonappearance of vortices in fast mechanical expansions of liquid ^{4}He through the lambda transition", Phys. Rev. Lett. **81**, 3703–3706, URL https://link.aps.org/doi/10.1103/PhysRevLett.81.3703 (1998).

Donaire, M., T. Kibble and A. Rajantie, "Spontaneous vortex formation on a superconductor film", New J. Phys. **9**, 148 (2007).

Donini, A., S. Palomares-Ruiz and J. Salvado, "Neutrino tomography of Earth", Nature Phys. **15**, 1, 37–40 (2019).

Dorey, P. and T. Romańczukiewicz, "Resonant kink-antikink scattering through quasinormal modes", Phys. Lett. B **779**, 117–123 (2018).

Drukier, A. and L. Stodolsky, "Principles and Applications of a Neutral Current Detector for Neutrino Physics and Astronomy", Phys. Rev. D **30**, 2295 (1984).

Duba, C. A. *et al.*, "HALO: The helium and lead observatory for supernova neutrinos", J. Phys. Conf. Ser. **136**, 042077 (2008).

Ducci, S., P. L. Ramazza, W. González-Viñas and F. T. Arecchi, "Order parameter fragmentation after a symmetry-breaking transition", Phys. Rev. Lett. **83**, 5210–5213, URL https://link.aps.org/doi/10.1103/PhysRevLett.83.5210 (1999).

Dufaux, J.-F., D. G. Figueroa and J. Garcia-Bellido, "Gravitational Waves from Abelian Gauge Fields and Cosmic Strings at Preheating", Phys. Rev. D **82**, 083518 (2010).

Durrer, R., M. Heusler, P. Jetzer and N. Straumann, "General relativistic collapse of textures", Phys. Lett. B **259**, 48–52 (1991).

Dutta, S. I., S. Ratkovic and M. Prakash, "The photo - neutrino process in astrophysical systems", Phys. Rev. D **69**, 023005 (2004).

Eguchi, K. *et al.*, "First results from KamLAND: Evidence for reactor anti-neutrino disappearance", Phys. Rev. Lett. **90**, 021802 (2003).

Eichler, D., M. Livio, T. Piran and D. N. Schramm, "Nucleosynthesis, Neutrino Bursts and Gamma-Rays from Coalescing Neutron Stars", Nature **340**, 126–128 (1989).

Eitel, K., "Direct neutrino mass experiments", Nucl. Phys. B Proc. Suppl. **143**, 197–204 (2005).

El-Neaj, Y. A. *et al.*, "AEDGE: Atomic Experiment for Dark Matter and Gravity Exploration in Space", EPJ Quant. Technol. **7**, 6 (2020).

Elliott, S. R. and J. Engel, "Double-beta decay", Journal of Physics G: Nuclear and Particle Physics **30**, 9, R183 (2004).

Elliott, S. R. and P. Vogel, "Double beta decay", Annual Review of Nuclear and Particle Science **52**, 1, 115–151 (2002).

Eltsov, V. B., M. Krusius and G. E. Volovik, "Vortex Formation and Dynamics in Superfluid 3He and Analogies in Quantum Field Theory", arXiv e-prints pp. cond–mat/9809125 (1998).

Engel, K., T. Lewis, M. S. Muzio and T. M. Venters, "Advancing the Landscape of Multimessenger Science in the Next Decade", in "2022 Snowmass Summer Study", (2022).

Epstein, R., "The Generation of Gravitational Radiation by Escaping Supernova Neutrinos", Astrophys. J. **223**, 1037–1045 (1978).

Erler, J. and M. J. Ramsey-Musolf, "The Weak mixing angle at low energies", Phys. Rev. D **72**, 073003 (2005).

Ertl, T., H. T. Janka, S. E. Woosley, T. Sukhbold and M. Ugliano, "A two-parameter criterion for classifying the explodability of massive stars by the neutrino-driven mechanism", Astrophys. J. **818**, 2, 124 (2016).

Esmaili, A., O. L. G. Peres and P. D. Serpico, "Impact of sterile neutrinos on the early time flux from a galactic supernova", Phys. Rev. D **90**, 3, 033013 (2014).

Esteban-Pretel, A., R. Tomas and J. W. F. Valle, "Probing non-standard neutrino interactions with supernova neutrinos", Phys. Rev. D **76**, 053001 (2007).

Evans, P. A. *et al.*, "Swift and NuSTAR observations of GW170817: detection of a blue kilonova", Science **358**, 1565 (2017).

Farhi, E., N. Graham, V. Khemani, R. Markov and R. Rosales, "An Oscillon in the SU(2) gauged Higgs model", Phys. Rev. D **72**, 101701 (2005).

Farzan, Y. and M. Tortola, "Neutrino oscillations and Non-Standard Interactions", Front. in Phys. **6**, 10 (2018).

Favata, M., "The gravitational-wave memory effect", Class. Quant. Grav. **27**, 084036 (2010).

Favata, M., "The Gravitational-wave memory from eccentric binaries", Phys. Rev. D **84**, 124013 (2011).

Fermi, E., "Tentativo di una teoria dell'emissione dei raggi beta", Ric. Sci. **4**, 491–495 (1933).

Fermi, E., "An attempt of a theory of beta radiation. 1.", Z. Phys. **88**, 161–177 (1934a).

Fermi, E., "Trends to a Theory of beta Radiation. (In Italian)", Nuovo Cim. **11**, 1–19 (1934b).

Feynman, R. P. and M. Gell-Mann, "Theory of Fermi interaction", Phys. Rev. **109**, 193–198 (1958).

Fischer, T., N.-U. F. Bastian, M.-R. Wu, P. Baklanov, E. Sorokina, S. Blinnikov, S. Typel, T. Klähn and D. B. Blaschke, "Quark deconfinement as a supernova explosion engine for massive blue supergiant stars", Nature Astron. **2**, 12, 980–986 (2018).

Fischer, T., S. C. Whitehouse, A. Mezzacappa, F. K. Thielemann and M. Liebendorfer, "The neutrino signal from protoneutron star accretion and black hole formation", Astron. Astrophys. **499**, 1 (2009).

Fischer, V., T. Chirac, T. Lasserre, C. Volpe, M. Cribier, M. Durero, J. Gaffiot, T. Houdy, A. Letourneau, G. Mention, M. Pequignot, V. Sibille and M. Vivier, "Prompt directional detection of galactic supernova by combining large liquid scintillator neutrino detectors", "JCAP" **2015**, 8, 032 (2015).

Fodor, G., P. Forgacs, Z. Horvath and A. Lukacs, "Small amplitude quasi-breathers and oscillons", Phys. Rev. D **78**, 025003 (2008).

Foot, R., H. Lew, X. G. He and G. C. Joshi, "Seesaw Neutrino Masses Induced by a Triplet of Leptons", Z. Phys. C **44**, 441 (1989).

Ford, L. H., "Cosmological particle production: a review", Rept. Prog. Phys. **84**, 11 (2021).

Fowler, W. A. and F. Hoyle, "Neutrino Processes and Pair Formation in Massive Stars and Supernovae.", "Astro. Phys. J."s **9**, 201 (1964).

Fox, D. B. *et al.*, "The afterglow of grb050709 and the nature of the short-hard gamma-ray bursts", Nature **437**, 845–850 (2005).

Freedman, D. Z., "Coherent Neutrino Nucleus Scattering as a Probe of the Weak Neutral Current", Phys. Rev. D **9**, 1389–1392 (1974).

Freedman, D. Z., D. N. Schramm and D. L. Tubbs, "The Weak Neutral Current and Its Effects in Stellar Collapse", Ann. Rev. Nucl. Part. Sci. **27**, 167–207 (1977).

Freund, M., "Analytic approximations for three neutrino oscillation parameters and probabilities in matter", Phys. Rev. D **64**, 053003 (2001).

Friedland, A., C. Lunardini and M. Maltoni, "Atmospheric neutrinos as probes of neutrino-matter interactions", Phys. Rev. D **70**, 111301 (2004a).

Friedland, A., C. Lunardini and C. Pena-Garay, "Solar neutrinos as probes of neutrino matter interactions", Phys. Lett. B **594**, 347 (2004b).

Fryer, C. L., D. E. Holz and S. A. Hughes, "Gravitational wave emission from core collapse of massive stars", Astrophys. J. **565**, 430–446 (2002).

Fryer, C. L., D. E. Holz and S. A. Hughes, "Gravitational waves from stellar collapse: Correlations to explosion asymmetries", Astrophys. J. **609**, 288–300 (2004).

Fukuda, Y. *et al.*, "Solar neutrino data covering solar cycle 22", Phys. Rev. Lett. **77**, 1683–1686 (1996).

Fukuda, Y. *et al.*, "Evidence for oscillation of atmospheric neutrinos", Phys. Rev. Lett. **81**, 1562–1567 (1998).

Fukuda, Y. *et al.*, "Measurement of the solar neutrino energy spectrum using neutrino electron scattering", Phys. Rev. Lett. **82**, 2430–2434 (1999).

Fuller, G. M., W. A. Fowler and M. J. Newman, "Stellar weak-interaction rates for sd-shell nuclei. I - Nuclear matrix element systematics with application to Al-26 and selected nuclei of importance to the supernova problem", "Astro. Phys. J."s **42**, 447–473 (1980).

Fuller, G. M., W. A. Fowler and M. J. Newman, "Stellar weak interaction rates for intermediate-mass nuclei. II - A = 21 to A = 60", "Astro. Phys. J." **252**, 715–740 (1982a).

Fuller, G. M., W. A. Fowler and M. J. Newman, "Stellar weak interaction rates for intermediate mass nuclei. III - Rate tables for the free nucleons and nuclei with A = 21 to A = 60", "Astro. Phys. J."s **48**, 279–319 (1982b).

Fuller, G. M., W. A. Fowler and M. J. Newman, "Stellar weak interaction rates for intermediate-mass nuclei. IV - Interpolation procedures for rapidly varying lepton capture rates using effective log (ft)-values", "Astro. Phys. J." **293**, 1–16 (1985).

Fuller, J., M. Cantiello, D. Lecoanet and E. Quataert, "THE SPIN RATE OF PRE-COLLAPSE STELLAR CORES: WAVE-DRIVEN ANGULAR MOMENTUM TRANSPORT IN MASSIVE STARS", The Astrophysical Journal **810**, 2, 101, URL https://doi.org/10.1088%2F0004-637x%2F810%2F2%2F101 (2015).

Gaia Collaboration, "Gaia Data Release 2. Summary of the contents and survey properties", "AAP" **616**, A1 (2018).

Gando, A. *et al.*, "Reactor On-Off Antineutrino Measurement with KamLAND", Phys. Rev. D **88**, 3, 033001 (2013).

Gehrels, N., M. Leventhal and C. J. MacCallum, "Prospects for gamma-ray line observations of individual supernovae", The Astrophysical Journal **322**, 215–233 (1987).

Gerke, J. R., C. S. Kochanek and K. Z. Stanek, "The Search for Failed Supernovae with The Large Binocular Telescope: First Candidates", Mon. Not. Roy. Astron. Soc. **450**, 3, 3289–3305 (2015).

Gibbons, G. W. and N. S. Manton, "Classical and Quantum Dynamics of BPS Monopoles", Nucl. Phys. B **274**, 183–224 (1986).

Giunti, C. and C. W. Kim, *Fundamentals of Neutrino Physics and Astrophysics* (2007).

Glashow, S. L., "Partial Symmetries of Weak Interactions", Nucl. Phys. **22**, 579–588 (1961).

Gleiser, M. and D. Sicilia, "A General Theory of Oscillon Dynamics", Phys. Rev. D **80**, 125037 (2009).

Goldhaber, M., L. Grodzins and A. W. Sunyar, "Helicity of Neutrinos", Phys. Rev. **109**, 1015–1017 (1958).

Goldstone, J. and R. Jackiw, "Quantization of Nonlinear Waves", Phys. Rev. D **11**, 1486–1498 (1975).

Gonzalez-Garcia, M. C., M. Maltoni and T. Schwetz, "Global Analyses of Neutrino Oscillation Experiments", Nucl. Phys. B **908**, 199–217 (2016).

Gossan, S. E., "Core-Collapse Supernova Physics in the Multi-Messenger Era", Dissertation (Ph.D.), California Institute of Technology URL https://resolver.caltech.edu/CaltechTHESIS:01312019-123521450 (2019).

Graham, N., "An Electroweak oscillon", Phys. Rev. Lett. **98**, 101801, [Erratum: Phys.Rev.Lett. 98, 189904 (2007)] (2007).

Graham, P. W., J. M. Hogan, M. A. Kasevich and S. Rajendran, "Resonant mode for gravitational wave detectors based on atom interferometry", Phys. Rev. D **94**, 104022, URL https://link.aps.org/doi/10.1103/PhysRevD.94.104022 (2016).

Graham, P. W., J. M. Hogan, M. A. Kasevich, S. Rajendran and R. W. Romani, "Mid-band gravitational wave detection with precision atomic sensors", (2017).

Graves, G. J. M. *et al.*, "Limits from the Hubble Space Telescope on a point source in SN 1987A", Astrophys. J. **629**, 944–959 (2005).

Gribov, V. N. and B. Pontecorvo, "Neutrino astronomy and lepton charge", Phys. Lett. B **28**, 493 (1969).

Großschedl, J. E., J. Alves, P. S. Teixeira, H. Bouy, J. Forbrich, C. J. Lada, S. Meingast, Á. Hacar, J. Ascenso, C. Ackerl, B. Hasenberger, R. Köhler, K. Kubiak, I. Larreina, L. Linhardt, M. Lombardi and T. Möller, "VISION - Vienna survey in Orion. III. Young stellar objects in Orion A", "AAP" **622**, A149 (2019).

Gueron, E. and P. S. Letelier, "Textures and Newtonian gravity", Phys. Rev. D **56**, 5272–5275 (1997).

Guo, G., Y.-Z. Qian and A. Heger, "Presupernova neutrino signals as potential probes of neutrino mass hierarchy", Phys. Lett. **B796**, 126–130 (2019).

Guo, X. *et al.*, "A Precision measurement of the neutrino mixing angle θ_{13} using reactor antineutrinos at Daya-Bay", arXiv e-prints (2007).

Halliwell, J. J., "Effective theories of coupled classical and quantum variables from decoherent histories: A New approach to the back reaction problem", Phys. Rev. D **57**, 2337–2348 (1998).

Halperin, B., "Statistical mechanics of topological defects", Physics of Defects, proceedings of Les Houches, Session XXXV NATO ASI, Editors Balian, Kléman and Poirier (North-Holland Press) p. 816 (1980).

Hampel, W. *et al.*, "GALLEX solar neutrino observations: Results for GALLEX IV", Phys. Lett. B **447**, 127–133 (1999).

Hannestad, S., G. G. Raffelt, G. Sigl and Y. Y. Y. Wong, "Self-induced conversion in dense neutrino gases: Pendulum in flavour space", Phys. Rev. D **74**, 105010, [Erratum: Phys.Rev.D 76, 029901 (2007)] (2006).

Hasinger, G., B. Aschenbach and J. Trumper, "The X-ray light curve of SN1987A", Astron. Astrophys. **312**, L9–L12 (1996).

Hawking, S. W., "Particle Creation by Black Holes", Commun. Math. Phys. **43**, 199–220, [Erratum: Commun.Math.Phys. 46, 206 (1976)] (1975).

Haxton, W. C., R. G. Hamish Robertson and A. M. Serenelli, "Solar Neutrinos: Status and Prospects", Ann. Rev. Astron. Astrophys. **51**, 21–61 (2013).

Helm, R. H., "Inelastic and Elastic Scattering of 187-Mev Electrons from Selected Even-Even Nuclei", Phys. Rev. **104**, 1466–1475 (1956).

Hendry, P. C., N. S. Lawson, R. A. M. Lee, P. V. E. McClintock and C. D. H. Williams, "Generation of defects in superfluid 4he as an analogue of the formation of cosmic strings", Nature **368**, 6469, 315–317, URL https://doi.org/10.1038/368315a0 (1994).

Hertzberg, M. P., "Quantum Radiation of Oscillons", Phys. Rev. D **82**, 045022 (2010).

Hertzberg, M. P., "Quantum and Classical Behavior in Interacting Bosonic Systems", JCAP **11**, 037 (2016).

Hindmarsh, M. and A. Rajantie, "Defect formation and local gauge invariance", Phys. Rev. Lett. **85**, 4660–4663 (2000).

Hindmarsh, M. B. and T. W. B. Kibble, "Cosmic strings", Rept. Prog. Phys. **58**, 477–562 (1995).

Hiramatsu, D. *et al.*, "The electron-capture origin of supernova 2018zd", Nature Astron. **5**, 9, 903–910 (2021a).

Hiramatsu, T., M. Kawasaki, K. Saikawa and T. Sekiguchi, "Axion cosmology with long-lived domain walls", JCAP **01**, 001 (2013).

Hiramatsu, T., E. I. Sfakianakis and M. Yamaguchi, "Gravitational wave spectra from oscillon formation after inflation", JHEP **03**, 021 (2021b).

Hirata, K. S., T. Kajita, M. Koshiba, M. Nakahata, Y. Oyama, N. Sato, A. Suzuki, M. Takita, Y. Totsuka, T. Kifune, T. Suda, K. Takahashi, T. Tanimori, K. Miyano, M. Yamada, E. W. Beier, L. R. Feldscher, W. Frati, S. B. Kim, A. K. Mann, F. M. Newcomer, R. Van Berg, W. Zhang and B. G. Cortez, "Observation in the kamiokande-ii detector of the neutrino burst from supernova sn1987a", Phys. Rev. D **38**, 448–458, URL https://link.aps.org/doi/10.1103/PhysRevD.38.448 (1988).

Hirata, K. S. *et al.*, "Real time, directional measurement of B-8 solar neutrinos in the Kamiokande-II detector", Phys. Rev. D **44**, 2241, [Erratum: Phys.Rev.D 45, 2170 (1992)] (1991).

Honda, M., T. Kajita, K. Kasahara and S. Midorikawa, "Atmospheric neutrinos", Progress of Theoretical Physics Supplement **123**, 483–490 (1996).

Hopkins, A. M. and J. F. Beacom, "On the normalisation of the cosmic star formation history", Astrophys. J. **651**, 142–154 (2006).

Horiuchi, S. and J. F. Beacom, "Revealing Type Ia supernova physics with cosmic rates and nuclear gamma rays", Astrophys. J. **723**, 329–341 (2010).

Horiuchi, S., J. F. Beacom, C. S. Kochanek, J. L. Prieto, K. Z. Stanek and T. A. Thompson, "The Cosmic Core-collapse Supernova Rate does not match the Massive-Star Formation Rate", Astrophys. J. **738**, 154–169 (2011).

Horowitz, C. J., K. J. Coakley and D. N. McKinsey, "Supernova observation via neutrino - nucleus elastic scattering in the CLEAN detector", Phys. Rev. D **68**, 023005 (2003).

Hosseinzadeh, G. *et al.*, "Short-Lived Circumstellar Interaction in the Low-Luminosity Type IIP SN 2016bkv", Astrophys. J. **861**, 1, 63 (2018).

Hu, B. L., "Scalar waves in the mixmaster universe. ii. particle creation", Phys. Rev. D **9**, 3263–3281 (1974).

Hu, B. L. and L. Parker, "Effect of gravitation creation in isotropically expanding universes", Phys. Lett. A **63**, 217–220 (1977).

Hu, B. L. and L. Parker, "Anisotropy Damping Through Quantum Effects in the Early Universe", Phys. Rev. D **17**, 933–945, [Erratum: Phys.Rev.D 17, 3292 (1978)] (1978).

Hu, W., D. J. Eisenstein and M. Tegmark, "Weighing neutrinos with galaxy surveys", Phys. Rev. Lett. **80**, 5255–5258 (1998).

Huang, K. and R. Tipton, "Vortex Excitations in the Weinberg-Salam Theory", Phys. Rev. **D23**, 3050 (1981).

Ibaceta, D. and E. Calzetta, "Counting defects in an instantaneous quench", Phys. Rev. E **60**, 2999–3008 (1999).

Ikeda, M. *et al.*, "Search for Supernova Neutrino Bursts at Super-Kamiokande", Astrophys. J. **669**, 519–524 (2007).

Itoh, N., H. Hayashi, A. Nishikawa and Y. Kohyama, "Neutrino Energy Loss in Stellar Interiors. VII. Pair, Photo-, Plasma, Bremsstrahlung, and Recombination Neutrino Processes", "Astro. Phys. J."s **102**, 411–+ (1996).

Itoh, N. and Y. Kohyama, "Neutrino-pair bremsstrahlung in dense stars. i-liquid metal case", The Astrophysical Journal **275**, 858–866 (1983).

Jani, K. and A. Loeb, "Gravitational-wave lunar observatory for cosmology", (2020).

Janka, H. T., "Neutrino Emission from Supernovae", (2017).

Janka, H. T., R. Buras, K. Kifonidis, M. Rampp and T. Plewa, "Explosion mechanisms of massive stars: A Critical review of possibilities and perspectives", (2002).

Janka, H. T., F. Hanke, L. Huedepohl, A. Marek, B. Mueller and M. Obergaulinger, "Core-collapse supernovae: Reflections and directions", URL https://arxiv.org/abs/1211.1378 (2012).

Janka, H. T. and W. Hillebrandt, "Neutrino emission from type II supernovae : an analysis of the spectra.", AAP **224**, 49–56 (1989).

Janka, H.-T., W. Keil, G. Raffelt and D. Seckel, "Nucleon spin fluctuations and the supernova emission of neutrinos and axions", Phys. Rev. Lett. **76**, 2621–2624 (1996).

Janka, H.-T., K. Langanke, A. Marek, G. Martinez-Pinedo and B. Mueller, "Theory of Core-Collapse Supernovae", Phys. Rept. **442**, 38–74 (2007).

Janka, H. T., T. Melson and A. Summa, "Physics of Core-Collapse Supernovae in Three Dimensions: a Sneak Preview", Ann. Rev. Nucl. Part. Sci. **66**, 341–375 (2016).

Jaranowski, P. and A. Krolak, "Data analysis of gravitational wave signals from spinning neutron stars. 2. Accuracy of estimation of parameters", Phys. Rev. D **59**, 063003 (1999).

Jaranowski, P. and A. Krolak, "Data analysis of gravitational wave signals from spinning neutron stars. 3. Detection statistics and computational requirements", Phys. Rev. D **61**, 062001 (2000).

Jaranowski, P. and A. Krolak, "Gravitational-Wave Data Analysis. Formalism and Sample Applications: The Gaussian Case", Living Rev. Rel. **8**, 3 (2005).

Jaranowski, P., A. Krolak and B. F. Schutz, "Data analysis of gravitational - wave signals from spinning neutron stars. 1. The Signal and its detection", Phys. Rev. D **58**, 063001 (1998).

Kajita, T., "The Measurement of Neutrino Properties with Atmospheric Neutrinos", Ann. Rev. Nucl. Part. Sci. **64**, 343–362 (2014).

Karra, G. and R. Rivers, "Initial vortex densities after a quench", Phys. Lett. B **414**, 28–33 (1997).

Kasliwal, M. M. *et al.*, "Illuminating Gravitational Waves: A Concordant Picture of Photons from a Neutron Star Merger", Science **358**, 1559 (2017).

Kasper, V., F. Hebenstreit, M. Oberthaler and J. Berges, "Schwinger pair production with ultracold atoms", Phys. Lett. B **760**, 742–746 (2016).

Kato, C., M. Delfan Azari, S. Yamada, K. Takahashi, H. Umeda, T. Yoshida and K. Ishidoshiro, "Pre-supernova Neutrino Emissions from ONe Cores in the Progenitors of Core-collapse Supernovae: Are They Distinguishable from Those of Fe Cores?", "Astro. Phys. J." **808**, 2, 168 (2015).

Kato, C., H. Nagakura, S. Furusawa, K. Takahashi, H. Umeda, T. Yoshida, K. Ishidoshiro and S. Yamada, "Neutrino Emissions in All Flavors up to the Pre-bounce of Massive Stars and the Possibility of Their Detections", Astro. Phys. J. **848**, 1, 48 (2017).

Kawamura, S., M. Ando, N. Seto and e. Sato, Shuichi, "Current status of space gravitational wave antenna DECIGO and B-DECIGO", Progress of Theoretical and Experimental Physics **2021**, 5, 05A105 (2021).

Kawamura, S. *et al.*, "Current status of space gravitational wave antenna DECIGO and B-DECIGO", (2020).

Kayser, B., "On the Quantum Mechanics of Neutrino Oscillation", Phys. Rev. D **24**, 110 (1981).

Keil, M. T., G. G. Raffelt and H.-T. Janka, "Monte Carlo study of supernova neutrino spectra formation", Astrophys. J. **590**, 971–991 (2003).

Keil, W., H.-T. Janka, D. N. Schramm, G. Sigl, M. S. Turner and J. R. Ellis, "A Fresh look at axions and SN-1987A", Phys. Rev. D **56**, 2419–2432 (1997).

Khaitan, D., "Supernova neutrino detection in LZ", JINST **13**, 02, C02024 (2018).

Kibble, T., "Topology of Cosmic Domains and Strings", J. Phys. A **9**, 1387–1398 (1976).

Kibble, T., "Some Implications of a Cosmological Phase Transition", Phys. Rept. **67**, 183 (1980).

Kibble, T., "Phase-Transition Dynamics in the Lab and the Universe", Physics Today **60**, 9, 47 (2007).

Kibble, T. W. B., "Testing cosmological defect formation in the laboratory", Physica C **369**, 87 (2002).

Kiefer, C., D. Polarski and A. A. Starobinsky, "Quantum to classical transition for fluctuations in the early universe", Int. J. Mod. Phys. **D7**, 455–462 (1998).

Kiers, K., S. Nussinov and N. Weiss, "Coherence effects in neutrino oscillations", Phys. Rev. D **53**, 537–547 (1996).

King, B., H. Gies and A. Di Piazza, "Pair production in a plane wave by thermal background photons", Phys. Rev. D **86**, 125007, [Erratum: Phys.Rev.D 87, 069905 (2013)] (2012).

Kirshner, R. P., G. Sonneborn, D. M. Crenshaw and G. E. Nassiopoulos, "Ultraviolet observations of sn 1987a", The Astrophysical Journal **320**, 602–608 (1987).

Kistler, M. D., W. C. Haxton and H. Yüksel, "Tomography of Massive Stars from Core Collapse to Supernova Shock Breakout", Astrophys. J. **778**, 81 (2013).

Kistler, M. D., H. Yuksel, S. Ando, J. F. Beacom and Y. Suzuki, "Core-Collapse Astrophysics with a Five-Megaton Neutrino Detector", Phys. Rev. D **83**, 123008 (2011).

Kluger, Y., J. M. Eisenberg, B. Svetitsky, F. Cooper and E. Mottola, "Pair production in a strong electric field", Phys. Rev. Lett. **67**, 2427–2430 (1991).

Kochanek, C. S. *et al.*, "The All-Sky Automated Survey for Supernovae (ASAS-SN) Light Curve Server v1.0", Publ. Astron. Soc. Pac. **129**, 980, 104502 (2017).

Kodama, K. *et al.*, "Observation of tau neutrino interactions", Phys. Lett. B **504**, 218–224 (2001).

Kofman, L., A. D. Linde and A. A. Starobinsky, "Reheating after inflation", Phys. Rev. Lett. **73**, 3195–3198 (1994).

Konopinski, E. J. and H. M. Mahmoud, "The Universal Fermi interaction", Phys. Rev. **92**, 1045–1049 (1953).

Kotake, K., "Multiple physical elements to determine the gravitational-wave signatures of core-collapse supernovae", Comptes Rendus Physique **14**, 318–351 (2013).

Kotake, K., W. Iwakami, N. Ohnishi and S. Yamada, "Ray-Tracing Analysis of Anisotropic Neutrino Radiation for Estimating Gravitational Waves in Core-Collapse Supernovae", Astrophys. J. **704**, 951–963 (2009a).

Kotake, K., W. Iwakami, N. Ohnishi and S. Yamada, "Ray-tracing analysis of anisotropic neutrino radiation for estimating gravitational waves in core-collapse supernovae", The Astrophysical Journal **704**, 2, 951 (2009b).

Kotake, K., N. Ohnishi and S. Yamada, "Gravitational Radiation from Standing Accretion Shock Instability in Core-Collapse Supernovae", Astrophys. J. **655**, 406–415 (2007a).

Kotake, K., N. Ohnishi and S. Yamada, "Gravitational radiation from standing accretion shock instability in core-collapse supernovae", The Astrophysical Journal **655**, 1, 406–415, URL https://doi.org/10.1086%2F509320 (2007b).

Kotake, K., K. Sato and K. Takahashi, "Explosion mechanism, neutrino burst, and gravitational wave in core-collapse supernovae", Rept. Prog. Phys. **69**, 971–1144 (2006).

Kotake, K., T. Takiwaki, Y. Suwa, W. I. Nakano, S. Kawagoe, Y. Masada and S.-i. Fujimoto, "Multimessengers from core-collapse supernovae: multidimensionality as a key to bridge theory and observation", Adv. Astron. **2012**, 428757 (2012).

Koyama, T., M. Machida, M. Kato and T. Ishida, "Spontaneous vortex formation in a quench process in superconducting films with small holes", Physica C: Superconductivity and its Applications **445-448**, 257 – 259, URL http://www.sciencedirect.com/science/article/pii/S0921453406002784, proceedings of the 18th International Symposium on Superconductivity (ISS 2005) (2006).

Kraus, C. and S. J. M. Peeters, "The rich neutrino programme of the SNO+ experiment", Prog. Part. Nucl. Phys. **64**, 273–277 (2010).

Krauss, L. M., S. L. Glashow and D. N. Schramm, "Anti-neutrinos Astronomy and Geophysics", Nature **310**, 191–198 (1984).

Kresse, D., T. Ertl and H.-T. Janka, "Stellar Collapse Diversity and the Diffuse Supernova Neutrino Background", Astrophys. J. **909**, 2, 169 (2021).

Kulkarni, S. R., "Modeling supernova-like explosions associated with gamma-ray bursts with short durations", (2005).

Kunxian, H., Ph.D. thesis, Kyoto University, available at http://www-he.scphys.kyoto-u.ac.jp/theses/doctor/khuang_dt.pdf (2015).

Kuroda, T., K. Kotake, K. Hayama and T. Takiwaki, "Correlated Signatures of Gravitational-Wave and Neutrino Emission in Three-Dimensional General-Relativistic Core-Collapse Supernova Simulations", Astrophys. J. **851**, 1, 62 (2017).

Kuroda, T., K. Kotake, T. Takiwaki and F.-K. Thielemann, "A full general relativistic neutrino radiation-hydrodynamics simulation of a collapsing very massive star and the formation of a black hole", Mon. Not. Roy. Astron. Soc. **477**, 1, L80–L84 (2018).

Kuroda, T., T. Takiwaki and K. Kotake, "Gravitational Wave Signatures from Low-mode Spiral Instabilities in Rapidly Rotating Supernova Cores", Phys. Rev. D **89**, 4, 044011 (2014).

Kuroda, T., T. Takiwaki and K. Kotake, "A New Multi-Energy Neutrino Radiation-Hydrodynamics Code in Full General Relativity and Its Application to Gravitational Collapse of Massive Stars", Astrophys. J. Suppl. **222**, 2, 20 (2016).

Kutschera, M., A. Odrzywołek and M. Misiaszek, "Presupernovae as Powerful Neutrino Sources", Acta Physica Polonica B **40**, 11, 3063 (2009).

Kyutoku, K. and K. Kashiyama, "Detectability of thermal neutrinos from binary neutron-star mergers and implications for neutrino physics", Phys. Rev. D **97**, 103001, URL https://link.aps.org/doi/10.1103/PhysRevD.97.103001 (2018).

Laguna, P. and W. H. Zurek, "Density of kinks after a quench: When symmetry breaks, how big are the pieces?", Phys. Rev. Lett. **78**, 2519–2522 (1997).

Landau, L. D., "On the conservation laws for weak interactions", Nucl. Phys. **3**, 127–131 (1957).

Langanke, K. and G. Martínez-Pinedo, "Shell-model calculations of stellar weak interaction rates: II. Weak rates for nuclei in the mass range /A=45-65 in supernovae environments", Nuclear Physics A **673**, 481–508 (2000).

Langanke, K. and G. Martínez-Pinedo, "The role of electron capture in core-collapse supernovae", Nuclear Physics A **928**, 305–312 (2014).

Leaman, J., W. Li, R. Chornock and A. V. Filippenko, "Nearby Supernova Rates from the Lick Observatory Supernova Search. I. The Methods and Database", Mon. Not. Roy. Astron. Soc. **412**, 1419 (2011).

Lee, T. D. and C.-N. Yang, "Question of Parity Conservation in Weak Interactions", Phys. Rev. **104**, 254–258 (1956).

Lee, T. D. and C. N. Yang, "Parity nonconservation and a two-component theory of the neutrino", Phys. Rev. **105**, 1671–1675, URL https://link.aps.org/doi/10.1103/PhysRev.105.1671 (1957).

Leisos, A., A. G. Tsirigotis and S. E. Tzamarias, "A feasibility study for the detection of supernova explosions with an undersea neutrino telescope", Nucl. Instrum. Meth. A **725**, 89–93 (2013).

Leonor, I. *et al.*, "Searching for prompt signatures of nearby core-collapse supernovae by a joint analysis of neutrino and gravitational-wave data", Class. Quant. Grav. **27**, 084019 (2010).

Li, H.-L., Y.-F. Li, L.-J. Wen and S. Zhou, "Prospects for Pre-supernova Neutrino Observation in Future Large Liquid-scintillator Detectors", arXiv e-prints p. arXiv:2003.03982 (2020).

Li, J.-T., G. M. Fuller and C. T. Kishimoto, "Neutrino Burst-Generated Gravitational Radiation From Collapsing Supermassive Stars", Phys. Rev. D **98**, 2, 023002 (2018).

Li, L.-X. and B. Paczynski, "Transient events from neutron star mergers", Astrophys. J. Lett. **507**, L59 (1998).

Li, S. W., L. F. Roberts and J. F. Beacom, "Exciting Prospects for Detecting Late-Time Neutrinos from Core-Collapse Supernovae", (2020).

Li, Y.-F., "Overview of the Jiangmen Underground Neutrino Observatory (JUNO)", in "International Journal of Modern Physics Conference Series", vol. 31 of *International Journal of Modern Physics Conference Series*, p. 1460300 (2014).

Lim, B., Y. Nazé, E. Gosset and G. Rauw, "A Gaia view of the two OB associations Cygnus OB2 and Carina OB1: the signature of their formation process", "Monthly Notices of the RAS" **490**, 1, 440–454 (2019).

Liu, F. and G. F. Mazenko, "Nonequilibrium autocorrelations in phase-ordering dynamics", Physical Review B **44**, 17, 9185 (1991).

Liu, F. and G. F. Mazenko, "Defect-defect correlation in the dynamics of first-order phase transitions", Physical Review B **46**, 10, 5963 (1992a).

Liu, F. and G. F. Mazenko, "Growth kinetics of systems with continuous symmetry", Physical Review B **45**, 13, 6989 (1992b).

Long, A. J., C. Lunardini and E. Sabancilar, "Detecting non-relativistic cosmic neutrinos by capture on tritium: phenomenology and physics potential", JCAP **08**, 038 (2014).

LSST Science Collaboration, "LSST Science Book, Version 2.0", arXiv e-prints p. arXiv:0912.0201 (2009).

Lunardini, C., *Diffuse Neutrino Flux from Supernovae*, p. 1637 (2017).

Lunardini, C. and A. Y. Smirnov, "Neutrinos from SN1987A, earth matter effects and the LMA solution of the solar neutrino problem", Phys. Rev. D **63**, 073009 (2001).

Lund, T., A. Wongwathanarat, H.-T. Janka, E. Muller and G. Raffelt, "Fast time variations of supernova neutrino signals from 3-dimensional models", Phys. Rev. D **86**, 105031 (2012).

Luo, J., L.-S. Chen, H.-Z. Duan, Y.-G. Gong, S. Hu, J. Ji, Q. Liu, J. Mei, V. Milyukov, M. Sazhin and et al., "Tianqin: a space-borne gravitational wave detector", Classical and Quantum Gravity **33**, 3, 035010, URL http://dx.doi.org/10.1088/0264-9381/33/3/035010 (2016).

M Punturo, M. A. and e. F Acernese, "The einstein telescope: a third-generation gravitational wave observatory", Classical and Quantum Gravity **27**, 19, 194002, URL https://doi.org/10.1088%2F0264-9381%2F27%2F19%2F194002 (2010).

Majorana, E., "Teoria simmetrica dell'elettrone e del positrone", Nuovo Cim. **14**, 171–184 (1937).

Maki, Z., M. Nakagawa and S. Sakata, "Remarks on the unified model of elementary particles", Prog. Theor. Phys. **28**, 870–880 (1962).

Manchester, R. N., B. M. Gaensler, L. Staveley-Smith, M. J. Kesteven and A. K. Tzioumis, "Imaging of the radio remnant of SN 1987A at 12 mm wavelength", Astrophys. J. Lett. **628**, L131–L134 (2005).

Mandelstam, S., "Soliton Operators for the Quantized Sine-Gordon Equation", Phys. Rev. D **11**, 3026 (1975).

Maniv, A., E. Polturak and G. Koren, "Observation of magnetic flux generated spontaneously during a rapid quench of superconducting films", Phys. Rev. Lett. **91**, 197001, URL https://link.aps.org/doi/10.1103/PhysRevLett.91.197001 (2003).

Martinez-Pinedo, G., K. Langanke and D. J. Dean, "Competition of electron capture and beta decay rates in supernova collapse", Astrophys. J. Suppl. **126**, 493–500 (2000).

Mavromatos, N. E. and V. A. Mitsou, "Magnetic monopoles revisited: Models and searches at colliders and in the Cosmos", Int. J. Mod. Phys. A **35**, 23, 2030012 (2020).

Mayle, R., J. R. Wilson, J. R. Ellis, K. A. Olive, D. N. Schramm and G. Steigman, "Constraints on Axions from SN 1987a", Phys. Lett. B **203**, 188–196 (1988).

Metzger, B. D., G. Martinez-Pinedo, S. Darbha, E. Quataert, A. Arcones, D. Kasen, R. Thomas, P. Nugent, I. V. Panov and N. T. Zinner, "Electromagnetic Counterparts of Compact Object Mergers Powered by the Radioactive Decay of R-process Nuclei", Mon. Not. Roy. Astron. Soc. **406**, 2650 (2010).

Michele Maggiore, C. V. D. B. and e. Nicola Bartolo, "Science case for the einstein telescope", Journal of Cosmology and Astroparticle Physics **2020**, 03, 050–050, URL https://doi.org/10.1088%2F1475-7516%2F2020%2F03%2F050 (2020).

Mikheev, S. P. and A. Y. Smirnov, "Resonant amplification of neutrino oscillations in matter and solar neutrino spectroscopy", Nuovo Cim. C **9**, 17–26 (1986).

Mikheyev, S. P. and A. Y. Smirnov, "Resonance Amplification of Oscillations in Matter and Spectroscopy of Solar Neutrinos", Sov. J. Nucl. Phys. **42**, 913–917 (1985).

Minkowski, P., "$\mu \to e\gamma$ at a Rate of One Out of 10^9 Muon Decays?", Phys. Lett. B **67**, 421–428 (1977).

Mirizzi, A., I. Tamborra, H.-T. Janka, N. Saviano, K. Scholberg, R. Bollig, L. Hudepohl and S. Chakraborty, "Supernova Neutrinos: Production, Oscillations and Detection", Riv. Nuovo Cim. **39**, 1-2, 1–112 (2016).

Misch, G. W., Y. Sun and G. M. Fuller, "Neutrino Spectra from Nuclear Weak Interactions in sd-Shell Nuclei under Astrophysical Conditions", "Astro. Phys. J." **852**, 1, 43 (2018).

Misiaszek, M., A. Odrzywolek and M. Kutschera, "Neutrino spectrum from the pair-annihilation process in the hot stellar plasma", "Phys. Rev. D" **74**, 043006 (2006).

Misner, C. W., K. Thorne and J. Wheeler, *Gravitation* (W. H. Freeman, San Francisco, 1973).

Mohapatra, R. N. and G. Senjanovic, "Neutrino Mass and Spontaneous Parity Nonconservation", Phys. Rev. Lett. **44**, 912 (1980).

Monaco, R., M. Aaroe, J. Mygind, R. J. Rivers and V. P. Koshelets, "Experiments on spontaneous vortex formation in josephson tunnel junctions", Phys. Rev. B **74**, 144513, URL https://link.aps.org/doi/10.1103/PhysRevB.74.144513 (2006a).

Monaco, R., J. Mygind, M. Aaroe, R. J. Rivers and V. P. Koshelets, "Zurek-kibble mechanism for the spontaneous vortex formation in Nb$-$Al/al$_{ox}$/Nb josephson tunnel junctions: New theory and experiment", Phys. Rev. Lett. **96**, 180604, URL https://link.aps.org/doi/10.1103/PhysRevLett.96.180604 (2006b).

Monaco, R., J. Mygind and R. J. Rivers, "Zurek-kibble domain structures: The dynamics of spontaneous vortex formation in annular josephson tunnel junctions", Phys. Rev. Lett. **89**, 080603, URL https://link.aps.org/doi/10.1103/PhysRevLett.89.080603 (2002).

Monzani, M. E., "Supernova neutrino detection in Borexino", Nuovo Cim. C **29**, 269–280 (2006).

Moore, C. J., R. H. Cole and C. P. L. Berry, "Gravitational-wave sensitivity curves", Classical and Quantum Gravity **32**, 1, 015014, URL https://doi.org/10.1088/0264-9381/32/1/015014 (2014).

Moore, C. J., R. H. Cole and C. P. L. Berry, "Gravitational-wave sensitivity curves", Class. Quant. Grav. **32**, 1, 015014 (2015).

Morozova, V., D. Radice, A. Burrows and D. Vartanyan, "The gravitational wave signal from core-collapse supernovae", Astrophys. J. **861**, 1, 10 (2018).

Morse, P. and H. Feshbach, *Methods of Theoretical Physics*, International series in pure and applied physics (McGraw-Hill, 1953), URL https://books.google.es/books?id=l8ENAQAAIAAJ.

Mrowczynski, S. and B. Muller, "Wigner functional approach to quantum field dynamics", Phys. Rev. **D50**, 7542–7552 (1994).

Mueller, B., H.-T. Janka and A. Marek, "A New Multi-Dimensional General Relativistic Neutrino Hydrodynamics Code of Core-Collapse Supernovae III. Gravitational Wave Signals from Supernova Explosion Models", Astrophys. J. **766**, 43 (2013).

Mueller, E. and H. T. Janka, "Gravitational radiation from convective instabilities in Type II supernova explosions.", AAP **317**, 140–163 (1997a).

Mueller, E. and H. T. Janka, "Gravitational radiation from convective instabilities in Type II supernova explosions.", AAP **317**, 140–163 (1997b).

Mukhanov, V. F. and G. V. Chibisov, "Quantum Fluctuations and a Nonsingular Universe", JETP Lett. **33**, 532–535, [Pisma Zh. Eksp. Teor. Fiz.33,549(1981)] (1981).

Mukhopadhyay, M., C. Cardona and C. Lunardini, "The neutrino gravitational memory from a core collapse supernova: phenomenology and physics potential", JCAP **07**, 055 (2021a).

Mukhopadhyay, M., Z. Lin and C. Lunardini, "Memory-triggered supernova neutrino detection", (2021b).

Mukhopadhyay, M., C. Lunardini, F. X. Timmes and K. Zuber, "Presupernova neutrinos: directional sensitivity and prospects for progenitor identification", Astrophys. J. **899**, 2, 153 (2020a).

Mukhopadhyay, M., E. I. Sfakianakis, T. Vachaspati and G. Zahariade, "Kink-antikink scattering in a quantum vacuum", JHEP **04**, 118 (2022).

Mukhopadhyay, M. and T. Vachaspati, "Rolling classical scalar field in a linear potential coupled to a quantum field", Phys. Rev. D **100**, 9, 096018 (2019).

Mukhopadhyay, M., T. Vachaspati and G. Zahariade, "Emergence of classical structures from the quantum vacuum", Phys. Rev. D **102**, 5, 056021 (2020b).

Mukhopadhyay, M., T. Vachaspati and G. Zahariade, "Quantum Formation of Topological Defects", Phys. Rev. D **102**, 11, 116002 (2020c).

Müller, B., "Neutrino Emission as Diagnostics of Core-Collapse Supernovae", Ann. Rev. Nucl. Part. Sci. **69**, 253–278 (2019).

Müller, B. and H.-T. Janka, "A New Multi-Dimensional General Relativistic Neutrino Hydrodynamics Code for Core-Collapse Supernovae IV. The Neutrino Signal", Astrophys. J. **788**, 82 (2014).

Müller, B., H.-T. Janka and A. Marek, "A New Multi-dimensional General Relativistic Neutrino Hydrodynamics Code of Core-collapse Supernovae. III. Gravitational Wave Signals from Supernova Explosion Models", "Astro. Phys. J." **766**, 1, 43 (2013).

Muller, E., H. T. Janka and A. Wongwathanarat, "Parametrized 3D models of neutrino-driven supernova explosions: Neutrino emission asymmetries and gravitational-wave signals", Astron. Astrophys. **537**, A63 (2012).

Müller, E., M. Rampp, R. Buras, H.-T. Janka and D. H. Shoemaker, "Toward gravitational wave signals from realistic core-collapse supernova models", The Astrophysical Journal **603**, 1, 221 (2004).

Murphy, J. W., C. D. Ott and A. Burrows, "A Model for Gravitational Wave Emission from Neutrino-Driven Core-Collapse Supernovae", Astrophys. J. **707**, 1173–1190 (2009).

Nakamura, K., S. Horiuchi, M. Tanaka, K. Hayama, T. Takiwaki and K. Kotake, "Multimessenger signals of long-term core-collapse supernova simulations: synergetic observation strategies", "Monthly Notices of the RAS" **461**, 3, 3296–3313 (2016).

Nakamura, K., S. Horiuchi, M. Tanaka, K. Hayama, T. Takiwaki and K. Kotake, "Multimessenger signals of long-term core-collapse supernova simulations: synergetic observation strategies", Mon. Not. Roy. Astron. Soc. **461**, 3, 3296–3313 (2016).

Nakamura, K. *et al.*, "Review of particle physics", J. Phys. G **37**, 075021 (2010).

Nambu, Y., "Strings, Monopoles and Gauge Fields", Phys. Rev. D **10**, 4262 (1974).

Narayan, R., B. Paczynski and T. Piran, "Gamma-ray bursts as the death throes of massive binary stars", Astrophys. J. Lett. **395**, L83–L86 (1992).

Narlikar, J. V., "Quantum fluctuations in gravitational collapse and cosmology.", MNRAS **183**, 159–168 (1978).

Neddermeyer, S. H. and C. D. Anderson, "Note on the Nature of Cosmic Ray Particles", Phys. Rev. **51**, 884–886 (1937).

Newstead, J. L., L. E. Strigari and R. F. Lang, "Detecting CNO solar neutrinos in next-generation xenon dark matter experiments", "Phys. Rev. D" **99**, 4, 043006 (2019).

Ni, W.-T., "Gravitational Wave (GW) Classification, Space GW Detection Sensitivities and AMIGO (Astrodynamical Middle-frequency Interferometric GW Observatory)", EPJ Web Conf. **168**, 01004 (2018).

Ni, W.-T., G. Wang and A.-M. Wu, "Astrodynamical middle-frequency interferometric gravitational wave observatory AMIGO: Mission concept and orbit design", Int. J. Mod. Phys. D **29**, 04, 1940007 (2020).

Notzold, D., "Gravitational Effects of Global Textures", Phys. Rev. D **43**, R961–R964 (1991).

Nunokawa, H., S. J. Parke and J. W. F. Valle, "CP Violation and Neutrino Oscillations", Prog. Part. Nucl. Phys. **60**, 338–402 (2008).

Nussinov, S., "Solar Neutrinos and Neutrino Mixing", Phys. Lett. B **63**, 201–203 (1976).

Ochoa-Ricoux, J. P., "The Daya Bay neutrino oscillation experiment", Nucl. Phys. B Proc. Suppl. **217**, 140–142 (2011).

O'Connor, E. and C. D. Ott, "Black Hole Formation in Failing Core-Collapse Supernovae", Astrophys. J. **730**, 70 (2011).

Oda, T., M. Hino, K. Muto, M. Takahara and K. Sato, "Rate Tables for the Weak Processes of sd -Shell Nuclei in Stellar Matter", Atom. Data Nucl. Data Tabl. **56**, 231–403 (1994).

Odrzywolek, A., "Plasmaneutrino spectrum", Eur. Phys. J. **C52**, 425–434 (2007).

Odrzywolek, A., "Nuclear statistical equilibrium neutrino spectrum", "Phys. Rev. C" **80**, 4, 045801 (2009).

Odrzywolek, A. and A. Heger, "Neutrino signatures of dying massive stars: From main sequence to the neutron star", Acta Phys. Polon. **B41**, 1611–1628 (2010).

Odrzywolek, A., M. Misiaszek and M. Kutschera, "Detection possibility of the pair - annihilation neutrinos from the neutrino - cooled pre-supernova star", Astropart. Phys. **21**, 303–313 (2004a).

Odrzywolek, A., M. Misiaszek and M. Kutschera, "Neutrinos from pre-supernova star", Acta Phys. Polon. **B35**, 1981 (2004b).

Olle, J., O. Pujolas, T. Vachaspati and G. Zahariade, "Quantum Evaporation of Classical Breathers", JHEP (2019).

Otsuki, K., H. Tagoshi, T. Kajino and S.-y. Wanajo, "General relativistic effects on neutrino driven wind from young, hot neutron star and the r process nucleosynthesis", Astrophys. J. **533**, 424 (2000).

Ott, C., "The Gravitational Wave Signature of Core-Collapse Supernovae", Class. Quant. Grav. **26**, 063001 (2009).

Ott, C. D., A. Burrows, L. Dessart and E. Livne, "A new mechanism for gravitational-wave emission in core-collapse supernovae", Physical Review Letters **96**, 20, 201102 (2006).

Ott, C. D., H. Dimmelmeier, A. Marek, H. T. Janka, I. Hawke, B. Zink and E. Schnetter, "3D Collapse of Rotating Stellar Iron Cores in General Relativity with Microphysics", Phys. Rev. Lett. **98**, 261101 (2007).

Ott, C. D., S. Ou, J. E. Tohline and A. Burrows, "One-armed spiral instability in a slowly rotating, post-bounce supernova core", Astrophys. J. Lett. **625**, L119–L122 (2005).

Ott, C. D., C. Reisswig, E. Schnetter, E. O'Connor, U. Sperhake, F. Loffler, P. Diener, E. Abdikamalov, I. Hawke and A. Burrows, "Dynamics and Gravitational Wave Signature of Collapsar Formation", Phys. Rev. Lett. **106**, 161103 (2011).

Paczynski, B., "Gamma-ray bursters at cosmological distances", Astrophys. J. Lett. **308**, L43–L46 (1986).

Pagliaroli, G., F. Vissani, E. Coccia and W. Fulgione, "Neutrinos from supernovae as a trigger for gravitational wave search", Phys. Rev. Lett. **103**, 031102, URL https://link.aps.org/doi/10.1103/PhysRevLett.103.031102 (2009).

Pal, V., C. Tradonsky, R. Chriki, A. A. Friesem and N. Davidson, "Observing dissipative topological defects with coupled lasers", Phys. Rev. Lett. **119**, 013902, URL https://link.aps.org/doi/10.1103/PhysRevLett.119.013902 (2017).

Pan, K.-C., C. Mattes, E. P. O'Connor, S. M. Couch, A. Perego and A. Arcones, "The Impact of Different Neutrino Transport Methods on Multidimensional Core-collapse Supernova Simulations", J. Phys. G **46**, 1, 014001 (2019).

Park, S., S. A. Zhekov, D. N. Burrows, G. P. Garmire and D. McCray, "Supernova remnant 1987A: The Latest report from the Chandra X-ray Observatory", Adv. Space Res. **35**, 991 (2005a).

Park, S., S. A. Zhekov, D. N. Burrows, G. P. Garmire, J. L. Racusin and R. McCray, "Evolutionary Status of SNR 1987A at the Age of Eighteen", Astrophys. J. **646**, 1001–1008 (2006).

Park, S., S. A. Zhekov, D. N. Burrows and R. McCray, "Supernova remnant 1987a: opening the future by reaching the past", Astrophys. J. Lett. **634**, L73–L76 (2005b).

Patton, K., C. Lunardini, R. Farmer and F. Timmes, "Neutrinos from Beta Processes in a Presupernova: Probing the Isotopic Evolution of a Massive Star", "Astro. Phys. J." **851**, 6 (2017a).

Patton, K. M., C. Lunardini and R. J. Farmer, "Presupernova Neutrinos: Realistic Emissivities from Stellar Evolution", "Astro. Phys. J." **840**, 2 (2017b).

Patton, K. M., C. Lunardini, R. J. Farmer and F. X. Timmes, "Neutrinos from Beta Processes in a Presupernova: Probing the Isotopic Evolution of a Massive Star", Zenodo, doi 10.5281/zenodo.2626645, URL https://doi.org/10.5281/zenodo.2626645 (2019).

Pau Amaro-Seoane, H. A. and e. Stanislav Babak, "Laser interferometer space antenna", (2017).

Pauli, W., "On the Earlier and more recent history of the neutrino", Camb. Monogr. Part. Phys. Nucl. Phys. Cosmol. **14**, 1–22 (2000).

Pejcha, O. and T. A. Thompson, "The physics of the neutrino mechanism of core-collapse supernovae", The Astrophysical Journal **746**, 1, 106 (2012).

Pena-Garay, C. and A. Serenelli, "Solar neutrinos and the solar composition problem", (2008).

Perrin, F., "Possibilité d'émission de particules neutres de masse intrinsèque nulle dans les radioactivités beta", Comptes-Rendus **197** (1933).

Peskin, M. E. and D. V. Schroeder, *An Introduction to quantum field theory* (Addison-Wesley, Reading, USA, 1995), URL http://www.slac.stanford.edu/~mpeskin/QFT.html.

Piran, T., "Neutrino Mass and Detection of Neutrino Supernova Bursts", Phys. Lett. B **102**, 299–302 (1981).

Pontecorvo, B., "Inverse beta processes and nonconservation of lepton charge", Zh. Eksp. Teor. Fiz. **34**, 247 (1957a).

Pontecorvo, B., "Mesonium and anti-mesonium", Sov. Phys. JETP **6**, 429 (1957b).

Pontecorvo, B., "Electron and Muon Neutrinos", Zh. Eksp. Teor. Fiz. **37**, 1751–1757 (1959).

Pontecorvo, B., "Neutrino Experiments and the Problem of Conservation of Leptonic Charge", Zh. Eksp. Teor. Fiz. **53**, 1717–1725 (1967).

Qian, Y. Z. and S. E. Woosley, "Nucleosynthesis in neutrino driven winds: 1. The Physical conditions", Astrophys. J. **471**, 331–351 (1996).

Raffelt, G. and D. Seckel, "Bounds on Exotic Particle Interactions from SN 1987a", Phys. Rev. Lett. **60**, 1793 (1988).

Raffelt, G., D. Seckel and G. Sigl, "Supernova neutrino scattering rates reduced by nucleon spin fluctuations: Perturbative limit", Phys. Rev. D **54**, 2784–2792 (1996).

Raffelt, G. G., J. Redondo and N. Viaux Maira, "The meV mass frontier of axion physics", Phys. Rev. **D84**, 103008 (2011).

Raj, N., V. Takhistov and S. J. Witte, "Presupernova neutrinos in large dark matter direct detection experiments", Phys. Rev. D **101**, 4, 043008 (2020).

Rajaraman, R., *Solitons and Instantons: An Introduction to Solitons and Instantons in Quantum Field Theory*, North-Holland personal library (North-Holland Publishing Company, 1982), URL https://books.google.es/books?id=1XucQgAACAAJ.

Ramsey, S. A. and B. L. Hu, "Nonequilibrium inflaton dynamics and reheating. 1. Back reaction of parametric particle creation and curved space-time effects", Phys. Rev. **D56**, 678–705, [Erratum: Phys. Rev.D57,3798(1998)] (1997).

Ratkovic, S., S. I. Dutta and M. Prakash, "Differential neutrino rates and emissivities from the plasma process in astrophysical systems", Phys. Rev. C **67**, 123002 (2003).

Reichard, S., R. F. Lang, C. McCabe, M. Selvi and I. Tamborra, "Supernova Neutrino Physics with Xenon Dark Matter Detectors", J. Phys. Conf. Ser. **888**, 1, 012260 (2017).

Reines, F., "The neutrino: From poltergeist to particle", Rev. Mod. Phys. **68**, 317–327 (1996).

Reines, F., C. L. Cowan, F. B. Harrison, A. D. McGuire and H. W. Kruse, "Detection of the free anti-neutrino", Phys. Rev. **117**, 159–173 (1960).

Reitze, D. *et al.*, "Cosmic Explorer: The U.S. Contribution to Gravitational-Wave Astronomy beyond LIGO", Bull. Am. Astron. Soc. **51**, 7, 035 (2019).

Rivers, R., "Vortex densities and correlations at phase transitions", in "4th Workshop on Thermal Field Theories and Their Applications", pp. 261–272 (1995).

Roy, D. P., "Eighty Years of Neutrino Physics", Physics News India **39**, 51 (2009).

Ruan, W.-H., Z.-K. Guo, R.-G. Cai and Y.-Z. Zhang, "Taiji program: Gravitational-wave sources", Int. J. Mod. Phys. A **35**, 17, 2050075 (2020).

Ruutu, V. M. H., V. B. Eltsov, A. J. Gill, T. W. B. Kibble, M. Krusius, Y. G. Makhlin, B. Placais, G. E. Volovik and W. Xu, "Vortex formation in neutron-irradiated superfluid 3he as an analogue of cosmological defect formation", Nature **382**, 6589, 334–336, URL https://doi.org/10.1038/382334a0 (1996).

Saffin, P. M., P. Tognarelli and A. Tranberg, "Oscillon Lifetime in the Presence of Quantum Fluctuations", JHEP **08**, 125 (2014).

Sagert, I., T. Fischer, M. Hempel, G. Pagliara, J. Schaffner-Bielich, A. Mezzacappa, F. K. Thielemann and M. Liebendorfer, "Signals of the QCD phase transition in core-collapse supernovae", Phys. Rev. Lett. **102**, 081101 (2009).

Sago, N., K. Ioka, T. Nakamura and R. Yamazaki, "Gravitational wave memory of gamma-ray burst jets", Phys. Rev. D **70**, 104012 (2004).

Saikawa, K., "Gravitational waves from cosmic domain walls: a mini-review", J. Phys. Conf. Ser. **1586**, 1, 012039 (2020).

Sajjad Athar, M. *et al.*, "Status and perspectives of neutrino physics", Prog. Part. Nucl. Phys. **124**, 103947 (2022).

Sako, M. *et al.*, "The Sloan Digital Sky Survey-II Supernova Survey: Search Algorithm and Follow-up Observations", Astron. J. **135**, 348–373 (2008).

Sakurai, J. J., "MASS REVERSAL AND WEAK INTERACTIONS", Nuovo Cim. **7**, 649–660 (1958).

Salam, A., "On parity conservation and neutrino mass", Nuovo Cim. **5**, 299–301 (1957).

Salam, A., "Weak and Electromagnetic Interactions", in "in Elementary particle theory. Relativistic groups and analyticity. Proceedings of the Eighth Nobel Symposium held May 19-25", pp. 367–377 (1968).

Sathyaprakash, B. S. and B. F. Schutz, "Physics, astrophysics and cosmology with gravitational waves", Living Reviews in Relativity **12**, 1, URL http://dx.doi.org/10.12942/lrr-2009-2 (2009a).

Sathyaprakash, B. S. and B. F. Schutz, "Physics, Astrophysics and Cosmology with Gravitational Waves", Living Rev. Rel. **12**, 2 (2009b).

Sato, S. *et al.*, "The status of DECIGO", J. Phys. Conf. Ser. **840**, 1, 012010 (2017).

Schechter, J. and J. W. F. Valle, "Neutrino Masses in SU(2) x U(1) Theories", Phys. Rev. D **22**, 2227 (1980).

Scheidegger, S., S. C. Whitehouse, R. Kappeli and M. Liebendorfer, "Gravitational waves from supernova matter", Class. Quant. Grav. **27**, 114101 (2010).

Schinder, P. J., D. N. Schramm, P. J. Wiita, S. H. Margolis and D. L. Tubbs, "Neutrino Emission by the Pair, Plasma, and Photo Processes in the Weinberg-Salam Model", "Astro. Phys. J." **313**, 531 (1987).

Schmitz, K., "New Sensitivity Curves for Gravitational-Wave Signals from Cosmological Phase Transitions", JHEP **01**, 097 (2021).

Scholberg, K., "The SuperNova Early Warning System", Astron. Nachr. **329**, 337–339 (2008).

Scholberg, K., "Supernova Neutrino Detection", Ann. Rev. Nucl. Part. Sci. **62**, 81–103 (2012).

Schramm, D. N., "Neutrinos from Supernova SN 1987a", Comments Nucl. Part. Phys. **17**, 5, 239–278 (1987).

Schwinger, J. S., "On gauge invariance and vacuum polarization", Phys. Rev. **82**, 664–679 (1951).

Seljak, U. *et al.*, "Cosmological parameter analysis including SDSS Ly-alpha forest and galaxy bias: Constraints on the primordial spectrum of fluctuations, neutrino mass, and dark energy", Phys. Rev. D **71**, 103515 (2005).

Serenelli, A., S. Basu, J. W. Ferguson and M. Asplund, "New Solar Composition: The Problem With Solar Models Revisited", Astrophys. J. Lett. **705**, L123–L127 (2009).

Serenelli, A. M., W. C. Haxton and C. Pena-Garay, "Solar models with accretion. I. Application to the solar abundance problem", Astrophys. J. **743**, 24 (2011).

Seto, N., S. Kawamura and T. Nakamura, "Possibility of direct measurement of the acceleration of the universe using 0.1-Hz band laser interferometer gravitational wave antenna in space", Phys. Rev. Lett. **87**, 221103 (2001).

Sharp, M. K., J. F. Beacom and J. A. Formaggio, "Potential for Supernova Neutrino Detection in MiniBooNe", Phys. Rev. D **66**, 013012 (2002).

Shibagaki, S., T. Kuroda, K. Kotake and T. Takiwaki, "Characteristic Time Variability of Gravitational-Wave and Neutrino Signals from Three-dimensional Simulations of Non-Rotating and Rapidly Rotating Stellar Core-Collapse", Mon. Not. Roy. Astron. Soc. **502**, 2, 3066–3084 (2021).

Shtykovskiy, P., A. Lutovinov, M. Gilfanov and R. Sunyaev, "Constraints on the luminosity of the stellar remnant in SNR1987A", Astron. Lett. **31**, 258–262 (2005).

Shuichi Sato, S. K. and e. Masaki Ando, "The status of DECIGO", Journal of Physics: Conference Series **840**, 012010, URL https://doi.org/10.1088%2F1742-6596%2F840%2F1%2F012010 (2017).

Sikivie, P., "Of Axions, Domain Walls and the Early Universe", Phys. Rev. Lett. **48**, 1156–1159 (1982).

Simpson, e. a., C., "Sensitivity of Super-Kamiokande with Gadolinium to Low Energy Anti-neutrinos from Pre-supernova Emission", arXiv e-prints p. arXiv:1908.07551 (2019).

Smartt, S. J., "Observational constraints on the progenitors of core-collapse supernovae : the case for missing high mass stars", Publ. Astron. Soc. Austral. **32**, e016 (2015).

Smith, M. W. E. *et al.*, "The Astrophysical Multimessenger Observatory Network (AMON)", Astropart. Phys. **45**, 56–70 (2013).

Sonneborn, G., B. Altner and R. P. Kirshner, "The progenitor of sn 1987a-spatially resolved ultraviolet spectroscopy of the supernova field", The Astrophysical Journal **323**, L35–L39 (1987).

Sonneborn, G., B. Altner and R. P. Kirshner, "The Progenitor of SN 1987A: Spatially Resolved Ultraviolet Spectroscopy of the Supernova Field", APJL **323**, L35 (1987).

Sotani, H. and T. Takiwaki, "Gravitational wave asteroseismology with protoneutron stars", Phys. Rev. D **94**, 4, 044043 (2016).

Spergel, D. N. and N. G. Turok, "Textures and cosmic structure", Sci. Am. **266**, 36–43 (1992).

Spiro, S., A. Pastorello, M. Pumo, L. Zampieri, M. Turatto, S. Smartt, S. Benetti, E. Cappellaro, S. Valenti, I. Agnoletto *et al.*, "Low luminosity type ii supernovae–ii. pointing towards moderate mass precursors", Monthly Notices of the Royal Astronomical Society **439**, 3, 2873–2892 (2014).

Stein, E. M. and G. Weiss, *Introduction to Fourier Analysis on Euclidean Spaces (PMS-32)* (Princeton University Press, 1971), URL http://www.jstor.org/stable/j.ctt1bpm9w6.

Stephens, G., E. Calzetta, B. Hu and S. Ramsey, "Defect formation and critical dynamics in the early universe", Phys. Rev. D **59**, 045009 (1999).

Street, J. C. and E. C. Stevenson, "New Evidence for the Existence of a Particle of Mass Intermediate Between the Proton and Electron", Phys. Rev. **52**, 1003–1004 (1937).

Strigari, L. E., M. Kaplinghat, G. Steigman and T. P. Walker, "The Supernova relic neutrino backgrounds at KamLAND and Super-Kamiokande", JCAP **03**, 007 (2004).

Strominger, A., "On BMS Invariance of Gravitational Scattering", JHEP **07**, 152 (2014).

Strominger, A. and A. Zhiboedov, "Gravitational Memory, BMS Supertranslations and Soft Theorems", JHEP **01**, 086 (2016).

Strumia, A. and F. Vissani, "Precise quasielastic neutrino/nucleon cross-section", Phys. Lett. B **564**, 42–54 (2003).

Strumia, A. and F. Vissani, "Neutrino masses and mixings and...", (2006).

Sudarshan, E. C. G. and R. e. Marshak, "Chirality invariance and the universal Fermi interaction", Phys. Rev. **109**, 1860–1860 (1958).

Sugerman, B. E. K., A. P. S. Crotts, W. E. Kunkel, S. R. Heathcote and S. S. Lawrence, "A New view of the circumstellar environment of SN1987A", Astrophys. J. **627**, 888–903 (2005).

Sugiyama, T., "KINK - ANTIKINK COLLISIONS IN THE TWO-DIMENSIONAL PHI**4 MODEL", Prog. Theor. Phys. **61**, 1550–1563 (1979).

Sukhbold, T., T. Ertl, S. E. Woosley, J. M. Brown and H. T. Janka, "Core-Collapse Supernovae from 9 to 120 Solar Masses Based on Neutrino-powered Explosions", Astrophys. J. **821**, 1, 38 (2016).

Sumiyoshi, K., S. Yamada, H. Suzuki and S. Chiba, "Neutrino signals from the formation of black hole: A probe of equation of state of dense matter", Phys. Rev. Lett. **97**, 091101 (2006).

Suwa, Y. and K. Murase, "Probing the central engine of long gamma-ray bursts and hypernovae with gravitational waves and neutrinos", Physical Review D **80**, 12, URL http://dx.doi.org/10.1103/PhysRevD.80.123008 (2009).

Szczepanczyk, M., J. Antelis, M. Benjamin, M. Cavaglia, D. Gondek-Rosinska, T. Hansen, S. Klimenko, M. Morales, C. Moreno, S. Mukherjee *et al.*, "Detecting and reconstructing gravitational waves from the next galactic core-collapse supernova in the advanced detector era", arXiv preprint arXiv:2104.06462 (2021).

't Hooft, G., "Magnetic Monopoles in Unified Gauge Theories", Nucl. Phys. B **79**, 276–284 (1974).

Tamborra, I., F. Hanke, B. Müller, H.-T. Janka and G. Raffelt, "Neutrino signature of supernova hydrodynamical instabilities in three dimensions", Phys. Rev. Lett. **111**, 12, 121104 (2013).

Tamborra, I., G. Raffelt, F. Hanke, H.-T. Janka and B. Mueller, "Neutrino emission characteristics and detection opportunities based on three-dimensional supernova simulations", Phys. Rev. D **90**, 4, 045032 (2014).

Tanaka, H. and H. Watanabe, "^{6}Li-loaded directionally sensitive anti-neutrino detector for possible geo-neutrinographic imaging applications", Scientific Reports **4**, 4708 (2014).

Tegmark, M. *et al.*, "Cosmological parameters from SDSS and WMAP", Phys. Rev. D **69**, 103501 (2004).

Thompson, T. A., A. Burrows and B. S. Meyer, "The Physics of protoneutron star winds: implications for r-process nucleosynthesis", Astrophys. J. **562**, 887 (2001).

Thorne, K. S., "Gravitational-wave bursts with memory: The Christodoulou effect", Phys. Rev. **D45**, 2, 520–524 (1992).

Tomalak, O. and R. J. Hill, "Theory of elastic neutrino-electron scattering", Phys. Rev. D **101**, 3, 033006 (2020).

Tomas, R., D. Semikoz, G. G. Raffelt, M. Kachelriess and A. S. Dighe, "Supernova pointing with low-energy and high-energy neutrino detectors", Phys. Rev. D **68**, 093013 (2003).

Trimble, V., "Supernovae. part i: the events", Rev. Mod. Phys. **54**, 1183–1224, URL https://link.aps.org/doi/10.1103/RevModPhys.54.1183 (1982).

Trimble, V., "Supernovae. part ii: the aftermath", Reviews of modern physics **55**, 2, 511 (1983).

Turck-Chieze, S., S. Cahen, M. Casse and C. Doom, "Revisiting the standard solar model", Astrophys. J. **335**, 415–424 (1988).

Turck-Chieze, S. and I. Lopes, "Toward a unified classical model of the sun: On the sensitivity of neutrinos and helioseismology to the microscopic physics", Astrophys. J. **408**, 347–367 (1993).

Turck-Chieze, S., D. Vignaud, W. Daeppen, E. Fossat, J. Provost and E. Schatzman, "The Solar Interior", Phys. Rept. **230**, 57–235 (1993).

Turck-Chieze, S. *et al.*, "Solar neutrino emission deduced from a seismic model", Astrophys. J. Lett. **555**, L69–L73 (2001).

Turner, M. S., "Gravitational Radiation from Supernova Neutrino Bursts", Nature **274**, 565–566 (1978).

Turner, M. S., "Axions from SN 1987a", Phys. Rev. Lett. **60**, 1797 (1988).

Turok, N., "Global Texture as the Origin of Cosmic Structure", Phys. Rev. Lett. **63**, 2625 (1989).

Ugliano, M., H. T. Janka, A. Marek and A. Arcones, "Progenitor-Explosion Connection and Remnant Birth Masses for Neutrino-Driven Supernovae of Iron-Core Progenitors", Astrophys. J. **757**, 69 (2012).

Vachaspati, T., "Topological defects in the cosmos and lab", Contemp. Phys. **39**, 225–237 (1998).

Vachaspati, T., "Schrodinger Picture of Quantum Gravitational Collapse", Class. Quant. Grav. **26**, 215007 (2009).

Vachaspati, T., *Kinks and domain walls: An introduction to classical and quantum solitons* (Cambridge University Press, 2010).

Vachaspati, T., "Quantum Backreaction on Classical Dynamics", Phys. Rev. D **95**, 12, 125002 (2017).

Vachaspati, T., "Unexciting classical backgrounds", Phys. Rev. D **105**, 5, 056008 (2022a).

Vachaspati, T., "Unexciting non-Abelian electric fields", (2022b).

Vachaspati, T. and A. Vilenkin, "Formation and Evolution of Cosmic Strings", Phys. Rev. D **30**, 2036 (1984).

Vachaspati, T. and A. Vilenkin, "Gravitational Radiation from Cosmic Strings", Phys. Rev. D **31**, 3052 (1985).

Vachaspati, T. and G. Zahariade, "Classical-quantum correspondence and backreaction", Phys. Rev. **D98**, 6, 065002 (2018a).

Vachaspati, T. and G. Zahariade, "Classical-Quantum Correspondence for Fields", Phys. Rev. (2018b).

Vachaspati, T. and G. Zahariade, "Classical-Quantum Correspondence and Hawking Radiation", JCAP **1904**, 04, 013 (2019).

Valenti, S. *et al.*, "The diversity of Type II supernova versus the similarity in their progenitors", Mon. Not. Roy. Astron. Soc. **459**, 4, 3939–3962 (2016).

Van Dissel, F. and E. I. Sfakianakis, "Symmetric multi-field oscillons", (2020).

van Leeuwen, F., "Validation of the new Hipparcos reduction", "AAP" **474**, 2, 653–664 (2007).

Vartanyan, D. and A. Burrows, "Gravitational Waves from Neutrino Asymmetries in Core-Collapse Supernovae", Astrophys. J. **901**, 2, 108 (2020).

Vartanyan, D., A. Burrows and D. Radice, "Temporal and Angular Variations of 3D Core-Collapse Supernova Emissions and their Physical Correlations", Mon. Not. Roy. Astron. Soc. **489**, 2, 2227–2246 (2019).

Vedder, J. D., "Simple approximations for the error function and its inverse", American Journal of Physics **55**, 8, 762–763, URL https://doi.org/10.1119/1.15018 (1987).

Vilenkin, A., "Cosmic Strings and Domain Walls", Phys. Rept. **121**, 263–315 (1985).

Vilenkin, A. and A. E. Everett, "Cosmic Strings and Domain Walls in Models with Goldstone and PseudoGoldstone Bosons", Phys. Rev. Lett. **48**, 1867–1870 (1982).

Vilenkin, A. and E. S. Shellard, *Cosmic Strings and Other Topological Defects* (Cambridge University Press, 2000).

Vinyoles, N., A. M. Serenelli, F. L. Villante, S. Basu, J. Bergström, M. C. Gonzalez-Garcia, M. Maltoni, C. Peña Garay and N. Song, "A new Generation of Standard Solar Models", Astrophys. J. **835**, 2, 202 (2017).

Vitagliano, E., I. Tamborra and G. Raffelt, "Grand Unified Neutrino Spectrum at Earth: Sources and Spectral Components", Rev. Mod. Phys. **92**, 45006 (2020).

Vogel, P. and J. Beacom, "Angular distribution of neutron inverse beta decay, ν_e+p–>e^++n", "Phys. Rev. D" **60**, 5, 053003 (1999).

Vogel, P. and J. F. Beacom, "Angular distribution of neutron inverse beta decay, anti-neutrino(e) + p —> e+ + n", Phys. Rev. D **60**, 053003 (1999).

Walk, L., I. Tamborra, H.-T. Janka and A. Summa, "Identifying rotation in SASI-dominated core-collapse supernovae with a neutrino gyroscope", Phys. Rev. D **98**, 12, 123001 (2018).

Walk, L., I. Tamborra, H.-T. Janka and A. Summa, "Effects of the standing accretion-shock instability and the lepton-emission self-sustained asymmetry in the neutrino emission of rotating supernovae", Phys. Rev. D **100**, 6, 063018 (2019).

Walk, L., I. Tamborra, H.-T. Janka, A. Summa and D. Kresse, "Neutrino emission characteristics of black hole formation in three-dimensional simulations of stellar collapse", Phys. Rev. D **101**, 12, 123013 (2020a).

Walk, L., I. Tamborra, H.-T. Janka, A. Summa and D. Kresse, "Neutrino emission characteristics of black hole formation in three-dimensional simulations of stellar collapse", Physical Review D **101**, 12, URL http://dx.doi.org/10.1103/PhysRevD.101.123013 (2020b).

Weinberg, S., "A Model of Leptons", Phys. Rev. Lett. **19**, 1264–1266 (1967).

Weinberg, S., *Gravitation and Cosmology: Principles and Applications of the General Theory of Relativity* (John Wiley and Sons, New York, 1972).

Wilkinson, D. H., "G(V), CKM unitarity, neutron decay, W(R)?", Z. Phys. A **348**, 129–138 (1994).

Wolfenstein, L., "Neutrino Oscillations in Matter", Phys. Rev. D **17**, 2369–2374 (1978).

Woosley, S. and T. Janka, "The physics of core-collapse supernovae", Nature Phys. **1**, 147 (2005).

Woosley, S. E., A. Heger and T. A. Weaver, "The evolution and explosion of massive stars", Rev. Mod. Phys. **74**, 1015–1071, URL https://link.aps.org/doi/10.1103/RevModPhys.74.1015 (2002).

Woosley, S. E. and T. A. Weaver, "The Physics of supernova explosions", Ann. Rev. Astron. Astrophys. **24**, 205–253 (1986).

Wu, C. S., E. Ambler, R. W. Hayward, D. D. Hoppes and R. P. Hudson, "Experimental test of parity conservation in beta decay", Phys. Rev. **105**, 1413–1415, URL https://link.aps.org/doi/10.1103/PhysRev.105.1413 (1957).

Yagi, K. and N. Seto, "Detector configuration of decigo/bbo and identification of cosmological neutron-star binaries", Physical Review D **83**, 4, URL http://dx.doi.org/10.1103/PhysRevD.83.044011 (2011a).

Yagi, K. and N. Seto, "Detector configuration of decigo/bbo and identification of cosmological neutron-star binaries", Phys. Rev. D **83**, 044011, URL https://link.aps.org/doi/10.1103/PhysRevD.83.044011 (2011b).

Yakunin, K. N. *et al.*, "Gravitational Waves from Core Collapse Supernovae", Class. Quant. Grav. **27**, 194005 (2010).

Yakunin, K. N. *et al.*, "Gravitational wave signatures of ab initio two-dimensional core collapse supernova explosion models for 12–25 $m_\odot$ stars", Phys. Rev. D **92**, 8, 084040 (2015).

Yates, A. and W. H. Zurek, "Vortex formation in two-dimensions: When symmetry breaks, how big are the pieces?", Phys. Rev. Lett. **80**, 5477–5480 (1998).

Yoshida, T., K. Takahashi, H. Umeda and K. Ishidoshiro, "Presupernova neutrino events relating to the final evolution of massive stars", "Phys. Rev. D" **93**, 12, 123012 (2016).

Zatespin, G., "Probability of Determining the Upper Limit of the Neutrino Mass from the Time of Flight", JETP Lett. **8**, 6, 333 (1968).

Zel'dovich, Y. B. and A. G. Polnarev, "Radiation of gravitational waves by a cluster of superdense stars", Sov. Astron. **18**, 17 (1974).

Zeldovich, Y. B. and A. A. Starobinsky, "Particle production and vacuum polarization in an anisotropic gravitational field", Zh. Eksp. Teor. Fiz. **61**, 2161–2175 (1971).

Zhan, M.-S. *et al.*, "ZAIGA: Zhaoshan Long-baseline Atom Interferometer Gravitation Antenna", Int. J. Mod. Phys. D **29**, 04, 1940005 (2019).

Zhang, H. *et al.*, "Supernova Relic Neutrino Search with Neutron Tagging at Super-Kamiokande-IV", Astropart. Phys. **60**, 41–46 (2015).

Zhang, H.-Y., "Gravitational effects on oscillon lifetimes", JCAP **03**, 102 (2021).

Zhang, H.-Y., M. A. Amin, E. J. Copeland, P. M. Saffin and K. D. Lozanov, "Classical Decay Rates of Oscillons", JCAP **07**, 055 (2020).

Zhekov, S. A., R. McCray, K. J. Borkowski, D. N. Burrows and S. Park, "Chandra observations of shock kinematics in supernova remnant 1987A", Astrophys. J. Lett. **628**, L127–L130 (2005).

Zhou, S.-Y., E. J. Copeland, R. Easther, H. Finkel, Z.-G. Mou and P. M. Saffin, "Gravitational Waves from Oscillon Preheating", JHEP **10**, 026 (2013).

Zurek, W., "Cosmological Experiments in Superfluid Helium?", Nature **317**, 505–508 (1985).

Zurek, W., "Cosmic strings in laboratory superfluids and the topological remnants of other phase transitions", Acta Phys. Polon. B **24**, 1301–1311 (1993).

Zurek, W., "Cosmological experiments in condensed matter systems", Phys. Rept. **276**, 177–221 (1996).

Zurek, W. H., U. Dorner and P. Zoller, "Dynamics of a quantum phase transition", Phys. Rev. Lett. **95**, 105701 (2005).

APPENDIX A

TWO FLAVOR NEUTRINO OSCILLATION

In this appendix, we derive and discuss the neutrino oscillation probabilities for the two flavor osciilation scenario (see Sec. 1.4 for details). The neutrinos come in three flavour (or interaction) eigenstates and three mass eigenstates. Since they have non zero mass, hence there is no reason for the above mentioned states to coincide. Thus, there occurs coherent mixing between them. We will study the mixing between two neutrinos, which is a fair approximation. In this treatment of two flavours the interaction eigenstates are related to the mass eigenstates by a 2×2 unitary rotation matrix from the mass basis to the interaction basis, as shown below:

$$\begin{pmatrix} \nu_e \\ \nu_\mu \end{pmatrix} = \begin{pmatrix} \cos\theta & \sin\theta \\ -\sin\theta & \cos\theta \end{pmatrix} \begin{pmatrix} \nu_1 \\ \nu_2 \end{pmatrix} \tag{A.1}$$

where ν_e and ν_μ are the interaction eigenstates, ν_1 and ν_2 are the mass eigenstates with eigenvalues m_1 and m_2; θ is the mixing angle. If we take m_1 to be the lower mass; then in its rest frame; ν_2 has higher energy, m_2 which is is its mass and some kinetic energy of its own. Since this is a quantum mechanical phenonmenon this coherent mixture ($\nu_e = \nu_1 \cos\theta + \nu_2 \sin\theta$) leads to breaking of energy conservation for short time intervals, which is taken care by the uncertainity principle. This leads to the phenomenon of neutrino oscillation.

Consider a nuclear beta decay which produces a ν_e state ($N(A, Z) \rightarrow N'(A, Z - 1) + e^+ + \nu_e$). Its ν_1 and ν_2 components will travel with different velocities sine they differ in mass. Because of this their relative wave-packet sizes will change with distance, which means transformation of ν_e to ν_μ. Due to the uncertainity principle, the neutrinos of definite mass and momentum do not travel as point particles, rather they travel as plane monochromatic waves, whose wave-function is given by;

$$\Psi = e^{-i(Et - pl)} \tag{A.2}$$

Since, the mass of the neutrinos is very small ($< eV$) as compared to their energies which are high ($\sim MeV$), they are extreme relativistic particles. Thus, in natural units,

$$t \cong l$$

and,

$$E \cong p + \frac{m^2}{2p} \cong p + \frac{m^2}{2E}$$

On substituting the above to Eq. A.2, we get,

$$\Psi = e^{-i(E-p)l} = e^{-i(\frac{m^2 l}{2E})} \tag{A.3}$$

So the neutrino mass eigenstate propagates with a phase of $e^{-i(\frac{m^2 l}{2E})}$. After travelling a distance l, the wave function of the produced ν_e is of the form

$$\nu_e \rightarrow \nu_1 \cos\theta e^{-i(\frac{{m_1}^2 l}{2E})} + \nu_2 \sin\theta e^{-i(\frac{{m_2}^2 l}{2E})} \tag{A.4}$$

Eq. A.4 can be written in terms of the interaction eigenstates using the inverse of Eq. A.1;

$$\begin{pmatrix} \nu_1 \\ \nu_2 \end{pmatrix} = \begin{pmatrix} \cos\theta & -\sin\theta \\ \sin\theta & \cos\theta \end{pmatrix} \begin{pmatrix} \nu_e \\ \nu_\mu \end{pmatrix} \tag{A.5}$$

From above, we have

$$\nu_1 = \nu_e \cos\theta - \nu_\mu \sin\theta$$

and

$$\nu_2 = \nu_e \sin\theta + \nu_\mu \cos\theta$$

Thus from Eq. A.4,

$$\nu_e \rightarrow (\nu_e \cos\theta - \nu_\mu \sin\theta)\cos\theta e^{-i(\frac{m^2 l}{2E})} + (\nu_e \sin\theta + \nu_\mu \cos\theta)\sin\theta e^{-i(\frac{m^2 l}{2E})}$$

or

$$\nu_e \rightarrow (\nu_e \cos^2 - \nu_\mu \sin\theta\cos\theta)e^{-i(\frac{{m_1}^2 l}{2E})} + (\nu_e \sin^2\theta + \nu_\mu \sin\theta\cos\theta)e^{-i(\frac{{m_2}^2 l}{2E})}$$

or

$$\nu_e \rightarrow \nu_e(\cos^2\theta e^{-i(\frac{{m_1}^2 l}{2E})} + \sin^2\theta e^{-i(\frac{{m_2}^2 l}{2E})}) + \nu_\mu \sin\theta\cos\theta(-e^{-i(\frac{{m_1}^2 l}{2E})} + e^{-i(\frac{{m_2}^2 l}{2E})})$$

Therefore, the probability of ν_e oscillation into ν_μ is given by the modulus square of the coefficient of ν_μ.

$$P_{e\mu}(l) = |\sin\theta\cos\theta(-e^{-i(\frac{{m_1}^2 l}{2E})} + e^{-i(\frac{{m_2}^2 l}{2E})})|^2 \tag{A.6}$$

$$= \sin^2\theta\cos^2\theta\left(2 - 2\cos\frac{\Delta m^2 l}{2E}\right)$$

$$= (\sin^2\theta\cos^2\theta)\left(4\sin^2\frac{\Delta m^2 l}{4E}\right)$$

$$P_{e\mu} = \sin^2 2\theta\left(\sin^2\frac{\Delta m^2 l}{4E}\right) \tag{A.7}$$

where, $\Delta m^2 = {m_2}^2 - {m_1}^2$. We convert the above equation from natural to more convenient units by writing Δm^2 in eV^2, l in metres and E in MeV. Using the relation, 200 MeV fm = $\hbar c$, we obtain

$$\frac{\Delta m^2 c^4 l}{4\hbar E} = \frac{1.3\Delta m^2 l}{E}$$

Thus,

$$P_{e\mu} = \sin^2 2\theta\left(\sin^2\frac{1.3\Delta m^2 l}{E}\right) \tag{A.8}$$

In the above expression the first factor gives the amplitude, whereas the second factor gives the phase of neutrino oscillation. For a phase angle θ, we know,

$$\frac{\pi}{\theta} = \frac{\lambda}{l}$$

l	$<< \lambda$	$\sim \lambda/2$	$>> \lambda$
$P_{e\mu}$	0	$\sin^2 2\theta \sim 1$	$\frac{1}{2}\sin^2 2\theta \sim \frac{1}{2}$

Table A.1: Table Showing The Values Of $P_{e\mu}$ For Limiting Cases Of l.

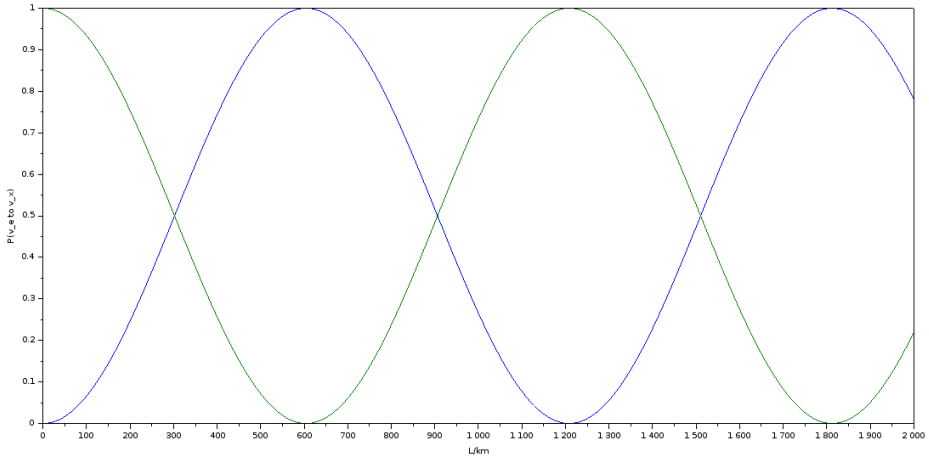

Figure A.1: The two flavour oscillation and survival probability, plotted as function of l for $E_\nu = 1GeV$,$\Delta m^2 = 0.002eV^2$ and $sin^2 2\theta = 1.0$

the repetition of phase occurs after π, since the period of $\sin^2 2\theta$ is π. Therefore, the wavelength of neutrino oscillations is given by,

$$\lambda \text{ [m]} = \frac{\pi}{1.3}\frac{E}{\Delta m^2} \simeq \frac{2.4E \text{ [MeV]}}{\Delta m^2 \text{ [eV}^2\text{]}} \tag{A.9}$$

For a large mixing angle θ, the amplitude is large ($\sin^2 2\theta \sim 1$). We can calculate $P_{e\mu}$ over a distance l, which is shown in Table. A.1. The corresponding survival probability is given by

$$P_{ee} \equiv P_{\nu_e \to \nu_e} = 1 - P_{e\mu} \tag{A.10}$$

Recent experiments measure the survival probability, not the oscillation probability, because neutrinos are detected by the production of their lepton partners, and producing an electron takes less energy than producing a muon ($m_e = 0.5MeV$, $m_\nu = 100$ MeV). It is possible to measure Δm^2 in any experiment subject to the condition, $l \geq \frac{\lambda}{2}$.

$$\frac{\lambda}{2} \simeq \frac{1.2E}{\Delta m^2}$$

So if we know l and E, we can calculate the lowest order of Δm^2 that can be measured.

$$\Delta m^2 \simeq \frac{1.2E}{l}$$

For solar and reactor neutrino experiments, the source of ν_e is nuclear reactions (see Sec. 1.6) and the energy is in the order of MeV. The distance between the reactor(source) and the detector l, for a long baseline experiment like KamLAND is of the order of $10^5 m$. Thus,

$$\Delta m^2 \geq \frac{1 \text{ MeV}}{10^5 \text{ m}}$$

or,

$$\Delta m^2 \geq 10^{-5}\ \text{eV}^2$$

For solar neutrinos, l is the distance between the earth and the sun, which is of the order 10^{11} m.

$$\Delta m^2 \geq \frac{1\ \text{MeV}}{10^{11}\ \text{m}}$$

or,

$$\Delta m^2 \geq 10^{-11}\ \text{eV}^2$$

These orders of magnitude are far beyond the reach of any other methods of mass measurement. In case of accelerator and atmospheric neutrinos the energy is in the order of GeV. For a long baseline accelerator neutrino experiment like MINOS the distance between the source and the detector, $l \sim 10^3$ km.

$$\Delta m^2 \geq \frac{1\ \text{GeV}}{10^3\ \text{km}}$$

or,

$$\Delta m^2 \geq 10^{-3}\ \text{eV}^2$$

While for atmospheric neutrinos traversing the earth l is given by the diameter of the earth, $l \sim 10^4$km.

$$\Delta m^2 \geq \frac{1\ \text{GeV}}{10^4\ \text{km}}$$

or,

$$\Delta m^2 \geq 10^{-4}\ \text{eV}^2$$

.

APPENDIX B

NEUTRINO EMISSION SPECTRAL PARAMETERS

Spectral Parameters for Selected PROMETHEUS-VERTEX and PROMETHEUS-HOTB Models

Model	$E^{\rm tot}_{\bar{\nu}_e}$	$E^{\rm tot}_{\nu_e}$ (10^{52} erg)	$E^{\rm tot}_{\nu_x}$	$\langle E_{\bar{\nu}_e}\rangle$	$\langle E_{\nu_e}\rangle$ (MeV)	$\langle E_{\nu_x}\rangle$	$\bar{\alpha}_{\bar{\nu}_e}$	$\bar{\alpha}_{\nu_e}$	$\bar{\alpha}_{\nu_x}$	Remnant	$M_{\rm NS,b}$ ($M_\odot$)
VERTEX, 8.8 $M_\odot$ ECSN ("Sf")	2.67	3.20	2.62	11.6	9.5	11.5	2.49	3.06	2.10	NS	1.366
VERTEX, z9.6co, LS220	2.93	3.28	3.17	12.4	9.7	12.4	2.51	2.82	2.03	NS	1.361
VERTEX, z9.6co, SFHo	3.13	3.49	3.31	12.1	9.6	12.0	2.83	3.03	2.24	NS	1.363
VERTEX, s11.2co, LS220	3.09	3.56	3.02	13.7	10.6	13.6	2.90	2.76	2.34	NS	1.366
VERTEX, s27.0co, LS220	5.72	5.99	5.37	13.7	10.9	13.1	2.25	2.15	1.82	NS	1.776
VERTEX, s27.0co, SFHo	5.91	6.24	5.68	13.6	10.9	13.2	2.61	2.50	2.11	NS	1.772
VERTEX, s20.0, SFHo	7.36	7.53	6.96	14.0	11.3	13.5	2.48	2.31	2.02	NS	1.947
VERTEX, s40s7b2c, LS220	4.49	5.44	2.81	17.6	14.4	18.8	2.52	2.08	1.61	BH (0.57 s)	(2.320)
VERTEX, s40.0c, LS220	8.62	9.38	4.83	18.7	15.7	17.6	1.95	1.58	1.41	BH (2.11 s)	(2.279)
s10.0, Z9.6, $\alpha = 3.5$, "L"	4.41	5.01	4.56	15.1	11.6	14.9	$3.32^{3.78}_{2.85}$	$3.32^{3.78}_{2.85}$	$2.67^{3.04}_{2.29}$	NS	1.430
s12.25, W18, $\alpha = 3.5$, "L"	5.55	6.30	5.74	14.7	11.5	14.6	$3.29^{3.75}_{2.83}$	$3.32^{3.79}_{2.86}$	$2.64^{3.01}_{2.27}$	NS	1.551
s27.0, W18, $\alpha = 3.0$, "H"	7.21	7.51	6.84	14.9	11.7	14.3	$2.83^{3.28}_{2.36}$	$2.84^{3.31}_{2.38}$	$2.29^{2.66}_{1.91}$	NS	1.742
s21.7, W18, $\alpha = 3.0$, "H"	7.87	8.20	7.46	15.0	12.1	14.5	$2.82^{3.28}_{2.36}$	$2.82^{3.28}_{2.36}$	$2.29^{2.66}_{1.91}$	NS	1.870
s40, W18, $\alpha_{\rm BH} = 2.0$, "F"	5.93	7.19	3.71	14.9	12.7	15.9	$1.90^{2.37}_{1.43}$	$1.79^{2.23}_{1.35}$	$1.21^{1.51}_{0.91}$	BH (1.03 s)	(2.7)
s23.3, W18, $\alpha_{\rm BH} = 2.0$, "F"	8.67	10.51	5.42	15.4	13.2	16.4	$1.87^{2.33}_{1.41}$	$1.76^{2.19}_{1.32}$	$1.19^{1.49}_{0.90}$	BH (1.67 s)	(2.7)
s24.1, W18, $\alpha_{\rm BH} = 2.0$, "S"	10.83	11.78	6.07	15.6	13.5	14.7	$1.85^{2.31}_{1.39}$	$1.74^{2.16}_{1.31}$	$1.34^{1.67}_{1.01}$	BH (2.01 s)	(2.7)
s24.7, W18, $\alpha_{\rm BH} = 2.0$, "S"	12.30	13.39	6.90	16.0	13.8	15.0	$1.82^{2.27}_{1.37}$	$1.70^{2.11}_{1.28}$	$1.32^{1.64}_{0.99}$	BH (2.46 s)	(2.7)
s22.1, W18, $\alpha_{\rm BH} = 2.0$, "S"	14.30	15.56	8.01	16.4	14.1	15.4	$1.80^{2.24}_{1.36}$	$1.68^{2.09}_{1.27}$	$1.30^{1.62}_{0.98}$	BH (3.32 s)	(2.7)
s28.0, W18, $\alpha_{\rm BH} = 2.0$, "S"	14.53	15.81	8.14	16.7	14.6	15.7	$1.76^{2.18}_{1.33}$	$1.62^{2.00}_{1.22}$	$1.27^{1.58}_{0.96}$	BH (3.79 s)	(2.7)
"	8.72	9.49	4.89	15.1	12.8	14.2	$1.89^{2.36}_{1.42}$	$1.79^{2.23}_{1.35}$	$1.37^{1.71}_{1.03}$	BH (2.04 s)	(2.3)
"	18.46	20.09	10.35	18.1	16.1	17.0	$1.63^{2.01}_{1.24}$	$1.45^{1.79}_{1.10}$	$1.18^{1.45}_{0.89}$	BH (5.64 s)	(3.1)
"	22.06	24.01	12.37	19.3	17.4	18.1	$1.53^{1.89}_{1.17}$	$1.34^{1.65}_{1.02}$	$1.11^{1.36}_{0.85}$	BH (7.51 s)	(3.5)
s27.9, W18, $\alpha_{\rm BH} = 2.0$, "S"	14.61	15.90	8.19	17.3	15.1	16.2	$1.69^{2.09}_{1.28}$	$1.51^{1.87}_{1.14}$	$1.22^{1.51}_{0.92}$	BH (5.11 s)	(2.7)
s18.0, W18, $\alpha_{\rm BH} = 2.0$, "S"	14.49	15.77	8.12	17.5	15.4	16.4	$1.67^{2.07}_{1.26}$	$1.46^{1.80}_{1.10}$	$1.21^{1.50}_{0.91}$	BH (9.12 s)	(2.7)

Figure B.1: Table showing the various neutrino luminosity spectra parameters. This is taken from Kresse *et al.* (2021).

The figure B.1 in this section consists of a table that has been taken from Kresse *et al.* (2021). The table provides the various neutrino emission spectral parameters, the final fate of the collapse and the mass of the compact object formed. The spectral parameters are discussed in Sec. 2.4.6. $E^{tot}_{\nu_i}$ is the total energy radiated in neutrino of species i, mean neutrino energy is given by $\langle E_{\nu_i}\rangle$ and spectral shape parameter α_{ν_x} (this is denoted by $\beta_{\nu)x}$ in the text in Sec. 2.4.6).

APPENDIX C

SOME NOTES FOR DIRECTIONAL POINTING USING PRESUPERNOVA NEUTRINOS

Obtaining an analytical expression for angular uncertainty

In this section we show the steps involved in going from Eq. 3.9 to Eq. 3.12. From eq. 3.9 we have,

$$P(p_x, p_y, p_z) = \frac{1}{\left(2\pi\sigma^2\right)^{\frac{3}{2}}} \exp\left(\frac{-p_x^2 - p_y^2 - (p_z - |\vec{p}|)^2}{2\sigma^2}\right). \tag{C.1}$$

$$\begin{aligned} P(p_x, p_y, p_z) = \frac{1}{\sqrt{2\pi{\sigma_x}^2}} \frac{1}{\sqrt{2\pi{\sigma_y}^2}} \frac{1}{\sqrt{2\pi{\sigma_z}^2}} \exp\left(\frac{-{p_x}^2}{2{\sigma_x}^2}\right) \exp\left(\frac{-{p_y}^2}{2{\sigma_y}^2}\right) \\ \exp\left(\frac{-(p_z - |\vec{p}|)^2}{2{\sigma_z}^2}\right) \end{aligned} \tag{C.2}$$

The angular uncertainty on the direction to the supernova progenitor is given by the angular aperture, β, of the cone around the vector $\vec{p}_m$, containing a chosen fraction of the total probability. The mathematical expression for the above statement is:

$$\frac{\int_0^\infty p^2 dp \int_{\cos\beta}^1 d\cos\theta \int_0^{2\pi} d\phi P(p_x, p_y, p_z)}{\int_0^\infty p^2 dp \int_{-1}^1 d\cos\theta \int_0^{2\pi} d\phi P(p_x, p_y, p_z)} = I \tag{C.3}$$

Transforming to polar coordinates, we have,

$$\begin{aligned} p_x &= p\sin\theta\cos\phi \\ p_y &= p\sin\theta\sin\phi \\ p_z &= p\cos\theta \end{aligned} \tag{C.4}$$

For this particular case which is *linear*,

$$\sigma_x = \sigma_y = \sigma_z = \frac{1}{\sqrt{3N}} = \sigma\,. \tag{C.5}$$

We choose a reference frame where, $p_x = 0$ and $p_y = 0$, and $p_z = |\vec{p}|$ as the mean.On doing the above substitutions, the integral in the numerator looks like,

$$\frac{1}{\sqrt{2\pi}}(3N)^{\frac{3}{2}} \int_0^\infty dp\ p^2 \int_{\cos\beta}^1 d\cos\theta\ \exp\left(-\frac{3N}{2}\left(p^2 + |\vec{p}|^2 - 2|\vec{p}|p\cos\theta\right)\right) \tag{C.6}$$

In the above expression, the phi-integral being trivial has already been done. For the denominator we just replace the limits of $d\cos\theta$ from -1 to, 1, which gives us 1 as

expected. We first solve the $d\cos\theta$ integral,

$$\frac{1}{\sqrt{2\pi}}(3N)^{\frac{3}{2}}\int_0^\infty dp\ p^2\ \exp\left(-\frac{3N}{2}\left(p^2+|\vec{p}|^2\right)\right)\ \int_{\cos\beta}^1 d\cos\theta\ \exp\left(3N\ |\vec{p}|p\cos\theta\right)\right)$$
$$=\sqrt{\frac{3N}{2\pi}}\ \frac{\exp\left(-\frac{3N}{2}|\vec{p}|^2\right)}{|\vec{p}|}\int_0^\infty dp\ p\ \exp\left(-\frac{3N}{2}p^2\right)\left(\exp\left(3N\ |\vec{p}|\ p\right)\right.$$
$$\left.-\exp\left(3N\ |\vec{p}|\ p\ \cos\beta\right)\right) \tag{C.7}$$

The denominator is obtained by substituting -1 in place of $cos\beta$ which gives us 1 as expected. On doing the above integral we obtain,

$$\frac{1}{2}\left[1+Erf\left(\sqrt{\frac{3N}{2}}|\vec{p}|\right)+\left(\cos\beta\ \exp\left(\frac{3N}{2}|\vec{p}|^2(\cos^2\beta-1)\right)\right.\right.$$
$$\left.\left.\left(-2+Erfc\left(\sqrt{\frac{3N}{2}}|\vec{p}|\cos\beta\right)\right)\right)\right]=I \tag{C.8}$$

The above expression can be simplified, Let,

$$k=\sqrt{\frac{3N}{2}}|\vec{p}| \tag{C.9}$$

We also know, $Erfc(x)=1-Erf(x)$. Then the above equation becomes,

$$\frac{1}{2}\left[1+Erf(k)-\cos\beta\ \exp\left(-k^2\sin^2\beta\right)\left(1+Erf(k\cos\beta)\right)\right]=I \tag{C.10}$$

The above expression is what we have in Eq. 3.12.

Plotting error cones in Mollweide projections

This appendix includes the relevant steps to plot an error cone corresponding to a given angle β, corresponding to the discussions in Sec. 3. The list of red and blue supergiants is given in Tab. D.1. The Mollweide projections can be made using the angles of declination (Dec) and right ascension (RA) given in the table. The next obvious step is to have a visualization of the error cone from the angular uncertainty (β) calculated in Sec. 3.2.1. The steps to do that are as follows:

1. Create a list of points to form a circle taking the zenith as the centre. These will be points at a constant Dec, and variable RA (0 to, 2 π). The radius will be the size of the error cone β (in radians) because, $S = r\theta$, but r = 1; so $s = \theta$ $(radians)$.

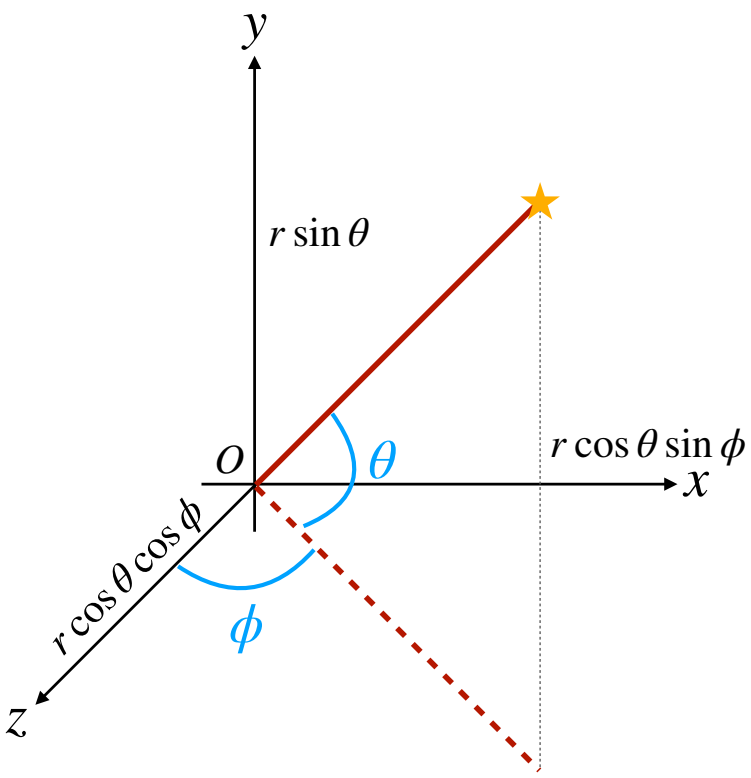

Figure C.1: Coordinate Arrangement.

2. Find the RA and Dec of the star around which you want to plot the error cone, and rotate each point to that RA and Dec.
   RA $= \phi$
   Dec $= \theta$
   $\tilde{\theta} = \frac{\pi}{2} - \theta$
   $\tilde{\phi} = \frac{\pi}{2} - \phi$

3. From spherical coordinates convert to Cartesian Coordinates (see Fig. C.1):

$$\begin{aligned} x &= (\cos\tilde{\theta})(\sin\tilde{\phi}) \\ y &= \sin\tilde{\theta} \\ z &= (\cos\tilde{\theta})(\cos\tilde{\phi}) \end{aligned} \tag{C.11}$$

4. Rotation matrices for rotating to the required RA and Dec

$$R(z,\tilde{\theta}) = \begin{bmatrix} \cos(-\tilde{\theta}) & -\sin(-\tilde{\theta}) & 0 \\ \sin(-\tilde{\theta}) & \cos(-\tilde{\theta}) & 0 \\ 0 & 0 & 1 \end{bmatrix} \tag{C.12}$$

$$R(y,\tilde{\phi}) = \begin{bmatrix} \cos(\tilde{\phi}) & 0 & \sin(\tilde{\phi}) \\ 0 & 1 & 0 \\ -\sin(\tilde{\phi}) & 0 & \cos(\tilde{\phi}) \end{bmatrix} \tag{C.13}$$

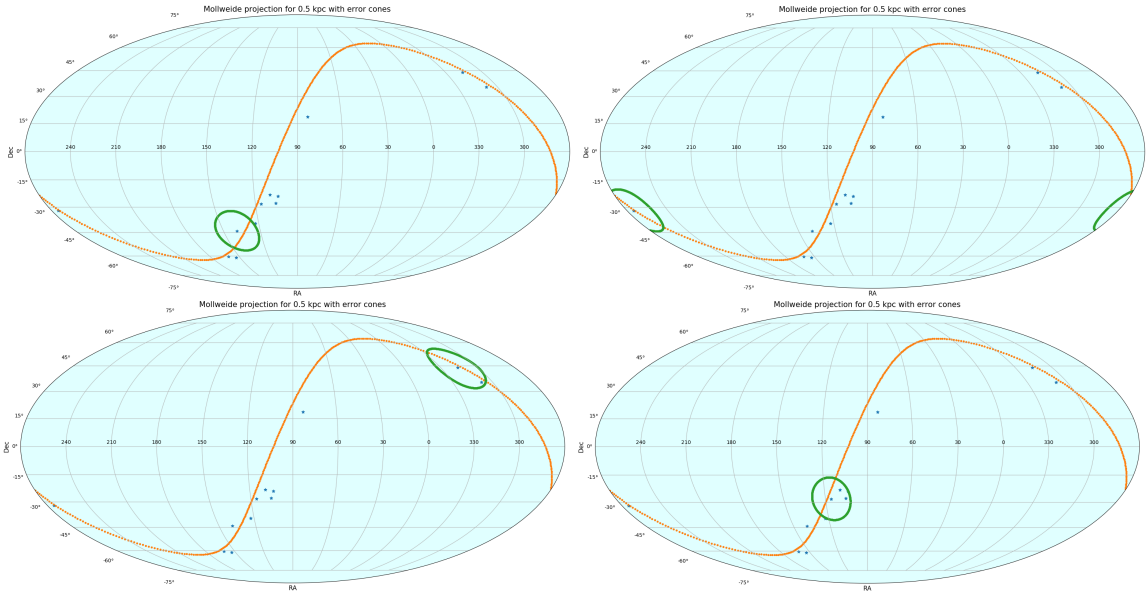

Figure C.2: Some examples of error cone of size β plotted on a Mollweide projection for different pre-supernova candidates.

5. Perform the rotation using matrix multiplication. Here I first rotate to the required Declination by rotating about z - axis, then rotate about y-axis for the RA

$$\begin{bmatrix} x' \\ y' \\ z' \end{bmatrix} = R(y,\phi)R(z,\theta) \begin{bmatrix} x \\ y \\ z \end{bmatrix} \tag{C.14}$$

6. Rotate back to the spherical coordinates:

$$\begin{aligned} \theta &= \arctan \frac{y}{\sqrt{x^2+z^2}} \\ \phi &= \arctan \frac{x}{z} \end{aligned} \tag{C.15}$$

7. Take care of the tan values of phi, based on what coordinate they are in because $\tan^{-1}$ has range from $(-\pi/2, \pi/2)$.

8. Once you have these points throw it to the Mollweide Projection Algorithm to plot the error cones.

In Fig. C.2, we show some examples of error cone of size β plotted on a Mollweide projection for different pre-supernova candidates.

The case of an exponential distribution

We extended our mathematical analysis to a more general case of exponential distribution and re-calculated all the quantities relevant to our problem and found

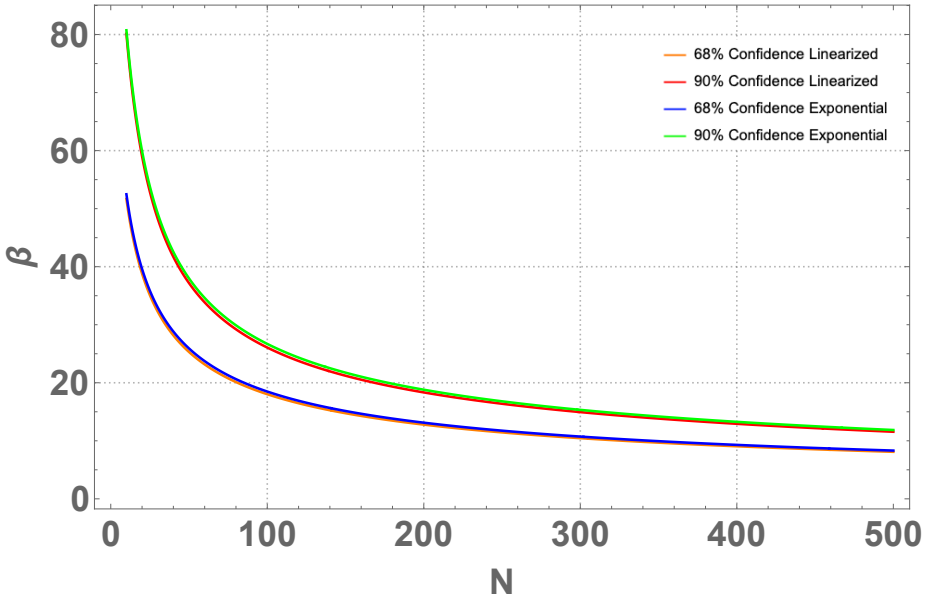

Figure C.3: Angular uncertainty (β) comparison for linear and exponential distributions for different confidence levels.

out that the linearized approximation works extremely well for our case (Reason yet to be thought of). Fig. C.3 shows the result. The agreement is seen both, for 68% and 90% confidence levels.

APPENDIX D

PRESUPERNOVA CANDIDATES

Table D.1 compiles a list of 31 red and blue core-collapse supernova progenitors within 1 kpc that have both distance and mass estimates. Table D.1 gives the star number (sorted by distance), Henry Draper (HD) catalog number, common name, constellation, distance, mass, J2000 right ascension (RA) and J2000 declination (Dec). For stars with multiple distance measurements, precedence is given to distances provided by the Gaia Collaboration (2018), van Leeuwen (2007), and individual determinations, in this order. Earlier compilations (e.g., Nakamura *et al.*, 2016) considered only red supergiant progenitors and did not require a mass estimate.

Table D.2 lists the angular distance $\Delta\theta$ of each star to its nearest neighbor. Table D.2 gives the star number, HD catalog and common name, the minimum angular separation between the star and its nearest neighbor, the HD catalog and common name of the nearest neighbor, and the star number of the nearest neighbor. The RA and Dec for each star is taken from Table D.1 when calculating angular separations. The algorithm to produce Table D.2 is discussed below (Sec. D).

Algorithm to calculate angular distance to nearest neighbour

1. From the list of stars extract only the stars lying within the required distance cuts.

2. From the extracted list read of the Star Name, Star RA and, Star Dec for each star. The RA is in the form HH:MM:SS (Hours:Minutes:Seconds), whereas the Dec is in the form + or - DD:MM:SS (Degrees:Arcminutes:Arcseconds). We need to convert each into decimal degrees.

3. Convert the RA and Dec into degrees using the following:

$$RA(in\ degrees) = 15\Big(HH + \frac{MM}{60} + \frac{SS}{3600}\Big) \tag{D.1}$$

$$Dec(in\ degrees) = \pm\Big(DD + \frac{MM}{60} + \frac{SS}{3600}\Big) \tag{D.2}$$

4. For each star calculate the angular distance to every other star using the above calculated RA and Dec in decimal degrees. Lets say the two stars being considered have RA and Dec as: RA1, Dec1 and RA2, Dec2. Then:

$$\begin{aligned}\cos A = \{&\sin(Dec\ 1)\sin(Dec\ 2)\} + \{(\cos(Dec\ 1)\cos(Dec\ 2))\\ &(\cos(RA\ 1 - RA\ 2)\}\end{aligned} \tag{D.3}$$

$$\implies A = \cos^{-1}(\cos A) \tag{D.4}$$

5. Once you have all these distances corresponding to each star from a given star, find the smallest distance and store the corresponding stars name. You can also extend it to finding the second smallest distance, giving you the nearest and the second-nearest neighbours respectively.

N	Catalog Name	Common Name	Constellation	Distance (kpc)	Mass ($M_\odot$)	RA	Dec
1	HD 116658	Spica/α Virginis	Virgo	0.077 ± 0.004 [a]	$11.43^{+1.15}_{-1.15}$ [b]	13:25:11.58	−11:09:40.8
2	HD 149757	ζ Ophiuchi	Ophiuchus	0.112 ± 0.002 [a]	20.0 [g]	16:37:09.54	−10:34:01.53
3	HD 129056	α Lupi	Lupus	0.143 ± 0.003 [a]	$10.1^{+1.0}_{-1.0}$ [f]	14:41:55.76	−47:23:17.52
4	HD 78647	λ Velorum	Vela	0.167 ± 0.003 [a]	$7.0^{+1.5}_{-1.0}$ [h]	09:07:59.76	−43:25:57.3
5	HD 148478	Antares/α Scorpii	Scorpius	0.169 ± 0.030 [a]	$11.0 - 14.3$ [l]	16:29:24.46	−26:25:55.2
6	HD 206778	ϵ Pegasi	Pegasus	0.211 ± 0.006 [a]	$11.7^{+0.8}_{-0.8}$ [f]	21:44:11.16	+09:52:30.0
7	HD 39801	Betelgeuse/α Orionis	Orion	0.222 ± 0.040 [d]	$11.6^{+5.0}_{-3.9}$ [m]	05:55:10.31	+07:24:25.4
8	HD 89388	q Car/V337 Car	Carina	0.230 ± 0.020 [c]	$6.9^{+0.6}_{-0.6}$ [f]	10:17:04.98	−61:19:56.3
9	HD 210745	ζ Cephei	Cepheus	0.256 ± 0.006 [c]	$10.1^{+0.1}_{-0.1}$ [f]	22:10:51.28	+58:12:04.5
10	HD 34085	Rigel/β Orion	Orion	0.264 ± 0.024 [a]	$21.0^{+3.0}_{-3.0}$ [j]	05:14:32.27	−08:12:05.90
11	HD 200905	ξ Cygni	Cygnus	0.278 ± 0.029 [c]	8.0 [r]	21:04:55.86	+43:55:40.3
12	HD 47839	S Monocerotis A	Monoceros	0.282 ± 0.040 [a]	29.1 [i]	06:40:58.66	+09:53:44.71
13	HD 47839	S Monocerotis B	Monoceros	0.282 ± 0.040 [a]	21.3 [i]	06:40:58.57	+09:53:42.20
14	HD 93070	w Car/V520 Car	Carina	0.294 ± 0.023 [c]	$7.9^{+0.1}_{-0.1}$ [f]	10:43:32.29	−60:33:59.8
15	HD 68553	NS Puppis	Puppis	0.321 ± 0.032 [c]	9.7 [f]	08:11:21.49	−39:37:06.8
16	HD 36389	CE Tauri/119 Tauri	Taurus	0.326 ± 0.070 [c]	$14.37^{+2.00}_{-2.77}$ [k]	05:32:12.75	+18:35:39.2
17	HD 68273	γ^2 Velorum	Vela	0.342 ± 0.035 [a]	$9.0^{+0.6}_{-0.6}$ [o]	08:09:31.95	−47:20:11.71
18	HD 50877	o^1 Canis Majoris	Canis Major	0.394 ± 0.052 [c]	$7.83^{+2.0}_{-2.0}$ [f]	06:54:07.95	−24:11:03.2
19	HD 207089	12 Pegasi	Pegasus	0.415 ± 0.031 [c]	$6.3^{+0.7}_{-0.7}$ [f]	21:46:04.36	+22:56:56.0
20	HD 213310	5 Lacertae	Lacerta	0.505 ± 0.046 [a]	$5.11^{+0.18}_{-0.18}$ [q]	22:29:31.82	+47:42:24.8
21	HD 52877	σ Canis Majoris	Canis Major	0.513 ± 0.108 [c]	$12.3^{+0.1}_{-0.1}$ [f]	07:01:43.15	−27:56:05.4
22	HD 208816	VV Cephei	Cepheus	0.599 ± 0.083 [c]	$10.6^{+1.0}_{-1.0}$ [f]	21:56:39.14	+63:37:32.0
23	HD 196725	θ Delphini	Delphinus	0.629 ± 0.029 [c]	$5.60^{+3.0}_{-3.0}$ [n]	20:38:43.99	+13:18:54.4
24	HD 203338	V381 Cephei	Cepheus	0.631 ± 0.086 [c]	12.0 [s]	21:19:15.69	+58:37:24.6
25	HD 216946	V424 Lacertae	Lacerta	0.634 ± 0.075 [c]	$6.8^{+1.0}_{-1.0}$ [p]	22:56:26.00	+49:44:00.8
26	HD 17958	HR 861	Cassiopeia	0.639 ± 0.039 [c]	$9.2^{+0.5}_{-0.5}$ [f]	02:56:24.65	+64:19:56.8
27	HD 80108	HR 3692	Vela	0.650 ± 0.061 [c]	$12.1^{+0.2}_{-0.2}$ [f]	09:16:23.03	-44:15:56.6
28	HD 56577	145 Canis Major	Canis Major	0.697 ± 0.078 [c]	$7.8^{+0.5}_{-0.5}$ [f]	07:16:36.83	−23:18:56.1
29	HD 219978	V809 Cassiopeia	Cassiopeia	0.730 ± 0.074 [c]	$8.3^{+0.5}_{-0.5}$ [f]	23:19:23.77	+62:44:23.2
30	HD 205349	HR 8248	Cygnus	0.746 ± 0.039 [c]	$6.3^{+0.7}_{-0.7}$ [f]	21:33:17.88	+45:51:14.5
31	HD 102098	Deneb/α Cygni	Cygnus	0.802 ± 0.066 [e]	$19.0^{+4.0}_{-4.0}$ [e]	20:41:25.9	+45:16:49.0

Note— [a]van Leeuwen (2007), [b]Tkachenko et al. (2016), [c]Gaia Collaboration et al. (2018), [d]Harper et al. (2017), [e]Schiller & Przybilla (2008), [f]Tetzlaff et al. (2011), [g]Howarth & Smith (2001), [h]Carpenter et al. (1999), [i]Cvetkovic et al. (2009), [j]Shultz et al. (2014), [k]Montargès et al. (2018), [l]Ohnaka et al. (2013), [m]Neilson et al. (2011), [n]van Belle et al. (2009); Malagnini et al. (2000), [o]North et al. (2007), [p]Lee et al. (2014), [q]Baines et al. (2018), [r]Reimers & Schroeder (1989), [s]Tokovinin (1997)

Figure D.1: Figure Of A Table For Candidate Pre-supernova Stars.

N	Catalog/Common Name	Min. Ang. Separation (degree)	Nearest Neighbor Name	Nearest Neighbor Number
1	HD 116658/Spica	39.66	HD 129056/α Lupi	3
2	HD 149757/ζ Ophiuchi	15.97	HD 148478/Antares	5
3	HD 129056/α Lupi	29.73	HD 148478/Antares	5
4	HD 78647/λ Velorum	1.73	HD 80108/HR 3692	27
5	HD 148478/Antares	15.97	HD 149757/ζ Ophiuchi	2
6	HD 206778/ϵ Pegasi	13.08	HD 207089/12 Pegasi	19
7	HD 39801/Betelgeuse	11.59	S Mono A/B	12/13
8	HD 89338/q Car	3.30	HD 93070/w Car	14
9	HD 210745/ζ Cephei	5.69	HD 208816/VV Cephei	22
10	HD 34085/Rigel	18.60	HD 39801/Betelgeuse	7
11	HD 200905/ζ Cygni	4.39	HD 102098/Deneb	31
12	HD 47839/S Mono A	11.60	HD 39801/Betelgeuse	7
13	HD 47839/S Mono B	11.60	HD 39801/Betelgeuse	7
14	HD 93070/w Car	3.30	HD 89338/q Car	8
15	HD 68553/NS Puppis	7.72	HD 68273/γ^2 Velorum	17
16	HD 36389/119 Tauri	12.50	HD 39801/Betelgeuse	7
17	HD 68273/γ^2 Velorum	7.72	HD 68553/NS Puppis	15
18	HD 50877/o^1 Canis Majoris	4.12	HD 52877/σ Canis Majoris	21
19	HD 207089/12 Pegasi	13.08	HD 206778/ϵ Pegasi	6
20	HD 213310/5 Lacertae	4.88	HD 216946/V424 Lacertae	25
21	HD 52877/σ Canis Majoris	4.12	HD 50877/o^1 Canis Majoris	18
22	HD 208816/VV Cephei	5.69	HD 210745/ζ Cephei	9
23	HD 196725/θ Delphini	16.39	HD 206778/ϵ Pegasi	6
24	HD 203338/V381 Cephei	6.72	HD 208816/VV Cephei	22
25	HD 216946/V424 Lacertae	4.88	HD 213310/5 Lacertae	20
26	HD 17958/HR 861	23.49	HD 219978/V809 Cassiopeia	29
27	HD 80108/HR 3692	1.73	HD 78647/λ Velorum	4
28	HD 56577/145 Canis Majoris	5.22	HD 50877/o^1 Canis Majoris	18
29	HD 219978/V809 Cassiopeia	9.33	HD 208816/VV Cephei	22
30	HD 205349/HR 8248	5.38	HD 200905/ζ Cygni	11
31	HD 102098/Deneb	4.39	HD 200905/ζ Cygni	11

Figure D.2: Figure Of A Table For Minimum Angular Separation Between Pre-supernova Candidates.

APPENDIX E

SOME DETAILED CALCULATIONS FOR THE NEUTRINO GW MEMORY EFFECT FORMALISM

Formalism Addendum

In this appendix we would like to collect some details to complement section 4.1

The weak field equations

Consider a metric $g_{\mu\nu}$ nearly flat[1] as given in Eq. (4.2),

$$g_{\mu\nu} = \eta_{\mu\nu} + h_{\mu\nu}. \tag{E.1}$$

i.e, $h_{\mu\nu}$ is a small perturbation and we will only keep terms up to first order in $h_{\mu\nu}$. The Ricci tensor is defined as,

$$R_{\mu\nu} = \partial_\nu \Gamma^\lambda_{\lambda\mu} - \partial_\lambda \Gamma^\lambda_{\nu\mu}, \tag{E.2}$$

where,

$$\Gamma^\lambda_{\mu\nu} = \frac{1}{2}\eta^{\lambda\rho}\Big(\partial_\mu h_{\rho\nu} + \partial_\nu h_{\rho\mu} - \partial_\rho h_{\mu\nu} + \mathcal{O}(h^2)\Big). \tag{E.3}$$

Using Eq. E.2 and E.3, we have;

$$R_{\mu\nu} \approx R^{(1)}_{\mu\nu} \equiv \frac{1}{2}\Big(\Box^2 h_{\mu\nu} - \partial_\lambda\partial_\mu h^\lambda_\nu - \partial_\lambda\partial_\nu h^\lambda_\mu + \partial_\mu\partial_\nu h^\lambda_\lambda\Big). \tag{E.4}$$

Recall the Einstien's field equation is defined as,

$$R_{\mu\nu} - \frac{1}{2}R g_{\mu\nu} = -8\pi G T_{\mu\nu}, \tag{E.5}$$

(Note that, $R = 8\pi G T^\mu_\mu$).
Using Eq. E.4 in Eq. E.5 after some massaging we obtain the following field equation,

$$\Box^2 h_{\mu\nu} - \partial_\lambda\partial_\mu h^\lambda_\nu - \partial_\lambda\partial_\nu h^\lambda_\mu + \partial_\mu\partial_\nu h^\lambda_\lambda = -16\pi G S_{\mu\nu} \tag{E.6}$$

where $S_{\mu\nu}$ is defined in terms of the conventional stress-energy tensor $T_{\mu\nu}$ as,

$$S_{\mu\nu} = T_{\mu\nu} - \frac{1}{2}\eta_{\mu\nu}T^\lambda_\lambda. \tag{E.7}$$

As we mention in section 4.1, the field equation above is gauge invariant. We choose a particular gauge

$$g^{\mu\nu}\Gamma^\lambda_{\mu\nu} = 0. \tag{E.8}$$

which from (E.3) implies the following condition on the metric perturbation,

$$\partial_\alpha h^\alpha_\lambda = \frac{1}{2}\partial_\lambda h^\mu_\mu, \tag{E.9}$$

This finally gives us,

$$\Box^2 h_{\mu\nu} = -16\pi G S_{\mu\nu} \tag{E.10}$$

[1] We use signature $\eta_{\mu\nu} = diag(-1, 1, 1, 1)$.

One can write a solution by using the retarded Green's function and explicitly take,

$$h_{\mu\nu} = 4G \int d^3\vec{x}' \Big(\frac{S_{\mu\nu}(\vec{x}', t - |\vec{x} - \vec{x}'|)}{|\vec{x} - \vec{x}'|} \Big). \tag{E.11}$$

Following Epstein (1978), we use the following ansatz for the sources,

$$S^{ij}(t, x) = n^i n^j r^{-2} \sigma(t - r) f(\Omega, t - r), \tag{E.12}$$

where, $\vec{n} = x/r$, $r = |x|$. This stress-tensor represents a point source that releases matter at $x = 0$ at the speed of light, with $\sigma(t)$ the rate of energy loss and $f(\Omega, t)$ the angular distribution of emission and hence it satisfies $f(\Omega, t) \geq 0$ and $\int f(\Omega, t) d\Omega = 1$. A convenient way of writing the source ansatz E.12 is,

$$S^{ij}(t, x) = n^i n^j r^{-2} \int_{-\infty}^{\infty} f(\Omega', t') \sigma(t') \delta(t - t' - r) dt'. \tag{E.13}$$

In order to fix the residual gauge freedom (see for example Misner *et al.* (1973)), we should project the source stress-tensor into its transverse-traceless component, which we denote by $(n^i n^j)_{TT}$ and write explicitly in the wave form as [2],

$$h^{ij}_{TT}(t, x) = 4 \int_{-\infty}^{\infty} \int_{4\pi} \int_0^{\infty} \frac{(n^i n^j)_{TT} f(\Omega', t') \sigma(t')}{|\vec{x} - \vec{x'}|} \delta(t - |\vec{x} - \vec{x'}| - t' - r') dr' d\Omega' dt' \tag{E.14}$$

We know by the property of Dirac-Delta functions:

$$\delta\Big(g(x)\Big) = \sum_i \frac{\delta\Big(x - x_i\Big)}{|g'(x_i)|_{x_i = x_0}}. \tag{E.15}$$

We have from Eq. E.14, $\delta(t - |\vec{x} - \vec{x'}| - t' - r')$. This implies for our case $g(r') = t - |\vec{x} - \vec{x'}| - t' - r'$. The roots are found by solving for r' in the equation, $g(r') = 0$. We can either solve for r' or just simply write,

$$|\vec{x} - \vec{x'}|^{1/2} = t - t' - r'. \tag{E.16}$$

Next we evaluate, $g'(r')$, which gives us,

$$g'(r') = -\frac{d}{dr'} |\vec{x} - \vec{x'}| - 1. \tag{E.17}$$

We know from the law of sines that,

$$|x - x'|^2 = r^2 + r'^2 - 2rr' \cos\theta. \tag{E.18}$$

[2] We delay an explicit computation of $(n^i n^j)_{TT}$ to appendix E below.

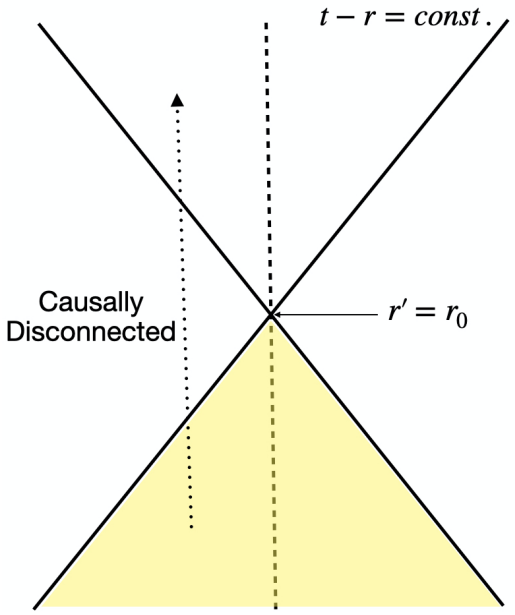

Figure E.1: A light cone to understand the integration limits for t' in Eq. E.22.

So the derivative, $\frac{d}{dr'}|\vec{x}-\vec{x'}| = \frac{r'-r\cos\theta}{|\vec{x}-\vec{x'}|}$. Using this and Eq. E.17 we obtain,

$$|g'(r')| = \Big(\frac{|\vec{x}-\vec{x'}| + r' - r\cos\theta}{|\vec{x}-\vec{x'}|}\Big). \tag{E.19}$$

But we need, $|g'(r')|_{r'=r_0}$ which is;

$$|g'(r')|_{r'=r_0} = \frac{t-t'-r\cos\theta'}{|\vec{x}-\vec{x'}|}, \tag{E.20}$$

where we have used, Eq. E.16 in the numerator and defined the angle $\theta(r'=r_0)=\theta'$. Now we have all the pieces to evaluate the Delta function and integrate over r' in Eq. E.14. Using Eq. E.15, E.20 in Eq. E.14 we have;

$$\theta^{ij}_{TT}(t,x) = 4G\int_{-\infty}^{\infty}\int_{4\pi}\frac{(n^i n^j)_{TT} f(\Omega',t')\sigma(t')}{t-t'-r\cos\theta'}d\Omega' dt'. \tag{E.21}$$

Comparing Eq. E.21 with Eq. E.22 we see that the limits for the t' integration do not yet match. So to understand this let us look at Fig E: We see the existing limit of $t' \to (-\infty,\infty)$, is unphysical in our case cause then the event of the astrophyscal phenomenon is causally disconnected for certain cases. Hence, for the limits to be physically meaningful $t' \to (-\infty, t-r)$, which when introduces in Eq. E.21 gives us Eq. E.22.

$$h^{ij}_{TT}(t,x) = 4G\int_{-\infty}^{t-r}\int_{4\pi}\frac{(n^i n^j)_{TT} f(\Omega',t')\sigma(t')}{t-t'-r\cos\theta}d\Omega' dt'. \tag{E.22}$$

For the derivation of the equations in this appendix, we have followed Mueller and Janka (1997a); Li *et al.* (2018); Ott (2009); Burrows and Hayes (1996); Kotake *et al.* (2012). The observer is situated at a distance $r = |x| \to \infty$ from the source, *i.e.*, very far away from the event, and sees the radiation from the source at a time t which was emitted at time $t' = t - r/c$. We are interested in the gravitation wave created by the neutrino pulse. By defining the direction dependent neutrino luminosity as[3] $\frac{dL_\nu(\Omega',t')}{d\Omega'} = f(\Omega', t')\sigma(t')$, we can now rewrite (E.22) in this approximation as,

$$h^{ij}_{TT}(t,x) = \frac{4G}{rc^4}\int_{-\infty}^{t-r/c} dt' \int_{4\pi} \frac{(n^i n^j)_{TT}}{1-\cos\theta}\frac{dL_\nu(\Omega',t')}{d\Omega'}d\Omega', \tag{E.23}$$

The wave $h^{ij}_{TT}(t,x)$ can be either '+' or '×' polarized. We denote the + polarization as, $h^{xx}_{TT} = -h^{yy}_{TT} = -h^{+}_{TT}$.

Special Case: I

We will now choose some special cases and see how Eq. 4.8 looks. When we have, $\varphi = 0$ and $\vartheta = 0$, the (XYZ) system coincides with the $(X'Y'Z')$ system. In this case one can see from Fig. 4.1, $\theta = \vartheta'$ and $\phi = \varphi'$. The expression in Eq 4.8 then becomes,

$$(h^{xx}_{TT})_p = \frac{2G}{rc^4}\int_{-\infty}^{t-r/c} dt' \int_{4\pi} (1+\cos\vartheta')\cos 2\varphi' \frac{dL_\nu(\Omega',t')}{d\Omega'}d\Omega' \,. \tag{E.24}$$

In the above equation Eq. E.24, when $dL_\nu/d\Omega$ is axially symmetric. In this case, when the observer is located at the symmetry axis the amplitude vanishes, $(h^{xx}_{TT})_p = 0$. This is because, for this arrangement $dL_\nu/d\Omega$ is independent of ϕ (since axis-symmetric), so $\int_0^{2\pi}\cos 2\phi\, d\phi = 0$ and hence the integral vanishes.

Special Case: II

Now, let us look at a scenario when $\varphi = 0$. In this situation the Y and Y' axes coincide. The two coordinate systems (XYZ and $X'Y'Z'$) are related by rotation about Z- axis by an angle ϑ. Thus we have,

$$\begin{aligned}
\sin\theta\cos\phi &= \sin\vartheta'\cos\varphi'\cos\vartheta - \cos\vartheta'\sin\vartheta \\
\sin\theta\sin\phi &= \sin\vartheta'\sin\varphi' \\
\cos\theta &= \sin\vartheta'\cos\varphi'\sin\vartheta - \cos\vartheta'\cos\vartheta.
\end{aligned}$$

Now consider the observer to be perpendicular to the source's Z' axis, *i.e.*, $\vartheta = \pi/2$ (refer to Fig. 4.1, here Z and X' axes coincide). Therefore, we now have,

$$\begin{aligned}
\sin\theta\cos\phi &= -\cos\vartheta' \\
\sin\theta\sin\phi &= \sin\vartheta'\sin\varphi' \\
\cos\theta &= \sin\vartheta'\cos\varphi'
\end{aligned} \tag{E.25}$$

[3] In other words, the energy radiated at time t per unit of time and per unit of solid angle into the direction Ω'.

The expression in Eq. 4.8 now becomes,

$$(h_{TT}^{xx})_e = \frac{2G}{rc^4}\int_{-\infty}^{t-r/c} dt' \int_{4\pi} (1+\sin\vartheta'\cos\varphi')\frac{(\cos^2\vartheta' - \sin^2\vartheta'\cos^2\varphi')}{(\cos^2\vartheta' + \sin^2\vartheta'\cos^2\varphi')}\frac{dL_\nu(\Omega',t')}{d\Omega'}d\Omega'. \tag{E.26}$$

Our main conclusion from illustratiing these special cases is, we can conveniently rewrite the wave form as,

$$h_{TT}^{xx} = \frac{2G}{rc^4}\int_{-\infty}^{t-r/c} dt' L_\nu(t')\alpha(t')\,, \tag{E.27}$$

by defining the *anisotropy parameter* $\alpha(t)$ in the x-direction as given by,

$$\alpha(t) = \frac{1}{L_\nu(t)}\int_{4\pi} d\Omega' \,\frac{(n^x n^x)_{TT}}{1-\cos\theta}\,\frac{dL_\nu(\Omega',t)}{d\Omega'}\,, \tag{E.28}$$

where the total neutrino luminosity is given by,

$$L_\nu(t) = \int_{4\pi} d\Omega' \,\frac{dL_\nu(\Omega',t)}{d\Omega'}. \tag{E.29}$$

Calculation of transverse-traceless amplitude

There is still an important piece $(n^i n^j)_{TT}$ at equations (E.23) and (E.28) that requires some work since it contains the angular dependence for the integrand of the wave form. In this section we will compute the transverse traceless component of the wave form.

From Fig. E.2 one can read the vectors,

$$\begin{aligned}\hat{n} &= \frac{\vec{x'}}{|\vec{x'}|}\\ \hat{n}' &= \frac{\vec{x}-\vec{x'}}{|\vec{x}-\vec{x'}|}\end{aligned} \tag{E.30}$$

or in components,

$$\begin{aligned}n_x &= \sin\theta\cos\phi\\ n_y &= \sin\theta\sin\phi\\ n_z &= \cos\theta\end{aligned} \tag{E.31}$$

$$\begin{aligned}n'_x &= -\sin\psi\cos\phi\\ n'_y &= -\sin\psi\sin\phi\\ n'_z &= \cos\psi\end{aligned} \tag{E.32}$$

From Eq. E.31, E.32, it is easy to show that,

$$\hat{n}.\hat{n}' = \cos(\theta+\psi). \tag{E.33}$$

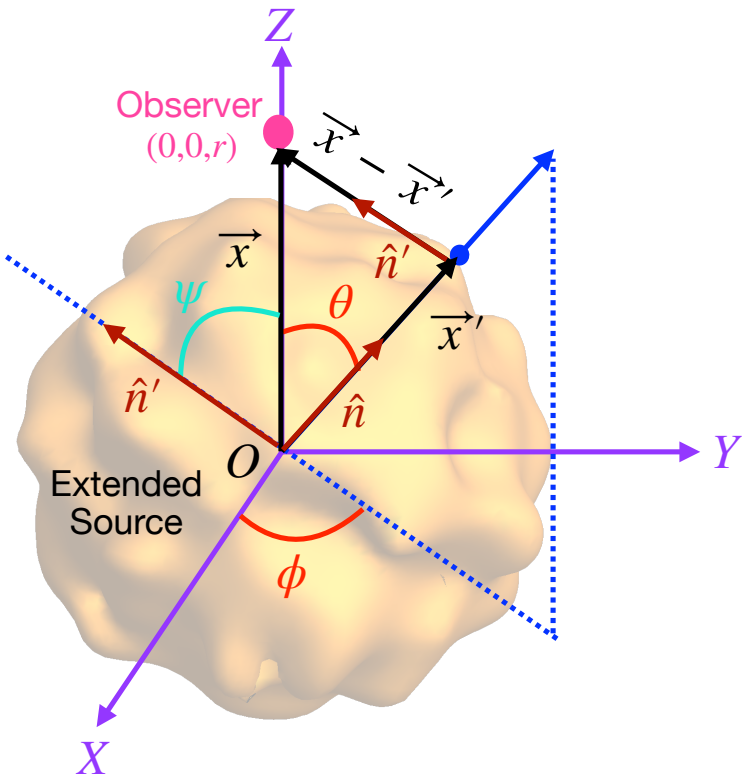

Figure E.2: Setup to show the different vectors involved. Same as Fig. 4.1 (including the colors used) but only the observer's coordinate system is shown along with the extended source. The blue dot is a point on the surface of the extended source and the corresponding position vector is shown as a blue arrow.

Also, from the figure (Fig. E.2) we see that $\vec{x}.\hat{n}' = r\cos\psi$. The operator that projects into the transverse-traceless component is given in the standard way,

$$P^i_j = \delta^i_j - n'^i n'_j. \tag{E.34}$$

More explicitly, the transverse-traceless (TT) part of a given tensor T^{kl} is given by,

$$T^{ij}_{TT} = \left(P^i_k P^j_l - \frac{1}{2}P^{ij}P_{kl}\right)T^{kl}. \tag{E.35}$$

Let us now check that our operator in Eq. E.34 does what it is supposed to, namely project out the transverse-traceless part of a tensor. First, we check that the component E.35 is transverse to the direction of wave propagation. In other words, T^{ij}_{TT} should be perpendicular (transverse) to n' and therefore its dot product with n' should vanish,

$$n'_i T^{ij}_{TT} = (n'_k - n'_i n'^i n'_k)(\delta^j_l - n'^j n'_l)T^{kl} - \frac{1}{2}(n'_j - n'_i n'^i n'_j)(\delta^k_l - n'^k n'_l)T^{kl} = 0,$$

which is what we required. Next, we want to show that the tensor component T^{ij}_{TT} is also traceless by showing $\delta^i_j T^{ij}_{TT} = 0$. Once again substituting the expressions from Eq. E.34, E.35 and doing the appropriate contractions give us,

$$\begin{aligned}\delta^i_j T^{ij}_{TT} &= (\delta^j_k - n'^j n'_k)(\delta^j_l - n'^j n'_l)T^{kl} - \frac{1}{2}(3-1)(\delta^k_l - n'^k n'_l)T^{kl} \\ &= (\delta^k_l - n'^k n'_l)T^{kl} - (\delta^k_l - n'^k n'_l)T^{kl} = 0,\end{aligned}$$

which is what we intended to show. Now we want to evaluate the expression $(n^x n^x)_{TT}$,

$$(n^x n^x)_{TT} = \Big(P^x_k P^x_l - \frac{1}{2}P^{xx}P_{kl}\Big)n^k n^l = \Big(P^x_k n^k n^l P^x_l - \frac{1}{2}P^{xx}P_{kl}n^k n^l\Big) \tag{E.36}$$

Let us first calculate each term separately appearing in the above expression.

$$P^x_k n^k = (\delta^x_k - n'^x n'_k)n^k = n^x - n'^x \cos(\theta+\psi) = \sin\theta\cos\phi + \sin\psi\cos\phi\cos(\theta+\psi)$$

$$P^x_k n^k = \cos\psi\cos\phi\sin(\theta+\psi) \tag{E.37}$$

In the above computations we have used the expressions in Eq. E.31, E.32, E.33, E.34. Similarly one can find the following projections,

$$P^y_k n^k = \cos\psi\sin\phi\sin(\theta+\psi) \tag{E.38}$$

$$P^z_k n^k = \sin\psi\sin(\theta+\psi) \tag{E.39}$$

Next we have,

$$\begin{aligned}P_{kl}n^k n^l = (\delta_{kl} - n'_k n'_l)n_k n_l = 1 - \cos^2(\theta+\psi), \\ P_{kl}n^k n^l = \sin^2(\theta+\psi),\end{aligned} \tag{E.40}$$

and finally,

$$P^{xx} = (\delta^x_x - n'^x n'_x) = 1 - \sin^2\psi\cos^2\phi. \tag{E.41}$$

So now we have all the terms required for the evaluation of $(n^x n^x)_{TT}$. Substituting Eq. E.37, E.40, E.41 in Eq. E.36 gives,

$$(n^x n^x)_{TT} = \frac{1}{2}\sin^2(\psi+\theta)\Big(\cos^2\phi(1+\cos\psi) - 1\Big). \tag{E.42}$$

In Sec. 4.1 we discuss the setup where the observer is at ∞, *i.e.*, $r = |\vec{x}| \to \infty$, in that case the angle $\psi = 0$. Putting, $\psi = 0$ in Eq. E.42 results in,

$$(n^x n^x)_{TT} = \frac{1}{2}(1-\cos^2\theta)\Big(2\cos^2\phi - 1\Big). \tag{E.43}$$

An alternative proof of property (4.16)

It is worth to clarify that in the usual treatment for the Fourier transform, property (4.16) is usually proven by applying integration by parts and it follows after assuming that

$$\lim_{t\to\pm\infty} g(t) \to 0\,. \tag{E.44}$$

However, in the case for gravitational memory, we can not make this assumption as by definition of memory,

$$\lim_{t\to\pm\infty} h(t) \to h_{\rm final}\,. \tag{E.45}$$

Here we want to provide a proof for the given property that does not rely on the vanishing of the boundary term, but only assumes the existence (finiteness) of the Fourier transform for the function under consideration.

We want to compute $\tilde{\dot{g}}(f)$. By using the rigorous definition of the derivative, we can write,

$$\tilde{\dot{g}}(f) = \mathcal{F}\left(\lim_{\delta\to 0}\frac{g(t+\delta)-g(t)}{\delta}\right) \tag{E.46}$$

where for notation's convenience we have denote the Fourier transform as $\mathcal{F}$. Assuming the existence of the Fourier transform, and henceforth its inverse, we have,

$$\begin{aligned}
\tilde{\dot{g}}(f) &= \mathcal{F}\left(\lim_{\delta\to 0}\int_{-\infty}^{\infty}\frac{e^{-2\pi i\delta f'}-1}{\delta}e^{-2\pi i f' t}\tilde{g}(f')df'\right)\\
&= \mathcal{F}\left(\int_{-\infty}^{\infty}-2\pi i f' e^{-2\pi i f' t}\tilde{g}(f')df'\right)\\
&= \int_{-\infty}^{\infty}e^{2\pi i f t}\left(\int_{-\infty}^{\infty}-2\pi i f' e^{-2\pi i f' t}\tilde{g}(f')df'\right)dt\,,
\end{aligned} \tag{E.47}$$

In the last line we have used the definition of Fourier transform. Due again to the existence of the Fourier transform of $g(t)$ (and it's inverse), we can commute the integrations, obtaining,

$$\tilde{\dot{g}}(f) = \int_{-\infty}^{\infty}\delta(f-f')(-2\pi)if'\tilde{g}(f')df' = -2\pi i f\tilde{g}(f)\,. \tag{E.48}$$

We are unaware of this treatment in the literature.

APPENDIX F

NOTES ON MEMORY-TRIGGERED SN NEUTRINO DETECTION

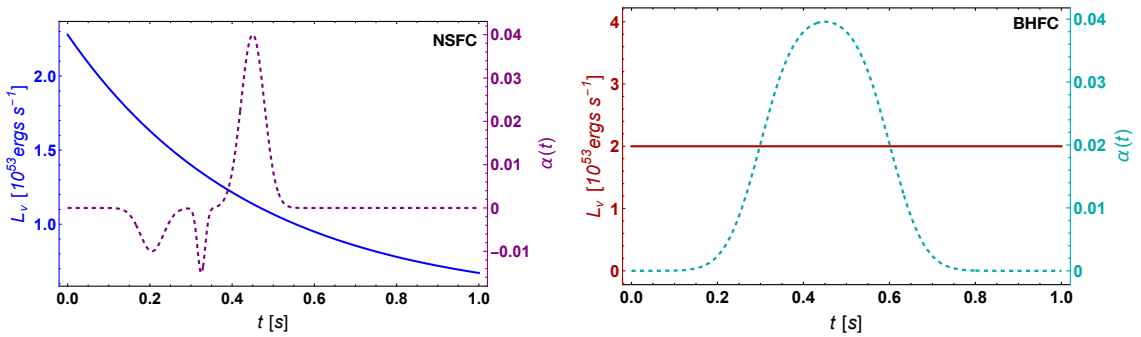

Figure F.1: The neutrino luminosity and anisotropy parameter for the NSFC and BHFC models.

Neutrino luminosity and anisotropy for NSFC and BHFC

The two different models considered in chapter 5 are - neutron star forming collapses (NSFCs) an black hole forming collapses (BHFCs). The characteristic strain for the two cases is plotted in Fig. 5.3. In this section of the appendix we show the corresponding neutrino luminosity ($L_\nu(t)$) and anisotropy ($\alpha(t)$) considered for the two cases. Fig. F.1 shows the relevant information.

The two models are based on the phenomenological models described in Sec. 4.3.1. In particular, the NSFC is based on the Ac3G model and the BHFC is based on the LAc3G model. In both cases we only consider a non-zero anisotropy only in the accretion phase. For the NSFC, we model the neutrino luminosity in the accretion phase using a decaying exponential. The anisotropy parameter consists of three-Gaussian bumps. In case of the BHFC, the neutrino luminosity in the accretion phase is modeled using a constant. The anisotropy parameter is broader that is lasts for a longer duration and is modeled using three-Gaussians combined together.

Detection probability for GW detectors

The detection of event signals at a detector is a probabilistic phenomenon. Hence, it is important to quantify the probability that the detector sees or misses a signal given the background noise. We will talk about the probability of detection for GW detectors in this section.

We follow the procedure outlined in Jaranowski and Krolak (1999); Jaranowski *et al.* (1998); Jaranowski and Krolak (2000); Astone *et al.* (2002); Jaranowski and Krolak (2005) to calculate the probability of detection and false alarm probabilities for the GW detectors. From the maximum likelihood principle, one can derive the detection statistics for the signal and calculate the probability density function for the statistics. This requires performing a χ^2-analysis on the signal. This way, the signal and the background noise is both taken into account and the probability that the detector sees a signal is quantified. A well-known fact about χ^2-analysis is that the number of independent degrees of freedom (DOF[1]) being considered for the analysis

[1]In this context, DOF alwyas refers to the independent χ^2 DOFs and *not* the degrees of freedom

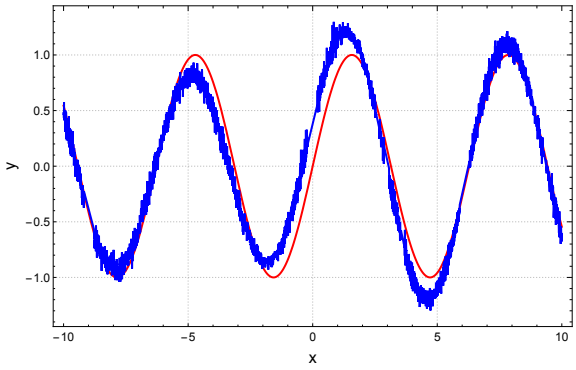

Figure F.2: Example of signal and corresponding prediction from theoretical models to illustrate the significance of χ^2 DOFs.

becomes an important factor. In general, one is allowed to choose as many DOFs as one wants till the time it is physically motivated and independent. Once the signal is detected, different DOFs of the model can be estimated based on the predictions from the physical model.

Let us think of an example to make this aspect clear: say we have a signal in the detector which is given by the blue line in Fig. F.2. We can choose a model (Model A) that predicts the signal as $y = \alpha_1 \sin(x)$. We perform a χ^2-distribution and derive that we have 2 independent DOFs. One can simply estimate the 2 DOFs given the signal. We show it as the red line in Fig. F.2. The fit is good and hence the physical model we use is a possible explanation of the signal/phenomena with parameters estimated from the signal. Now imagine, we have a second model (Model B) which predicts $y = \alpha_1 \sin(x) + \alpha_2 \cos(\beta x)$ and a χ^2-analysis gives 3 DOFs for this case. We can again estimate the 3 DOFs by using the observed signal. This fit will also be good and the model will also be a probable explanation of the phenomenon with the corresponding estimated parameters. The parameters estimated from Model A and B would be different and so would be the results, but both the models are equally good.

The probability distribution function when the signal is absent is given by Jaranowski and Krolak (2000) (See Eq. 27),

$$p_0(\mathcal{F}) = \frac{\mathcal{F}^{n/2-1}}{(n/2-1)!} \exp\Big(-\mathcal{F}\Big)\,. \tag{F.1}$$

The corresponding normalized probability distribution function when the signal is present is given by Jaranowski and Krolak (2000) (See Eq. 28),

$$\begin{aligned} p_1(\rho, \mathcal{F}) &= \frac{1}{N} \frac{(2\mathcal{F})^{(n/2-1)/2}}{\rho^{(n/2-1)}} I_{n/2-1}(\rho\sqrt{2\mathcal{F}}) \exp\left(-\mathcal{F} - \frac{1}{2}\rho^2\right), \\ N &= \int_0^\infty \frac{(2\mathcal{F})^{(n/2-1)/2}}{\rho^{(n/2-1)}} I_{n/2-1}(\rho\sqrt{2\mathcal{F}}) \exp\left(-\mathcal{F} - \frac{1}{2}\rho^2\right) d\mathcal{F} = \exp(\rho^2)\,, \end{aligned} \tag{F.2}$$

(or parameters) in the model itself.

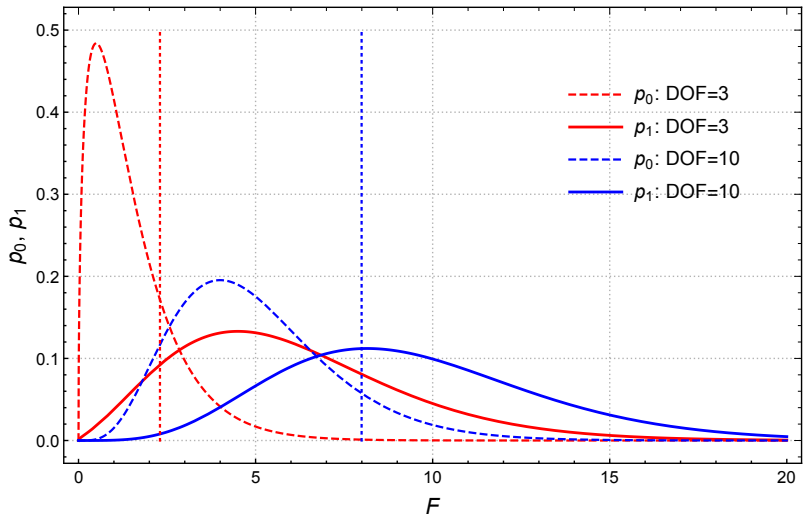

Figure F.3: The probability distribution functions versus $\mathcal{F}$ when the signal is absent (F.1) (Dashed lines) and when the signal is present (F.2) (Solid lines) for 3 DOFs (Red) and 10 DOFs (Blue) respectively. The corresponding $\mathcal{F}_0$ is shown for each case in the vertical dotted lines, where the significance level α is chosen to be 0.1. The SNR, $\rho = 3$.

where, N is the normalization factor such that $\int_0^\infty p_1(\rho, \mathcal{F})\, d\mathcal{F} = 1$, n is the number of DOFs, $I_{n/2} - 1$ is the modified Bessel function of the first kind and order $n/2 - 1$. ρ is the non-centrality parameter which for our case is the signal-to-noise ratio (SNR) as defined in (5.2). $\mathcal{F}$ is the reduced log likelihood function. The *false alarm probability* is defined as the probablility that $\mathcal{F}$ exceeds a certain threshold $\mathcal{F}_0$ when there is no signal.

$$P_F(\mathcal{F}_0) = \int_{\mathcal{F}_0}^{\infty} p_0(\mathcal{F}) d\mathcal{F}\,. \tag{F.3}$$

So in principle, the signal detection problem is basically a statistical hypothesis testing problem. The *null hypothesis* is that the signal is absent from the data and the *alternative hypothesis* is that the signal is present. The *test statistics* is the functional $\mathcal{F}$. This leads to the question how does one obtain $\mathcal{F}_0$. In order to do that, we need to fix a *significance level* α (different from the α defined in (4.28)). $\mathcal{F}_0$ is obtained by solving the equation for a given α, $\alpha = P_F(\mathcal{F}_0)$. The *confidence level* is defined as $1 - \alpha$. The *probability of detection* is defined as the probability that $\mathcal{F}$ exceeds the threshold $\mathcal{F}_0$ when the SNR is ρ,

$$P_D(\rho, \mathcal{F}_0) = \frac{1}{N} \int_{\mathcal{F}_0}^{\infty} p_1(\rho, \mathcal{F})\, d\mathcal{F}\,. \tag{F.4}$$

In Fig. F.3 we show the probability distribution functions versus $\mathcal{F}$ when the signal is absent and when the signal is present. The corresponding $\mathcal{F}_0$ is calculated using $\alpha = P_F(\mathcal{F}_0)$ and plotted with dotted lines. The probability of false alarm (shown in Fig. F.4, Dashed lines) is the area under the dashed curves from $\mathcal{F}_0$ to ∞. Similarly, the probability of detection is the area under the solid curves in Fig. F.3 for $\mathcal{F}$ going

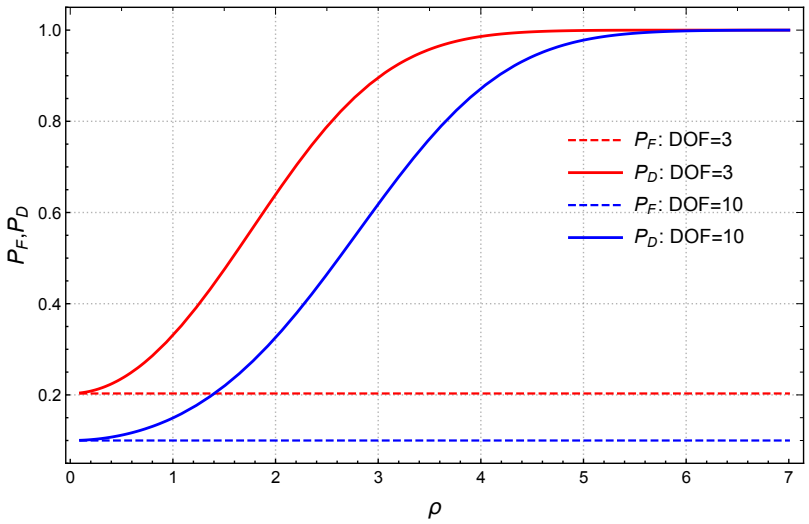

Figure F.4: The probability of false alarm (P_F) (F.3) (Dashed lines) and the normalized probability of detection (F.4) (P_D) (Solid lines) versus the SNR (ρ) (5.2) for 3 DOFs (Red) and 10 DOFs (Blue) respectively. The significance level α is chosen to be 0.1.

from $\mathcal{F}_0$ to ∞. We show the probability of detection for the two DOFs as solid lines in Fig. F.4. An important feature to note in Fig. F.4 is, given a confidence level α the probability of false alarm is constant when the SNR is varied. At low SNRs, *i.e.,* when the signal is comparable to the noise the probability of detection is equal to the probability of false alarm. Another important feature is, at high SNRs the probability of detection is equal to 1 and independent of the SNR. We do see that at low SNRs there is a difference in the value of P_D depending on the choice of DOFs. But as discussed previously, this difference is expected and should not be a cause of concern since changing the DOFs is equivalent to looking at a different model and hence the results are subject to change. To further solidify our understanding regarding this, in Fig. F.5 we show a density plot of probability of detection with SNR and DOFs. It is evident right away that above a SNR of ~ 6, P_D becomes independent of both the SNR and DOFs.

In this work, we choose to be conservative and thus we will restrict our probability of detection to 50% at 90% confidence level. We choose the DOFs $n = 3$ corresponding to the 3-Gaussians we use in the NSFC and BHFC models (more details about this in Sec. F). Then the restricted probability of detection (P_{det}) becomes,

$$P_{det}(r) = \begin{cases} P_D(\rho(r), \mathcal{F}_0), & \text{for } P_D \geq 0.5 \\ 0, & \text{otherwise} \end{cases} . \tag{F.5}$$

The restricted detection probability also ensures that we are well above the probability of false alarm. Thus any signal event that is detected is extremely likely to be a true event. The restricted probability also puts a distance cut - the GW detector would be sensitive upto a certain distance where $P_{det} \geq 0.5$ and then would not see anything beyond that distance. It is important to note here that the improvement we suggest to DECIGO in the form of DECIGO+, may seem arbitrary but is actually a

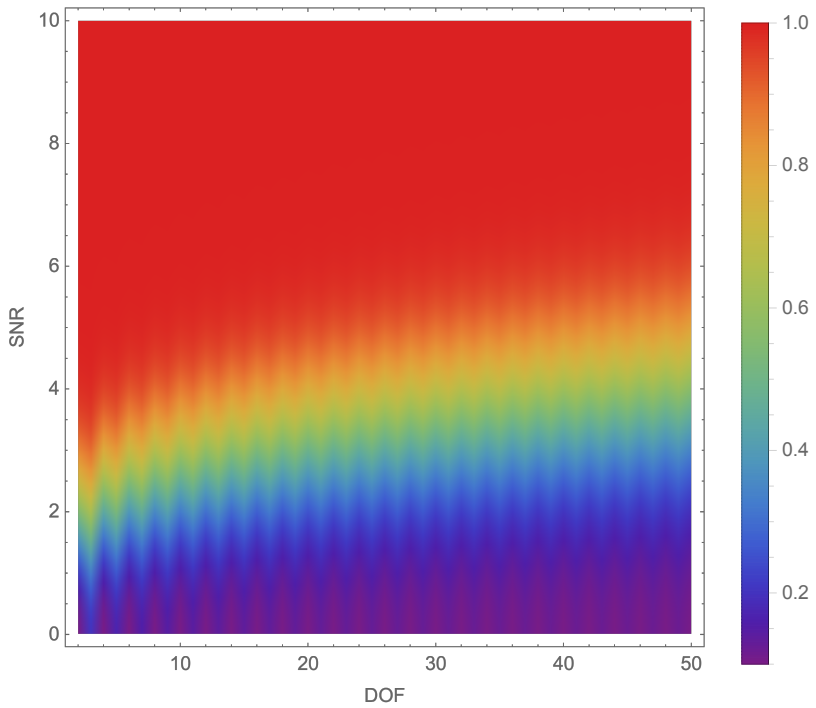

Figure F.5: The density plot of probability of detection (P_D) with varying SNR (ρ) and DOFs. We choose the significance level $\alpha = 0.1$.

motivated choice. We choose the noise ($h_n(f)$) of DECIGO+ such that for the BHFC model, DECIGO+ has $P_{det} \approx 0.5$ at $r \sim 350$ Mpc. Hence, the upper limit on distances considered in this work ~ 350 Mpc. This helps in two ways - a) the distances are small enough such that redshift $z \sim 0$[2] and b) the background for large distances is huge since the R_{CCSN} increases as a power-law with distance. Thus, limiting to $r \sim 350$ Mpc seems a reasonable assumption.

Triggered versus untriggered backgrounds

This section provides some additional information on the various neutrino detector backgrounds. Fig. F.6 shows the main background event rates in Hyper Kamiokande (Hyper-K) from various sources (see Sec. 1.6 for details on different neutrino sources) in the units of per MeV per year per kiloton for the cases when no Gadolinium (Gd) is present (left) and when Gd is present (right). As expected, the addition of Gd reduces the background and also reduces the threshold energy. This is evident from Fig. F.7 where we show the total background per MeV per year per kiloton for the cases of without (solid black line) and with (dashed blue line) Gd. For Hyper-K without Gd the threshold energy of the detector is ~ 18 MeV, whereas, when Gd is added the threshold is ~ 10 MeV.

The total background rate in a detector like Hyper-K is $\lambda = 1313$ events/year. The number of background events that a megaton-scale detector will accumulate

[2] $z = 0.08$ for a distance of 350 Mpc.

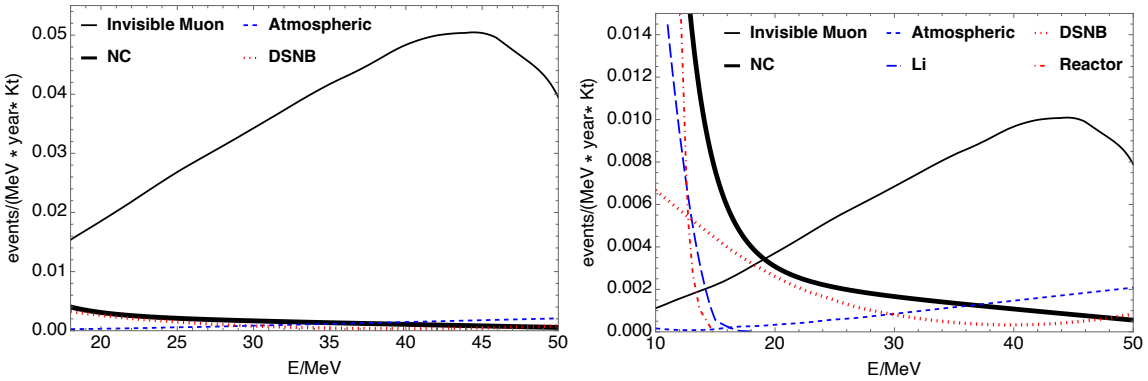

Figure F.6: The main background event rates in Hyper Kamiokande from various sources per MeV per year per kiloton.*Left:* When Gadolinium (Gd) is not present. *Right:* When Gd is added.

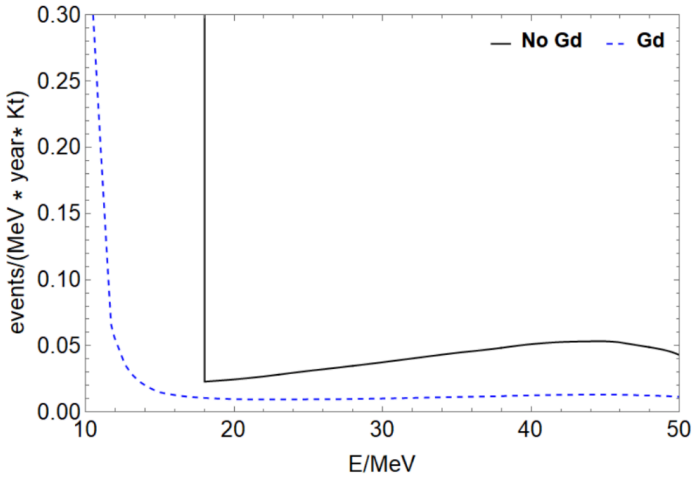

Figure F.7: Total background event rates in Hyper Kamiokande from various sources per MeV per year per kiloton for the case when no Gd is present (solid black line) and when Gd is present (blue dashed line).

in 30 years is shown in Fig. F.8 as a green dashed line. This is what we call the *untriggered background*, that is, the background in the absence of triggers or time windows for analyzing the neutrino detector data. But when we perform a triggered search, the background level is reduced by a factor $\epsilon_{bckg=} N_{SN}^{trig}(D)\Delta t/\Delta T$ compared to the untriggered search. This is shown in Fig. F.8 as the solid brown line. A remarkable thing about triggered searches as evident from the plot is, for distances below $\sim$ 50 Mpc the triggered search allows to get rid of background events. However, as we move further in distance, the number of supernovae go up, leading to a rapid increase in the number of time windows. This leads to an increase in the background. This is because the longer the total duration of time-windows is, the more background events are present. We considered distances $\sim$ 350 Mpc, for which the triggered and untriggered backgrounds differ by $\mathcal{O}(2)$. This gives another good reason to put an upper bound on the distance sensitivity of the gravitational wave detectors.

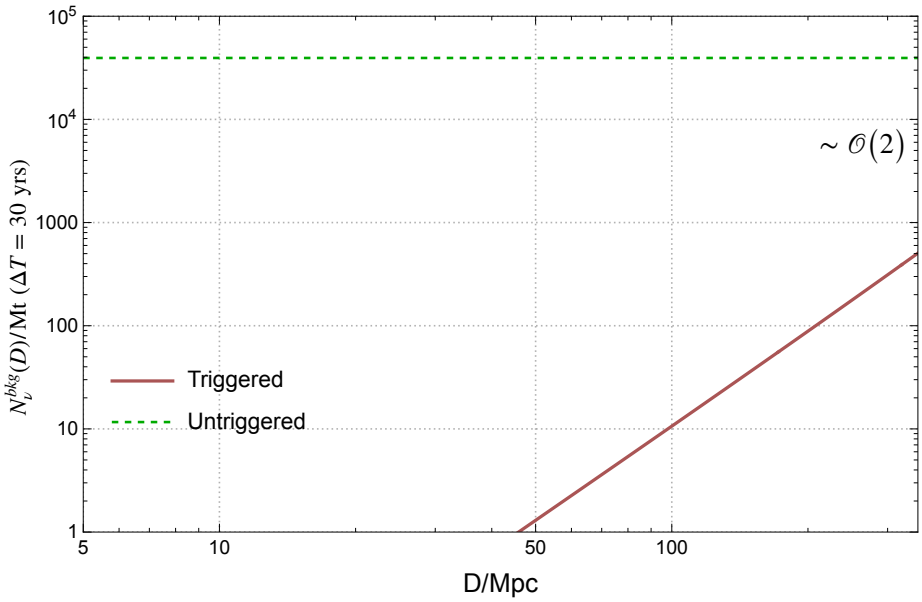

Figure F.8: The comparison between total number of triggered (solid brown line) and untriggered (dashed green line) background events in the neutrino detector per megaton in 30 years.

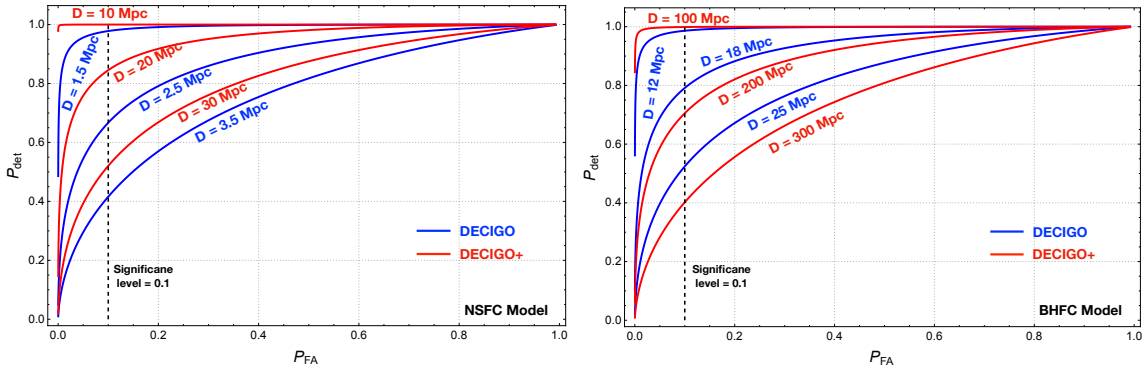

Figure F.9: Receiver Operating Characteristic curves for DECIGO (blue) and DECIGO+ (red) for the NSFC (left) and BHFC (right) models. The significance level is shown by a black dashed line.

Receiver Operating Characteristic curves(ROC)

The parametric plot of the probability of detection versus probability of false alarm with optimal signal to noise ratio as a parameter is called the receiver operating characteristic (ROC) (Jaranowski and Krolak, 2000). Fig. F.9 shows the ROC curves for DECIGO and DECIGO+, for the NSFC (left) and BHFC (right) models. We do not go into the details of the ROC curves, it can be found in Jaranowski and Krolak (2000). Information can be read off from the ROC curve in this way that: we first choose a SNR for a given detector, which depends on the distance. Corresponding to the SNR (or distance) we draw the ROC curve. We then decide on a false alarm

probability (or significance level[3]). This is the vertical dashed black line shown in the two figures. The point of intersection of this vertical line with one of the ROC curves gives the probability of detection at that particular distance for the detector.

[3]Confidence Level = 1- Signifiance Level.

APPENDIX G

SOME ADDITIONAL DETAILS FOR KINK-ANTIKINK COLLISIONS IN THE QUANTUM VACUUM

Structure of the radiation bursts

We provide a detailed look at the spatial form of the radiation burst that is generated during the first kink-antikink collision. In order to get a "clean" signal, we restrict the present analysis to the case where back-reaction of the ψ field on the ϕ background is neglected. This is an increasingly good approximation for smaller values of λ.

Fig. G.1 shows the resulting radiation bursts, where they are sufficiently far away from the collision region. We choose to present two significantly different values for each of the three parameters of the problem: the velocity ($v = 0.1, 0.3$), the ψ field mass ($\mu = 0.1, 0.7$) and the coupling strength ($\lambda = 0.1, 0.9$).

An immediate realization concerns the effect of changing the initial kink-antikink velocity v. We see that the radiation waveform is almost identical for each pair of (μ, λ) when we change the velocity. Furthermore, the energy contained in the radiation burst is almost equal for the two curves in each panel of Fig. G.1. Hence, our numerical results given in the main text are corroborated by Fig. G.1, showing that the quantum radiation emitted during the kink-antikink collision essentially loses the memory of the initial velocity.

A further observation is related to the amplitude and shape of the renormalized energy density $\rho_{\psi}^{(R)}$ in the radiation burst in each of the four panels of Fig. G.1, corresponding to the four different combinations of λ and μ. Each radiation burst is seen to form a wave packet with a spectral content that is highly dependent on the parameters. Most importantly, we see that increasing λ increases the overall energy in ψ radiation. This is to be expected, since λ is the coupling strength between the classical background field ϕ and the quantum radiation field ψ. On the contrary, increasing μ leads to a decreased energy in the radiation burst. This can also be qualitatively understood. As shown in Fig. 10.2, the initial ψ configuration deviates from the trivial vacuum more for smaller values of μ. Simply put, it is easier to excite a lighter quantum field. Finally, we see that the front of the wavepacket is at a slightly larger distance from the origin for $\mu = 0.1$ than for $\mu = 0.7$. Since all panels correspond to snapshots taken at the same time $\tau = 40$, this translates into a larger velocity of the radiation burst in the case of smaller ψ mass (μ), as one could have guessed from simple kinematical arguments.

Quality of numerics

In this appendix, we discuss the quality of the numerics in our simulations. In Fig. G.2, we illustrate the independence of the physical observables on the choice of the temporal time step used in the simulation, dt. In Fig. G.2a we see that the total energy is conserved to an accuracy of $\sim 0.1\%$ over the entire time of evolution (for a time step $dt = 0.004$). As expected, energy is conserved to an even better accuracy when dividing the time step by two. However, given the trade-off in computational time we think $dt = 0.004$ is sufficient for the task at hand. Our choice is further justified by Fig. G.2b where we show the energy in ϕ (E_{ϕ}) computed for two values of dt, 0.004 and 0.002. Indeed the two plots superimpose each other. Moreover, Fig. G.3 clearly shows that, at least for the physical observables that we are interested in (i.e. E_{ϕ}), decreasing the lattice spacing $a = L/N$ or increasing the size of the box L do

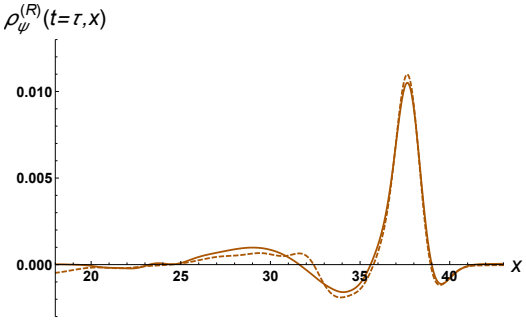

$\mu = 0.1,\ \lambda = 0.1,\ E_{0.1}^{RB} = 0.0161,\ E_{0.3}^{RB} = 0.0136$

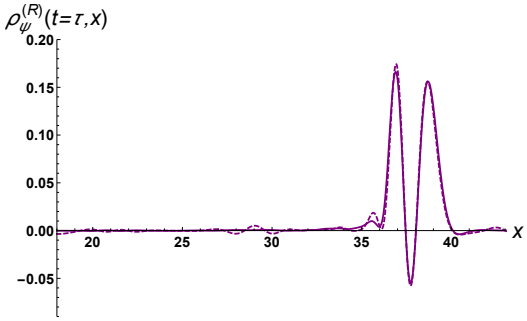

$\mu = 0.1, \lambda = 0.9, E_{0.1}^{RB} = 0.2799, E_{0.3}^{RB} = 0.2698$

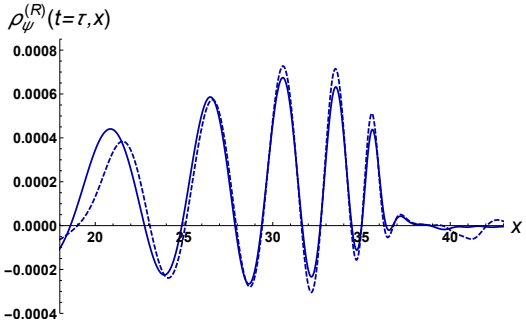

$\mu = 0.7, \lambda = 0.1, E_{0.1}^{RB} = 0.0033, E_{0.3}^{RB} = 0.0030$

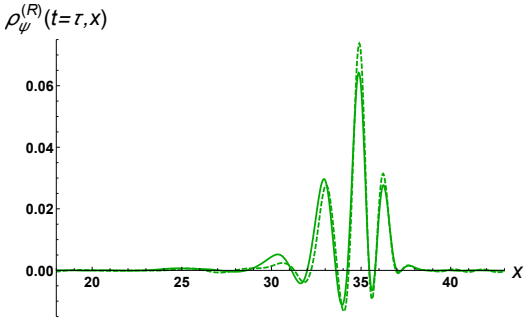

$\mu = 0.7, \lambda = 0.9, E_{0.1}^{RB} = 0.0908, E_{0.3}^{RB} = 0.0848$

Figure G.1: Snapshots (taken at time $\tau = 40$) of the renormalized energy density of the radiation bursts for different parameters in the case without backreaction. The solid lines are for $v = 0.1$ and the dashed lines are for $v = 0.3$. E_v^{RB} is the energy in the radiation burst for $v = 0.1$ and $v = 0.3$. The other parameters are $L = 100$, $N = 500$, $\kappa \to 0$, $m_{\text{phys}} = m = 1$ and $t_0 = -100$.

not sensibly change our results. In other words, our choices of parameters are good enough and the results shown in the main text are independent of both the UV and the IR cutoffs.

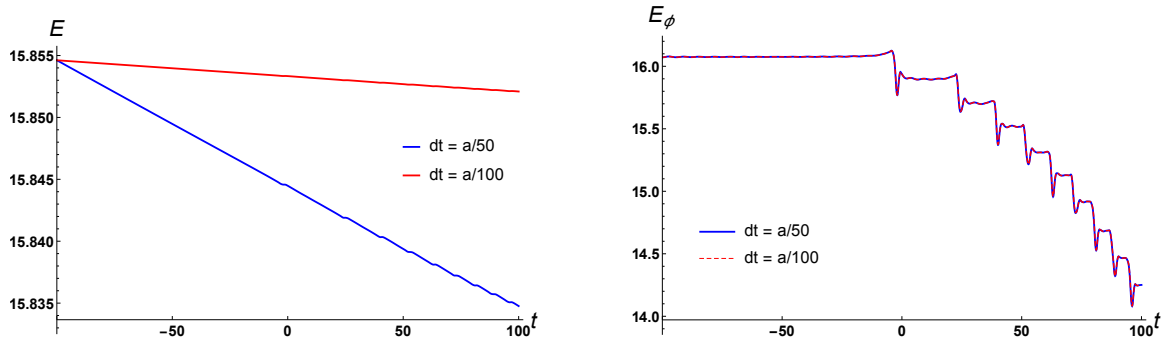

Figure G.2: (a) Time evolution of the total energy (10.38) for $dt = a/50 = 0.004$ and $dt = a/100 = 0.002$. (b) Time evolution of the energy in ϕ (E_ϕ) for $dt = a/50 = 0.004$ (solid blue) and $dt = a/100 = 0.002$ (dashed red). The parameters are $L = 100$, $N = 500$, $v = 0.1$, $\mu = 0.1$, $\lambda = 0.3$ and $m_{\text{phys}} = 1$, $\kappa = 1$ and $t_0 = -100$. The collision happens at $t = 0$. Recall that $a = L/N$. These plots illustrate the independence of our results on the choice of time step.

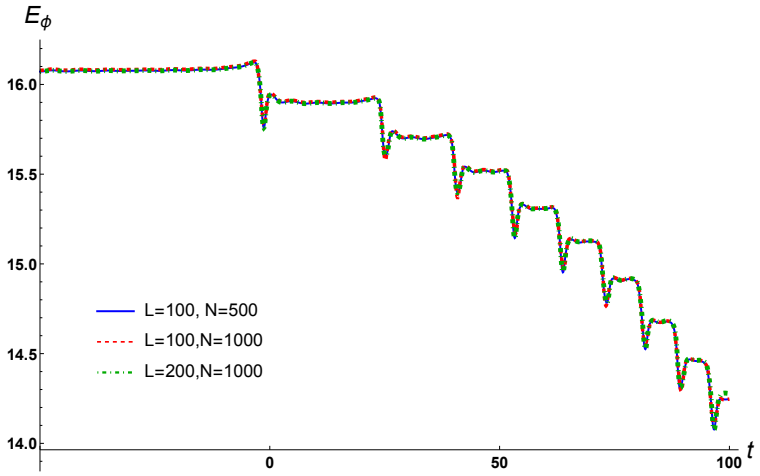

Figure G.3: Time evolution of the energy in ϕ (E_ϕ) for different values of L and N. The parameters are $v = 0.1$, $\mu = 0.1$, $\lambda = 0.3$ and $m_{\text{phys}} = 1$, $\kappa = 1$ and $t_0 = -50$. The collision happens at $t = 0$. Recall that $a = L/N$ and we have chosen $dt = a/50$. This illustrates the independence of our results on the lattice spacing a and on the size of the box L.